The University of Adelaide

Department of Mechanical Engineering

A Numerical Study of Bluff Body Flow

submitted by

Kwok Leung LAI, BEng (Hons)

Thesis for the Degree of Doctor of Philosophy

August 2000

Contents

Summary

A numerical scheme, based on discrete-vortex and surface-vorticity boundary-integral methods, has been developed for simulating time-dependent, two-dimensional, viscous flow over arbitrary arrays of solid bodies of arbitrary cross-section. Flow-induced fluctuating forces on bluff bodies immersed in the wakes of upstream bodies are major sources of dipole sound, and the motivation was to make possible the calculation of such forces and hence of the aerodynamic noise which they generate. A further objective was to identify the various possible flow regimes which can occur on an array and their dependence on array geometry, and to uncover the detailed flow mechanisms of wake-body interaction associated with each of them.

In the analysis, the flow is considered to be started impulsively from rest and its development with time is calculated. The numerical scheme models the natural processes of generation of vorticity at solid boundaries and its diffusion into the flow domain, and the evolution of the vorticity field in the flow domain by convection and diffusion. The time-histories of the distributions of elemental vortices and fluid-dynamic pressures on the bodies are the prime results of the calculations, from which streamline patterns, isovorticity contours, pressure distributions in the general flow field, and Strouhal numbers of vortex shedding are deduced.

The underlying principles and development of the numerical scheme, and the implementation procedures for calculation of inviscid-flow over single bodies, viscous flow over single bodies, and finally viscous flow over arrays are presented. In the development of the method, a number of refinements to accepted procedures have been made. Amongst these are the introduction of an innovative numerical procedure for calculation of the pressure distribution in the general flow field from the evolution of vorticity field; the use of a modified cell-to-cell algorithm to improve computation efficiency of the discrete vortex method; and the implementation of what has been termed the *zero circulation correction*, to improve accuracy of the surface-vorticity boundary-integral method.

For validation, the numerical scheme has been applied to the flow over circular cylinders at Reynolds numbers in the range $100 \leq Re_d \leq 10^4$, and thick rectangular plates with chord-to-thickness ratios $C = 1$, $C = 2$ and $C = 4$, at $100 \leq Re_h \leq 10^3$. Extensive comparisons with published experimental data show that the procedure gives a true representation of real flow

patterns and regimes, and, in general, gives quantitatively accurate predictions of flow parameters. In many cases, the calculations additionally provide fine details of the flow not revealed by and therefore usefully complementing experimental findings. They also draw attention to the effects of three-dimensionality in real flows and to the Reynolds-number limitations that these impose on two-dimensional numerical calculations.

In light of the success of the simulation of the flow over circular cylinders and thick rectangular plates, the procedures have been applied with confidence to array flows, a class of bluff-body flows which has been very much less extensively studied, either experimentally or numerically, than the flow over individual bluff bodies. Simulations of flow over tandem arrays of two rectangular plates with ($C1 = 1$, $C2 = 1$), ($C1 = 1$, $C2 = 4$) and ($C1 = 4$, $C2 = 4$), at a Reynolds number of $Re_h = 500$, have been made. The broad flow regimes which have been identified, based on the position of impingement on the array of the shear layers separated from the leading corners of the upstream plate, are in accord with the limited available experimental results. More significantly, the fine detail provided by the simulations reveals a progressively changing flow in the gap between the plates as the gap is varied from negligible to very large values. In this progression, a number of characteristic sub-regimes can be identified: periodically-reversing transverse flow through the gap for very small gaps $G < 0.5$; trapped-vortex flow in the gap for $0.5 < G < 1$; periodic vortex-formation in the gap, without or with very little vortex convection, for $1 < G < 2$; and fully-established vortex-street flow within the gap for large gaps $G > 2$. The nature of the interaction between the downstream plate and vortices shed from the upstream plate varies from progressive loss of vorticity from the gap vortices to the external flow, for $G < 1$, to vortex-street impingement on the downstream plate for large gaps, $G > 2$. In the case of gaps large enough to accommodate a fully-established vortex street, the simulations show up the relation between vortices impinging on the downstream plate and vortex formation from the trailing edge of the downstream plate. In particular, they identify the condition under which phase-locking of vortex shedding from the upstream and downstream plates occurs, and, when it does, accurately predict phase differences. Flow parameters, such as Strouhal number of vortex shedding, pressure coefficients and drag coefficients, vary with G, and in most cases, a change in the form of variation indicates a change from one flow regime to another. Overall, the results of the simulations provide detailed insights into the mechanisms of flow over tandem arrays of rectangular plates which it would be difficult or impossible to obtain experimentally.

Statement of Originality

The material in this thesis is original and has not been submitted or accepted for the award of a degree or diploma at any other university. To the best of my knowledge and belief, the thesis contains no material previously published or written by another person except where due reference is made in the text of the thesis.

Name : Kwok-leung LAI

Date : 18 August, 2000

Permission to Copy

The author consents to the thesis being made available for loan and photocopying provided that the thesis is accepted for the award of the degree.

Name : Kwok-leung LAI

Date : 18 August, 2000

Acknowledgements

In the course of this research project in computational fluid dynamics, there have been many people who have given their advice, assistance and support at various stages of the project, and to whom I express my sincere thanks and gratitude. To my supervisor, Dr. M.K. Bull, thanks are due for advice and guidance which have been instrumental in this project. I am grateful to him for his time and efforts in the preparation of this thesis. His sharp scientific mind, attention to detail and enthusiasm towards his work are most inspiring.

Thanks are due to Mr. Antoni Blazewicz and Mr. Yi Li for use of their experimental results in this thesis, and to Dr. Peter Lanspeary for providing expertise in computing. I extend my thanks to Mr. Jonathan May and Ms. Vera Melissaratos, of the Computer Aided Teaching Suite of the Faculty of Engineering, for their assistance and advice.

I am most grateful to my parents in Hong Kong for encouragement and support which have carried me through the toughest times, to all my friends in Adelaide who have made my stay in a new country most enjoyable and, last but not least, to my beloved Ling-Ming for her support and patience.

I gratefully acknowledge the financial support from the S.L. Pao Education Foundation Scholarship, the University of Adelaide Scholarship and the HECS Postgraduate Scholarship.

Nomenclature

Vector quantities are characterised by **bold** type, and their components are enclosed in brackets in either of the following forms :

$$\boldsymbol{a} = [\boldsymbol{i}, \boldsymbol{j}, \boldsymbol{k}] \quad or \quad \boldsymbol{a} = \begin{bmatrix} \boldsymbol{i} \\ \boldsymbol{j} \\ \boldsymbol{k} \end{bmatrix} .$$

$\boldsymbol{B}$	diffusive flux of circulation, per unit length per unit time
b	element of *tangential surface velocity matrix* **[b]**
C	chord-to-thickness ratio $\equiv c/h$; also binomial coefficient and contour
C_p	coefficient of static pressure, $= (\bar{p} - p_\infty)/\frac{1}{2}\rho U_\infty^2$
$C_{p'}$	coefficient of r.m.s. pressure fluctuation
C_D	coefficient of total drag
C_{Dp}	coefficient of pressure drag
C_L	coefficient of lift
C_{pb}	base suction coefficient
c	chord
$\boldsymbol{D}$	drag force; also flow domain
d	diameter
ds	segment length
δe	error level
$\boldsymbol{F}$	force
f	weighting factor; also frequency
G	gap-to-thickness ratio $\equiv g/h$
g	gap width between plates in tandem arrays (of rectangular plates); also acceleration due to gravity
h	plate thickness
i	$\sqrt{-1}$
$\boldsymbol{i}, \boldsymbol{j}, \boldsymbol{k}$	unit vectors in x-, y-, z-directions
K	element of *coupling coefficient matrix* **[K]**
k	coupling coefficient
$\boldsymbol{L}$	lift force
L	characteristic length
l	length

M_k	(*k*)*th* moment of discrete vortex about cell centre (for implementation of cell-to-cell method); also the number of a segment on the (*k*)*th* body of the system
N	number of solid bodies in the system
N_t	maximum number of terms used in cell-to-cell algorithm
$\boldsymbol{n}$	unit normal vector
O	Order of magnitude
p	static pressure
p_o	total pressure
$p_{o\gamma}$	total pressure induced by surface vorticity
p_{ov}	total pressure induced by vortex motion
p_∞	ambient static pressure
Re	Reynolds Number, $\equiv U_\infty L/\upsilon$
St	Strouhal Number, $\equiv f L/U_\infty$
S	surface
s	length along path
t	time
$\boldsymbol{t}$	unit tangential vector
$\boldsymbol{U}_\infty$	Main stream velocity
$\boldsymbol{u}$	vector velocity field
u	velocity component in x-direction
$\boldsymbol{V}$	transport velocity of discrete vortex
v	velocity component in y-direction
v_s	potential-flow surface velocity
v_θ	velocity component in θ-direction
x, y, z	Cartesian coordinates
$\boldsymbol{Z}$	complex coordinates
Z	number of discrete vortex in solution domain
$\boldsymbol{z}$	complex coordinate of discrete vortex relative to cell centre
∇	Gradient operator
$\nabla\cdot$	divergence operator
$\nabla\times$	curl operator
∇^2	Laplacian operator, $\equiv\nabla\cdot\nabla$
α	angle of inclination of the main stream to the x-axis

β	angle between tangent to a body segment and the x-axis
δ	boundary layer thickness; also Kronecker delta function
ω	vorticity, $\equiv\nabla\times\boldsymbol{u}$
γ	strength of vortex sheet; also element of solution matrix $[\gamma]$
υ	kinematic viscosity
ρ	fluid density
ϕ	velocity potential
ψ	stream function
σ	core radius of the assumed vortex structure
Γ	circulation
$\Delta\Gamma$	circulation (strength) of discrete vortex
θ	polar coordinate angle

List of Figures

8.101 Predicted streamline patterns in flow over the ($C1 = 1$, $C2 = 4$) array: (a) $G = 1.5$, (b) $G = 2$, (c) $G = 3$, (d) $G = 4$ and (e) $G = 6$; calculated in a reference frame moving at a velocity of $U_{ref} = 0.8\ U_{\infty}$.

8.102 Elemental-vortex distributions in flow over the ($C1 = 4$, $C2 = 4$, $G = 1$) array, showing flow development from an impulsive start to the fully-developed flow.

8.103 Calculated streamline patterns in flow over the ($C1 = 4$, $C2 = 4$, $G = 1$) array, showing flow development from an impulsive start to the fully-developed flow.

8.104 Vorticity contours in flow over the ($C1 = 4$, $C2 = 4$, $G = 1$) array, showing flow development from an impulsive start from rest to the fully-developed flow.

8.105 Elemental-vortex distributions in flow over the ($C1 = 4$, $C2 = 4$, $G = 1.5$) array, showing flow development from an impulsive start from rest to the fully-developed flow.

8.106 Calculated streamline patterns in flow over the ($C1 = 4$, $C2 = 4$, $G = 1.5$) array, showing flow development from an impulsive start from rest to the fully-developed flow.

8.107 Vorticity contours in flow over the ($C1 = 4$, $C2 = 4$, $G = 1.5$) array, showing flow development from an impulsive start from rest to the fully-developed flow.

8.108 Elemental-vortex distributions in flow over the ($C1 = 4$, $C2 = 4$, $G = 2$) array, showing flow development from an impulsive start from rest to the fully-developed flow.

8.109 Calculated streamline patterns in flow over the ($C1 = 4$, $C2 = 4$, $G = 2$) array, showing flow development from an impulsive start from rest to the fully-developed flow.

8.110 Vorticity contours in flow over the ($C1 = 4$, $C2 = 4$, $G = 1.5$) array, showing flow development from an impulsive start from rest to the fully-developed flow.

8.111 Instantaneous pressure fields and streamline patterns in fully-developed flow around the ($C1 = 4$, $C2 = 4$, $G = 2$) array.

8.112 Vorticity contours over one vortex-shedding period in flow over the ($C1 = 4$, $C2 = 4$, $G = 2$) array.

8.113 Calculated distributions of mean and r.m.s. pressure coefficients on the ($C1 = 4$, $C2 = 4$, $G = 1$) array.

8.114 Time-histories of drag and lift on the ($C1 = 4$, $C2 = 4$, $G = 1$) array, (a) upstream plate, (b) downstream plate. Drag and lift are calculated for $\Delta t = 0.02$; highlighted values are averaged over $\Delta t = 0.4$.

8.115 Calculated distributions of mean and r.m.s. pressure coefficients on the ($C1 = 4$, $C2 = 4$, $G = 1.5$) array.

8.116 Time-histories of drag and lift on the ($C1 = 4$, $C2 = 4$, $G = 1.5$) array, (a) upstream plate, (b) downstream plate. Drag and lift are calculated for $\Delta t = 0.02$; highlighted values are averaged over $\Delta t = 0.4$.

8.117 Calculated distributions of mean and r.m.s. pressure coefficients on the ($C1 = 4$, $C2 = 4$, $G = 2.0$) array.

8.118 Time-histories of drag and lift on the ($C1 = 4$, $C2 = 4$, $G = 2.0$) array, (a) upstream plate, (b) downstream plate. Drag and lift are calculated for $\Delta t = 0.02$; highlighted values are averaged over $\Delta t = 0.4$.

8.119 Elemental-vortex distributions in flow over the ($C1 = 4$, $C2 = 4$, $G = 4$) array, showing flow development from an impulsive start from rest to the fully-developed flow.

8.120 Calculated streamline patterns in flow over the ($C1 = 4$, $C2 = 4$, $G = 4$) array, showing flow development from an impulsive start from rest to the fully-developed flow.

8.121 Vorticity contours in flow over the ($C1 = 4$, $C2 = 4$, $G = 4$) array, showing flow development from an impulsive start from rest to the fully-developed flow.

8.122 Instantaneous pressure fields and streamline patterns in fully-developed flow over the ($C1 = 4$, $C2 = 4$, $G = 4$) array.

8.123 Elemental-vortex distributions in flow over the ($C1 = 4$, $C2 = 4$, $G = 6$) array, showing evolution of flow from the impulsive start to the fully-developed state.

8.124 Streamline patterns in flow over the ($C1 = 4$, $C2 = 4$, $G = 6$) array, showing evolution of flow from the impulsive start to the fully-developed state.

8.125 Vorticity contours in flow over the ($C1 = 4$, $C2 = 4$, $G = 6$) array, showing evolution of flow from the impulsive start to the fully-developed state.

8.126 Elemental-vortex distributions in flow over the ($C1 = 4$, $C2 = 4$, $G = 8$) array, showing development of flow from the impulsive start to the fully-developed state.

8.127 Calculated streamline patterns in flow over the ($C1 = 4$, $C2 = 4$, $G = 8$) array, showing development of flow from the impulsive start to the fully-developed state.

8.128 Vorticity contours in flow over the ($C1 = 4$, $C2 = 4$, $G = 8$) array, showing development of flow from the impulsive start to the fully-developed state.

8.129 Calculated distributions of mean and r.m.s. pressure coefficients on the ($C1 = 4$, $C2 = 4$, $G = 4.0$) array.

8.130 Time-histories of drag and lift on the ($C1 = 4$, $C2 = 4$, $G = 4.0$) array, (a) upstream plate, (b) downstream plate. Drag and lift are calculated for $\Delta t = 0.02$; highlighted values are averaged over $\Delta t = 0.4$.

8.131 Calculated distributions of mean and r.m.s. pressure coefficients on the ($C1 = 4$, $C2 = 4$, $G = 6.0$) array.

8.132 Time-histories of drag and lift on the ($C1 = 4$, $C2 = 4$, $G = 6.0$) array, (a) upstream plate, (b) downstream plate. Drag and lift are calculated for $\Delta t = 0.02$; highlighted values are averaged over $\Delta t = 0.4$.

8.133 Calculated distributions of mean and r.m.s. pressure coefficients on the ($C1 = 4$, $C2 = 4$, $G = 8.0$) array.

8.134 Time-histories of drag and lift on the ($C1 = 4$, $C2 = 4$, $G = 8.0$) array, (a) upstream plate, (b) downstream plate. Drag and lift are calculated for $\Delta t = 0.02$; highlighted values are averaged over $\Delta t = 0.4$.

8.135 Power spectra of fluctuating lift of the ($C1 = 4$, $C2 = 4$) array with various gap-to-thickness ratio in the range $1.0 \leq G \leq 8.0$.

8.136 Variation of flow parameters with gap-to-thickness ratio G for the ($C1 = 4$, $C2 = 4$) array: (a) Strouhal numbers of vortex shedding into the wake of the array, (b) pressure coefficients and (c) drag coefficients.

8.137 Predicted streamline patterns in flow over the ($C1 = 4$, $C2 = 4$) array in various flow regimes; calculated in a reference frame moving at a velocity of $U_{ref} = 0.8\ U_{\infty}$.

List of Tables

Chapter 1

Introduction

1.1 The Aim of the Project

The aim of the present work is the calculation of the flow around arrays of bluff bodies and the fluctuating forces on the bodies in the array, with a view to supporting and clarifying conclusion deduced from experimental investigations, and, if sufficient confidence can be established in the calculation procedures, to uncovering details of the flow which are not readily obtained by experiment. Although the study of bluff body flows is of direct significance in a wide range of practical applications such as the design of vehicles, turbo-machinery, and off-shore structures and the solution of practical problems such as flow-excited vibration of chimney, steel tower suspension bridges, buildings and other structures, the motivation for it in the present case has come predominantly from its relevance to studies of aerodynamic noise generation by bluff-body arrays; in this case, experimental investigations have indicated that one of the most important sources of acoustic noise is the fluctuating fluid-dynamic forces on rigid non-vibrating bodies immersed in the wakes of upstream bodies, which constitute dipole sound sources.

Consequently, in this introductory chapter, a brief review of typical examples of aerodynamic noise generation by bluff-body flow will be given, to illustrate the types of flow of interest; the methods which might be adopted for the solution of the flow equations will then be considered.

1.2 Generation of Aerodynamic Noise by Bluff Body Arrays and Its Dependence on Flow Characteristics

The noise from an idling circular saw is a typical example of aerodynamic noise generated by a bluff body flow. Cho and Mote [1979] found that the air flow over the saw rotating blade is very nearly in the tangential direction and therefore interaction is possible between the wake of any one tooth and the array of subsequent teeth. Some of the earliest work in this field, conducted by Dugdale [1969], Cho and Mote [1979], and Stewart [1978] led to the conclusion that the dominant source of aerodynamic noise is the flow of air over the saw teeth.

There have, however, been contradictory conclusions among researchers on the detailed mechanism of acoustic radiation from circular saw blades. Leu and Mote [1984] measured the pressure fluctuation on tooth surfaces and deduced from their measurement that vortices shed from the leading edges of the teeth are a major source of surface pressure fluctuations and of aerodynamic noise generation in idling circular saws. They also concluded that the vortex shedding mechanism was directly influenced by the configuration of tooth cascades.

Pickles *et al.* [1988], carried out flow visualisation in a wind tunnel and a water tunnel, and measured the sound power from rotating model circular saw blades. They concluded that the dominant noise generation mechanism of an idling circular saw is the interaction of the vortex wake of each tooth with the leading edge of the following tooth, rather than the vortex shedding process from individual teeth itself. Experiments conducted by Bull *et al.* [1990] and Martin and Bies [1990] also led to this conclusion.

Stewart [1978] and Kanapathipillai [1982] found a distinct change in the variation of radiated sound pressure level with the ratio of gap between teeth (denoted by g) to the tooth thickness (denoted by h) when the ratio g/h was around a critical value of about 2. As shown later in this report, the ratio g/h also plays an important role in vortex shedding in linear plate arrays. This correspondence provides further evidence that vortex-body interaction effects are the primary source of noise generation by an idling circular saw.

Investigations of tandem arrays of thick plates, Fig. 1.1, which can be regarded as simplified representations of arrays of saw teeth, by Bull *et al.* [1990, 1991, 1992a, 1992b] have identified a number different flow regimes, and shown that changes from one regime to another when flow velocity varies can produce large changes in radiated sound power level. An understanding of the fluid flow around such bluff-body combination can therefore be expected to lead to increased understanding of the characteristics of the aerodynamic noise generated.

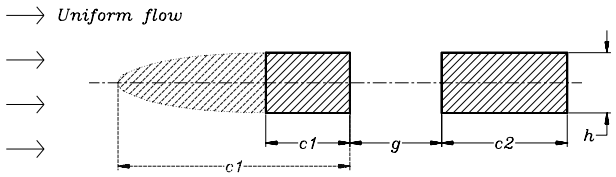

Figure 1.1. Schematic arrangement of two plates in tandem; the leading edge of the upstream plate can be faired or blunt.

Sakamoto *et al.* [1987] investigated the vortex shedding from two square prisms in a tandem configuration for various spacings between the prisms, and identified three vortex shedding regimes. For $g/h < 3$, where g is the gap between prisms and h their thickness, vortex shedding takes place only from the leading edge of the upstream prism, that from the leading edge of the downstream prism being suppressed. In the range $3 < g/h < 27$ vortex shedding occurs from both leading edges and at the same frequency. In the range $g/h > 27$ the two prisms shed vortices independently and at different frequencies.

On the other hand, experiments conducted by Bull *et al.* [1989] showed that when the upstream plate of two plates in tandem has a faired (semi-elliptical) leading edge, shown as dotted line in Fig. 1.1, the results are quite different from those obtained by Sakamoto. It was concluded that in this case the shedding frequencies are influenced by the boundary layer thickness on the plate surfaces and the gap between the two plates. For $g/h < 2$ vortex shedding from the trailing edge of the upstream plate is suppressed, vortex shedding then taking place only at the trailing edge of the downstream plate. For $g/h > 2$ vortices are shed from the trailing edges of both plates. It was found that the effect of vortex shedding from the trailing edge of the upstream plate is to produce a very thick shear layer on the downstream plate and, consequently, vortices are shed from the trailing edge of the downstream plate at a lower frequency than those from the upstream plate. Measurements of pressure fluctuations on the downstream plate in the vicinity of its leading edge by Li [1991] support the conclusion that forces on the downstream plate, generated by its interaction with the incident vortex wake, are the major noise sources.

Consideration of results such as these makes it clear that, to be of value, calculated results must provide an accurate representation of the interaction between a body and an impinging vortex wake. Furthermore, the calculations should provide details of the effects of array geometry on the behaviour of the flow within the gaps in bluff-body arrays, the effects of downstream bodies on flow separation and reattachment on upstream bodies, the frequencies of vortex shedding and the forces induced on the bodies in the array.

1.3 Consideration of Numerical Solution Procedures

To achieve the aim set out in the previous section, it is necessary to obtain solutions to the fundamental governing equations for fluid flow, the Navier-Stokes equations, applied to bluff-body arrays and taking full account of the effects of fluid viscosity. The governing equations form a set of coupled, non-linear, partial differential equations which must be solved within an irregular domain, subject to various initial and boundary conditions. Analytical solutions to such problems are limited to very simple cases with simplified boundary and initial conditions.

Numerical schemes for the simulation of viscous rotational flows may employ either the Eulerian or the Lagrangian framework of reference. In the Euler methods, the whole of the relevant flow regime is dealt with, usually by means of a spatially discretised grid. Such data as the local velocity and fluid properties associated with the fixed grids are updated at each stage of a time stepping calculation procedure. In contrast, in the Lagrangian models, attention is focused on individual particles as they move through the fluid; knowledge of the flow field is thus derived from the behaviour of these individual particles.

As a numerical solution is an approximation to the real behaviour, accuracy depends on the suitability of the particular numerical scheme chosen for a given problem. One approach to approximation is to replace the partial derivatives in the governing equations by their Taylor series expansions, and sub-divide the domain into cells which may be either structured or unstructured. The governing equations are applied to each cell to relate the values of the dependent variables to those of the neighbouring cells, thus forming a set of algebraic equations. Numerical schemes such as finite difference and finite volume methods are typical examples of this approach.

In numerical schemes involving a grid system, the grid formation is a crucial first step of the exercise, and has a very significant influence on the accuracy of the result. Grid formation can be very tedious, particularly for complex geometric configurations, and becomes extremely difficult in the case of multiple bodies.

1.3.1 Finite Difference Schemes

Many researchers have approached the problem of flow around bluff bodies by solving finite-difference analogues of the full Navier-Stokes equations in two dimensions. All such procedures have an upper bound on the Reynolds number, since the methods suffer from numerical instability or require grids of impracticably small size to retain stability at high Reynolds numbers. In addition, the solution of the complete set of equations is extremely costly in terms of computing memory capacity and computing time. Ozono *et al.* [1992] studied the problem of viscous flow around a flat plate at Reynolds number of $O(10^3)$, using finite difference methods with a boundary-fitted grid and co-ordinate transformation in order to distribute a sufficient number of grid points in the boundary layer. In their calculation, a grid system of 435 × 81 points was used for a flat plate with a ratio of length to thickness of 8, at Reynolds number of $O(10^3)$.

For the analysis of a boundary layer problem, it is necessary that at least a few mesh points fall within the boundary layer. In general, boundary layer thickness decreases as Reynolds number increases (in proportion to $Re^{-½}$ for a laminar layer). If a finite difference procedure is used with a grid characterised near the boundary and in the wake by a mesh length δ, then for a laminar flow the condition $\delta^2 Re = O(1)$ must be satisfied. We therefore require a very fine grid system to deal with flows at high Reynolds number.

Analysis by Chorin [1969] suggests that a more stringent condition, $\delta Re = O(1)$, must be satisfied. This condition indicates that as Reynolds number is increased the numbers of mesh points and the computational loading required to obtain a solution rapidly become prohibitive. Another difficulty associated with finite difference methods is that the mesh surrounding the solid body needs to be defined for each geometric configuration, and this may become extremely difficult when bodies of complex geometry are to be investigated. The difficulties of mesh generation are further intensified for multiple-body arrays.

From considerations such as these, it becomes clear that numerical schemes which rely on grid systems are not particularly appropriate for analysis of bluff body flows at high Reynolds number, and that a grid-free calculation method is to be preferred.

1.3.2 The Discrete Vortex Method

The most highly developed grid-independent calculation procedure is the discrete vortex method.

In real flows, except at very low Reynolds numbers, the vorticity is only significant in thin boundary layers adjacent to solid boundaries and within the wakes. Outside these regions the flow is essentially inviscid. Thus, instead of concentrating attention on the velocity and pressure fields of the flow, it is conceptually correct to consider the flow as compact regions of concentrated vorticity contained in an otherwise irrotational flow. The motion of these regions of vorticity follows the local fluid velocity of the external irrotational flow field, which is itself determined by the vorticity field. If the distributed vorticity is now approximated and replaced by a number of discrete (potential-flow) vortices, a potential-flow model of the flow is obtained. Now, according to the laws of vortex motion as enunciated by Helmholtz [1858], in an inviscid fluid flow vortex lines remain always composed of the same fluid particles and move with the fluid, and their strength remains constant with time. In conjunction with a model of the type just outlined, this leads to the possibility of a Lagrangian scheme of tracking vortices for flow analysis, and is the basis of the Discrete Vortex Method.

The vortex method makes use of the (inviscid flow) Euler equations, formulated in terms of vorticity, and the Biot-Savart law for the velocity field of a discrete vortex. Flow development within the solution domain is then derived from the vorticity trajectories. If solutions are to be obtained for real time-dependent flows, the discrete vortex model must be extended to include the effects of vorticity generation at solid boundaries and vorticity diffusion within the flow. This leads to techniques such as the random walk procedure introduced by Chorin [1973] which will be referred to in greater detail later. If these features can be successfully introduced, the method has the potential to produce solutions to viscous flow problems which correctly include the development of boundary layers and wakes, that is to produce solution to the Navier-Stokes equation.

When practical time-stepping procedures are derived to implement discrete vortex methods, the number of vortices Z in the flow field increases with time and at each time step computation of $O(Z^2)$ vortex interactions is required. This quickly leads to heavy demands on computing power. Modified procedures such as the cloud-in-cell and the cell-to-cell methods can reduce the computing load for the calculation of vortex interactions. The cloud-in-cell method, for example, makes use of a grid system to encompass the discrete vortices in the flow field, and, according to Leonard [1980], can reduce the computing load to about $O(M \log_2 M)$ where M is the number of grid points. Detailed discussion of the cell-to-cell method will be presented later.

Despite the inherent computing difficulties the discrete vortex method is a very attractive one for bluff body flows, and has been adopted for the present work. As will be seen later, the numerical scheme developed is based on the discrete vortex and the surface-vorticity boundary-integral methods: the discrete vortex method is employed to simulate the vorticity evolution in the flow field, while the surface-vorticity boundary-integral method is adopted to model the interaction between the bluff-bodies and the flow field. However, before the methods used are discussed in detail, the equations of fluid motion and vortex motion which the method uses as its basis will be set out, and the development of vortex methods reviewed.

Chapter 2

Basic Vortex and Vorticity Equations

As indicated in chapter 1, the calculation procedures to be adopted for bluff-body flows are concentrated on vorticity and discrete vortex motion. It is therefore appropriate to set out the relationship between the velocity field and the vorticity field, relevant mathematical relations which describe the motion of discrete vortices in the flow field, and the derivation of the vorticity transport equation which is the form in which the fundamental Navier-Stokes equation for the conservation of momentum will be applied. The work is confined to the analysis of incompressible fluid flow.

2.1 The Relation Between Vorticity Field and Velocity Field in Fluid Flow

The relation between velocity and vorticity is analogous to that between magnetic field and current density. The vorticity vector ω can be interpreted as a local angular-momentum density: the angular momentum of a fluid particle rotating with angular velocity $\omega/2$. In an ideal barotropic fluid under the action of conservative external forces, fluid particles originally free of vorticity remain free of vorticity at all times. In a real fluid a particle without vorticity can acquire it by viscous diffusion or the action of non-conservative external forces. For fluid motion described by a vector velocity field $\boldsymbol{u}(\boldsymbol{x},t)$, the vorticity vector $\omega(\boldsymbol{x},t)$ is defined as the curl of the velocity :

$$\omega(\boldsymbol{x},t) \equiv \mathit{curl}\ \boldsymbol{u} = \left(\frac{\partial w}{\partial y} - \frac{\partial v}{\partial z}, \frac{\partial u}{\partial z} - \frac{\partial w}{\partial x}, \frac{\partial v}{\partial x} - \frac{\partial u}{\partial y} \right) = (\xi, \eta, \zeta), \tag{2.1}$$

where ξ, η, and ζ are its components in the x, y, and z directions respectively. The theoretical foundations of the vortex method for calculating fluid flow are based on the two facts (Saffman

[1992]) : first, that Eq. (2.1) may be inverted to give the velocity field as an integral over the vorticity field; and, second, that when the fluid is barotropic and inviscid (or when vorticity diffusion is negligible) and external forces are conservative, the vorticity satisfies the conservation principles of Helmholtz's laws and can be tracked, and therefore a Lagrangian calculation scheme can be used. Saffman summarises the conditions for which the inversion of Eq. (2.1) is possible and $\boldsymbol{u}$ is determined uniquely as follows:

i. The velocity field is solenoidal, i.e. div $\boldsymbol{u} = 0$.
ii. The region occupied by the fluid is singly connected.
iii. The normal component of fluid velocity is given on bounding surfaces *S*.
iv. The velocity vanishes at infinity when the fluid is unbounded.
v. The normal component of vorticity vanishes on *S*.
vi. The vorticity field is compact.

The velocity is then given uniquely by the sum of a solenoidal vector potential component and an irrotational scalar component

$$\boldsymbol{u}(x,t) = \boldsymbol{u}_v(x,t) + \nabla\Phi \quad , \tag{2.2}$$

where $\boldsymbol{u}_v$ is a solenoidal field satisfying

$$curl\ \boldsymbol{u}_v = \omega \tag{2.3}$$

and $\nabla\Phi$ is the irrotational solenoidal field which can be added to satisfy a single boundary condition on the velocity field on *S*. If there are no bounding surfaces, $\Phi = 0$.

2.2 Vortex Terminology

First, it is appropriate to define *vortex lines*, that is lines which are everywhere in the direction of the vorticity vector, and are given by

$$\frac{dx}{\xi} = \frac{dy}{\eta} = \frac{dz}{\zeta} \quad , \tag{2.4}$$

where ξ, η, ζ are the components of the vorticity vector $\gamma = \xi i + \eta j + \zeta k$. Second, the expression for the circulation around a closed reducible curve *C* which is

$$\Gamma = \oint \boldsymbol{u} \cdot d\boldsymbol{s} \quad , \tag{2.5}$$

where *s* is the curvilinear coordinate along *C*.

A *vortex tube* consists of the surface formed by all the vortex lines passing through a closed reducible curve; the circulation Γ around a vortex tube is the same for all curves embracing it, and is a measure of the strength of the vortex tube. The term *vortex filament* is generally used to denote a vortex tube of small cross section. A vortex filament with infinitesimal cross section and finite circulation is called a *line vortex* or simply, a *vortex*.

The velocity field of a line vortex of circulation Γ is given by the Biot-Savart law as

$$\boldsymbol{u} = \frac{\Gamma}{4\pi}\int \frac{\boldsymbol{ds} \times \boldsymbol{r}}{|\boldsymbol{r}|^3}, \tag{2.6}$$

where $\boldsymbol{r}(x,y,z)$ is the position vector of a point relative to the vortex line. The velocity field of a vortex is irrotational since curl $\boldsymbol{u} = 0$.

A *vortex sheet* is a limit in which the vorticity domain is of zero thickness. The velocity normal to the sheet is continuous; the tangential velocity experiences a discontinuity across the sheet of magnitude equal to the strength of the sheet.

The circulation Γ_c around any closed contour induced by a vortex external to the contour is given by

$$\begin{aligned}\Gamma_c &= \oint_{\partial S} \boldsymbol{u} \cdot \boldsymbol{ds} = \iint_S \boldsymbol{\omega} \cdot \boldsymbol{n}\, dA \\ &= 0\end{aligned} \tag{2.7}$$

where $\boldsymbol{n}$ is the unit outward normal to the open surface S. The transformation of a contour integral to a double integral is made possible by the Stokes theorem. However, if a vortex lies within the region S, the induced circulation Γ_c around ∂S is equal to the strength Γ of that vortex.

This is a very important conclusion about the circulation around any closed contour induced by a vortex. Thus, the induced circulation is zero if the vortex is outside the closed loop, but otherwise the induced circulation equals the strength of the vortex. This result is used extensively in the development of the discrete vortex numerical method.

2.3 The Vorticity Transport Equation

Like all other flows, bluff body flows are governed by the fundamental continuity and momentum equations. In a homogeneous incompressible flow in which the fluid velocity vector is $\boldsymbol{u}$, the equation for the conservation of mass is

$$\nabla\cdot\boldsymbol{u} = 0 \ ; \tag{2.8}$$

and the momentum equation for flow under the influence of an external force $\boldsymbol{F}$ per unit mass is the Navier-Stokes equation

$$\partial_t\boldsymbol{u} + \boldsymbol{u}\cdot\nabla\boldsymbol{u} = -(1/\rho)\nabla p + \boldsymbol{F} + \upsilon\nabla^2\boldsymbol{u} \ , \tag{2.9}$$

where p is the pressure, t the time, υ the viscosity, and ρ the density of fluid. By making use of the vector identity

$$\boldsymbol{u}\cdot\nabla\boldsymbol{u} = \nabla\left(\frac{\boldsymbol{u}^2}{2}\right) - \boldsymbol{u}\times\omega \ , \tag{2.10}$$

where $\omega = \nabla\times\mathbf{u}$ is the vorticity, Eq. (2.9) can be rewritten in the form

$$\partial_t\boldsymbol{u} - \boldsymbol{u}\times\omega = -(1/\rho)\nabla p_o + \boldsymbol{F} + \upsilon\nabla^2\boldsymbol{u} \ , \tag{2.11}$$

where $p_o = p + \tfrac{1}{2}\rho u^2$ denotes the stagnation pressure. The curl of this equation leads to

$$\partial_t\omega - \nabla\times(\boldsymbol{u}\times\omega) = -(1/\rho)\nabla\times(\nabla p_o) + \nabla\times\boldsymbol{F} + \upsilon\nabla^2\omega \ , \tag{2.12}$$

which, because of the vector identities $\nabla\times\nabla p_o \equiv 0$, and $\nabla\times\boldsymbol{F} \equiv 0$ (if $\boldsymbol{F}$ is a conservative external force so that it is the gradient of a single-valued scalar), becomes

$$\partial_t\omega - \nabla\times(\boldsymbol{u}\times\omega) = \upsilon\nabla^2\omega \ . \tag{2.13}$$

We now make use of the vector identity

$$\nabla\times(\boldsymbol{u}\times\omega) \equiv \boldsymbol{u}\nabla\cdot\omega - \omega\nabla\cdot\boldsymbol{u} - (\boldsymbol{u}\cdot\nabla)\omega + (\omega\cdot\nabla)\boldsymbol{u} \ . \tag{2.14}$$

Since $\nabla\cdot\omega = \nabla\cdot(\nabla\times\boldsymbol{u}) \equiv 0$, and since by Eq. (2.8) $\nabla\cdot\boldsymbol{u} = 0$, we then have

$$\nabla\times(\boldsymbol{u}\times\omega) \equiv -(\boldsymbol{u}\cdot\nabla)\omega + (\omega\cdot\nabla)\boldsymbol{u} \ . \tag{2.15}$$

Substituting Eq. (2.15) into Eq. (2.13), we obtain the vorticity transport equation in the form

$$\partial_t \omega + \boldsymbol{u} \cdot \nabla \omega = \omega \cdot \nabla \boldsymbol{u} + \upsilon \nabla^2 \omega \quad , \tag{2.16-a}$$

or

$$\frac{D\omega}{Dt} \equiv \left(\partial_t + \boldsymbol{u} \cdot \nabla\right) \omega = \omega \cdot \nabla \boldsymbol{u} + \upsilon \nabla^2 \omega \quad . \tag{2.16-b}$$

This equation shows that the rate of change of vorticity depends on the local values of the velocity and vorticity field alone; the pressure term is eliminated. It shows further that, in an incompressible fluid of uniform density ρ and viscosity υ, the rate of change of vorticity of a fluid element $D\omega/Dt$ depends only on the instantaneous value of the vorticity and the local velocity gradient.

Let us now introduce a dimensionless vorticity

$$\omega^* = \frac{\omega L}{U_\infty} \quad , \tag{2.17}$$

a dimensionless velocity

$$\boldsymbol{u}^* = \frac{\boldsymbol{u}}{U_\infty} \quad , \tag{2.18}$$

a dimensionless vortex sheet strength

$$\gamma = \frac{\gamma}{U_\infty} \quad , \tag{2.19}$$

a dimensionless circulation

$$\Delta\Gamma = \frac{\Delta\Gamma}{U_\infty L} \quad , \tag{2.20}$$

and a dimensionless time

$$t = \frac{t U_\infty}{L} \quad , \tag{2.21}$$

where U_∞ is the free stream velocity, and L a characteristic length. As well, we introduce the dimensionless coordinates $x^* = x/L$, $y^* = y/L$.

The vorticity transport equation can then be rewritten in dimensionless form as

$$\frac{D\omega^*}{Dt} \equiv \left(\partial_{t^*} + \boldsymbol{u}^* \cdot \nabla\right) \omega^* = \omega^* \cdot \nabla \boldsymbol{u}^* + \frac{1}{Re} \nabla^2 \omega^* \quad , \tag{2.22}$$

where Re denotes the Reynolds number defined as $Re = U_\infty L/\upsilon$. For simplicity the asterisk over dimensionless quantities will be omitted in subsequent text.

2.4 Physical Interpretation of the Vorticity Transport Equation

The term $\boldsymbol{u}\cdot\nabla\omega$ represents the rate of change of vorticity due to convection of the fluid. As vorticity is associated with fluid particles and carried along with them, its distribution varies as fluid particles move in the flow field. The term $\omega\cdot\nabla\boldsymbol{u}$ is the rate of increase of vorticity due to vortex line deformation and is interpreted physically as stretching of the vortex filaments. Although the strength (circulation) of any one filament remains constant in time, the vorticity distribution along it varies. Vortex filament stretching, and therefore $\omega\cdot\nabla\boldsymbol{u}$, can occur only in three-dimensional flow, since in two-dimensional flow, ω is everywhere normal to the plane of flow while $\nabla\boldsymbol{u}$ is in the plane of flow, and $\omega\cdot\nabla\boldsymbol{u} = 0$. The last term $(1/Re)\nabla^2\omega$ represents the rate of change of vorticity due to molecular diffusion.

2.5 Two-Dimensional Flows

In this work the concentration will be on two-dimensional flows, and therefore the form taken in this case by various relations in the earlier sections of this chapter will be specifically stated. For two-dimensional flow it is often more convenient to make use of the complex z-plane and express the relations in terms of the complex variable $\boldsymbol{z} = (x + iy)$ rather than in the form of the general three-dimensional vector relations.

2.5.1 Vortices in Two-Dimensional Flows

For two-dimensional flows, a *vortex* is referred to as a *point vortex*. The point vortex $\Delta\Gamma$ is a singularity with a vorticity field given by

$$\omega(z) = \frac{\Delta\Gamma}{2\pi}\,\delta(z-z_o)\,, \qquad \textbf{(2.23)}$$

where δ is the two-dimensional Dirac delta function, $\boldsymbol{z}_o$ is the location of the point vortex in the complex z-plane, and $\Delta\Gamma$ is its strength (circulation). The circulation of a point vortex is taken as positive if the vortex rotates clockwise, and vice versa. When the flow field contains a number of point vortices $\Delta\Gamma_j$, j = 1,2,...,Z, (as in calculation procedures to be developed later where a distributed

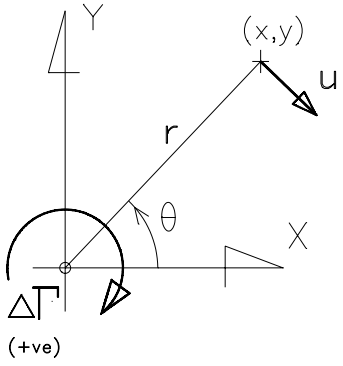

Figure 2.1. Notation for a point vortex and its velocity field.

vorticity field is approximated and replaced by a finite number of point vortices), the vorticity field ω becomes the summation of Z delta functions,

$$\omega(z) = \sum_{j=1}^{Z} \frac{\Gamma_j}{2\pi} \delta(z - z_j) \ , \tag{2.24}$$

The velocity $\boldsymbol{u}$ at a point (x,y) induced by a point vortex at the origin is given by

$$\boldsymbol{u} = \frac{\Delta\Gamma \times \boldsymbol{r}}{2\pi r^2} \ , \tag{2.25}$$

with components u and v in the x- and y-direction respectively given by

$$(u,v) = \frac{\Delta\Gamma}{2\pi r^2}[y \ , -x] \ , \tag{2.26}$$

where $\boldsymbol{r}(x,y)$ is the position vector at the point measured from the point vortex and $r^2 = x^2+y^2$. The velocity potential ϕ_v and stream function ψ_v of a point vortex $\Delta\Gamma$ are:

$$\phi_v = -\Delta\Gamma \frac{\theta}{2\pi} \ , \tag{2.27}$$

and

$$\psi_v = \frac{\Delta\Gamma}{2\pi} \ln(r) \ , \tag{2.28}$$

where θ is the angle between the x-axis and the position vector $\boldsymbol{r}$, positive in the clockwise direction.

It follows that the potential ϕ and stream function ψ at a point due to Z discrete vortices, $\Delta\Gamma_j$ for $j = 1,2,...,Z$, and a superimposed uniform flow $\boldsymbol{U}_\infty$ inclined at an angle α to the x-axis are

$$\phi = U_\infty(x \cos\alpha + y \sin\alpha) + \sum_{j=1}^{Z} -\Delta\Gamma_j \frac{\theta_j}{2\pi} \ , \tag{2.29}$$

and

$$\psi = U_\infty(y \cos\alpha - x \sin\alpha) + \sum_{j=1}^{Z} \frac{\Delta\Gamma_j}{2\pi} \ln(r_j) \ . \tag{2.30}$$

With the expression for the velocity field $\boldsymbol{u}(u,v)$ given by Eq. (2.26), we then have

$$(u,v) = \boldsymbol{U}_\infty[\cos\alpha, \sin\alpha] + \sum_{j=1}^{Z} \frac{\Delta\Gamma_j}{2\pi r_j^2}[(y-y_j), -(x-x_j)] \ . \tag{2.31}$$

Alternatively, the velocity field of a point vortex can be expressed in term of the complex variable $\boldsymbol{z} = (x + iy)$. The complex potential $\Omega(z)$ at point z in the complex plane, due to a single vortex $\Delta\Gamma_j$ at z_j, is given by

$$\Omega(z) = \frac{i\,\Delta\Gamma_j}{2\pi}\ln(z - z_j) \ . \tag{2.32}$$

The complex conjugate $\bar{\boldsymbol{u}}$ of the velocity is then

$$\bar{\boldsymbol{u}} = u - iv = \frac{i\,\Delta\Gamma_j}{2\pi(z - z_j)} \ . \tag{2.33}$$

The expression for the velocity field in terms of the complex variable by Eq. (2.33) is found useful when developing the cell-to-cell algorithm in a later chapter. As each of these vortices has a complex potential given by Eq. (2.32), and a ve locity field given by Eq. (2.33), the overall complex potential $\Omega(z)$ is obtained by superposition as

$$\Omega(z) = \frac{i}{2\pi}\sum_{j=1}^{Z} \Delta\Gamma_j \ln(z - z_j) \ , \tag{2.34}$$

and the overall velocity field $\boldsymbol{u}(z)$ is given by

$$\bar{\boldsymbol{u}} = u - iv = \frac{i}{2\pi}\sum_{j=1}^{Z} \frac{\Delta\Gamma_j}{z - z_j} \ . \tag{2.35}$$

2.5.2 The Vorticity Transport Equation in Two-Dimensional Flows

In a two-dimensional flow the vorticity vector ω has only one non-zero component $\omega = \zeta$, normal to the plane of the flow. The vorticity transport equation then becomes a scalar equation which is of the same form as the equation satisfied by the density of some conserved substance which is convected with the fluid and diffused within it, namely

$$\frac{D\omega}{Dt} = \frac{1}{Re}\nabla^2\omega \ . \tag{2.36}$$

This implies an important consequence that the motion of an incompressible fluid can be represented as the creation and subsequent evolution of a self-interacting vorticity field. Once the vorticity field as a function of space and time is known the motion of the fluid is determined. The detailed mechanism of vorticity creation and shedding from a solid surface, and the subsequent convective and diffusive motion will be taken up again in later chapters.

Chapter 3

Review of the Development of Discrete Vortex Methods

In this chapter, the development of the discrete vortex methods will be reviewed, from their early application to vortex-sheet stability to more recent application to viscous flow over solid bodies. Emphasis is placed on the surface-vorticity boundary-integral method and approximations to it by discrete vortex methods for numerical analysis of both potential flow and viscous flow over solid bodies. The solution procedures used in this project for the calculations of inviscid flow and viscous flow past a single body will be described in the first part of this chapter, followed by the development of solution procedures for the calculations of flow past a multi-body array.

3.1 The Kelvin-Helmholtz Instability of a Vortex Sheet

Early work on discrete vortex methods was concerned particularly with the effects of the Kelvin-Helmholtz instability of a vortex sheet, and has been reviewed by many authors. Notable reviews are those of Fink and Soh [1974] and Clements and Maull [1975], and further detailed discussion is given by Lewis [1991, Ch. 8].

A vortex sheet is in a state of critical equilibrium, the so-called Kelvin-Helmholtz instability; following a small perturbation of the sheet, self-convection causes the sheet to roll up into stable vortex clusters periodically distributed along its length. The first application of the discrete vortex method is usually attributed to Rosenhead [1931] who investigated this instability by approximating the vortex sheet by an array of point vortices. His calculated results showed smooth rolling-up of the vortex sheet. Rosenhead's calculation was later repeated by Birkhoff and Fisher [1959] and Hama and Burke [1960] using more discrete vortices to represent the vortex sheet and smaller time steps in the integration routine. They found that although the

vortices formed clusters their paths were highly irregular, and it was concluded that the self-induced motion of an array of point vortices would ultimately become random.

Similar procedures have been applied to the calculation of the rolling-up of the vortex sheet behind a wing to form wing-tip vortices, initially by Westwater [1935] and apparently with some success. However, in view of the problems arising from the Rosenhead calculations, Westwater's calculations were also repeated – by Takami [1964] and Moore [1971], who found the calculated vortex paths to be very complicated and in some respects (such as pairs of vortices orbiting about each other) at variance with vortex sheet behaviour in real flows.

Results such as these, together with problems associated with the singular nature of line vortices and the resulting unrealistically large induced velocities at points close to a line vortex (even in two-dimensional flow), led to a variety of smoothing techniques to produce better agreement between calculation and observation. These include the introduction of vortices with finite cores, vortex amalgamation schemes, rediscretisation of the vortex sheet, and others; discussion of them is given in a comprehensive review paper by Sarpkaya [1989].

3.2 Discrete Vortex Method for Analysis of Potential Flow Over Solid Bodies

The potential flow of a uniform stream over a body can be mathematically modelled by replacing the body by a source distribution or by a vortex sheet which constitutes a surface vorticity distribution. It is the latter case which is to be considered here, and descriptions of the methods are given by Lewis [1981, 1991].

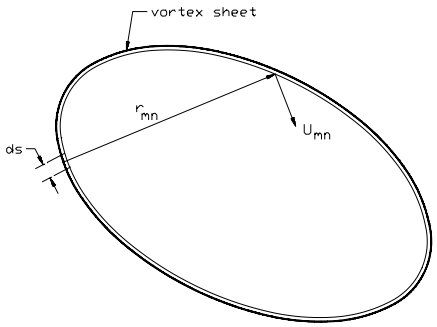

Figure 3.1. Velocity induced by vortex sheet.

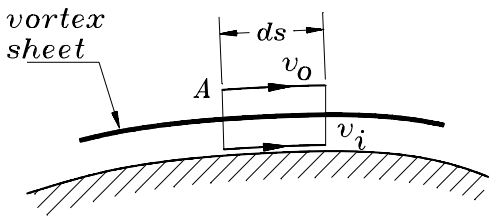

Figure 3.2. Schematic of vortex sheet.

Thus we consider the solid boundary to be replaced by a vortex sheet of strength $\gamma(s)$, as shown in Fig. 3.1, where s is the curvilinear coordinate along the body contour. The velocity induced at a point s_m on the vortex sheet by an element of vortex sheet of length ds and strength $\gamma(s_n)$ at the point s_n also on the vortex sheet, is given by the Biot-Savart law as

$$d\boldsymbol{u}_{mn} = \frac{\gamma(s_n)\, ds \times \boldsymbol{r}_{mn}}{2\pi |r_{mn}|^2} \qquad \textbf{(3.1)}$$

The component of this velocity tangential to the vortex sheet at s_m, where the unit normal vector is $\boldsymbol{n}_m$, is given by

$$d\boldsymbol{u}_{m_t} = \boldsymbol{n}_m \times (d\boldsymbol{u}_m \times \boldsymbol{n}_m) \ . \qquad \textbf{(3.2)}$$

Integration gives the tangential velocity at s_m due to the entire vortex sheet as

$$\boldsymbol{u}_{m_t} = \frac{1}{2\pi} \oint \frac{\boldsymbol{n}_m \times ((\gamma(s_n) \times \boldsymbol{r}_{mn}) \times \boldsymbol{n}_m)\ ds}{|r_{mn}|^2} \ . \qquad \textbf{(3.3)}$$

If we now consider the elementary region A, shown in Fig. 3.2, with arc length ds, which contains a total vortex strength of $\gamma(s)ds$, then by taking the circulation around the boundary of A, we have

$$(v_o - v_i)\, ds = \gamma(s)\, ds \ , \qquad \textbf{(3.4)}$$

where v_o and v_i are the tangential fluid velocities just outside and inside the vortex sheet. We require v_o to be the local potential-flow surface velocity v_s, and if the velocity v_i just under the vortex sheet is given the value zero (appropriate to a solid surface) then

$$\gamma(s) = v_s \ , \qquad \textbf{(3.5)}$$

that is the vortex sheet has a strength equal to the local potential-flow surface velocity. This is an important feature of surface vorticity modelling. The potential flow problem is then to determine $\gamma(s)$ in such a way that the resultant flow makes the body (i.e. the vortex sheet contour) a streamline of the flow. This requirement is met if the resultant flow is tangential to the vortex sheet contour at all points. Martensen [1959] has shown that application of a Dirichlet boundary condition on the inside of the vortex sheet satisfies this requirement. Then with $v_i = 0$ and the body located in an uniform stream with velocity $\boldsymbol{U}_\infty$ at infinity, the condition at a general point s_m on the vortex sheet contour becomes

$$-\frac{1}{2}\gamma(s_m) + \frac{1}{2\pi} \oint \frac{\boldsymbol{n}_m \times ((\gamma(s_n) \times \boldsymbol{r}_{mn}) \times \boldsymbol{n}_m)\ ds}{|r_{mn}|^2} + \boldsymbol{n}_m \times (\boldsymbol{U}_\infty \times \boldsymbol{n}_m) = 0 \ . \qquad \textbf{(3.6)}$$

The first term $-\gamma(s_m)/2$ accounts for the discontinuity of tangential velocity across the sheet, the second term represents the contribution of the vortex sheet to the tangential velocity at s_m, and the last term represents the resolved component of main stream velocity in the tangential direction at s_m. The equation can be rewritten in terms of a coupling coefficient $k(s_m,s)$, which is dependent only on the geometry of the body, in the form

$$-\frac{1}{2}\gamma(s_m)+\oint k(s_m,s)\,\gamma(s)\,ds+\boldsymbol{U}_\infty\cdot\boldsymbol{t}_m=0\ , \qquad \textbf{(3.7)}$$

where $\boldsymbol{t}_m$ denotes the unit tangential vector at s_m, the coupling coefficient is given by

$$k(s_m,s)=\frac{1}{2\pi}\left\{\frac{(y_m-y)\cos\beta_m-(x_m-x)\sin\beta_m}{(x_m-x)^2+(y_m-y)^2}\right\}, \qquad \textbf{(3.8)}$$

and β_m is the angle the tangent at s_m makes with the x-axis. Eq. (3.7) is the result given by Lewis [1980]. It is a non-singular Fredholm integral equation of the second kind for $\gamma(s)$.

It might be noted that in the derivation of Eq. (3.7), only one boundary condition, namely zero tangential velocity on the inside of the vortex sheet, has been used; the requirement of zero velocity normal to the surface has apparently been ignored. However, Martensen [1959] provided a rigorous proof that one boundary condition implies the other, and enforcement of only one is sufficient provided that there is no vortex or source distribution within the body profile.

3.2.1 Numerical Procedure for the Surface Vorticity Boundary Integral Method

The development of a practical numerical scheme for the surface vorticity boundary integral method starts with replacing the continuous body contour by a finite number of straight line segments (panels) whose end points are defined by specifying the data points along the body contour. Representing a closed body contour by M panels requires M+1 data points $(X_d\ ,\ Y_d)_n$, where n = 1, 2...M+1, with $(X_d\ ,\ Y_d)_{M+1} = (X_d\ ,\ Y_d)_1$. The collocation points (or pivotal points) $(x,y)_n$, where n = 1,2...M, at the mid-position of each panel are thus given by

$$x_n=\frac{X_{d_n}+X_{d_{n+1}}}{2},\quad y_n=\frac{Y_{d_n}+Y_{d_{n+1}}}{2}\ ,\qquad n=1,2\ldots M\ . \qquad \textbf{(3.9)}$$

Consider a system with a body approximated by M segments each of length Δs_m, where m = 1,2,...M, with the m*th* segment making an angle of β_m with the x-axis, and with the main stream $\boldsymbol{U}_\infty$ inclined at an angle α to the x-axis. The vorticity is assumed to be constant over any particular segment. The integral equation Eq. (3.7) can then be approximated by the discretised form

$$\sum_{n=1}^{M} K(s_m, s_n)\,\gamma(s_n) + \cos(\alpha - \beta_m) = 0 \ , \qquad \textbf{(3.10)}$$

suitable for numerical evaluation, where the modified coupling coefficient $K(s_m, s_n)$ is given by

$$K(s_m, s_n) = \Delta s_n k(s_m, s_n) - \frac{1}{2}\delta_{mn} \ , \qquad \textbf{(3.11)}$$

δ_{mn} is the Kronecker delta function (which has the value unity for $m = n$ but is otherwise zero), and $k(s_m , s_n)$ is given by Eq. (3.8). Note that Eq. (3.10) is in dimensionless form therefore the $\boldsymbol{U}_\infty$ has been deliberately omitted.

For the special case $m = n$, the coupling coefficient $k(s_m , s_m)$ determines the tangential velocity self-induced by the mth segment, and the value given by Eq. (3.8) is indeterminate. For a straight segment $k(s_m, s_m) = 0$, but for a body with significant surface curvature this is generally a poor approximation. To take account of the effect of curvature, it is necessary to consider Eq. (3.8) in the form

$$k(s_m, s_m) = \frac{1}{2\pi} \lim_{s_m \to s_n} \left[\frac{(y_m - y_n)\dfrac{dx_m}{ds} - (x_m - x_n)\dfrac{dy_m}{ds}}{(x_m - x_n)^2 + (y_m - y_n)^2} \right] , \qquad \textbf{(3.12)}$$

where dx_m/ds denotes the derivative dx/ds at s_m ($\equiv \cos\beta_m$), and similarly for $dy_m/ds \equiv \sin\beta_m$. Lewis [1980] showed that the expression for $k(s_m,s_m)$, Eq. (3.12), can be reduced to

$$k(s_m, s_m) = \frac{1}{4\pi} \left\{ \frac{-\dfrac{d^2 y_m}{dx^2}}{\left(1 + \left(\dfrac{dy_m}{dx} \right)^2 \right)^{3/2}} \right\} . \qquad \textbf{(3.13)}$$

The bracketed term in Eq. (3.13) is the expression for the inverse of the radius of curvature r_m of the contour at the location s_m. Thus, from Eq. (3.13) and Eq. (3.11),

$$K(s_m, s_m) = -\frac{1}{2} + \frac{\Delta s_m}{4\pi r_m} \approx -\frac{1}{2} - \frac{\Delta \beta_m}{4\pi} \quad , \tag{3.14}$$

where $\Delta\beta_m$ is the internal angle of segment *m*, which is approximately equal to half the change of slope between neighbouring elements,

$$\Delta \beta_m = \frac{1}{2}(\beta_{m+1} - \beta_{m-1}) \quad . \tag{3.15}$$

Therefore the corrected coupling coefficient $K(s_m,s_m)$, including the effect of surface curvature on the self-induced velocity, is

$$K(s_m, s_m) = -\frac{1}{2} - \frac{1}{8\pi}(\beta_{m+1} - \beta_{m-1}) \tag{3.16}$$

which is the result given by Lewis [1980].

Extension of the foregoing treatment to all the segments of the body results in a set of *M* simultaneous linear equations each similar to Eq. (3.10), for *M* unknown values of surface vorticity $\gamma(s_n)$. This set of equations can be written in matrix form as

$$[K]\,[\gamma] = [b] \quad , \tag{3.17}$$

where the *coupling coefficient matrix* **[*K*]** is an $M \times M$ matrix with elements $K_{mn} = K(s_m , s_n)$, the *tangential surface velocity matrix* **[*b*]** is a column matrix of the *M* elements $b_m = -\cos(\alpha - \beta_m)$, and the *solution matrix* **[γ]** is a column matrix of the *M* elements $\gamma(s_n)$.

3.2.2 Singularity of the Coupling Coefficient Matrix, [*K*]

The contribution of an element $\gamma(s_n)ds_n$ of the vortex sheet to the circulation around the vortex-sheet contour itself is given by

$$\gamma(s_n) ds_n \oint k(s_m, s_n)\, ds_m \quad . \tag{3.18}$$

We know that the circulation around a contour which intersects a vortex is half the strength of the vortex, and it follows that

$$\gamma(s_n)\, ds_n \oint k(s_m, s_n)\, ds_m = \frac{1}{2}\gamma(s_n)\, ds_n \quad , \tag{3.19}$$

and hence that

$$\oint k(s_m, s_n)\, ds_m = \frac{1}{2} \quad . \tag{3.20}$$

In the discretised summation approximation, this becomes

$$\sum_{m=1}^{M} k(s_m, s_n)\,\Delta s_m = \frac{1}{2} \,. \tag{3.21}$$

With Eq. (3.11) relating $k(s_m,s_n)$ and $K(s_m,s_n)$, we then have

$$\sum_{m=1}^{M} \frac{1}{\Delta s_n}\left[K(s_m, s_n) + \frac{1}{2}\delta_{mn}\right]\Delta s_m = \frac{1}{2} \,. \tag{3.22}$$

$$\therefore \quad \frac{1}{\Delta s_n}\sum_{m=1}^{M} K(s_m, s_n)\,\Delta s_m + \frac{1}{2} = \frac{1}{2} \tag{3.23}$$

$$\therefore \quad \sum_{m=1}^{M} K(s_m, s_n)\,\Delta s_m = 0 \tag{3.24}$$

It can readily be shown that this is also the condition for the circulation around a contour inside the vortex sheet to be zero.

If, in the approximation, Eq. (3.24) is satisfied exactly, then it follows that the rows of the matrix **[*K*]** are not linearly independent and the matrix is singular. It should be noted that the result Eq. (3.24) is valid for any general distribution $\gamma(s_n)$ of the strength of the vortex sheet. The total circulation of the sheet

$$\Gamma = \oint \gamma(s)\,ds \tag{3.25}$$

and therefore the circulation around the body may be zero or non-zero. In the case of a flow started impulsively from rest $\Gamma = 0$ initially and must remain so. But steady potential flows with non-zero circulation about the body (with, as usual in potential flow analysis, no specification of how such a circulation might arise) can also be considered. In both cases the matrix **[*K*]** should be singular.

In general if, in the approximation, the $K(s_m, s_n)$ values are all determined from the geometrical relation, Eq. (3.8), the sum in Eq. (3.24) will not be exactly zero. Experience shows that in this case, particularly for slender bodies, large errors may be introduced in the circulation around the body (see for example Lewis [1991] Ch.2). The errors are associated with the combined effects of segment m in conjunction with its opposite segment $(M+1-m)$ being poorly represented.

In their study of aerofoil sections of finite thickness, Jacob and Riegels [1963] addressed the problem of bodies with thin sections, and proposed correcting the coefficients $K_{M+1-m,m}$ on the back diagonal of the **[*K*]** matrix by satisfying Eq. (3.24) exactly to enforce zero internal circulation. For each n*th* column $\mathbf{[}\boldsymbol{K}_{mn}\mathbf{]}$ n = 1,2,...M, the $(M+1-n)$*th* element is assigned the value

$$K(s_j,s_n)\Delta s_j = -\sum_{\substack{m=1\\ m\neq j}}^{M} K(s_m,s_n)\Delta s_m \ , \qquad j=M+1-n \ , \tag{3.26}$$

instead of the value given by Eq. (3.11). Following Jacob and Riegels, this scheme is often referred to as *back diagonal correction*. However, when this correction is made, the consequent exact satisfaction of Eq. (3.24) implies that the rows of the matrix **[*K*]** are not linearly independent, and the matrix **[*K*]** becomes singular, as it should be.

Consider then the matrix equation Eq. (3.17), **[*K*][γ]** = **[*b*]** , of which **[*K*]** has been corrected for zero internal circulation. The element of **[*b*]**, $b_m = -\cos(\alpha-\beta_m)$, represents the tangential velocity at point m on the surface due to the irrotational uniform free-stream flow. The circulation around the contour induced by the free-stream must be zero. Therefore, the following condition must be satisfied:

$$\oint U_t\, ds = 0 \ , \tag{3.27}$$

or, in the summation approximation,

$$\sum_{m=1}^{M} b_m \Delta s_m = 0 \ . \tag{3.28}$$

Now, if in the set of simultaneous linear equations **[*K*][γ]** = **[*b*]** each n*th* equation is multiplied by the constant Δs_m for m = 1,2,...M, and the resulting equations added, the sum is zero. Thus any one equation is equal to minus the sum of all the others. There are therefore now only $(M-1)$ independent equations to be solved for M unknowns. Hence, when the zero induced circulation condition is imposed on the Martensen formulation, one additional condition is required to produce a unique solution.

3.2.3 Regularisation of the Coupling Coefficient Matrix, [*K*]

Several methods for overcoming the singularity of coupling coefficient matrix are discussed by Lewis [1991, Ch.2]. Jacob and Riegels [1963] applied the Martensen method to study the potential-flow of lifting aerofoils in a uniform stream. They made use of the Kutta-Joukowsky trailing edge condition, which essentially specifies that the rear stagnation point be at the trailing edge of the aerofoil. By prescribing one extra collocation point, namely n_{te}, at the trailing edge and imposing the Kutta condition of zero vorticity at n_{te}, appropriate to a stagnation point, the (t_e)*th* equation and column matrix can be deleted. The dimension of the system of equations is thus reduced by one and a unique solution becomes obtainable.

Wilkinson [1967] in analysing inviscid flow about aerofoils and cascades, overcame the problem of a singular matrix by imposing the Kutta trailing-edge condition in a form in which γ is specified on the two segments n_{te} and n_{te+1} adjacent to the trailing edge. Thus it is specified that $\gamma(s_{te}) = -\gamma(s_{te+1})$, thereby reducing the number of unknown values of surface vorticity by one. One equation of the system is eliminated by combining the (t_e)*th* and (t_e+1)*th* column matrices, and combining the (t_e)*th* and (t_e+1)*th* equations. The dimension of the coefficient matrix is thus reduced from M to $(M-1)$ to solve for $(M-1)$ unknown values of γ.

The above approaches, which have been generally used for surface vorticity modelling of aerofoils and cascades, make use of prior knowledge about the flow condition at the trailing edge of aerofoils to modify the coupling coefficient matrix. This allows a unique solution for the surface vorticity distribution (and hence the circulation and lift) to be obtained in these particular cases.

In the more general case of potential flow over a body of arbitrary shape with arbitrary prescribed circulation a more general additional condition is required. If the prescribed circulation around the body is Γ_b, then, by definition and Eq. (3.5),

$$\Gamma_b = \oint_{\partial S} v_s \, ds = \oint_{\partial S} \gamma(s) \, ds \quad . \tag{3.29}$$

This can be expressed in discretised approximation form as

$$\Gamma_b = \sum_{n=1}^{M} \gamma(s_n) \Delta s_n \quad . \tag{3.30}$$

This equation and the Martensen equation represented by Eq. (3.10) can be simultaneously satisfied by adding Eq. (3.30) to Eq. (3.10) and solving the resulting equation. The equation to be solved is

$$\sum_{n=1}^{M} \left[K(s_m, s_n) + \Delta s_n\right]\gamma(s_n) + \cos(\alpha - \beta_m) - \Gamma_b = 0 \quad . \tag{3.31}$$

The modified coupling coefficient matrix $[K(s_m,s_n) + \Delta s_n]$ is now non-singular and solution is possible. This system of simultaneous linear equations can be written in matrix form as $\mathbf{[}K^r\mathbf{][}\gamma\mathbf{]} = \mathbf{[}b\mathbf{]}$, where $\mathbf{[}K^r\mathbf{]}$ is the regularised *coupling coefficient matrix*. The elements of the matrices $\mathbf{[}K^r\mathbf{]}$ and $\mathbf{[}b\mathbf{]}$ are given by

$$\begin{aligned} K^r_{mn} &= K(s_m, s_n) + \Delta s_n \quad , \\ b_m &= -\cos(\alpha - \beta_m) + \Gamma_b \quad . \end{aligned} \tag{3.32}$$

Since $\mathbf{[}b\mathbf{]}$ contains two separate independent parts, $-\cos(\alpha - \beta_m)$ and Γ_b, the solution for $\mathbf{[}\gamma\mathbf{]}$ also has two independent parts, $\gamma_1(s_n)$ and $\gamma_2(s_n)$, which satisfy the equations

$$\begin{aligned} &\sum_{n=1}^{M} \left[K(s_m, s_n) + \Delta s_n\right]\gamma_1(s_n) = -\cos(\alpha - \beta_m) \quad , \\ &\sum_{n=1}^{M} \left[K(s_m, s_n) + \Delta s_n\right]\gamma_2(s_n) = \Gamma_b \quad . \end{aligned} \tag{3.33}$$

The vortex sheet $\gamma_1(s_n)$ is associated with the uniform free-stream, while $\gamma_2(s_n)$ is associated with the bound circulation Γ_b on the body. Further, if we let $\gamma_{o2}(s_n)$ denote the solution of the Martensen equation for a body with a positive unit bound circulation only, that is,

$$\sum_{n=1}^{M} \left[K(s_m, s_n) + \Delta s_n\right]\gamma_{o2}(s_n) = 1 \quad , \tag{3.34}$$

then by making use of the solutions of $\gamma_1(s_n)$ and $\gamma_{o2}(s_n)$, the resultant vortex sheet on a body immersed in a uniform free stream, and with bound circulation Γ_b, can be evaluated by

$$\gamma(s_n) = \gamma_1(s_n) + \Gamma_b \gamma_{o2}(s_n) \quad . \tag{3.35}$$

For a non-lifting body $\Gamma_b = 0$; Eq. (3.30) reduces to

$$\sum_{n=1}^{M} \gamma(s_n)\Delta s_n = 0 \tag{3.36}$$

and Eq. (3.31) to

$$\sum_{n=1}^{M} \left[K(s_m, s_n) + \Delta s_n\right]\gamma(s_n) + \cos(\alpha - \beta_m) = 0 \quad . \tag{3.37}$$

The solution of this equation $\gamma(s_n)$ satisfies Eq. (3.10) and Eq. (3.36) simultaneously. It might be noted that the above calculation method can be used to analyse the potential flow about aerofoils and cascades. In this case the Kutta trailing edge condition requires the surface velocities at the trailing edge on the upper and lower surfaces to be of the same magnitude. With reference to the condition set up by Wilkinson [1967], the Kutta condition implies $\gamma(s_{te}) = -\gamma(s_{te+1})$. By making use of Eq. (3.35), the bound circulation Γ_b around the aerofoil, which satisfies the Kutta trailing edge condition, can be determined from the relation

$$\gamma_1(s_{te}) + \Gamma_b \gamma_{o2}(s_{te}) = -\left[\gamma_1(s_{te+1}) + \Gamma_b \gamma_{o2}(s_{te+1})\right] . \qquad \textbf{(3.38)}$$

Thus the value of bound circulation Γ_b (in dimensionless form) on the aerofoil is determined, from which the coefficient of lift force C_L acting on the aerofoil in inviscid flow can be derived by the Kutta-Joukowski theorem as

$$C_L = \frac{L}{\frac{1}{2}\rho U_\infty^2 l} = \frac{\rho \Gamma_b U_\infty}{\frac{1}{2}\rho U_\infty^2 l} = 2\Gamma_b^* . \qquad \textbf{(3.39)}$$

For analysis of steady inviscid flow past solid bodies by the surface-vorticity boundary-integral method, the solution of the equation $\mathbf{[K^r][\gamma] = [b]}$ yields the values of $\gamma(s_n)$ and hence directly the potential flow velocity at the body surface by Eq. (3.5). The pressure coefficient C_p on the body surface can be calculated by

$$C_p = \frac{p - p_o}{\frac{1}{2}\rho U_\infty^2} = 1 - u^2 = 1 - \gamma(s_n)^2 \qquad \textbf{(3.40)}$$

where p_o is the ambient atmospheric pressure. From the $\gamma(s_n)$ values the general velocity field is easily calculated by using the Biot-Savart equation. For analysis of potential flow past a body, the surface vorticity integral equation generates the solution directly. This method can handle all arbitrary body shapes with the same ease, and can be extended to deal with multiple bodies; for which the mathematical modelling will be presented in section 3.7.

In the present study, analysis of potential flow over solid bodies using the surface-vorticity boundary-integral method is carried out in the following sequential steps:

i. Input the body geometry by defining data points $(X_d,Y_d)_n$ on its contour, and thus define the collocation points $(x,y)_n$ with reference to Eq. (3.9).

ii. Calculate the relevant geometrical data Δs_n and β_n, hence evaluate the elements K_{mn} of the *coupling coefficient matrix* **[*K*]** by Eqs. (3.8), (3.11) and (3.16), and determine the elements b_m of the *tangential surface velocity matrix* **[*b*]**.

iii. Implement the back-diagonal correction according to Eq. (3.26), and regularise **[*K*]** by using Eq. (3.30). Hence form the corrected matrix **[*K'*]** and **[*b*]** as given by Eq. (3.32). For analysis of a non-lifting body, the value of Γ_b is set to zero.

iv. Invert matrix **[*K'*]**, and hence find the value of **[γ]**. For analysis of inviscid flow past aerofoils and cascades, the value of Γ_b can be obtained by Eq. (3.35) so as to satisfy the Kutta trailing-edge condition.

v. Calculate the coefficients of lift force and surface pressure by using Eq. (3.39) and Eq. (3.40) respectively. The streamlines of the flow pattern can be constructed by using Eq. (2.31) to find the velocity at any point in the flow field.

3.3 Inviscid Flow Analysis of Vortex Shedding from Bluff Bodies by Discrete Vortex and Potential Flow Methods

The flow of a real fluid over a body is characterised by the presence of vorticity in the flow. Batchelor [1967] presents a thorough discussion of the origin of vorticity. It cannot be created or destroyed in the interior of a homogeneous fluid, but is produced only at the boundaries of fluid regions, from which it is diffused into the fluid by the action of viscosity. In general, the vorticity is confined to a finite region, outside which it is zero or at most exponentially small. It is continuously created and shed into the flow domain from the entire body surface. Vorticity thus introduced into the flow that is still close to the body surface forms the boundary layer, and further downstream under the action of diffusion and convection becomes the body wake. In flow over a bluff body, separation of the boundary layer from the body surface will generally occur, and in most cases this will result in the formation of a vortex wake. Virtually all the vorticity in the wake then originates at the boundary layer separation points on the body. If a numerical scheme for the calculation of such flows correctly simulated vorticity diffusion and convection, it would automatically represent boundary layer separation and identify the location of the boundary layer separation points.

However, if separation point locations can be specified (for example, from experimental data), full representation of vorticity diffusion and convection can be avoided and the vortex wake development calculated by inviscid flow procedures, without the necessity to take account of the effects of viscosity. The procedure starts with the introduction of nascent vortices into the flow, for each time step, at a position close to the body near the boundary layer separation point. The strength and position of the nascent vortices has to be specified. Then, a time-stepping procedure is used, and the velocity field calculated at each time step by potential flow methods, applied to a field of uniform flow containing a set of discrete vortices whose motion is determined by the overall interactive velocity field.

The most commonly used potential-flow procedures are conformal transformation with the method of images, and the surface vorticity method. The conformal transformation and image systems, in particular, have been used extensively for bodies of simple shape, but for bodies of complicated shape or for multi-body arrays these procedures present considerable mathematical and computational difficulties. In this connection, it should be noted that, when conformal mapping is used, the convection velocity field of a vortex in one plane does not give the correct

velocity field when transformed into another plane. The transformed velocity fields must be adjusted by a procedure such as Routh's correction. (See, for example, Naylor [1982]).

Most early studies of bluff-body flows made in this way were restricted to vorticity shedding from fixed separation points. The model is generally valid for sharp-edged bluff bodies as the separation points are usually at the sharp corners. However, special problems arise with smooth-profiled bodies such as circular cylinders, due to uncertainty in the location of separation points. In such cases, the determination of separation points must rely on boundary layer calculations or experimental information. In general, the rate at which vorticity is shed into a wake is given by

$$\int_0^{\delta} \left(\frac{\partial v}{\partial x} - \frac{\partial u}{\partial y} \right) u \, dy \ , \qquad \textbf{(3.41)}$$

where δ is the boundary layer thickness on the body at the shedding point. This may be closely approximated by

$$\frac{d\Gamma}{dt} = \frac{u_1^2 - u_2^2}{2} \approx \frac{u_1^2}{2} \ , \qquad \textbf{(3.42)}$$

where u_1 and u_2 are the velocities at the outer and inner edges of the separated shear layer, as shown in Fig. 3.3. This result may also be arrived at by considering the continuity of pressure across the vortex sheet, which requires the sheet to move locally at the mean velocity of its two surfaces. The convective velocity of the shear layer u_c is then given by

$$u_c = \frac{u_1 + u_2}{2} \ , \qquad \textbf{(3.43)}$$

and the vorticity in the sheet, $\gamma(s)$, is

$$\gamma(s) = u_1 - u_2 \ . \qquad \textbf{(3.44)}$$

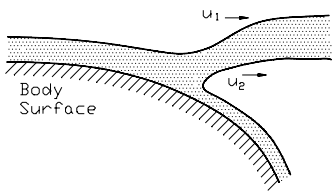

Figure 3.3. Schematic diagram of separating boundary layer.

The rate of vorticity shedding is the product of convective velocity and vorticity, i.e. $d\Gamma/dt = u_c\gamma(s)$, which reproduces Eq. (3.42). It must also be recognised that even when the separation points can be specified, the strength of the nascent vortices and the position at which they are introduced are subject to additional conditions. Vortex-shed ding from sharp-edged and smooth-profiled bodies in turn will now be discussed.

3.3.1 Vorticity Shedding from Sharp-Edged Bodies

For a sharp-edged body, fixed separation points may be assumed to be at the sharp edges. But, the nascent vortex of strength $\Delta\Gamma_o$ is introduced at a position z_o not at the separation point but close to it. The actual strength and position must be determined so that the Kutta condition is satisfied, which requires that the flow separates tangentially to the body surface at the edge. Both fixed and time-variable nascent vortex positions have been used in calculation procedures to satisfy the Kutta condition (Sarpkaya, 1975). The former approach of a fixed position involves the selection of a "suitable" point in the flow near the separation point and use of the velocity U_s at that point to evaluate the rate at which vorticity is shed into the wake from

$$\frac{d\Gamma}{dt} = \frac{1}{2} U_s^2 \ . \qquad \textbf{(3.45)}$$

This procedure, used by Clements [1973], Clements and Maull [1975] and Kuwahara [1973], allows no interaction between the shed vortices and the position of the point of appearance of the vortices. Yet, as shown by Kronauer [1964] and Gerrard [1967], the oscillation of the point of appearance of the nascent vortices influences the manner in which the wake vortex sheets roll up.

In the study of inviscid flow over an inclined plate using this discrete vortex method, Kuwahara [1973] modelled the vorticity shedding mechanism by the generation of nascent vortices of strength determined by Kutta condition, at two arbitrary fixed points near the edges of the plate. His calculation led to unrealistically high normal-force coefficient, and a parametric study of small variations in the point of appearance of the nascent vortices showed the normal-force coefficient depending strongly on the assumed positions of the two fixed points. Naylor [1982] summarises the results of a parametric study conducted by Bearman and Kamemoto [1978] to determine the effect of varying the position of introduction of nascent vortices in the flow over an inclined flat plate. Their calculations were based on a fixed position for the introduction of nascent vortices and a vortex strength adjusted to satisfy the Kutta condition at the trailing edge of the plate. They found that the flow features could be related to a non-dimensional parameter P_k defined as

$$P_k = \frac{a_s}{U_\infty \Delta t_i} \ , \qquad \textbf{(3.46)}$$

where a_s is the distance between the introduction point and the separation point on the circle in the transformed plane, Δt_i is the time interval between successive vortices. For $P_k > 0.3$, the

behaviour of the flow remained realistic. For $P_k < 0.3$, the calculated drag coefficient and the flow pattern of the vortex street were not realistic. Bearman and Kamemoto did not propose an upper bound for P_k, but tested up to $P_k = 1.9$. For $P_k > 0.3$ (and up to 1.9, the largest value tested), the numerical results compared favourably with previous theoretical results. In the latter approach, variable nascent vortex position, the strength of the nascent vortex is determined from

$$\frac{d\Gamma}{dt} = \frac{1}{2} U_{sh}^2 \qquad \textbf{(3.47)}$$

where U_{sh} is interpreted as a characteristic velocity in the free shear layers - for example the velocity at some point off the surface above the separation point intended to represent the outer edge of the boundary layer in the real fluid (Kiya *et al.* [1979] as referred to by Naylor [1982]). The position is calculated through a suitable iteration scheme, so as to maintain the Kutta condition at the edge of the body and thus it can move slightly with time. Thus this method can simulate the feedback from the wake fluctuations to the fluctuations in the rate of shedding of vorticity.

In a similar study to that of Kuwahara [1973], Sarpkaya [1975] used this procedure, taking U_{sh} as the average of the transport velocities of the first four vortices in the shear layer. His calculations showed the formation of a Karman vortex street with a Strouhal number (St = 0.154) in fair agreement with the experimental value found by Fage and Johansen [1927] (St = 0.148). The calculated force coefficient was 20–25% higher than that measured experimentally by Fage and Johansen, a result explained by Sarpkaya as a result of insufficient mixing in the wake.

Lewis [1981], in his vortex method with surface-vorticity modelling, introduces nascent vortices at a sharp edge with strength $\Delta\Gamma = \gamma(sp)^2\Delta t/2$, where $\gamma(sp)$ is the surface vorticity on the body segment just upstream of the separation point, in accord with Eq. (3.41). The surface vorticity leaves the surface tangentially with convective velocity $\gamma(sp)/2$. The point of origin of the nascent vortex is taken as the mid point of the length of the actual vorticity sheet self-convected from the separation point in the time step Δt, i.e. a point at a distance of $\gamma(sp)\Delta t/4$ from the sharp edge. Practically, the nascent vortex will be in close proximity to the separation point and will exercise undue influence over the value of $\gamma(sp)$ at the next time step $t + \Delta t$; the trajectory of the nascent vortex therefore requires adjustment in order to obtain realistic results.

3.3.2 Vorticity Shedding from Smooth-Profiled Bodies

In the case of bluff bodies with smooth profiles and without salient edges, both the position of separation point and trajectory of the separated shear layer are unknown, being determined by complex fluid motion in the boundary layer and in the vortex wake. In addition, the location of the separation points varies with the phase reached in the shedding cycle. As Gerrard [1967] found in calculations of the Karman vortex street behind a circular cylinder by the vortex method, analysis based on fixed separation points gives rise to erroneous results even when the model takes account of the velocity distribution around the body and the unsteady wake.

Sarpkaya [1968] produced a model to represent the moving separation point on a cylinder by introducing vortex at the mid-point between the first maximum o f absolute velocity encountered traversing the cylinder from the front stagnation point and the first maximum of absolute velocity on traversing the cylinder from the rear stagnation point. Calculated results agreed well with previous experimental results found by Sarpkaya [1966].

Various other schemes have been adopted by users of vortex methods to model vorticity shedding from a body surface. There is not a unique procedure for calculating the rate at which vorticity is shed into the wake. As remarked by Sarpkaya [1989], designing a numerical scheme to model the continuous process of vorticity shedding in discrete steps is not a simple matter.

3.3.3 Solution Procedure

For both the types of flow described in sections 3.3.1 and 3.3.2, the solution can be obtained by a time-stepping procedure (see, for example, Lewis 1991, Ch.8). This involves an initial potential flow solution of Eq. (3.31) as described in section 3.2, followed by the introduction of free vortices into the flow near the separation points and their convection during the time-step Δt, after which the potential flow calculation is repeated. The calculation then proceeds to the next time-step.

At all times after the initial instant at which the flow starts, there will be an additional potential-flow contribution to the velocity field due to the shed vortices, given by Eq. (2.27), and an additional term representing the component of the velocity tangential to the body surface in the

Martensen equation for the boundary condition on the body surface. Thus, when a system of Z discrete vortices $\Delta\Gamma_j$ is present in the flow, the elements b_m of the *tangential surface velocity matrix* **[*b*]** are modified to include the effect of the discrete vortices on the tangential surface velocity on the body; the element b_m of the matrix **[*b*]** has a value equal to the induced surface velocity at segment Δs_m due to the main stream and the discrete vortices, and is given by

$$b_m = -\sum_{j=1}^{Z} \Delta\Gamma_j (L_{mj} \cos\beta_m + M_{mj} \sin\beta_m) - \cos(\alpha - \beta_m) \ , \qquad \textbf{(3.48)}$$

where L_{ij} and M_{ij} denote the components in the x and y directions respectively of the dimensionless velocity induced at location (x_i , y_i) by a unit-strength vortex $\Delta\Gamma_j = 1$ located at (x_j, y_j). L_{ij} and M_{ij} are given by

$$L_{ij} = \frac{1}{2\pi}\left[\frac{y_i - y_j}{r_{ij}^2}\right] \quad , \quad M_{ij} = -\frac{1}{2\pi}\left[\frac{x_i - x_j}{r_{ij}^2}\right], \qquad \textbf{(3.49)}$$

with

$$r_{ij} = \sqrt{(x_i - x_j)^2 + (y_i - y_j)^2} \ . \qquad \textbf{(3.50)}$$

The Martensen equation in discretised form, the modified form of Eq. (3.10), can therefore be written as [Lewis 1991, Ch.8]

$$\sum_{n=1}^{M} K(s_m, s_n)\, \gamma(s_n) + \sum_{j=1}^{Z} \Delta\Gamma_j (L_{mj} \cos\beta_m + M_{mj} \sin\beta_m) + \cos(\alpha - \beta_m) = 0 \, . \qquad \textbf{(3.51)}$$

The coupling coefficient matrix **[*K*]** is again singular, and must be regularised by the imposition of an additional condition. In this case, considering the flow as impulsively started from rest, the net circulation in the flow is zero at time $t = 0$ and according to the Helmholtz theorem must remain so. This requires that

$$\sum_{n=1}^{M} \gamma(s_n) \Delta s_n + \sum_{j=1}^{Z} \Delta\Gamma_j = 0 \ , \qquad \textbf{(3.52)}$$

where the first sum accounts for the strength of the vortex sheet on the body and the second sum for the circulation of all discrete vortices in the flow domain.

Simultaneous satisfaction of the two sets of equations, Eq. (3.51) and Eq. (3.52), can be obtained by solving the set formed by their addition; the set of equations to be solved is therefore [Lewis 1991, Ch.8]

$$\sum_{n=1}^{M} [K(s_m, s_n) + \Delta s_n]\, \gamma(s_n) + \sum_{j=1}^{Z} \Delta\Gamma_j (1 + L_{mj} \cos\beta_m + M_{mj} \sin\beta_m) + \cos(\alpha - \beta_m) = 0 \, . \qquad \textbf{(3.53)}$$

The elements of the **[K^r]** matrix are therefore again formed, as in section 3.2.3, by back-diagonal correction of the elements of the **[*K*]** matrix followed by addition of Δs_n to each element of the n*th* row.

It is also to be noted that since the flow is irrotational everywhere at $t = 0$, the condition $\sum \Delta\Gamma_j = 0$ is satisfied. The potential flow solution at $t = 0$ therefore gives $\sum \gamma(s_n)\Delta s_n = 0$. If the total circulation of the discrete vortices shed within each time step is zero (i.e $\sum \Delta\Gamma_k = 0$, where k denotes the newly shed discrete vortices within each time step), $\sum \gamma(s_n)\Delta s_n$ will remain zero in all subsequent potential flow solutions. Thus, satisfaction of the condition

$$\sum_{n=1}^{M} \gamma(s_n)\Delta s_n = 0 \ , \qquad \textbf{(3.54)}$$

should be adequate to ensure satisfaction of Eq. (3.52). Then the set of equations obtained by addition of Eq. (3.51) and Eq. (3.54), namely,

$$\sum_{n=1}^{M} [K(s_m, s_n) + \Delta s_n]\gamma(s_n) + \sum_{j=1}^{Z} \Delta\Gamma_j (L_{mj}\cos\beta_m + M_{mj}\sin\beta_m) + \cos(\alpha - \beta_m) = 0 \ , \qquad \textbf{(3.55)}$$

should be exactly equivalent to Eq. (3.53). The solution procedure can be represented by the flow diagram, Fig. 3.4.

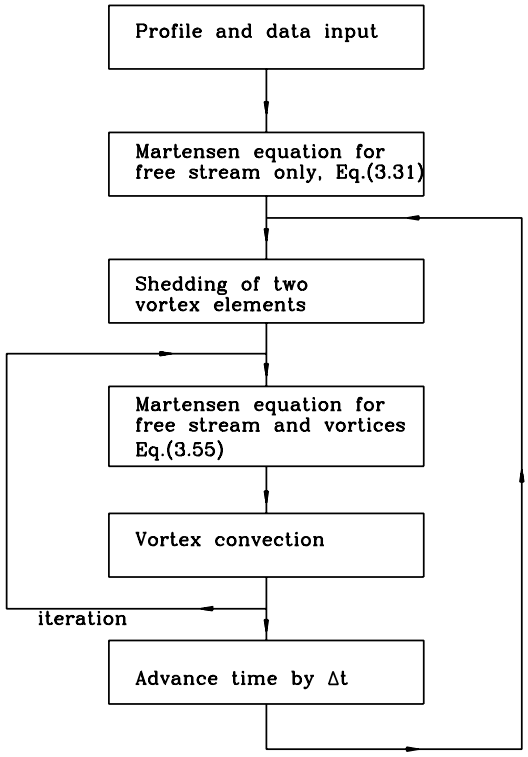

Figure 3.4. Solution procedure for inviscid flow analysis of vortex shedding from bluff bodies by discrete-vortex and surface-vorticity boundary-integral methods.

3.4 Extension of the Surface Vorticity Method to Analysis of Viscous Flow Over Bodies of Arbitrary Cross-section by Discrete Vortex Methods

3.4.1 Physical Significance of Surface Vorticity Modelling

The surface vorticity method discussed in section 3.2 is designed for analysis of potential flows, but the method provides the foundation for development of numerical schemes for rotational fluid motion, including boundary layer and wake simulation. In all real flows a boundary layer exists adjacent to any body surface, and when the viscosity of the fluid is non-zero the no-slip condition of zero tangential velocity must be satisfied at the solid surface. Sufficient vorticity is then present within the boundary layer to reduce the fluid velocity from its value outside the layer to zero at the boundary. Inviscid potential flow can be considered as the limiting case of real flow at infinite Reynolds number in which the boundary layer is of infinitesimal thickness. In this case the boundary layer becomes an infinitely thin sheet of vorticity, across which the fluid velocity experiences a discontinuity from zero at the boundary to the potential-flow value just outside the vortex sheet.

It can be observed that this condition is exactly that which is set up by the surface vorticity model for potential flow considered earlier in section 3.2, namely a flow satisfying the no-slip condition at body surfaces and with any solid body having a boundary layer of infinitesimal thickness (i.e. a vortex sheet) enveloping its surface. Two further observations are pertinent. The first is that the potential flow model of section 3.2 is truly representative of the initial state of a real flow started impulsively from rest; the second is that in a real (two-dimensional) flow vorticity is created only at solid boundary surfaces, and is diffused into the flow from the *entire* boundary surface (in contrast to the localised shedding of vorticity considered in section 3.3) under the action of viscosity. Since the surface vorticity model correctly sets up the initial surface vortex sheet which is physically representative of an impulsively-started flow, it can be expected that if a physically realistic extension to the model can be made to take account of boundary layer formation by diffusion of this vorticity into the flow and its subsequent convection, then the model should give a valid representation of the development of a real viscous flow. It is, as observed by Lewis [1991, Preface], considerations such as these, that the models can correctly represent the vortical nature of real flows, which make surface vorticity and discrete vortex methods attractive.

A complete numerical scheme for viscous flow analysis by vortex methods; i.e. to obtain a solution to the Navier-Stokes equation rather than the Euler equations, thus requires the additional modelling of the continuous creation of vorticity and its evolution in the flow. The procedures adopted for viscous flow modelling by the surface vorticity method therefore follow the discretisation procedure set out for potential flow analysis in section 3.2, with the addition of a discrete vortex approximation to the continuous vorticity field which forms around a body and in its wake in a real flow. In this way, inviscid potential-flow analysis can still be used to calculate the velocity field of the flow at each stage of the time-stepping procedure used to obtain the solution for the flow development. At any stage in the calculation, the flow is modelled as a body surrounded by a vortex sheet and with a number (which increases with time) of discrete vortices in the flow representing the process of vorticity diffusion from the body surface, after its creation there and subsequent convection past the body and into the wake.

3.4.2 Simulation of Vorticity Creation

In a real flow, which can be considered to be started impulsively from rest, a sheet of surface vorticity is created in the starting process and this vorticity immediately begins to diffuse away from the body surface. At any subsequent instant the resulting vorticity distribution in the flow determines the velocity field and the normal vorticity gradient at the body surface, and hence the rate of diffusion of vorticity away from the body surface at that instant; the generation of vorticity at the body surface and diffusion of vorticity away from the surface occur simultaneously and continuously. In the numerical model, the distributed vorticity in the surface vortex sheet generated when the flow is impulsively started from rest is approximated by a set of discrete vortices on the body surface. These vortices are considered to be shed ("diffused") into the flow in the first time-step. Their induced (potential-flow) velocity field at the end of the first time-step will give a new slip velocity at the body surface, which must be accommodated by a surface vortex sheet with a new distribution of vorticity; this vortex sheet is discretised, and shed into the flow as discrete vortices in the next time step. This process is then repeated for all ensuing time-steps.

As in the case of vortex shedding from bluff bodies considered in section 3.3, at all times after the initial instant at which the flow starts, there will be an additional potential-flow contribution to the velocity field due to the shed vortices, given by Eq. (2.27), and an additional term

representing the component of the velocity tangential to the body surface in the Martensen equation Eq. (3.17) for the boundary condition on the body surface. The matrix **[*b*]** therefore again takes the modified form given by Eq. (3.48), and the modified Martensen equation in discretised form takes the form of Eq. (3.51), repeated here for completeness,

$$\sum_{n=1}^{M} K(s_m, s_n)\,\gamma(s_n) + \sum_{j=1}^{Z} \Delta\Gamma_j (L_{mj}\cos\beta_m + M_{mj}\sin\beta_m) + \cos(\alpha - \beta_m) = 0\,, \qquad \textbf{(3.56)}$$

with L_{ij}, M_{ij} and r_{ij} given by equations Eq. (3.49) and Eq. (3.50), and $\Delta\Gamma_j$ representing the strengths of all discrete vortices previously shed from the body into the flow.

Since the discrete vortices and the uniform free-stream induce zero circulation around the body, Eq. (3.24) applies, and as in the previous cases considered, the *coupling coefficient matrix* **[*K*]** is singular; it must be regularised before the calculation can yield a unique solution for **[**γ**]**. Regularisation can be effected by making use of the condition for conservation of vorticity expressed by Eq. (3.52). As indicated above, diffusion into the flow of vorticity created at the body surface is modelled by replacing the vorticity distribution $\gamma(s_n)$ existing on each body segment of length Δs_n at the end of a given time-step by a discrete vortex of strength $\Delta\Gamma_n = \gamma(s_n)\Delta s_n$, and introducing the resulting discrete vortices into the flow at the beginning of the next time-step. Since initially $\sum\gamma(s_n)\Delta s_n = 0$ in a flow started impulsively from rest, it follows that $\sum\Delta\Gamma_n = 0$ in the first time step, and hence that throughout the calculation

$$\sum_{n=1}^{M} \gamma(s_n)\Delta s_n = 0 \qquad \textbf{(3.57)}$$

and

$$\sum_{j=1}^{Z} \Delta\Gamma_j = 0\,, \qquad \textbf{(3.58)}$$

where the latter summation is over all discrete vortices shed in the flow domain since $t = 0$. Hence, as in section 3.3.3, either Eq. (3.52) or Eq. (3.54) will ensure conservation of vorticity, in which case either Eq. (3.53) or Eq. (3.55) can yield the required solution.

It should be noted that if the conditions represented by Eq. (3.57) and Eq. (3.58) be satisfied, the modified Martensen equation in the form

$$\sum_{n=1}^{M} \left[K(s_m, s_n) + \Delta s_n\right]\gamma(s_n) + \sum_{j=1}^{Z} \Delta\Gamma_j (L_{mj}\cos\beta_m + M_{mj}\sin\beta_m) + \cos(\alpha - \beta_m) = 0 \qquad \textbf{(3.59)}$$

will give a unique solution for **[**γ**]** which satisfies the no-slip condition at the solid surface and the condition of zero net circulation of the vortex sheet created.

However, as will be seen later in section 3.4.7, some qualification of these considerations is required when the procedures for modelling diffusion by the motion of discrete vortices are developed. The way in which conservation of vorticity is taken into account will then be reconsidered.

3.4.3 Flow Simulation

We have to consider how the introduction of vorticity into the flow by diffusion from the solid boundaries, and its subsequent diffusion and convection within the flow can be represented in a discretised form suitable for numerical calculations. As already pointed out, in real viscous flows these processes occur simultaneously. Modelling of this simultaneous motion leads to extreme difficulties in numerical schemes and a widely used approach is to treat the effects of introduction of discrete vortices (equivalent to shedding of vorticity from the body surfaces), convection of vorticity, and diffusion sequentially rather than simultaneously.

For the sequential treatment of convection and diffusion, Chorin [1973] proposed the so-called *operator splitting method* to approximate the vorticity formulation of the Navier-Stokes equation i.e. the vorticity transport equation Eq. (2.22). According to this equation, the rate of change of vorticity $\partial\omega/\partial t$ consists of two distinct parts :

i) vorticity convection in the velocity field determined kinematically by the instantaneous vorticity field, and

ii) vorticity diffusion in the fluid by the action of viscosity.

The principle involved is to split the advective-diffusion motion in each time step into two fractional steps. The first step involves (inviscid) convection of vorticity according to the convection equation

$$\frac{D\omega}{Dt} = \partial_t \omega + \boldsymbol{u}\cdot\nabla\omega = 0 \ , \qquad \textbf{(3.60)}$$

without viscous diffusion. The second step involves diffusion of vorticity in the fluid without convection, to satisfy the diffusion equation

$$\partial_t \omega = \frac{1}{Re}\nabla^2\omega \ . \qquad \textbf{(3.61)}$$

An additional consideration which arises in practice is the distribution of vorticity associated with a discrete vortex. In the preceding considerations, it has been implicitly assumed that the discrete vortices are point vortices. However, the singularity of the point vortex leads to unrealistically high induced velocities at points close to the vortex, and experience indicates that the singularity must be removed before calculations can yield valid results.

3.4.4 Model Vortices

The problem of the velocity field singularity of a point vortex leads to the use of a modified vortex structure, with finite core, so that the velocity in the vortex remains finite even at the vortex center. Various vortex structures are discussed by Leonard [1980]. Chorin [1973] used a vortex with velocity distribution given by

$$v_\theta = \frac{\Gamma}{2\pi r} \qquad (r \geq \sigma)$$
$$v_\theta = \frac{\Gamma}{2\pi \sigma} \qquad (r < \sigma) \tag{3.62}$$

where σ is the radius of the vortex core. Chorin further pointed out that an array of such vortices, to some extent, retains the properties of the vortex sheet which it represents, in that the velocity field is bounded and changes direction abruptly at the vortex centre.

The velocity distribution of a Rankine vortex

$$v_\theta = \frac{\Gamma r}{2\pi \sigma^2} \qquad (r < \sigma)$$
$$v_\theta = \frac{\Gamma}{2\pi r} \qquad (r \geq \sigma) \tag{3.63}$$

has been used by Lewis [1991, Ch.9]. A further alternative employed by Leonard [1980] is the Gaussian vorticity distribution

$$\omega(r) = \frac{1}{\pi \sigma^2} \exp\left(\frac{-|r|^2}{\sigma^2}\right) \tag{3.64}$$

where σ is a measure of the size of the vortex core, which satisfies the viscous diffusion equation for an isolated vortex.

3.4.5 Simulation of Vorticity Shedding into the Flow from Boundary Surfaces

Two methods have generally been used to model the introduction into the flow of vorticity created on a body surface, in its representational form of discrete vortices : simulation of direct diffusion from the surface, and the offset method. These procedures are discussed by Lewis [1991, Ch.9].

In the first case, discrete vortices can be introduced directly into the flow by the model diffusion process which is adopted (such as the random walk which will be discussed later).

Alternatively, the vortices representing the surface vorticity can be introduced by the *offset method* whereby these vortices are placed initially at a finite distance above the surface. This method is similar to that used for introduction of nascent vortices in shedding from sharp-edged bodies (as discussed in section 3.3). For Chorin's vortex (section 3.4.4 above), the no-slip condition at the solid surface is maintained, at least locally, if the vortices are introduced at a distance ϵ above the surface given by $\epsilon=\sigma=\Delta s/2\pi$. Porthouse [1983] proposed $\epsilon=\sqrt{(4\upsilon\Delta t/3)}$ (or $\epsilon = \sqrt{(4\Delta t/(3Re))}$ in dimensionless form), for time-stepping with period Δt.

3.4.6 Simulation of Vorticity Convection and Diffusion within the Flow

According to the *operator splitting method* as discussed in section 3.4.3, the simultaneous motion of convection and diffusion is modelled sequentially during each time step of the calculation. In the first fractional step, the vortices are subject to inviscid convection determined by the local velocity field at their present locations. The velocity field can be computed by using the Biot-Savart equation Eq. (2.30), or as the solution to the Poisson equation for the stream function

$$\nabla^2\psi = -\omega \ , \qquad \textbf{(3.65)}$$

where the velocity components are given by $u = \partial\psi/\partial y$ and $v = -\partial\psi/\partial x$. Once the velocity field has been determined, the new vortex positions can be calculated by using, for example, the simple forward difference scheme as depicted in Eq. (3.67) below.

The second fractional step is the simulation of viscous diffusion of vorticity. The most commonly used method of modelling the diffusion of vorticity is the *random-walk* method. The

mathematical representation of the scheme, due to Chorin [1973], is then as follows:

$$x_i^{k+1} = x_i^k + \Delta t\, u^k + \eta_1 ,$$
$$y_i^{k+1} = y_i^k + \Delta t\, v^k + \eta_2 , \qquad \textbf{(3.66)}$$

with (u^k, v^k) denoting the velocity field corresponding to the vortex position (x^k, y^k). After the first fractional step, the vortices will arrive at the intermediate position (x_c^{k+1}, y_c^{k+1}) given by $(x^k, y^k) + \Delta t(u^k, v^k)$ which is a solution to the convection equation Eq. (3.61) (as discussed in section 3.4.3 above). The final vortex position (x^{k+1}, y^{k+1}) at the end of the time-step is obtained by adding to (x_c^{k+1}, y_c^{k+1}) the random walk components η_1 and η_2 in the x and y directions respectively. These random walk components are represented by Gaussianly distributed random variables with zero mean and variance $2\Delta t/Re$, Δt being the time step. The vorticity distribution in the x-y plane after k discrete time steps is expressed in terms of x_i^k and y_i^k, where $x_i^k \equiv x_i(k\Delta t)$ and $y_i^k \equiv y_i(k\Delta t)$. This is a robust algorithm which does not require any spatial differentiation, and retains the advantage of being grid-free. Long [1988] proved that this scheme converges to the exact flow equations.

Porthouse and Lewis [1981] developed a similar random walk technique based on Monte Carlo simulation. The random walk of a vortex is given by two independent components, the radial drift Δr and angular displacement $\Delta\theta$, where

$$\Delta r = \sqrt{\frac{4\,\Delta t}{Re} \ln P^{-1}} ,$$
$$\Delta\theta = 2\pi Q \quad . \qquad \textbf{(3.67)}$$

P and Q are random numbers in the range from 0 to 1. The displacements of the vortex in the x and y directions are then given by

$$\eta_1 = \Delta r \cos(\Delta\theta) ,$$
$$\eta_2 = \Delta r \sin(\Delta\theta) . \qquad \textbf{(3.68)}$$

As a preliminary calculation in the present work, a numerical experiment has been carried out to compare Porthouse and Lewis's random walk with that of Chorin. A population of two thousand point vortices was subjected to the random walk in accordance with Eq. (3.67) and Eq. (3.68). The mean values of the random displacements, η_1 and η_2, were very close to zero, and the variance agreed with the value $2\Delta t/Re$ as proposed by Chorin. We may conclude that the random walk of Chorin and of Porthouse and Lewis are identical, and can be used interchangeably.

An alternative scheme to represent viscous diffusion is that proposed by Leonard [1980], to account for vortex core spreading. The method is based on a vortex with the Gaussian vortex core as specified in section 3.4.4. In this case the core radius σ is allowed to grow in size in order to satisfy the equation

$$\frac{D\omega}{Dt} = \upsilon \nabla^2 \omega \ , \tag{3.69}$$

where υ is kinematic viscosity. This requires σ^2 to grow linearly in time as

$$\frac{d\sigma^2}{dt} = 4\upsilon \ . \tag{3.70}$$

Leonard's core spreading method exactly satisfies the equation for vorticity diffusion of a single isolated point vortex. However, this meth od fails to represent the viscous diffusion of vorticity macroscopically: it was proved by Greengard [1985] that the core spreading technique does not correctly approximate the Navier-Stokes equation.

3.4.7 Treatment of Vortices which Enter the Interior of the Body Contour

It was indicated in section 3.4.2 that the procedure used for modelling viscous diffusion might require reconsideration of the way in which conservation of vorticity is satisfied. This requirement arises because some vortices, predominantly as a result of the random walk but sometimes as a result of inaccuracies in the convection scheme used, take up positions within the body contour. The Martensen equation requires that there be no vortex or source distributions within the body contour. Discrete vortices which enter the interior of the contour must therefore be removed, and in such a way that the conservation of vorticity is maintained.

There are two possible treatments which may be used to deal with these vortices, namely *vortex reflection* and *vortex annihilation*.

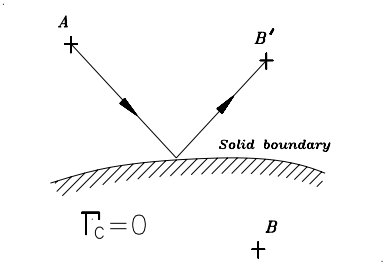

Figure 3.5. Schematic represenation of *vortex reflection.*

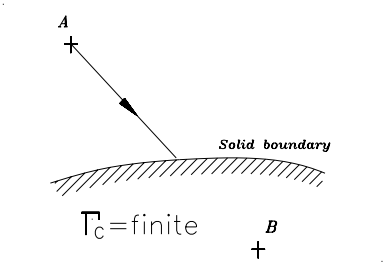

Figure 3.6. Schematic representation of *vortex removal.*

Vortex Reflection – Any discrete vortex which is found inside the contour, say at position B as shown in Fig. 3.5, is replaced by a vortex reflected from the solid boundary into the flow domain at position B'. In this way, the number of discrete vortices Z in the flow domain remains equal to the number shed from the body since time $t = 0$, and the total circulation of these vortices remains zero throughout. In this case, the conditions of Eq. (3.57) and Eq. (3.58) are met, and therefore equation Eq. (3.59) applies.

Vortex Annihilation – When any discrete vortex $\Delta\Gamma_j$ comes within the contour, say at position B, Fig. 3.6, it is removed permanently from the flow domain i.e. annihilated, and the total number of Z discrete vortices in the flow domain is reduced by Z_d the number of discrete vortices which enter the contour in a given time-step. The net total circulation of the discrete vortices in the flow (i.e. those vortices outside the contour) is also reduced by an amount Γ_c equal to the net strength of these Z_d discrete vortices. Thus, for vorticity to be conserved, the net circulation of these vortices,

$$\Gamma_c = \sum_{j=1}^{Z_d} \Delta\Gamma_j \ , \qquad \textbf{(3.71)}$$

must be restored to the external flow. This is achieved by redistributing the circulation Γ_c in the vortex sheet on the body contour, where its contribution to the strength of the vortex sheet will be given by

$$\sum_{n=1}^{M} \gamma(s_n)\Delta s_n = \sum_{j=1}^{Z_d} \Delta\Gamma_j = \Gamma_c \ . \qquad \textbf{(3.72)}$$

this implies that when the Martensen equation for the condition of zero fluid velocity at the solid surface is applied at the beginning of the next time-step to determine the strength of the new vortex sheet, it must be applied to a body which temporarily has a non-zero circulation of Γ_c.

By using the mathematical technique discussed in section 3.2.3, Eq. (3.72) for the circulation around the body contour can be used to regularise the coupling coefficient matrix in the basic Martensen equation, Eq. (3.56). The two sets of equation, Eq. (3.56) and Eq. (3.72) can be simultaneously satisfied by solving the set resulting from their addition. The set of equations to be solved is therefore

$$\sum_{n=1}^{M} \left[K(s_m, s_n) + \Delta s_n\right]\gamma(s_n) + \sum_{j=1}^{Z} \Delta\Gamma_j\left(L_{mj}\cos\beta_m + M_{mj}\sin\beta_m\right) + \cos(\alpha - \beta_m) - \Gamma_c = 0 \ . \qquad \textbf{(3.73)}$$

In Eq. (3.73), the discrete vortices $\Delta\Gamma_j$ for $j = 1,2,...Z$ in the second summation term are those vortices shed from the body and remaining outside the body contour. The circulation of the Z_d discrete vortices which moved inside the contour and were annihilated is represented by the term Γ_c.

When the vorticity of the vortex sheet as given by Eq. (3.73) is shed into the flow as discrete vortices $\Delta\Gamma_n = \gamma(s_n)\Delta s_n$, there will be an addition of circulation of amount Γ_c to the flow. In this way, the circulation of the Z_d discrete vortices which were previously annihilated is restored in the form of newly shed discrete vortices, and therefore the total vorticity of the system is conserved.

In these considerations, the numerical procedure for the conservation of vorticity is focused on the balance between the annihilation and generation of vorticity on the body. Since vorticity is created only at the surface of the solid body, and it is conserved at the source, then it must also be conserved for the entire system. This is an important factor to be considered when dealing with multi-body systems. In such cases, the equation of vorticity conservation for the whole system is not adequate to ensure unique solutions for $[\gamma]$ on each body in the multi-body array, and the condition of circulation for each individual body must be used to regularise the singular matrix $[K]$.

Finally, it should be noted that, as far as the solution of Eq. (3.73) is concerned, the circulation Γ_c around the body contour can have any finite value, zero or non-zero. If no discrete vortices move inside the body contour, as happens in the *vortex reflection* scheme, the circulation $\Gamma_c = 0$. In such case, Eq. (3.73) is reduced to Eq. (3.59). Therefore, Eq. (3.73) can be considered as a general equation which is applicable in conjunction with either the *vortex reflection* or the *vortex annihilation* scheme, with an appropriate assigned value of Γ_c.

3.4.8 Treatment of Vortices in Close Proximity to the Body Surface

The approximation of the body contour by discrete segments for calculation purposes, in conjunction with vortices close to the contour, can introduce significant numerical errors. In the exact potential flow solution for a body in a uniform main stream containing discrete vortices outside the body contour, the free stream and each discrete vortex induce zero circulation around the body contour. Thus equation Eq. (3.28), i.e. $\sum b_n \Delta s_n = 0$, applies in this

case also. (Note that the condition of zero induced circulation around a contour inside the vortex sheet, due to the vortex sheet itself, has been enforced by the back-diagonal correction as in section 3.2.2).

However, in the numerical calculation, this condition on the b_n is not always satisfied due to segmentation of the body. The velocity induced on a contour segment by a vortex is represented by a single value at the collocation point, and when this value represents a large variation in induced velocity over the length of the segments, errors in calculation can occur. The error is particularly severe for vortices in close proximity to the body - at a distance from the contour which is small compared with a segment length. This implies a spurious non-zero bound circulation around the body, and this kind of numerical error is often referred to as *numerical vorticity leakage*, Lewis [1991, Ch.8]. The consequences of *numerical vorticity leakage* are that the condition of vorticity conservation is upset and that the distribution of $\gamma(s_n)$ around the contour is distorted. This leads to errors in the strengths $\Delta\Gamma_j$ of the shed vortices, distortion of the resulting flow field and erroneous prediction of pressure forces on the body.

The expression $(L_{ij}\cos\beta_m + M_{ij}\sin\beta_m)$ established in Eq. (3.48) represents the component of the induced velocity tangential to the body surface at segment Δs_m by a positive unit-strength vortex at a point z_j on the complex plane. Therefore the circulation Γ_i induced around the contour by a unit positive vortex can then be expressed in numerical form as

$$\Gamma_i = \sum_{m=1}^{M} (L_{mj}\cos\beta_m + M_{mj}\sin\beta_m)\,\Delta s_m \quad . \qquad \textbf{(3.74)}$$

A preliminary study has been made in the present work aiming to determine how the proximity of a vortex affects the induced circulation Γ_i and to obtain some indication of the magnitude of circulation errors introduced. The general behaviour is that the ideal condition, i.e. $\Gamma_i = 0,\ 1/2,\ 1$ according as the vortex is outside, on, or inside the contour, is achieved when the vortex is exactly on the contour or far away from it on either side. When the vortex is close to the contour, the calculated circulation deviates substantially from the theoretical value. These considerations show that it is imperative in the calculation procedure to enforce zero induced circulation around the body contour in order to maintain the conservation of vorticity and the closure of surface pressure distribution.

The procedure recommended by Lewis [1991 Ch.8] is very similar to the back-diagonal correction Eq. (3.6) to the coupling coefficient matrix to ensure zero induced circulation around the contour. It entails correcting the induced velocity on the body segment closest, say Δs_p, to the vortex to a value given by

$$(L_{pj} \cos \beta_p + M_{pj} \sin \beta_p) \Delta s_p = -\sum_{\substack{n=1 \\ n \neq p}}^{M} (L_{nj} \cos \beta_n + M_{nj} \sin \beta_n) \Delta s_n \ . \qquad \textbf{(3.75)}$$

3.4.9 Merging of Vortices

Experience with calculation procedures of the type being considered shows that there are situations in which merging of two or more discrete vortices is desirable. A discussion of amalgamation of vortices is given by Sarpkaya [1989]. The two main reasons for merging are: i) to avoid vortices inducing excessively high velocities on each other due to their singular nature; and ii) to reduce computing time. The first reason has already been referred to in section 3.1. The second reason relates to the fact that to solve a problem of unsteady separated flows requires calculation of the velocity fields induced by the entire system of vortices at each time step. This involves calculating the effect of each vortex on every other vortex in the field in each time step; if the field contains Z vortices the number of calculations required is of order $O(Z^2)$. Since the number of vortices Z in the flow field grows continuously, the computing time soon becomes prohibitive unless some action is taken to reduce the total number of vortices.

The numerical strategy for vortex merging is based on the fact that the velocity field about the bluff body is mainly affected by the vortices in the boundary layer and those in the vortex wake immediately downstream of the body, and that the velocity field induced by a vortex decreases with the square of the distance from it, as given by Eq. (2.27). Therefore, as the vortices move downstream away from the bluff body, their influence on the body diminishes rapidly. In order to save computing time it is expedient to combine remote vortex clusters into single vortices. Vortex merging can be accomplished by searching for pairs of nearby vortices, for which the distance between two or more vortices is less than a prescribed merging distance r_c, in which case they are combined into to a single vortex. The coordinates of the combined vortex (x_c, y_c) recommended by Deffenbaugh and Marshall [1976] and used by Porthouse [1983] are based

on the magnitudes of the merging vortices as given by

$$x_c = \frac{\sum_{j=1}^{k} |\Delta\Gamma_j| x_j}{\sum_{j=1}^{k} |\Delta\Gamma_j|}, \qquad y_c = \frac{\sum_{j=1}^{k} |\Delta\Gamma_j| y_j}{\sum_{j=1}^{k} |\Delta\Gamma_j|}; \tag{3.76}$$

its strength equals the algebraic sum of circulations of the k discrete vortices being combined, i.e.

$$\Delta\Gamma_c = \sum_{j=1}^{k} \Delta\Gamma_j , \tag{3.77}$$

so that the merging process conserves the total circulation in the system. Since the effect of a vortex on the bluff body diminishes with the distance x of the vortex from the body, the merging distance r_c can be increased for remote vortex clusters. Lewis [1991, Ch.11] suggests the following merging arrangement

(i) for $x < 1.5L$, merge if $r_c \le \sigma$
(ii) for $1.5L < x < 4L$, $r_c \le 3\sigma$
(iii) for $4L < x$, $r_c \le 5\sigma$,

where L denotes the characteristic length of the system and σ the radius of the vortex core. Systematic study has revealed that the computing time required for the merging process is strongly affected by the efficiency of searching procedure. When the cell-to-cell method (CTC) is in use, the search for vortex pairs can take advantage of the CTC mesh system.

Further saving in computing load can be achieved by permanent removal from the flow field of those vortices which are at a great distance from the body. The total circulation Γ_s of the vortices eliminated is accounted for to keep track of the vorticity conservation in the system. In this case, the equation for the conservation of vorticity becomes

$$\sum_{n=1}^{M} \gamma(s_n)\Delta s_n + \sum_{j=1}^{Z} \Delta\Gamma_j + \Gamma_s = 0 . \tag{3.78}$$

The circulation $(\sum\Delta\Gamma_j + \Gamma_s)$ can be regarded as the total strength of discrete vortices in an infinite flow domain D_∞. Outside the active flow domain D the remote vortices have negligible effect on the flow field around the body, and therefore are ignored in the calculation. It should be noted that Eq. (3.92) does not enter into the numerical scheme but is simply used for monitoring the vorticity conservation in the system.

3.5 Calculation of Pressure Distribution in Discrete Vortex Methods

The numerical procedures discussed so far have been directed to the simulation of the motion of vorticity in viscous flow over solid bodies, as approximate solution of the Navier-Stokes equations. If they do indeed represent genuine solutions to the Navier-Stokes equations, they should also allow evaluation of pressure field and thus aerodynamic forces acting on the bluff bodies. However, as can be seen from the vorticity transport equation, which is equivalent to the Navier-Stokes equation in vorticity formulation, the pressure term has been eliminated from it. Therefore the calculations by the discrete vortex methods do not yield the pressure field directly. The pressure field is deduced from the evolution of the vorticity field which is given directly from discrete vortex calculations.

In the absence of any external force, the Navier Stokes equation (2.11) for an incompressible flow can be rewritten as

$$\frac{1}{\rho}\nabla p_o = (\boldsymbol{u} - \upsilon\nabla)\times\omega - \frac{\partial \boldsymbol{u}}{\partial t}, \qquad \textbf{(3.79)}$$

where use has been made of the vector identity

$$\nabla^2\boldsymbol{u} \equiv \nabla(\nabla\cdot\boldsymbol{u}) - \nabla\times(\nabla\times\boldsymbol{u}) \quad . \qquad \textbf{(3.80)}$$

Given a vorticity field ω and its evolution with time, the velocity field $\boldsymbol{u}$ and its time derivatives $\partial_t\boldsymbol{u}$ at any point can be obtained and hence Eq. (3.79) can be integrated to give the total pressure p_o at any point. In the present model, with the continuous vorticity field represented by a system of discrete vortices, the pressure field is a function of the motion of discrete vortices. In the flow domain the vorticity $\omega = 0$ except at the vortex singularities. Eq. (3.79) is therefore reduced to

$$\frac{1}{\rho}\nabla p_o = -\frac{\partial \boldsymbol{u}}{\partial t} \quad . \qquad \textbf{(3.81)}$$

Thus, ∇p_o can be obtained by evaluation of the time derivative of the velocity field $\partial_t\boldsymbol{u}$. Given the vorticity field at two distinct time instants, say $\omega(t)$ and $\omega(t+\Delta t)$, we are able to construct the associated velocity fields $\boldsymbol{u}(t)$ and $\boldsymbol{u}(t+\Delta t)$ and hence the time derivative of velocity field $\partial_t\boldsymbol{u}$ by finite difference methods, i.e. $[\boldsymbol{u}(t+\Delta t)-\boldsymbol{u}(t)]/\Delta t$. In the present numerical scheme, with the trajectories of discrete vortices being tracked, the evolution of the velocity field is a function of the motion of the discrete vortices, and $\partial_t\boldsymbol{u}$ can be derived directly from the vortex motion.

Expressing the velocity field $\boldsymbol{u}$ at a point (x,y) in terms of the uniform free stream velocity $\boldsymbol{U}_\infty$ and the vorticity field in the flow domain, which includes the effects of surface vorticity $\gamma \Delta s$ on solid boundaries and the discrete vortices $\Delta\Gamma_j$ in flow domain, we have

$$\boldsymbol{u} = \boldsymbol{U}_\infty + \sum_{j=1}^{Z} \frac{\Delta\Gamma_j}{2\pi r_j^2}\left[(y-y_j), -(x-x_j)\right] + \sum_{m=1}^{M} \frac{\gamma_m \Delta s_m}{2\pi r_m^2}\left[(y-y_m), -(x-x_m)\right] \quad , \tag{3.82}$$

where $r_j^2 = (x-x_j)^2 + (y-y_j)^2$, $r_m^2 = (x-x_m)^2 + (y-y_m)^2$, (x_m, y_m) denotes the coordinates of the pivotal point on segment s_m and γ_m is the solution of the Martensen equation corresponding to the system of Z discrete vortices at their current positions. Note that Eq. (3.82) describes a velocity field in which the boundary conditions on solid boundaries are satisfied. This is because the surface vorticity sheet γ_m has been created by the Martensen equation corresponding to the current vortex positions.

Eq. (3.82) can be differentiated with respect to time to give $\partial_t \boldsymbol{u}$ the time derivative of the velocity field. However, before the differentiation is carried out, a few comments regarding the solution procedures of the present numerical model for viscous flow past solid bodies, described in previous sections, are in order. Consider the beginning of a certain time step to be the instant just after shedding of surface vorticity γ_m into the flow domain. The entire vorticity field $\omega(t)$ then consists of a system of Z discrete vortices at positions (x^k, y^k), where Z includes the nascent vortices equivalent to the surface vorticity sheet which have just been shed from the surface. At this particular moment, the surface vorticity sheet has vanished, i.e. $\gamma_m = 0$. However, the boundary conditions are still satisfied because the nascent vortices are effectively equivalent to the surface vorticity sheet.

Evolution of this system of Z discrete vortices by convection and diffusion, over the duration of a timestep Δt, brings the discrete vortices to their new positions (x^{k+1}, y^{k+1}). Corresponding to these new vortex positions (x^{k+1}, y^{k+1}), a new surface vorticity sheet is created to restore the boundary condition at solid boundaries. It is conceptually correct to consider the surface vorticity sheet being changed from zero to a finite non-zero value over the duration of a timestep Δt. As a result of the motion of these Z discrete vortices and the creation of new

surface vorticity sheet, the entire vorticity field has evolved from $\omega(t)$ to $\omega(t+\Delta t)$, and the appropriate boundary conditions have been restored at solid boundaries in readiness for the next time step. At this point, the final instant in the time step, the newly created surface vorticity sheet is shed into the flow domain as nascent vortices at the very beginning of the next time step. It is at this moment that the system of Z discrete vortices is increased by the number of nascent vortices; Z remains constant throughout the remainder of the timestep.

It should be noted that the creation of surface vorticity on solid boundaries is associated with the motion of discrete vortices; and that the surface vorticity γ_m is the only quantity of vorticity that changes with time; the circulation of discrete vortices $\Delta\Gamma_j$ in the flow field remains constant. Thus, it follows that the time derivative of the velocity field of Eq. (3.82) is given by

$$\frac{\partial \boldsymbol{u}}{\partial t} = \frac{1}{2\pi}\sum_{j=1}^{Z}\Delta\Gamma_j\frac{d}{dt}\left(\frac{1}{r_j^2}\left[(y-y_j),-(x-x_j)\right]\right) + \frac{1}{2\pi}\sum_{m=1}^{M}\frac{d\gamma_m}{dt}\frac{\Delta s_m}{r_m^2}\left[(y-y_m),-(x-x_m)\right]. \qquad \textbf{(3.83)}$$

Carrying out the differentiation within the first summation on the right-hand side of Eq. (3.83) and simplifying, we have

$$\frac{d}{dt}\left(\frac{1}{r_j^2}\left[(y-y_j),-(x-x_j)\right]\right) = \frac{1}{r_j^4}\begin{bmatrix}2(x-x_j)(y-y_j)v_{xj}-[r_j^2-2(y-y_j)^2]v_{yj}\\ [r_j^2-2(x-x_j)^2]v_{xj}-2(x-x_j)(y-y_j)v_{yj}\end{bmatrix}, \qquad \textbf{(3.84)}$$

where $v_{xj} = dx_j/dt$ and $v_{yj} = dy_j/dt$ are the transport velocities in the x- and y-direction respectively of discrete vortices $\Delta\Gamma_j$ from their initial positions (x^k, y^k) at the beginning of a timestep to the final positions (x^{k+1}, y^{k+1}) at the end of that timestep. This transport velocity of vortex motion is the result of both convection and diffusion and is generally different from the local flow velocity at vortex position as denoted by (u^k, v^k) in Eq. (3.66).

It is clear that the transport velocity $\boldsymbol{V}_j = (v_{xj}, v_{yj})$ of discrete vortex $\Delta\Gamma_j$ is given by

$$\begin{aligned} \boldsymbol{V}_j = [v_{xj}, v_{yj}] &= \left[\frac{x_j^{k+1} - x_j^{k}}{\Delta t}, \frac{y_j^{k+1} - y_j^{k}}{\Delta t} \right] \\ &= \left[u^{k} + \frac{\eta_1}{\Delta t}, v^{k} + \frac{\eta_2}{\Delta t} \right], \end{aligned} \tag{3.85}$$

where η_1 and η_2 are random-walk displacements in the x- and y-direction respectively as given by Eq. (3.68). Substitution of Eq. (3.83) and (3.84) into Eq. (3.81) gives

$$\begin{aligned} -\frac{1}{\rho}\nabla p_o = \frac{\partial \boldsymbol{u}}{\partial t} &= \frac{1}{2\pi} \sum_{m=1}^{M} \frac{d\gamma_m}{dt} \frac{\Delta s_m}{r_m^2} [(y-y_m), -(x-x_m)] \\ &+ \frac{1}{2\pi} \sum_{j=1}^{Z} \Delta\Gamma_j \frac{1}{r_j^4} \begin{bmatrix} 2(x-x_j)(y-y_j)v_{xj} - [r_j^2 - (y-y_j)^2]v_{yj} \\ [r_j^2 - 2(x-x_j)^2]v_{xj} - 2(x-x_j)(y-y_j)v_{yj} \end{bmatrix}. \end{aligned} \tag{3.86}$$

With the knowledge of the derivative $\partial_t \boldsymbol{u}$ and hence the pressure gradient ∇p_o, one may compute the total pressure at any point by integrating Eq. (3.86) numerical ly by finite difference methods. In this case, it is vital to form a finite difference mesh system large enough to establish a reasonable boundary condition (i.e. total pressure at infinity $p_o = p_\infty + \frac{1}{2}\rho U_\infty^2$) and to use a finite difference step size small enough to reveal detail in regions of high pressure gradient as well as to minimise numerical error. These constraints on finite difference methods make direct numerical integration of Eq. (3.81) very inefficient in terms of computing time.

Alternatively, integration of Eq. (3.86) can be carried out analytically to give the total pressure distribution in the flow field. The two sums on the right-hand side of Eq. (3.86) relate the total pressure distribution to the change of surface vorticity with time and to the transport of vorticity in the flow, and will be treated separately.

It is worth noting that the moving vorticity in the flow domain is the principal source of change in the total pressure distribution in the flow, and that the surface vorticity on solid boundaries reacts dynamically to this moving vorticity in order to maintain the appropriate boundary conditions on solid surfaces: this is the essence of the present numerical model of the discrete vortex method with the surface-vorticity boundary-integral algorithm. From Eq. (3.86), the

change of total pressure due to the moving vortices only is

$$-\frac{1}{\rho}\nabla p_{ov} = \frac{1}{2\pi}\sum_{j=1}^{Z}\Delta\Gamma_j\frac{1}{r_j^4}\begin{bmatrix}2(x-x_j)(y-y_j)v_{xj}-[r_j^2-(y-y_j)^2]v_{yj}\\ [r_j^2-2(x-x_j)^2]v_{xj}-2(x-x_j)(y-y_j)v_{yj}\end{bmatrix}, \qquad \textbf{(3.87)}$$

where p_{ov} is the total pressure induced by the moving vortices. Integrating Eq. (3.87), we obtain a single-valued scalar function P_v (the specific total pressure induced by vortex motion) which is given by

$$\begin{aligned} P_v = \frac{p_{ov}}{\rho} &= \frac{1}{\rho}\int\nabla p_{ov}\cdot d\boldsymbol{s} = \sum_{j=1}^{Z}\Delta\Gamma_j\frac{1}{2\pi r^2}\left(yv_{xj}-xv_{yj}\right) \\ &= \sum_{j=1}^{Z}\boldsymbol{U}_{ij}\cdot\boldsymbol{V}_j \quad , \end{aligned} \qquad \textbf{(3.88)}$$

where $\boldsymbol{U}_{ij}$ is the velocity at i induced by a vortex $\Delta\Gamma_j$ at j. This result, Eq. (3.88), is identical to the expression presented by Porthouse [1983] who derived the total pressure from the term $(\boldsymbol{u}-\upsilon\nabla)\times\omega$, interpreted as vortex flux by Porthouse. The function P_v describing the total pressure satisfies the conditions of potential theory. Therefore the total pressure field p_{ov} is conservative. This allows us to use Eq. (3.88) to evaluate the total pressure at any point induced by the moving vortices.

As for the total pressure distribution $p_{o\gamma}$ induced by the changing surface vorticity, the pressure gradient can be written as

$$-\frac{1}{\rho}\nabla p_{o\gamma} = \frac{1}{2\pi}\sum_{m=1}^{M}\frac{d\gamma_m}{dt}\frac{\Delta s_m}{r_m^2}\left[(y-y_m),-(x-x_m)\right] \quad . \qquad \textbf{(3.89)}$$

Taking the curl of Eq. (3.89), it can be found that $\nabla\times\nabla p_{o\gamma} = 0$ as it must be since the expression for velocities induced by point vortices are based on potential theory. By Stokes's theorem, the integration of pressure gradient $\nabla p_{o\gamma}$ along any closed contour c can be transformed into a surface integral over the surface S enclosed by c:

$$\oint_c \nabla p_{o\gamma}\cdot d\boldsymbol{s} = \int_s(\nabla\times\nabla p_{o\gamma})\cdot\boldsymbol{n}\,dS = 0 \; . \qquad \textbf{(3.90)}$$

Thus, the integration of pressure gradient along any closed contour is equal to zero. This implies that the integration of $\nabla p_{o\gamma}$ between any two distinct points is independent of the path between the points. Therefore the total pressure distribution $p_{o\gamma}$ induced by the changing surface vorticity is conservative.

By integration of $\nabla p_{o\gamma}$ to give $p_{o\gamma}$, the solution to Eq. (3.89) is found to be

$$P_\gamma = \frac{p_{o\gamma}}{\rho} = \frac{1}{2\pi}\sum_{m=1}^{M}\frac{d\gamma_m}{dt}\Delta s_m\theta_m = \frac{1}{2\pi}\sum_{m=1}^{M}\frac{\gamma_m\Delta s_m}{\Delta t}\theta_m \quad , \tag{3.91}$$

where P_γ is a scalar function denoting the specific total pressure induced by the changing surface vorticity, γ_m the solution of the Martensen equation for surface vorticity created on solid boundaries during time Δt, and $\theta_m = \tan^{-1}(y-y_m)/(x-x_m)$ the angle made at the pivotal point on segment s_m by a point at (x, y). The term $d\gamma_m/dt$ in Eq. (3.91) is approximated and replaced by $\gamma_m/\Delta t$ because the magnitude of the surface vorticity sheet changes from 0 to γ_m over a timestep Δt. The velocity potential of a discrete point vortex $\Delta\Gamma$, as given by Eq. (2.26), is $\phi_v = -\Delta\Gamma\theta/2\pi$. Thus, it can be seen that P_γ given by Eq. (3.91), is the sum of the time rates of change of the velocity potentials of all the vortex sheet elements on the solid body. By this consideration, Eq. (3.91) can be rewritten in terms of the velocity potentials of the discrete vortices as

$$P_\gamma = \frac{p_{o\gamma}}{\rho} = \sum_{m=1}^{M}\frac{\gamma_m\Delta s_m}{\Delta t}\frac{\theta_m}{2\pi} = \sum_{m=1}^{M}\frac{-\phi_{vm}}{\Delta t} \quad . \tag{3.92}$$

By the principle of superposition, the two potential-flow total pressure fields p_{ov} and $p_{o\gamma}$ can be added to give the total pressure field p_o (= p_{ov} + $p_{o\gamma}$) which is a solution to the Navier-Stokes equation (2.11). However, before Eq. (3.92) is evaluated for $p_{o\gamma}$, consideration of the mathematical nature of the velocity potential ϕ_v of a discrete vortex is pertinent. Being a function of the angular displacement θ, the velocity potential ϕ_v of a point vortex $\Delta\Gamma$ is a multi-valued scalar function: as θ increase from zero, ϕ_v also increases till at $\theta = 2\pi$ it becomes $\phi_v = \Delta\Gamma$. Another circuit round the vortex increases ϕ_v by another $\Delta\Gamma$. It can be noted that a multi-valued function is not consistent with the single-valued and continuous nature of the pressure field. Therefore, it is necessary to clarify the calculation of $p_{o\gamma}$ from the velocity potential of vortex.

It is instructive to consider the particular case of an isolated discrete vortex $\Delta\Gamma$ in an unbounded fluid which induces a circulating motion in the fluid around it. The fluid is at rest except in so far as it is disturbed by the vortex; in particular the velocity and pressure tend to zero at great distances from the vortex. Assume that we are able to increase the circulation of

this vortex by $d\Delta\Gamma$ during a time increment of dt. Use of Eq. (3.92) to compute the pressure distribution associated with $d\Delta\Gamma/dt$, through the term $d\phi_v/dt$, would imply a multiplicity of values for the pressure and also a constant non-zero finite total pressure, $p_o \neq 0$, along any radial direction even at infinity; both these effects are physically impossible. Prandtl and Tietjens [1934, Art. 71] discussed this issue and concluded that if a motion with circulation exists, it will persist, but such motion cannot be produced from rest. It is physically impossible to change the total circulation in the fluid without temporarily upsetting the continuity of the fluid as, for example, by the insertion of a rigid body into the fluid. This conclusion is consistent with the Kelvin's circulation theorem which states that the circulation in a flow domain remains constant with time.

In a real flow, and also in the present numerical model, equal amounts of vorticity of opposite sign are generated on the body surface such that the net circulation created on the body is equal to zero (as will be discussed in later sections this is a necessary condition to ensure closure of surface pressure distribution on the body). Despite the change in circulation ($=\gamma\Delta s$) with time on each segment of the body, the time rate of change of circulation on the whole body remains unchanged and equals zero. An observer distant from the body will not experience any change in velocity or in the pressure field due to the change of surface vorticity on the body. Provided the condition of zero circulation generated around a body contour is satisfied, Eq. (3.92) is valid to predict the total pressure field associated with the time rate of change of surface vorticity on the body. In the present numerical scheme, the condition of zero circulation around a body contour has been satisfied by the enforcement of Eq. (3.75) and hence the prerequisite condition for the evaluation of $p_{o\gamma}$ from Eq. (3.92) is fulfilled. The practical problem remaining is the determination of θ values so as to avoid discontinuities and multiple values of ϕ_v.

As the circulation around the body contour corresponding to the vorticity created on the body surface is always equal to zero, $\sum\gamma\Delta s = 0$, it is legitimate to consider, from another point of view, that the vorticity on the body contour is being redistributed as a result of the movement of vortices in the flow domain, in such a way that the appropriate boundary conditions are always satisfied on the solid body surface. Vorticity redistribution on the solid boundary is complementary to the moving vorticity in the flow domain; together they account for the vorticity evolution in the flow.

Numerical evaluation of Eq. (3.92) for the total pressure at a point (x,y), induced by the vortex sheet, requires determination of the angles θ_m (m = 1,2,...M) which the lines joining the pivotal points on the body to that point make with the reference datum. Note that although the intrinsic multi-valuedness of ϕ_v can be eliminated by setting the range of θ to be 0 to 2π, ϕ_v experiences a discontinuity as θ moves across the datum axis, where its value jumps from 0 to 2π. When a point lies on the datum axis, ϕ_v has an indeterminate value between 0 or 2π. Because it is the entire vortex sheet on a body that determines the pressure distribution induced by the creation of surface vorticity, the pressure given by Eq. (3.92) will be correct only if the angle θ_m is finite and well defined and its variation around the body contour is smooth and continuous. Evidently, when these conditions are satisfied, the sum in Eq. (3.92) becomes independent of the selection of datum axis. We must therefore select a proper datum axis for measuring θ to ensure a smooth and continuous variation in θ around the body contour, and its orientation will be determined by the geometric relationship between a particular point and the body.

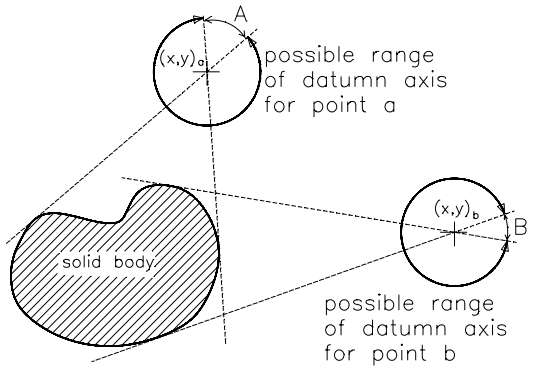

Figure 3.7. Determination of the reference datumn axis for the evaluation of θ_m.

Consider a point $(x, y)_a$ in the flow field as shown in Fig. 3.7. The angle between the tangents from it to the solid body is A. All the lines joining the pivotal points on the body and point (x, y)$_a$ must lie between these tangent lines. If the datum axis has an orientation which lies inside angle A, as in the case shown in Fig. 3.8, the values of θ_m measured from this datum axis will fall in the vicinity of the discontinuity. However, when the datum axis is rotated to such an angular position that it lies outside angle A, as shown in Fig. 3.9, the values of θ_m measured from the new datum axis will have a smooth and continuous variation. It can be noted that any angular position outside the angle A can be used as a proper orientation for the datum axis for point $(x, y)_a$.

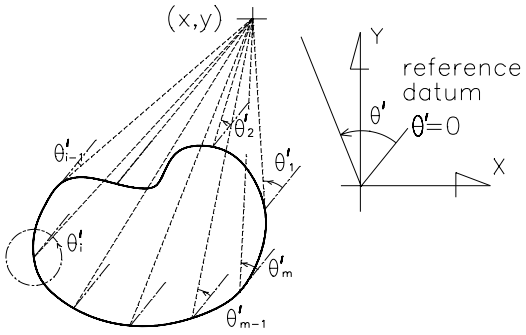

Figure 3.8. Angles made at the pivotal points on body by a point at (x,y).

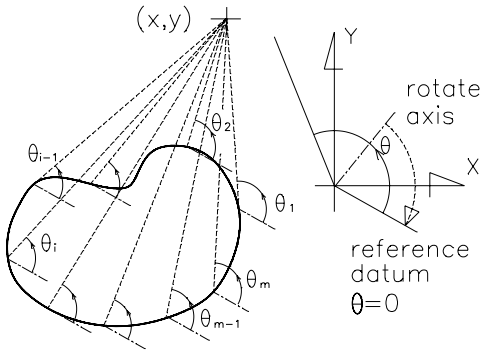

Figure 3.9. Rotating the datumn axis to avoid ambiguous measurement of angle θ.

Since the orientation of the datum axis for a particular point is determined by its geometric relationship with the body, it has to be determined independently for each point (for each body in multiple body systems). Fig. 3.7 shows the range of angular position that is possible as an orientation for the datum axis for two distinct points in the flow field: $(360° - A)$ for point $(x,y)_a$ and $(360° - B)$ for point $(x, y)_b$. In the present work, a solution procedure has been developed to determine the appropriate orientation of the datum axis for a particular point in association with the evaluation of Eq. (3.92).

Adding the total pressure induced by the uniform main stream, the moving vortices and the creation of surface vorticity, we have the total pressure at any point in the flow field given by

$$p_o = \left(p + \frac{\rho u^2}{2} \right) = \left(p_\infty + \frac{\rho U_\infty^2}{2} \right) + p_{ov} + p_{o\gamma} \quad , \tag{3.93}$$

with the values of p_{ov} and $p_{o\gamma}$ obtained from Eq. (3.88) and Eq. (3.92) respectively. One can compute the velocity field $\boldsymbol{u}$ by Eq. (3.82), and thus the dynamic pressure. The static pressure p is obtained by subtracting the dynamic pressure from the total pressure. With the pressure coefficient C_p defined as

$$C_p = \frac{p - p_\infty}{\frac{1}{2}\rho U_\infty^2} \quad , \tag{3.94}$$

the pressure coefficient at any point in the flow field can be expressed as

$$C_p = 1 + 2 \left(\sum_{j=1}^{Z} U_{ij} \cdot V_j + \frac{1}{2\pi} \sum_{m=1}^{M} \frac{\gamma_m \Delta s_m}{\Delta t} \theta_m \right) - u^2 \quad , \tag{3.95}$$

in which the values to be used are non-dimensional quantities.

The total pressure given by Eq. (3.93) is in fact an analytical solution to the contour integral of pressure gradient given by Eq. (3.86), along a path from infinity to a point in the flow domain or on the body contour. To be consistent with the condition required by Eq. (3.86) that $\omega = 0$ except at the singularities, the contour integral can be performed along any path provided it excludes the body contour. The proviso is necessary because vorticity is being continuously generated on the surface of solid bodies in the form of an infinitesimally thin vortex sheet, so that $\omega \neq 0$ on the entire body contour ∂S. Consequently, the condition necessary for Eq. (3.86) to apply is not satisfied along ∂S; the equation does not give the pressure gradient $\partial p_o/\partial s$ along ∂S (where s is the curvilinear coordinate along ∂S) correctly. The evaluation of $\partial p_o/\partial s$ along the body contour is established in the next section.

The total pressure given by Eq. (3.93) can also be obtained by the alternative procedure of considering the general Bernoulli equation for unsteady flow of an incompressible fluid. In the absence of external forces, the Bernoulli equation for unsteady flow is

$$\frac{\partial \phi}{\partial t} + \frac{p}{\rho} + \frac{u^2}{2} = F(t) \quad , \tag{3.96}$$

where ϕ is the velocity potential (the velocity field being $\boldsymbol{u} = \nabla\phi$) and $F(t)$ is a function of time alone. $F(t)$ can be taken to be constant ($= p_\infty + \rho U_\infty^2/2$) for unsteady flows in which the approach flow at infinity remains steady (which is appropriate for the present study of flow past stationary solid bodies). The velocity potential at a point due to a uniform flow $\boldsymbol{U}_\infty$ at an angle of attack α, a system of Z discrete vortices and the surface vorticity sheet is

$$\phi = U_\infty (x \cos\alpha + y \sin\alpha) - \frac{1}{2\pi} \sum_{j=1}^{Z} \Delta\Gamma_j \theta_j + \sum_{m=1}^{M} \phi_{vm} \quad , \tag{3.97}$$

where the last sum on the right-hand side is the velocity potential induced by the vortex sheet as defined in Eq. (3.92). Carrying out differentiation of Eq. (3.97) with respect to time, we have

$$\frac{\partial \phi}{\partial t} = -\sum_{j=1}^{Z} \boldsymbol{U}_{ij} \cdot \boldsymbol{V}_j + \sum_{m=1}^{M} \frac{d\phi_{vm}}{dt} \quad , \tag{3.98}$$

since $\partial\theta/\partial t = (v_{xj} \sin\theta - v_{yj} \cos\theta)/r$ at a point fixed in space for the vortex moving at velocity $\boldsymbol{V}_j = (v_{xj}, v_{yj})$. Substituting Eq. (3.88) and Eq. (3.92) into Eq. (3.98), we have

$$\frac{\partial \phi}{\partial t} = -\frac{p_{ov}}{\rho} - \frac{p_{o\gamma}}{\rho} \quad . \tag{3.99}$$

Substituting Eq. (3.99) in Eq. (3.96) and rearranging, we obtain an expression for the total pressure which is identical to Eq. (3.93).

3.5.1 Determination of Surface Pressure Distribution

To determine the surface pressure at a point on the body for a given vorticity field, for example the point *e* in Fig. 3.10, one may perform contour integration of total pressure from *c* to *e* along *L1* (letting *c* tend to infinity to establish the known boundary condition at infinity). The analytic solution to this contour integration for total pressure is readily obtainable from Eq. (3.93). However, one may also carry out the contour integration along another path including part of the body contour to get to the same point, such as the path *L2* + *L3* joining points *c*, *d* and *e* shown in Fig. 3.10. Despite the difference in path of integration, the two calculations should give the same total pressure at point *e* on the body surface.

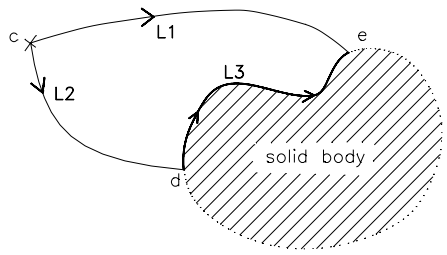

Figure 3.10. Integration for surface pressure via different paths.

When the contour integration is performed along a path on the body contour ∂S, such as *L3* in Fig. 3.10, it requires an expression for the pressure gradient $\partial p_o/\partial s$ along the body contour. In the potential flow models used in the present numerical scheme the fluid velocity is zero at the solid surface ∂S (as in the real flow), and so the total pressure is equal to the static pressure at the body surface. Applying the Navier Stokes equation Eq. (3.79) at the body surface and noting that $\boldsymbol{u} = 0$ on ∂S and $p_o = p$, we obtain the pressure gradient along ∂S as

$$\frac{1}{\rho}\frac{\partial p}{\partial s} = -\upsilon \nabla \times \boldsymbol{\omega} \quad . \tag{3.100}$$

The term $\upsilon \nabla \times \boldsymbol{\omega}$ of Eq. (3.100) may be regarded as the diffusive flux density of vorticity (per unit length per unit time) moving outwards from the body surface. Let us denote this quantity as $B(s)$ ($\equiv \upsilon \nabla \times \boldsymbol{\omega}$) for simplicity. This indicates that the pressure gradient is a local source of vorticity at a solid boundary, and further that the closure of pressure gradient around a closed contour implies zero net diffusive flux of vorticity outwards from the surface. Since the closure of pressure distribution on the body must be satisfied irrespective of the body shape and the flow condition, the net diffusive flux density of vorticity outwards from the surface must equal zero.

Morton [1984], with reference to Lighthill [1963], points out that the pressure gradient on a surface in a real viscous flow is related to the diffusive flux density of vorticity outwards from the surface. Porthouse [1983], in his study of flow simulation by vortex dynamics, discussed the derivation of pressure field in the equivalent potential flow with a system of moving vortices. He derived from the Navier-Stokes equation the result that the total pressure gradient along a contour is related to the vorticity flux across the contour. His conclusion is analogous to that of Morton [1984] in that both relate the outward diffusive flux density of vorticity from a solid surface to the pressure gradient on the surface.

In the present numerical model, $B(s)$ is a measurable quantity and is readily available from the calculation. Consider the simulation of viscous flow development, in which for each time-step Δt, the vortex sheet $\gamma(s_n)$ created at the solid boundary is diffused outwards into the flow as discrete vortices of strength $\Delta\Gamma_n = \gamma(s_n)\Delta s_n$. This gives rise to a diffusive flux of circulation moving outwards the solid surface whose density $B_o(s_n)$ (per unit length per unit time) at segment s_n is given by

$$B_o(s_n) = \frac{\gamma(s_n)}{\Delta t} \quad . \tag{3.101}$$

In the meantime, discrete vortices may get inside the body contour as a result of diffusion and convection. The point at which the vortex $\Delta\Gamma_j$ crosses the contour is assumed to be the collocation point of the nearest segment, say s_n. The equivalent diffusive flux density of vorticity entering the surface at segment s_n, $B_i(s_n)$, is

$$B_i(s_n) = \frac{1}{\Delta t}\sum_{j=1}^{Z_d(s_n)} \frac{\Delta\Gamma_j}{\Delta s_n} = \frac{\Gamma_j(s_n)}{\Delta s_n \Delta t} \quad , \tag{3.102}$$

where $Z_d(s_n)$ denotes the number of vortices which have entered the interior of contour through segment s_n in the duration of Δt, and $\Gamma_j(s_n)$ the accumulated vorticity of these $Z_d(s_n)$ vortices. Subtracting Eq. (3.102) from Eq. (3.101), we obtain the net diffusive flux density of circulation outwards from the surface at segment s_n in the time-step Δt considered, given by

$$B(s_n) = B_o(s_n) - B_i(s_n) = \frac{1}{\Delta t}\left[\gamma(s_n) - \frac{\Gamma_j(s_n)}{\Delta s_n}\right] . \tag{3.103}$$

With the values of net diffusive flux density of vorticity $B(s_n)$ at segment s_n given by Eq. (3.103) and the definition of pressure coefficient by Eq. (3.94), the expression for the pressure gradient on the body surface, Eq. (3.100), can be rewritten in discretised form suitable for numerical integration as

$$\Delta C_p(s_n) = -\frac{2}{\Delta t}\left[\gamma(s_n)\Delta s_n - \Gamma_j(s_n)\right] \qquad \textbf{(3.104)}$$

where $\Delta C_p(s_n)$ represents the change in pressure coefficient along the length Δs_n of segment s_n corresponding to the vorticity evolution in a time interval of Δt. For the satisfaction of the closure of pressure distribution around the closed body contour, the sum $\sum \Delta C_p(s_n)$ for n = 1,2,...M must be equal to zero.

To show that the closure of pressure distribution around the body is observed, let us consider that the bound circulation Γ_c on a body (due to vortices inside the contour) as given by Eq. (3.71). Γ_c is the sum of $\Gamma_j(s_n)$ around the entire body, and, further, the circulation of the vortex sheet created by the Martensen equation Eq. (3.73) is equal to Γ_c since Eq. (3.72) is always enforced in the Martensen equation. As a result of these considerations, we have

$$\sum_{n=1}^{M}\left[\gamma(s_n)\Delta s_n - \Gamma_j(s_n)\right] = \sum_{n=1}^{M}\gamma(s_n)\Delta s_n - \Gamma_c = 0 \ . \qquad \textbf{(3.105)}$$

By Eqs. (3.104) and (3.105), the sum of $\Delta C_p(s_n)$ around the entire body contour can be expressed as

$$\sum_{n=1}^{M}\Delta C_p(s_n) = -\frac{2}{\Delta t}\sum_{n=1}^{M}\left[\gamma(s_n)\Delta s_n - \Gamma_j(s_n)\right] = 0 \ . \qquad \textbf{(3.106)}$$

This shows that the condition for the closure of pressure distribution around the closed contour is satisfied. The distribution of pressure coefficient $C_p(s_m)$ on the surface can be obtained by integrating Eq. (3.104) around the contour from a reference point, which can be taken as one of the data points on the body, to the data point of segment s_m on the contour. Thus we have

$$C_p(s_m) = \sum_{n=1}^{m}\Delta C_p(s_n) = -\frac{2}{\Delta t}\sum_{n=1}^{m}\left[\gamma(s_n)\Delta s_n - \Gamma_j(s_n)\right] \ . \qquad \textbf{(3.107)}$$

The pressure coefficients $C_p(s_m)$ obtained from Eq. (3.107) are relative values with respect to $C_p(s_1)$ of segment s_1 from which the integration begins for numerical convenience. In order to obtain the absolute surface pressure coefficients, the pressure coefficient $C_p(s_1)$ at s_1 can be computed by Eq. (3.93) and then all other values of $C_p(s_m)$ adjusted by adding $C_p(s_1)$ to each.

For the calculation of surface pressure on solid bodies, either Eq. (3.93) or Eq. (3.107) can be used to compute the surface pressure coefficient. Successful numerical experiments have been carried out to verify the consistency of these equations. However, Eq. (3.107) is preferred because it demands less computing effort and assures closure of the surface pressure distribution.

Performing integration of surface pressure p around the body contour, we obtain the pressure force acting on the body and hence the lift and drag coefficients are given by

$$C_L = \frac{-1}{\frac{1}{2}\rho U_\infty^2 L} \int_c p \cos\beta \, ds \ , \qquad \textbf{(3.108)}$$

and

$$C_D = \frac{1}{\frac{1}{2}\rho U_\infty^2 L} \int_c p \sin\beta \, ds \ . \qquad \textbf{(3.109)}$$

The above integrations are expressed in discretised forms appropriate for numerical calculations, in terms of dimensionless variables, as:

$$C_L = -\sum_{n=1}^{M} C_p(s_n) \cos\beta_n \Delta s_n \ , \qquad \textbf{(3.110)}$$

and

$$C_D = \sum_{n=1}^{M} C_p(s_n) \sin\beta_n \Delta s_n \ , \qquad \textbf{(3.111)}$$

where the pressure coefficients $C_p(s_n)$ are values at mid-positions of the segment which are taken as the average of the values given by Eq. (3.107) at the end (data) points of the segment, $= \frac{1}{2}[C_p(s_{n-1}) + C_p(s_n)]$.

3.6 Summary of Solution Procedure for Viscous Flow Modelling

The solution procedure for viscous flow analysis by the surface-vorticity boundary-integral in conjunction with the discrete vortex methods can be summarised in the flow diagram, Fig. 3.11,

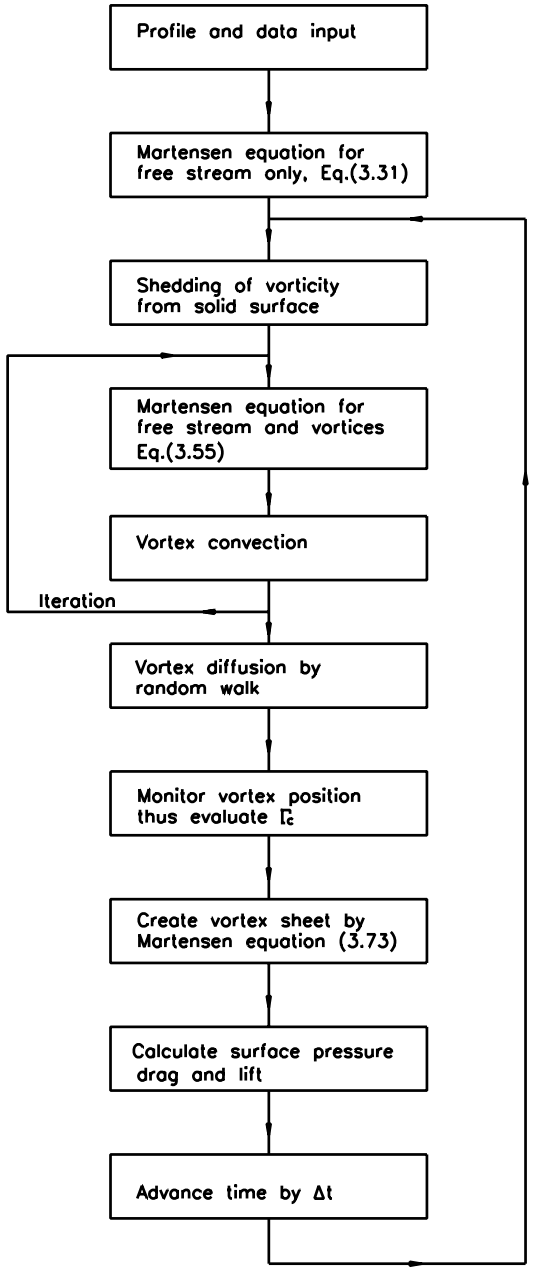

Figure 3.11. Solution procedure for viscous flow analysis by the surface-vorticity boundary-integral and discrete-vortex methods.

3.7 Extension to Calculation of Flow Past a Multi-Body Array

The calculation procedures of the surface-vorticity boundary-integral method for flow past a single body described in sections 3.2, 3.3 and 3.4, can be extended to flow past a multi-body array. Procedures for both inviscid and viscous flow past an array of multiple body will be established in this section.

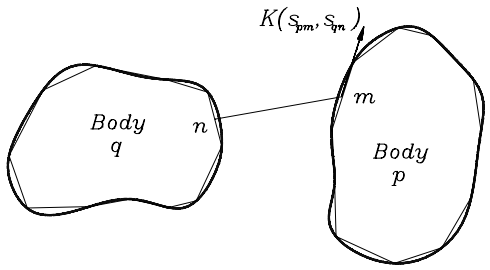

Figure 3.12. Definition of the coupling coefficient $K(s_{pm},s_{qn})$ in a multi-body system.

In a system containing more than one solid body, the potential-flow velocity field induced by the vortex sheet on each body is modified by the presence of the other bodies in the system. The mutual interaction between the bodies is reflected in the coupling coefficients, and the coupling coefficient matrix **[*K*]** in the Martensen equation is modified accordingly. Consider the simplest multi-body system, one which contains two solid bodies p and q as indicated in Fig. 3.12. The tangential component of the velocity at segment s_{pm} (the segment m of the body p) induced by the vortex sheet at segment s_{qn} is represented by the coupling coefficient $K(s_{pm}, s_{qn})$ which is determined by the geometric relation of the bodies as given by

$$K(s_{pm},s_{qn}) = \frac{\Delta s_{qn}}{2\pi}\left(\frac{(y_{pm}-y_{qn})\cos\beta_{pm}-(x_{pm}-x_{qn})\sin\beta_{pm}}{(x_{pm}-x_{qn})^2+(y_{pm}-y_{qn})^2} \right) - \frac{1}{2}\delta_{pm,qn} , \qquad \textbf{(3.112)}$$

where $\delta_{pm,qn}$ is the Kronecker delta function (which has the value of unity for $p = q$ and $m = n$ but is otherwise zero), (x_{pm}, y_{pm}) and β_{pm} are respectively the collocation point and the angle made with the x-axis by the tangent at segment s_{pm}, and Δs_{qn} is the length of segment s_{qn}. For the special case when $p = q$ and $m = n$, the self-induced coupling coefficient $K(s_{pm}, s_{pm})$ is the same as that given by Eq. (3.16) the notation of which is now modified to cater for multi-body system; it becomes

$$K(s_{pm},s_{pm}) = -\frac{1}{2} - \frac{1}{8\pi}\left(\beta_{p,m+1} - \beta_{p,m-1}\right) . \qquad \textbf{(3.113)}$$

For the analysis of potential flow past an array of N solid bodies, each of which has M_q segments, where $q = 1,2,...N$, the equation for zero tangential velocity at the collocation point of segment s_{pm} is given by

$$\sum_{q=1}^{N} \sum_{n=1}^{M_q} K(s_{pm}, s_{qn}) \gamma(s_{qn}) + \cos(\alpha - \beta_{pm}) = 0 \quad . \tag{3.114}$$

Extension of Eq. (3.114) to all the segments of the bodies in the system results in a set of M ($=\sum M_q$, where $q = 1,2,...N$) simultaneous linear equations for M unknown values of $\gamma(s_{qn})$ the vorticity distribution over the vortex sheets on the bodies.

The matrix form of this set of equations is similar to Eq. (3.17), i.e. $\mathbf{[K][\gamma] = [b]}$. But, now, the *coupling coefficient matrix* $\mathbf{[K]}$ can be considered to comprise $N \times N$ submatrices $\mathbf{[K_{pq}]}$ for $(p, q) = 1,2,...N$, and the *tangential surface velocity matrix* $\mathbf{[b]}$ and the *solution matrix* $\mathbf{[\gamma]}$ to comprise N subcolumns $\mathbf{[b_p]}$ and $\mathbf{[\gamma_p]}$ respectively, for $p = 1,2,...N$, corresponding to the values associated with body p. The matrix equation can be expressed in the form of

$$\begin{bmatrix} [K_{11}] & [K_{12}] & \cdots & [K_{1N}] \\ [K_{21}] & [K_{22}] & \cdots & [K_{2N}] \\ \cdots & \cdots & \cdots & \\ [K_{N1}] & [K_{N2}] & \cdots & [K_{NN}] \end{bmatrix} \begin{bmatrix} [\gamma_1] \\ [\gamma_2] \\ \cdots \\ [\gamma_N] \end{bmatrix} = \begin{bmatrix} [b_1] \\ [b_2] \\ \cdots \\ [b_N] \end{bmatrix} \quad . \tag{3.115}$$

When $p = q$ the submatrix $\mathbf{[K_{pp}]}$ on the leading diagonal represents the *self-induced coupling coefficient matrix* for the body p. It is an $M_p \times M_p$ (row × column) matrix and of the same form as the one given by Eq. (3.11) for a single isolated body. For $p \neq q$, the submatrix $\mathbf{[K_{pq}]}$ represents the influence of body q on body p. It is an $M_p \times M_q$ matrix with elements $K_{pq,mn} = K(s_{pm}, s_{qn})$. The *tangential surface velocity matrix* $\mathbf{[b]}$ is a column matrix of the M elements $b_{pm} = -\cos(\alpha - \beta_{pm})$, for $p = 1,2,...N$ and $m = 1,2,...M_p$, and the *solution matrix* $\mathbf{[\gamma]}$ is a column matrix of the M elements $\gamma(s_{qn})$, for $q = 1,2,...N$ and $n = 1,2,...M_q$.

3.7.1 Singularity and Regularisation of the Coupling Coefficient Matrix, $[K_{pq}]$

Following the same argument for ensuring zero circulation around a contour inside the vortex sheet described in section 3.2.2, the *self-induced coupling coefficient matrices* $\mathbf{[K_{pp}]}$ for p = 1,2,...N are corrected to enforce zero circulation according to Eq. (3.26). For the circulation around a body induced by a vortex sheet element of another body, the condition of zero circulation requires that the circulation $\Gamma_{p,qj}$ around the body p induced by the vortex sheet element $\gamma(s_{qj})\Delta s_{qj}$ on the body q be equal to zero, i.e.

$$\Gamma_{p,qj} = \sum_{m=1}^{M_p} K(s_{pm}, s_{qj})\,\Delta s_{pm} = 0 \ . \qquad \textbf{(3.116)}$$

However, this condition is not always complied with since the $K(s_{pm}, s_{qn})$ values are determined from the geometric configuration of the bodies. The deviation from zero circulation becomes apparent when the bodies are very close to each other and some vortex sheet elements are in close proximity to the neighbouring body. Satisfaction of Eq. (3.116) is ensured by correcting the $K(s_{pm}, s_{qn})$ values according to the following scheme.

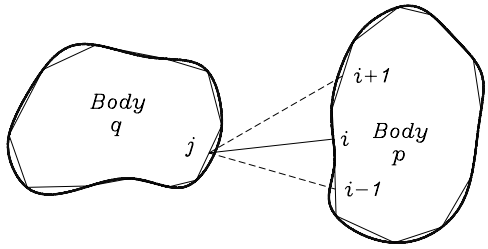

Figure 3.13. Schematic concept of the correction for zero induced circulation.

Consider a submatrix $\mathbf{[K_{pq}]}$, where $p \neq q$, which contains the columns $\mathbf{[K_{pq,j}]}$ for j = 1,2,...M_q. Zero induced circulation is enforced by adjusting the value of the element $K(s_{pi}\ ,\ s_{qj})$ corresponding to the segment s_{pi} which is closest to segment s_{qj}, as indicated in Fig. 3.13. $K(s_{pi}\ ,\ s_{qj})$ is assigned the value

$$K(s_{pi}, s_{qj}) = -\frac{1}{\Delta s_{pi}} \sum_{\substack{m=1 \\ m\neq i}}^{M_p} K(s_{pm}, s_{qj})\Delta s_{pm} \ , \quad j = 1,2,...M_q \ , \qquad \textbf{(3.117)}$$

instead of the one given by Eq. (3.112). Eq. (3.117) is applied to other off-diagonal submatrices $\mathbf{[K_{pq}]}$ for $p \neq q$ so that the condition of zero induced circulation is satisfied for all bodies.

Discussion of the singularity of the *coupling coefficient matrix* **[*K*]** for a single body system has been given in section 3.2.2 and the regularisation of the singular matrix described in section 3.2.3. In the present case, for multi-body systems, the problem of a singular **[*K*]** matrix also exists, as a result of the exact satisfaction of the condition of zero circulation on all the bodies.

After the submatrices $[K_{pq}]$, where $(p\ ,\ q) = 1,2,...N$, have been corrected by Eq. (3.26) and Eq. (3.117), the resultant coupling coefficient matrix **[*K*]** is singular and one additional condition is required to regularise the singular matrix. The equation for prescribed circulation, Eq. (3.30), can be used for the purpose of matrix regularisation since it is applicable to all the solid bodies in the system irrespective of their geometrical configuration and the flow condition. By using a procedure similar to the matrix regularisation described in section 3.2.3, the equation for the prescribed circulation Γ_{bp} around the body p in the form

$$\Gamma_{bp} = \sum_{m=1}^{M_q} \gamma(s_{pm})\Delta s_{pm}\ , \qquad p = 1,2,...N, \tag{3.118}$$

is added to the Martensen equation Eq. (3.114) to give the regularised equations

$$\sum_{q=1}^{N}\sum_{n=1}^{M_q}\left[K(s_{pm},s_{qn}) + \delta_{pq}\Delta s_{pm}\right]\gamma(s_{qn}) + \cos(\alpha-\beta_{pm}) - \Gamma_{bp} = 0\ , \tag{3.119}$$

where δ_{pq} is the Kronecker delta function which is used in order that Eq. (3.118) is added to each row of the *self-coupling coefficient matrix* $[K_{pp}]$ for $p = 1,2,...N$. The Martensen equation (3.119) for a multi-body system can be expressed in terms of the regularised *coupling coefficient matrix* **[*K*^{r}]** and the corresponding modified *tangential surface velocity matrix* **[*b*]** in the form of **[*K*^{r}][γ] = [*b*]**, where the elements of the matrices **[*K*^{r}]** and **[*b*]** are given by

$$\begin{aligned} K^{r}_{pq,mn} &= K(s_{pm},s_{qn}) + \delta_{pq}\Delta s_{pm}\ , \\ b_{pm} &= -\cos(\alpha-\beta_{pm}) + \Gamma_{bp}\ . \end{aligned} \tag{3.120}$$

For inviscid flow calculation, the prescribed circulation Γ_{bp} on a body can be assigned any finite value: zero for a non-lifting body and non-zero for lifting body in order to satisfy the Kutta trailing edge condition. For calculation of viscous flow past solid bodies with vorticity shedding, the bound circulation around the contour is designated as Γ_{cp} to distinguish it from the prescribed circulation Γ_{bp} as used in inviscid flow calculation. The detailed discussion of the use of the equation of circulation around a body contour to regularise the singular **[*K*]** matrix in viscous flow calculation will be taken up later again in section 3.9.

3.8 Inviscid Flow about a Multi-Body Array Consisting of Lifting and Non-lifting Bodies

Calculation of inviscid flow past a single lifting body requires the solution for Γ_b determined by Eq. (3.38) to satisfy the Kutta trailing edge condition on that body. However, in a multi-body system, the values of Γ_{bp} on the lifting bodies are determined in such a way that the Kutta trailing edge condition on all these bodies is satisfied and that the values of Γ_{bp} for the non-lifting bodies are always equal to zero. Due to the mutual interaction between bodies, the prescribed circulation on one body affects the vortex sheet distributions $\gamma(s_{pm})$ on all the bodies in the system. The solution procedure is to find a set of prescribed circulation values Γ_{bp} on the lifting bodies that give the resultant vortex sheet strengths $\gamma(s_{pm})$ on the bodies satisfying the Kutta trailing edge condition. The required values of Γ_{bp} can be estimated by iteration but can be evaluated in a more systematic way as follows.

In a single-body system, the solution of the Martensen equation for the vortex sheet distribution $\gamma(s_n)$, Eq. (3.33), can be considered to comprise two parts: $\gamma_1(s_n)$ and $\gamma_2(s_n)$ associated with the uniform main stream $\boldsymbol{U}_\infty$ and with the prescribed circulation Γ_b respectively. Similarly, for a multi-body system consisting of N solid bodies, the solution $\gamma(s_{pm})$ can be considered to be made up of (N+1) parts: one associated with the uniform main stream and the other N parts associated with the prescribed circulations on the N solid bodies.

Let $\gamma_1(s_{pm})$ denote the vortex sheet distribution on the bodies, for p = 1,2,...N, due to the uniform free stream $\boldsymbol{U}_\infty$ only. Thus, $\gamma_1(s_{pm})$ is the solution to the Martensen equation Eq. (3.119) with $\Gamma_{bp} = 0$ which is

$$\sum_{q=1}^{N}\sum_{n=1}^{M_q}\left[K(s_{pm},s_{qn}) + \delta_{pq}\Delta s_{pm}\right]\gamma_1(s_{qn}) + \cos(\alpha-\beta_{pm}) = 0 \quad . \qquad \textbf{(3.121)}$$

Let $\gamma^i_{o2}(s_{pm})$ denote the vortex sheet distribution on the bodies due to a positive unit circulation on the body i only. The values of $\gamma^i_{o2}(s_{pm})$ are obtained by assigning the prescribed circulations $\Gamma_{bp} = 1$ for $p = i$ and otherwise $\Gamma_{bp} = 0$ and then solving the corresponding Martensen equation for i = 1,2,...N in turn :

$$\sum_{q=1}^{N}\sum_{n=1}^{M_q}\left[K(s_{pm},s_{qn}) + \delta_{pq}\Delta s_{pm}\right]\gamma^i_{o2}(s_{qn}) = \delta_{pi}\ , \qquad i=1,2,\ldots N \ . \qquad \textbf{(3.122)}$$

With the values of $\gamma_1(s_{pm})$ and $\gamma^i_{o2}(s_{pm})$ for $(i, p) = 1,2,...N$ obtained from Eqs. (3.121) and (3.122), the vortex sheet strength distribution $\gamma(s_{pm})$ on a body for a given set of prescribed circulations Γ_{bp} on the bodies is

$$\gamma(s_{pm}) = \gamma_1(s_{pm}) + \sum_{q=1}^{N} \gamma^q_{o2}(s_{pm})\,\Gamma_{bq} \quad . \tag{3.123}$$

By making use of the expression for $\gamma(s_{pm})$ as given in Eq. (3.123), the Kutta trailing-edge condition for a lifting body p can be written in terms of the known values $\gamma_1(s_{pm})$ and $\gamma^i_{o2}(s_{pm})$ as

$$\gamma_1(s_{p,te}) + \sum_{q=1}^{N} \gamma^q_{o2}(s_{p,te})\,\Gamma_{bq} = -\gamma_1(s_{p,te+1}) - \sum_{q=1}^{N} \gamma^q_{o2}(s_{p,te+1})\,\Gamma_{bq} \quad . \tag{3.124}$$

Extension of Eq. (3.124) to all the N_L lifting bodies in a system of N solid bodies results in a set of N_L simultaneous linear equation for N_L unknown values of Γ_{bp}. The prescribed circulations Γ_{bp} on all the lifting bodies in the system can be determined from the following algebraic equations, obtained by rearrangement of Eq. (3.124),

$$\sum_{q=1}^{N} \left[\gamma^q_{o2}(s_{p,te}) + \gamma^q_{o2}(s_{p,te+1}) \right] \Gamma_{bq} = -\left[\gamma_1(s_{p,te}) + \gamma_1(s_{p,te+1}) \right] , \tag{3.125}$$

and those values of Γ_{bp} for the non-lifting bodies are set to zero in order to reflect the zero-lift condition of these bodies. It might be noted that when the system contains only one lifting body, i.e. $N_L = 1$, Eq. (3.125) reduces to Eq. (3.38) as given in section 3.2.3. The resultant vortex sheet distribution $\gamma(s_{pm})$ on all the bodies can be obtained from either the Martensen equation Eq. (3.100) or Eq. (3.104) with the calculated values of Γ_{bp} given by Eq. (3.125). For inviscid flow analysis, the lift coefficients and surface pressure distributions can be obtained by substituting the corresponding values into Eq. (3.38) and Eq. (3.39) respectively.

3.9 Simulation of Viscous Flow Past a Multi-Body Array

The solution procedures of the surface-vorticity boundary-integral method and the discrete vortex method for calculation of the time-dependent viscous flow past a single body have been given in section 3.4. Briefly, the viscosity of a real flow causes the vorticity created at the solid surfaces to diffuse in to the flow. The distributed vorticity in the flow is represented by a system of discrete vortices. The continuous processes of vorticity creation at solid surfaces, and the convection and diffusion of the distributed vorticity field are approximated as sequential processes as outlined in section 3.4. The numerical procedures for the calculation of time-dependent viscous flow past a multi-body array remain the same as those for a single body system. However, the Martensen equation is modified to reflect the mutual interaction between the bodies in a multi-body system.

In a viscous flow problem involving N solid bodies together with a system of Z discrete vortices, the discretised Martensen equation in its basic form, which is a statement of the no-slip condition at the collocation point of segment s_{pm}, is given by

$$\sum_{q=1}^{N}\sum_{n=1}^{M_q} K(s_{pm},s_{qn})\,\gamma(s_{qn}) + \sum_{j=1}^{Z}\Delta\Gamma_j\left(L_{pm,j}\cos\beta_{pm} + M_{pm,j}\sin\beta_{pm}\right) + \cos(\alpha-\beta_{pm}) = 0\,, \qquad \textbf{(3.126)}$$

with the values of $K(s_{pm},s_{qn})$ given by Eqs. (3.112) and (3.113), and those of $L_{pm,j}$ and $M_{pm,j}$ by Eq. (3.49). Extension of Eq. (3.126) to all the segments on the bodies results in a system of linear equation which can be written in the matrix form of $\mathbf{[}\boldsymbol{K}\mathbf{][}\gamma\mathbf{]} = \mathbf{[}\boldsymbol{b}\mathbf{]}$ as given by Eq. (3.115). Following the general procedure of zero-circulation correction of the matrix $\mathbf{[}\boldsymbol{K}\mathbf{]}$, this system of equation becomes singular and one additional condition is required to regularise the singularity. Consider the general equation for conservation of vorticity in the flow domain, which takes the form

$$\sum_{q=1}^{N}\sum_{n=1}^{M_q}\gamma(s_{qn})\Delta s_{qn} + \sum_{j=1}^{Z}\Delta\Gamma_j = 0\,, \qquad \textbf{(3.127)}$$

where the first summation term accounts for the vorticity of the vortex sheet enveloping the bodies and the second summation term for that of all discrete vortices in the flow domain. Eq. (3.127) states only the condition of vorticity conservation for the whole system but does not specify the vorticity distribution among the bodies in the system: $\sum\gamma(s_{qn})\Delta s_{qn}$ can take up any value and still satisfy Eq. (3.127). Therefore, the equation of vorticity conservation Eq. (3.127) is not sufficient to ensure an unique solution of $\mathbf{[}\gamma\mathbf{]}$ for a multi-body system.

Now, consider the bound circulation around the body contour as given by Eq. (3.72). The bound circulation Γ_{cq} around the body q can be expressed, in the notation for a multi-body system, in the form

$$\sum_{n=1}^{M_q} \gamma(s_{qn})\Delta s_{qn} = \sum_{j=1}^{Z_{dq}} \Delta\Gamma_j = \Gamma_{cq} \quad , \qquad q = 1,2,\ldots N \ . \tag{3.128}$$

Γ_{cq} is equal to the total strength of the Z_{dq} discrete vortices which have entered the interior of the contour of body q and have been annihilated according to the scheme described in section 3.4.7. It can be noted that Eq. (3.128) implicitly specifies the value of $\gamma(s_{qn})$ on each body. Thus, if Eq. (3.128) is used to regularise the singular matrix **[*K*]**, a unique solution of **[**γ**]** can be obtained.

Note that in a single-body system, when $N = 1$, the amount of vorticity created on the body surface exactly equals the amount of vorticity annihilated as bound circulation around the body; and the vorticity of the whole system is conserved. Consequently, the equation of vorticity conservation and the equation of circulation around the body imply each other. In this case, either Eq. (3.127) or Eq. (3.128) can be used to regularise the singular matrix **[*K*]** because both equations implicitly express the vortex sheet distribution $\gamma(s_n)$ on the body.

Adding Eq. (3.128) to Eq. (3.126), we obtain the modified Martensen equation,

$$\begin{aligned} &\sum_{q=1}^{N}\sum_{n=1}^{M_q} \left[K(s_{pm},s_{qn}) + \delta_{pq}\Delta s_{pm}\right]\gamma(s_{qn}) + \\ &\qquad \sum_{j=1}^{Z} \Delta\Gamma_j (L_{pm,j}\cos\beta_{pm} + M_{pm,j}\sin\beta_{pm}) + \cos(\alpha - \beta_{pm}) - \Gamma_{cp} = 0 \quad , \end{aligned} \tag{3.129}$$

that yields the solution of **[**γ**]** which satisfies Eq. (3.126) and Eq. (3.128) simultaneously.

As a result of regularisation, the elements of the regularised *coupling coefficient matrix* **[*K*^{r}]** and the modified *surface tangential velocity matrix* **[*b*]** take the forms

$$\begin{aligned} K^r_{pq,mn} &= K(s_{pm},s_{qn}) + \delta_{pq}\Delta s_{pm} \ , \\ b_{pm} &= -\cos(\alpha - \beta_{pm}) - \sum_{j=1}^{Z} \Delta\Gamma_j (L_{pm,j}\cos\beta_{pm} + M_{pm,j}\sin\beta_{pm}) + \Gamma_{cp} \ . \end{aligned} \tag{3.130}$$

A significant feature of the system of equations which results from the equation of bound circulation Eq. (3.128) and the Martensen equation (3.126) is that the vorticity of the Z_{dp} discrete vortices annihilated inside the body p is redistributed in the vortex sheet on that body when the Martensen equation Eq. (3.129) is applied to create a new vortex sheet. When these newly created vortex sheets are later shed into the flow as discrete vortices $\Delta\Gamma_{pm} = \gamma(s_{pm})\Delta s_{pm}$, the circulation associated with the annihilated vortices is now replenished into the flow. By this arrangement, the vorticity is conserved in such a way that the amount of vorticity generated on a body will exactly balance the amount of vorticity annihilated on that body. As vorticity is only created at solid surface of the bodies, the satisfaction of vorticity conservation for each body implies that the vorticity is conserved in the whole system.

Eq. (3.129), considered as the general equation for setting up the no-slip boundary condition at solid surface in the surface-vorticity boundary-integral method, is applicable to both inviscid and viscous flow calculations for both single and multiple body systems, i.e. N can be any non-zero finite value. When $N = 1$, Eq. (3.129) reduces to Eq. (3.73) for a single-body system. Thus, in the computational code developed in this numerical simulation project, Eq. (3.129) is implemented to perform the calculation.

Chapter 4

Description of Method Used in Present Calculations

This chapter addresses the implementation of the numerical procedures for the calculation of time-dependent two-dimensional viscous flow over a multi-body array by the discrete vortex and the surface-vorticity boundary-integral methods. Based on the established procedures for potential flow analysis and the extensions to viscous flow modelling outlined in chapter 3, we are able to develop a numerical scheme to simulate the real viscous flow over solid bodies.

4.1 Outline of the Numerical Procedures for Calculation of Time-Dependent Viscous Flow Over an Array of Solid Bodies

In the application of the surface vorticity method to bluff body flows, the body is enveloped by an infinitesimally thin vortex sheet whose strength distribution is so constructed that the body contour is a closed streamline. In addition a boundary condition of zero velocity tangential to the vortex sheet on its internal surface is prescribed, so that the body is represented by a solid surface covered by vortex sheet.

Within the framework of the discrete vortex and the surface-vorticity boundary-integral methods, the vortex sheet covering the bluff-body and the vorticity in the flow around it (in the boundary layer and in the wake) are replaced by a system of bound and free discrete vortices. The strength of the vortex sheet on each of the bodies in the system is determined so that it satisfies the boundary condition of zero velocity at solid boundaries and is approximated by a set of two-dimensional surface-vorticity elements with strengths $\gamma(s_{qn})$, q = 1,2,...N, n = 1,2,...M_q, each element being equivalent to a discrete vortex of strength $\gamma(s_{qn})\Delta s_{qn}$ (where Δs_{qn} is the length of the element). The vorticity that is created at solid boundaries and shed into the flow is represented by a set of point vortices, with circulation $\Delta\Gamma_j$, j = 1,2,...Z. Boundary

conditions are satisfied at the collocation points on the body contour. Thus mathematical modelling of bluff body flows by the method of discrete vortices involves determination of the circulations of the bound discrete vortices and their evolution in the flow: a solution is to be obtained for the vorticity distribution as a function of space and time. From the vorticity distribution, the velocity and pressure fields can be calculated at any point outside the bluff bodies or on the body surfaces.

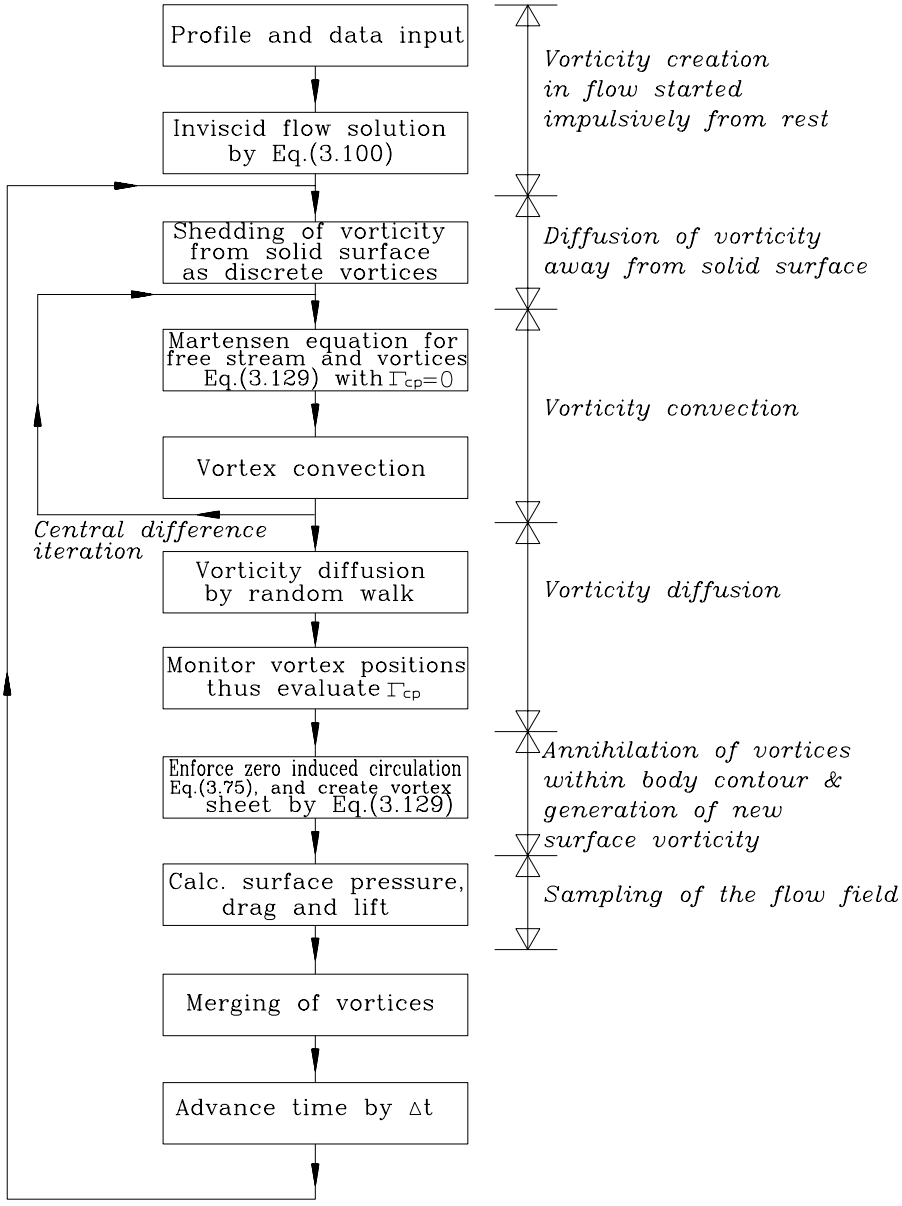

Figure 4.1. Solution procedures with the additional schemes of vortex merging and zero circulation correction.

The processes of vorticity creation, shedding, convection, and diffusion, which are taking place continuously and simultaneously in real fluid motion, are now modelled as successive discrete processes occurring over discrete time increments, using the basic numerical models described in section 3.4. The calculation of flow development over a period of time t is divided into finite time steps of size Δt. During each time step, the flow undergoes vorticity creation, vorticity shedding, vortex convection and diffusion in the flow field. Diffusion of vorticity is simulated by the random walk method described in section 3.4.6 and the vortex annihilation scheme is used to treat free vortices which enter the interior of the body contour.

The significant feature of the numerical model used in this project is that vorticity is shed from the entire body surface; so that we are able to model the development of the boundary layer, and the formation of a vortex wake in an impulsively started flow. The calculation procedures is essentially that illustrated in Fig. 3.11; with some additional detail it is presented again in Fig. 4.1. The various stages summarised in the figure are described in more detail in the following sections.

4.2 Generation of Vorticity and Equivalent Discrete Vortices

In the present calculation, the vortex sheet generated on the solid boundaries of body q is partitioned into discrete vortices of strength given by $\Delta\Gamma = \gamma(s_{qn})\Delta s_{qn}$ and shed into the flow, the values of $\gamma(s_{qn})$ being determined by the Eq. (3.129), which is repeated here for completeness

$$\sum_{q=1}^{N}\sum_{n=1}^{M_q}\left[K(s_{pm},s_{qn})+\delta_{pq}\Delta s_{pm}\right]\gamma(s_{qn}) + \sum_{j=1}^{Z}\Delta\Gamma_j\left(L_{pm,j}\cos\beta_{pm}+M_{pm,j}\sin\beta_{pm}\right)+\cos(\alpha-\beta_{pm})-\Gamma_{cp}=0\ . \qquad \textbf{(4-1)}$$

For the calculation of impulsively started flow, the first set of discrete vortices are determined by Eq. (4.1) with $Z = 0$ and $\Gamma_{cp} = 0$ for $p = 1,2,...N$, which is now equivalent to Eq. (3.119) derived for inviscid flow with the uniform main stream only. After this initial instant, these vortices are shed into the flow which then contains a system of Z discrete vortices. The discrete vortices in the flow are taken into account in all subsequent solutions of the Martensen equation, the value of Z increasing as time progresses. In all later time-steps generation of new

vorticity (at the end of each step) must account for circulation removed by annihilation of vortices which enter the interior of the body contour as a result of the random walk process. Γ_{cp}, p = 1,2,...N, represents the total circulation of these vortices in any given time-step.

4.3 Numerical Procedure for the Introduction of Discrete Vortices into the Flow

The vorticity shedding process takes place at the beginning of each time step after the application of the Martensen equation at the end of the previous step. In the present calculations, the vortices are considered to have a structure given by Eq. (3.62). Based on the considerations given in section 3.4.4, the new vortices are introduced into the flow at a distance $\epsilon = \sqrt{(4\Delta t/(3Re))}$ above the solid surface. The strength and structure of the vortices in the flow remain unchanged with time.

The vorticity distribution in the flow, and hence the velocity field, is determined by the evolution of the discrete vortices in the flow by convection and diffusion. The vorticity distribution after k time-steps is obtained by performing the time integration. Let us denote the time step by Δt, the position of the i*th* discrete vortex at time $k\Delta t$ by (x_i^k, y_i^k), and the velocity field derived from these positions by (u^k, v^k). Given (x^k, y^k) and hence (u^k, v^k), the positions of vortices at the next time step (x^{k+1}, y^{k+1}) are determined as follows.

4.4 Numerical Procedure for the Simulation of Vorticity Convection and Diffusion

The simulation of vorticity convection and diffusion in the present work is carried out by using the operator splitting method, with two sequential fractional steps in each time-step as outlined in section 3.4.6. The calculation procedures are as follows.

In the first fractional step, the discrete vortices are convected at the local velocity, as determined by the vorticity field. For a flow with a uniform main stream inclined at an angle α to the x-axis, a system of Z discrete vortices and a solid body enveloped by a vortex sheet $\gamma(s_n)$, the velocity field can be calculated by the Biot-Savart equation.

With the notation introduced in Eq. (3.49), the velocity field is given by

$$u_i^k = \cos\alpha + \sum_{\substack{j=1 \\ j\neq i}}^{Z} \Delta\Gamma_j L_{ij} + \sum_{n=1}^{m} \gamma(s_n)\Delta s_n L_{in} \quad ,$$

$$v_i^k = \sin\alpha + \sum_{\substack{j=1 \\ j\neq i}}^{Z} \Delta\Gamma_j M_{ij} + \sum_{n=1}^{m} \gamma(s_n)\Delta s_n M_{in} \quad , \qquad \textbf{(4-2)}$$

where (u_i^k, v_i^k) is the velocity at the reference point i, and cos α and sin α represent the components of free stream velocity in the x and y directions respectively. The first sum in Eq. (4.2) is the velocity field of the discrete vortices. Each $\gamma(s_n)$ of the second sum in Eq. (4.2) is determined by the Martensen equation Eq. (4.1) to satisfy the no-slip boundary condition on the body surface in the current vorticity field. The effect of all $\gamma(s_n)$ on the overall velocity field, given by the second summation term in Eq. (4.2), can be regarded as that of the interaction between the discrete vortices and the solid bodies in the flow.

The satisfaction of the convection equation Eq. (3.60), for initial vortex position (x^k, y^k), amounts to tracking the points of the discrete vortices which implies solution of the system of ordinary differential equations (ODEs)

$$\frac{dx_i}{dt} = u(x_i, y_i, t)$$

$$\frac{dy_i}{dt} = v(x_i, y_i, t) \quad , \qquad \textbf{(4-3)}$$

with u^k and v^k as given by Eq. (4.2). The solution can be approximated by, for example, a forward difference scheme to advance the vortices, as discussed in section 3.4.6; it is

$$x_{ci}^{k+1} = x_i^k + \Delta t\, u_i^k$$

$$y_{ci}^{k+1} = y_i^k + \Delta t\, v_i^k \quad . \qquad \textbf{(4-4)}$$

This takes the vortices to intermediate positions, after the convection step, denoted by $(x_{ci}^{k+1}, y_{ci}^{k+1})$.

The accuracy of the procedure outlined above depends on the size of the finite time-step Δt and on the particular finite difference scheme which is used. As pointed out by Porthouse [1983] and Lewis [1991, Ch.8], the inviscid convection process is a thermodynamically and fluid-dynamically reversible process. If the convection process is reversed after a number of time-steps by changing Δt to $-\Delta t$, and performing the same number of time-steps, the final positions

of vortices should coincide with their initial positions. A comparison of the final and initial positions provides a measure of the accuracy of the numerical strategy.

The consequence of an inaccurate convection process is that the vortices do not follow the true streamline paths. With a forward difference scheme, the problem is intensified in flow regions with high-curvature streamlines. Instead of moving in the true streamline path, a vortex would follow a path of smaller curvature, spiralling away from the center of curvature. The errors introduced are analogous to the effect of viscous diffusion and are therefore sometimes referred to as "numerical viscosity", Lewis [1991, Ch.8].

The problems of numerical viscosity can be alleviated by the use a higher-order scheme, but at the expense of computing time. A central difference scheme for the convection process, as follows, has been used in this project (Lewis [1991, Ch.2]). For the initial positions of vortices (x^k , y^k) and the corresponding velocity field (u^k , v^k) given by Eq. (4.2), a forward difference step, Eq. (4.4), is first applied to move vortices to the intermediate positions (x_{ca}^{k+1}, y_{ca}^{k+1}); the velocity field (u_{ca}^{k+1}, v_{ca}^{k+1})$_a$ is again calculated by Eq. (4.2). The vortices are then convected to their corrected intermediate positions (x_{cb}^{k+1}, y_{cb}^{k+1}) according to the expressions

$$x_{cb}^{k+1} = x^k + \frac{1}{2}\Delta t\,(u^k + u_{ca}^{k+1}) \quad ,$$
$$y_{cb}^{k+1} = y^k + \frac{1}{2}\Delta t\,(v^k + v_{ca}^{k+1}) \quad . \qquad \textbf{(4-5)}$$

This procedure can be made iterative by determining the new velocity field (u_{cb}^{k+1}, v_{cb}^{k+1}) for the new vortex positions (x_{cb}^{k+1}, y_{cb}^{k+1}), and then using the velocity field (u_{cb}^{k+1}, v_{cb}^{k+1}) in place of (u_{ca}^{k+1}, v_{ca}^{k+1}) in Eq. (4.5) to calculate new approximate vortex positions. The iteration can be repeated as many times as required to achieve a desired level of accuracy and to ensure reversibility of the process. It is imperative to update the values of $\gamma(s_{pn})$ so as to maintain the boundary condition at the solid surface during each stage of the iteration process. This is accomplished by using the Martensen equation Eq. (4.1) to evaluate $\gamma(s_{pn})$ in the current vorticity field. Since in any given time step the convection calculation is immediately preceded by shedding of all surface vorticity from the body, the appropriate form of the Martensen equation to be solved in each iteration of the convection calculation is Eq. (4.1) with $\Gamma_{cp} = 0$. Any annihilated discrete vortices within the time step are temporarily bound to the segment at which they cross the body, so that their effect on the external velocity field is maintained. By using the notation introduced in section 3.4.9, the vorticity on segment s_{pn} due to vorticity annihilation is $\Gamma_f(s_{pn})/\Delta s_{pn}$. Therefore the resultant vorticity on the contour during the iterative

convection calculation is $[\gamma(s_{pn}) + \Gamma_j(s_{pn})/\Delta s_{pn}]$, and the velocity field is given by the modified equation Eq. (4.2) in the form

$$u_i^k = \cos\alpha + \sum_{\substack{j=1 \\ j\neq i}}^{Z} \Delta\Gamma_j L_{ij} + \sum_{p=1}^{N}\sum_{n=1}^{M_p} \left[\gamma(s_{pn})\Delta s_{pn} + \Gamma_j(s_{pn})\right] L_{i,pn} \quad ,$$

$$v_i^k = \sin\alpha + \sum_{\substack{j=1 \\ j\neq i}}^{Z} \Delta\Gamma_j M_{ij} + \sum_{p=1}^{N}\sum_{n=1}^{M_p} \left[\gamma(s_{pn})\Delta s_{pn} + \Gamma_j(s_{pn})\right] M_{i,pn} \quad , \qquad \textbf{(4-6)}$$

where the $\gamma(s_{pn})$ are given by the Martensen equation (4.1) with $\Gamma_{cp} = 0$. In the present work, two iterations have been used, as a balance between numerical accuracy and computing time.

Upon completion of the first fractional step which simulates vortex convection, the vortices are at the intermediate positions (x_c^{k+1}, y_c^{k+1}). The second of the fractional steps is to satisfy the vorticity diffusion Eq. (3.57), starting with initial vortex positions (x_c^{k+1}, y_c^{k+1}). The viscous diffusion of vorticity is simulated by using the random walk process originally proposed by Chorin [1973], in the form given by Porthouse and Lewis [1981] as discussed in section 3.4.5.

Each vortex is given a radial drift Δr and an angular displacement $\Delta\theta$ according to Eq. (3.67) in order to determine the random walk components η_1 and η_2 in the x and y directions respectively. The values of Δr and $\Delta\theta$ are determined independently for each vortex. The final positions (x^{k+1}, y^{k+1}) of the discrete vortices are obtained by adding the convection and the diffusion displacements, i.e. $(x^{k+1}, y^{k+1}) = (x_c^{k+1}, y_c^{k+1}) + (\eta_1, \eta_2)$ as given by Eq. (3.66).

In order to advance all vortices by one convective step, the velocity field (u_i^k, v_i^k) due to all vortices has to be calculated at each vortex position (x_i^k, y_i^k), for the superposition required by Eq. (4.2). Therefore the number of calculation required for each convection step is of the order of $O(Z^2)$, where Z is the number of vortices. When there is a large number of vortices in the flow field, the evaluation of velocity field by Eq. (4.2) imposes a heavy computational loading; we have found that this may take up to 95% of the total computing time. Unless some action is taken to deal with this problem, the computing time required to obtain solution for a long flow development time may become prohibitive. Computing time can be reduced by the numerical process of vortex amalgamation and the use of a grid system to facilitate cell-to-cell calculation, a detailed description of which is given in chapter 5.

4.5 Implementation of Vorticity Conservation and Induced Circulation Conditions

Upon completion of the convection and diffusion processes at the end of each time-step, the final positions of some of the vortices (especially those close to the solid boundary where viscous effects are dominant) may be inside the contour of body p, p = 1,2,...N. These vortices with total net circulation Γ_{cp} must be removed from the interior of body p to satisfy the prerequisite condition for the Martensen equation, that the interior of the body contour contains no vortex or source distributions. In addition some vortices will take up position outside the body contour, but so close to it that a correction to the *tangential surface velocity* matrix is necessary to enforce the condition that they each induce zero circulation around the body contour.

Therefore, at each time when the Martensen equation is applied, the positions of all vortices are examined to check whether they lie inside the body contour. This monitoring of vortex locations is performed as a complementary part of setting up Eq. (4.1), and therefore it does not involve any extra computing load.

In the present calculation, the vortex positions are monitored by examining the values Γ_{ip} of induced circulation around a body contour due to a unit vortex at each of the particular vortex positions. The value of Γ_{ip} is given by a equation similar to Eq. (3.74) in the following form:

$$\Gamma_{ip} = \sum_{m=1}^{M_p} \left(L_{pm,j} \cos\beta_{pm} + M_{pm,j} \sin\beta_{pm} \right) \Delta s_{pm} \quad , \quad p = 1,2,\ldots N. \qquad \textbf{(4-7)}$$

If the calculated value of Γ_{ip} is greater than 0.5, the vortex is considered to be inside the contour of body p and vice versa.

Those vortices which are found to be lie inside a body contour are eliminated and conservation of vorticity then maintained by the procedure for the vortex annihilation scheme given in section 3.4.7. The total net circulation Γ_{cp} of the vortices which move inside the body contour as a result of the random walk, and are annihilated, is redistributed in the vortex sheet and reintroduced into the flow as free vortices in the next time step.

For those vortices lying outside the contour, if their value of Γ_{ip} given by Eq. (4.7) deviates from zero (the theoretical value for external vortices) by more than a predetermined value δe, for example $\delta e = 10^{-8}$, the condition of zero induced circulation around the contour is enforced. The induced velocity on the nearest segment, say s_{pk}, is corrected according to a scheme similar to Eq. (3.75) in the form:

$$(L_{pk,j}\cos\beta_{pk}+M_{pk,j}\sin\beta_{pk})\,\Delta s_{pk} = -\sum_{\substack{n=1\\ n\neq k}}^{M_p} (L_{pn,j}\cos\beta_{pn}+M_{pn,j}\sin\beta_{pn})\,\Delta s_{pn} \ . \qquad \textbf{(4-8)}$$

Note that the procedures for monitoring vortex positions and enforcing zero induced circulation are carried out when setting up Eq. (4.1). Therefore th ese procedures are complementary to the main calculation routine and do not impose an extra computing requirement.

4.6 Procedure for Vortex Merging

In the present calculations, vortex merging is carried out by following a slightly modified form of the Lewis [1991, Ch.11] proposal (see section 3.4.10). Since recirculation is likely to be present in the wake behind the body, the vortices at a short distance from the rearward face of the body may be convected towards the body. In order to maintain a reasonable resolution for the vorticity field near the body, the extent to which vortex merging occurs in the vicinity of the body is minimised. The arrangement for vortex merging in the present procedure is as follows:

(i) for $x<3L$, merge if $r_c \le \sigma$
(ii) for $3L<x<8L$, merge if $r_c \le 3\sigma$
(iii) for $8L<x$, merge if $r_c \le 5\sigma$.

The single resulting vortex is taken to have a strength $\Delta\Gamma_c$ given by Eq. (3.91) and to be located at the position given by Eq. (3.90).

The total circulation in the system, which should be zero, is monitored through Eq. (3.92) and it is generally found to have a value of the order of 10^{-12}. The boundary of the active flow domain D is set at a distance $20L$ (L is the characteristic length) from the bluff-body so as to allow the vortex wake to develop. Discrete vortices which have travelled beyond this boundary are removed permanently from the flow domain D and have their strength added to Γ_s (see Eq. (3.78)). Though the value of $20L$ is found adequate in most cases, it can be altered to suit a particular situation.

4.7 Summary of the Numerical Scheme for Viscous Separated Flows

With reference to the flow diagram of Fig. 4.1, the calculation procedures of the present numerical scheme for viscous bluff body flows can be categorised into the following functional modules. Note that the equations being solved by the numerical procedures are those for multi-body systems in non-dimensional form derived in sections 3.7, 3.8 and 3.9. These are general equations that they are readily applicable to single-body systems without any need for modification.

a) *Data Input*

The numerical calculation starts with the data input to specify the body contour, and the uniform main stream as characterised by the Reynolds number *Re* and its inclination α to the x-axis. This is followed by the formation of the basic coupling coefficient matrix **[*K*]** by equations Eq. (3.112) and Eq. (3.113) and its correction for zero induced circulation by Eq. (3.26) and Eq. (3.117). The resulting singular matrix **[*K*]** is then regularised by the condition of circulation Eq. (3.128). This results in the general Martensen equation Eq. (4.1). Inversion of the regularised *coupling coefficient matrix* **[*K*]** gives the working matrix $\mathbf{[K]}^{-1}$ which is stored for later use throughout the calculation.

b) *Potential Flow Calculation*

For calculation of impulsively started flow, the first potential flow calculation is performed to create the initial surface vorticity which is to be shed into the flow domain as discrete vortices. To obtain this initial surface vorticity, the prescribed circulations on all the solid bodies (lifting and non-lifting) are set to zero, i.e. $\Gamma_{bp} = 0$ for $p = 1,2,...N$; and Eq. (3.119) is then solved for **[γ]**. Note that the Kutta trailing-edge condition is not enforced in this case as the viscous flow will develop of its own accord to generate lift on lifting body.

After the first potential flow calculation, by Eq. (3.119), the first set of discrete vortices are shed from surface segments of the bodies. To facilitate later calculation of pressure distribution, the stagnation points on the body surface corresponding to the potential flow with the free stream only are determined. These are the points at which the contour integration of surface pressure around a body is started.

c) *Calculation of Flow Containing a System of Discrete Vortices*

After the initial shedding of vortices at $t = 0$, there exists a system of Z discrete vortices evolving in the flow. The numerical procedures in each step of the time-stepping calculation for viscous separated flow past a multi-body array are carried out as follows.

i. Initialise the annihilated vorticity on segments $\Gamma_j(s_{pm})$ for $p = 1,2,...N$ and $m = 1,2,...M_p$, so that the bound circulation Γ_{cp} on all bodies is equal to zero.

ii. Convect vortices according to Eq. (4.2) and Eq. (4.5), using appropriate central differencing scheme to achieve desired accuracy. Save the initial vortex positions (x^k, y^k), before commencing the convection process, for later use in calculating vortex transport velocities.

Monitor vortex positions while setting up Eq. (4.1) during the convection iteration process. If vortices are convected to positions inside the body contour, reflect them back to the flow domain. For those vortices which are outside the body contour but in close proximity to it, enforce the zero-induced-circulation condition around the contour according to Eq. (4.8).

iii. Carry out simulation of vorticity diffusion by the random walk process according to Eq. (3.67) and Eq. (3.68).

Monitor vortex positions while setting up Eq. (4.1) for the creation of surface vorticity. If vortices are diffused to positions inside the body contour, annihilate them, and incorporate their vorticity into Γ_{cp} and update $\Gamma_j(s_{pn})$. Discard the influences of vortices so annihilated on the other bodies in the system.

iv. Calculate the strength of the vortex sheet $\gamma(s_{pm})$ created at the body surfaces according to Eq. (4.1).

v. From the vortex positions (x^{k+1}, y^{k+1}) after completion of the convection and diffusion processes, calculate the vortex transport velocities $\boldsymbol{V}_j$ by Eq. (3.85). $\boldsymbol{V}_j$ is used to obtain other parameters of the flow field such as the velocity field $\boldsymbol{u}$, and the pressure distribution by Eq. (3.95).

Calculate surface pressure distributions with values of the latest calculated vortex-sheet strengths $\gamma(s_{pm})$ and $\Gamma_j(s_{pm})$ according to Eq. (3.107). Hence calculate the drag and lift coefficients acting on the bodies using Eq. (3.110) and Eq. (3.111).

vi. Merge vortices according to the condition of section 4.6.

vii. Save data to disk for analysis or future resumption of calculation.

viii. Shed surface vorticity into the flow domain as nascent vortices of equivalent strength, $\Delta\Gamma_{pm} = \gamma(s_{pm})\Delta s_{pm}$, placed at a distance ϵ from the solid surface.

ix. Reset $\Gamma_j(s_{pm})$ and Γ_{cp} to zero, for p = 1,2,...N and m = 1,2,...M_p, ready for calculation in next time step.

x. Repeat steps (ii) through (ix) until a state of fully developed flow is established.

Chapter 5

Uses of Grid Systems in Discrete Vortex Methods

As indicated in previous chapters, discrete vortex methods have advantages over other numerical methods in that they do not rely on a grid system to obtain a solution of the flow equations, and they therefore avoid the tedious grid formation process. Another special attraction of vortex methods for external fluid flow is that only the regions of key interest are dealt with. In contrast, the solution domain in grid-dependent methods has to be sufficiently large to allow acceptable peripheral boundary conditions to be established.

However, there is a computational difficulty of a different kind associated with vortex methods. Solution of a problem of unsteady separated flow by discrete vortex methods requires calculation of the velocity field induced by the entire system of discrete vortices at any given time. This is done by performing the Biot-Savart integral for each vortex to evaluate its effect on all other vortices. The number of calculations is proportional to the square of the number of vortices. Since the number of discrete vortices in the active flow domain continuously increases, as new vortices are created into flow field, the computing time for a time step is ever increasing. Eventually, the calculation becomes prohibitive.

Modified calculation procedures for vortex-to-vortex interactions are introduced to tackle this problem. Examples of the modified procedures are the cloud-in-cell method, which originates from plasma and high-energy physics, and the cell-to-cell method, which makes use of the Taylor series expansion to approximate the interactions between remote vortices. It is the latter method which has been incorporated in the present calculation procedure.

The basis of the cell-to-cell (CTC) method is the fact that the velocity field of a point vortex decreases with distance as $1/r$, as given by Eq. (2.24). Thus, instead of calculating the vortex-to-vortex interaction for individual, widely-separated, vortices, it is more efficient to calculate the group-to-group interaction, and this can be done without substantial loss of accuracy. In effect all the vortices in a cell can be referred to the cell centre and treated as a single vortex, with correction for the first, second, and higher order moments of the discrete vortices about their cell centre.

In the cell-to-cell method, a grid encompassing the entire active flow domain is employed to facilitate the grouping process. The grid may use square or rectangular cells (mesh), which is adequate as long as it covers the active domain. The noteworthy feature of the grid used in the cell-to-cell method (and also in the cloud-in-cell method) is its independence of the bluff body geometry. The grid is wholly used for allocation of vortices to their respective cells in order to perform the group-to-group calculation. This contrasts with the grid systems used for the finite difference methods in which the boundary conditions are imposed at the mesh points at the boundaries; such grid systems have to follow the body contour in order to allow boundary conditions to be applied at body surface. This constraint is not a feature of the cell-to-cell grids.

5.1 Mathematical Foundation of the Cell-to-Cell Algorithm

The calculation method of cell-to-cell algorithm is due to Spalart and Leonard [1981]. Lewis [1991, Ch.12] illustrates its application to the velocity induced at a particular vortex by all vortices within another cell. In the following, the result is expressed in terms of the distance between cell centres and the positions of vortices relative to the cell centres. By Eq. (2.33), the complex conjugate of the velocity $\boldsymbol{U}_{ji}$ induced at coordinate $\boldsymbol{Z}_j$ by a vortex of strength $\Delta\Gamma_i$ at coordinate $\boldsymbol{Z}_i$ is expressed by

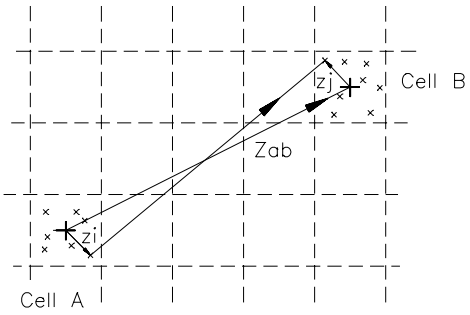

Figure 5.1. Schematic of the cell-to-cell method.

$$\bar{\boldsymbol{U}}_{ji} = u - iv = \frac{i\,\Delta\Gamma_i}{2\pi(\boldsymbol{Z}_j - \boldsymbol{Z}_i)} \quad . \tag{5.1}$$

The complex vector $(\boldsymbol{Z}_j - \boldsymbol{Z}_i)$ can be expressed in terms of the complex coordinates of the cell centres $\boldsymbol{Z}_a$, $\boldsymbol{Z}_b$ and the complex coordinates $\boldsymbol{z}_i$, $\boldsymbol{z}_j$ of the vortices relative to their respective cell centres as

$$\boldsymbol{Z}_j - \boldsymbol{Z}_i = (\boldsymbol{Z}_b - \boldsymbol{Z}_a) - (\boldsymbol{z}_i - \boldsymbol{z}_j) \ . \tag{5.2}$$

Substitution of Eq. (5.2) in Eq. (5.1), and expansion by Taylor's theorem about $(\boldsymbol{Z}_b - \boldsymbol{Z}_a)$ then gives

$$\bar{\boldsymbol{U}}_{ji} = \frac{i\,\Delta\Gamma_i}{2\pi(\boldsymbol{Z}_b - \boldsymbol{Z}_a)}\left(1 + \left(\frac{\boldsymbol{z}_i - \boldsymbol{z}_j}{\boldsymbol{Z}_b - \boldsymbol{Z}_a}\right) + \left(\frac{\boldsymbol{z}_i - \boldsymbol{z}_j}{\boldsymbol{Z}_b - \boldsymbol{Z}_a}\right)^2 + \left(\frac{\boldsymbol{z}_i - \boldsymbol{z}_j}{\boldsymbol{Z}_b - \boldsymbol{Z}_a}\right)^3 + \ldots\right) \ . \tag{5.3}$$

The extension to an array of I discrete vortices contained within the cell A gives the total induced velocity at $\boldsymbol{Z}_j$ as

$$\bar{\boldsymbol{U}}_j = \sum_{i=1}^{I} \bar{\boldsymbol{u}}_{ji} \ . \tag{5.4}$$

Letting $(\boldsymbol{Z}_b - \boldsymbol{Z}_a) \equiv \boldsymbol{Z}_{ab}$, we then have

$$\bar{\boldsymbol{U}}_j = \frac{i}{2\pi \boldsymbol{Z}_{ab}} \sum_{i=1}^{I} \Delta\Gamma_i \left(1 + \left(\frac{\boldsymbol{z}_i - \boldsymbol{z}_j}{\boldsymbol{Z}_{ab}}\right) + \left(\frac{\boldsymbol{z}_i - \boldsymbol{z}_j}{\boldsymbol{Z}_{ab}}\right)^2 + \left(\frac{\boldsymbol{z}_i - \boldsymbol{z}_j}{\boldsymbol{Z}_{ab}}\right)^3 + \ldots\right) \ , \tag{5.5}$$

or

$$\bar{\boldsymbol{U}}_j = \frac{i}{2\pi \boldsymbol{Z}_{ab}} \sum_{i=1}^{I} \Delta\Gamma_i \sum_{n=0}^{\infty} \left(\frac{\boldsymbol{z}_i - \boldsymbol{z}_j}{\boldsymbol{Z}_{ab}}\right)^n \ . \tag{5.6}$$

Introduce now the zeroth, first, second and higher order of moments of the discrete vortices about the cell centre, denoted by M_0, M_1, M_2,... etc. respectively. They are given by

$$M_k = \sum_{i=1}^{I} \Delta\Gamma_i \boldsymbol{z}_i^{\,k} \ , \qquad (k = 0,1,2,\ldots) \ . \tag{5.7}$$

By expansion of the series in Eq. (5.6) and rearrangement, the induced velocity $\bar{\boldsymbol{U}}_j$ is obtained as

$$\bar{\boldsymbol{U}}_j = \frac{i}{2\pi \boldsymbol{Z}_{ab}} \sum_{n=0}^{n_t} (-\boldsymbol{z}_j)^n \sum_{k=0}^{n_t - n} \frac{C_{n+1,k+1} M_k}{\boldsymbol{Z}_{ab}^{n+k}} \ . \tag{5.8}$$

Here n_t denotes the number of terms used in the truncated Taylor series, and $C_{n+1,k+1}$, the coefficient for the moment terms M_k, $k = 0,1,\ldots(n_t - n)$, is given by the binomial coefficient as

$$C_{n+1,k+1} = \binom{n+k}{n} = \frac{(n+k)!}{n!\,k!} \ . \tag{5.9}$$

For computational convenience, the $C_{n+1,k+1}$ values can be calculated at the outset of the cell-to-cell method and stored in an array, an example of which is shown in Eq. (5.10), corresponding to $n_t = 5$,

$$C = \begin{bmatrix} 1 & 1 & 1 & 1 & 1 & 1 \\ 1 & 2 & 3 & 4 & 5 & 0 \\ 1 & 3 & 6 & 10 & 0 & 0 \\ 1 & 4 & 10 & 0 & 0 & 0 \\ 1 & 5 & 0 & 0 & 0 & 0 \\ 1 & 0 & 0 & 0 & 0 & 0 \end{bmatrix}. \qquad \textbf{(5.10)}$$

The C values can thus be read from this array when required. For example, the C value corresponding to $n = 1$, $k = 2$ is $C_{2,3} = 3$.

5.2 Selection of Parameters

The computational saving is not obvious at first glance as extra overheads are required to calculate the vorticity moment terms, to allocate vortices to their respective cells, and also to calculate the complex coordinate of each vortex relative to the cell centre. Experiment reveals that optimal computing saving can be achieved by the cell-to-cell method by proper selection of two parameters :

(i) the number of terms n_t to be used in the truncated Taylor series expansion to achieve the desired accuracy, and

(ii) the optimum number of vortices per cell I_o as given by the mesh size.

5.2.1 Determination of the Number of Terms, *n*

Eq. (5.3) reveals the fact that the accuracy a cell-to-cell calculation can achieve depends on the magnitude of the vector $(\boldsymbol{z}_i - \boldsymbol{z}_j)$ relative to $\boldsymbol{Z}_{ab}$. Clearly, if both $\boldsymbol{Z}_i$ and $\boldsymbol{Z}_j$ are close to their respective cell centres, i.e. $(\boldsymbol{z}_i - \boldsymbol{z}_j)$ very small, fewer terms are required in the expansion to achieve the desired accuracy. On the other hand, if vortices are located far from centres, the approximation has to be corrected by the higher order moments of the vortices. Furthermore, the number of terms n_t used in the truncated Taylor series expansion depends on the accuracy demanded by the proximity of cells *A* and *B*, but is independent of the mesh size.

In Eq. (5.3), the term $1/(\boldsymbol{Z}_i - \boldsymbol{Z}_j) \equiv 1/\boldsymbol{Z}_{ij}$ is expressed by the Taylor series

$$\frac{1}{Z_{ij}} \approx \frac{1}{Z_{ab}}\left(1 + \left(\frac{z_i - z_j}{Z_{ab}}\right) + \left(\frac{z_i - z_j}{Z_{ab}}\right)^2 + \left(\frac{z_i - z_j}{Z_{ab}}\right)^3 + \ldots\right), \qquad \textbf{(5.11)}$$

which is exact only when the number of terms n_t in the series on the right-hand side tends to infinity. However, in practical computation, the Taylor series on the right-hand side of Eq. (5.11) is approximated by a finite number of terms (n_t is finite). The error δe of the approximation for $\overline{\boldsymbol{U}}_{ji}$ in Eq. (5.3) is therefore given by the ratio of (L.H.S.– R.H.S.) to (L.H.S.) of Eq. (5.11). In order to establish the relation between δe and n_t for a given grid system, we consider a square grid system of cell size Δl, with $\boldsymbol{z}_i$ and $\boldsymbol{z}_j$ located at opposite corners of their respective cells, so that $(\boldsymbol{z}_i - \boldsymbol{z}_j)$ has the maximum possible value. The values of $\boldsymbol{z}_i$ and $\boldsymbol{z}_j$ are given by

$$z_i = \frac{\Delta l}{2}(1 - i), \qquad z_j = \frac{\Delta l}{2}(-1 + i). \qquad \textbf{(5.12)}$$

Consider two cells A and B which are c columns and r rows apart, in which case $\boldsymbol{Z}_{ab} = \Delta l(c + ir)$ and $\boldsymbol{Z}_{ij} = \Delta l((c-1) + i(r + 1))$. Rewriting Eq. (5.11) in terms of c and r, and with $(\boldsymbol{z}_i - \boldsymbol{z}_j)$ as given by Eq. (5.12), we have

$$\frac{1}{(c-1)+i(r+1)} \approx \frac{1}{c+ir}\sum_{n=0}^{n_t}\left(\frac{1-i}{c+ir}\right)^n. \qquad \textbf{(5.13)}$$

Substituting the appropriate values of c and r into Eq. (5.13) and computing the difference between the left-hand side and right-hand side, we are able to establish the error δe for a given n_t associated with two particular cells.

	c=0	c=1	c=2	c=3	c=4	c=5	c=6	c=7	c=8
r=0	nil	nil	19	10	6	6	5	5	3
r=1	nil	nil	18	10	7	5	4	4	3
r=2	19	18	9	8	6	6	5	5	4
r=3	10	10	8	6	5	5	5	4	4
r=4	6	7	6	5	4	4	4	4	4
r=5	6	5	6	4	4	4	4	3	3
r=6	5	4	5	4	4	4	3	3	3
r=7	5	4	5	4	3	3	3	3	3
r=8	3	3	4	4	3	3	3	3	3

Table 5.1. Number of terms, n_t, required to maintain error level δe = 0.0001 in cell-to-cell method.

Table 5.1 summarises the minimum numbers of terms n_t required to maintain an error δe = 0.0001 for various cell proximities. Clearly, the more terms used, the higher will be the accuracy of approximation for $\bar{\boldsymbol{u}}_{ji}$. The values of n_t established here are for the case that the vector $(\boldsymbol{z}_i - \boldsymbol{z}_j)$ has its maximum possible value. Since most of the vortices will lie closer to their respective cell centres, the accuracy of approximation is ensured by using the established value of n_t. Table 5.1 shows that as many as 19 terms are required to achieve the set error level for cells in close proximity. However, in most cases only ten terms or less are required. In order to avoid excessive computational overheads in calculating the vorticity moment terms and excessive requirements of computer memory for temporary data storage, the maximum number of terms N_t has been set to 10 in the present work. Vortex interactions within cells as well as between adjacent cells are still obtained by direct vortex-to-vortex interaction for any cases which would require $n_t > N_t$.

The computational savings come from the fact that the moment terms M_0 , M_1 , M_2 etc. of each cell need only be calculated once and can be used unchanged to compute the velocity of any number vortices $\Delta\Gamma_j$ at all other cells. The complex coordinate of a vortex relative to its cell centre $\boldsymbol{z}_j$ and its higher powers can be calculated and saved during the cell allocation procedure for each time instant. Furthermore the complex coordinate $\boldsymbol{Z}_{ab}$ and its powers are fixed for a given mesh configuration; these values can be calculated once and for all at the outset.

5.2.2 Determination of the Optimum Number of Vortices Per Cell, I_o

For every calculation of the interaction between two cells, the second summation term of Eq. (5.8)

$$\sum_{k=0}^{n_t-n} \frac{C_{n+1,k+1} M_k}{Z_{ab}^{n+k}} \qquad \textbf{(5.14)}$$

of the participating cells is first of all evaluated. The induced velocity at each vortex position is obtained by substituting the appropriate $(-\boldsymbol{z}_j)^n$ into Eq. (5.8). Computing time is saved because these summation terms in are the same for all vortices in the two cells. However, the presence of too many vortices in a single cell, as a result of a mesh which is too coarse, leads to the need for more terms n_t to achieve a given error level, the more frequent calculation of direct vortex-to-vortex interactions, and little or no computational saving.

To obtain an indication of the optimal number of vortices per cell, two numerical experiments were conducted. In the first, 1500 uniformly distributed vortices were used to evaluate the effect of the number vortices per cell, I, on computational efficiency. The selection of n, for a specified error level δe, was based on the condition determined in section 5.2.1. The computing time corresponding to various values of I are listed in Table 5.2, in which the values are normalised by the computing time taken for the direct vortex-to-vortex interaction.

Number of vortices, Z : 1500 Error level, δe : 0.0001 Maximum number of term, N_t : 5	
Number of vortices per cell, I	Computing time
direct interaction	1.00
2.7	2.35
11.1	0.75
16	0.70
20	0.65
25	0.75
44	0.85
69.4	1.02

Table 5.2. Comparison of computing time of direct summation and cell-to-cell method.

The second experiment with 2500 uniformly distributed vortices showed that a 40% reduction in computing time can be achieved at an error level of 0.0001, and that as much as 60% reduction can be achieved at an error level of 0.01. For a given distribution of vortices, the efficiency of the cell-to-cell calculation can vary drastically depending on the number of vortices in the cell. Too fine a grid structure and thus too few vortices per cell, can lead to extra computing time due to more frequent evaluation of the summation terms in Eq. (5.8). Too coarse a grid structure will mean the more frequent use of the direct vortex-to-vortex interaction, and hence the wasting of the overhead of calculating moments terms. In practice, the vortices within the flow domain are not uniformly distributed, and it is not possible to arrange that every cell has the same number of vortices. In order to make the cell-to-cell method work efficiently, it is essential to choose a grid size so that the average number of vortices per cell can be kept in the range 15 to 40.

5.3 Operational Procedure for the Basic Cell-to-Cell Method

The numerical procedure developed in the present study for implementing the basic cell-to-cell method can be summarised as follows:

i. Determine the desirable level of accuracy δe, and the maximum number of terms N_t. These values are then fixed throughout the course of calculation.

ii. Design a grid structure to cover the entire active flow domain, and to keep the number of vortices per cell between about 15 and 40. The grid structure so formed is fixed throughout the course of calculation.

iii. Allocate vortices to cells, and during the same process determine the complex coordinates $\boldsymbol{z}_j$ of vortices relative to cell centres. Hence, calculate the moment terms M_k for $k = 0,1,2,...N_t$, according to Eq. (5.7).

iv. Calculate vortex velocities starting with the first cell of the grid structure, denoted as A = Cell(1) in the flow diagram Fig. 5.2, where A is a cell variable. The mutually induced velocities for vortices within A are calculated by the direct vortex-to-vortex summation, VTV(A).

Perform cell-to-cell calculation for all possible pairs of cells, A and B, for the required number of terms n_t determined by a given $\boldsymbol{Z}_{ab}$. If n_t is less than or equal to N_t, proceed to calculate higher order terms $\boldsymbol{Z}_{ab}^{-n}$ for $n = 1,2,...N_t$; then calculate mutually induced vortex velocities in the two cells, denoted by CTC(A, B) in the flow diagram. For vortices in any two cells requiring $n_t > N_t$, calculate induced velocities by the Biot-Savart equation, i.e. by the summation of direct vortex-to-vortex interactions, denoted by VTV(A, B) in the flow diagram.

Steps (iii) and (iv) are repeated in all the subsequent cell-to-cell calculations.

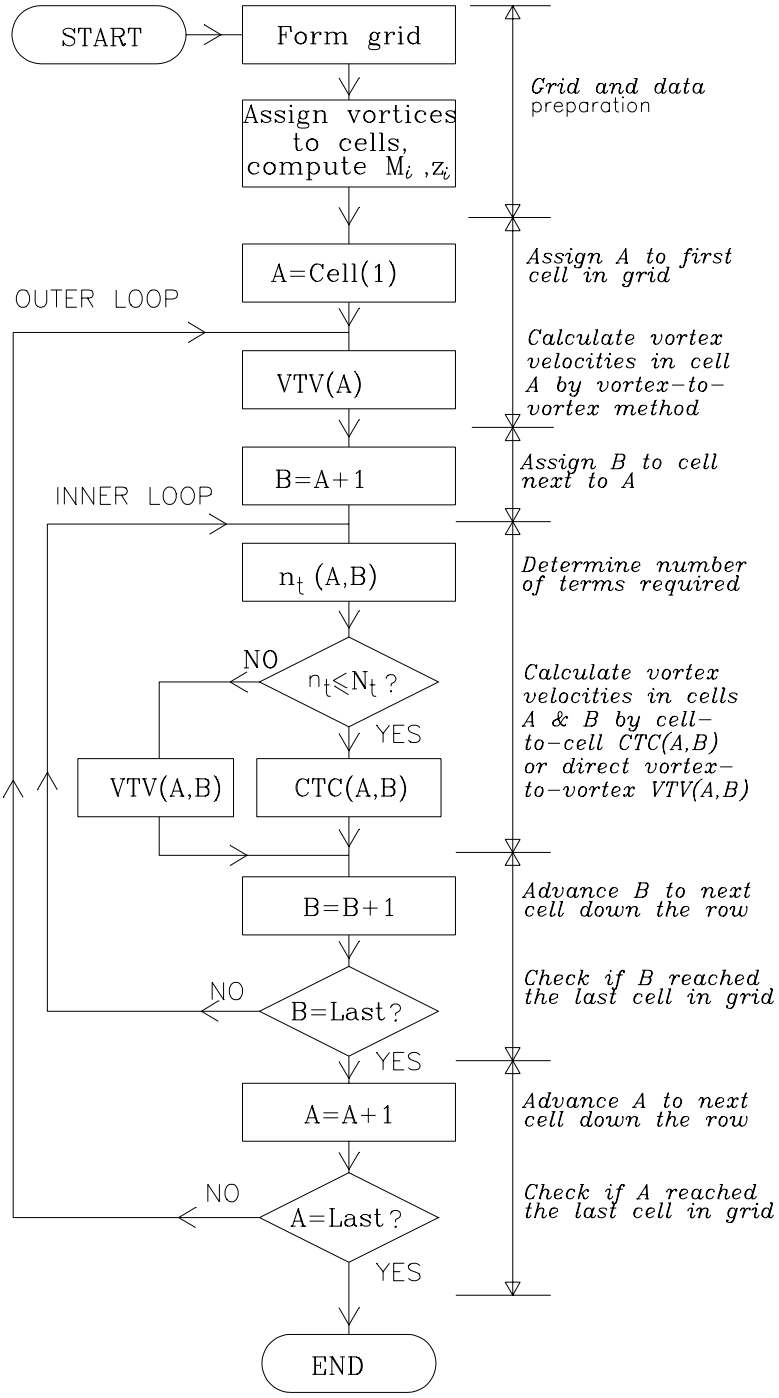

Figure 5.2. Operational procedures of the basic cell-to-cell method.

5.4 Modifications to the Basic Cell-to-Cell Algorithm

The basic configuration of the cell-to-cell method described in previous sections is a grid structure of uniform mesh. With this basic arrangement, calculation of the induced velocity at each vortex positions requires treatment of two cells at a time. Computing time is saved because a number of discrete vortices can be grouped as one equivalent vortex for calculation of the induced velocity at distant points. In practice, this means that fewer terms are required in the Taylor series expansion for a given degree of accuracy for distant cells.

Moreover, the moment terms (the second summation term in Eq. (5.8)) are calculated once and used for all vortices in the two cells being considered. Let the number of vortices in the two cells be I_1 and I_2. The number of calculations required by the cell-to-cell method is of the order of $O(I_1+I_2)$ in contrast to $O(I_1 \times I_2)$ as required by the direct vortex-to-vortex summation. It would seem that the larger the number of vortices per cell the greater the benefit of the cell-to-cell method in terms of computing time. However, for a given level of accuracy, the need for direct vortex-to-vortex calculation within each cell and for cells in close proximity, occasioned by increasing the number of vortices per cell, will eventually lead to longer computing time.

With a view to taking advantage of the efficient calculation procedure that the cell-to-cell method can offer and, at the same time, avoiding excessive use of direct vortex-to-vortex calculations, modifications to the basic cell-to-cell method have been implemented in the present numerical scheme.

5.4.1 Use of Sub-Grid Structures to Enhance Cell-to-Cell Calculations

There are two main reasons for the use of sub-grid structures. Firstly, the number of vortices in any single cell can be kept as large as possible to take advantage of the efficient cell-to-cell calculation. When the vortex-to-vortex procedure is required for calculation within one cell or between two cells requiring $n_t > N_t$, calculation can be switched to cell-to-cell procedures at the sub-cell level. In this way, the use of direct vortex-to-vortex calculation is minimised.

Secondly, the computing times quoted in Table 5.2, which apply for a uniform grid structure, are ideal, and can be achieved in practice only when the discrete vortices are distributed uniformly throughout the grid structure. In the case of bluff body flows, the distribution of discrete vortices depends on the phase of the flow reached at any particular time instant. In general their distribution is not uniform. In this project, it has been found that the number of vortices per cell may range from $I < 10$ to $I > 200$. In order to make the cell-to-cell method more efficient in dealing with non-uniformly distributed vortices, a sub-grid structure has been implemented in the present work with the primary purpose of evening out the number of vortices to be handled in each cell-to-cell calculation.

Implementation of the cell-to-cell algorithm with a sub-grid structure requires a systematic procedure to form grid structures at a number of levels. Let h denote the level of any particular sub-grid system, and H the highest sub-grid level of the grid structure. With this notation, the flow with no grid structure is $h = 0$, and the basic grid structure on which the sub-grids are built is $h = 1$; and the various sub-grid structures in the system may then be at levels $h = 2, 3,...H$. Fig. 5.3 shows a grid system with two levels of sub-grid structure, i.e. $H = 3$. The vectors $\boldsymbol{z}_i(1)$ and $\boldsymbol{z}_i(2)$ shown in Fig. 5.3 are the complex coordinates of the discrete vortex relative to the centre of the cells at level $h = 1$ and $h = 2$ respectively. Note that the vector $\boldsymbol{z}_i(3)$ is intentionally omitted in the figure for clarity.

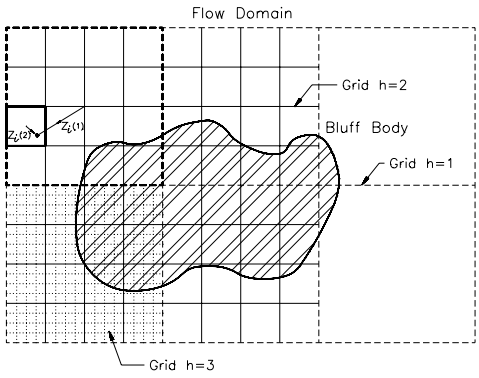

Figure 5.3. Schematic of cell-to-cell grid structure with two levels of sub-grid, H=2.

The grid formation process starts with the basic grid structure $h = 1$ which covers the entire flow domain. By constructing a grid structure in each cell of the basic grid $h = 1$, the sub-grid structure $h = 2$ is formed. For simplicity in the calculation procedure and consistency with the basic grid structure, a square mesh is used in all the sub-grid structures, and the number of rows and columns J to be formed in each cell at any level is 4. This grid formation procedure is repeated for each cell of the grid $h = 2$ to form the sub-grid at level $h = 3$. The process can go on until the required number of levels of sub-grid structures is reached. It may be noted that there is no limit imposed on the number of levels of sub-grid structure which can be formed in a system, as long as the demand for computer memory for these structures can be satisfied.

In the cell-to-cell method with sub-grid structure, the moment terms that a discrete vortex has with respective to the cell centres at each level of the grid structure are calculated. Let $\boldsymbol{z}_i(h)$, where h = 1,2...H, denote the complex coordinates of a discrete vortex relative to the centre of the cell in level h. The zeroth, first, second and higher order of moments $M_k(h)$ of the discrete vortices about the cell centre in the various levels of grid structure are given by

$$M_k(h) = \sum_{i=1}^{I(h)} \Delta\Gamma_i z_i(h)^k \ , \qquad k = 0,1,2,\ldots, \quad h = 1,2,\ldots H \ . \tag{5.15}$$

Eq. (5.8) for the induced velocity $\bar{U}_j$ is now extended to cater for cell-to-cell calculation with sub-grid structure. With $\boldsymbol{Z}_{ab}(h)$ denoting the complex vector between the centres of cells which are in the sub-grid level h, it takes the form

$$\bar{U}_j = \frac{i}{2\pi Z_{ab}(h)} \sum_{n=0}^{n_t} (-z_j(h))^n \sum_{k=0}^{n_t-n} \frac{C_{n+1,k+1} M_k(h)}{Z_{ab}^{n+k}(h)} \ . \tag{5.16}$$

The concept of a grid system has been greatly expanded by the use of sub-grid structure. A cell in a grid system is itself a grid system, and the entire flow domain can be considered as a (rectangular) cell. The cell-to-cell calculation becomes the grid-to-grid calculation. A standard procedure that operates on a cell can thus be used to handle a grid system at all levels, as well as the entire flow domain. This feature simplifies the calculation procedures for the cell-to-cell methods and thus enhances computational efficiency.

Evaluation of the induced velocity at each vortex position starts with the basic grid h =1; the operation follows the procedures outlined in section 5.3. The number of terms n_t required is determined by the proximity of the two cells concerned. If the n_t required is higher than the maximum number of moment terms N_t, the calculation proceeds with the grid structure at the next level; otherwise the normal cell-to-cell algorithm, Eq. (5.16), is used. If the highest level of grid system is reached ($h = H$) and the number of terms n_t required is higher than the maximum order of moment terms ($n_t > N_t$), then direct summation is used to calculate the induced velocities. For a given cell-to-cell grid system, the vectors $\boldsymbol{Z}_{ab}(h)$ for h = 1,2,...H are constant and so are all the associated values $\boldsymbol{Z}_{ab}^{-k}(h)$ for k = 1,2,...,N_t. These constant values, once determined, apply for all subsequent calculations with that given grid system. Therefore, further saving in computing time can be achieved by storing these values and retrieving them when needed.

5.4.2 Continuous Monitoring of the Cell-to-cell Performance

One difficulty encountered in using the cell-to-cell method is the determination of the size of the mesh structure in order to house the vortices with the optimum number of vortices per cell. Numerical experiments show that the efficiency, in term of computing time, of the cell-to-cell calculation depends on the number of vortices per cell: either too many and too few will lead to poor efficiency.

It has been suggested in section 5.2.2 that the optimum number of vortices per cell ranges from about 15 to 40. However, since the distribution of vortices continuously changes in the course of calculation, the optimum grid structure changes with time. In order to monitor the suitability of a particular grid structure for the current distribution of vortices, a procedure has been implemented to monitor the cell-to-cell performance. The vortex distribution over the grid system is surveyed, and if the number of vortices per cell deviates from the acceptable range, the grid is reconstructed. This procedure works continuously so that the best possible grid structure can be maintained at all times.

5.5 Operational Procedure for the Modified Cell-to-Cell Method with Sub-Grid Structure

In order to perform the modified cell-to-cell method with sub-grid structure, a huge amount of computer memory is required for the storage of temporary data such as $\boldsymbol{z}_i(h)$, $\boldsymbol{z}_i^2(h)$, $\boldsymbol{z}_i^3(h)$,...$\boldsymbol{z}_i^{Nt}(h)$, $h = 1,2,...H$, for all the discrete vortices and $\boldsymbol{Z}_{ab}(h)$, $\boldsymbol{Z}_{ab}^{-1}(h)$, $\boldsymbol{Z}_{ab}^{-2}(h)$, ... $\boldsymbol{Z}_{ab}^{-Nt}(h)$ associated with the grid system. Thus, the amount of available computer memory determines the number of sub-grid levels which can be used.

In the present work, with 32M byte RAM of computer memory available, the set up is $H = 2$, $J = 4$ and $N_t = 12$. The maximum number of discrete vortices which can be handled is about 27,000. With the use of one level of sub-grid structure, the efficiency of the cell-to-cell calculation has been improved by 25%, and the overall computing time reduced by 60% compared with the time taken by direct summation of the Biot-Savart equation. To conclude this section on the use of a sub-grid structure in the cell-to-cell method with the modified cell-to-cell algorithm, the flow diagram for the procedure is presented in Fig. 5.4 and summarised as follows.

i. Determine the number of sub-grid levels H, the number of rows and columns J in each sub-grid, the desirable level of accuracy δe, and the maximum number of vortex moment terms N_t.

ii. Form the basic grid structure, $h = 1$, to cover the entire active flow domain, and then form the sub-grid structure for $h = 2,3,...H$.

iii. Allocate vortices to cells of the basic grid $h = 1$ first and then to cells of the respective sub-grid systems. During this allocation process, calculate the complex coordinates $\boldsymbol{z}_i(h)$, $\boldsymbol{z}_i^2(h)$, $\boldsymbol{z}_i^3(h)$, $...\boldsymbol{z}_i^{Nt}(h)$, $h = 1,2,...H$.

Monitor the suitability of the current grid structure for the distribution of vortices. Redesign grid structure to suit changes of distribution of vortices with time, as the need arises.

iv. Calculate vortex velocities starting with the basic grid structure $h = 1$. The velocities mutually induced by vortices within one single cell are calculated, for which the mode of calculation depends on the number of discrete vortices I in the cell. If the value of I is larger than 20 and a sub-grid is available in that cell, perform cell-to-cell calculation in the next available sub-grid level. Otherwise, if $I < 20$ or $h = H$, carry out direct vortex-to-vortex summation for the cell concerned.

Perform cell-to-cell calculation for all possible pairs of cells, A and B, in the basic grid $h = 1$, and determine the number of terms n_t required for a given $\boldsymbol{Z}_{ab}(1)$. If $n_t \le N_t$, proceed to calculate higher order terms $\boldsymbol{Z}_{ab}^{-2}(1)$, $\boldsymbol{Z}_{ab}^{-3}(1)$, etc. and carry out cell-to-cell calculation by Eq. (5.16). If $n_t > N_t$ and $I > 20$, perform cell-to-cell calculation at the next available sub-grid level.

Otherwise, if the highest level of sub-grid structure is reached, $h = H$, or the number of vortices in the cell is less than 20, $I < 20$, calculate vortex velocities by direct summation of the Biot-Savart equation.

v. Save data such as $\boldsymbol{Z}_{ab}(h)$ and higher order terms, and n_t for subsequent calculations.

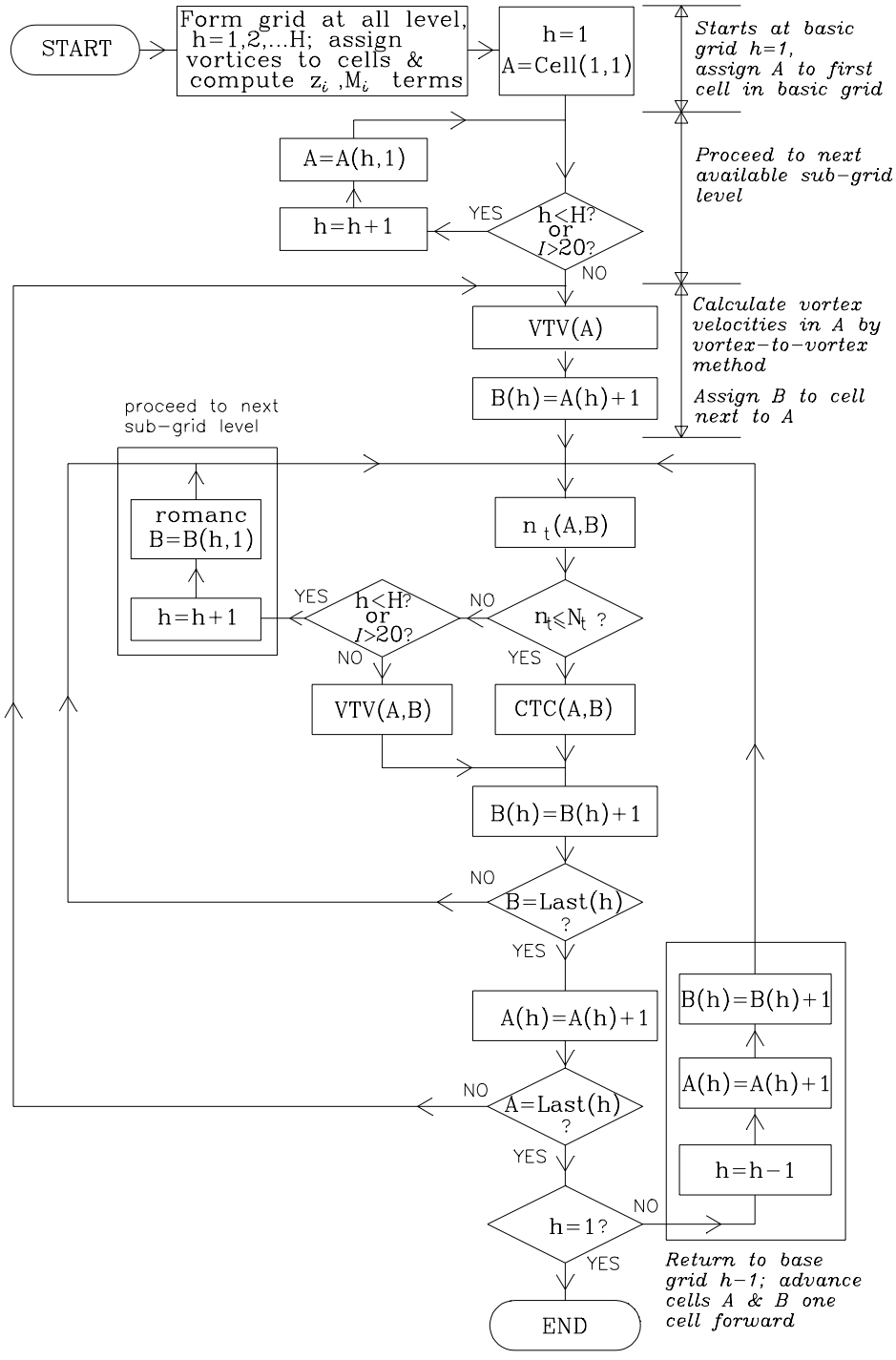

Figure 5.4. Operational procedures for cell-to-cell method with sub-grid structure.

5.6 Other Uses of the Cell-to-Cell Algorithm

The cell-to-cell algorithm developed in the above sections has been set up primarily for the calculation of velocities mutually induced by discrete vortices, as required in the simulation of vorticity convection in the flow. However, the algorithm, with suitable modification, also provides an efficient calculation procedure for other quantities of fluid flow. This section highlights the modification that can be made to extend the cell-to-cell methods to calculations of other flow quantities.

Firstly, consider the calculation of induced velocity at a general point *j* in the flow field due to a system of discrete vortices, otherwise given by the Biot-Savart equation. In this case, the Taylor series of Eq. (5.1) is expanded about $\boldsymbol{Z_{aj}}$ the complex coordinate of point *j* relative to the centre of cell *A*, as shown in Fig. 5.5, which is given by

$$\boldsymbol{Z_j - Z_i = Z_{aj} - z_i} \ . \qquad \textbf{(5.17)}$$

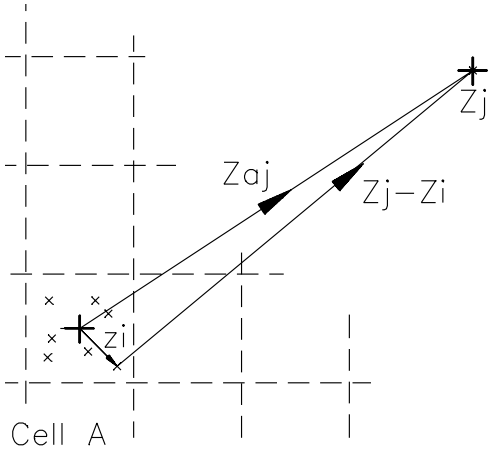

Figure 5.5. Calculation of induced velocity at a point by the Cell-to-cell method.

Expanding the Taylor series of Eq. (5.1) about $\boldsymbol{Z_{aj}}$ and rearranging, we obtain the conjugate of the induced velocity $\bar{\boldsymbol{U}}_j$ due to an array of *I* vortices contained in cell *A* as

$$\bar{\boldsymbol{U}}_j = \frac{i}{2\pi \boldsymbol{Z_{aj}(h)}} \sum_{k=0}^{n_t} \frac{M_k(h)}{\boldsymbol{Z_{aj}^k(h)}} \ , \qquad \textbf{(5.18)}$$

where $M_k(h)$ are the moment terms given by Eq. (5.15). Note that Eq. (5.18) is expressed in general form, thus making provision for the use of the cell-to-cell method with the sub-grid structure derived in the present study.

The conjugate of the induced velocity at a point, due to the entire system of discrete vortices in the flow domain, can thus be obtained by summing Eq. (5.18) over all the cells in a cell-to-cell system. The operational procedures for this calculation are the same as those given in section 5.5. By the use of Eq. (5.18), we can extend the cell-to-cell algorithm to calculation of other quantities induced by the discrete vortices.

Secondly, consider the evaluation of Eq. (3.88) for the stagnation pressure induced at a point by a system of discrete vortices which are moving at velocities $\boldsymbol{V}_i = (v_{xi}, v_{yi})$. It requires summation of the vector dot product $\boldsymbol{U}_{ji} \cdot \boldsymbol{V}_i$ over all the discrete vortices in the flow field. When this calculation is performed at a large number of points, such as when constructing the pressure distribution in the entire flow domain, direct summation of Eq. (3.88) becomes very inefficient. Alternatively, and more efficiently, we can make use of the cell-to-cell algorithm to calculate the term $\boldsymbol{U}_{ji} \cdot \boldsymbol{V}_i$.

By expressing the velocities in complex-variable form, it can be seen that the dot product $\boldsymbol{U}_{ji} \cdot \boldsymbol{V}_i$ is equivalent to the real part of the complex-variable product $\bar{\boldsymbol{U}}_{ji} \boldsymbol{V}_i$. Multiplying Eq. (5.1) by $\mathbf{V}_i$, we have the product $\bar{\boldsymbol{U}}_{ji} \boldsymbol{V}_i$ given by

$$\bar{\boldsymbol{U}}_{ji} \boldsymbol{V}_i = \left(\frac{i \, \Delta\Gamma_i v_{xi}}{2\pi (Z_j - Z_i)} \right) + i \left(\frac{i \, \Delta\Gamma_i v_{yi}}{2\pi (Z_j - Z_i)} \right)$$

$$= \boldsymbol{A}_{ji} + i \boldsymbol{B}_{ji} \quad . \tag{5.19}$$

Each of the bracketed terms on the right-hand side of Eq. (5.19) resembles Eq. (5.1) but with $\Delta\Gamma_i$ replaced by $\Delta\Gamma_i v_{xi}$ and $\Delta\Gamma_i v_{yi}$ respectively. It follows that, in the present case, we can use the same cell-to-cell solution procedures developed in previous sections for Eq. (5.1). For simplicity, two auxiliary complex variables $\boldsymbol{A}_{ji}$ and $\boldsymbol{B}_{ji}$ each representing the corresponding bracketed term in Eq. (5.19), have been introduced.

By applying the cell-to-cell solution procedures to Eq. (5.19), the solutions for $\boldsymbol{A}_j$ and $\boldsymbol{B}_j$ at point j due to an array of I discrete vortices in a cell are given by

$$\boldsymbol{A}_j = \sum_{i=1}^{I} A_{ji} = \frac{i}{2\pi Z_{aj}(h)} \sum_{k=0}^{n_t} \frac{W_{xk}(h)}{Z_{aj}^{k}(h)} \quad ,$$

$$\boldsymbol{B}_j = \sum_{i=1}^{I} B_{ji} = \frac{i}{2\pi Z_{aj}(h)} \sum_{k=0}^{n_t} \frac{W_{yk}(h)}{Z_{aj}^{k}(h)} \quad , \tag{5.20}$$

where $W_{xk}(h)$ and $W_{yk}(h)$ are the moment terms (or moments of vorticity flux in the x- and y-direction) of the discrete vortices about the cell centre.

The expressions for $W_{xk}(h)$ and $W_{yk}(h)$ are

$$W_{xk}(h) = \sum_{i=1}^{I} (\Delta\Gamma_i v_{xi})\, z_i^k(h) \quad ,$$
$$W_{yk}(h) = \sum_{i=1}^{I} (\Delta\Gamma_i v_{yi})\, z_i^k(h) \quad , \qquad k = 0,1,2,\ldots N_t \ , \ h = 1,2,\ldots H \ . \tag{5.21}$$

Extension of the above calculation to all the cells in a cell-to-cell system gives the solutions for $\boldsymbol{A}_j$ and $\boldsymbol{B}_j$ at point j due to all discrete vortices in the flow domain; the stagnation pressure induced by the moving vortices is hence obtained as the real part of $(\boldsymbol{A}_j + i\boldsymbol{B}_j)$. Note that, with proper data management, the need for temporary storage for $W_{xk}(h)$, $W_{yk}(h)$, $\Delta\Gamma_i v_{xi}$ and $\Delta\Gamma_i v_{yi}$ will not impose any extra demand for computer memory. However, since the above calculation of $\boldsymbol{U}_{ji}\cdot\boldsymbol{V}_i$ with the cell-to-cell algorithm involves two computations by the cell-to-cell method, for $\boldsymbol{A}_j$ and $\boldsymbol{B}_j$ separately, its use is justified only when a large number of calculations (typically more than 500) is required.

Eq. (5.18) and Eq. (5.19) have been used in the construction of the velocity field and stagnation pressure field over the entire flow domain, when thousands of calculations are required. These equations provide an efficient calculation procedure through the use of cell-to-cell algorithm. Calculation of velocities induced by a system of discrete vortices by the cell-to-cell algorithm, Eq. (5.18), can also be applied in setting up of the matrix equation $\mathbf{[}\boldsymbol{K}\mathbf{][}\gamma\mathbf{]=[}\boldsymbol{b}\mathbf{]}$. The expression $(L_{pm,j}\cos\beta_{pm} + M_{pm,j}\sin\beta_{pm})$ in the elements of matrix $\mathbf{[}\boldsymbol{b}\mathbf{]}$ is the tangential surface velocity at a solid surface. The values of $L_{pm,j}$ and $M_{pm,j}$ can be obtained by Eq. (3.18) according to the efficient cell-to-cell algorithm. As the matrix equation is applied in every timestep, saving in computing time has been achieved by using the cell-to-cell method in the evaluation of $\mathbf{[}\boldsymbol{b}\mathbf{]}$.

Chapter 6

Validation of Numerical Procedures

The numerical procedures appropriate to surface vorticity modelling of bluff body flows, described in Chapters 4 and 5, have been developed into a computational code in PASCAL programming language. The code was designed initially to run in a personal computer which is an IBM compatible machine, model DX4/100 with 32 mega byte of RAM. In order to cater for the vast demand for memory for temporary data storage, the code is programmed in DOS protected-mode which gives the program access to virtually all the computer's memory. With this computing capacity, the number of discrete vortices which can be handled is about 3×10^4 and the cell-to-cell method with one level of sub-grid structure $H = 2$ can be effected. This setup permits the calculations of flow about a single body to be carried out.

In a later stage of this project, when calculations of viscous flow about a multi-body array are carried out, the number of discrete vortices required may increase to about 8×10^4; hence more levels of sub-grid structure in the cell-to-cell procedure are needed to enhance computing efficiency and to contain the computing time within a practical range. In this case, the demands for computing power and computer memory are beyond the capacity of the above-mentioned personal computer system. Consequently, use has been made of a computer system with greater capacity, a DEC AXP machine, for calculations of flow over multi-body arrays. For these calculations, the numerical code has been extended, in PASCAL programming language, to be compatible with the UNIX systems in this machine.

All calculations have been made for impulsively started incompressible viscous flows about bluff bodies, and are based on non-dimensional equations of fluid motion. The Reynolds number $Re = U_\infty L/\upsilon$, based on the free-stream velocity U_∞, the characteristic length L of the body and the kinematic viscosity of the fluid υ, is then the primary parameter defining the flow. Some

common bluff-body shapes, such as the circle, ellipse, triangle, rectangle, flat plate with elliptical leading edge, and aerofoil section of the NACA 4-digit series are included in the program for user selection. Other shapes can be defined by the user in a text file.

Validation of the numerical scheme developed in this study requires consideration of bodies with both smooth and sharp-edged profiles. Since potential flow calculations are an essential element of the general viscous flow calculation, the results of such calculations for both types of body will be examined in the first part of this chapter. For viscous flow over bluff bodies with a smooth profile, the circular cylinder is used as a datum case – firstly because of the wealth of theoretical and experimental data available, and secondly because this case exhibits most of the important features of bluff body flows in general. Circular cylinder results, for various values of Reynolds numbers, are presented and discussed in the second part of this chapter. Validation of the present methods for viscous flow over bluff-bodies with sharp corners is considered later, in chapter 7, which is devoted to results of their application to flow over thick plates of rectangular cross-section.

6.1 Potential Flow Solutions

The crux of the present numerical simulation is the creation of surface vorticity at solid boundaries by a given external flow field; this requires solution of Eq. (3.129), $\mathbf{[}\boldsymbol{K}\mathbf{][}\gamma\mathbf{]=[}\boldsymbol{b}\mathbf{]}$, for the surface vorticity distribution represented by $\mathbf{[}\gamma\mathbf{]}$. An accurate formulation of the coupling coefficient matrix $\mathbf{[}\boldsymbol{K}\mathbf{]}$ is thus a vital first part of the calculation procedures; and for verification of formulation accuracy, calculations of inviscid uniform flows past solid bodies have been carried out and results compared with available theoretical results. In the first part of this chapter, these comparisons are presented for a wide range of body shapes including smooth profiles, sharp-edged profiles, and slender sections in single and multi-body arrays. Consideration of these results leads to a modification of the generally accepted *back-diagonal correction* of the $\mathbf{[}\boldsymbol{K}\mathbf{]}$ matrix.

6.1.1 Potential Flow Over Smooth-Profiled Bodies

For the calculation of inviscid flow over smooth bodies, the circular cylinder, for which the exact analytical solution for potential flow is available, has been chosen as typical. For inviscid flow, the fluid velocity on the cylinder surface is given by (for example Batchelor [1967])

$$v_s = 2\sin\theta + \frac{\Gamma_b}{\pi}\ , \qquad \textbf{(6.1)}$$

where v_s denotes the non-dimensional fluid velocity (referred to the velocity of the incident uniform free stream U_∞) on the cylinder surface at angular position θ, and Γ_b is the prescribed circulation around the cylinder (non-dimensionalised by the product of U_∞ and the cylinder diameter d), taken as positive for clockwise rotation.

The numerical solution is obtained according to the calculation procedures described in section 3.2.3. Thus, the coupling coefficient matrix **[*K*]** is formulated according to the geometry of the solid body, and regularised for singularity by the *back-diagonal correction*. The regularised matrix **[*K*′]** so formed is then inverted and used to calculate **[**γ**]**. The potential-flow fluid velocity at the solid surface is given by the local strength γ of the surface vorticity sheet, according to Eq. (3.5).

In a study of the effect of the *back diagonal correction* on the numerical results, two sets of results have been obtained, one without and one with the *back diagonal correction*. A comparison of the numerical results with the exact values, given by Eq. (6.1), is tabulated in Table 6.1. The values shown are the surface velocities at the collocation points, $\theta = 9°, 27°$, etc., for a circular cylinder represented by 20 uniform straight segments. The table shows that the numerical solutions obtained both with and without the *back diagonal correction* are in close agreement with the exact solution. Those obtained using the surface-vorticity boundary-integral method with the basic coupling coefficient matrix are essentially identical to those obtained by Lewis [1991, Ch. 1]. However, although the error of calculation, defined as $(e-n)/e$ with n denoting the numerical result and e the exact solution, is very small (in both cases less than 1%), it is rather greater in the case in which the back-diagonal correction has been made. This point will be returned to later.

The resultant velocity field $\boldsymbol{u}(u,v)$ is obtained by superimposing the uniform flow field $\boldsymbol{U}_\infty$ on that due to the distribution of surface vorticity represented by the calculated strength of vortex sheet $[\gamma]$ as given by the Biot-Savart equation Eq. (2.30). Streamlines can then be constructed by solving the differential equation,

$$\frac{dy}{dx} = \frac{v}{u} \,. \tag{6.2}$$

In the present work, the differential equation Eq. (6.2) is solved by using the Runge-Kutta method. The calculated streamline patterns of uniform flow over a circular cylinder is depicted in Fig. 6.1(a); the stagnation points are at $\theta = 0°$ and $180°$. The numerical results compare well with the standard theoretical solution.

$\theta°$	Exact (e)	Numerical $(n_1)^*$	Error $(e-n_1)/e$	Numerical with BDC** (n_2)	Error $(e-n_2)/e$
9	0.31287	0.31274	4.15E-04	0.31029	8.24E-03
27	0.90798	0.90760	4.15E-04	0.90050	8.24E-03
45	1.41421	1.41363	4.15E-04	1.40256	8.24E-03
63	1.78201	1.78127	4.15E-04	1.76733	8.24E-03
81	1.97538	1.97456	4.15E-04	1.95910	8.24E-03
99	1.97538	1.97456	4.15E-04	1.95910	8.24E-03
117	1.78201	1.78127	4.15E-04	1.76733	8.24E-03
135	1.41421	1.41363	4.15E-04	1.40256	8.24E-03
153	0.90798	0.90760	4.15E-04	0.90050	8.24E-03
171	0.31287	0.31274	4.15E-04	0.31029	8.24E-03

* Numerical results obtained with the basic coupling coefficient matrix.
** BDC - Back Diagonal Correction.

Table 6.1. Comparison between exact and numerical solutions with back-diagonal correction of potential flow past circular cylinder; number of segments $M = 20$; because of symmetry of the solution, only results on the upper cylinder surface are presented.

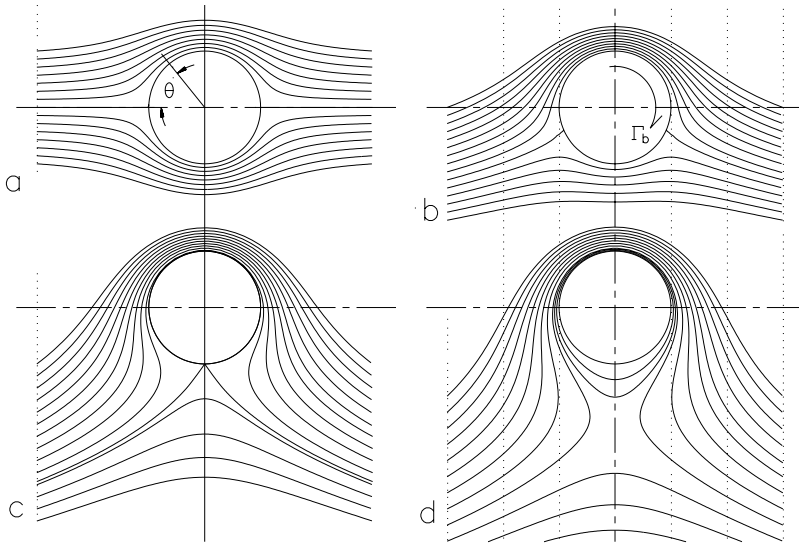

Figure 6.1. Calculated streamline patterns of potential flow past a circular cylinder: (a) $\Gamma_b = 0$, (b) $\Gamma_b = \pi$, (c) $\Gamma_b = 2\pi$ and, (d) $\Gamma_b = 2.5\pi$.

As observed earlier, the results obtained with the *back diagonal correction* are apparently less accurate than those obtained without it. This is apparently because the correction, applied only to the elements on the back diagonal of the **[*K*]** matrix, changes the character of the matrix. With reference to Eq. (3.26), suppose that for the n*th* column the sum $\sum K(s_m , s_n)\Delta s_m$ deviates from zero by a finite error value $\delta\Gamma_n$; so that

$$\sum_{m=1}^{M} K(s_m,s_n)\Delta s_m - \delta\Gamma_n = 0 \ . \qquad \textbf{(6.3)}$$

For the case of circular cylinder, due to angular symmetry of the body and uniformity of segment length, the **[*K*]** matrix is symmetric about the diagonal, and all off-diagonal elements have the same value. When the *back diagonal correction* is applied, the error $\delta\Gamma_n$ is nullified wholly by changing only the $(M+1-n)$*th* element of the n*th* column leaving all other elements unchanged. As a result, the symmetry of the **[*K*]** matrix is upset. This suggests that the accuracy of the numerical approximation might be improved by an alternative form of correction for zero induced circulation which preserves the character of the **[*K*]** matrix. On the other hand, the nature of the *back diagonal correction* should be maintained for thin bodies, in which case the elements on the back diagonal of the **[*K*]** matrix are strongly dominant and its use is appropriate.

6.1.2 Zero Circulation Correction of the [*K*] Matrix

Based on the above considerations, a modified scheme, which will be referred to as the *zero circulation correction*, which corrects all but the diagonal elements of the **[*K*]** matrix for zero circulation is proposed as follows. Each element of the n*th* column, except the n*th* element $K(s_n, s_n)$ which retains its value for self-induced velocity given by Eq. (3.16), is assigned the value $K'(s_m, s_n)$ given by

$$K'(s_j,s_n)\Delta s_j = K(s_j,s_n)\Delta s_j - f_{j,n}\,\delta\Gamma_n \ , \qquad j=1,2,\ldots M, \qquad \textbf{(6.4)}$$

where the weighing factor $f_{j,n}$ for the element $K(s_j,s_n)$ is determined by its contribution to the total circulation around the contour. One possible form is

$$f_{j,n} = \frac{\left[\,|K(s_j,s_n)\,\Delta s_j|\,\right]^a}{\sum_{\substack{m=1 \\ m\neq n}}^{M}\left[\,|K(s_m,s_n)\Delta s_m|\,\right]^a} \ , \qquad j\neq n \ , \qquad \textbf{(6.5)}$$

with $f_{j,n} = 0$ when j = n, and a is a positive real number (a = 1 is used in the present calculations). It can readily be seen that the elements modified according to Eq. (6.4) satisfy

the condition $\sum K(s_j,s_n)\Delta s_j = 0$ provided that $\sum f_{j,n} = 1$, and Eq. (6.5) ensures that the latter condition is satisfied. In fact, any function which satisfies the condition $\sum f_{j,n} = 1$ can be used, but the function given by Eq. (6.5), with $a = 1$, maintains the character of the **[*K*]** matrix and keeps the alterations to minimum. As for the *back diagonal correction*, the matrix **[*K*]** after correction by Eqs. (6.4) and (6.5) becomes singular and requires to be regularised by adding Eq. (3.30) to it.

When Eq. (6.4) is applied to the circular cylinder case, with uniform Δs_j and constant $K(s_j, s_n)$ for $j \neq n$, the error $\delta\Gamma_n$ is distributed over the off-diagonal elements so that the symmetric structure of the original **[*K*]** matrix is preserved in the resultant matrix. With the *zero circulation correction*, the previous calculations for the circular cylinder have been repeated; the results are tabulated in Table 6.2. Comparison of the calculated results in Tables 6.1 and 6.2 shows that the error levels are very significantly reduced with the new correction scheme.

θ°	Exact (e)	Numerical* (n_1)	Error (e-n_1)/e	Numerical with ZCC** (n_3)	Error (e-n_3)/e
9	0.31287	0.31274	4.15E-04	0.31287	-6.24E-11
27	0.90798	0.90760	4.15E-04	0.90798	-2.30E-11
45	1.41421	1.41363	4.15E-04	1.41421	-1.90E-11
63	1.78201	1.78127	4.15E-04	1.78201	-1.31E-11
81	1.97538	1.97456	4.15E-04	1.97538	-4.92E-12
99	1.97538	1.97456	4.15E-04	1.97536	-4.92E-12
117	1.78201	1.78127	4.15E-04	1.78201	-1.31E-11
135	1.41421	1.41363	4.15E-04	1.41421	-1.90E-11
153	0.90798	0.90760	4.15E-04	0.90798	-2.30E-11
171	0.31287	0.31274	4.15E-04	0.31287	-6.24E-11

* Numerical results obtained with the basic coupling coefficient matrix.
** ZCC - Zero circulation correction by equations (6.4) and (6.5).

Table 6.2. Comparison between exact and numerical solutions with zero-circulation correction of potential flow past circular cylinder; number of segments $M = 20$; because of symmetry, only results on the upper cylinder surface are shown.

Calculations of inviscid flow over a circular cylinder with finite bound circulation $\Gamma_b \neq 0$ have also been carried out and the result checked against the exact solution. The circulation specified by Eq. (3.30), $\Gamma_b = \sum \gamma(s_n)\Delta s_n$, has been incorporated in the coupling coefficient matrix during the matrix regularisation process. The calculated values of surface velocity on the cylinder match the exact values to a very high degree of accuracy (with relative errors, as defined above, of order 10^{-11}).

When the cylinder has circulation, the flow becomes asymmetric, with higher fluid velocity over the upper side of the cylinder (where the surface moves in the same direction as the incident flow), as reflected by the densely concentrated streamlines shown by the calculated streamline patterns of Fig. 6.1(b) and (c) for $\Gamma_b = \pi$ and $\Gamma_b = 2\pi$ respectively. The stagnation points shift towards the lower side of the cylinder as Γ_b increases, to $\theta = -30°$ and $210°$ for $\Gamma_b = \pi$, and to $\theta = 270°$ (for both stagnation points) for $\Gamma_b = 2\pi$. Further increase in Γ_b moves the stagnation points off the cylinder surface; Fig. 6.1(d) shows the case when $\Gamma_b = 2.5\pi$.

m	Exact (e)	Numerical with BDC (n_1)	Error (n_1-e)/e	Numerical with ZCC (n_2)	Error (n_2-e)/e	Numerical no BDC/ZCC (n_3)	error (n_3-e)/e
1	2.50030	2.61398	4.55E-02	2.61452	4.57E-02	-3.58112	-2.43E-00
2	1.57664	1.59038	8.71E-03	1.59035	8.70E-03	-0.28164	-1.18E-00
3	1.34482	1.34583	7.53E-04	1.34584	7.58E-04	0.36179	-7.31E-01
4	1.23464	1.23503	3.11E-04	1.23503	3.16E-04	0.62165	-4.96E-01
5	1.16575	1.16593	1.53E-04	1.16593	1.56E-04	0.76240	-3.46E-01
6	1.11495	1.11501	5.54E-05	1.11501	5.64E-05	0.85309	-2.35E-01
7	1.07274	1.07272	-2.20E-05	1.07272	-2.30E-05	0.92045	-1.42E-01
8	1.03405	1.03395	-9.40E-05	1.03395	-9.70E-05	0.97820	-5.40E-02
9	0.99524	0.99507	-1.70E-04	0.99506	-1.70E-04	1.03584	4.08E-02
10	0.95263	0.95239	-2.50E-04	0.95239	-2.60E-04	1.10284	1.58E-01
11	0.90098	0.90067	-3.50E-04	0.90066	-3.60E-04	1.19274	3.24E-01
12	0.83027	0.82991	-4.40E-04	0.82989	-4.50E-04	1.33184	6.04E-01
13	0.71556	0.71541	-2.10E-04	0.71541	-2.20E-04	1.58784	1.22E-00
14	0.46739	0.47907	2.50E-02	0.47910	2.50E-02	2.22677	3.76E-00
15	-0.63276	-0.52489	-1.70E-01	-0.52518	-1.70E-01	5.43946	-9.59E-00
16	-2.50031	-2.61398	4.55E-02	-2.61452	4.57E-02	3.58111	-2.43E-00
17	-1.57665	-1.59038	8.71E-03	-1.59035	8.70E-03	0.28165	-1.18E-00
18	-1.34482	-1.34583	7.53E-04	-1.34584	7.58E-04	-0.36179	-7.31E-01
19	-1.23464	-1.23503	3.11E-04	-1.23503	3.16E-04	-0.62165	-4.96E-01
20	-1.16575	-1.16593	1.53E-04	-1.16593	1.56E-04	-0.76240	-3.46E-01
21	-1.11495	-1.11501	5.54E-05	-1.11501	5.64E-05	-0.85309	-2.35E-01
22	-1.07274	-1.07272	-2.20E-05	-1.07272	-2.30E-05	-0.92045	-1.42E-01
23	-1.03405	-1.03395	-9.40E-05	-1.03395	-9.70E-05	-0.97820	-5.40E-02
24	-0.99524	-0.99507	-1.70E-04	-0.99506	-1.70E-04	-1.03584	4.08E-02
25	-0.95263	-0.95239	-2.50E-04	-0.95239	-2.60E-04	-1.10284	1.58E-01
26	-0.90098	-0.90067	-3.50E-04	-0.90066	-3.60E-04	-1.19274	3.24E-01
27	-0.83027	-0.82991	-4.40E-04	-0.82989	-4.50E-04	-1.33184	6.04E-01
28	-0.71556	-0.71541	-2.10E-04	-0.71541	-2.20E-04	-1.58784	1.22E-00
29	-0.46739	-0.47907	2.50E-02	-0.47909	2.50E-02	-2.22677	3.76E-00
30	0.63276	0.52489	-1.70E-01	0.52518	-1.70E-01	-5.43946	-9.60E-00

Table 6.3. Comparison between exact and numerical solutions of potential flow past ellipse of 5% thickness; inclined at $10°$ to main stream, $M = 30$.

As a preliminary comparison of the performance of the *back diagonal correction* and the *zero circulation correction* on thin bodies, the two procedures have been applied to potential flow past thin ellipses of 10% and 5% thickness, inclined at 10° to the incident flow. The exact solution can be obtained by taking the Joukowski transformation of the exact solution for a circular cylinder (see, for example, Lewis (1991, Ch.2)). Exact results and numerical results for a 30-segment representation of the 5% thick ellipse are tabulated in Table 6.3. It can be seen that the numerical results obtained without any corrections for zero induced circulation are considerably less accurate than those with either of the corrections implemented, and quite unrealistically inaccurate for the 5% thick ellipse.

The calculations which have been carried out lead to the conclusion that there is little to choose between the *zero circulation correction* and the *back diagonal correction* for bodies of thin section, but that the zero circulation correction scheme is preferable for bodies with a cross-section like the circular cylinder.

6.1.3 Potential Flow Over Sharp-Edged Bodies

Flows past sharp edged bodies present numerical difficulties as the flow velocity is singular at the angular points. This is a major problem in some numerical schemes, such as those which utilise conformal transformation. However, in surface vorticity modelling, the fluid velocity at each collocation point is the average value over a segement of finite length, and the method gives finite values for the fluid velocity at the angular points. The ability of the present numerical program to handle sharp-edged bodies has been tested with a square cylinder.

In this case, the body contour has been represented by 60 uniform straight segments, 15 on each side of the square. Because of symmetry of the body, the potential flow past the square must be symmetrical. Numerical experiments have shown that the surface vorticity on the square cylinder generated with the *back-diagonal correction* is not symmetrical, because the correction upsets the symmetry of **[*K*]** matrix. By contrast, the *zero-circulation correction* derived in the present study preserves the symmetry of the **[*K*]** matrix and thus ensures a symmetric distribution of surface vorticity.

The calculated streamlines of flows past a square cylinder at different angle of inclination are shown in Fig. 6.2. An exact solution is not available and therefore a direct comparison between numerical and theoretical results cannot be made, but the calculated streamline patterns are consistent with those for related shapes for which exact solutions can be obtained.

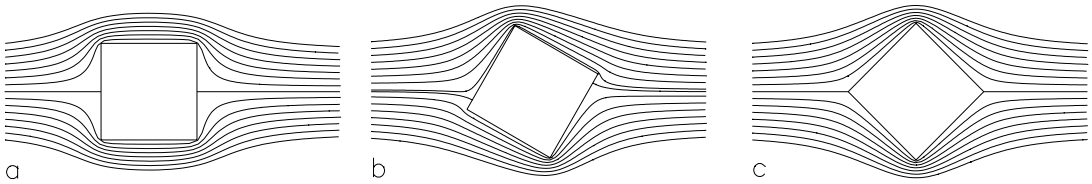

Figure 6.2. Calculated streamline patterns of inviscid flow past a square cylinder; at angle of inclination: (a) 0°, (b) 30° and (c) 45°.

Calculations of inviscid flow past another type of sharp-edged body namely an NACA 4412 wing section have also been performed. These calculations, dealing with a body of thin and sharp-edged section, serve as a rigorous test of the the effectiveness of the *zero-circulation correction* in the formulation of the **[*K*]** matrix. The calculated streamlines for potential flow past the wing section, at 30° angle of attack, without and with the Kutta trailing-edge condition enforced are shown in Fig. 6.3. In the first case, Fig. 6.3(a), the rear stagnation point lies on the upper surface of the aerofoil and the fluid flows from the lower surface round the sharp traling edge to the upper side of the aerofoil. When the Kutta trailing edge condition is satisfied by imposing a bound circulation of $\Gamma_b = 1.93$ as given by Eq. (3.38), Fig. 6.3(b), the flow at the trailing edge leaves the aerofoil tangentially to the surface.

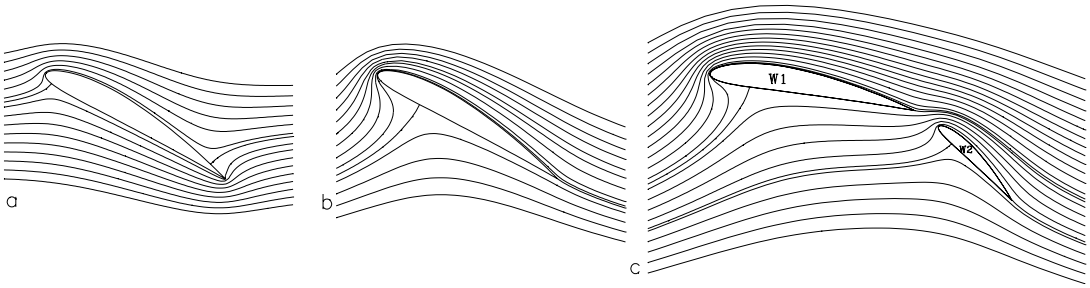

Figure 6.3. Calculated inviscid flow past an NACA 4412 wing section: (a) 30° attack angle, without Kutta trailing edge correction, (b) with Kutta trailing edge correction, (c) two wing sections of chord ratio 2:1, angles of attack of 10° and 45°.

Angle of attack α, degrees	Calculated lift coefficient (This study)	Theoretical lift coefficient Abbott & Von Doenhoff [1959]
-12	-0.93	-0.94
-8	-0.45	-0.46
-4	0.03	0.0
0	0.52	0.52
4	1.00	1.0
8	1.48	1.48
12	1.94	1.94
16	2.40	2.39
20	2.84	-
30	3.86	-

Table 6.4. Comparison between theoretical and calculated lift coefficients of NACA 4412 wing section.

For further verification of the numerical programme, again with the use of *zero-circulation correction*, a comparison of calculated lift coefficients C_L, given by Eq. (3.39), with published theoretical data has been made. Values of C_L for the NACA 4412 wing section at various angle of attack from $-12°$ to $30°$ are tabulated in Table 6.4, together with the theoretical values (from Abbott and Von Doenhoff [1959]), calculated by conformal mapping from the potential flow solution for a circular cylinder. The table shows that the lift coefficients calculated by the surface-vorticity boundary-integral method in the present study are in good agreement with the published data.

As an illustration of calculation of potential flow past a multi-body array, using the solution procedures for multi-body systems described in sections 3.6 to 3.8, the flow over two NACA 4412 wing sections ($W1$ and $W2$) has been considered. The result is shown in Fig. 6.3(c). The chord lengths of $W1$ and $W2$ are in the ratio 2:1, and the angles of attack α are $10°$ and $45°$ respectively. The bound circulations Γ_b on the two aerofoils for the satisfaction of the Kutta trailing edge condition are given by Eq. (3.106) as $\Gamma_b(W1) = 2.01$ and $\Gamma_b(W2) = 0.83$ respectively. Hence the predicted lift coefficients for $W1$ and $W2$ are $C_L(W1) = 4.02$ and $C_L(W2) = 1.66$ (compared with $C_L = 1.71$ of a single NACA 4412 wing section with $\alpha = 10°$). The streamline pattern, Fig. 6.3(c), shows the flow leaving the trailing edges of $W1$ and $W2$ tangentially, in satisfaction of the Kutta trailing-edge condition on each of the aerofoils.

All these results indicate that the formulation of the surface-vorticity boundary-integral method being used in the present work gives valid results for potential flow about a variety of body shapes. In particular, they indicate that the *zero-circulation correction* derived in this study leads to a more accurate formulation of the **[*K*]** matrix than the direct *back-diagonal correction*.

6.2 Numerical Calculations of Flow Over Circular Cylinder

6.2.1 Flow Regimes for Circular Cylinder Flow

Viscous bluff-body flows are generally significantly different from the idealised potential flows. Obvious differences are the occurrence of boundary layer separation from solid surfaces and in many cases the establishment of a Karman vortex street behind the body. The flow regime established is often strongly dependent on Reynolds number; and the surface-pressure distribution, the drag and lift forces, and the vortex-shedding frequency can change dramatically when the flow moves from one regime to another. Viscous flow over a circular cylinder is a typical example; for this flow there exists a sequence of flow regimes determined by the Reynolds number Re_d based on the cylinder diameter and the main stream velocity U_∞. Cylinder flows have been the subject of extensive experimental investigation and numerical simulation and therefore provide an appropriate standard for testing the computational codes developed in the present work.

Physical experiments on flow over circular cylinders have shown that at low Reynolds numbers, Re_d less than about 50, laminar boundary layer separation produces a steady recirculation region downstream of the cylinder. At $Re_d \sim 50$, this flow becomes unstable and vortices are formed at some distance downstream of the cylinder. Over the range $50 < Re_d < 140-195$, the flow is laminar throughout, and the shed vortices form a classical Karman street behind the cylinder (Kovasznay [1949], Roshko [1953], Bloor [1964]). At these Reynolds numbers the flow is two-dimensional, but at higher Reynolds numbers, the vortex shedding becomes three-dimensional in character (Williamson [1988,1996]). For $200 < Re_d < 300-400$, the vortices are laminar on formation but transition to turbulence occurs in the fully-formed vortices (Bloor [1964]). For $Re_d > 400$, transition to turbulence occurs in the laminar shear layer separating from the cylinder, before vortex formation takes place, and this type of flow persists to much higher Reynolds numbers. As Re_d is increased from about 10^3 to 2×10^5, the transition point moves forward towards the cylinder, eventually reaching the cylinder surface. For Reynolds numbers greater than about 2×10^5, the cylinder boundary layers become turbulent before separation; the separation point then moves towards the rear of the cylinder and the well-known dramatic reduction in drag occurs.

6.2.2 Numerical Parameters for Calculation of Circular Cylinder Flows

Calculations of flow over a circular cylinder at Reynolds numbers Re_d = 100, 500, 1000 and 10,000 have been carried out, according to the scheme detailed in Chapter 4, for the purpose of verifying the numerical procedures developed. Specifically, the cylinder is represented by an inscribed polygon of 60 equal sides (M = 60), and the collocation points taken at the mid-points of the sides of the polygon. In the solutions of the Martensen equation the *zero-circulation correction* is applied to the basic coupling coefficient matrix **[*K*]** and the resulting singular matrix regularised; the tangential surface velocity matrix **[*b*]** is corrected by Eq. (4.8) to ensure that each external vortex induces zero circulation around the body contour. *Vortex reflection* is applied to those vortices which enter the body contour. The solution matrix **[**γ**]** then yields the distribution of surface vorticity on the cylinder surface. In each time-step, following vortex sheet creation, calculations of the surface pressure distribution on the cylinder, and drag and lift coefficients are carried out. Vortex merging is implemented in accordance with section 4.6. Discrete vortices equivalent to the surface vorticity are introduced into the flow by the offset method at a distance $\epsilon = \sqrt{(4\Delta t/(3Re))}$ above the solid surface. These vortices are assumed to have the Chorin structure (Eq. (3.62)) with $\sigma = \Delta s/\sqrt{Re}$, invariant with time. The time-step was taken as Δt = 0.02. The solution procedures were repeated for a sufficiently large number of time-steps to yield the fully-developed-flow solution. From the distributions of elemental vortices, the streamline patterns, vorticity contours, instantaneous pressure fields and pressure forces on the body are calculated.

6.2.3 Simulation Results

In this section, the calculated results for circular-cylinder flow at Reynolds numbers Re_d = 100, 500, 1,000 and 10^4 are presented. The elemental-vortex distributions, streamline patterns, instantaneous pressure fields and vorticity contours for Re_d = 100 are shown in Figs. 6.4–6.7, and the corresponding results for Re_d = 500, 1,000 and 10^4 are shown, respectively, in Figs. 6.8–6.11, Figs. 6.15–6.18 and Figs. 6.19–6.22. They indicate that, over this range of Reynolds number, the developing flows on the cylinder are very similar to each other and the fully-developed flows are characterised by virtually the same processes of flow separation, vortex shedding and wake formation downstream of the cylinder, but with increasing irregularity in the vortex street at higher Reynolds numbers.

6.2.3.1 Flow Development

Consider the flow development at Re_d = 500 from the impulsive start to the fully-developed state. Because of symmetry of the body shape, the initial flow is symmetrical about the streamwise centre-line of the cylinder. The flow on both the upper and lower front surfaces of the cylinder is fully-attached from the stagnation point at $\theta = 0°$ to about $\theta = 80°$ where separation occurs; the separated shear layers subsequently roll up to form vortices downstream of the cylinder. In the early development ($t \leq 3$), the vortices downstream of the cylinder, in the form of a pair of stationary counter-rotating vortices, are confined in a closed recirculation region. Enlarged views of streamline patterns, over the time from t = 0.75 to t = 2.5 are shown in Fig. 6.10; the predicted streamline patterns for the same flow conditions obtained by Collins and Dennis [1973] using a finite difference method, and by Stansby [1993] using the discrete vortex method are also reproduced in Fig. 6.12. There are clearly strong similarities between the three sets of computed streamline patterns of the developing flow. Experimental visualisations of the developing flow at Re_d = 500 by Bouard and Coutanceau [1977], reproduced here as Fig. 6.13, (similar to those of Prandtl and Tietjens, 1934/1957) show the patterns of the counter-rotating vortices at times t = 1 and 3. These patterns appear to be quite accurately reproduced by the present simulations, the results of which are also shown in Fig. 6.13.

Extension of the closed recirculation region in the streamwise direction with time, and the associated symmetrical growth of vortices within it, can be clearly seen in these figures. The length of the closed recirculation region l, normalised by the cylinder diameter d, increases almost linearly with time in the early part of development, $t \leq 3$, as found experimentally by Honji and Taneda [1969] and Bouard and Coutanceau [1980] for Re_d = 550, and Schwabe [1935] for Re_d = 560. These experimental results are shown in Fig. 6.14 together with the present numerical results and those calculated by Thoman and Szewczyk [1969] for Re_d = 600, and Panikker and Lavan [1975] and Collin and Dennis [1973] for Re_d = 500. There is fair agreement amongst all calculated l/d values, and the present calculations agree particularly well with the experimental data.

Further growth of the two counter-rotating vortices, leading to vortex shedding, is asymmetric. The upper vortex (of positive vorticity) grows bigger and occupies most of the space in the near-wake ($t \approx 4$) whereas the lower vortex (of negative vorticity) shrinks by losing vorticity

into the wake. As is evident from the time-histories of lift (Fig. 6.26), generation of (positive) lift on the cylinder coincides with this departure of (negative) vorticity from the near-wake of the cylinder. This represents the onset of vortex shedding, and the large (upper) vortex is shed into the wake at $t \approx 6$. The closed recirculation region then gives way to periodic vortex shedding into the wake. For $t > 10$, the fully-developed flow becomes established: vortices are shed alternately from the upper and lower sides of the cylinder, forming a vortex street in the wake. The lift on the cylinder then varies in phase with the vortex shedding cycle: shedding of the positive vorticity of an upper vortex produces negative circulation around the cylinder and hence negative lift; and, similarly, shedding of a (negative) lower vortex gives rise to positive lift on the cylinder. This correspondence can be readily identified by comparing the time-history of lift (Fig. 6.26) with the time-history of vortex shedding (Fig. 6.8); for example, over the time $8 < t < 10$, shedding of lower-vortex (negative) vorticity causes increasing lift, while over the time $10 < t < 12$ shedding of an upper (positive) vortex gives decreasing lift.

While the two counter-rotating vortices extend symmetrically behind the cylinder in the initial part of development ($t < 4$), the lift on the cylinder is virtually equal to zero (Fig. 6.26) and the drag increases from zero to, and fluctuates slightly about, a mean value $C_D \approx 0.9$. In association with the establishment of fully-developed flow, the mean drag on the cylinder gradually increases from $C_D \approx 0.9$ to $C_D \approx 1.1$, the value which persists throughout the fully-developed state. A similar variation of lift and drag with flow development is noted in the circular cylinder flow at $Re_d = 200$ calculated by Graham [1993] using a hybrid vortex method. The increase in drag appears to be related to the decrease in vortex formation length from $l/d \approx 1.5$ in the developing flow ($t < 8$) to $l/d \approx 1$ in the fully-developed flow ($t > 10$).

6.2.3.2 Mechanism of Vortex Formation and Shedding

The process of vortex formation and shedding from the cylinder at $Re_d = 500$ can be seen in greater detail from the enlarged streamline patterns and instantaneous pressure fields of Fig. 6.10. These figures show the variation of flow patterns over a number of vortex shedding cycles from $t = 70$ onwards. At $t = 70$, a nascent upper vortex emerges in the near-wake by the upper boundary-layer separation point of the cylinder, while the lower vortex in the near-wake is being shed. The upper vortex grows by gaining vorticity from the upper separated shear layer, and simultaneously moves downwards along the rear surface of the cylinder. When it is at its maximum size, just before being shed into the wake, it has taken up a position close

to the streamwise centre-line of the cylinder ($t \approx 72$). At the same time, a nascent lower vortex appears immediately downstream of the lower separation point of the cylinder. As this vortex grows by gaining vorticity from the lower separating shear layer, it moves upwards along the rear surface of the cylinder and replaces the already-formed upper vortex downstream ($t = 72$). During this movement, an upward transverse flow on the rear face of the cylinder sets in, marking the shedding of the upper vortex into the wake. At $t \approx 74$, the lower vortex reaches its maximum size and takes up a position near the streamwise centre-line while a nascent vortex is forming from the shear layers separating from the upper surface of the cylinder. The newly-formed upper vortex grows, moves downwards along the rear surface and establishes a downward transverse flow over it ($t = 74$) which corresponds to shedding of the lower vortex. The vortex shedding cycle is then repeated. This periodic vortex shedding, alternately from the upper and lower sides of the cylinder, produces a regular Karman vortex street in the wake.

The processes of vortex formation on the cylinder and shedding into the wake are similar for Reynolds numbers $Re_d = 100$, 1,000 and 10^4. The similarities can be seen by comparing the streamline patterns and instantaneous pressure fields over the time period $t = 70–81$ (Figs. 6.6, 6.10, 6.17 and 6.21) for these four Reynolds numbers. In all these cases, the flow on the front surfaces of the cylinder is fully-attached, boundary-layer separation occurring at $\theta \approx 80^\circ$; wake vortices are formed by rolling up of the separated shear layers. With increasing Reynolds number, the vortex formation length decreases and the vortices formed in the near-wake become more compact. At high Reynolds numbers, $Re_d > 1{,}000$, however, secondary small-scale vortices are formed on the rear surfaces of the cylinder and are shed into the wake with the main vortices. As can be clearly seen in the flow patterns for $Re_d = 10^4$ (Figs. 6.19–22), these vortices remain as separate identities in the wake vortex street. The vortex street has a regular periodicity for Reynolds numbers 100 and 500, but becomes less regular as the Reynolds number increases. At $Re_d = 10^4$, the irregularities become extremely pronounced, as a result of the presence of persisting secondary vortices. Despite the irregularity of the vortex street pattern at $Re_d = 1{,}000$ and 10^4, the pressure forces on the cylinder still exhibit quite regular periodicity as can be seen from the time-histories of lift on the cylinder (Figs. 6.27 and 6.28), although somewhat less so than at lower Reynolds numbers, and for $Re_d = 10^4$ the presence of high-frequency modulation is becoming apparent.

6.2.3.3 Influence of Reynolds Number on the Flow Parameters

The effects of Reynolds number on pressure distributions (Fig. 6.23), lift and drag on the cylinder (Figs. 6.25–6.28) and the frequency of vortex shedding into the wake (Fig. 6.29) can now be considered.

The distributions of $\bar{p}$, the time-average of the static pressure p over the surfaces of the cylinder, expressed as the pressure coefficient $C_p = (\bar{p} - p_\infty)/\frac{1}{2}\rho U_\infty^2$ at the four selected Reynolds numbers are presented in Fig. 6.23(a); the surface pressure distribution in an ideal inviscid flow is also shown. The present pressure distributions can be compared with the experimental data of Linke [1931], reproduced from Goldstein [1938] in Fig. 6.23(b). The general character of the calculated pressure distribution and its variation with Reynolds number are broadly similar to the experimental observations: the pressure decreases gradually over the forward part of the cylinder from $C_p \approx 1$ to a minimum value and then rises towards the rear part of the cylinder. However, direct comparison of calculated and experimental pressure distributions can be made in only one (high Reynolds number) case: calculations for $Re_d = 10{,}000$ with the experimental data of Linke for $Re_d = 9{,}900$. In this case, while the calculated pressure coefficients over the front surface of the cylinder, from $\theta = 0°$ to about $50°$, agree fairly well with the experimental values, the calculated minimum pressure coefficient is considerably lower than the experimental values and occurs at about $\theta = 80°$ compared with the $\theta \approx 70°$ indicated by experiment, and the calculated base pressure coefficient is also lower than the measured value.

A more general comparison between present calculations and experiments for Reynolds numbers in the range $Re_d \leq 1{,}000$ can be made of the base-pressure coefficient $-C_{pb}$. The computed values of $-C_{pb}$ for $Re_d = 100$, 500 and 1,000 are presented in Fig. 6.24, where they are compared with the experimental results of Williamson and Roshko [1990]. At low Reynolds numbers $Re_d \lesssim 500$, the present base-pressure coefficients ($-C_{pb} = 0.75$ and 0.91 for $Re_d = 100$ and 500) generally agree well with the experimental results. However, with an increase in Reynolds number to $Re_d = 1{,}000$, the calculated base pressure coefficient $-C_{pb} = 0.93$ deviates from the experimental value $-C_{pb} \approx 0.8$. Similarly, for $Re_d = 10^4$, the calculated value $-C_{pb} = 1.4$ is greater than the experimental value of Linke, $-C_{pb} = 1.05$ for $Re_d = 9{,}900$.

The predicted time-averaged drag coefficients, as determined from the time-histories of drag of the cylinder (Fig. 6.25–6.28), for the four selected Reynolds numbers are tabulated in Table 6.6, together with the experimental data of Thom [1929]. The predicted total drag coefficients, obtained by increasing the predicted form drag coefficients by the empirical frictional drag coefficient $C_{Df} = 4Re^{-½}$ derived by Thom [1929] (see Goldstein [1938] Ch. 9), are shown in Fig. 6.30 as a function of Reynolds number. The experimental results for total drag coefficients obtained by Thom [1929] as given by Goldstein [1938], and the results of other computations and experiments as given by Graham [1992] are also shown. The calculated drag coefficients of the present work for two-dimensional flow are generally similar to other numerical two-dimensional results and show similar trends with Reynolds number. However, it is clear that the calculated values in general are in good agreement with experiment only for Reynolds numbers lower than about 200, and that significant divergence between calculation and experiment occurs for higher Reynolds numbers. For example, in the present work, the calculated form drag coefficient $C_{Dp} = 0.98$ agrees well with the experimental value of 0.99 at $Re_d = 100$, but the calculated values for $Re_d = 500$, 1000 and 10,000 are about 10% to 30% higher than the experimental values. The disagreement at the higher Reynolds numbers is a reflection of the poor prediction of pressure distribution around the cylinder, as previously discussed, particularly over the rear part where the predicted pressures are significantly lower than those found experimentally; this leads to calculated form drag coefficients considerably higher than the experimental values. The discrepancies are attributed by Graham [1992] primarily to the neglect of three-dimensionality in the flow for Reynolds numbers greater than 200.

Values of the Strouhal number $St = fD/U_\infty$, determined from the power spectrum of fluctuating lift of the cylinder (Fig. 6.29), which characterises vortex shedding from the cylinder are summarised in Table 6.5. The table also lists experimental data given by Roshko [1953], and it can be seen that there is good agreement between the calculated and experimental values for $Re_d \leq 1{,}000$. The comparison between experimental and numerical Strouhal numbers made by Graham [1992] is reproduced in Fig. 6.31 together with the present computational results. The present numerically-predicted Strouhal numbers are in close agreement with experimental data for Reynolds numbers up to 1,000 but a quite large discrepancy between calculation and experiment appears at the highest Reynolds number for which calculations have been made, $Re_d = 10^4$.

Re_d	Strouhal Number, St		Normal Pressure Drag, C_{Dp}	
	This study	Experimental, Roshko [1953]	This study	Experimental, Thom [1929]
100	0.16	0.17	0.98	1.0
500	0.21	0.207-0.212	1.05	0.92
1,000	0.22	0.21-0.214	1.08	0.87
10,000	0.226	0.205	1.27	1.14

Table 6.5. Comparison of calculated Strouhal number and pressure drag coefficients with experimental values.

6.2.4 Concluding Remarks for Calculations of Circular Cylinder Flows

Simulations of flow over a circular cylinder at Reynolds numbers Re_d = 100, 500, 1,000 and 10^4 have been performed as datum cases for purposes of validating the present numerical scheme, which is based on the discrete vortex method. From the distributions of elemental vortices which are the prime result of the calculations, vorticity fields, streamline patterns, pressure distributions, drag coefficients and Strouhal numbers of vortex shedding have been calculated. The results generally accord well with experimental data; and the level of agreement is as good as or, in many cases, better than that for previously-published results obtained by similar or different computational procedures.

The calculations give a good representation of the detailed initial flow development and of the steady state Strouhal numbers and force coefficients, particular at low Reynolds numbers, 500 or less. Discrepancies between calculated and experimental values become greater as Reynolds number is increased; it is clear that the pressure distributions are not being very precisely predicted, especially over the rear part of the cylinder where boundary layer separation occurs. The loss of accuracy at higher Reynolds number appears to result, to some extent, from neglect of three-dimensionality in the real flow, which the present numerical scheme (for two-dimensional flows) does not deal with. As already noted, Graham [1992] attributes poor agreement between the results of two-dimensional computational codes and experiment for Reynolds number above 200 to increasing significance of the effects of three-dimensionality. Roshko [1993] points out that the three-dimensionality, arising from natural instabilities, generally appears in real bluff-body flows at Reynolds numbers greater than 180. At high Reynolds numbers, typically 10^4–10^5, greater discrepancies can be expected because the effects of turbulence are not directly modelled.

The inablility to represent three-dimensionality is an inherent weakness of two-dimensional numerical schemes for the calculation of flow at high Reynolds numbers. Nevertheless, comparisons of the results obtained by the present numerical scheme with experiment provide strong evidence that, for Reynolds numbers up to about 500 (and in some cases up to 1000), the procedure can be used with confidence to provide physically realistic predictions of flow patterns, boundary-layer development, boundary-layer separation, wake formation and vortex shedding in viscous flow over bluff bodies such as circular cylinders.

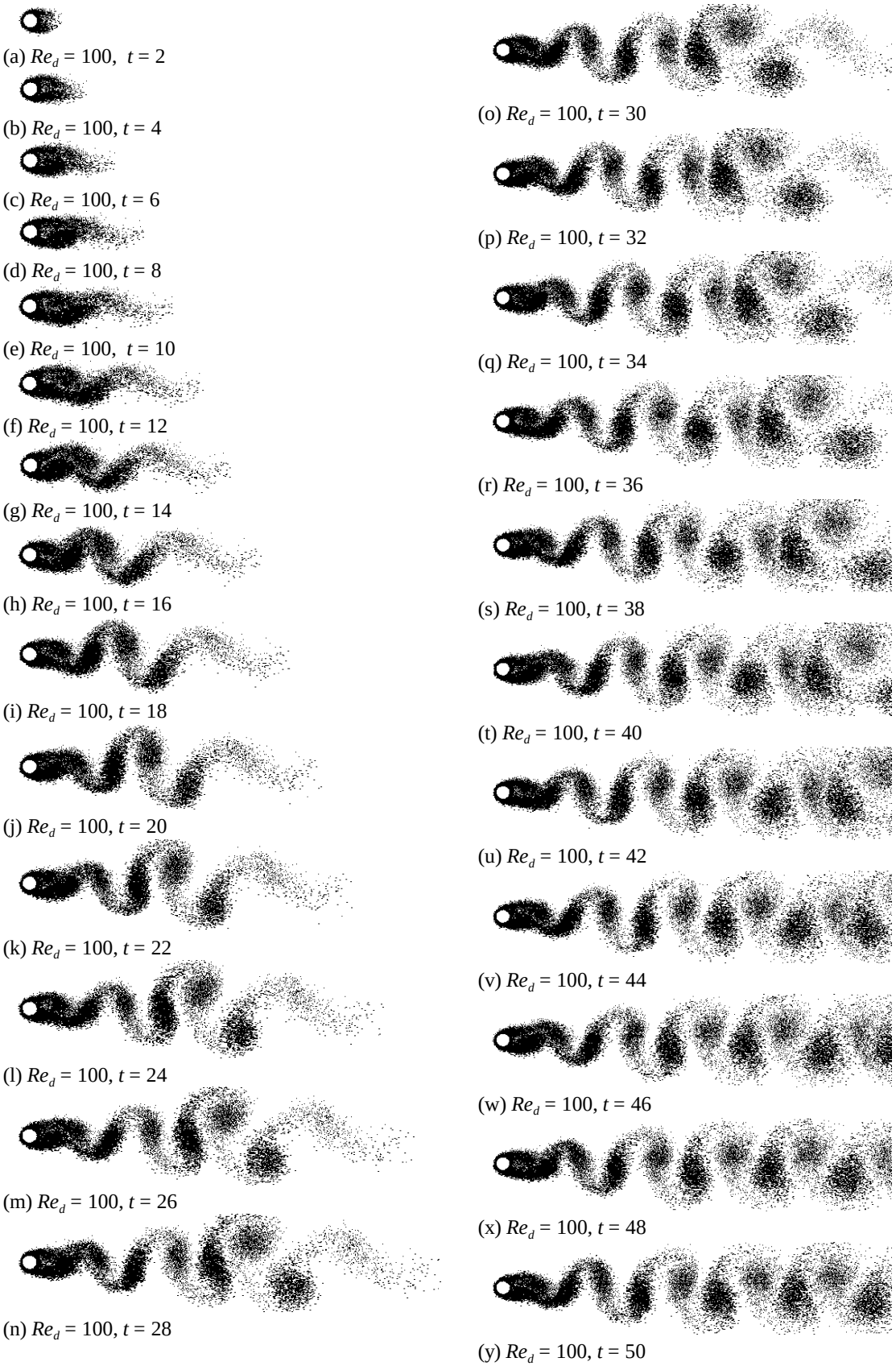

(a) Re_d = 100, t = 2

(b) Re_d = 100, t = 4

(c) Re_d = 100, t = 6

(d) Re_d = 100, t = 8

(e) Re_d = 100, t = 10

(f) Re_d = 100, t = 12

(g) Re_d = 100, t = 14

(h) Re_d = 100, t = 16

(i) Re_d = 100, t = 18

(j) Re_d = 100, t = 20

(k) Re_d = 100, t = 22

(l) Re_d = 100, t = 24

(m) Re_d = 100, t = 26

(n) Re_d = 100, t = 28

(o) Re_d = 100, t = 30

(p) Re_d = 100, t = 32

(q) Re_d = 100, t = 34

(r) Re_d = 100, t = 36

(s) Re_d = 100, t = 38

(t) Re_d = 100, t = 40

(u) Re_d = 100, t = 42

(v) Re_d = 100, t = 44

(w) Re_d = 100, t = 46

(x) Re_d = 100, t = 48

(y) Re_d = 100, t = 50

Figure 6.4. Elemental-vortex distributions in flow over a circular cylinder at Re_d = 100, showing sequence of flow evolution from the impulsive start to the fully-developed state.

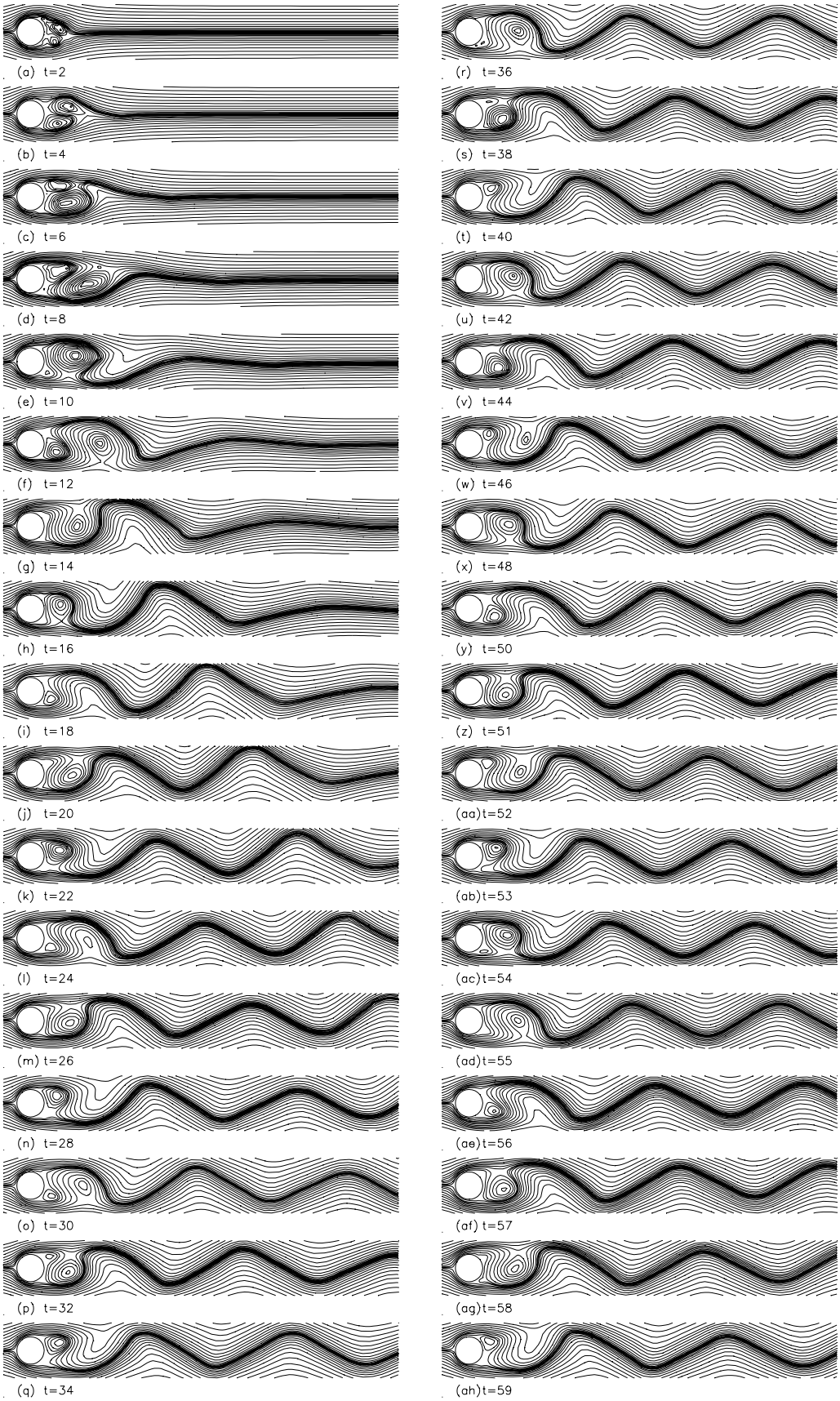

Figure 6.5. Calculated streamline patterns in flow over circular cylinder at Re_d = 100, showing sequence of flow evolution from the impulsive start to the fully-developed state.

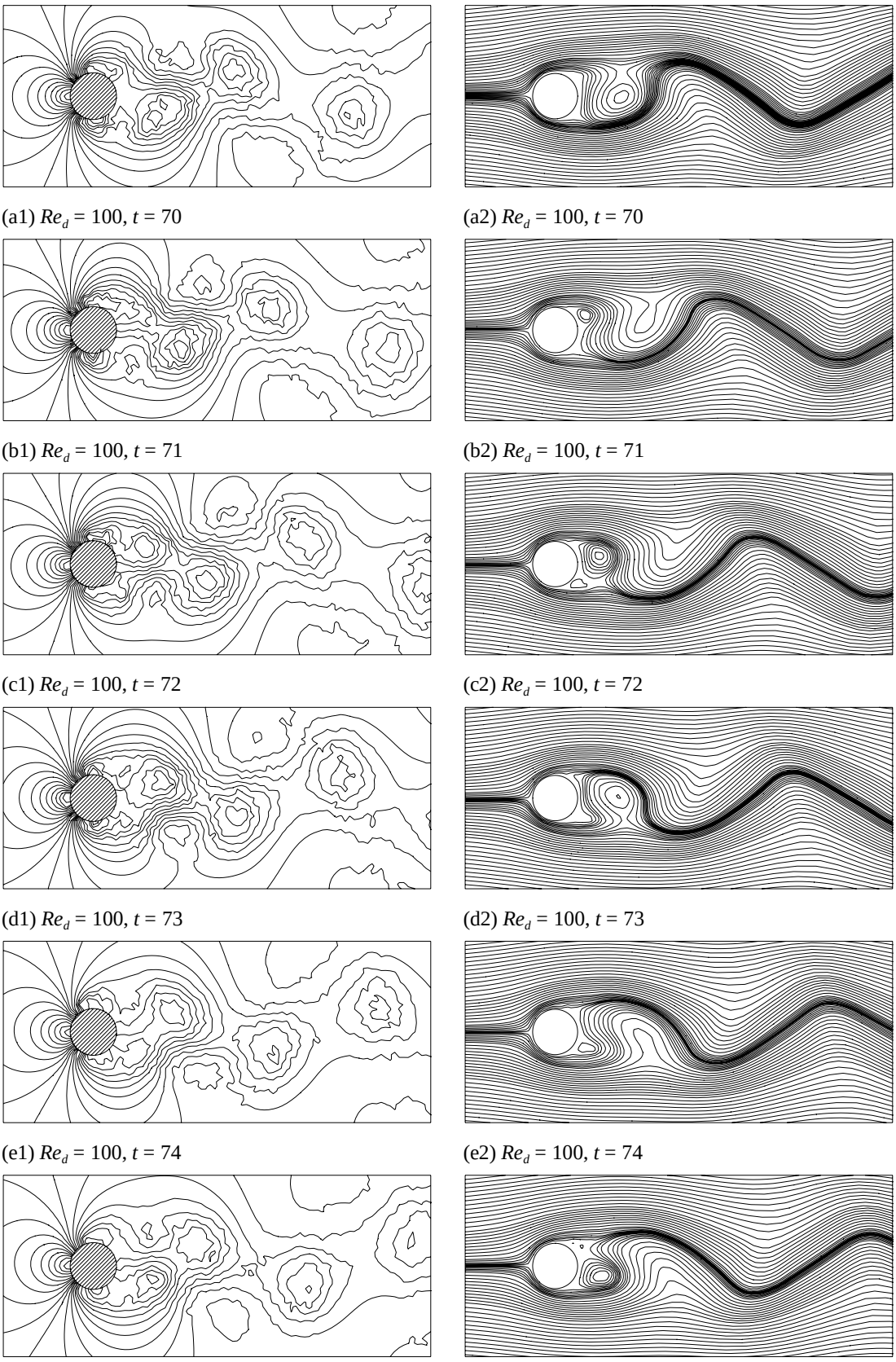

(a1) Re_d = 100, t = 70 (a2) Re_d = 100, t = 70

(b1) Re_d = 100, t = 71 (b2) Re_d = 100, t = 71

(c1) Re_d = 100, t = 72 (c2) Re_d = 100, t = 72

(d1) Re_d = 100, t = 73 (d2) Re_d = 100, t = 73

(e1) Re_d = 100, t = 74 (e2) Re_d = 100, t = 74

(f1) Re_d = 100, t = 75 (f2) Re_d = 100, t = 75

Figure 6.6. Instantaneous pressure fields and streamline patterns in fully-developed flow over a circular cylinder at Re_d = 100.

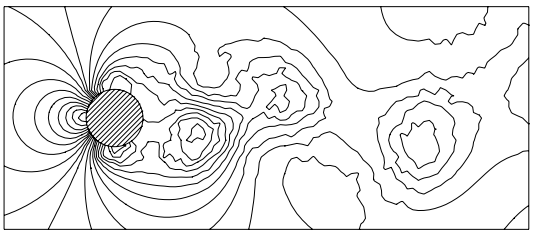

(g1) Re_d = 100, t = 76

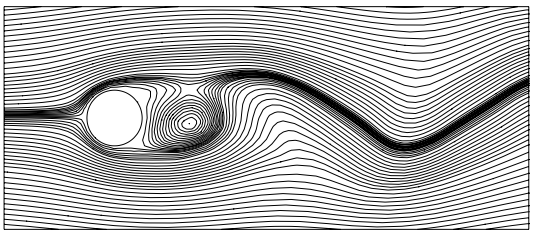

(g2) Re_d = 100, t = 76

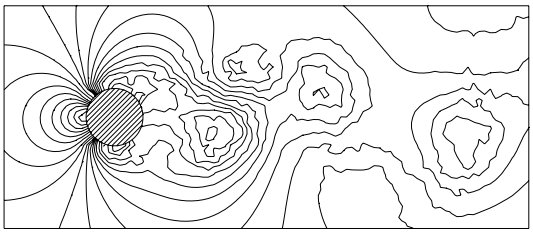

(h1) Re_d = 100, t = 77

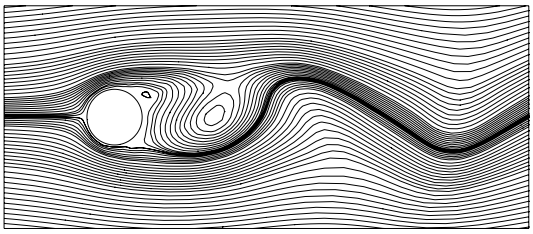

(h2) Re_d = 100, t = 77

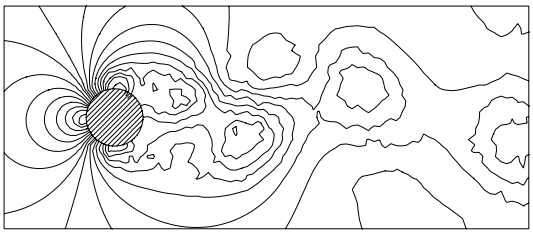

(i1) Re_d = 100, t = 78

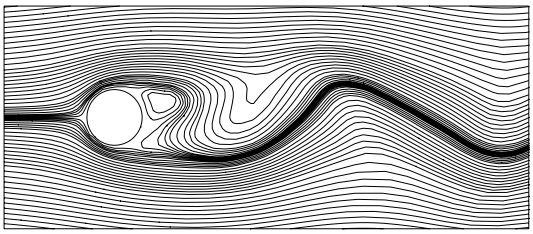

(i2) Re_d = 100, t = 78

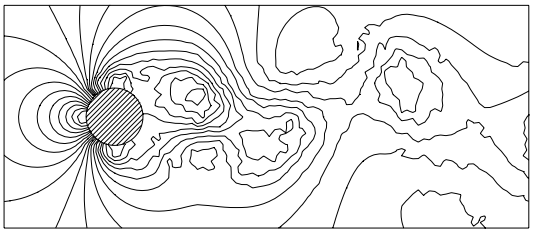

(j1) Re_d = 100, t = 79

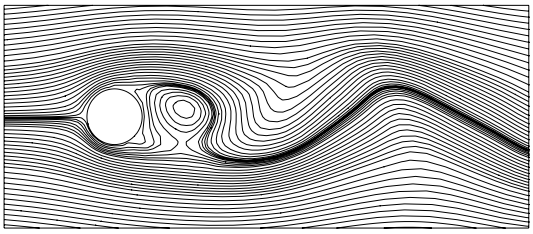

(j2) Re_d = 100, t = 79

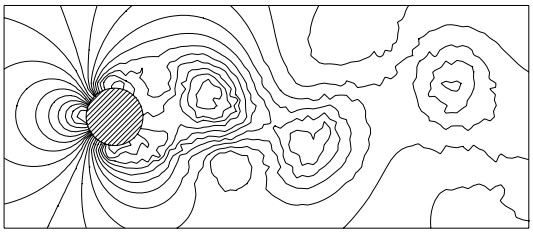

(k1) Re_d = 100, t = 80

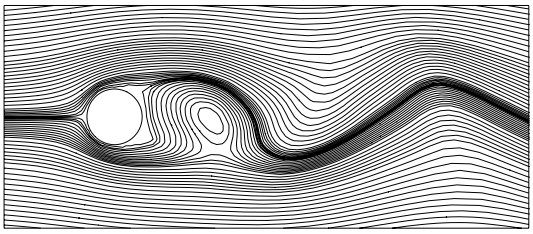

(k2) Re_d = 100, t = 80

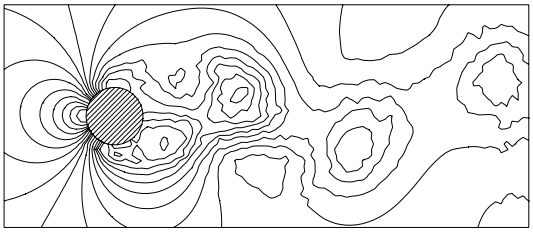

(k1) Re_d = 100, t = 81

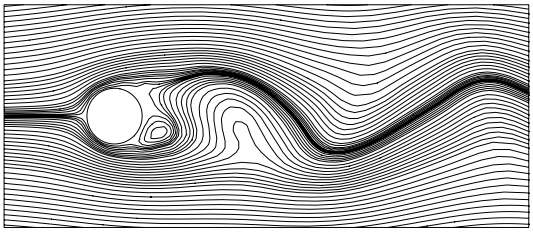

(l2) Re_d = 100, t = 81

Figure 6.6. Cont'd.

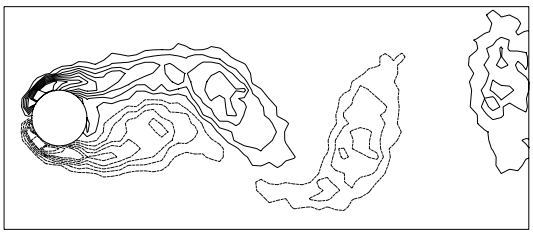

(a) Re_d = 100, t = 70

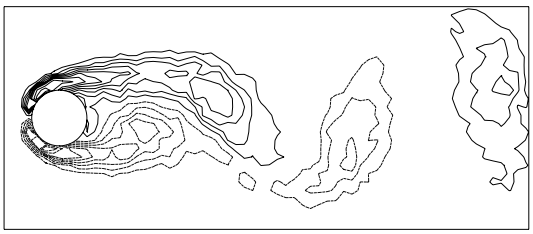

(g) Re_d = 100, t = 76

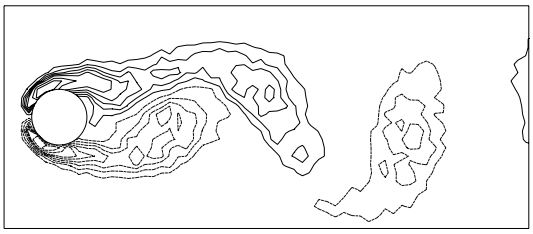

(b) Re_d = 100, t = 71

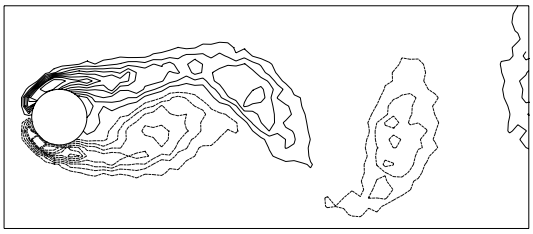

(h) Re_d = 100, t = 77

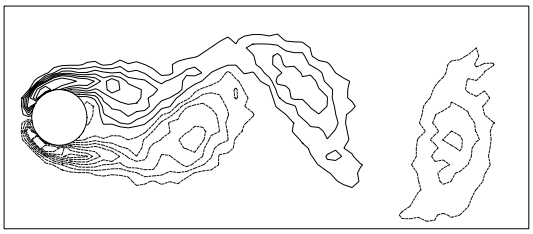

(c) Re_d = 100, t = 72

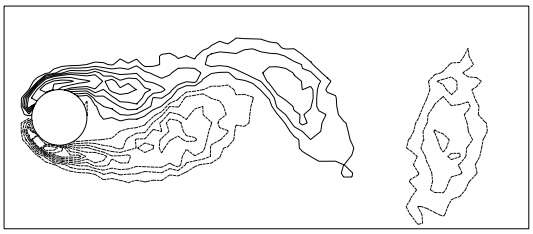

(i) Re_d = 100, t = 78

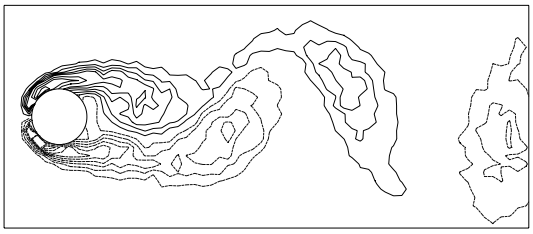

(d) Re_d = 100, t = 73

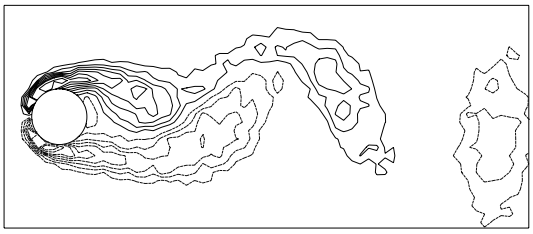

(j) Re_d = 100, t = 79

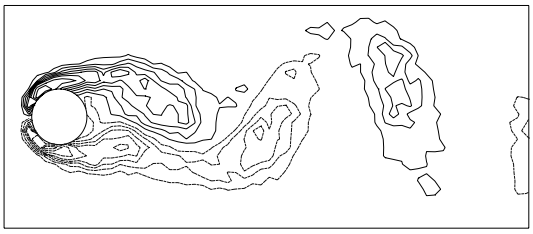

(e) Re_d = 100, t = 74

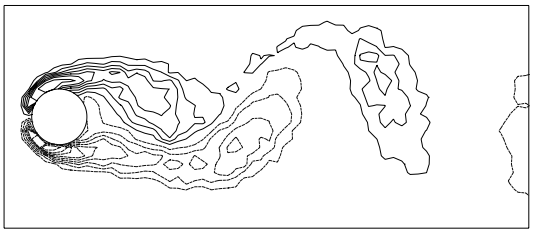

(k) Re_d = 100, t = 80

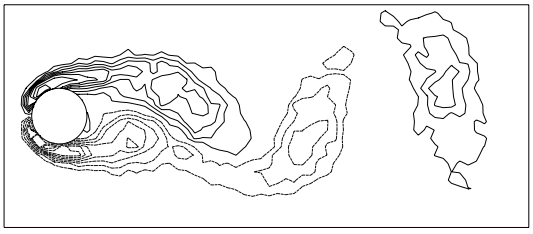

(f) Re_d = 100, t = 75

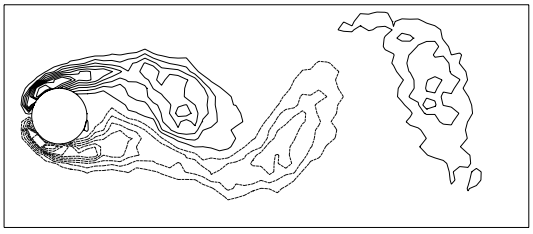

(l) Re_d = 100, t = 81

Figure 6.7. Vorticity contours in fully-developed flow over a circular cylinder at Re_d = 100.

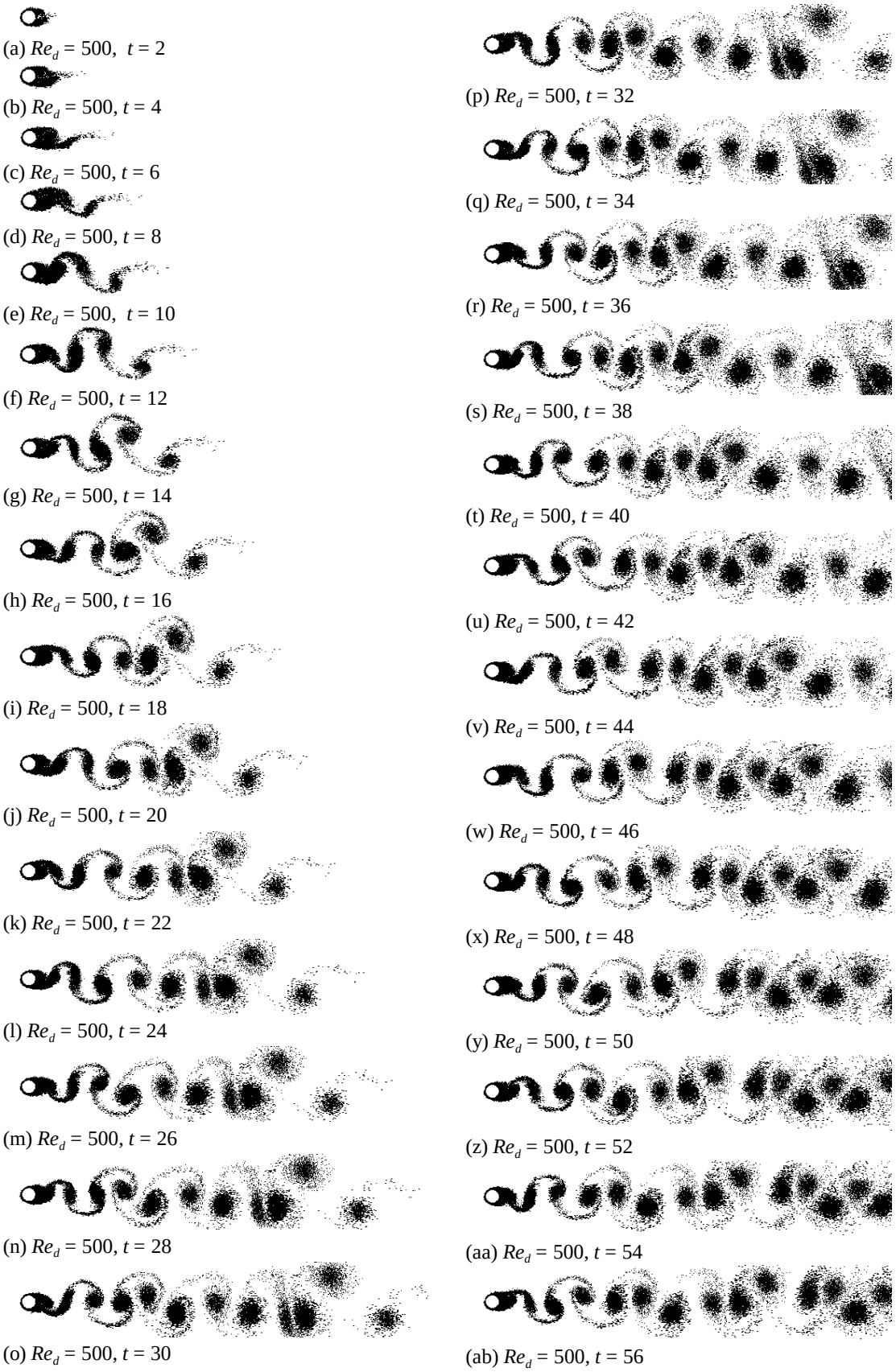

(a) Re_d = 500, t = 2

(b) Re_d = 500, t = 4

(c) Re_d = 500, t = 6

(d) Re_d = 500, t = 8

(e) Re_d = 500, t = 10

(f) Re_d = 500, t = 12

(g) Re_d = 500, t = 14

(h) Re_d = 500, t = 16

(i) Re_d = 500, t = 18

(j) Re_d = 500, t = 20

(k) Re_d = 500, t = 22

(l) Re_d = 500, t = 24

(m) Re_d = 500, t = 26

(n) Re_d = 500, t = 28

(o) Re_d = 500, t = 30

(p) Re_d = 500, t = 32

(q) Re_d = 500, t = 34

(r) Re_d = 500, t = 36

(s) Re_d = 500, t = 38

(t) Re_d = 500, t = 40

(u) Re_d = 500, t = 42

(v) Re_d = 500, t = 44

(w) Re_d = 500, t = 46

(x) Re_d = 500, t = 48

(y) Re_d = 500, t = 50

(z) Re_d = 500, t = 52

(aa) Re_d = 500, t = 54

(ab) Re_d = 500, t = 56

Figure 6.8. Elemental-vortex distributions in flow over a circular cylinder at Re_d = 500, showing development from the impulsive start to the fully-developed flow.

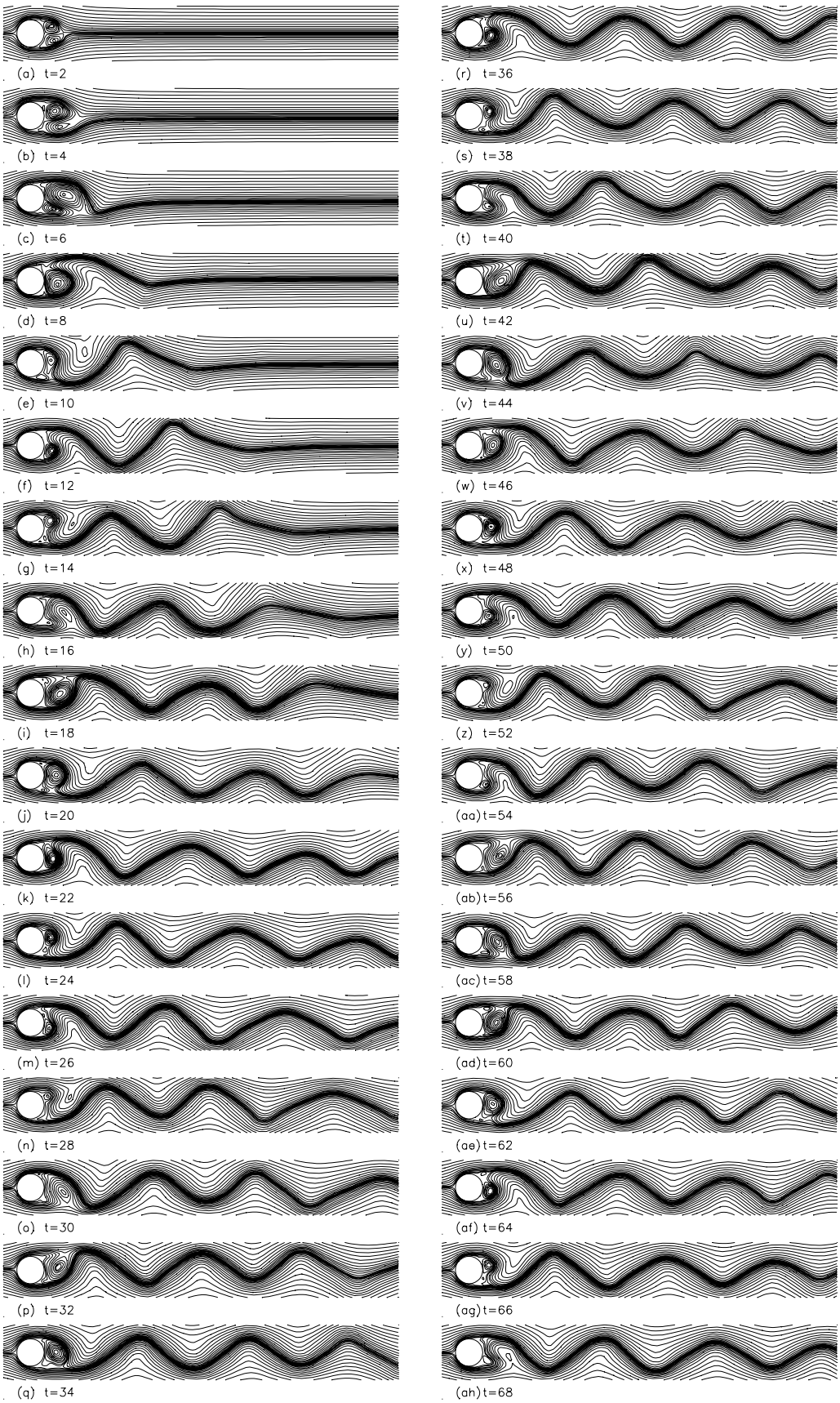

Figure 6.9. Calculated streamline patterns in flow over a circular cylinder at Re_d = 500, showing development from the impulsive start to the fully-developed flow.

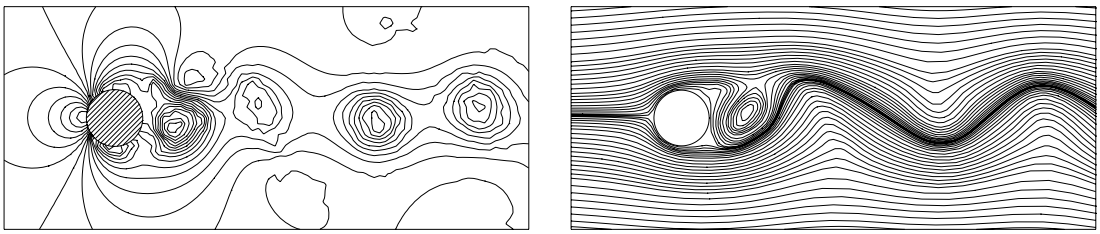

(a1) Re_d = 500, t = 70 (a2) Re_d = 500, t = 70

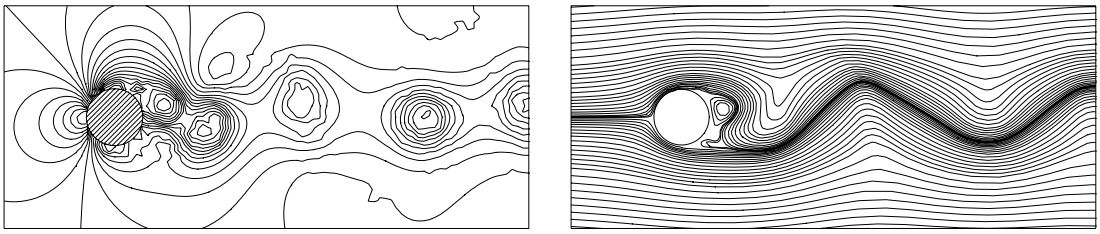

(b1) Re_d = 500, t = 71 (b2) Re_d = 500, t = 71

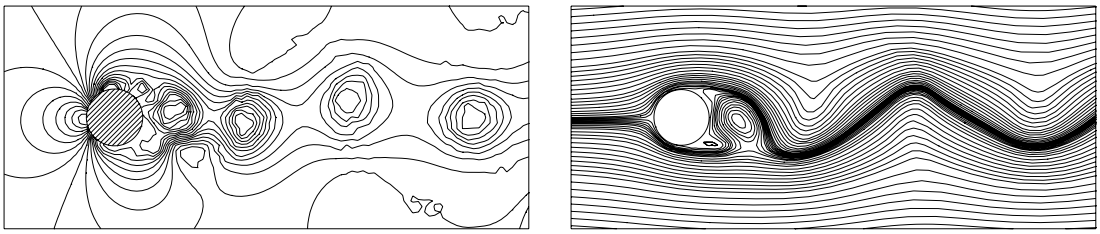

(c1) Re_d = 500, t = 72 (c2) Re_d = 500, t = 72

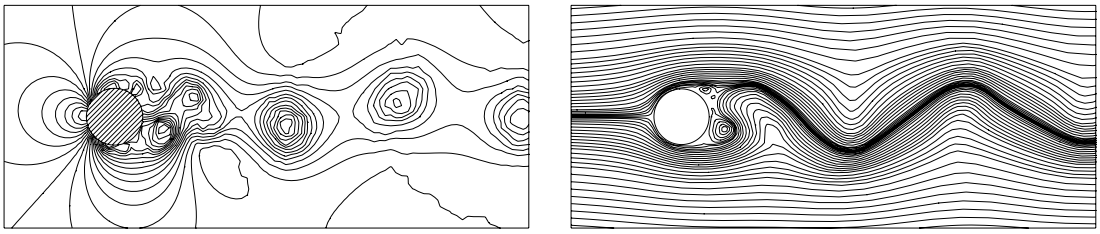

(d1) Re_d = 500, t = 73 (d2) Re_d = 500, t = 73

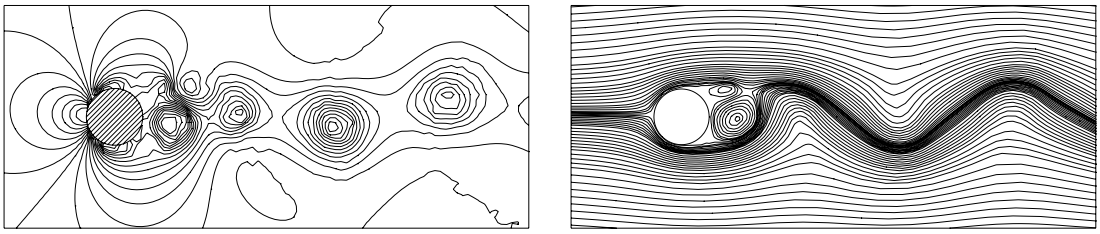

(e1) Re_d = 500, t = 74 (e2) Re_d = 500, t = 74

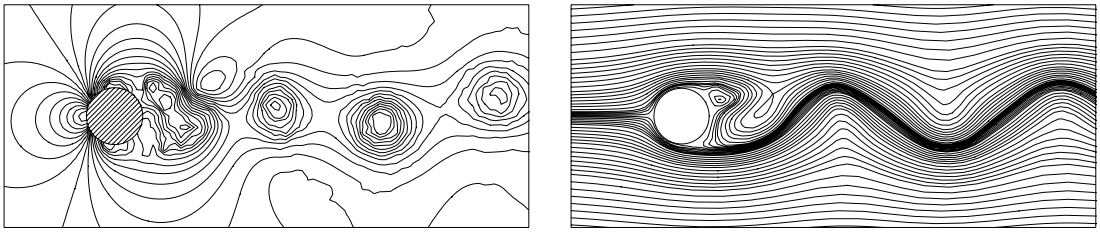

(f1) Re_d = 500, t = 75 (f2) Re_d = 500, t = 75

Figure 6.10. Instantaneous pressure fields and streamline patterns in fully-developed flow over the circular cylinder at Re_d = 500.

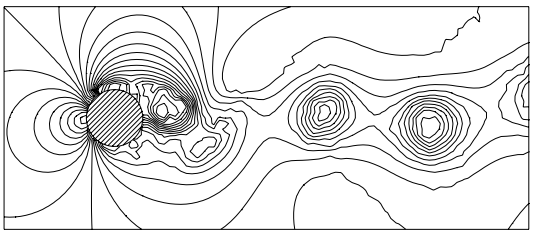

(g1) Re_d = 500, t = 76

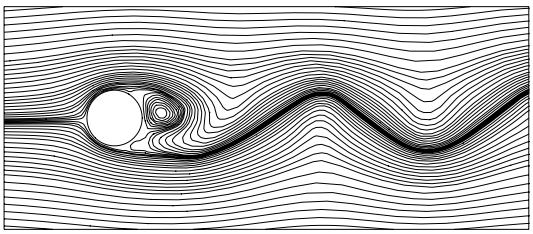

(g2) Re_d = 500, t = 76

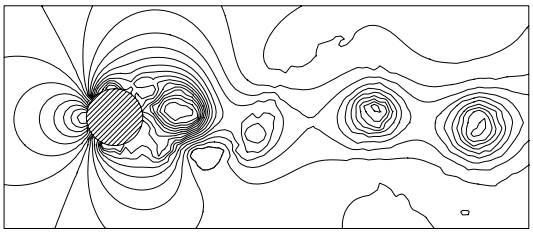

(h1) Re_d = 500, t = 77

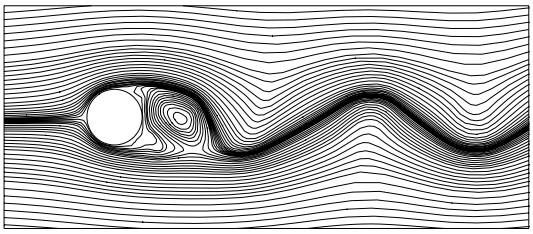

(h2) Re_d = 500, t = 77

(i1) Re_d = 500, t = 78

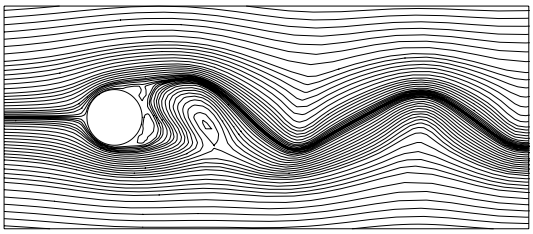

(i2) Re_d = 500, t = 78

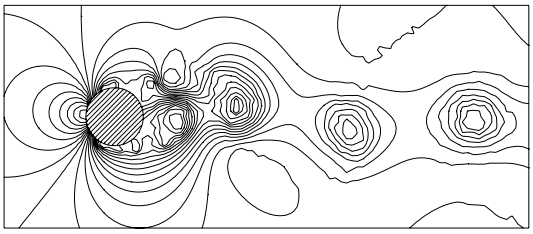

(j1) Re_d = 500, t = 79

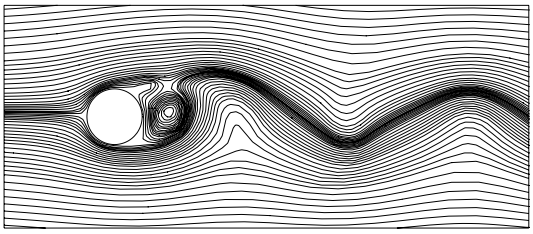

(j2) Re_d = 500, t = 79

(k1) Re_d = 500, t = 80

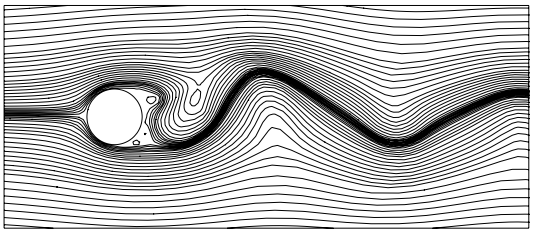

(k2) Re_d = 500, t = 80

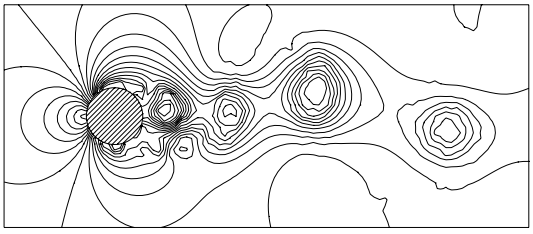

(l1) Re_d = 500, t = 81

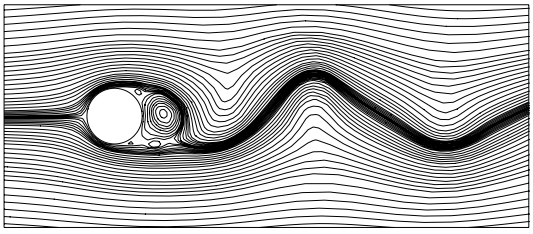

(l2) Re_d = 500, t = 81

Figure 6.10. Cont'd.

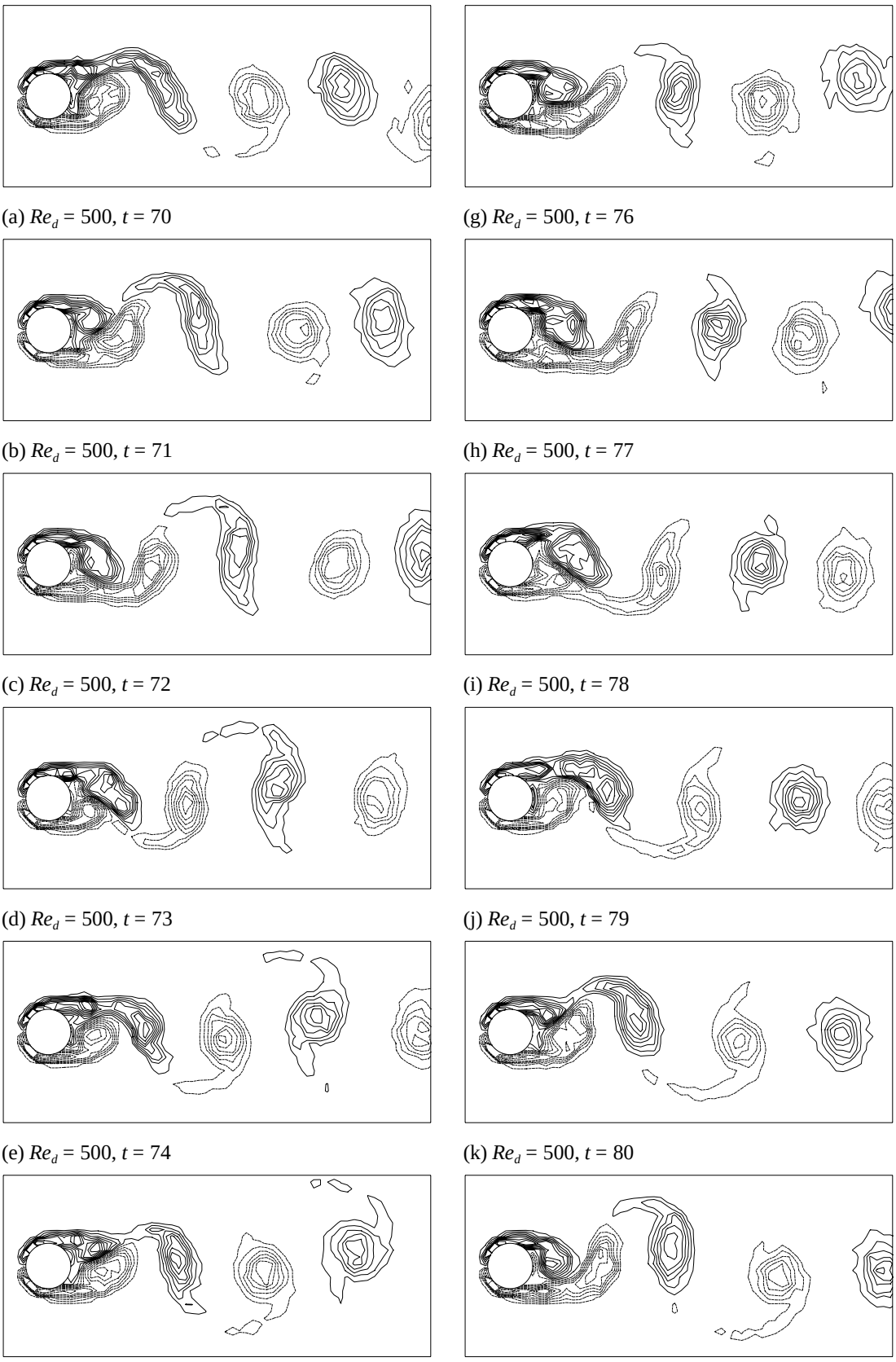

(a) Re_d = 500, t = 70

(b) Re_d = 500, t = 71

(c) Re_d = 500, t = 72

(d) Re_d = 500, t = 73

(e) Re_d = 500, t = 74

(f) Re_d = 500, t = 75

(g) Re_d = 500, t = 76

(h) Re_d = 500, t = 77

(i) Re_d = 500, t = 78

(j) Re_d = 500, t = 79

(k) Re_d = 500, t = 80

(l) Re_d = 500, t = 81

Figure 6.11. Vorticity contours in fully-developed flow over a circular cylinder at Re_d = 500.

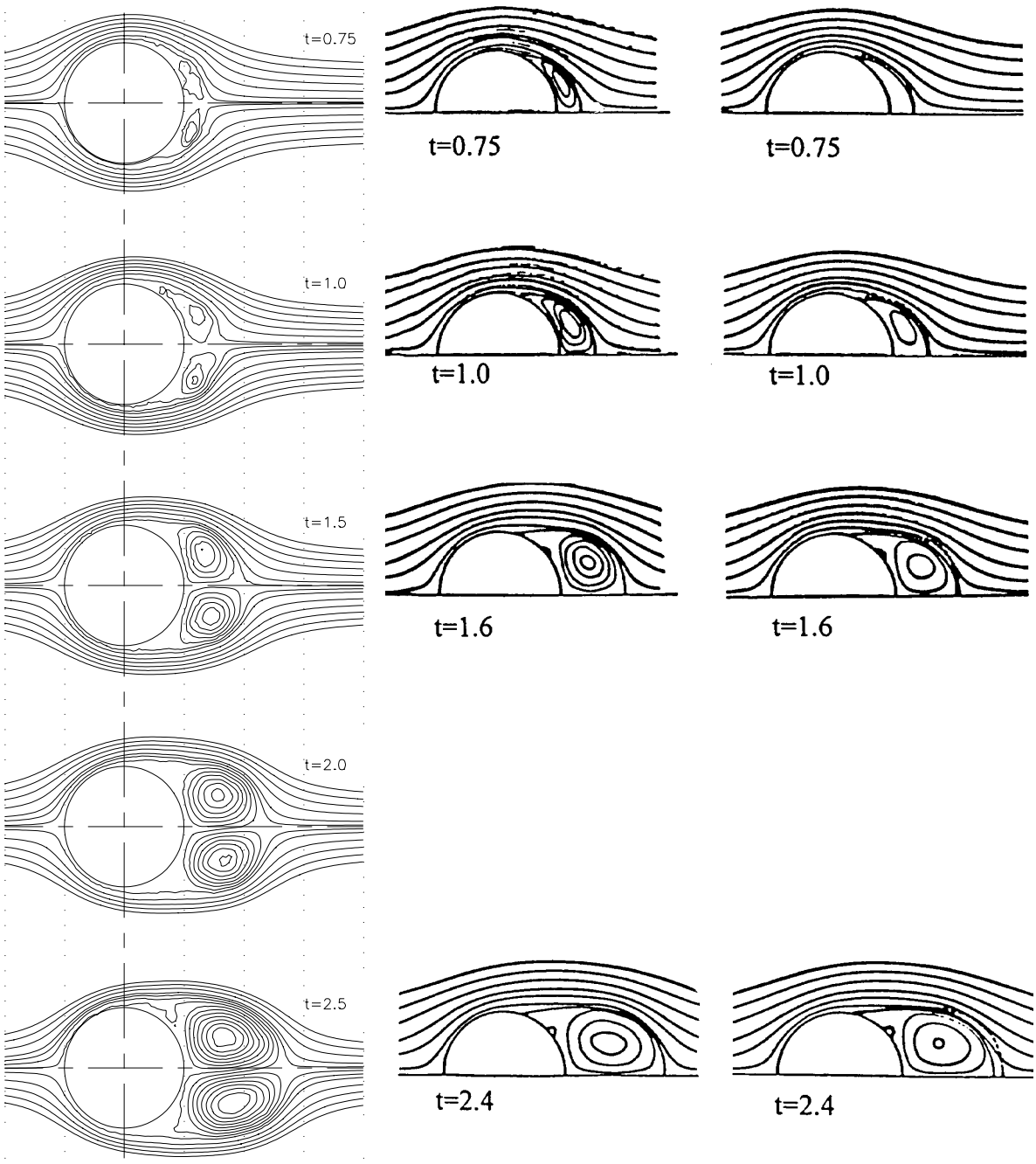

Figure 6.12. Calculated initial development of impulsively started flow past a circular cylinder at $Re_d = 500$: (a) this study, (b) Collins and Dennis [1973] (finite difference method), (c) Stansby [1993] (discrete vortex method).

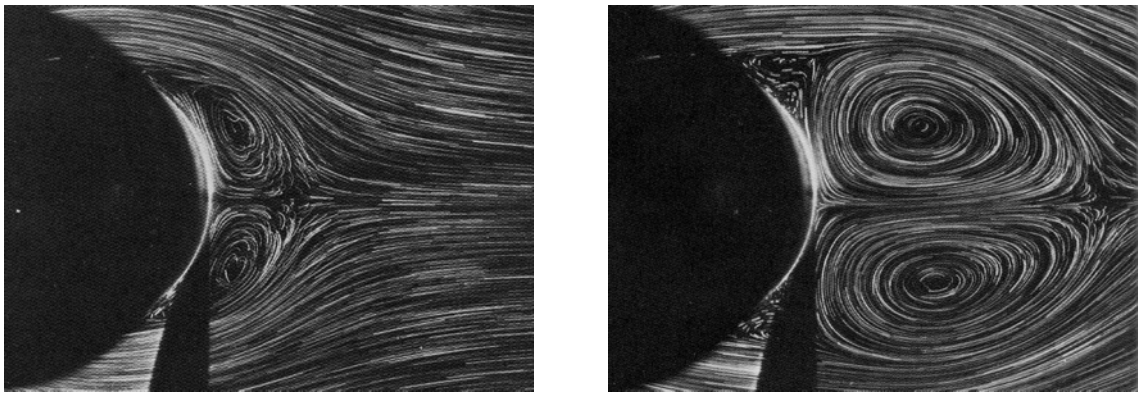

(a1) Re_d = 500, t = 1.0 (a2) Re_d = 500, t = 3.0

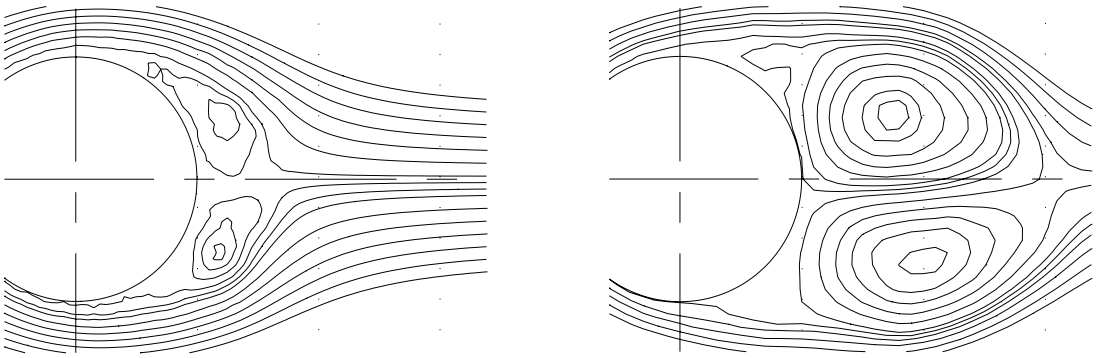

(b1) Re_d = 500, t = 1.0 (b2) Re_d = 500, t = 3.0

Figure 6.13. Comparison between visualised flow patterns and calculated results for circular cylinder flow at Re_d = 500: (a) Coutanceau and Bouard [1977], (b) this study.

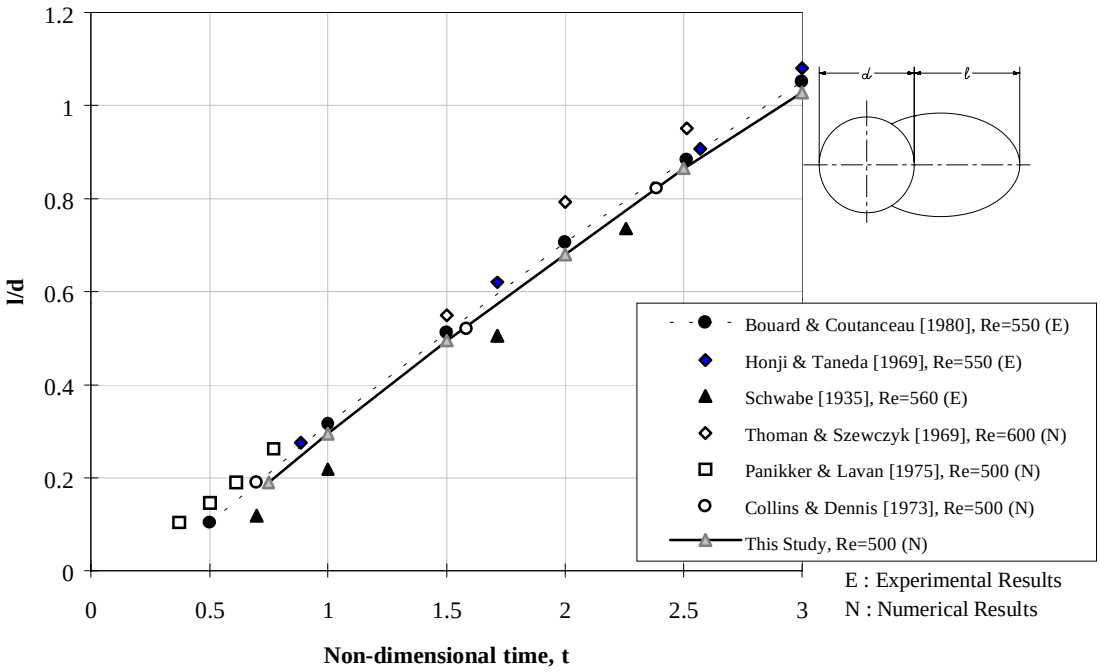

Figure 6.14. Evolution with time of the closed wake length of a circular cylinder at Re_d = 500.

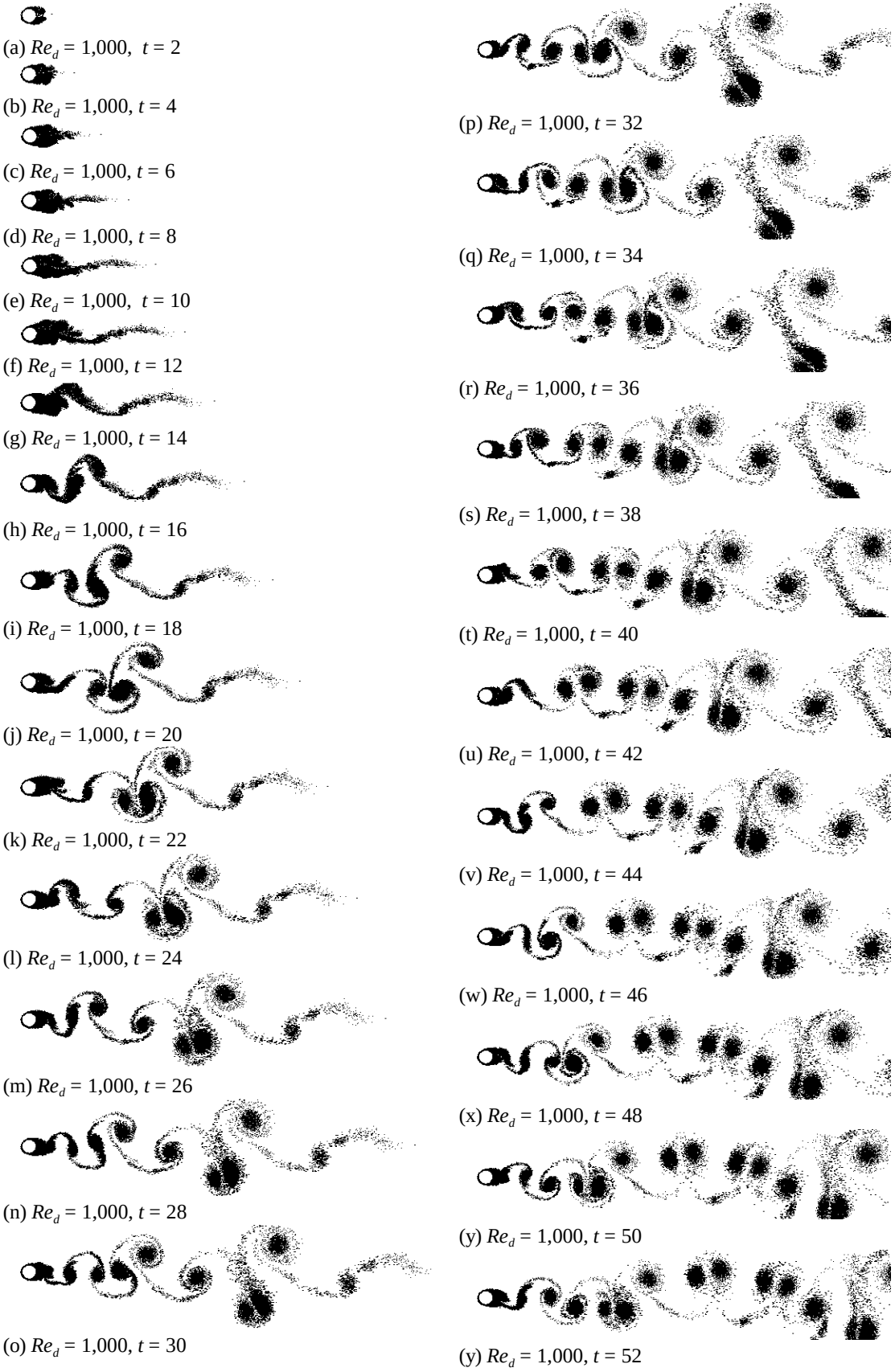

(a) Re_d = 1,000, t = 2

(b) Re_d = 1,000, t = 4

(c) Re_d = 1,000, t = 6

(d) Re_d = 1,000, t = 8

(e) Re_d = 1,000, t = 10

(f) Re_d = 1,000, t = 12

(g) Re_d = 1,000, t = 14

(h) Re_d = 1,000, t = 16

(i) Re_d = 1,000, t = 18

(j) Re_d = 1,000, t = 20

(k) Re_d = 1,000, t = 22

(l) Re_d = 1,000, t = 24

(m) Re_d = 1,000, t = 26

(n) Re_d = 1,000, t = 28

(o) Re_d = 1,000, t = 30

(p) Re_d = 1,000, t = 32

(q) Re_d = 1,000, t = 34

(r) Re_d = 1,000, t = 36

(s) Re_d = 1,000, t = 38

(t) Re_d = 1,000, t = 40

(u) Re_d = 1,000, t = 42

(v) Re_d = 1,000, t = 44

(w) Re_d = 1,000, t = 46

(x) Re_d = 1,000, t = 48

(y) Re_d = 1,000, t = 50

(y) Re_d = 1,000, t = 52

Figure 6.15. Elemental-vortex distributions in flow over a circular cylinder at Re_d = 1,000, showing sequence of flow development from the impulsive start to the fully-developed state.

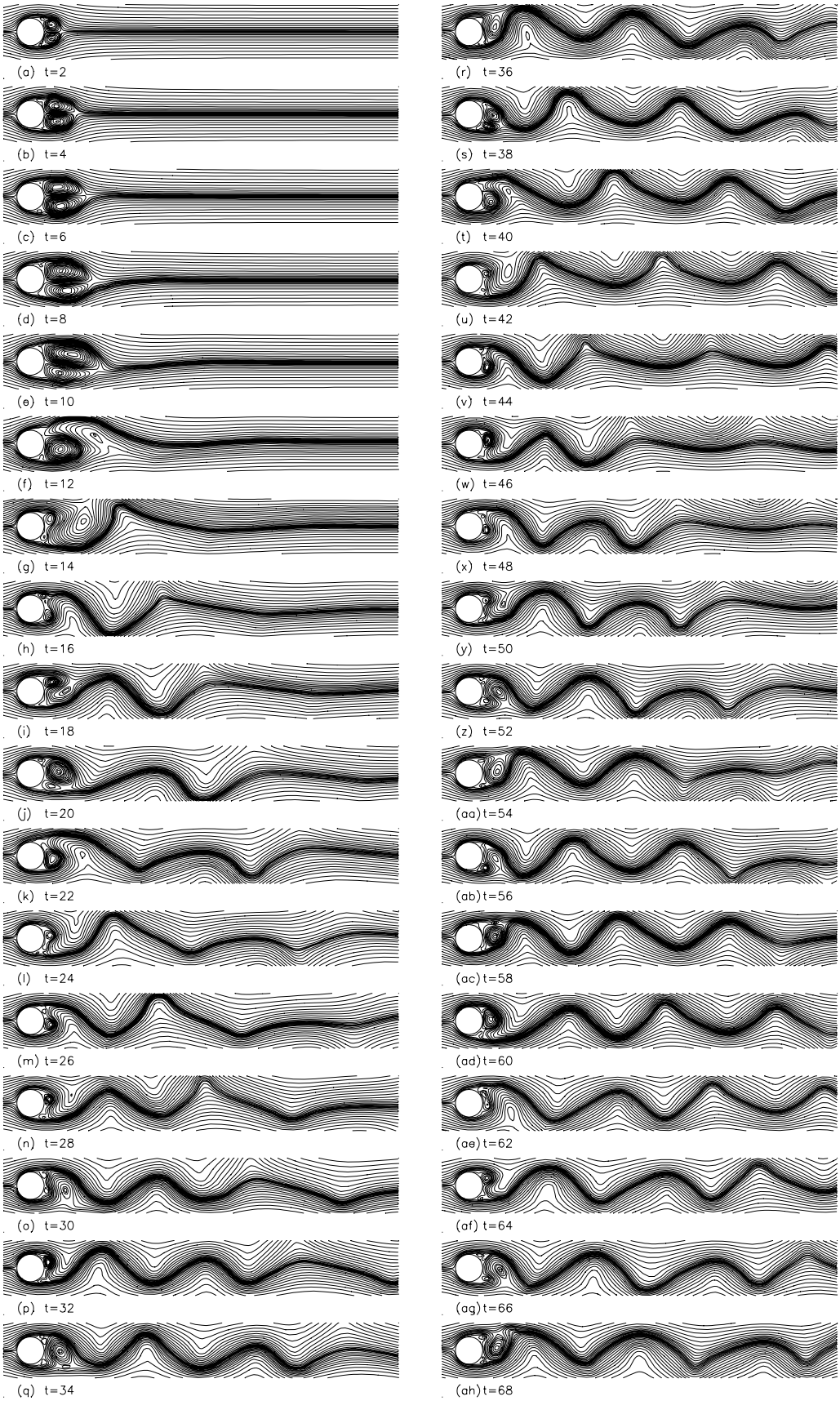

Figure 6.16. Calculated streamline patterns in flow over a circular cylinder at Re_d = 1,000, showing sequence of flow development from the impulsive start to the fully-developed state.

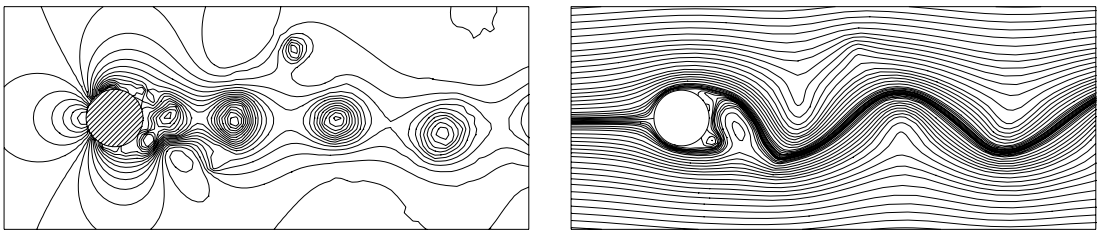

(a1) Re_d = 1,000, t = 70 (a2) Re_d = 1,000, t = 70

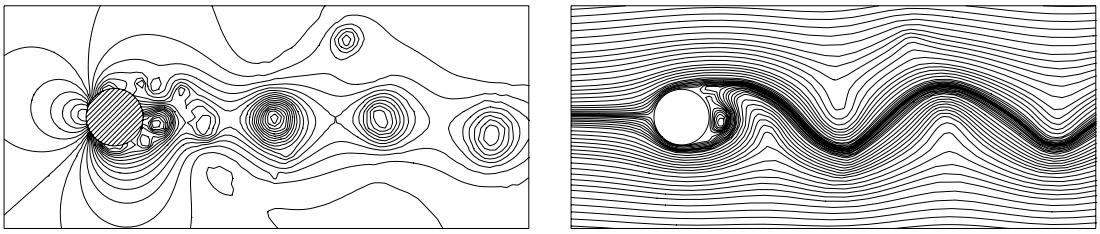

(b1) Re_d = 1,000, t = 71 (b2) Re_d = 1,000, t = 71

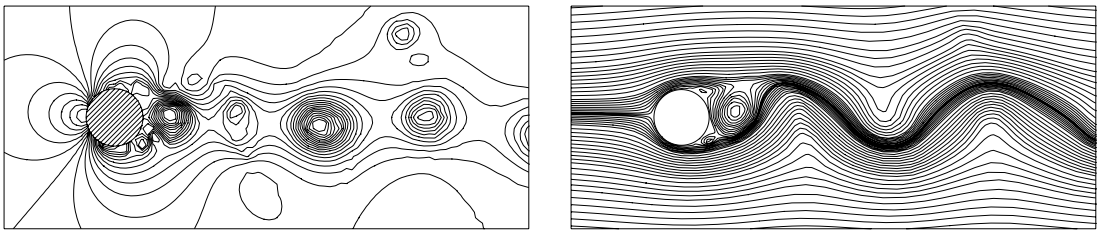

(c1) Re_d = 1,000, t = 72 (c2) Re_d = 1,000, t = 72

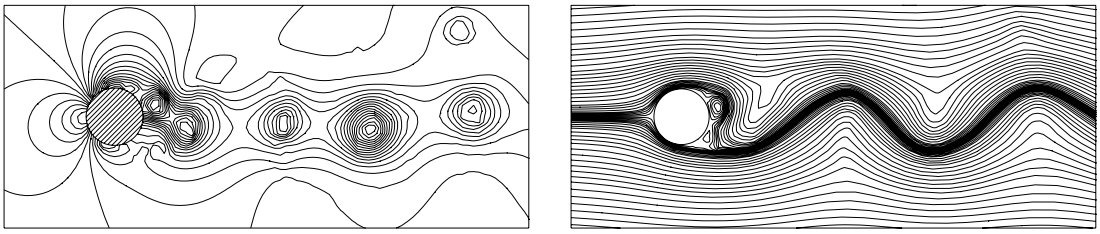

(d1) Re_d = 1,000, t = 73 (d2) Re_d = 1,000, t = 73

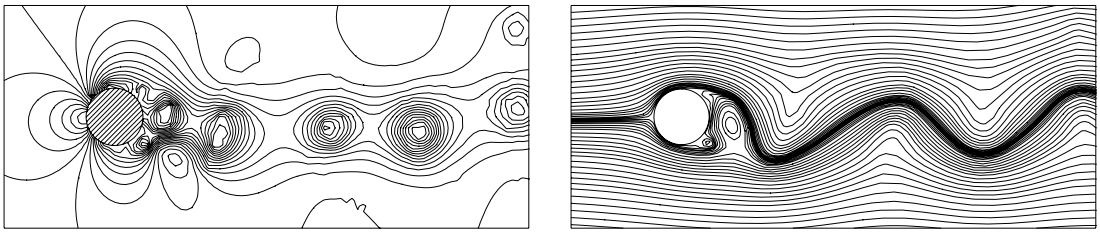

(e1) Re_d = 1,000, t = 74 (e2) Re_d = 1,000, t = 74

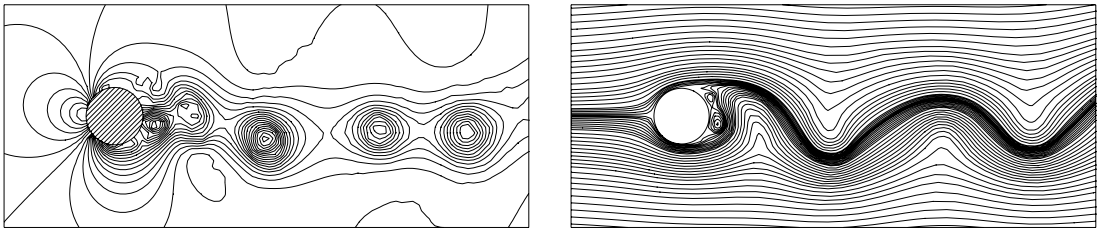

(f1) Re_d = 1,000, t = 75 (f2) Re_d = 1,000, t = 75

Figure 6.17. Instantaneous pressure fields and streamline patterns in fully-developed flow over a circular cylinder at Re_d = 1,000.

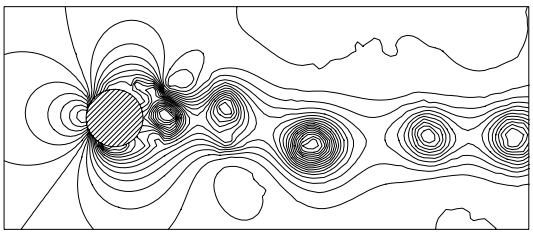

(g1) Re_d = 1,000, t = 76

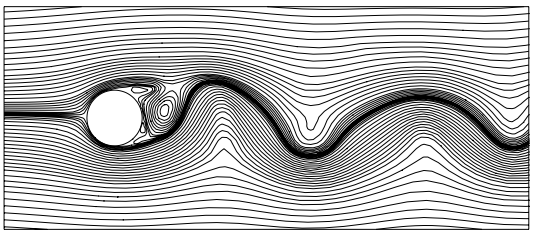

(g2) Re_d = 1,000, t = 76

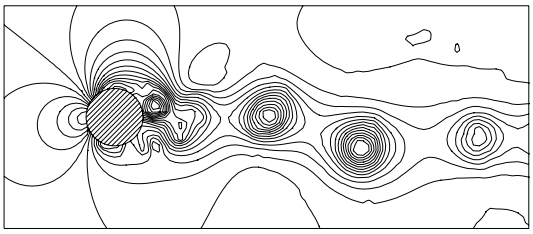

(h1) Re_d = 1,000, t = 77

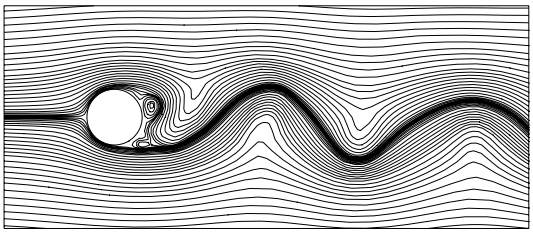

(h2) Re_d = 1,000, t = 77

(i1) Re_d = 1,000, t = 78

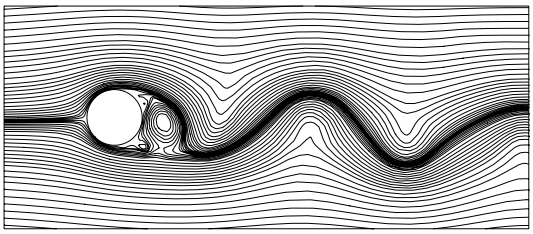

(i2) Re_d = 1,000, t = 78

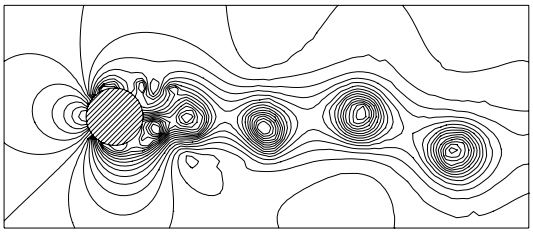

(j1) Re_d = 1,000, t = 79

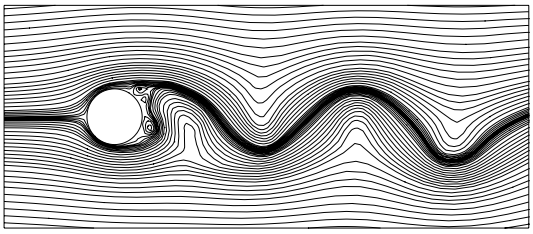

(j2) Re_d = 1,000, t = 79

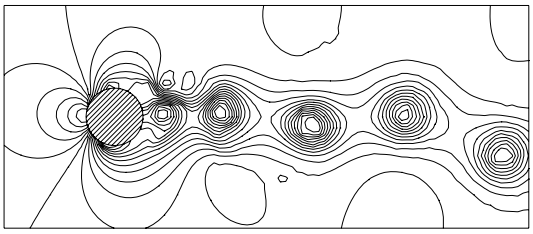

(k1) Re_d = 1,000, t = 80

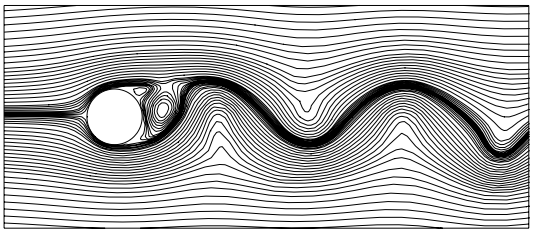

(k2) Re_d = 1,000, t = 80

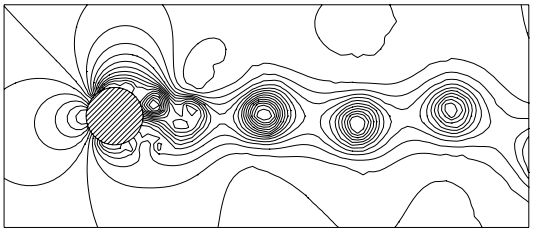

(l1) Re_d = 1,000, t = 81

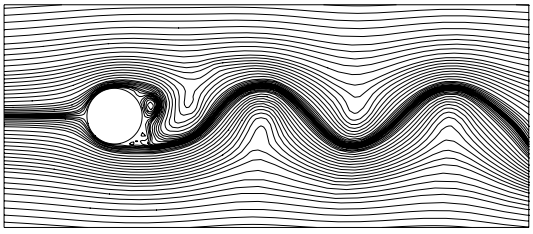

(l2) Re_d = 1,000, t = 81

Figure 6.17. Cont'd.

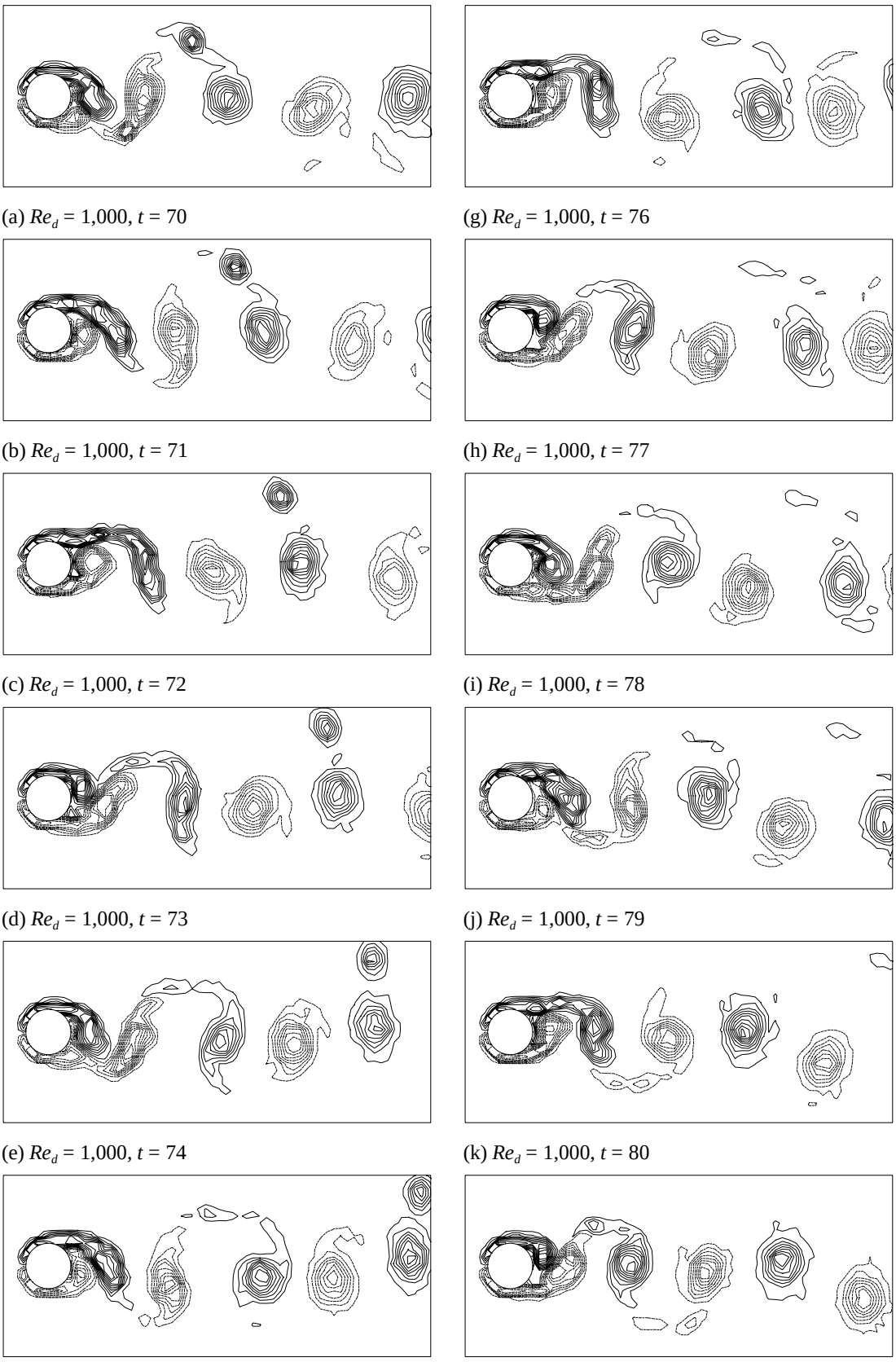

(a) Re_d = 1,000, t = 70

(b) Re_d = 1,000, t = 71

(c) Re_d = 1,000, t = 72

(d) Re_d = 1,000, t = 73

(e) Re_d = 1,000, t = 74

(f) Re_d = 1,000, t = 75

(g) Re_d = 1,000, t = 76

(h) Re_d = 1,000, t = 77

(i) Re_d = 1,000, t = 78

(j) Re_d = 1,000, t = 79

(k) Re_d = 1,000, t = 80

(l) Re_d = 1,000, t = 81

Figure 6.18. Vorticity contours in fully-developed flow over a circular cylinder at Re_d = 1,000.

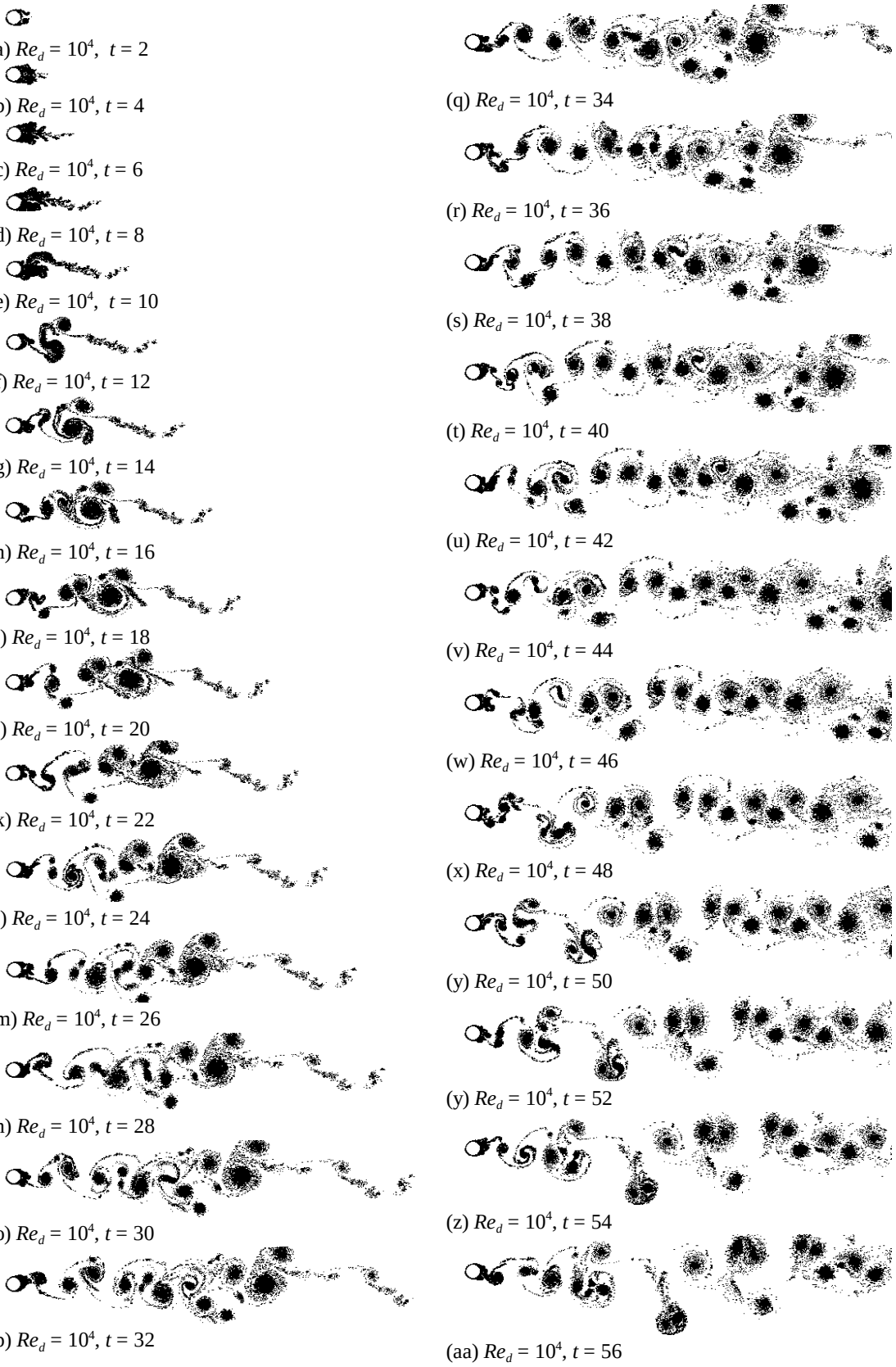

(a) $Re_d = 10^4$, $t = 2$

(b) $Re_d = 10^4$, $t = 4$

(c) $Re_d = 10^4$, $t = 6$

(d) $Re_d = 10^4$, $t = 8$

(e) $Re_d = 10^4$, $t = 10$

(f) $Re_d = 10^4$, $t = 12$

(g) $Re_d = 10^4$, $t = 14$

(h) $Re_d = 10^4$, $t = 16$

(i) $Re_d = 10^4$, $t = 18$

(j) $Re_d = 10^4$, $t = 20$

(k) $Re_d = 10^4$, $t = 22$

(l) $Re_d = 10^4$, $t = 24$

(m) $Re_d = 10^4$, $t = 26$

(n) $Re_d = 10^4$, $t = 28$

(o) $Re_d = 10^4$, $t = 30$

(p) $Re_d = 10^4$, $t = 32$

(q) $Re_d = 10^4$, $t = 34$

(r) $Re_d = 10^4$, $t = 36$

(s) $Re_d = 10^4$, $t = 38$

(t) $Re_d = 10^4$, $t = 40$

(u) $Re_d = 10^4$, $t = 42$

(v) $Re_d = 10^4$, $t = 44$

(w) $Re_d = 10^4$, $t = 46$

(x) $Re_d = 10^4$, $t = 48$

(y) $Re_d = 10^4$, $t = 50$

(y) $Re_d = 10^4$, $t = 52$

(z) $Re_d = 10^4$, $t = 54$

(aa) $Re_d = 10^4$, $t = 56$

Figure 6.19. Elemental-vortex distributions in flow over a circular cylinder at $Re_d = 10^4$, showing evolution of flow from the impulsive start to the fully-developed state.

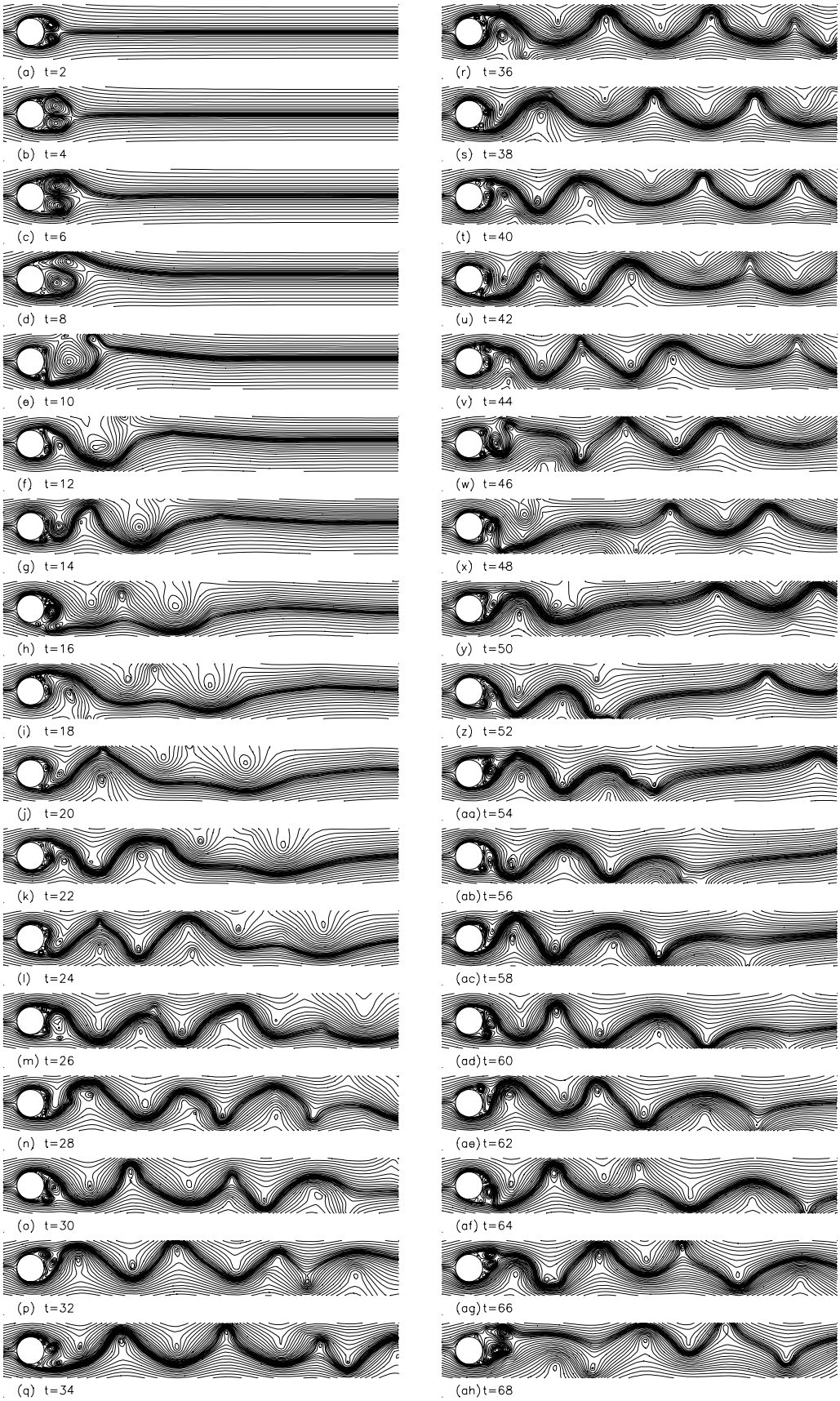

Figure 8.20. Streamline patterns in flow over a circular cylinder at Re_d = 10,000, showing evolution of flow from the impulsive start to the fully-developed state.

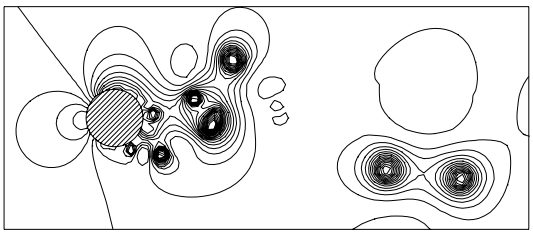

(a1) $Re_d = 10^4$, $t = 70$

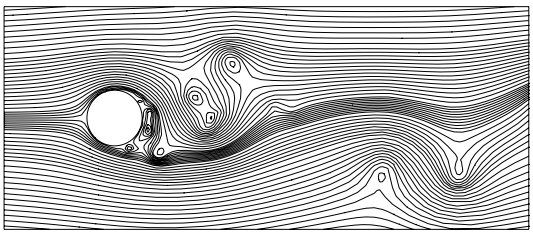

(a2) $Re_d = 10^4$, $t = 70$

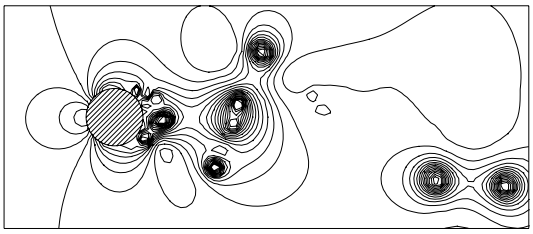

(b1) $Re_d = 10^4$, $t = 71$

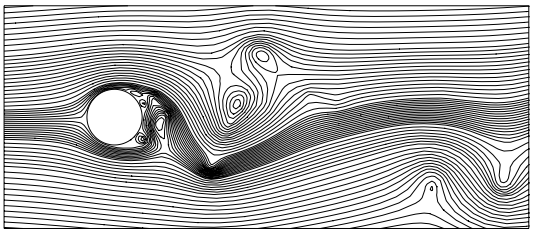

(b2) $Re_d = 10^4$, $t = 71$

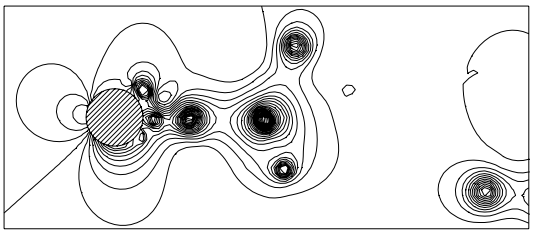

(c1) $Re_d = 10^4$, $t = 72$

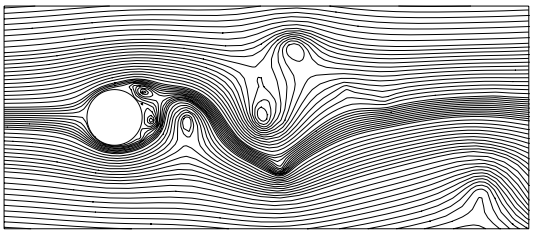

(c2) $Re_d = 10^4$, $t = 72$

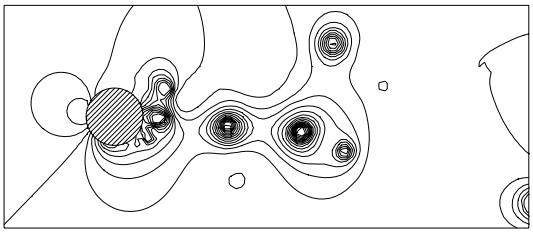

(d1) $Re_d = 10^4$, $t = 73$

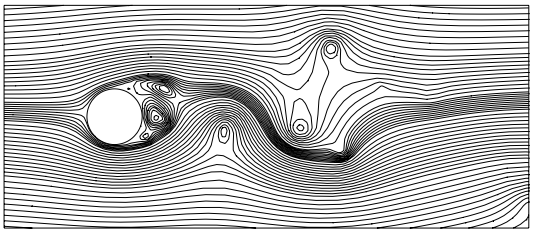

(d2) $Re_d = 10^4$, $t = 73$

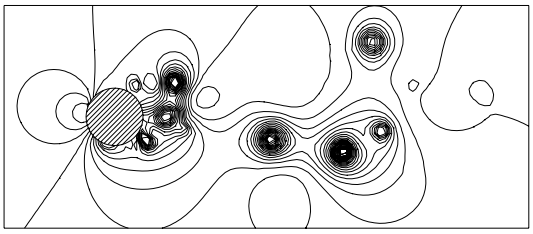

(e1) $Re_d = 10^4$, $t = 74$

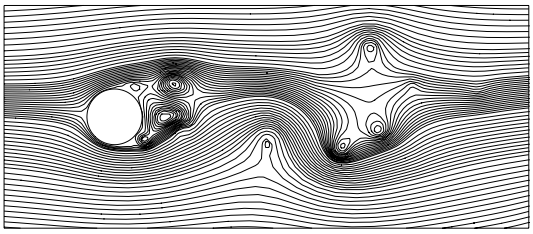

(e2) $Re_d = 10^4$, $t = 74$

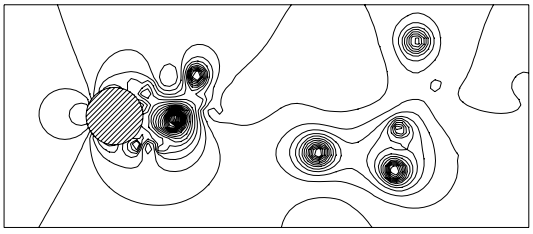

(f1) $Re_d = 10^4$, $t = 75$

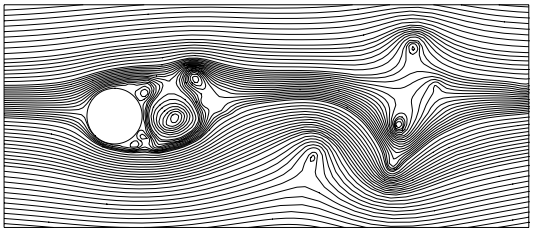

(f2) $Re_d = 10^4$, $t = 75$

Figure 6.21. Instantaneous pressure fields and streamline patterns in fully-developed flow over a circular cylinder at $Re_d = 10^4$.

(g1) $Re_d = 10^4$, $t = 76$

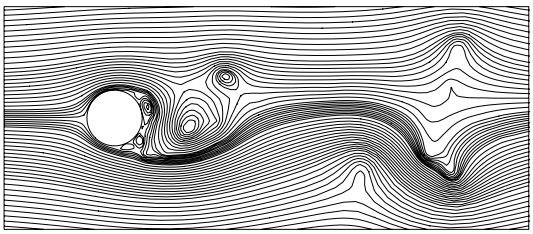

(g2) $Re_d = 10^4$, $t = 76$

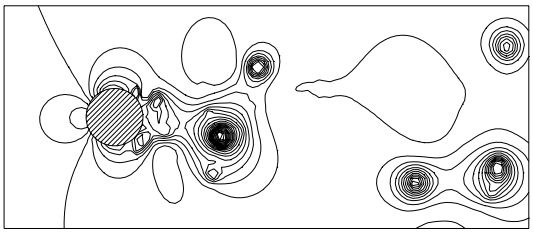

(h1) $Re_d = 10^4$, $t = 77$

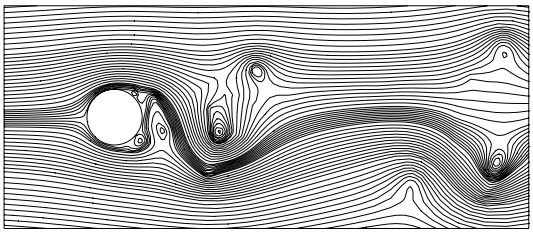

(h2) $Re_d = 10^4$, $t = 77$

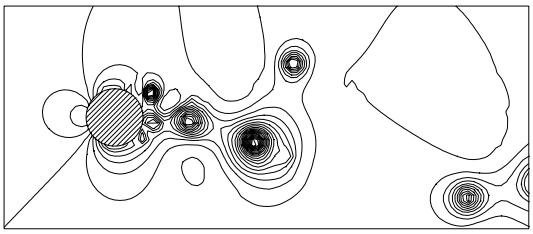

(i1) $Re_d = 10^4$, $t = 78$

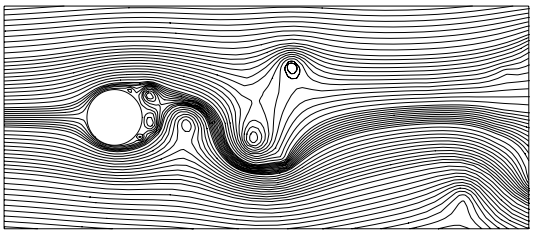

(i2) $Re_d = 10^4$, $t = 78$

(j1) $Re_d = 10^4$, $t = 79$

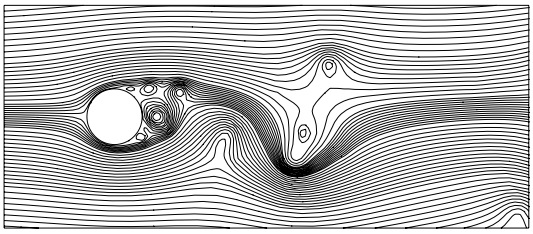

(j2) $Re_d = 10^4$, $t = 79$

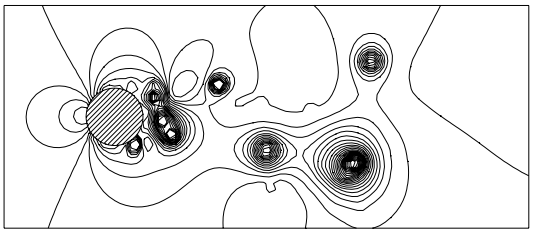

(k1) $Re_d = 10^4$, $t = 80$

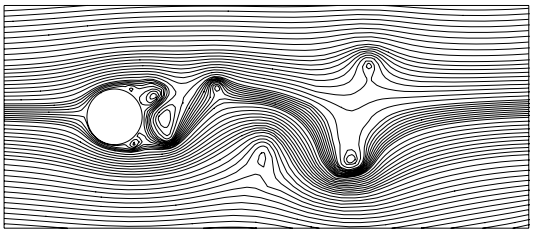

(k2) $Re_d = 10^4$, $t = 80$

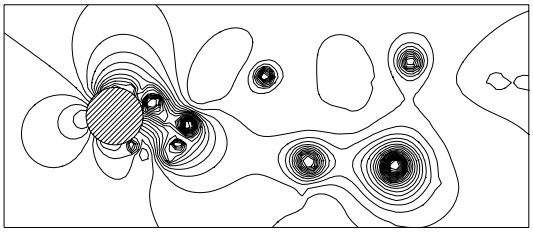

(l1) $Re_d = 10^4$, $t = 81$

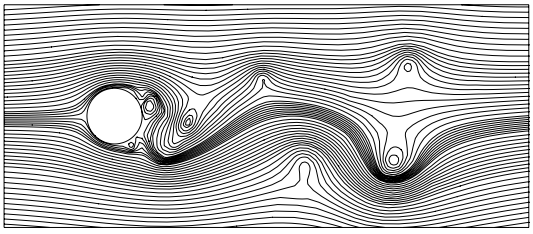

(l2) $Re_d = 10^4$, $t = 81$

Figure 6.21. Cont'd.

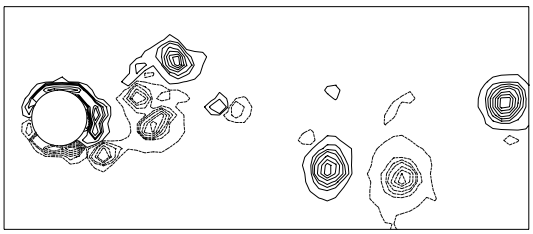

(a) $Re_d = 10^4$, $t = 70$

(g) $Re_d = 10^4$, $t = 76$

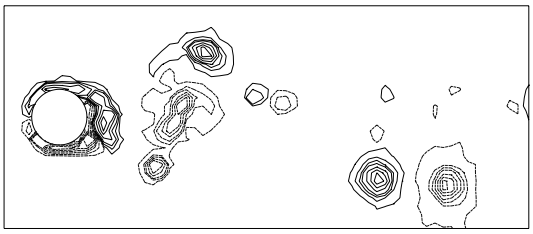

(b) $Re_d = 10^4$, $t = 71$

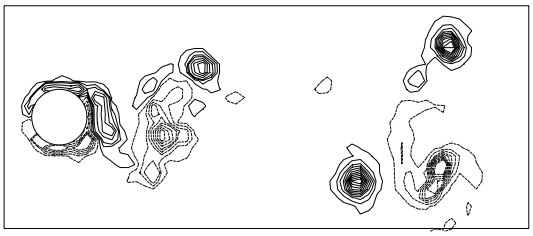

(h) $Re_d = 10^4$, $t = 77$

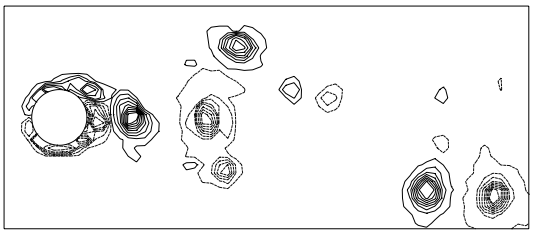

(c) $Re_d = 10^4$, $t = 72$

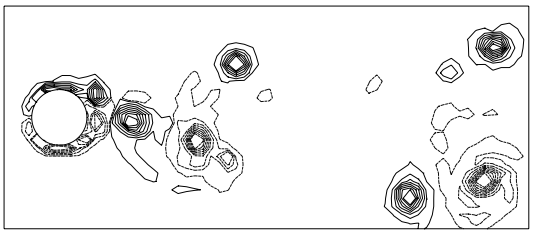

(i) $Re_d = 10^4$, $t = 78$

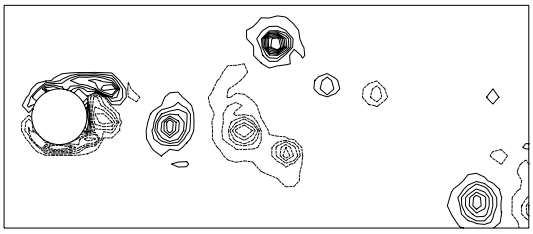

(d) $Re_d = 10^4$, $t = 73$

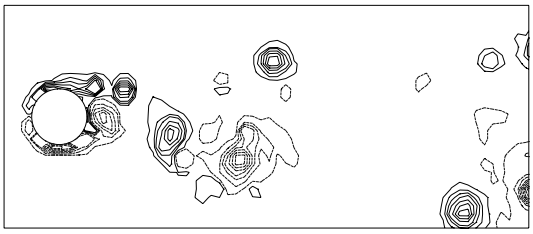

(j) $Re_d = 10^4$, $t = 79$

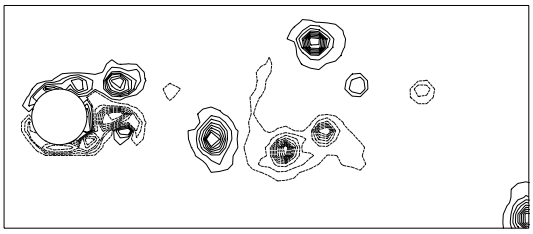

(e) $Re_d = 10^4$, $t = 74$

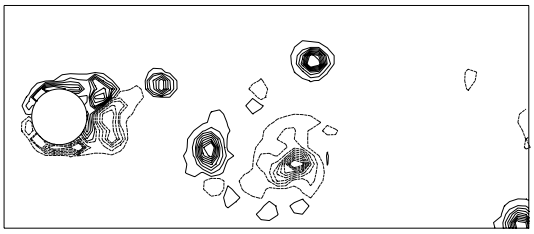

(k) $Re_d = 10^4$, $t = 80$

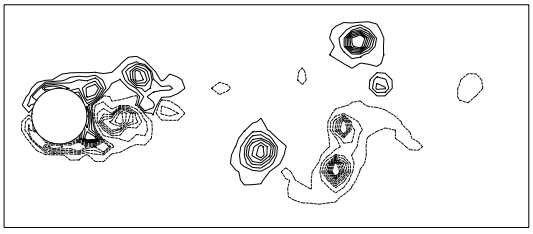

(f) $Re_d = 10^4$, $t = 75$

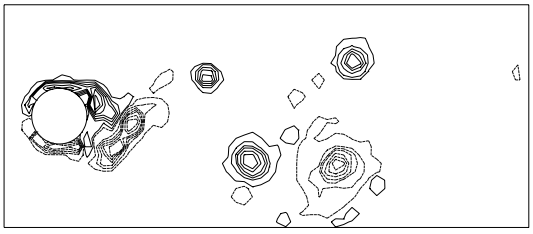

(l) $Re_d = 10^4$, $t = 81$

Figure 6.22. Vorticity contours in fully-developed flow over a circular cylinder at $Re_d = 10^4$.

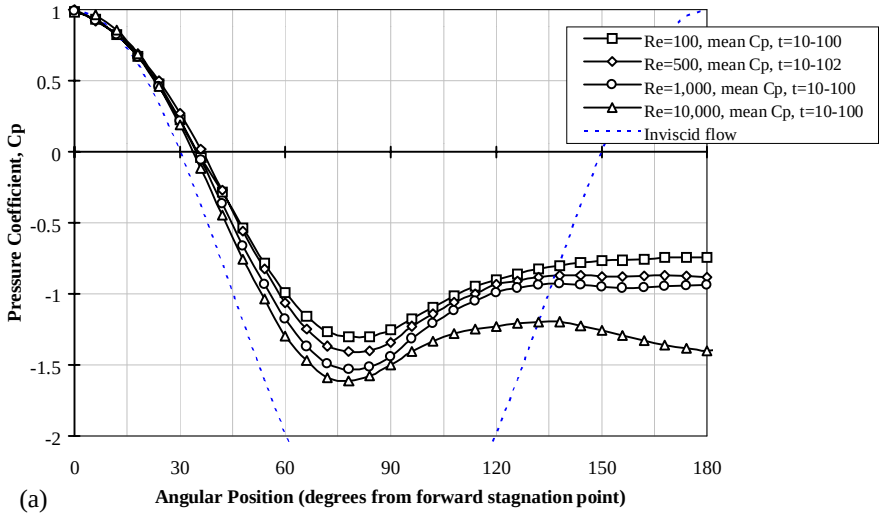

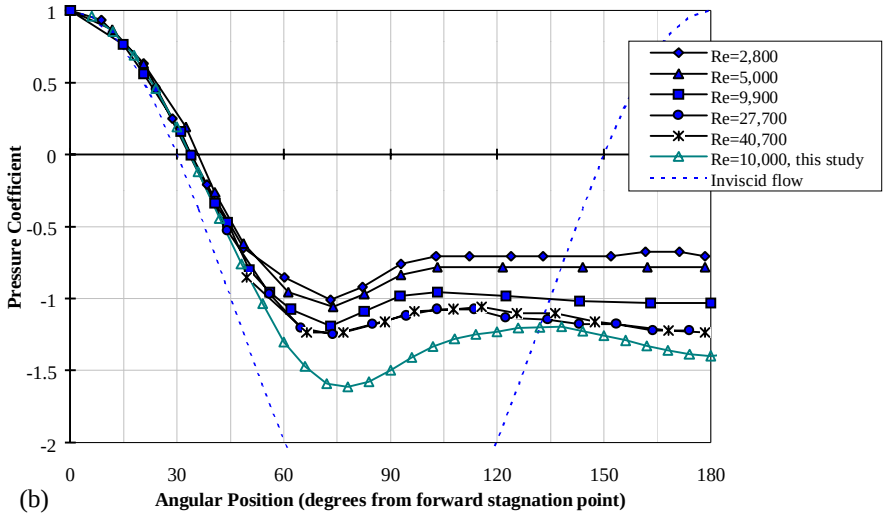

Figure 6.23. Variation with Reynolds number of the pressure distributions on a circular cylinder: (a) numerical results of this study, (b) experimental data measured by Linke [1931] as given by Goldstein [1938].

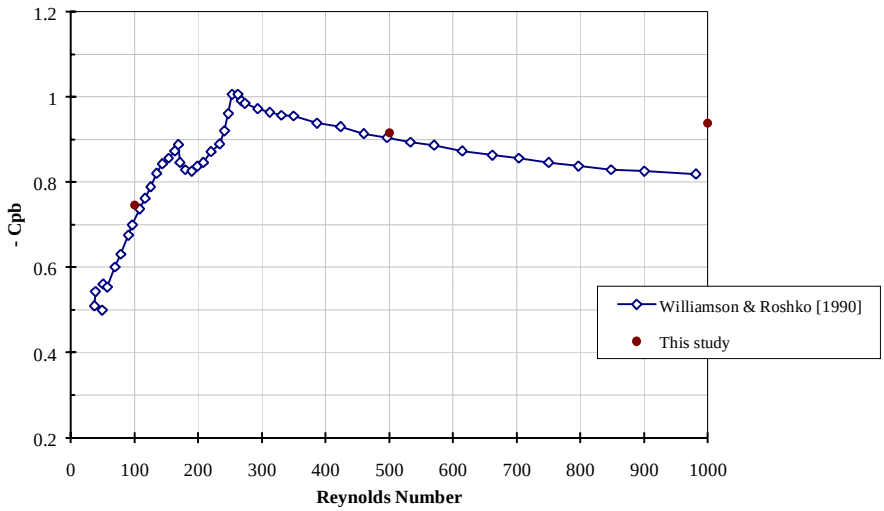

Figure 6.24. Variation of base pressure coefficient with Reynolds number for circular cylinder flow.

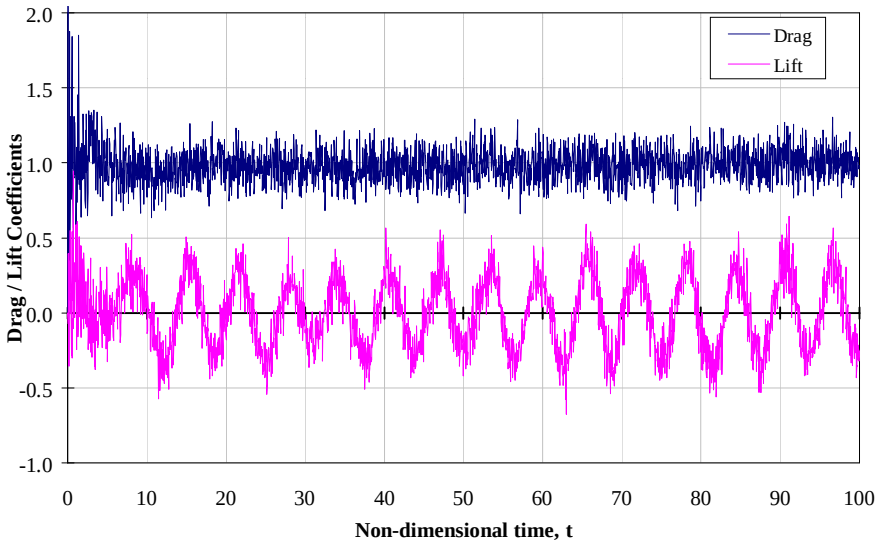

Figure 6.25. Calculated time-histories of drag and lift for cylinder flow at Re_d = 100.

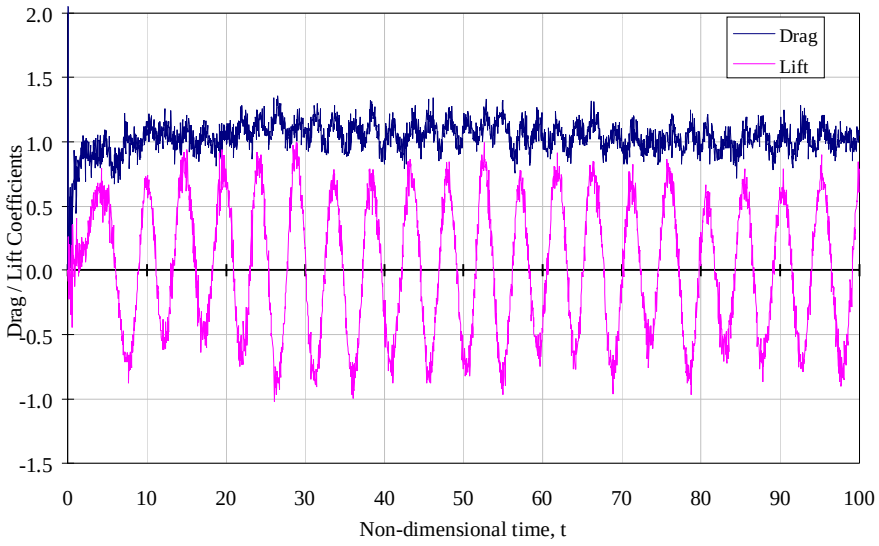

Figure 6.26. Calculated time-histories of drag and lift for cylinder flow at Re_d = 500.

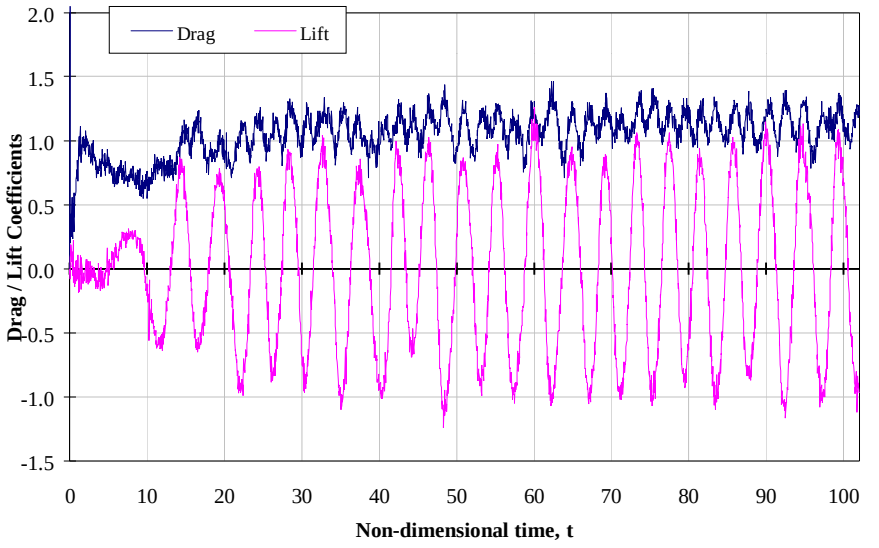

Figure 6.27. Calculated time-histories of drag and lift for cylinder flow at Re_d = 1,000.

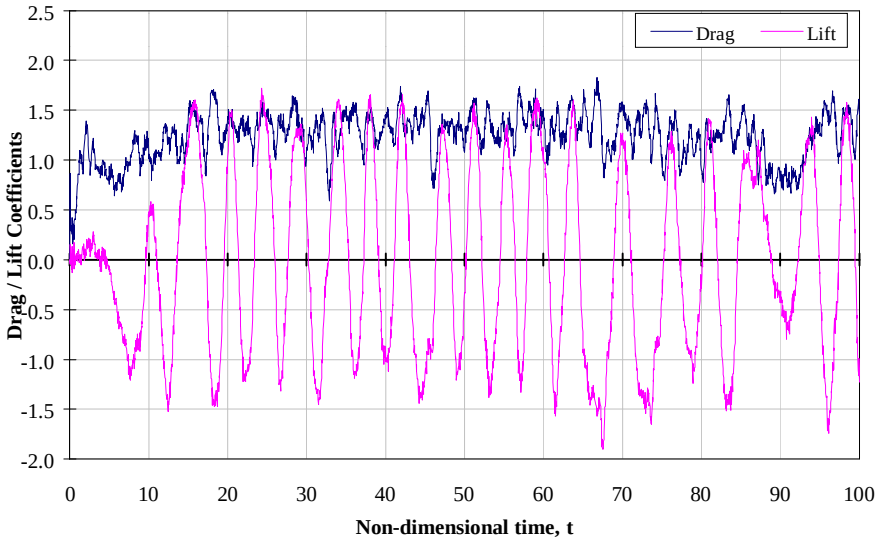

Figure 6.28. Calculated time-histories of drag and lift for cylinder flow at Re_d = 10,000.

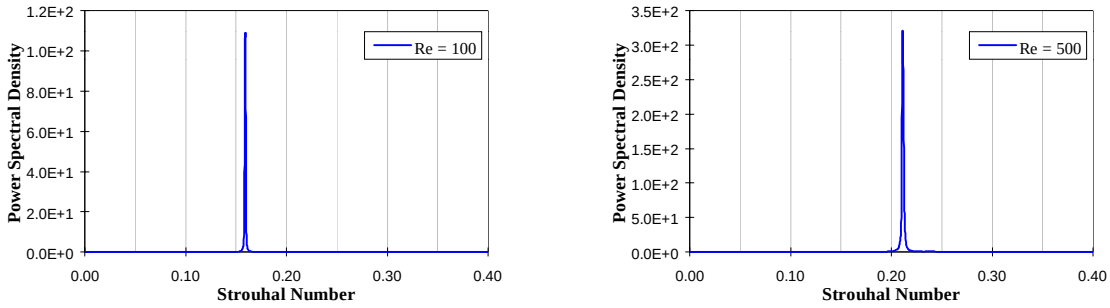

(a) Re_d = 100

(b) Re_d = 500

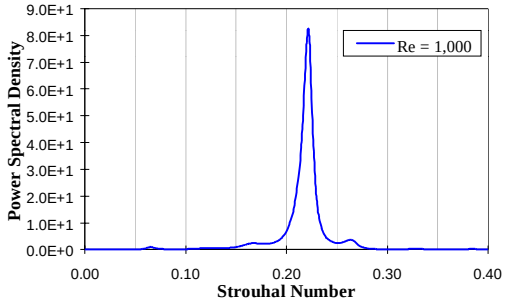

(c) Re_d = 1,000

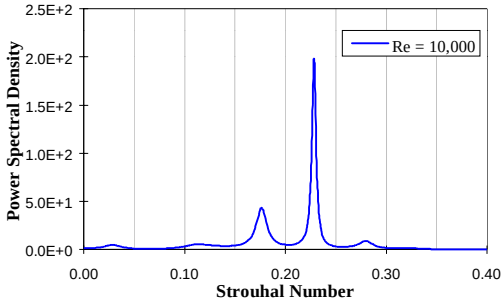

(d) Re_d = 10,000

Figure 6.29. Power spectra of fluctuating lift on a circular cylinder at Reynolds numbers: (a) Re_d = 100, (b) 500, (c) 1,000 and (d) 10,000.

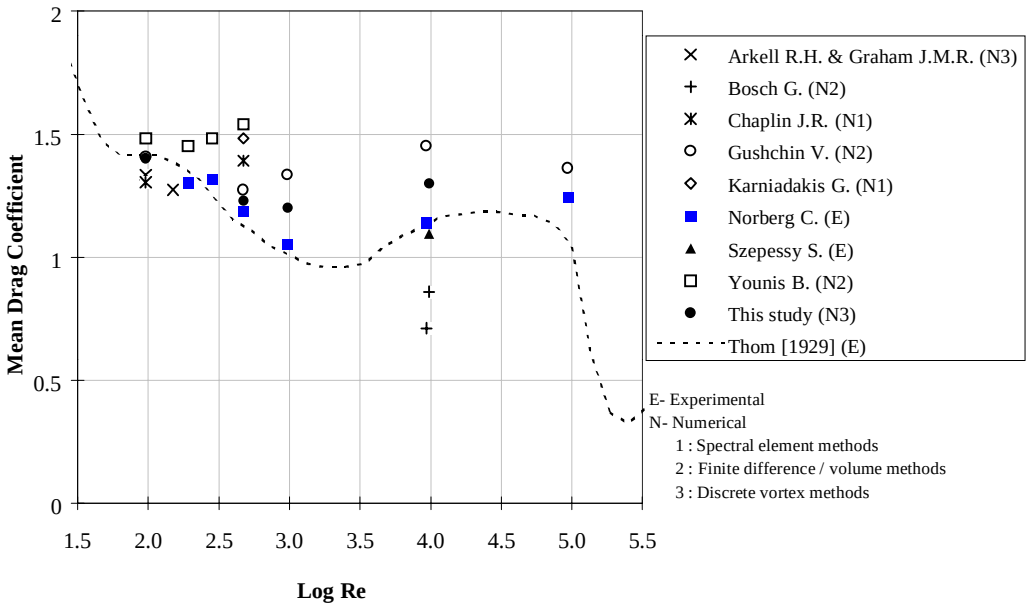

Figure 6.30. Variation of mean drag coefficient with Reynolds number for circular-cylinder flow.

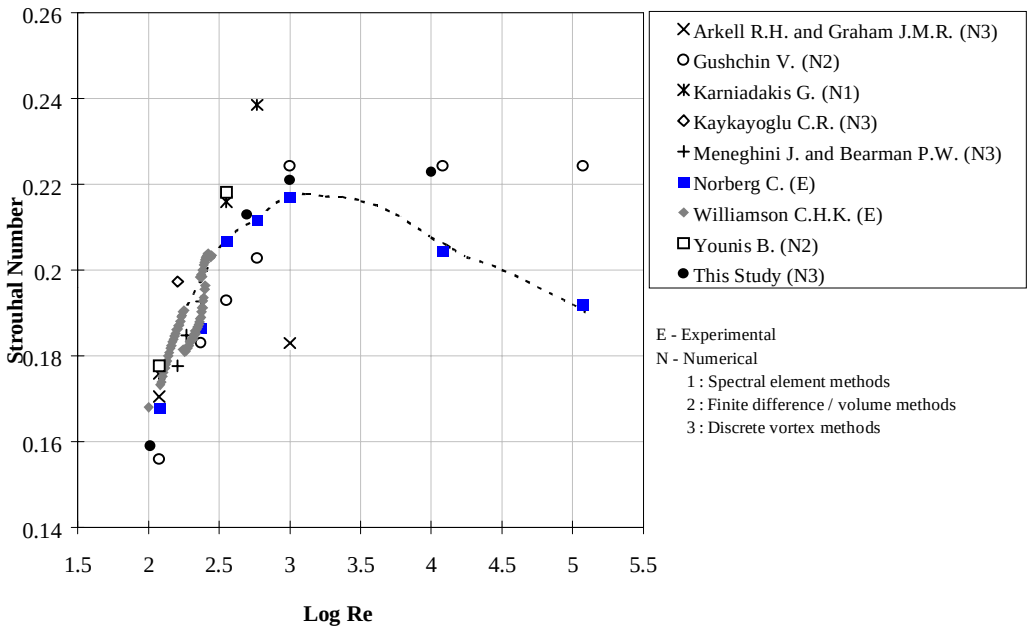

Figure 6.31. Variation of Strouhal number with Reynolds number for circular-cylinder flow.

Chapter 7

Flow Over Thick Plates with Sharp Corners

The calculations of flow over circular cylinders presented in chapter 6 provide evidence of the validity of the present numerical scheme for bodies of smooth cross-section. Before the method was applied to arrays of rectangular plates, evidence that its validity extends to bluff bodies with sharp edges was obtained by making calculations of flow over single plates of rectangular cross-section with various chord-to-thickness ratios. The results of these calculations are presented in this chapter.

7.1 Previous Investigations

The flow over thick plates of rectangular cross-section, or rectangular cylinders, has been investigated extensively by both experiment and numerical calculation. Of the experimental studies of the vortex-shedding characteristics of rectangular plates and the associated flow patterns, most – including those by Vickery [1966], Bearman and Trueman [1972], Lee [1975], Rockwell [1977], Hillier and Cherry [1981], Bearman and Obasaju [1982], Kiya and Sasaki [1983, 1985], Cherry, Hillier and Latour [1984], Nakamura and Nakashima [1986], Sasaki and Kiya [1991] – have been made at fairly high Reynolds numbers, in the range 5×10^3 to 2.5×10^5. Experiments at lower Reynolds numbers, in the range 40 to 5×10^3 include those of Lane and Loehrke [1980], Ota, Asano and Okawa [1981], Okajima [1982], Okajima, Mizota and Tanida [1983], Nakamura, Ohya and Tsuruta [1991], Sasaki and Kiya [1991], Norberg [1993] and Suzuki, Inoue, Nishimura, Fukutani and Suzuki [1993].

Numerical studies of two-dimensional flow over single rectangular plates have generally been confined to the low Reynolds number range of about 50 to 1000. Such studies have been carried out by Davis and Moore [1982], Stansby [1985], Franke, Rodi and Schönung [1990], Okajima [1990], Okajima, Nagahisa and Rokugoh [1990], Tamura and Kuwahara [1990],

Arnal, Goering and Humphrey [1991], Tafti and Vanka [1991], Kelkar and Patankar [1992], Okajima, Ueno and Sakai [1992], Ohya, Nakamura, Ozono, Tsuruta and Nakayama [1992], Ozono, Ohya, Nakamura and Nakayama [1992], Suzuki, Inoue, Nishimura, Fukutani and Suzuki [1993], Tamura, Itoh and Kuwahara [1993] and Sohankar, Davidson and Norberg [1995].

The flow regime established on a rectangular cylinder depends on whether flow separation occurs and, if it does occur, on the location of the separation point. In the flow over a sharp-edged body separation from the body surface will generally take place at the salient points of the body. In the case of a rectangular cylinder, this means either the leading corners or trailing corners of the section. When separation occurs at the leading corners of a long plate the separated shear layer reattaches to the side surfaces, so forming a closed leading-edge separation bubble, while for a short plate reattachment may or may not occur. The two dominant parameters determining which of these various processes occur, and thereby the flow regime, are the Reynolds number, $Re_h \equiv U_\infty h/\upsilon$, and the chord-to-thickness ratio, $C \equiv c/h$, where c is the chord length, h the plate thickness, υ the kinematic viscosity of the fluid and U_∞ the main stream velocity.

The effects of Reynolds number on the leading-edge flow and leading-edge separation bubble on very long rectangular plates have been studied, by flow visualisation, by Lane and Loehrke [1980], Ota, Asano and Okawa [1981], and Sasaki and Kiya [1991]. The flow was found to remain laminar and attached to the leading edge of the plate for Re_h less than about 100 (Lane and Loehrke, 100; Sasaki and Kiya, 80). When the Reynolds number is increased beyond this value a leading-edge separation bubble is formed, with the shear layer laminar at both separation and reattachment. The length of the bubble x_R increases rapidly with Re_h, reaching a maximum value of $x_R = 6.5h–7h$ at $Re_h \approx 300$ (Lane and Loehrke, 325; Ota *et al*., 270; Sasaki and Kiya, 320). At this value of Re_h, unstable oscillations start to occur in the separated shear layer. Further increase of Reynolds number results in transition from laminar to turbulent flow within the separated shear layer, in the onset of rolling-up of the shear layer to form discrete vortices, and in reduction of the bubble length to an asymptotic value of about $x_R \approx 4h$. As Re_h is increased beyond about 400 and towards 1000, flow structure in the reattachment region and downstream becomes increasingly three-dimensional (Lane and Loehrke [1980]; Kiya and Sasaki [1983]; Sasaki and Kiya [1991]; Soria *et al*. [1993]) – and consequently results of two-dimensional calculations for such flows must be treated with some caution. Ota *et al*. associate the Reynolds number at which the separation bubble has its minimum length with the

Reynolds number at which the separated shear layer becomes turbulent immediately before or immediately after separation. This gives $Re_h \approx 1{,}500$ as characterising the onset of turbulent separation and turbulent reattachment.

At very low Reynolds number, in accord with the observations of Lane and Loehrke, Ota *et al*., and Sasaki and Kiya, the flow regimes established on rectangular plates at all values of C are similar, so long as the Reynolds number does not exceed a value at which the leading-edge separation bubble formed on the side surfaces by laminar separation and laminar reattachment no longer persists. Thus, for Re_h typically less than about 50, the flow around the plate can be expected to be viscous and without separation (as in the numerical results of Kelkar and Patankar [1992]). At somewhat higher Reynolds numbers, $50 < Re_h < 100$, the flow remains attached to the leading edges and side faces of the plate, but separates at the trailing corners giving rise to trailing-edge vortex shedding and the formation of a Karman street downstream of the plate (Franke, Rodi and Schönung [1990]). When the Reynolds number exceeds about 100 and a leading-edge separation bubble with laminar reattachment is formed, the reattached flow on the side faces again separates at the trailing corners with trailing-edge vortex shedding.

For short plates, those with chord length less than the maximum length of the leading-edge separation bubble on a very long plate, i.e. those with $C \lesssim 7$, at higher Reynolds numbers, the long-plate flow regimes are modified. As C is decreased below this value, instead of permanent reattachment of the separated shear layer, the reattachment may become intermittent. Continued reduction of C eventually leads to flows in which reattachment no longer occurs, and vortices are formed downstream of the plate by direct interaction of the shear layers separating from the two leading corners of the plate.

The experimental results of Lane and Loehrke [1980] for plates with $C = 2$ and 4, Okajima [1982] for plates with $C = 1$–4, and Okajima, Mizota and Tanida [1983] for plates with $C = 1.5$–3, indicate laminar separation from the leading corners and laminar reattachment over a range of Reynolds numbers from 100 to 250–400, laminar separation with intermittent laminar reattachment for Re_h up to 500–800, and separated flow without reattachment as Re_h is further increased. For Reynolds numbers in the range of about 5×10^3 to 5×10^4, the experiments of Okajima, Mizota and Tanida [1983] and Parker and Welsh [1983] identify turbulent separation without reattachment for $C \lesssim 3$, and turbulent separation with intermittent (turbulent) reattachment for roughly $3 \lesssim C \lesssim 7$. The flow on long plates, those with $C \gtrsim 7$, for $Re_h \gtrsim 300$, is characterised by a permanent, but not steady, leading-edge separation bubble formed by

laminar separation and turbulent reattachment at moderate Reynolds numbers and by turbulent separation and turbulent reattachment at high Reynolds numbers (Okajima *et al.*, 1983; Parker and Welsh, 1983).

The flow regimes corresponding to the experimental data cited above can be generally associated with regions of the C–Re_h plane, as shown in Fig. 7.1, although, because of the effects of experimental variations and the effects of additional parameters such as free-stream turbulence levels which are not represented, the boundaries of the various regions cannot be regarded as rigidly defined.

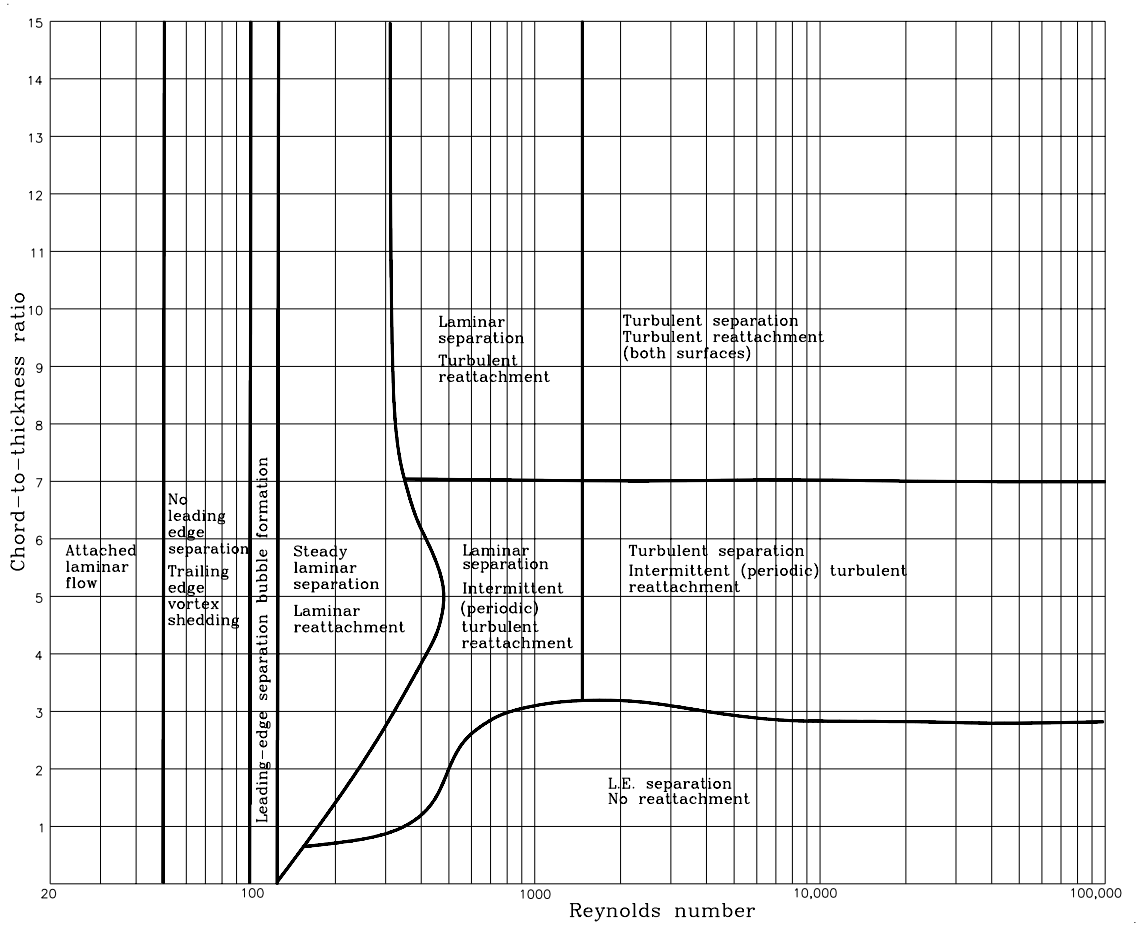

Figure 7.1. Flow regimes for a rectangular plate.

Fig. 7.1 clearly indicates that variation of Reynolds number of the flow over a given plate, from very low to very high values, will generally lead to several changes in flow regime, the sequence of changes depending very much on the chord-to-thickness ratio. In some cases these flow changes bring about dramatic changes in flow parameters. For short plates with chord-to-thickness ratio in the range $1.5 \leq C \leq 3$, the measurements of Okajima [1982] and Okajima*et al.* [1983] show that the change from flow with laminar separation at the leading corners and

intermittent turbulent reattachment to flow with leading-corner separations and no reattachment is accompanied by a dramatic discontinuity in the variation of the Strouhal number of vortex shedding with Reynolds number. Plates with $C = 3$ fall close to boundaries in the C–Re_h plane over a wide range of Re_h, and are subject to more flow regime changes than plates with slightly smaller or larger C values. Thus Okajima [1982], Okajima *et al*. [1983] and Norberg [1993] all find multiple vortex-shedding frequencies and several discontinuities in the variation of Strouhal number with Reynolds number for $Re_h \gtrsim 10^3$.

The large top right hand region of Fig. 7.1, corresponding roughly to $C \gtrsim 3$ and $Re_h \gtrsim 300$ – 400, represents flow regimes characterised by the so-called impinging-shear-layer instability, which occurs for turbulent reattachment of the separated leading-edge shear layers (whether separation is laminar or turbulent) and for both intermittent ($3 \leq C \leq 7$) and permanent reattachment ($C > 7$).

As pointed out by Nakamura and Nakashima [1986], when the separated shear layers on the upper and lower sides of an elongated rectangular plate impinge on the plate at reattachment, they can become unstable in the presence of the sharp trailing edges of the plate. As a result of this instability the shear layers roll up to form discrete vortices, which then impinge on the trailing edges of the plate. Vortices from the upper and lower sides of the plate interact with each other downstream of the plate, adjusting phase, to form a Karman street with the same frequency. Nakamura, Ohya and Tsuruta [1991], in experiments on vortex shedding from rectangular plates with $C = 3$–16 for $Re_h = (1–3)\times10^3$, concluded that the vortex-shedding from the plate is governed by the impinging-shear-layer instability. The shedding frequency generally decreases with increase of C, but at particular values of C jumps to a higher value; at these particular C values two characteristic frequencies appear intermittently. The Strouhal number St_c ($= f\,c/U_\infty$, based on plate chord c) is approximately constant at $St_c = 0.6$ for $C = 3$ to 5, and increases stepwise with further increase in C to values which are roughly integral multiples of 0.6. Parker and Welsh's [1983] investigations at higher Reynolds numbers, $(1.5–4)\times10^6$, indicate that for $C > 16$ the impinging-shear-layer instability no longer occurs, the flow then taking the form of a leading-edge separation bubble followed by trailing-edge vortex shedding.

The results of numerical studies of flow around rectangular plates with C = 3 to 9 at Re_h = 1,000 by Ozono, Ohya, Nakamura and Nakayama [1992] are in accord with the experimental data and provide additional detail of the flow associated with the impinging-shear-layer instability. They show St_c increasing stepwise with C and in accord with the number of vortices formed on a streamwise face. For C = 3, 6 and 9, the predicted flow patterns indicate that the shear layer separates at the leading edge of the plate and reattaches on the streamwise face, forming a separation bubble which oscillates in length at the same frequency as that of the vortex shedding which subsequently occurs at the trailing edge of the plate. The separation bubble grows until the bounding shear layer, half way along the bubble, deflects towards the plate surface and reattaches; the bubble is thus split in two. The upstream part then starts to grow again while the downstream part is convected dowstream as a discrete vortex (referred to as the 'L-vortex' by Ozono *et al*. 1992). The number of vortices on a streamwise face and their spacing are related to the plate chord. Before the L-vortex reaches the trailing edge, the reattached shear layer separates at the trailing edge to form a new vortex (the 'T-vortex') on the vertical trailing face of the plate. The L- and T-vortices interact with each other and are shed as a pair into the wake. The interaction between the L- and T-vortices occurs alternately at the upper and lower trailing edge corners, producing a regular Karman street behind the plate and a regular variation of lift coefficient. For C = 4, 5, 7 and 8 (in contrast to 3, 6 and 9), the calculations show irregular vortex shedding from the trailing edge and corresponding irregular fluctuations in lift coefficient, even though there are still dominant frequencies appearing in the power spectra. L- and T-vortices are shed separately from the trailing edge; irregularities in the flow field are apparently attributable to the phasing of shedding of the L- and T-vortices at the upper and lower trailing edge corners.

Calculated St_c values are in good agreement with the experimental results of Nakamura *et al*. [1991], the stepwise increase of Strouhal number with increasing C supporting the conclusion that the impinging-shear-layer instability governs the vortex shedding. Ozono *et al*. [1992] regard the flow for plates with C = 3, 6 and 9, which exhibit regular vortex shedding, as basic; the flow regimes on plates with intermediate values of C, for which irregularities appear, are regarded as departure from the basic flows resulting from break down of the regular interaction between L- and T- vortices. The calculated results also show that a particular plate may exhibit St_c values belonging to two groups, as detected in the experimental work.

In the present work, calculations of flow over single rectangular plates with chord-to-thickness ratios C = 1, C = 2 and C = 4 have been made for the Reynolds number range $100 \leq Re_h \leq$ 1,000. These values of C correspond to three different representative sequences of variation of flow regime with Reynolds number over the chosen Reynolds number range. Plates with C = 1, square cylinders, have been extensively investigated exper imentally and numerically. In this case, Fig. 7.1 indicates that there will be a change from flow with a laminar leading-edge separation bubble and trailing-edge vortex shedding to flow with laminar leading-edge separation and intermittent reattachment, and finally to flow fully-separated from the leading edges, as the Reynolds number is progressively increased. However, experimental results such as those of Okajima [1982] for Strouhal number and Okajima and Sugitani [1990] for base pressure, indicate a continuous variation of flow parameters with Reynolds number, despite the changes in flow regime. The sequence of changes in flow regime indicated for plates with C = 2 is similar to that for square cylinders, but with discontinuity in flow parameter variation, such as the discontinuity in Strouhal-number variation referred to earlier in this section. The flow on a plate with C = 4 can be expected to change from the laminar-separation-bubble/ trailing-edge-vortex-shedding regime to a regime of laminar leading-edge separation with periodic turbulent reattachment, subject to impinging-shear-layer instability.

The calculations yield vorticity fields, streamline pa tterns, pressure fields, Strouhal numbers and force coefficients. The predicted flow patterns and associated flow parameters are presented in the following sections and compared with existing experimental results and the results of calculations by others using similar or different procedures.

7.2 Calculation Parameters in the Present Work

For all rectangular cylinders for which results are presented, C = 1, 2, and 4, flow calculations have been performed for Reynolds numbers Re_h = 100, 250, 500 and 1,000. The boundaries of the cylinder are represented by uniform straight segments of length $h/20$ (or Δs = 0.05, in non-dimensional terms); thus the numbers of segments used in the calculations are M = 80, 120 and 200 for the C = 1, 2 and 4 cylinders respectively. In all cases, the flow is started impulsively from rest at t = 0 and the time-histories of its development calculated using non-dimensional time steps of Δt = 0.02.

In relation to these parameter choices there are two additional points which might be noted: first, that several time steps are required for discrete vortices to be convected past a body segment; and, second, that when the convection velocity of a discrete vortex closer than one segment length to the body surface is to be calculated, nearby body segments are subdivided and the contributions of the surface vorticity on all sub-segments individually calculated. Subsidiary calculations indicate that this procedure gives a satisfactory representation of the near-body velocity field, even at sharp corners.

Diffusion into the flow of vorticity generated at the body surface is modelled by the offset method. In the majority of the results presented the non-dimensional offset distance is $\epsilon = \sqrt{(4\Delta t/3Re_h)} = 1.15\sqrt{(\Delta t/Re_h)}$. Some exploration of the effect of varying ϵ has been made. It has been found that the calculated results are insensitive to the value used for $C = 1$ and 4 at all Reynolds numbers investigated. However, for the $C = 2$ flows which undergo abrupt changes in flow regime at particular Reynolds numbers, there is some sensitivity to the value used. In these cases, better agreement with existing data is obtained for a somewhat greater value of ϵ. Hence, the results presented are for $\epsilon = 1.7\sqrt{(\Delta t/Re_h)}$ for $C = 2$ at $Re_h = 250$, 500 and 1,000, while in all other cases the results are based on $\epsilon = 1.15\sqrt{(\Delta t/Re_h)}$.

Calculations of instantaneous pressure fields are carried out by using Eq. (3.95); for this purpose the transport velocities of elemental vortices are calculated from their total displacements (convective plus diffusive) over a timestep of $\Delta t = 0.02$, beginning at the time instant being considered.

7.3 Flow over a Single Square Cylinder, $C = 1$

7.3.1 Flow Development on a Square Cylinder

In these calculations, the boundary of the square cylinder is represented by $M = 80$ uniform straight segments, 20 on each side of the square. The value of ϵ is $\sqrt{(4\Delta t/3Re_h)}$.

The predicted flow development from rest, represented in terms of discrete-vortex distributions, is presented for Reynolds numbers Re_h = 100, 250, 500 and 1,000 in Figs. 7.2 to 7.5. The corresponding streamline patterns are shown in Figs. 7.6 to 7.9, and vorticity contours in Figs. 7.10 to 7.13.

Consider first the flow development at $Re_h = 100$. It is evident from Figs. 7.2(a), 7.6(a) and 7.10(a) that the initial flow pattern exhibits symmetry about the centre-line of the cylinder, as a result of geometrical symmetry of the cylinder shape, and that very soon after the beginning of flow development flow separation occurs at the leading-edge corners. The shear layers separating from the leading-edges coalese downstream of the body to form a closed recirculation region, the dominant feature of which is two standing counter-rotating wake vortices (twin-vortex structure) immediately behind the cylinder. As the flow further develops, the recirculation region elongates in the streamwise direction and eventually becomes unstable. The instability leads to vortex shedding. Fig. 7.6(b) shows the departure of the upper wake vortex. The lower wake vortex then grows and is eventually shed into the wake, Fig. 7.6(c), while at the same time a new vortex is forming at the upper trailing-edge corner. A state of periodic vortex shedding is thus established in which vortices with positive and negative vorticity are shed alternately from the upper and lower surfaces of the cylinder. The combination of shed vortices with the main stream leads to a sinuous wake behind the cylinder, as shown in Figs. 7.6(d) to 7.6(f).

The calculations indicate that the initial flow development at Re_h = 250, 500 and 1,000 is broadly similar to that at $Re_h = 100$: in each case, a closed recirculation region, comprising two counter-rotating vortices is formed, although, with an increase in Reynolds number, the wake vortices are formed closer to the cylinder and become more compact. More significant differences appear in the subsequent flow development. The computed flow patterns for Re_h = 500 and 1,000 show that, at an early stage of flow development, reattachment of the leading-

edge shear layers to the side surfaces of the cylinder is accompanied by the formation of rolled-up, discrete, vortices on the side surfaces. This process becomes more pronounced as the Reynolds number increases. It can be clearly seen in the streamline patterns of Fig. 7.9 and the isovorticity contours of Fig. 7.13 for the flow at Re_h = 1,000, and is characteristic of flow at high Reynolds number. These vortices are convected along the side surfaces and shed into the wake. They are shed together with the vortices formed on the trailing face of the cylinder without the two merging (see again the vorticity contours of Fig. 7.13). This leads to the vortex street behind the cylinder becoming less regular as the Reynolds number is increased, as is evident in the elemental-vortex patterns for fully-developed flow shown later in Fig. 7.15. The process of formation of discrete vortices on the side surfaces in fully-developed flow over the cylinder will be taken up again in the next section.

(a) Re_h = 100, C = 1, t = 2

(b) Re_h = 100, C = 1, t = 4

(c) Re_h = 100, C = 1, t = 8

(d) Re_h = 100, C = 1, t = 12

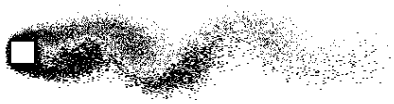

(e) Re_h = 100, C = 1, t = 16

(f) Re_h = 100, C = 1, t = 20

Figure 7.2. Elemental-vortex distributions in flow over a square cylinder at Re_h=100.

(a) Re_h = 250, C = 1, t = 2

(b) Re_h = 250, C = 1, t = 4

(c) Re_h = 250, C = 1, t = 8

(d) Re_h = 250, C = 1, t = 12

(e) Re_h = 250, C = 1, t = 16

(f) Re_h = 250, C = 1, t = 20

Figure 7.3. Elemental-vortex distributions in flow over a square cylinder at Re_h= 250.

(a) Re_h = 500, C = 1, t = 3

(b) Re_h = 500, C = 1, t = 6

(c) Re_h = 500, C = 1, t = 9

(d) Re_h = 500, C = 1, t = 12

(e) Re_h = 500, C = 1, t = 15

(f) Re_h = 500, C = 1, t = 18

Figure 7.4. Elemental-vortex distributions in flow over a square cylinder at Re_h=500.

(a) Re_h = 1,000, C = 1, t = 3

(b) Re_h = 1,000, C = 1, t = 6

(c) Re_h = 1,000, C = 1, t = 9

(d) Re_h = 1,000, C = 1, t = 12

(e) Re_h = 1,000, C = 1, t = 15

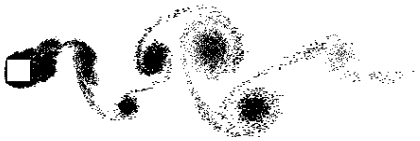

(f) Re_h = 1,000, C = 1, t = 18

Figure 7.5. Elemental-vortex distributions in flow over a square cylinder at Re_h = 1,000.

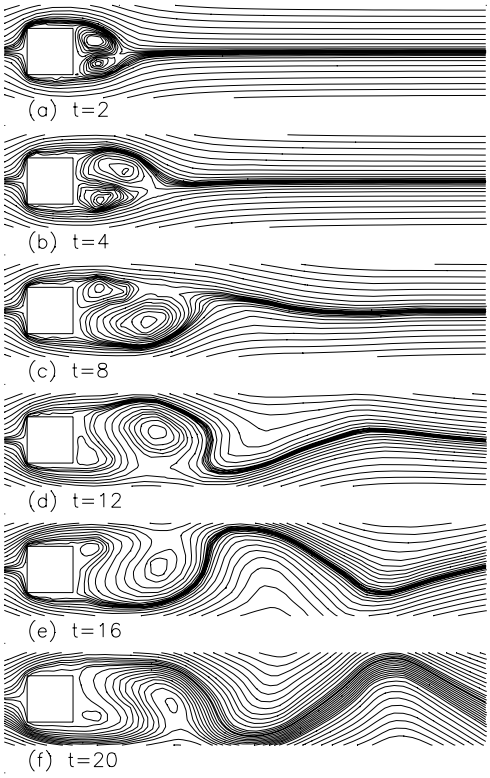

Figure 7.6. Streamline patterns in flow over a square cylinder at Re_h = 100.

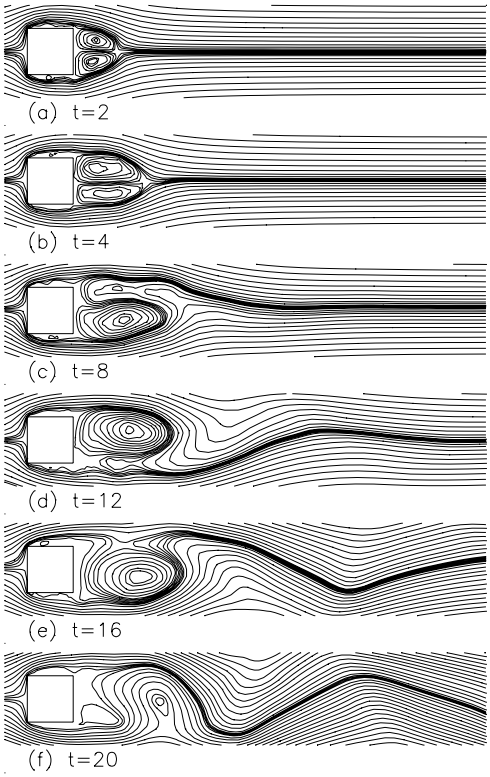

Figure 7.7. Streamline patterns in flow over a square cylinder at Re_h = 250.

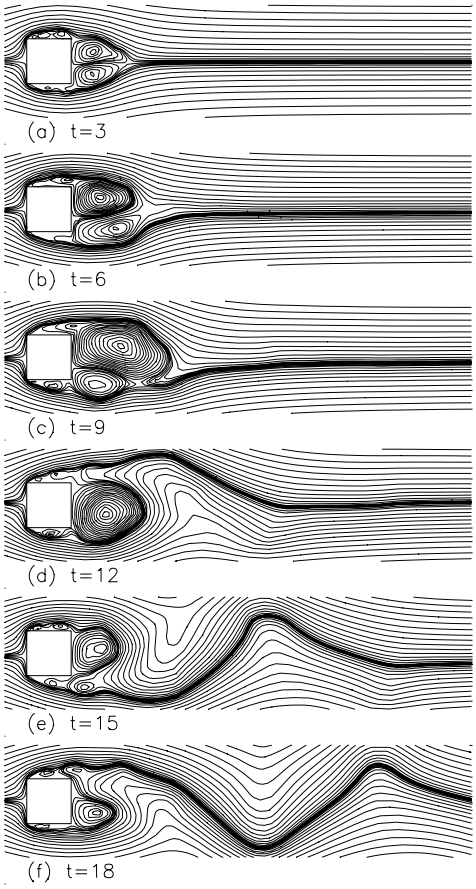

Figure 7.8. Streamline patterns in flow over a square cylinder at Re_h = 500.

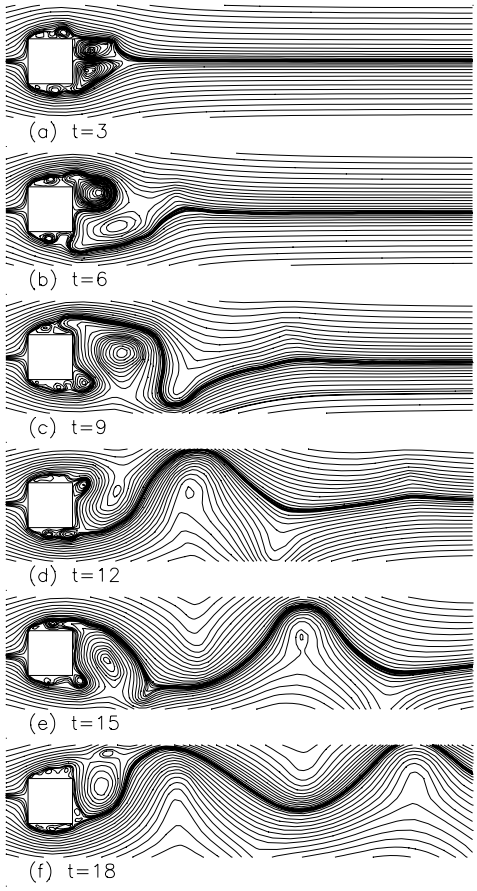

Figure 7.9. Streamline patterns in flow over a square cylinder at Re_h = 1,000.

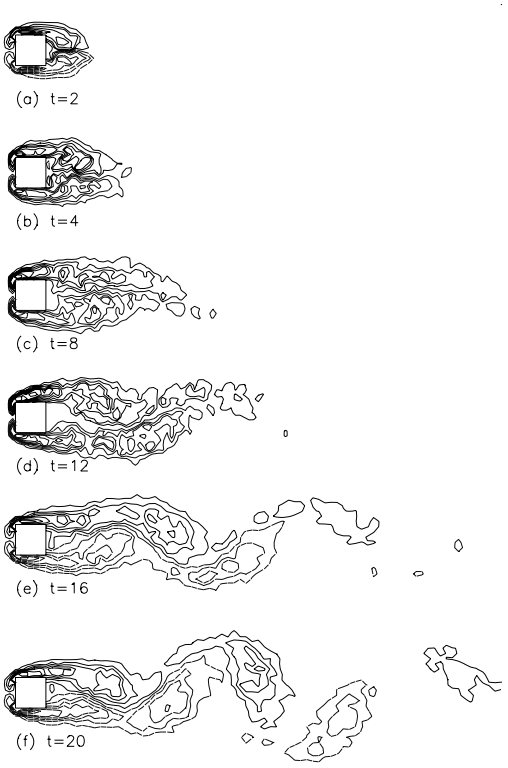

Figure 7.10. Vorticity contours in flow over a square cylinder at Re_h = 100.

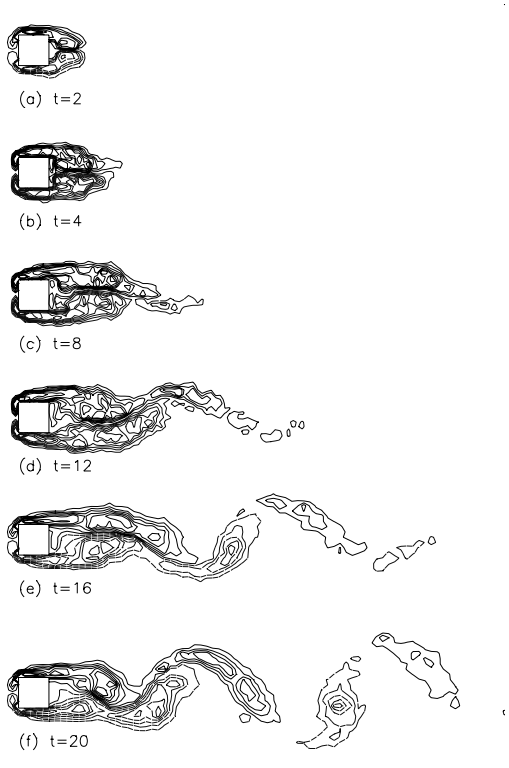

Figure 7.11. Vorticity contours in flow over a square cylinder at Re_h = 250.

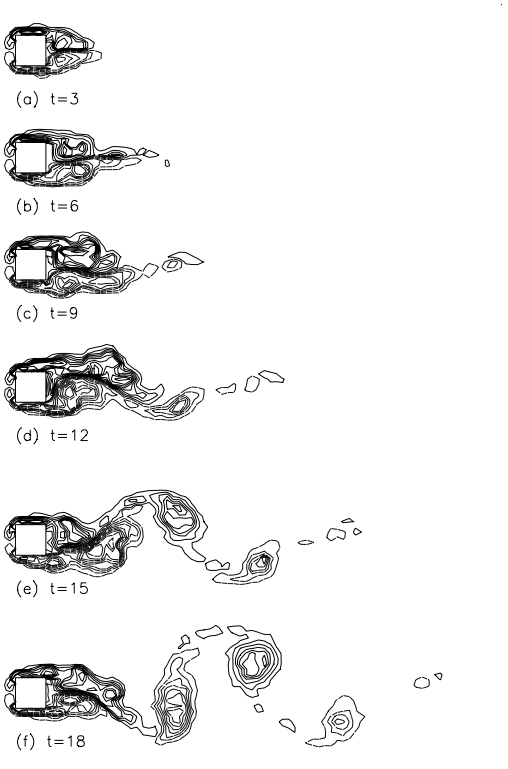

Figure 7.12. Vorticity contours in flow over a square cylinder at Re_h = 500.

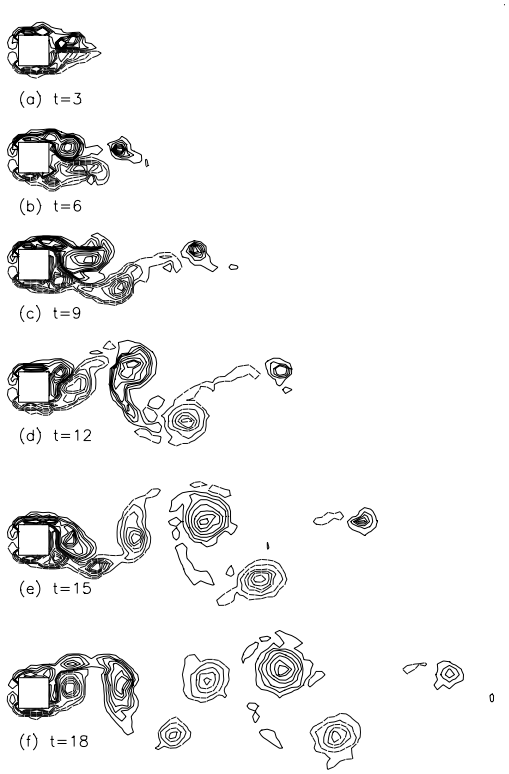

Figure 7.13. Vorticity contours in flow over a square cylinder at Re_h = 1,000.

7.3.2 Fully-Developed Flow Over a Square Cylinder

7.3.2.1 Comparisons of Calculated Flow Patterns with Existing Data

In this section, calculated flow patterns for fully-develop ed flow over a square cylinder obtained in the present work are compared with a range of existing experimental and computed results. Davis and Moore [1982] present calculated results for streaklines of the flow around a square cylinder at Re_h = 250 and 1,000. They also show that the particle concentrations characterising streaklines correspond to the vortex structures in the flow as determined by isovorticity contours. Thus it is valid to compare the streakline patterns calculated by Davis and Moore with the patterns of elemental discrete vortices obtained in the present work. Comparison of present fully-developed elemental-vortex and vorticity patterns for Re_h = 250 at t = 55.7 and Re_h = 1,000 at t = 92.4 with streakline patterns of Davis and Moore (their Figures 8a and b) is made in Fig. 7.14. A more general comparison of wake structure for Re_h = 1,000 (at t = 94.4 in the present work) is made (with Figure 21 of Davis and Moore) in Fig. 7.15. These show that there is a very good correspondence between the two sets of computed flow patterns.

Experimental and calculated streamline patterns for C = 1 at Re_h = 250 are given by Okajima [1982] and reproduced in Fig. 7.16. The figure also shows calculated patterns from the present work (t = 44 and 46). There are obviously close similarities of all three patterns at each of the two stages in the flow.

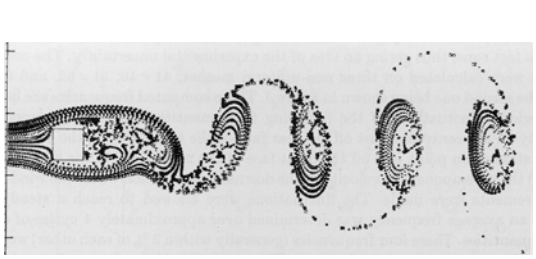

(a) Streaklines for Re_h = 250

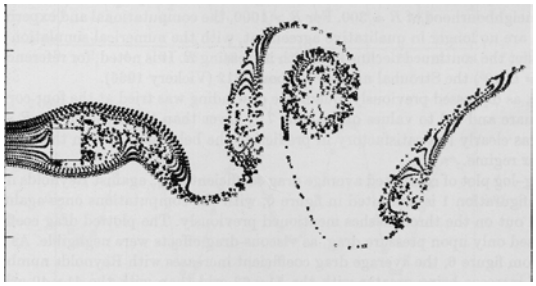

(c) Streaklines for Re_h = 1,000

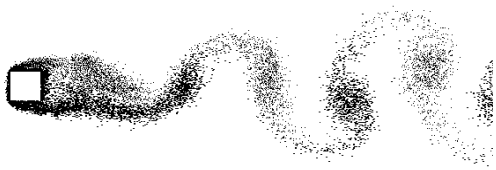

(b) Elemental-vortex patterns for Re_h = 250, t = 55.7

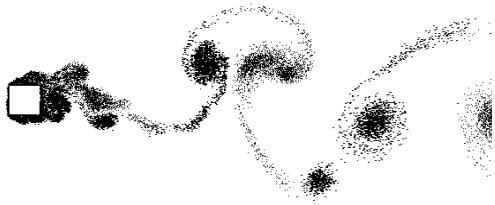

(d) Elemental-vortex patterns for Re_h =1,000, t = 92.4

Figure 7.14. Fully-developed flow patterns at Re_h = 250 and 1,000. Streakline patterns reproduced from Davis and Moore [1982]; elemental-vortex distributions obtained in present study.

(a) Streaklines for Re_h = 1,000

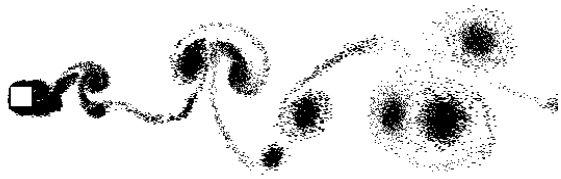

(b) Elemental-vortex patterns for Re_h = 1,000, t = 94.4

Figure 7.15. Wake structure behind a square cylinder at Re_h = 1,000: (a) calculated streakline patterns reproduced from Davis and Moore [1982], (b) distribution of elemental-vortices obtained in this study.

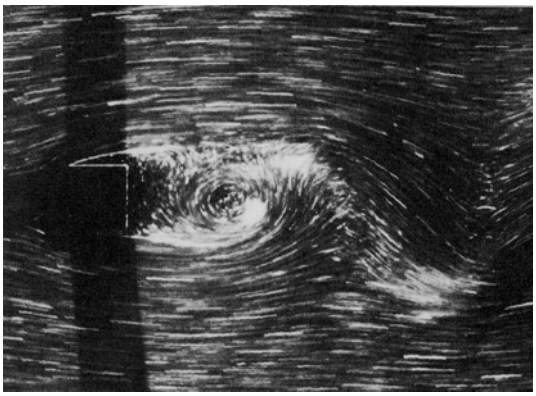

(a) Re_h = 250, C = 1

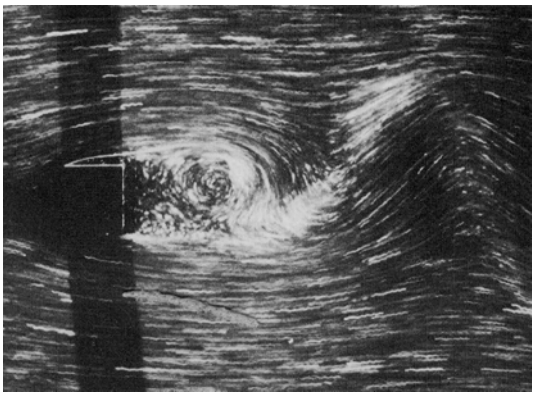

(d) Re_h = 250, C = 1

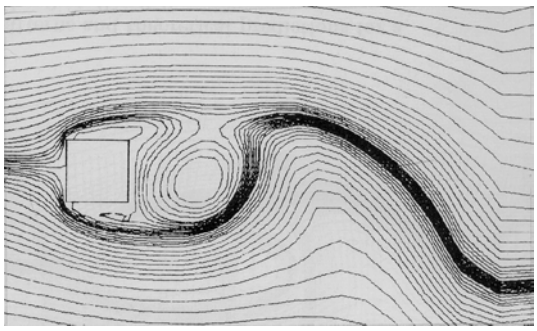

(b) Re_h = 250, C = 1

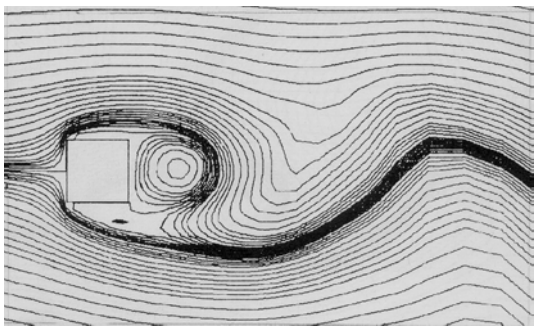

(e) Re_h = 250, C = 1

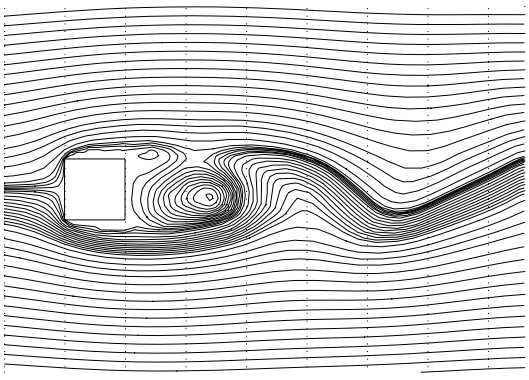

(c) Re_h = 250, C = 1, t = 44

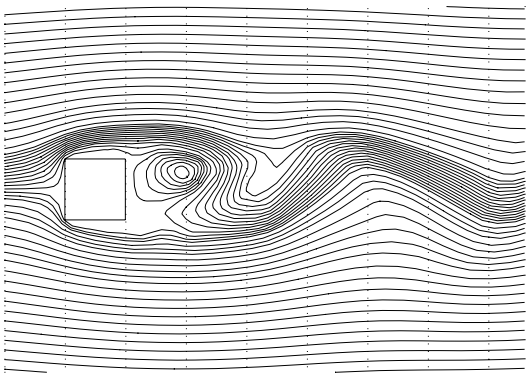

(f) Re_h = 250, C = 1, t = 46

Figure 7.16. Comparison between visualised flow patterns and numerical calculation for square cylinder flow at Re_h = 250: (a) and (d) flow visualisation of Okajima [1982], (b) and (e) calculated streamline patterns of Okajima [1982], (c) and (f) calculated streamline patterns of this study.

Okajima [1990] gives calculated flow patterns for $C = 1$ at $Re_h = 500$. These are compared with present results (for $t = 70.6$ and 74.1) in Fig. 7.17. Again there is close agreement between the calculated patterns. Streamlines and isovorticity contours obtained in the present work for $Re_h = 1{,}000$ (at $t = 95.4$) also compare well with the computations of Okajima, Ueno and Sakai [1992], as shown by Fig 7.18.

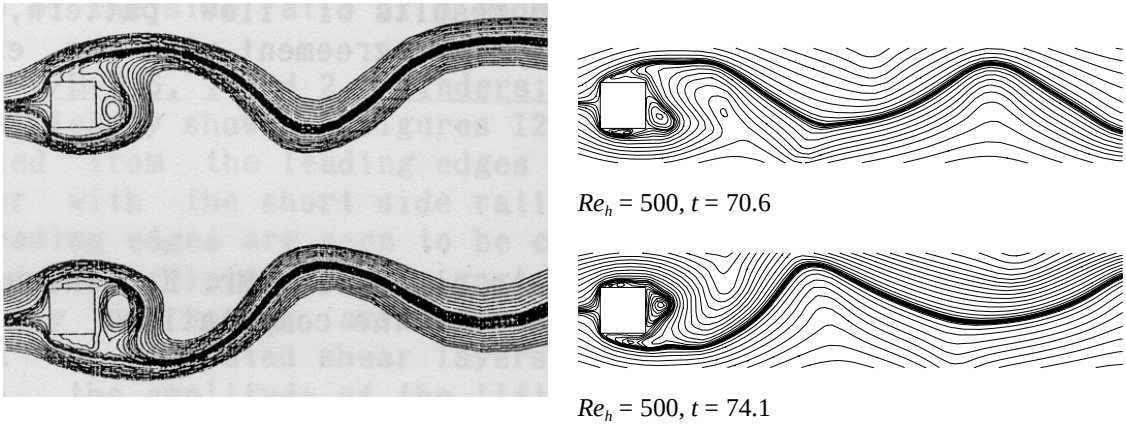

Figure 7.17. Streamline patterns of fully-developed flow over a square cylinder at $Re_h = 500$: (a) calculated results of Okajima [1990], (b) this study.

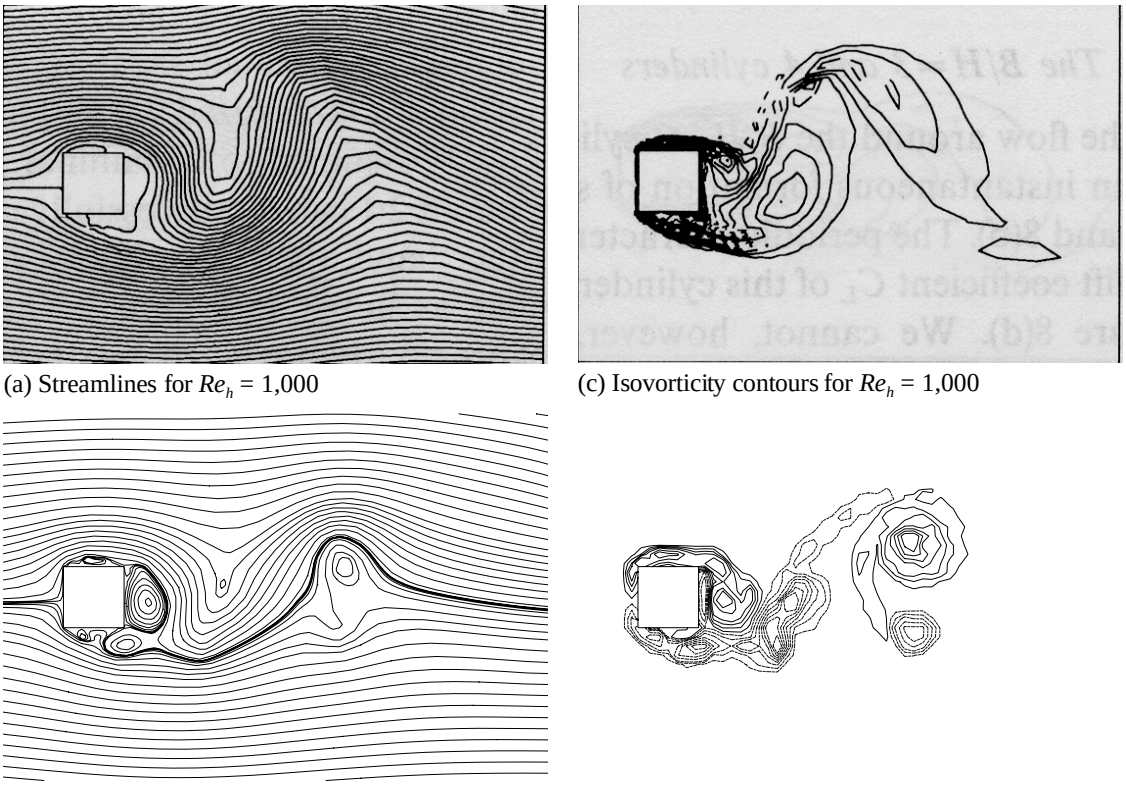

Figure 7.18. Streamlines and isovorticity contours for flow over a square cylinder at $Re_h = 1{,}000$: (a) and (c) calculated results of Okajima, Ueno and Sakai [1992], (b) and (d) calculated results of this study.

7.3.2.2 Mechanisms of Vortex Formation and Shedding

The flow patterns produced by the present method are shown by the broad comparisons made in the preceding section to be in good agreement with existing data. However, when the patterns are examined more closely, they can also provide greater detail of the mechanisms of vortex formation than is evident in these comparisons.

Calculated elemental vortex patterns for $Re_h = 100$, over several vortex-shedding cycles, are shown in Fig. 7.19, and the corresponding streamline patterns and isovorticity contours in Figs. 7.20 and 7.21. More detailed streamline patterns, high lighting the flow on the side surfaces and in the near-body wake of the cylinder over one vortex-shedding cycle, together with the corresponding instantaneous pressure fields shown in Fig. 7.22. The corresponding results for Re_h = 250, 500 and 1,000 are presented in Figs. 7.23–7.26, Figs. 7.27–7.30, and Figs. 7.31–7.34 respectively.

The computed flow patterns (Figs. 7.19–7.22) indicate that at $Re_h = 100$ the predominant process of vortex formation downstream of the cylinder is the rolling up of the shear layers separating from the trailing corners of the cylinder. However, they also indicate that this is accompanied by a process of weak vortex formation and convection on the side (streamwise) surfaces of the cylinder. In this latter process, flow separation occurs at the leading corners of the cylinder at all times, followed by reattachment of the separated shear layer to the side surfaces, with the formation of leading-edge-separation bubbles. Weak vortices are formed in the separation bubble. The bubble grows, divides and then contracts. When the bubble divides, a discrete vortex, detached from the bubble, is formed on the side surface; this vortex is convected along the side surface, past the trailing corner. The frequency of formation of these discrete vortices appears to be higher than the frequency of formation of wake vortices, but there is some suggestion of synchronism – the onset of the formation of a large trailing-edge vortex generally appears to coincide with the passage of one of these vortices over the trailing corner. At other times, the convected side-surface vortex appears to merge with the vortex already forming on the rear face of the cylinder, before the latter is shed into the wake. The sequence of events, as it occurs on the lower surface, from time $t = 93$ onwards, can be seen in the streamline patterns of Figs. 7.20 and the isovorticity contours of Fig. 7.21.

A similar process of vortex formation, from the upper surface, can be seen in the elemental-vortex, streamline, isovorticity and isobar patterns (Figs. 7.23–7.26) for $Re_h = 250$, from $t = 48.2$ onwards. Calculations indicate that the flow pattern at $Re_h = 250$ is essentially identical to that at $Re_h = 100$. At the higher Reynolds number the discrete vortices formed on the side surfaces of the cylinder are stronger and more pronounced, but they are still significantly weaker than the vortices formed from the shear layers separating from the trailing edge.

At $Re_h = 500$, the calculations (Figs. 7.27–7.30) indicate flow separation from the leading corners of the cylinder at all times, but not always reattachment. Reattachment of the separated shear layer occurs intermittently, alternating with completely detached flow in which there is reversed flow over the side surface. A typical sequence of events in the flow over the upper surface can be seen, for example, in Fig. 7.28 from $t = 70.1$ onwards, and in the corresponding enlarged streamline patterns over one vortex-shedding cycle shown in Fig. 7.30. (Fig. 7.30 also includes isobar patterns of the pressure field around the cylinder, which frequently give a clearer indication of flow separation and reattachment than do the streamline patterns.) Following a period of detached flow, reattachment of the leading-edge shear layer on the side surface produces a short leading-edge-separation bubble ($t = 71.1$). The bubble then increases in length, discrete vortices are formed within it, the bubble divides and discrete vortices are convected along the side surface ($t = 71.6, 72.1$). A discrete vortex, after passing the trailing corner takes up a position on the rear face of the cylinder near the trailing corner ($t = 73.1, 73.6$), where it forms the seed of a vortex which develops on the trailing face; this trailing-face vortex grows ($t = 74.1$) and is eventually shed into the wake ($t = 76.1$). Interaction between the flow around this vortex and vortical motion in the now full-chord leading-edge-separation bubble leads to re-establishment of separated reversed flow over the side surface.

It should be noted that the frequency of formation and convection of discrete vortices along the side surfaces is greater than the wake-vortex frequency – not all vortices convected past the trailing corner lead to wake-vortex formation. Occasionally a trailing-face vortex is shed into the wake in isolation. However, in general, a trailing-face vortex and a side-face vortex newly arriving at the trailing corner are shed into the wake simultaneously. After shedding, the two vortices, at least initially, retain their separate identities, and their centres rotate about a common centre. Following this initial motion, the two in some cases merge to form a single discrete vortex while in others they separate to form two discrete vortices (with the same sense of rotation). Consequently, there is some irregularity in the vortex street developed

downstream of the cylinder, as is evident in the elemental-vortex patterns of Fig. 7.27, and the isovorticity contours of Fig. 7.29. On the other hand, the vortex shedding process itself at this Reynolds number is closely regular, as can be seen from the time-history of lift variation shown later in Fig. 7.39.

For Re_h = 1,000, the calculated flow patterns (Figs. 7.31–7.34) indicate a process of vortex formation which is essentially similar to that for Re_h = 500 but even more sharply defined. The sequence of events on the lower surface, from t = 85.4 onwards can be seen in the streamline patterns and pressure fields in Figs. 7.32 and 7.34. Fig. 7.34 clearly shows the reattachment of the leading-edge shear layer on the side surface accompanied by formation of leading-edge-separation bubble (t = 88.4); this is followed by the splitting of the leading-edge-separation bubble and the resulting formation of discrete vortices and their convection along the side surface (t = 89.4, 90.4). A discrete vortex, convected past the trailing corner, forms the seed of a trailing-face vortex (t = 91.4), which grows (t = 92.4) before being shed into the wake (t = 93.4). The subsequent formation of full-chord leading-edge-separation bubble and the re-establishment of separated reversed flow over the side surface can then be seen at t = 93.4 and 94.4.

As for Re_h = 500, the frequency of formation and convection of discrete vortices along the side surfaces is greater than the vortex-shedding frequency. Similarly, the flow exhibits occasional shedding of an isolated trailing-face vortex into the wake, and, more generally, simultaneous shedding of a trailing-face vortex and a newly-arrived side-face vortex. In the latter case, as for Re_h = 500, the two vortices may merge to form a single discrete vortex or separate to form two discrete vortices. At this Reynolds number, the elemental-vortex patterns of Fig. 7.31, and the isovorticity contours of Fig. 7.33 show that the irregularity in the vortex street developed downstream of the cylinder is more pronounced than at Re_h = 500, and the vortex shedding process itself, although still characterised by a dominant frequency, is significantly less regular, as can be seen from the time-histories of lift variation shown later in Figs. 7.39 and 7.41.

In summary, the calculations indicate that the formation and shedding of wake vortices from the cylinder is linked with the formation of discrete vortices on the side surfaces. At low Reynolds numbers, Re_h = 100 and 250, whereas a weak process of discrete-vortex formation on the side surfaces occurs, there is continuous flow of vorticity along the side surfaces into the wake. This signifies that the wake vortices gain vorticity primarily from the shear layers separating from the

trailing edge. Thus, vortex-shedding from the cylinder consists of the trailing-face vortices only. With an increase in Reynolds number, the discrete vortices formed on the side surfaces are of larger size and stronger vortical flow. The isovorticity contours for Re_h = 1,000 indicate that vorticity is fed into the wake predominantly in the form of discrete-vortices. In this case, vortex-shedding involves both trailing-face vortices and discrete vortices formed on the side surfaces.

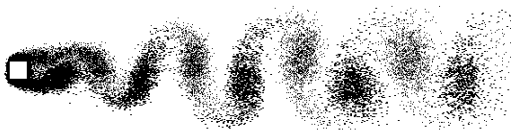

(a) Re_h = 100, C = 1, t = 57.3

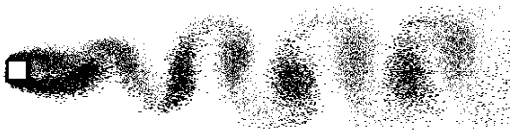

(k) Re_h = 100, C = 1, t = 87.3

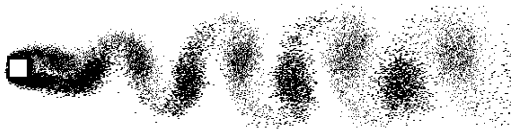

(b) Re_h = 100, C = 1, t = 60.3

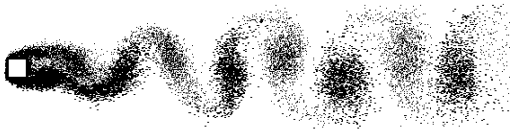

(l) Re_h = 100, C = 1, t = 90.3

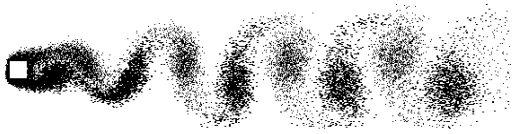

(c) Re_h = 100, C = 1, t = 63.3

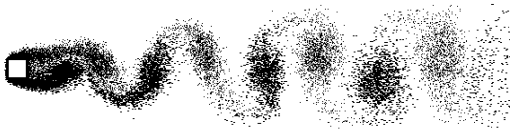

(m) Re_h = 100, C = 1, t = 92.4

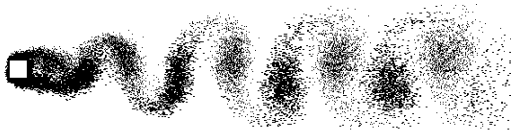

(d) Re_h = 100, C = 1, t = 66.3

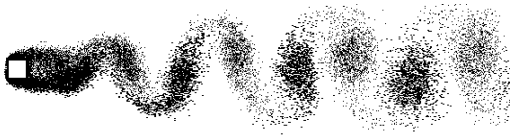

(n) Re_h = 100, C = 1, t = 94.4

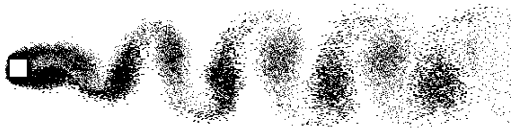

(e) Re_h = 100, C = 1, t = 69.3

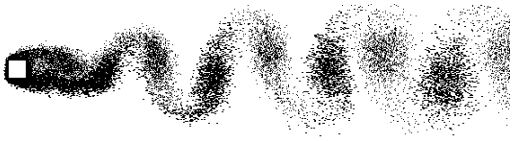

(o) Re_h = 100, C = 1, t = 96.4

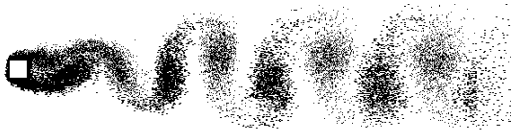

(f) Re_h = 100, C = 1, t = 72.3

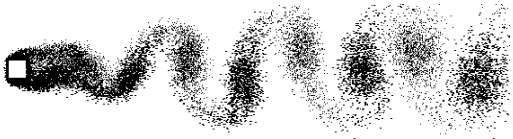

(p) Re_h = 100, C = 1, t = 98.4

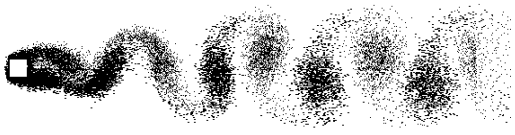

(g) Re_h = 100, C = 1, t = 75.3

(q) Re_h = 100, C = 1, t = 100.4

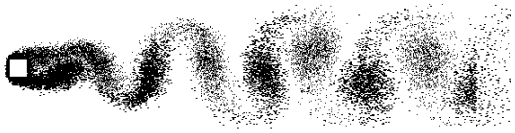

(h) Re_h = 100, C = 1, t = 78.3

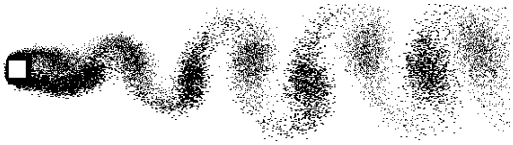

(r) Re_h = 100, C = 1, t = 102.4

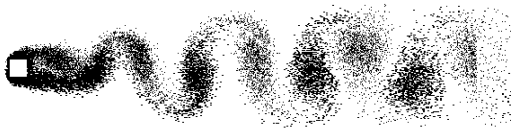

(i) Re_h = 100, C = 1, t = 81.3

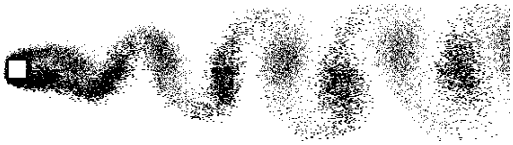

(s) Re_h = 100, C = 1, t = 104.4

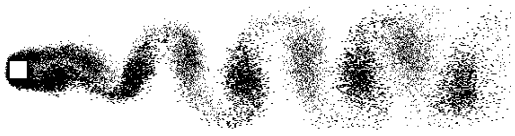

(j) Re_h = 100, C = 1, t = 84.3

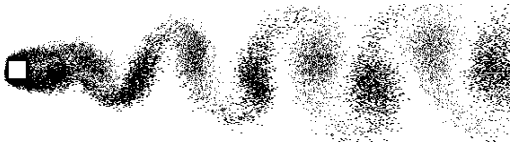

(t) Re_h = 100, C = 1, t = 106.4

Figure 7.19. Elemental-vortex distributions in fully-developed flow over a square cylinder at Re_h = 100.

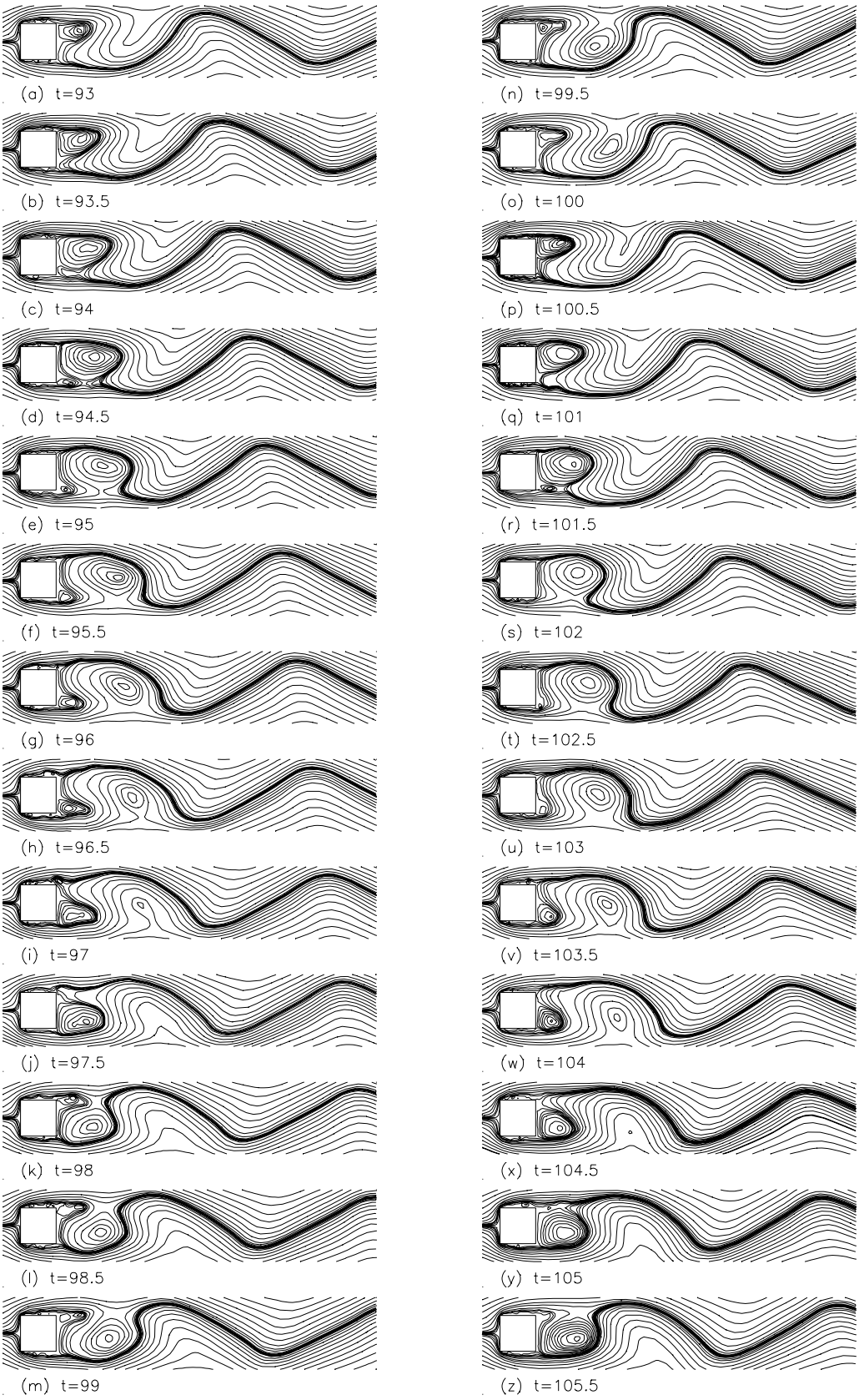

Figure 7.20. Streamline patterns in fully-developed flow over a square cylinder at Re_h = 100.

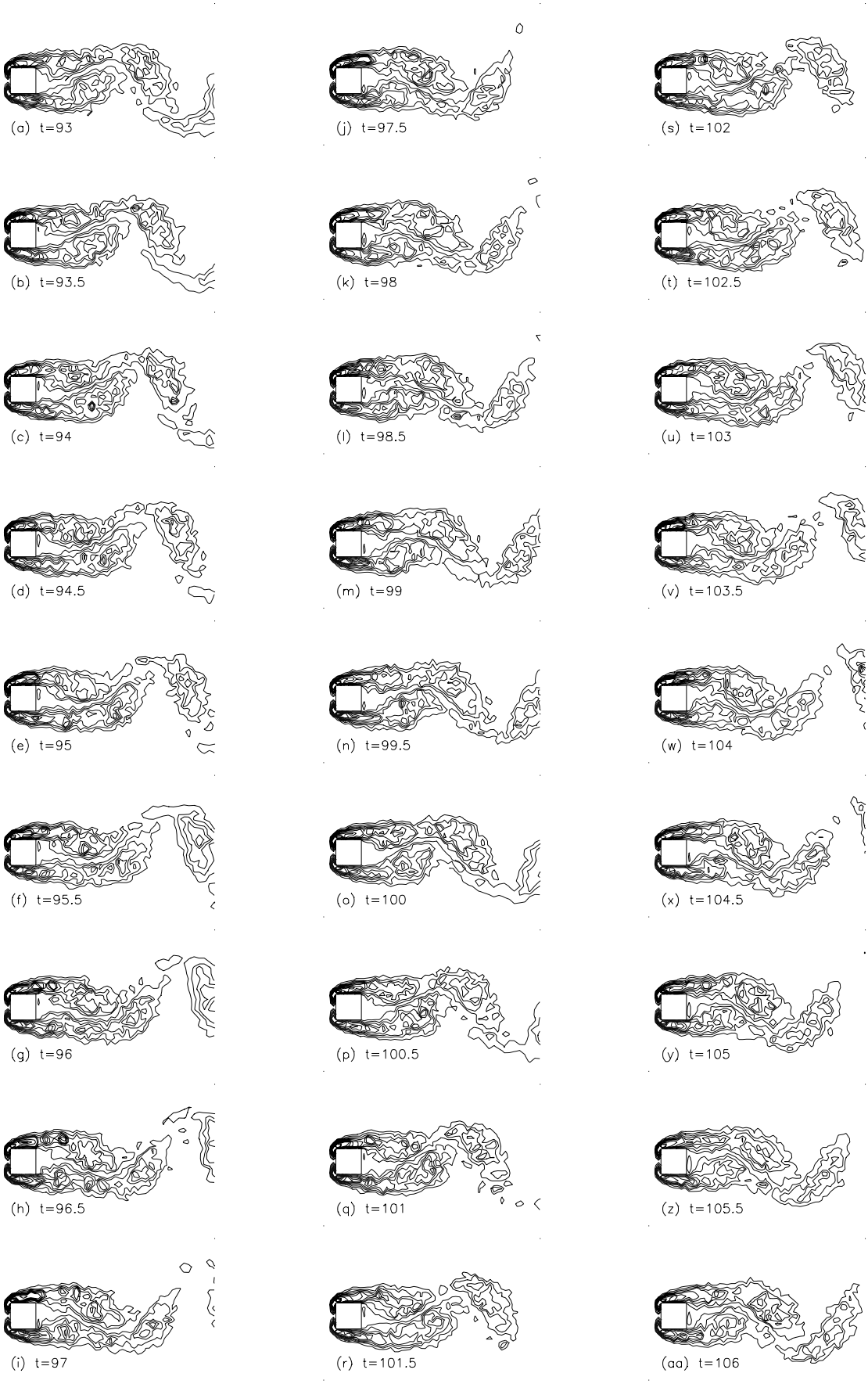

Figure 7.21. Vorticity contours in fully-developed flow over a square cylinder at Re_h = 100.

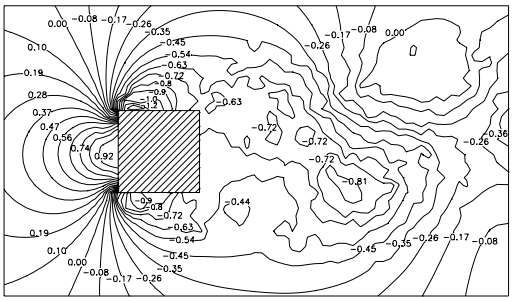

(a1) Re_h = 100, C = 1, t = 93

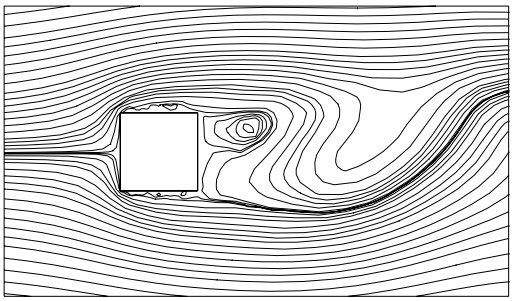

(a2) Re_h = 100, C = 1, t = 93

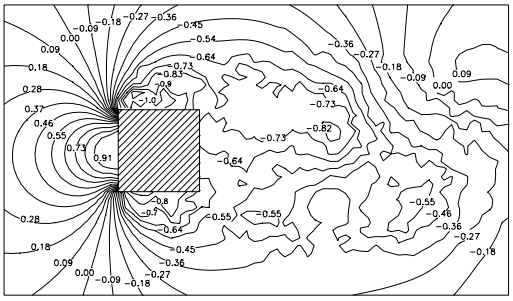

(b1) Re_h = 100, C = 1, t = 94.5

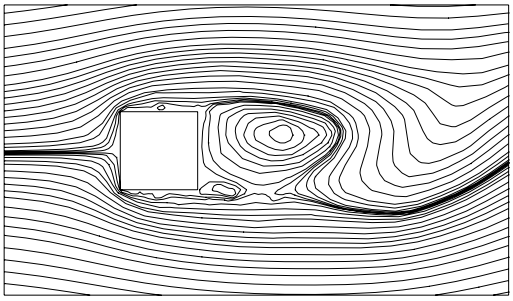

(b2) Re_h = 100, C = 1, t = 94.5

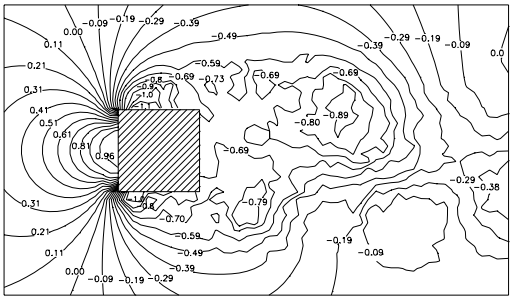

(c1) Re_h = 100, C = 1, t = 96

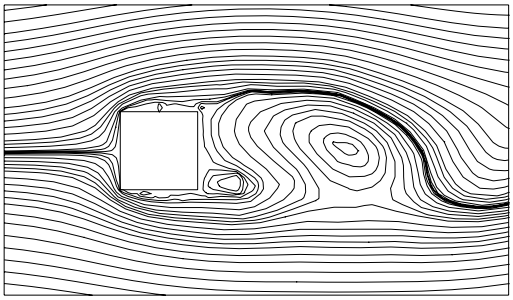

(c2) Re_h = 100, C = 1, t = 96

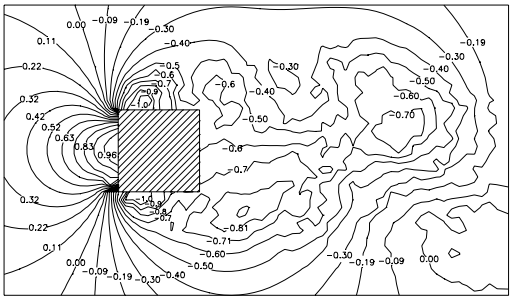

(d1) Re_h = 100, C = 1, t = 97.5

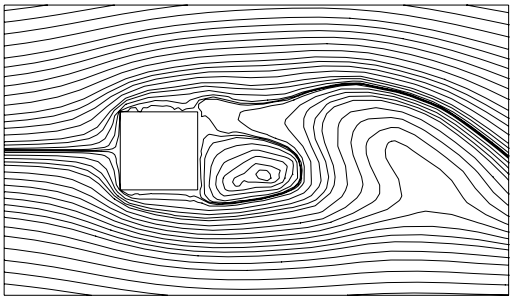

(d2) Re_h = 100, C = 1, t = 97.5

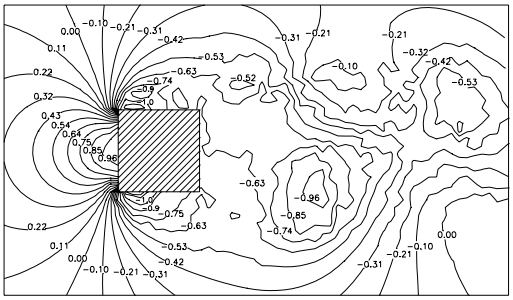

(e1) Re_h = 100, C = 1, t = 99

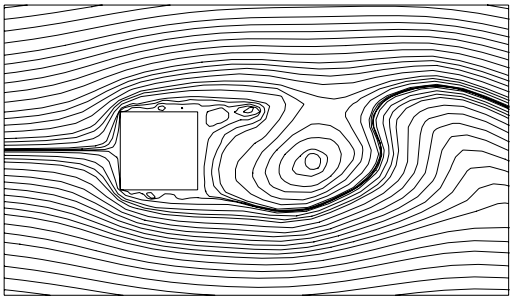

(e2) Re_h = 100, C = 1, t = 99

Figure 7.22. Instantaneous pressure fields and streamline patterns around a square cylinder at Re_h = 100. Numbers shown are coefficients of static pressure.

(a) Re_h = 250, C = 1, t = 36

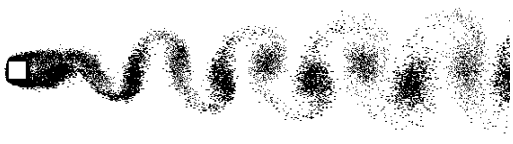

(k) Re_h = 250, C = 1, t = 51.2

(b) Re_h = 250, C = 1, t = 38

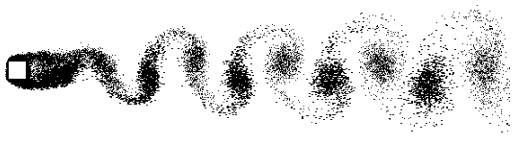

(l) Re_h = 250, C = 1, t = 52.2

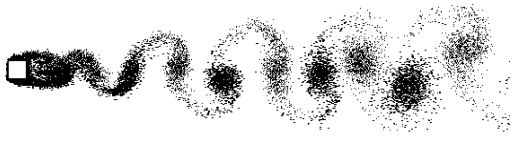

(c) Re_h = 250, C = 1, t = 40

(m) Re_h = 250, C = 1, t = 53.2

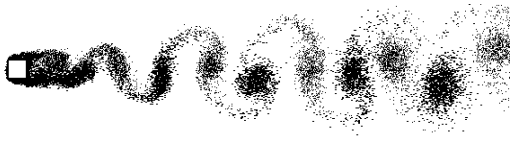

(d) Re_h = 250, C = 1, t = 42

(n) Re_h = 250, C = 1, t = 54.2

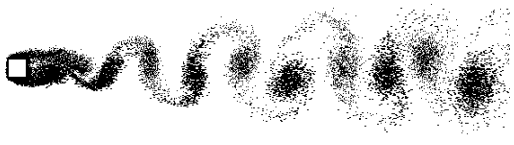

(e) Re_h = 250, C = 1, t = 44

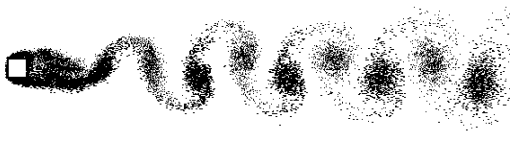

(o) Re_h = 250, C = 1, t = 55.2

(f) Re_h = 250, C = 1, t = 46

(p) Re_h = 250, C = 1, t = 56.2

(g) Re_h = 250, C = 1, t = 47.2

(q) Re_h = 250, C = 1, t = 57.2

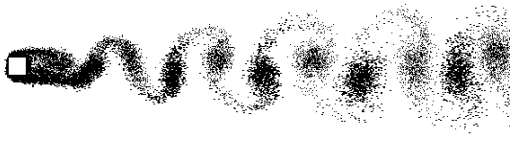

(h) Re_h = 250, C = 1, t = 48.2

(r) Re_h = 250, C = 1, t = 58.2

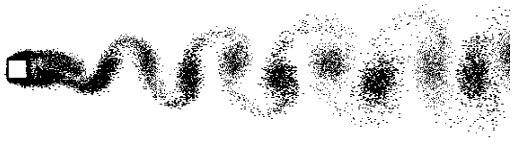

(i) Re_h = 250, C = 1, t = 49.2

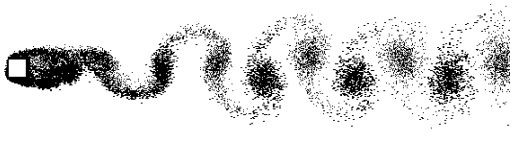

(s) Re_h = 250, C = 1, t = 59..2

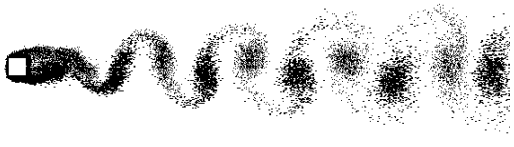

(j) Re_h = 250, C = 1, t = 50.2

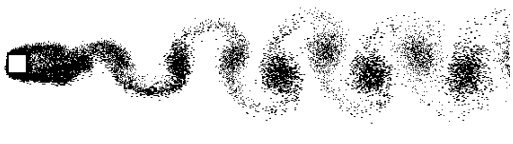

(t) Re_h = 250, C = 1, t = 60.2

Figure 7.23. Elemental-vortex distributions in fully-developed flow over a square cylinder at Re_h = 250.

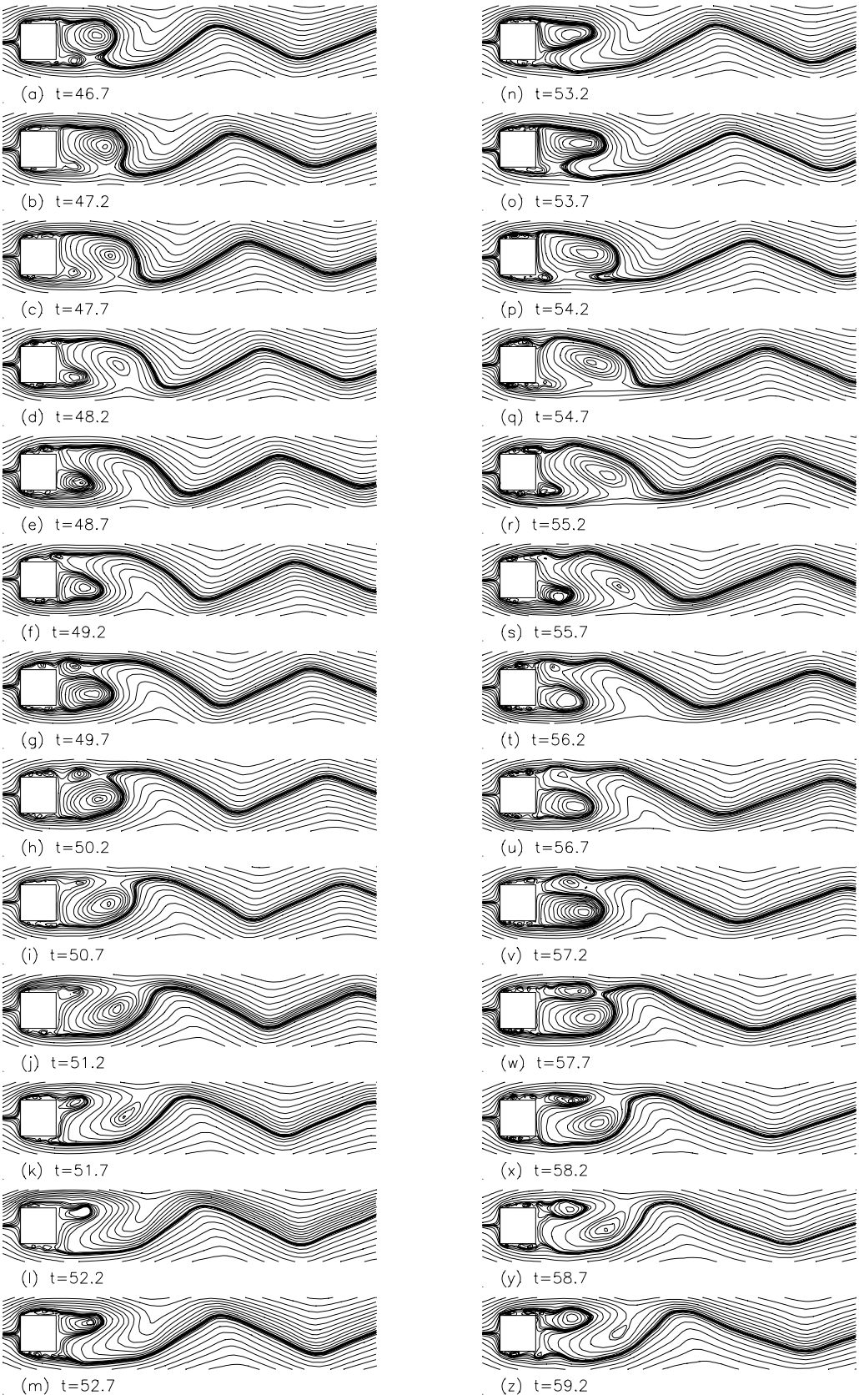

Figure 7.24. Streamline patterns in fully-developed flow over a square cylinder at Re_h = 250.

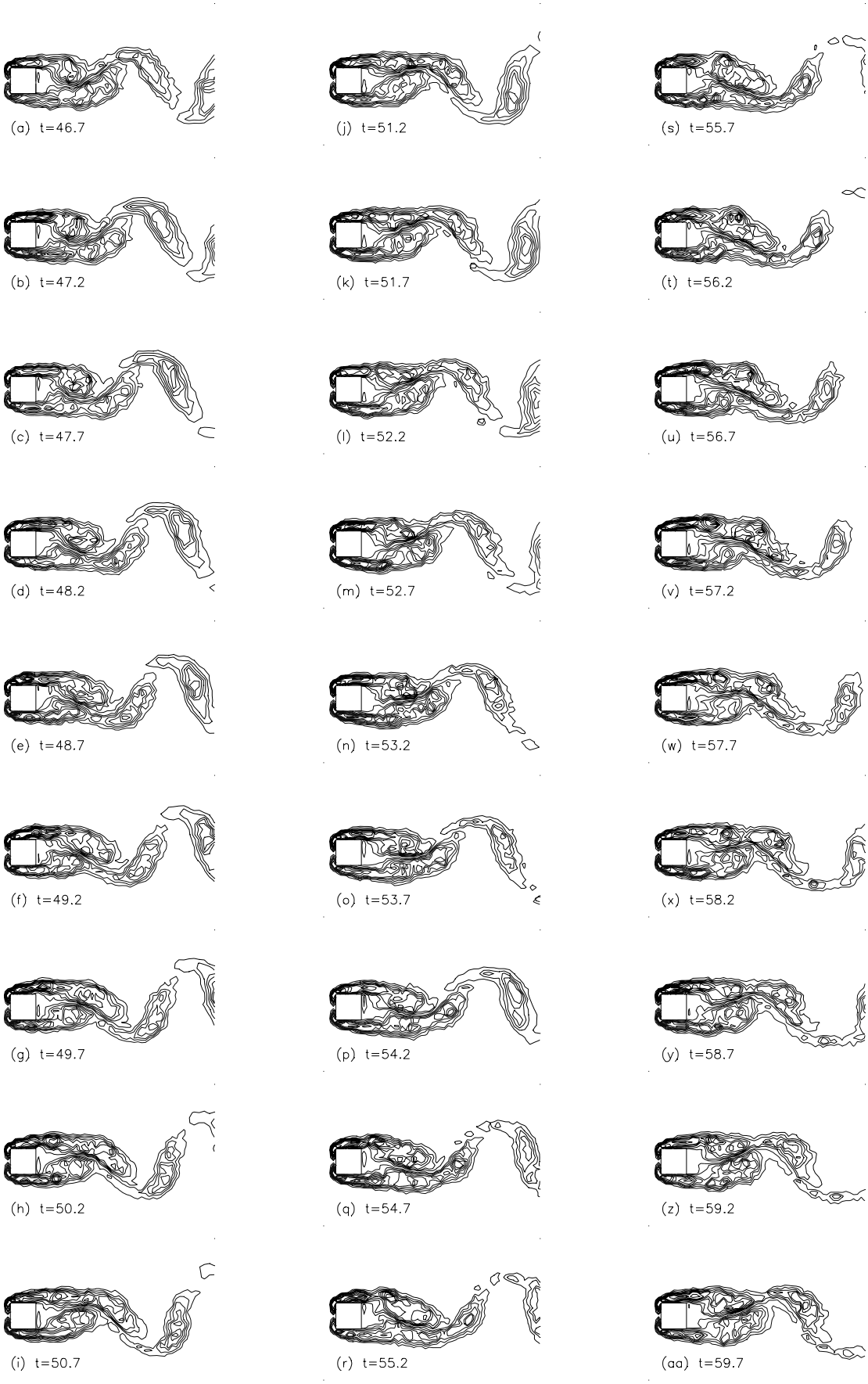

Figure 7.25. Vorticity contours in fully-developed flow over a square cylinder at Re_h = 250.

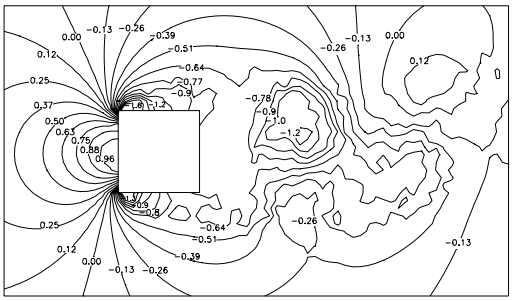

(a1) Re_h = 250, C = 1, t = 46.7

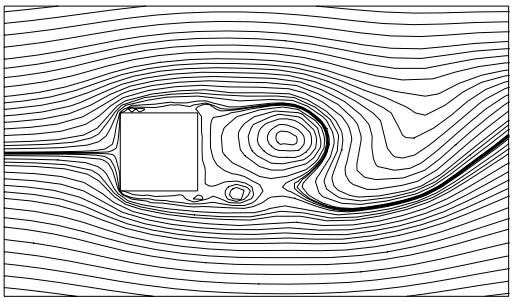

(a2) Re_h = 250, C = 1, t = 46.7

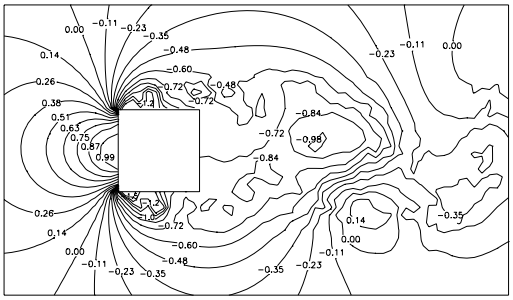

(b1) Re_h = 250, C = 1, t = 48.2

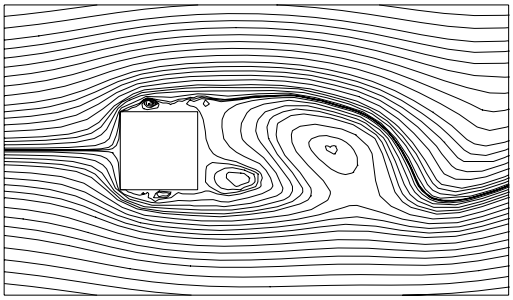

(b2) Re_h = 250, C = 1, t = 48.2

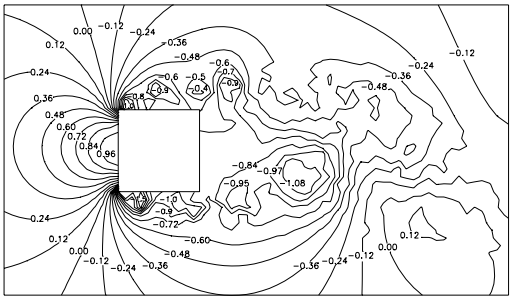

(c1) Re_h = 250, C = 1, t = 49.7

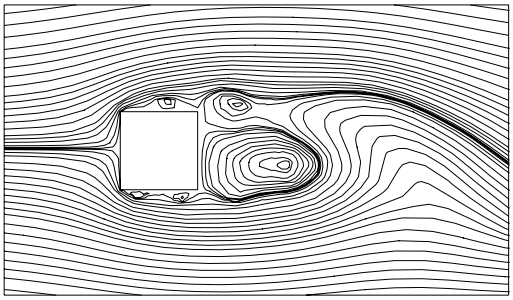

(c2) Re_h = 250, C = 1, t = 49.7

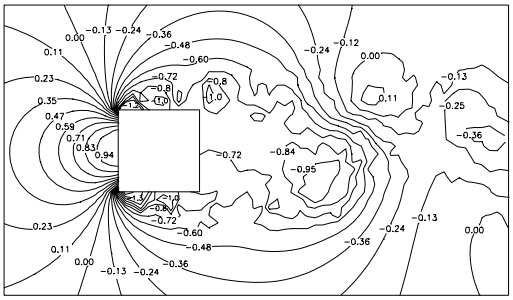

(d1) Re_h = 250, C = 1, t = 51.2

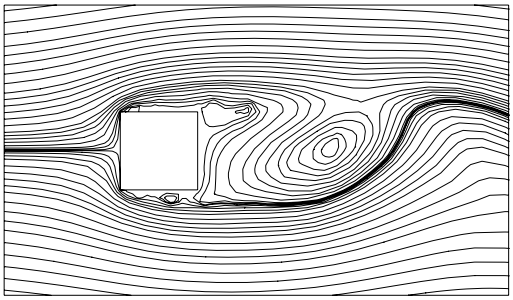

(d2) Re_h = 250, C = 1, t = 51.2

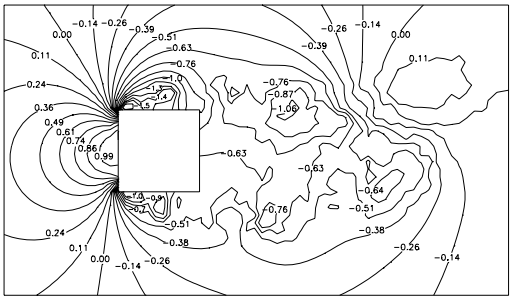

(e1) Re_h = 250, C = 1, t = 52.7

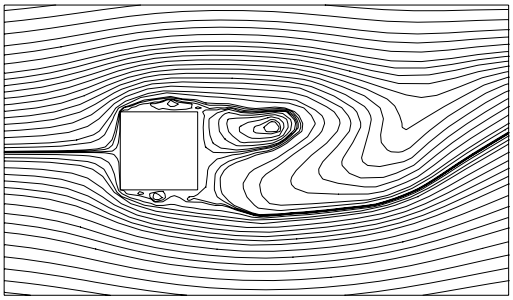

(e2) Re_h = 250, C = 1, t = 52.7

Figure 7.26. Instantaneous pressure fields and streamline patterns around a square cylinder at Re_h = 250. Numbers shown are coefficients of static pressure.

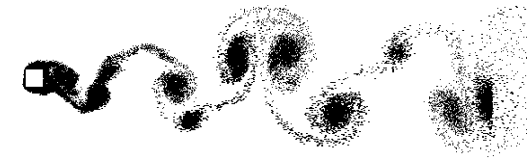

(a) Re_h = 500, C = 1, t = 40.6

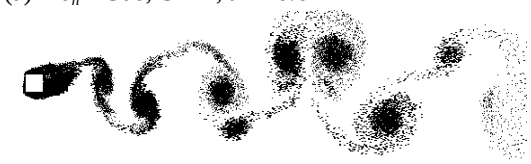

(b) Re_h = 500, C = 1, t = 43.6

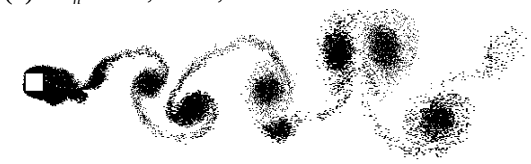

(c) Re_h = 500, C = 1, t = 46.6

(d) Re_h = 500, C = 1, t = 49.6

(e) Re_h = 500, C = 1, t = 52.6

(f) Re_h = 500, C = 1, t = 55.6

(g) Re_h = 500, C = 1, t = 58.6

(h) Re_h = 500, C = 1, t = 61.6

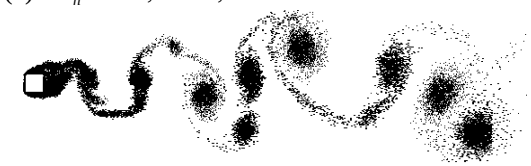

(i) Re_h = 500, C = 1, t = 64.6

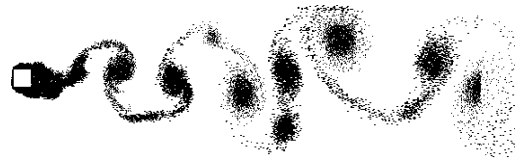

(j) Re_h = 500, C = 1, t = 67.6

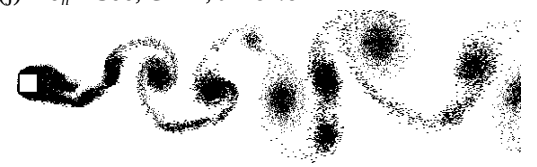

(k) Re_h = 500, C = 1, t = 69.6

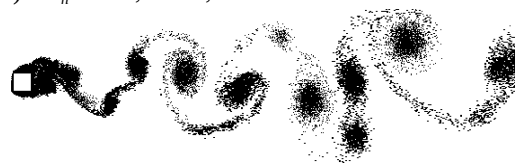

(l) Re_h = 500, C = 1, t = 71.6

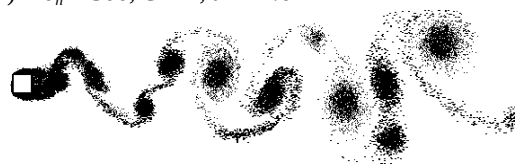

(m) Re_h = 500, C = 1, t = 73.6

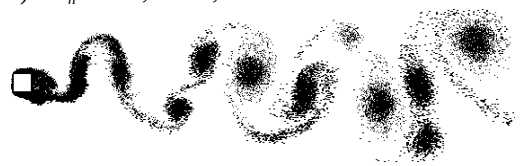

(n) Re_h = 500, C = 1, t = 75.6

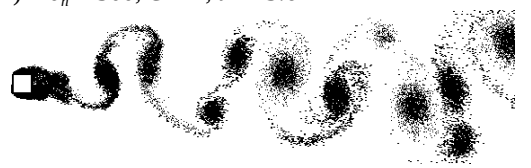

(o) Re_h = 500, C = 1, t = 77.6

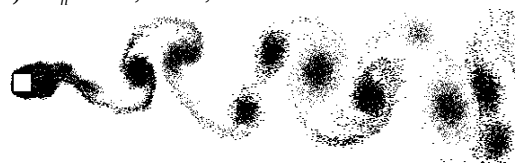

(p) Re_h = 500, C = 1, t = 79.6

(q) Re_h = 500, C = 1, t = 81.6

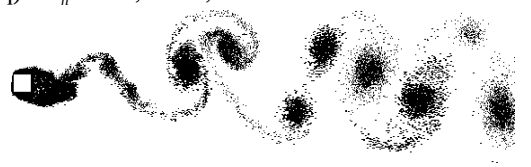

(r) Re_h = 500, C = 1, t = 82.6

Figure 7.27. Elemental-vortex distributions in fully-developed flow over a square cylinder at Re_h = 500.

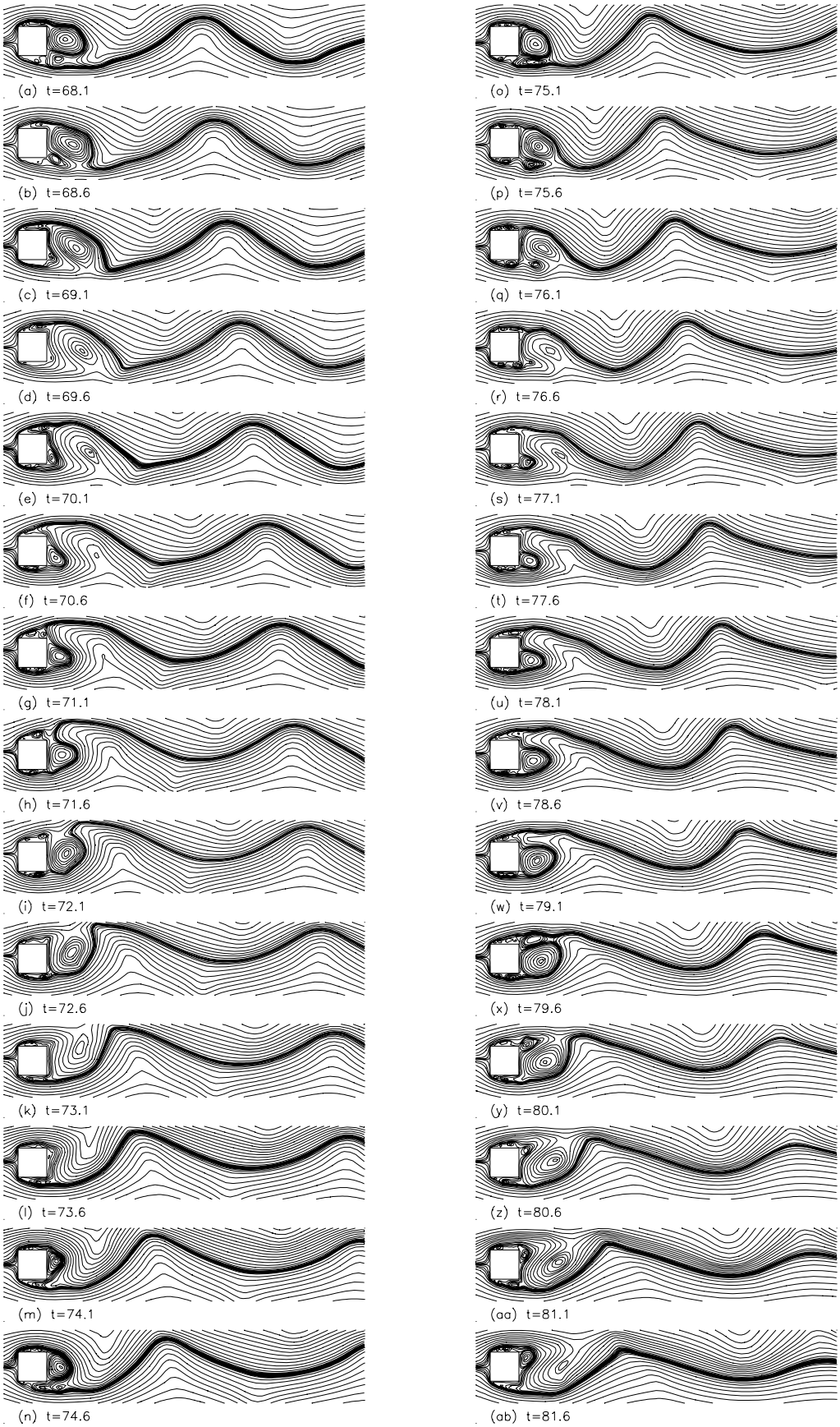

Figure 7.28. Streamline patterns in fully-developed flow over a square cylinder at Re_h = 500.

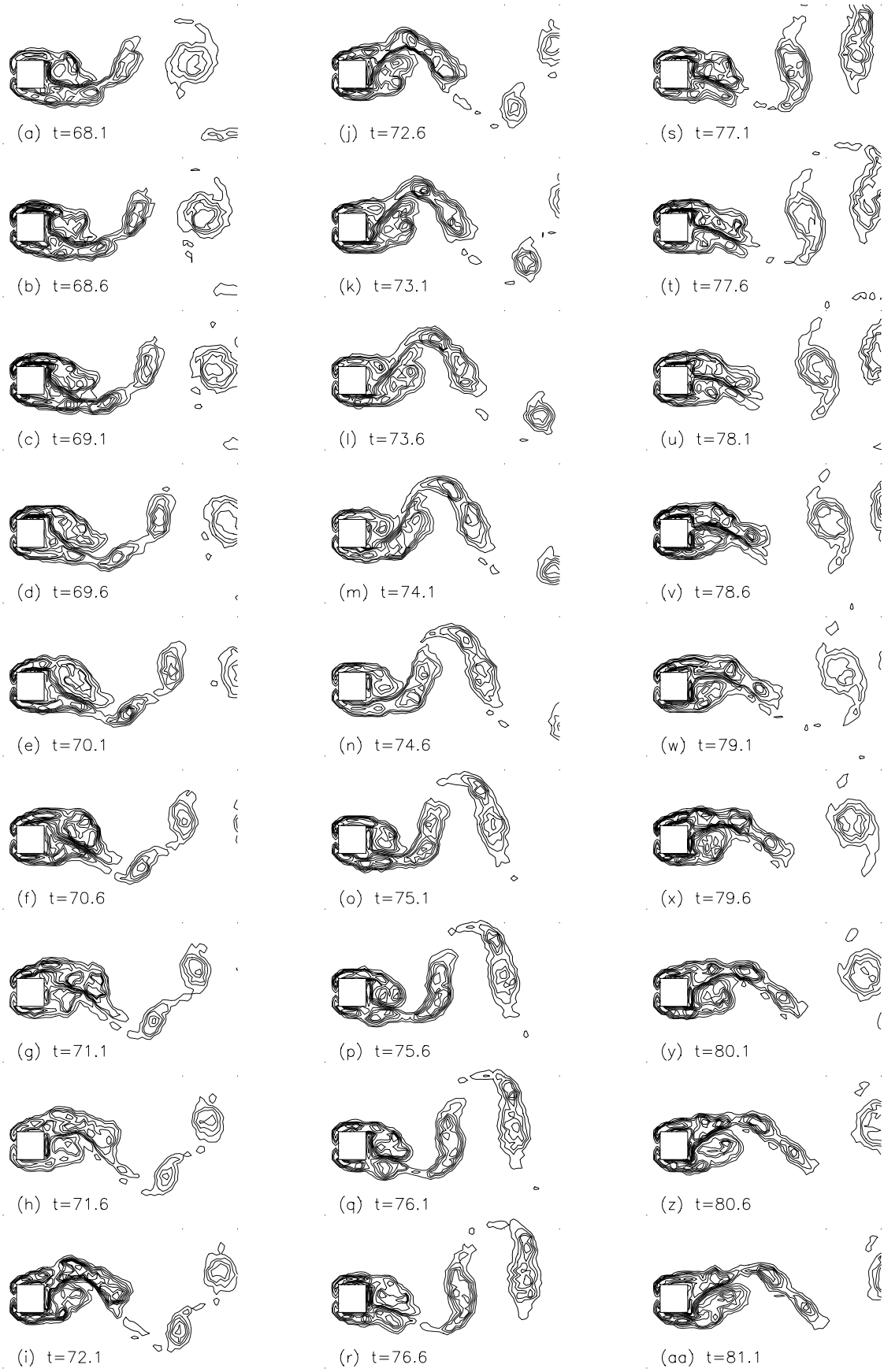

Figure 7.29. Vorticity contours in fully-developed flow over a square cylinder at Re_h = 500.

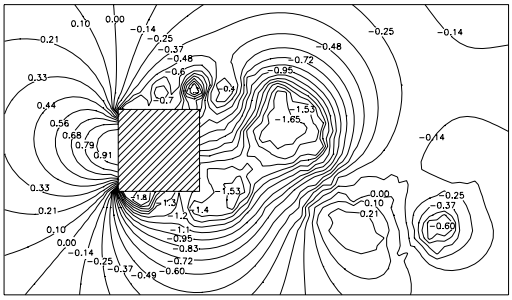

(a1) Re_h = 500, C = 1, t = 70.1

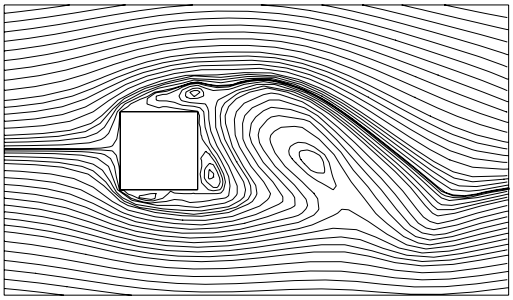

(a2) Re_h = 500, C = 1, t = 70.1

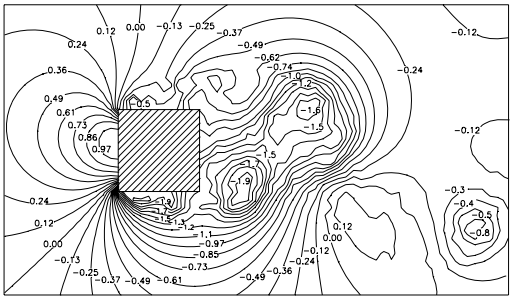

(b1) Re_h = 500, C = 1, t = 70.6

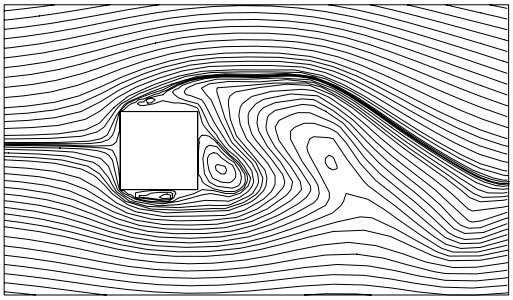

(b2) Re_h = 500, C = 1, t = 70.6

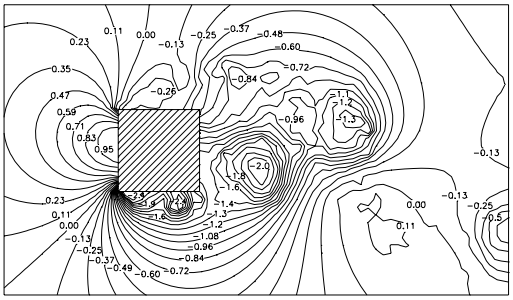

(c1) Re_h = 500, C = 1, t = 71.1

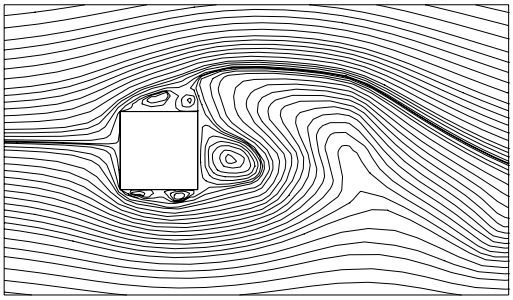

(c2) Re_h = 500, C = 1, t = 71.1

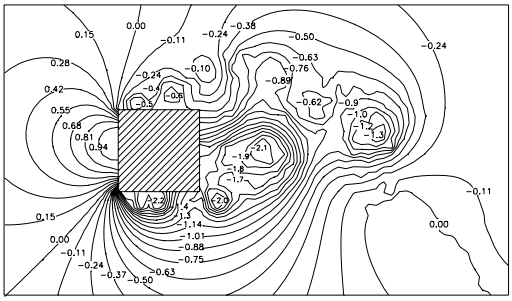

(d1) Re_h = 500, C = 1, t = 71.6

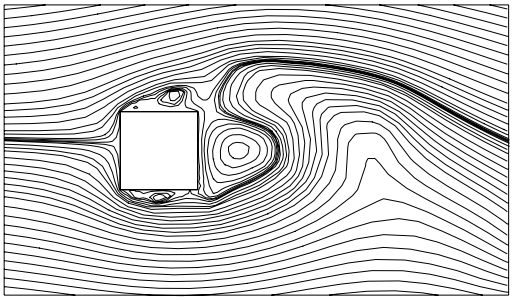

(d2) Re_h = 500, C = 1, t = 71.6

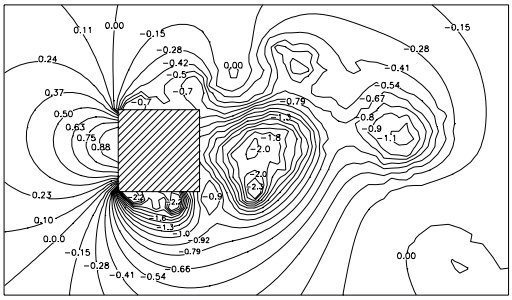

(e1) Re_h = 500, C = 1, t = 72.1

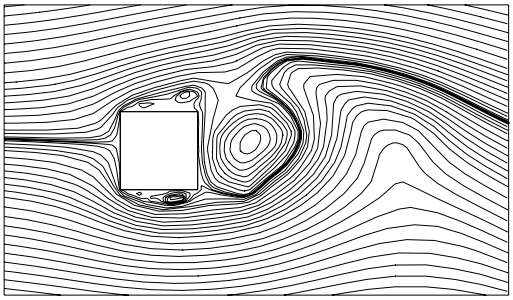

(e2) Re_h = 500, C = 1, t = 72.1

Figure 7.30. Instantaneous pressure fields and streamline patterns around a square cylinder at Re_h = 500. Numbers shown are coefficients of static pressure.

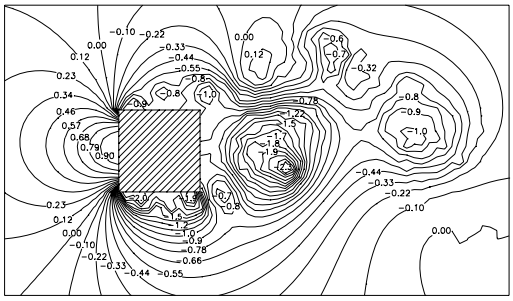

(f1) Re_h = 500, C = 1, t = 72.6

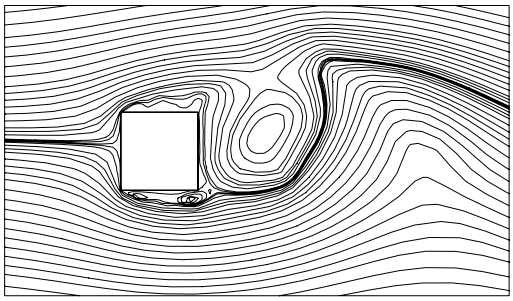

(f2) Re_h = 500, C = 1, t = 72.6

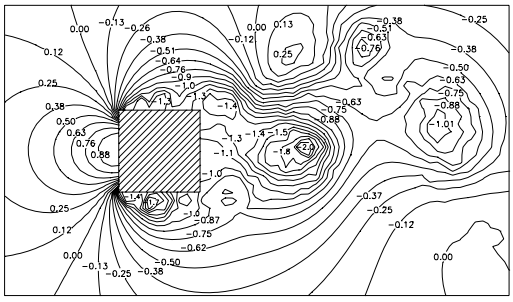

(g1) Re_h = 500, C = 1, t = 73.1

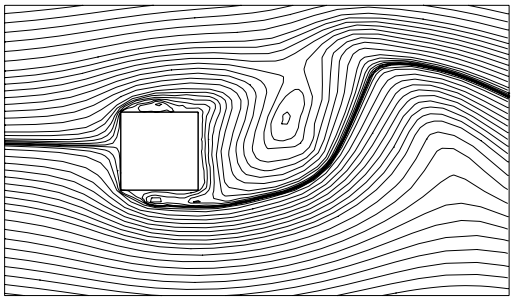

(g2) Re_h = 500, C = 1, t = 73.1

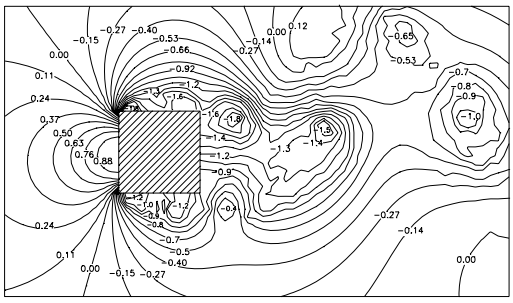

(h1) Re_h = 500, C = 1, t = 73.6

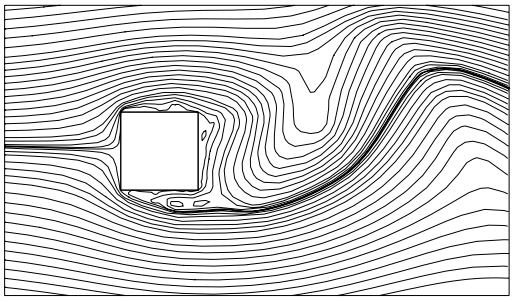

(h2) Re_h = 500, C = 1, t = 73.6

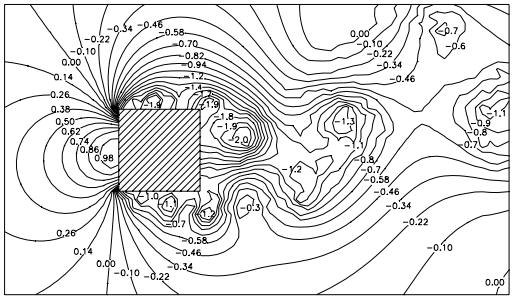

(i1) Re_h = 500, C = 1, t = 74.1

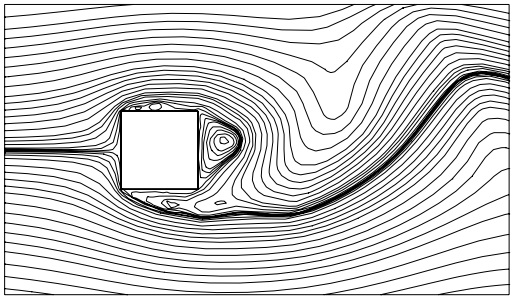

(i2) Re_h = 500, C = 1, t = 74.1

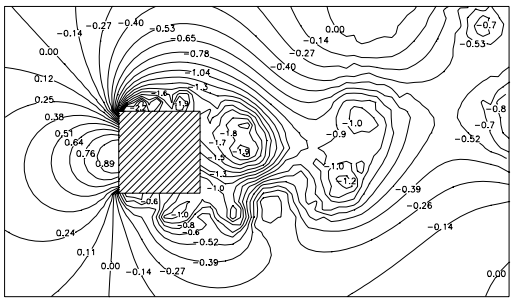

(j1) Re_h = 500, C = 1, t = 74.6

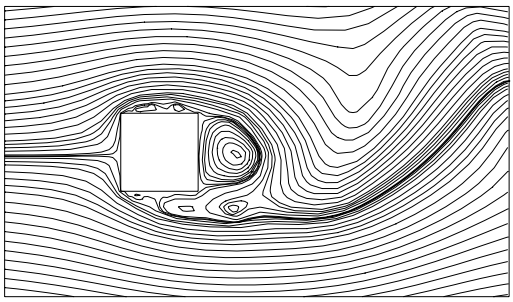

(j2) Re_h = 500, C = 1, t = 74.6

Figure 7.30. Cont'd.

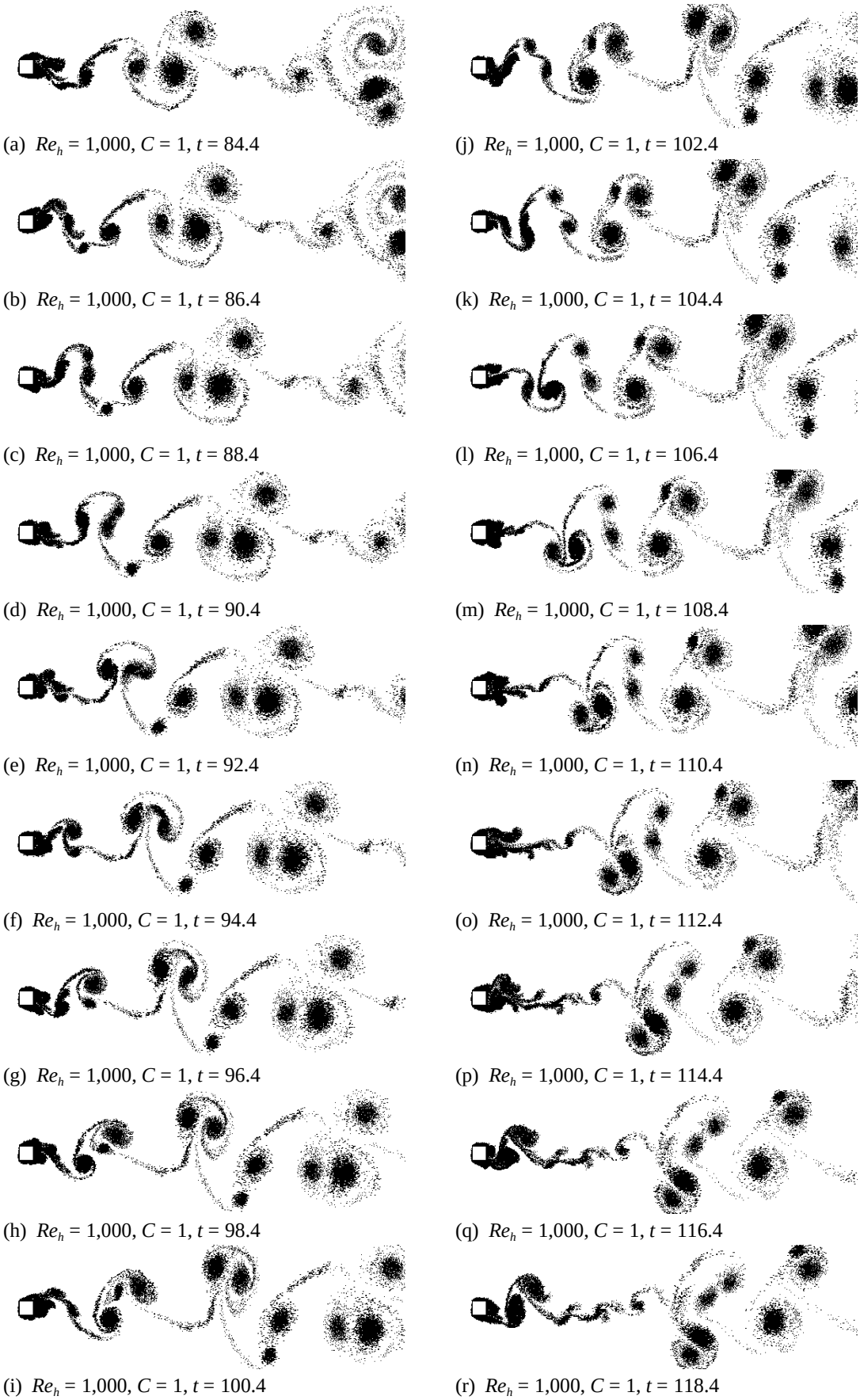

(a) Re_h = 1,000, C = 1, t = 84.4

(b) Re_h = 1,000, C = 1, t = 86.4

(c) Re_h = 1,000, C = 1, t = 88.4

(d) Re_h = 1,000, C = 1, t = 90.4

(e) Re_h = 1,000, C = 1, t = 92.4

(f) Re_h = 1,000, C = 1, t = 94.4

(g) Re_h = 1,000, C = 1, t = 96.4

(h) Re_h = 1,000, C = 1, t = 98.4

(i) Re_h = 1,000, C = 1, t = 100.4

(j) Re_h = 1,000, C = 1, t = 102.4

(k) Re_h = 1,000, C = 1, t = 104.4

(l) Re_h = 1,000, C = 1, t = 106.4

(m) Re_h = 1,000, C = 1, t = 108.4

(n) Re_h = 1,000, C = 1, t = 110.4

(o) Re_h = 1,000, C = 1, t = 112.4

(p) Re_h = 1,000, C = 1, t = 114.4

(q) Re_h = 1,000, C = 1, t = 116.4

(r) Re_h = 1,000, C = 1, t = 118.4

Figure 7.31. Elemental-vortex distributions in fully-developed flow over a square cylinder at Re_h = 1,000.

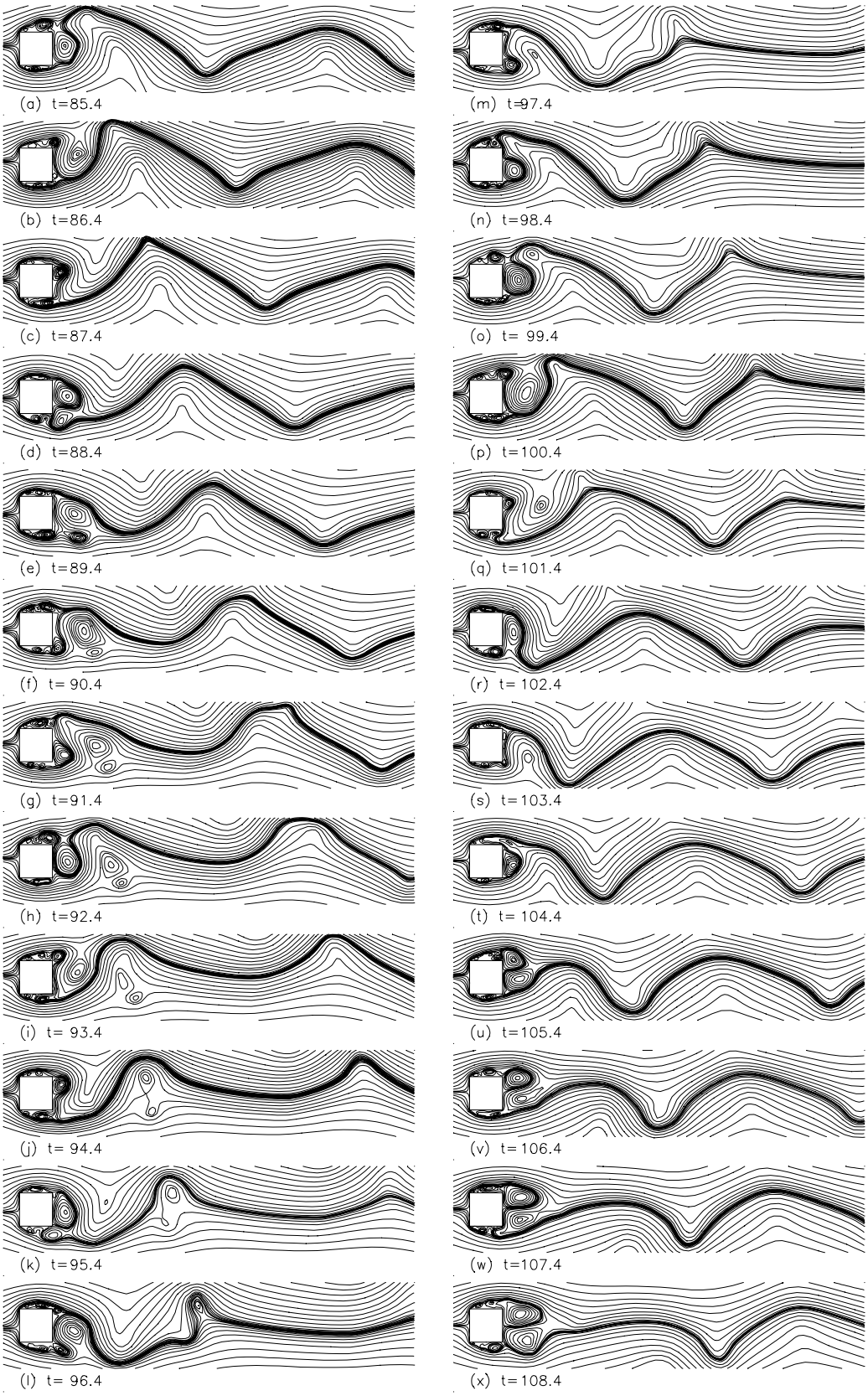

Figure 7.32. Streamline patterns in fully-developed flow over a square cylinder at Re_h = 1,000.

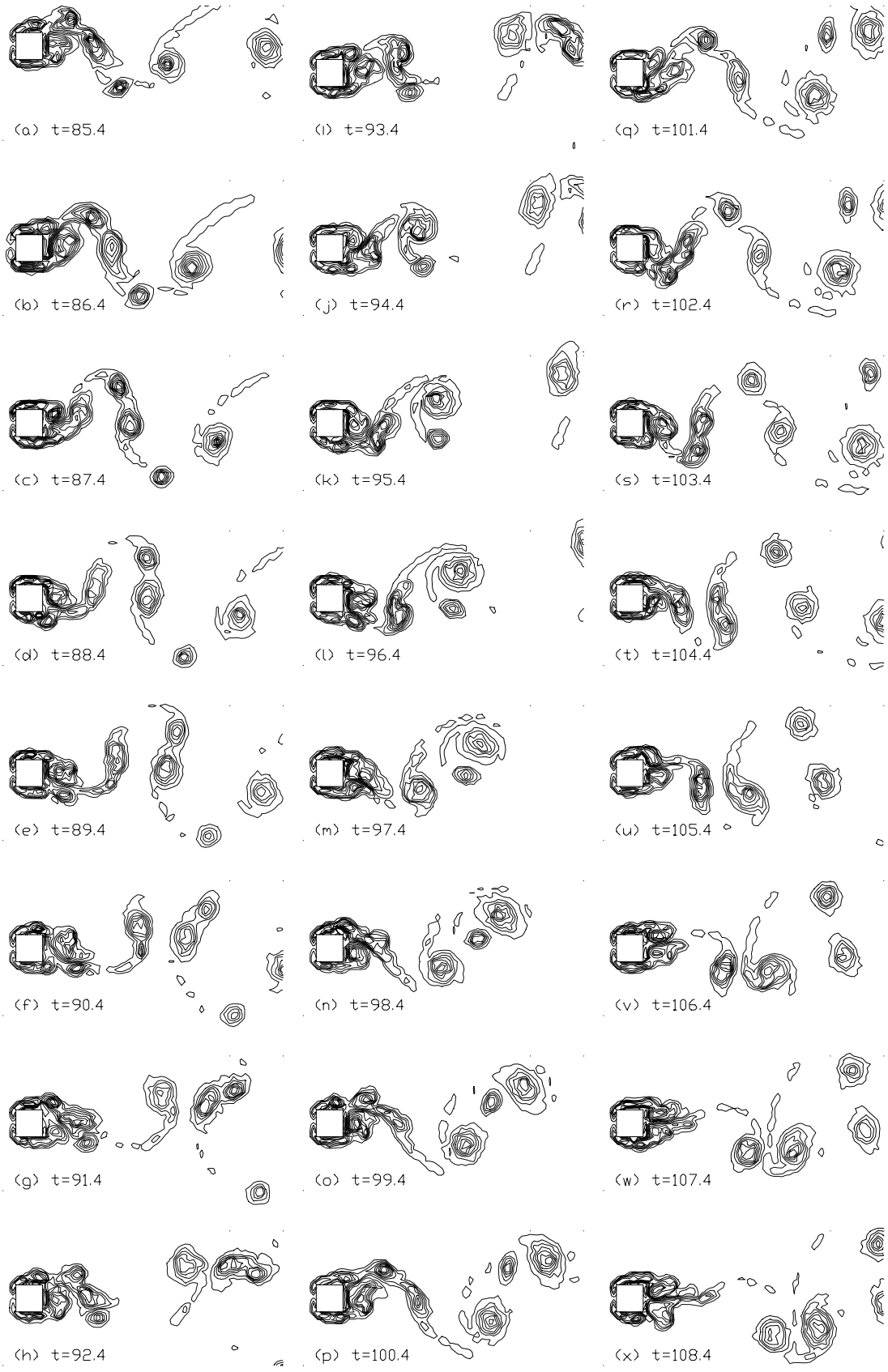

Figure 7.33. Vorticity contours in fully-developed flow over a square cylinder at Re_h = 1,000.

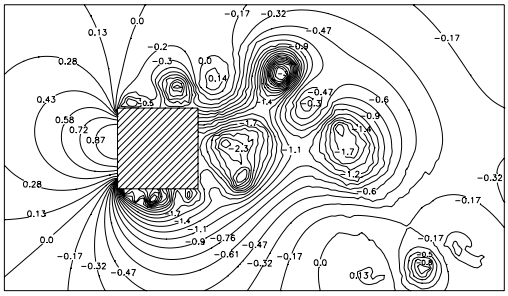

(a1) Re_h = 1,000, C = 1, t = 85.4

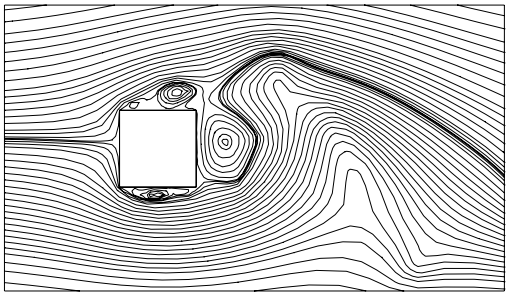

(a2) Re_h = 1,000, C = 1, t = 85.4

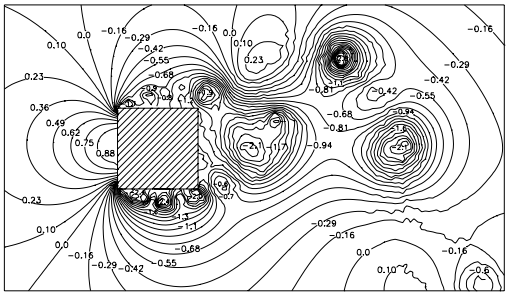

(b1) Re_h = 1,000, C = 1, t = 86.4

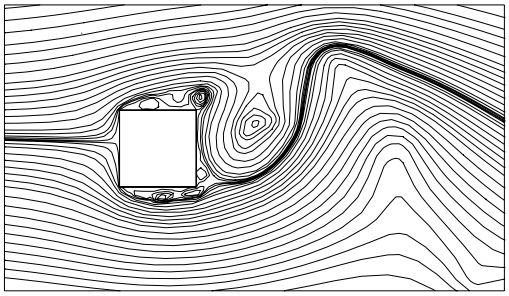

(b2) Re_h = 1,000, C = 1, t = 86.4

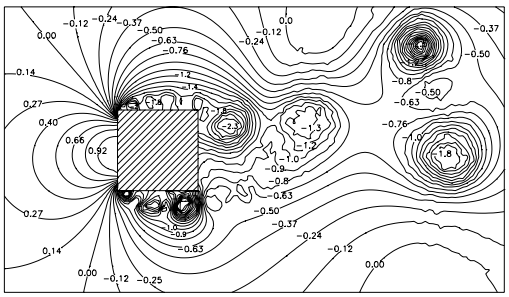

(c1) Re_h = 1,000, C = 1, t = 87.4

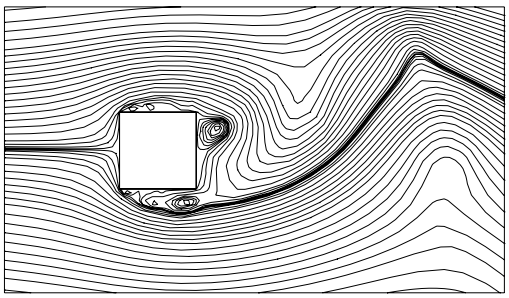

(c2) Re_h = 1,000, C = 1, t = 87.4

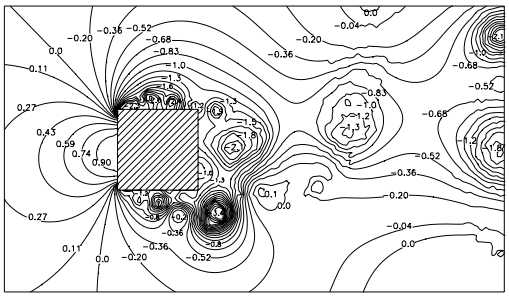

(d1) Re_h = 1,000, C = 1, t = 88.4

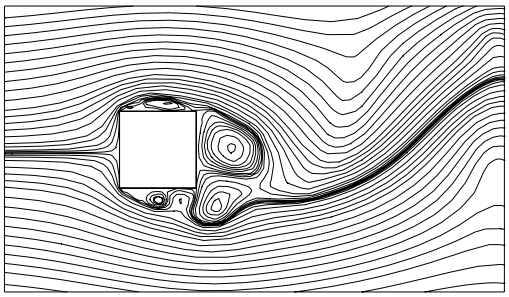

(d2) Re_h = 1,000, C = 1, t = 88.4

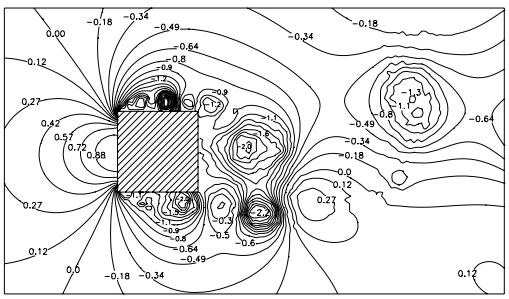

(e1) Re_h = 1,000, C = 1, t = 89.4

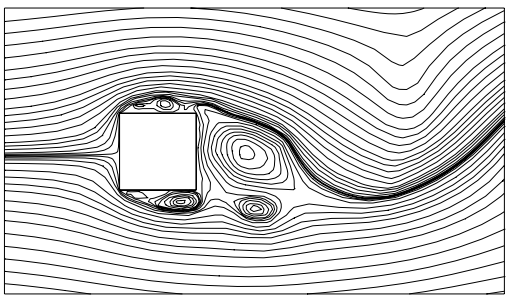

(e2) Re_h = 1,000, C = 1, t = 89.4

Figure 7.34. Instantaneous pressure fields and streamline patterns around a square cylinder at Re_h = 1,000. Numbers shown are coefficients of static pressure.

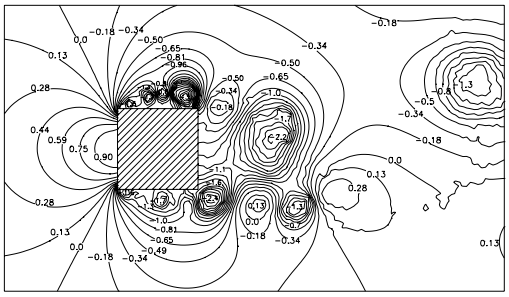

(f1) Re_h = 1,000, C = 1, t = 90.4

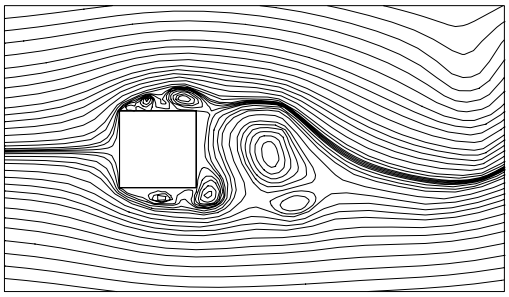

(f2) Re_h = 1,000, C = 1, t = 90.4

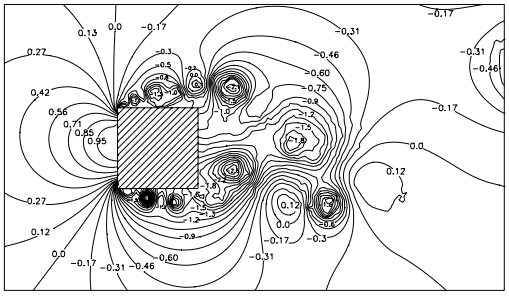

(g1) Re_h = 1,000, C = 1, t = 91.4

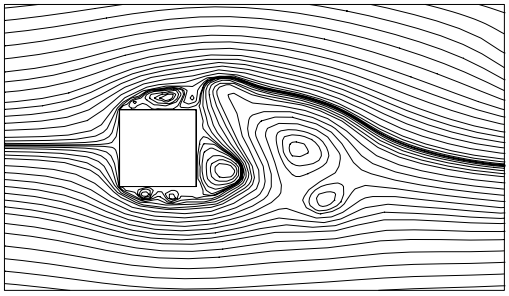

(g2) Re_h = 1,000, C = 1, t = 91.4

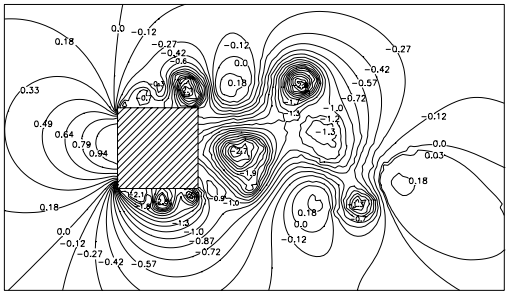

(h1) Re_h = 1,000, C = 1, t = 92.4

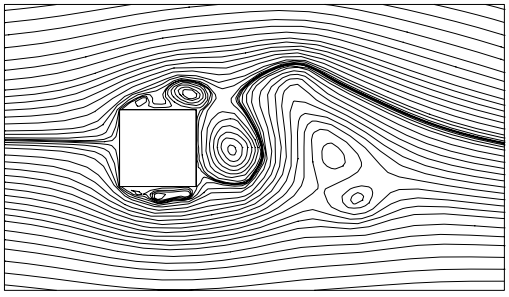

(h2) Re_h = 1,000, C = 1, t = 92.4

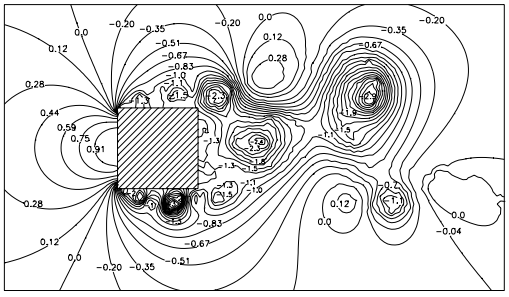

(i1) Re_h = 1,000, C = 1, t = 93.4

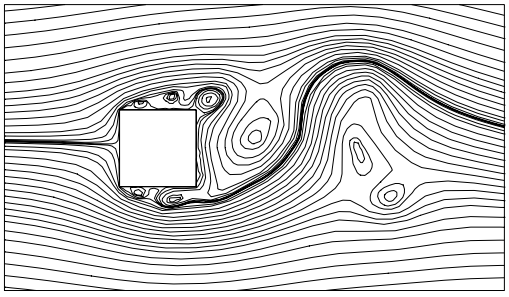

(i2) Re_h = 1,000, C = 1, t = 93.4

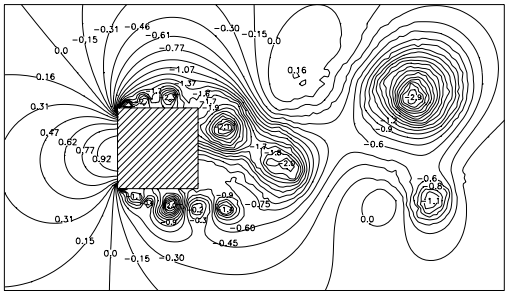

(j1) Re_h = 1,000, C = 1, t = 94.4

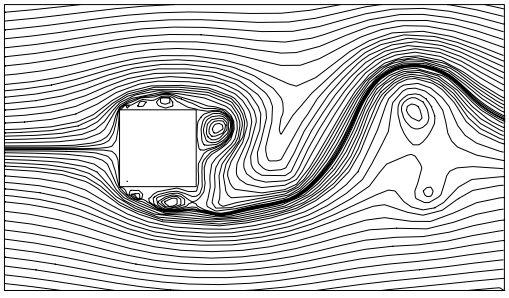

(j2) Re_h = 1,000, C = 1, t = 94.4

Figure 7.34. Cont'd.

7.3.2.3 Surface Pressures, Lift and Drag

The distributions of $\bar{p}$, the time-average of the static pressure p over the surfaces of the cylinder, expressed as the pressure coefficient $C_p = (\bar{p} - p_\infty)/\frac{1}{2}\rho U_\infty^2$ and the coefficient of r.m.s. pressure fluctuation $C_{p'} = p'/\frac{1}{2}\rho U_\infty^2$ (where the mean square pressure fluctuation p'^2 is the time-averaged value of $(p - \bar{p})^2$) at the four Reynolds numbers considered are presented in Fig. 7.35; the surface pressure distribution in an ideal inviscid flow is also shown. The inviscid-flow pressure field around the cylinder is presented in Fig. 7.36. The distance along the surface, s (scaled with the plate thickness), is measured from the lower leading-edge corner of the plate; so s runs from 0 to 1 along the front (windward) surface, 1 to 2 the upper surface, 2 to 3 along the base (leeward) surface and 3 to 4 along the lower surface. The pressure field is sampled at the end of each time step. This makes the sampling period equal to $\Delta t = 0.02$. The averages shown are for time ranges (indicated in Fig. 7.35) beginning when the flow appears to be essentially fully developed and ending at the limit of the calculations.

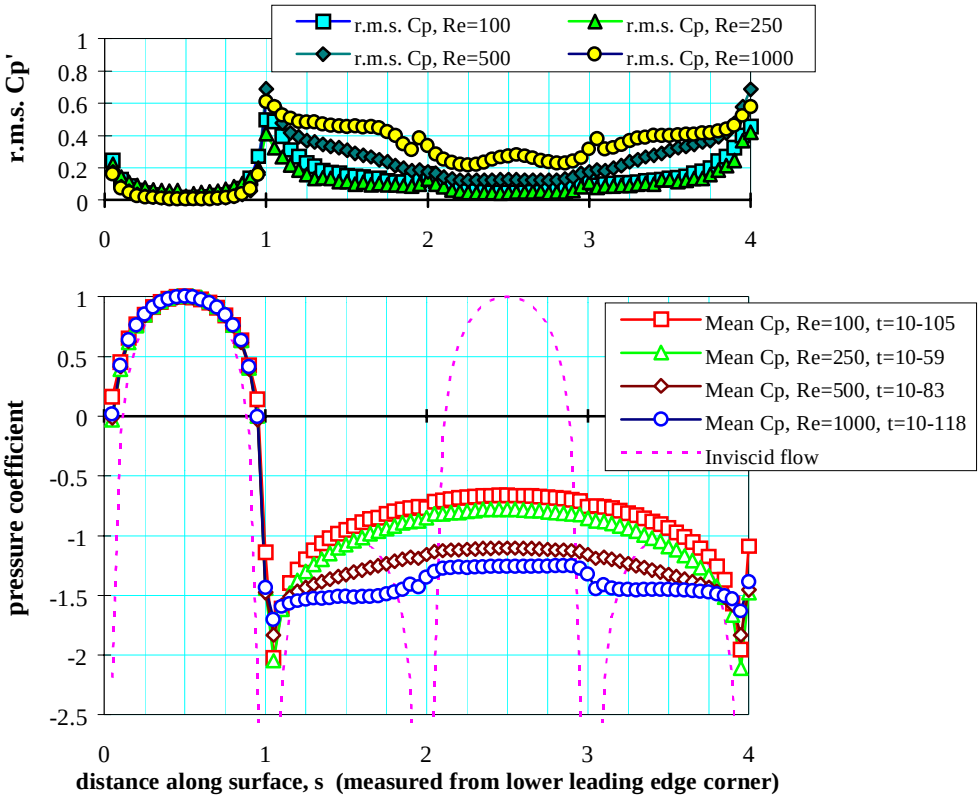

Figure 7.35. Predicted distributions of mean and r.m.s. pressure coefficients along surface of a square cylinder at Re_h = 100, 250, 500 and 1,000.

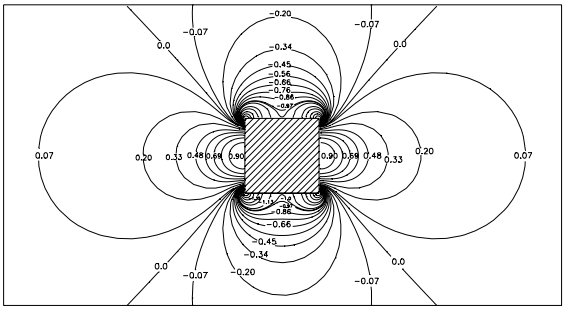

Figure 7.36. Inviscid-flow pressure field around a square cylinder. Numbers shown are coefficients of static pressure.

It can be seen from Fig. 7.35 that the pressure distribution on the leading face is essentially independent of Reynolds number and is very similar to the inviscid-flow pressure distribution (Fig. 7.36). The surface pressure decreases from $C_p \approx 1$ at the front stagnation point ($s = 0.5$) to the lowest pressure $C_p \approx -2$ on the side surfaces near the leading edge corners. On both the upper and lower surfaces, the pressure gradually rises and reaches the base pressure on the leeward surface. The base pressure, and with it the pressure rise along the side surfaces, decreases as the Reynolds number is increased.

The r.m.s. pressure fluctuation $C_{p'}$ on the front face increases from the front stagnation point to the leading corners where the highest value of $C_{p'}$ overall occurs, and is insensitive to Reynolds number. The distributions of surface-pressure shown in Fig. 7.35 are consistent with the changes in the instantaneous pressure fields around the cylinder over one vortex-shedding cycle at the selected Reynolds numbers shown in Figs. 7.22, 7.26, 7.30 and 7.34. The latter figures show that the pressure field upstream of the cylinder is very similar to the inviscid-flow pressure field (Fig. 7.36); and that high pressure gradients occur in the flow near the leading-edge corners of the cylinder and in the regions of flow reattachment on the side surfaces. Figures 7.30 and 7.34 show that the pressure gradients associated with flow reattachment become stronger as Re_h increases. Thus fluctuations in the location of flow reattachment on the side surfaces lead to greater surface-pressure-fluctuations as the Reynolds number is increased. This is reflected in the high values of r.m.s. pressure fluctuation on the side surfaces of the cylinder at $Re_h = 500$ and 1,000 shown in Fig. 7.35.

Computed mean base pressures $-C_{pb}$, numerical results of Sohankar *et al.* [1995] and experimental results of Okajima [1982] and Okajima *et al.* [1992] are tabulated in Table 7.1. In making comparisons, observed three-dimensionalities in flow over long-chord plates for $Re_h > 200$ (section 7.1) should be remembered. On this account, agreement here (and for plates with

larger values of C, discussed later) between calculated and experimental pressure and force coefficients, at significantly higher Reynolds numbers, has to be treated with some reserve. However, for square cylinders, computed base pressures in the present study are in fair agreement with those of Sohankar *et al*. at Re_h =100 and 250; and the computed $-C_{pb}$ =1.3 at Re_h =1,000 is in very good agreement with the experimental result, 1.28, of Okajima *et al*.

Re_h	St^a	St^b	St^c	St^d	$-C_{pb}{}^a$	$-C_{pb}{}^b$	$-C_{pb}{}^d$	$C_{Dp}{}^a$	$C_{Dp}{}^b$	$C_{Dp}{}^d$
100	0.142	0.145	0.14	0.14 - 0.145	0.63	0.623	—	1.4	1.398	—
250	0.146	0.151	—	0.14 - 0.142	0.75	0.832	—	1.5	1.501	—
500	0.132	—	0.143	0.125	1.15	—	—	1.8	—	—
1,000	0.125	—	0.132	0.13	1.3	—	1.28	2.0	—	1.95

a This study, numerical results by discrete vortex method.

b Computed $-C_{pb}$ and C_{Dp} at Re_h = 100 and 250 by Sohankar *et al.* [1995] using finite volume method.

c Computed *St* value by Arnal, Goering and Humphrey [1991] using finite difference method.

d Experimental results of *St*, $-C_{pb}$ and C_{Dp} at Re_h = 1,000 obtained by Okajima *et al.* [1992]; experimental results of *St* at Re_h = 100, 250 and 500 based on the fluctuating velocities in the wake, obtained by Okajima [1982].

Table 7.1. Comparison between calculations of the present study and experimental data and other numerical results for Strouhal number, base pressure coefficient and pressure drag coefficient for square cylinder flow.

The time histories of drag and lift coefficients obtained in the present study for Re_h = 100, 250, 500 and 1,000 are presented in Figs. 7.37, 7.38, 7.39 and 7.41 respecti vely, where the computed results for C_D and C_L at each time step, Δt = 0.02, of the calculation are plotted against time t. (Note, however, that for the Re_h = 100 and Re_h = 1,000 plots, Figs. 7.37 and 7.41, the values shown are the averages of every two successive time-steps, for convenience in reducing the record length for data plotting). In the cases of the Re_h = 100 and 250 data, because of the small amplitude of lift and drag variations in relation to "numerical noise", values of C_D and C_L averaged over every forty successive time-steps are shown in order to highlight the genuine periodicities. It can be seen from these figures that, in general, after the initial flow development stage the variations of drag and lift become periodic with fairly constant amplitude, and the amplitude of variation increases with Reynolds number. At Reynolds numbers Re_h = 100, 250 and 500, the time histories are quite regular, although there is some slight modulation of the traces for Re_h = 500, which appears to be consistent with the irregularities in vortex shedding noted earlier in section 7.2.2.2. Similar, but stronger, modulation of the lift and drag time-histories at this Reynolds number occurs in the results of the finite-difference calculation of Arnal *et al*. [1991].

For Re_h = 500, the general patterns and magnitudes of lift and drag variation obtained in the present study are very similar to those calculated by Okajima [1990] using the finite difference method, which are reproduced in Fig. 7.40. With an increase of Reynolds number to Re_h = 1,000, the subharmonic content in the time histories becomes greater and the modulation more pronounced. This is a reflection of the greater irregularity in vortex shedding at this Reynolds number than at Re_h = 500 discussed earlier in section 7.2.2. The finite-difference calculations of Okajima *et al.* [1992] and Arnal *et al.* [1991] also show frequency modulation in the lift and drag histories at Re_h = 1,000. There are clearly strong similarities between the traces obtained by Okajima *et al*. which are reproduced in Fig. 7.42 and those of the present work shown in Fig. 7.41.

The values of mean pressure drag coefficients C_{Dp} obtained from the time-histories of fluctuating drag coefficients at the four selected Reynolds numbers are summarised in Table 7.1. Comparison of them with other published data shows that they are, in general, in good agreement with the results of experiment and other numerical schemes over this Reynolds number range: values at Re_h = 100 and 250 agree well with the numerical results of Sohankar *et al.* [1995]; and the computed pressure drag coefficient C_{Dp} = 2 at Re_h = 1,000, is in very good agreement with the experimental value C_{Dp} = 1.95 obtained by Okajima [1992].

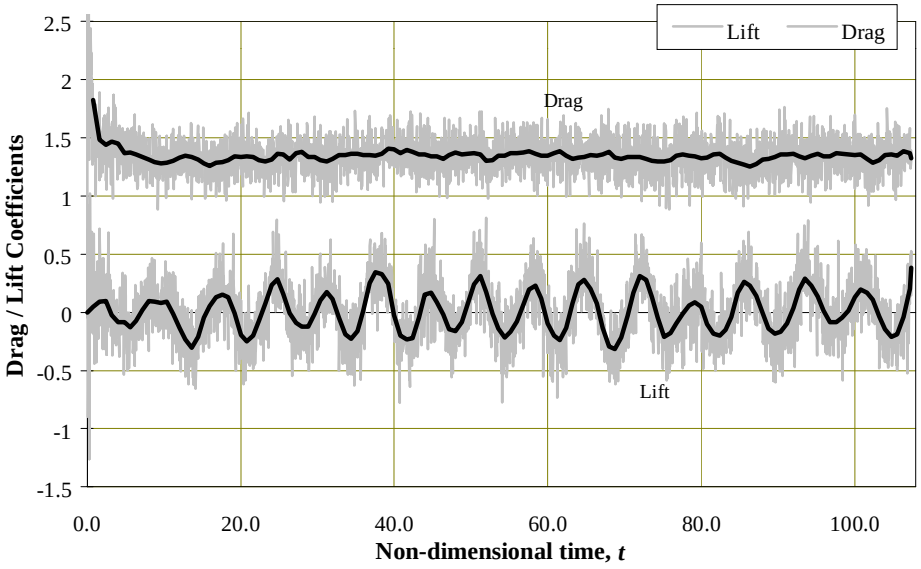

Figure 7.37. Time-histories of calculated drag and lift coefficients on a square cylinder at Re_h = 100. Drag and lift are calculated for Δt = 0.02, averaged over Δt = 0.04; highlighted mean drag and lift are averaged over Δt = 0.8.

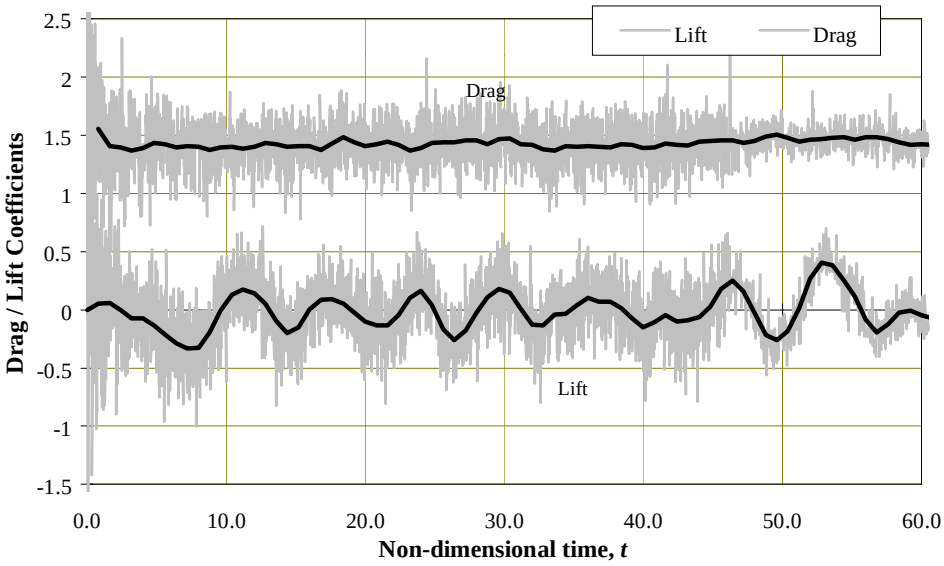

Figure 7.38. Time-histories of calculated drag and lift coefficients on a square cylinder at $Re_h = 250$. Drag and lift are calculated for $\Delta t = 0.02$; highlighted mean drag and lift are averaged over $\Delta t = 0.8$.

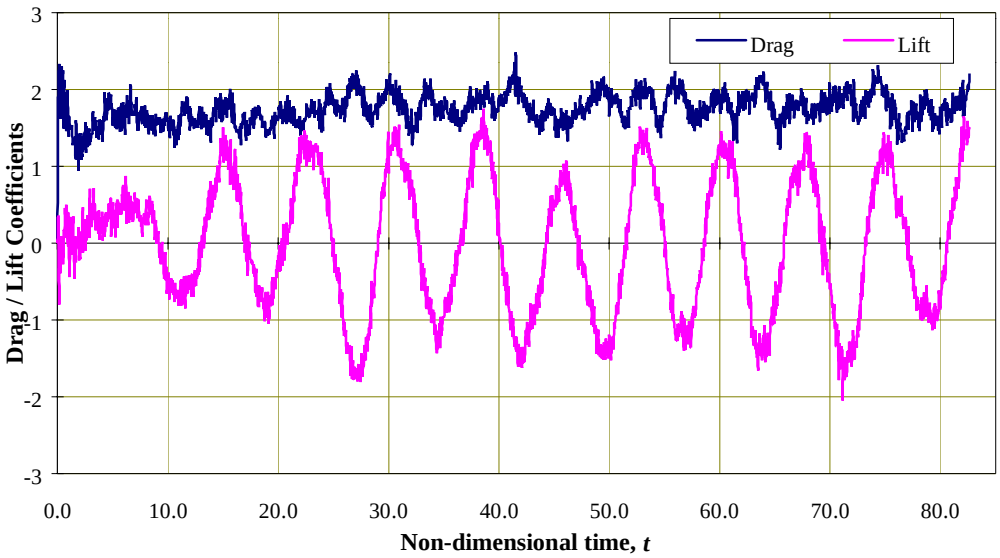

Figure 7.39. Time-histories of calculated drag and lift coefficients on a square cylinder at $Re_h = 500$. Drag and lift are calculated for $\Delta t = 0.02$.

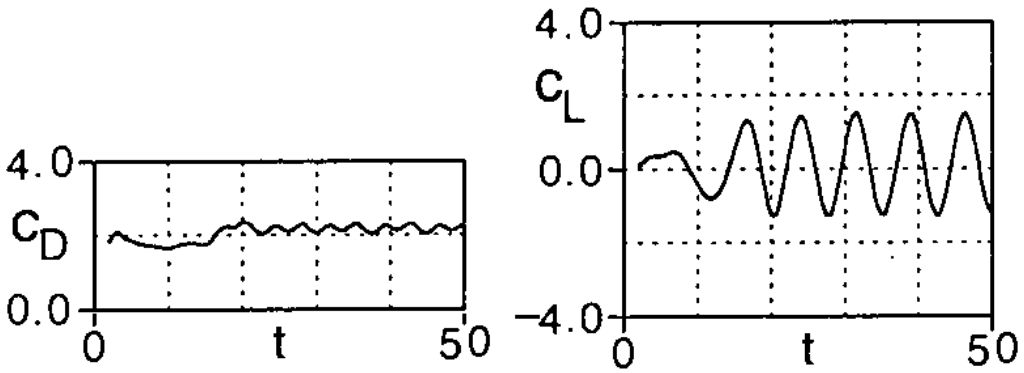

Figure 7.40. Time-histories of drag and lift coefficients on a square cylinder at $Re_h = 500$ calculated by Okajima [1990] using finite difference method.

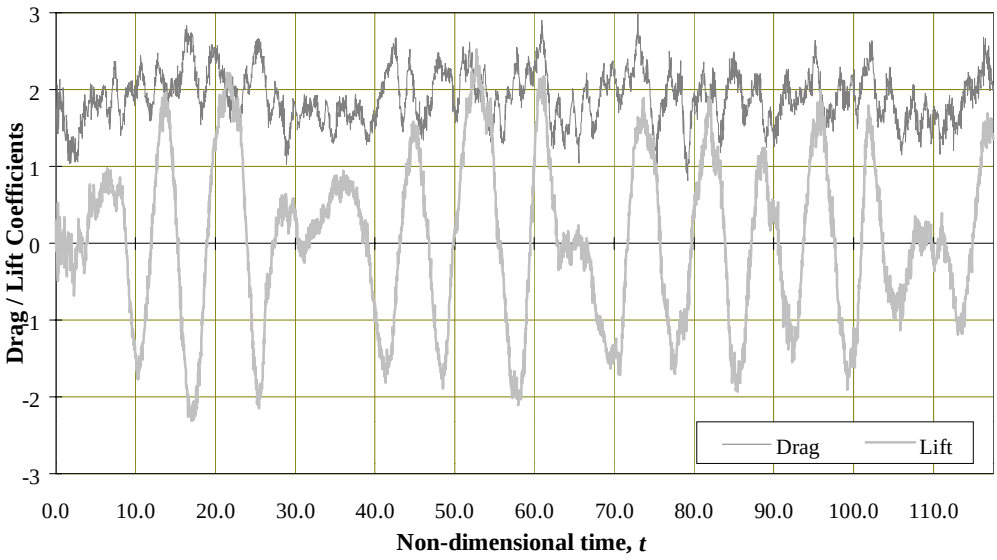

Figure 7.41. Time-histories of calculated drag and lift coefficients on a square cylinder at Re_h = 1,000. Drag and lift are calculated for Δt = 0.02.

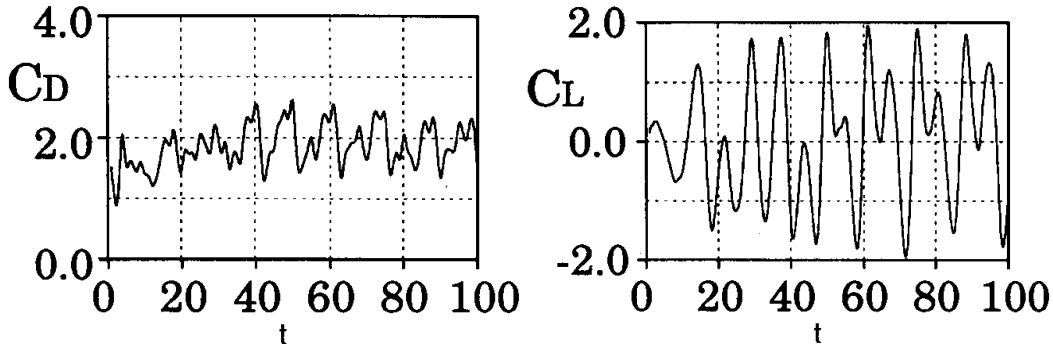

Figure 7.42. Time-histories of drag and lift coefficients on a square cylinder at Re_h = 1,000 calculated by Okajima, Ueno and Sakai [1992] using finite difference method.

7.3.2.4 Strouhal Numbers

The power spectra of fluctuating lift for square-cylinder flow at the four Reynolds numbers considered in the present calculation are presented in Fig. 7.43. They have been estimated by using the maximum entropy method, the data used for signal analysis being averages over 10 time-steps which gives a sampling period of Δt = 0.2. A dominant sharp peak occurs in the spectrum for all four Reynolds numbers. The frequency of this peak is identified with the dominant frequency of vortex shedding from the cylinder.

For Re_h = 100, 250 and 500 this peak is the only one which appears in the spectrum. In the case of Re_h = 500, as previously noted, the time histories of lift and drag are slightly modulated, but the modulation is apparently too weak to affect the spectrum. The corresponding calculations of Arnal *et al*. [1991] show rather stronger modulation at this Reynolds number, leading to the appearance of spectral harmonics and subharmonics of the main vortex-shedding frequency and other frequencies.

The strongly modulated lift and drag histories at Re_h = 1,000 give spectra with multiple peaks. The main peak in the lift spectrum indicates a vortex-shedding frequency of St = 0.125. As expected, the drag spectrum shows a peak at twice this frequency. But this peak is not the major one in the drag spectrum; the main peak occurs at the much lower frequency of St = 0.035. In fact, all the peaks in the drag spectrum occur at Strouhal numbers which are close to integer multiples of the Strouhal number corresponding to that of the major peak – i.e. given by 0.035n, where n is an integer, generally odd – while the peaks in the lift spectrum occur close to 0.035(n + ½). The same pattern occurs in the results of Arnal *et al*.; they find St = 0.132 as the dominant vortex-shedding frequency from the lift spectrum, but their maximum drag peak occurs at St = 0.07, corresponding to n = 2 rather than 1. They attribute a large part of the cycle-to-cycle variation in lift and drag to variation in strength of the shed vortices.

Strouhal numbers, $St \equiv fh/U_\infty$, corresponding to the spectral peaks of Fig. 7.43, are listed in Table 7.1 for the four Reynolds numbers considered. Experimental results for these same Reynolds numbers obtained by Okajima [1982] and by Okajima *et al*. [1992] are also summarised in Table 7.1, together with numerical results obtained by Sohankar *et al*. [1995] using the finite volume method and by Arnal *et al*. [1991] using finite differences. There is fairly good agreement amongst the computed results, and the calculated St values obtained in the present study agree particularly well with the experimental results. A more general picture of the variation with Reynolds number of the Strouhal number for square-cylinder flow is given by Fig. 7.44 which shows the experimental results of Okajima [1982] and Davis and Moore [1982] as well as the numerical results of Davis and Moore [1982], Franke, Rodi and Schönung [1990], Arnal, Goering and Humphrey [1991] and of the present calculations.

As previously observed by Franke, Rodi and Schönung [1990], there are large discrepancies between the experimental results of Okajima [1982] and Davis and Moore [1982]. Franke *et al.* suggest that the sharpness of the cylinder corners in the experiments and the treatment of the corners in numerical procedures may be significant factors contributing to the discrepancies.

The Strouhal numbers predicted by the present calculations are in very good agreement with the experimental results of Okajima [1982], both in magnitude and in the general pattern of variation with the Reynolds number.

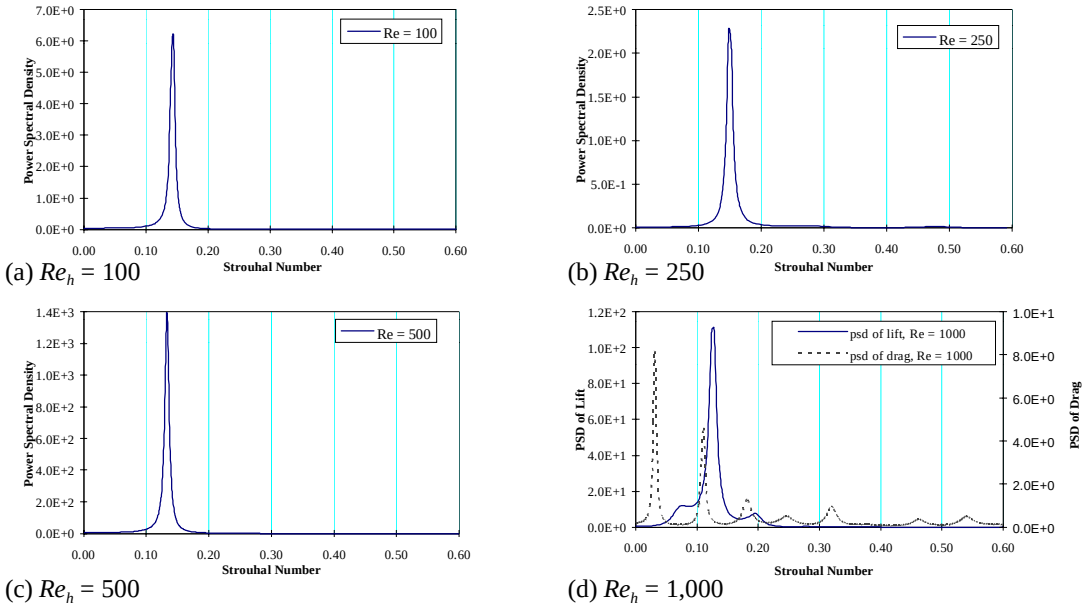

Figure 7.43. Power spectra of fluctuating lift on a square cylinder at Reynolds numbers of (a) Re_h = 100, (b) 250, (c) 500 and (d) 1,000.

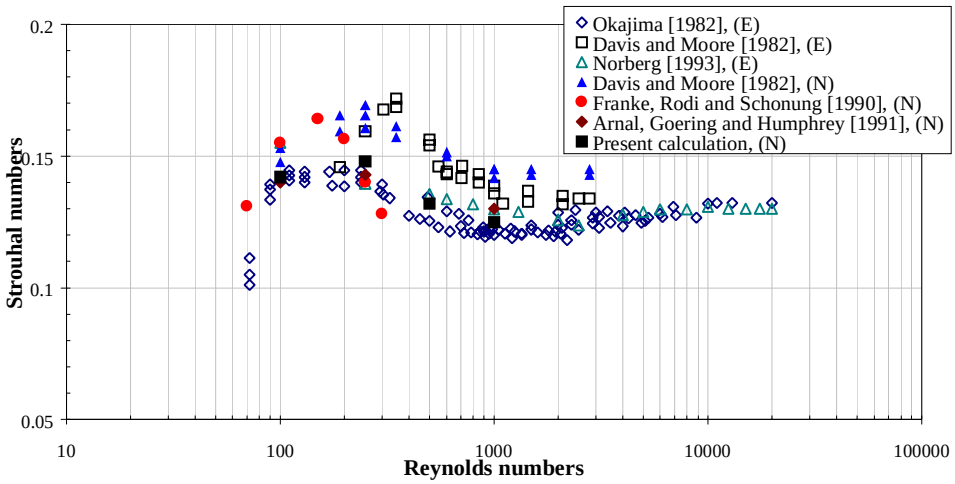

Figure 7.44. Variation of Strouhal number with Reynolds number for a square cylinder, C = 1.

7.4 Flow Over Single Rectangular Plates with $C = 2$ and $C = 4$

Calculations of flow over a single rectangular plate have also been performed on plates with chord-to-thickness ratio $C = 2$ and 4 at the Reynolds numbers of $Re_h = 100$, 250, 500 and 1,000. For the plate with $C = 2$, the body contour is represented by 120 uniform straight segments ($M = 120$), with 20 and 40 segments on each of the short and long sides respectively; the plate with $C = 4$ is represented by 200 uniform straight segments ($M = 200$), with 20 and 80 segments on each of the short and long sides respectively. For $C = 2$, the value of ϵ is $1.15\sqrt{(\Delta t/Re_h)}$ for $Re_h = 100$, and $1.7\sqrt{(\Delta t/Re_h)}$ for $Re_h = 250$, 500 and 1,000; for $C = 4$, the value of ϵ is $1.15\sqrt{(\Delta t/Re_h)}$ throughout.

7.4.1 Flow Development on Rectangular Plates with $C = 2$ and $C = 4$

Flow development on the plates with $C = 2$ at Reynolds numbers of $Re_h = 100$, 250, 500 and 1,000 is shown in terms of elemental-vortex distributions in Figs. 7.45–48, streamline patterns in Figs. 7.49–52 and vorticity contours in Figs 7.53–56. Corresponding results for the plate with $C = 4$ are shown in Figs. 7.57–7.68. For both plates, the figures indicate that in the initial stage of flow development, shear layers separate from the leading corners of the plate and reattach to the side surfaces. Downstream of reattachment, the flow remains fully-attached along the side faces and finally separates from the trailing corners. The shear layers separating from the trailing corners quickly roll up (within the time range $0 \le t < 2$) to form a closed recirculation region, comprising two counter-rotating vortices, immediately behind the plate.

For the $C = 2$ plate at Reynolds numbers of $Re_h = 100$ and 250, the recirculation region gains vorticity from the shear layers separating from the trailing corners and extends in the streamwise direction. Instability in the extended recirculation region leads to vortex shedding: positive and negative vortices are shed alternately from the upper and lower surfaces of the plate to form a vortex street. The computed flow patterns for $Re_h = 500$ and 1,000 indicate that, in the initial stage of flow development (before $t = 2$), shear layer separation from a leading corner and reattachment to a side surface results in formation of a separation bubble on the side surface. A short time later (before $t = 4$) large-scale discrete vortices form in the separation bubble and are convected along the side surface. The first arrival of a convected vortex at the trailing corner appears to coincide with the transition from a closed recirculation region downstream of the plate to the vortex shedding regime at these Reynolds numbers.

For the C = 4 plate, the flow patterns for Re_h = 100 and 250 indicate that reattachment of leading-edge shear layers is accompanied by a weak process of vortex formation on the side surfaces, similar to that occurring on the C = 2 plate at higher Reynolds numbers. Because the vortical motion of the rolled-up vortices at these Reynolds numbers is so weak, the flow is essentially fully attached to the side surfaces downstream of reattachment at all times. Thus, the closed recirculation region gains vorticity mainly from the shear layers separating from the trailing edges. As the flow develops, this recirculation region grows and extends in the streamwise direction. Instability of the extended recirculation region then leads to periodic vortex shedding from the cylinder.

At the higher Reynolds numbers Re_h = 500 and 1,000, discrete vortices, stronger than on the cylinder with C = 2, form on the side surfaces of the C = 4 cylinder. These vortices are convected along the side surfaces. Thus, for the C = 4 plate, with its longer chord, the flow downstream of reattachment is fully attached, with intermittent passage of discrete vortices. The closed recirculation region therefore gains vorticity from both convected discrete vortices and the shear layers separating from the trailing edges of the cylinder. Instability of the recirculation region, as before, leads to periodic vortex shedding from the cylinder.

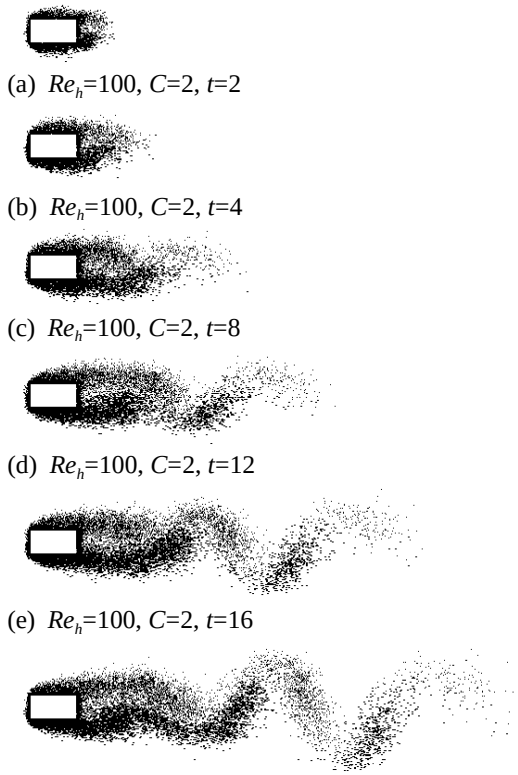

(a) Re_h=100, C=2, t=2

(b) Re_h=100, C=2, t=4

(c) Re_h=100, C=2, t=8

(d) Re_h=100, C=2, t=12

(e) Re_h=100, C=2, t=16

(f) Re_h=100, C=2, t=20

Figure 7.45. Elemental-vortex distributions in flow over C = 2 cylinder at Re_h = 100.

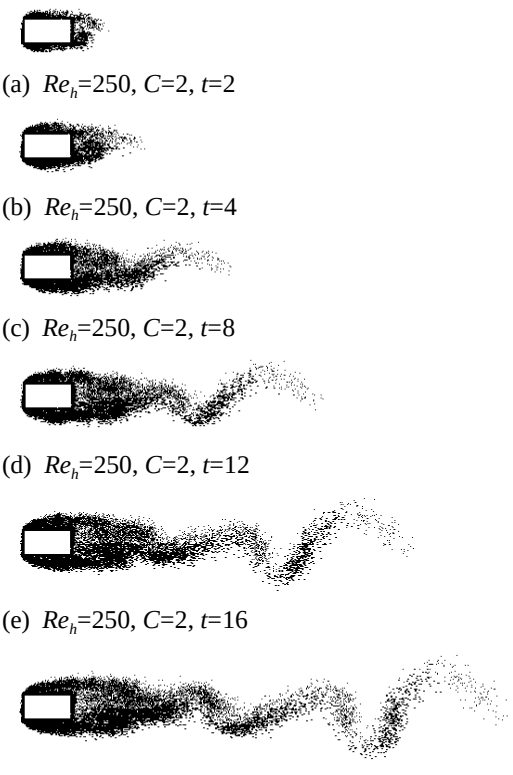

(a) Re_h=250, C=2, t=2

(b) Re_h=250, C=2, t=4

(c) Re_h=250, C=2, t=8

(d) Re_h=250, C=2, t=12

(e) Re_h=250, C=2, t=16

(f) Re_h=250, C=2, t=20

Figure 7.46. Elemental-vortex distributions in flow over C = 2 cylinder at Re_h = 250.

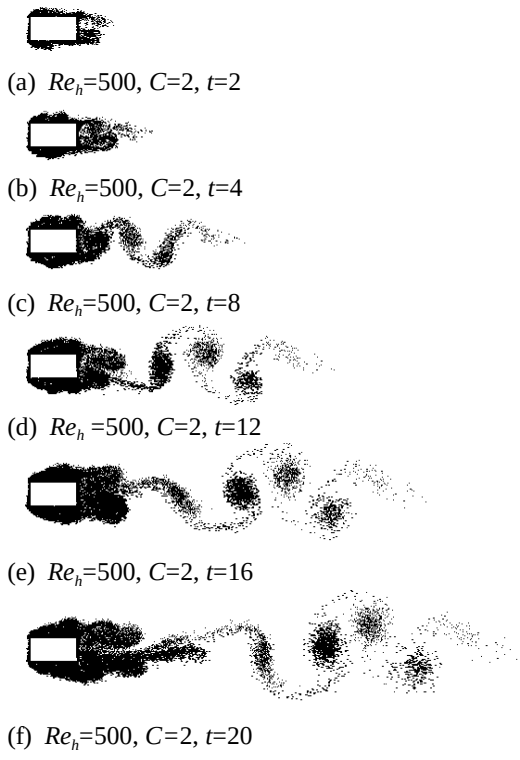

(a) Re_h=500, C=2, t=2

(b) Re_h=500, C=2, t=4

(c) Re_h=500, C=2, t=8

(d) Re_h =500, C=2, t=12

(e) Re_h=500, C=2, t=16

(f) Re_h=500, C=2, t=20

Figure 7.47. Elemental-vortex distributions in flow over C = 2 cylinder at Re_h = 500.

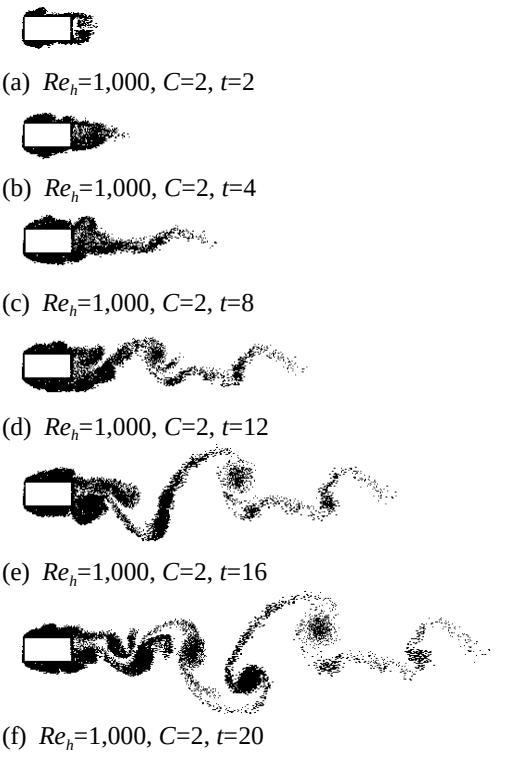

(a) Re_h=1,000, C=2, t=2

(b) Re_h=1,000, C=2, t=4

(c) Re_h=1,000, C=2, t=8

(d) Re_h=1,000, C=2, t=12

(e) Re_h=1,000, C=2, t=16

(f) Re_h=1,000, C=2, t=20

Figure 7.48. Elemental-vortex distributions in flow over C = 2 cylinder at Re_h=1,000.

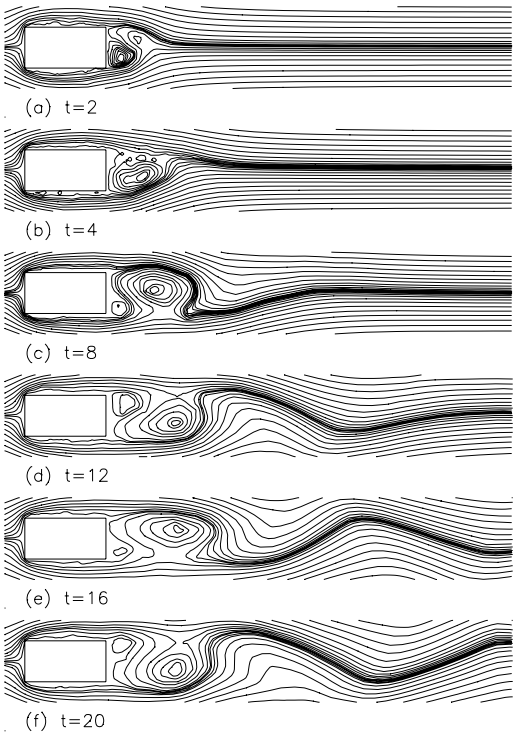

Figure 7.49. Streamline patterns in flow over $C = 2$ cylinder at $Re_h = 100$.

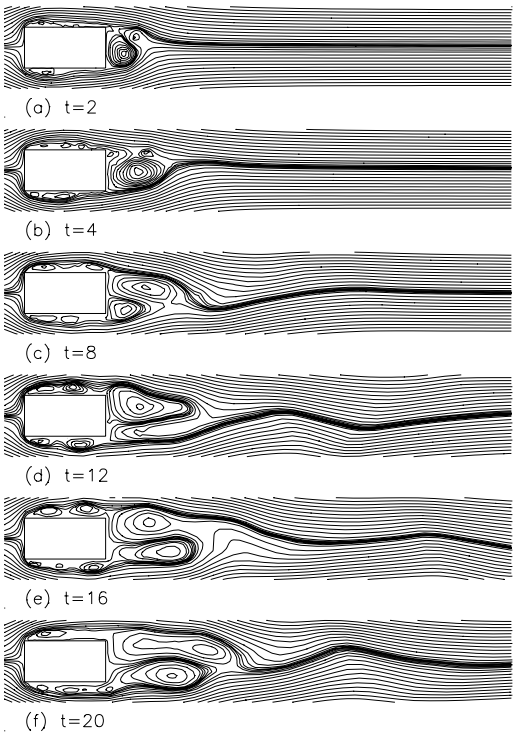

Figure 7.50. Streamline patterns in flow over $C = 2$ cylinder at $Re_h = 250$.

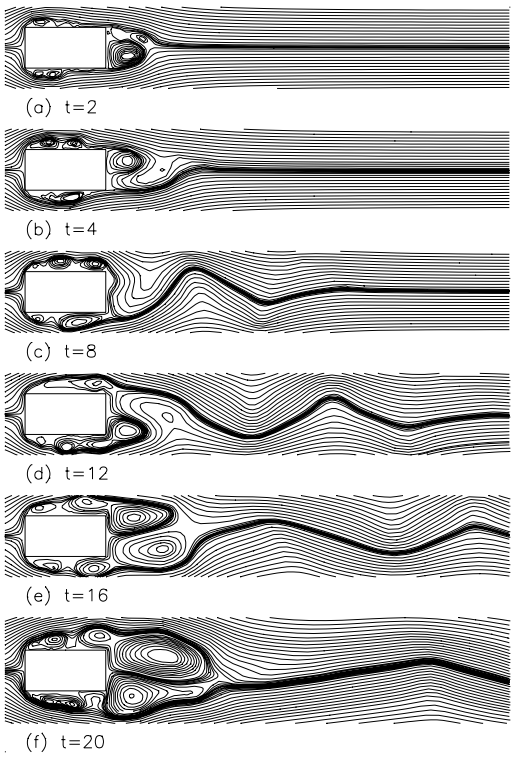

Figure 7.51. Streamline patterns in flow over $C = 2$ cylinder at $Re_h = 500$.

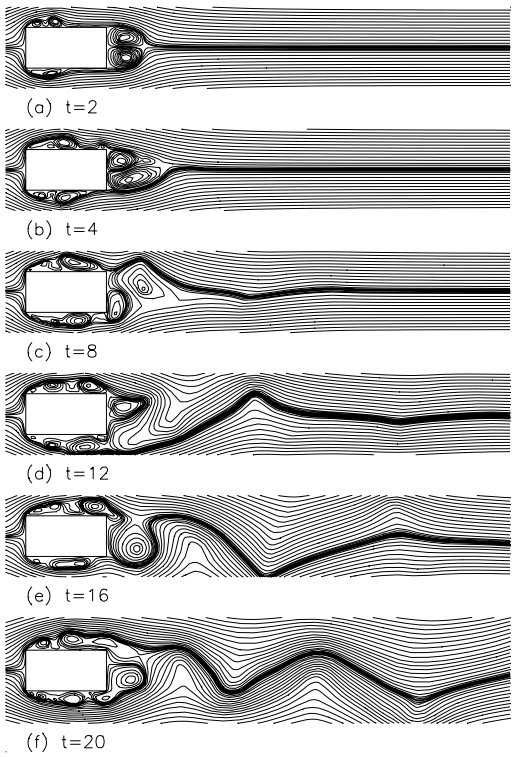

Figure 7.52. Streamline patterns in flow over $C = 2$ cylinder at $Re_h = 1{,}000$.

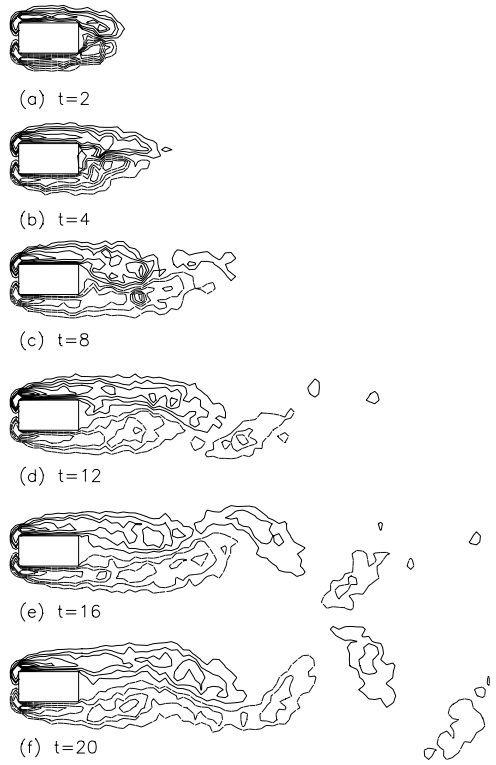

Figure 7.53. Vorticity contours in flow over C = 2 cylinder at Re_h = 100.

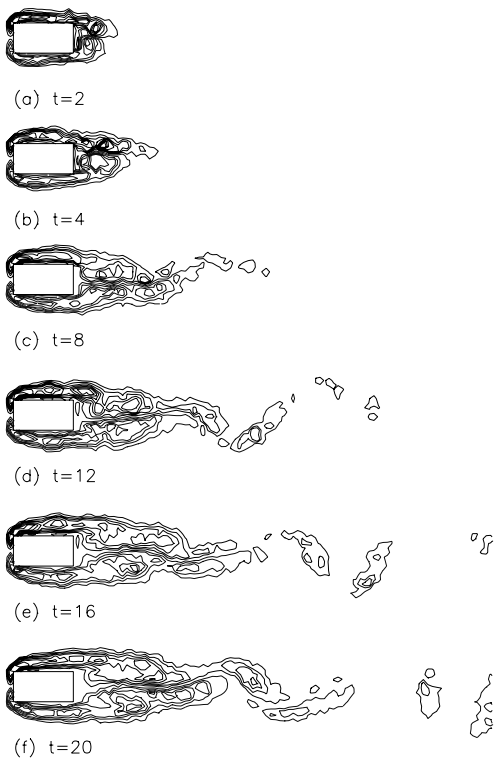

Figure 7.54. Vorticity contours in flow over C = 2 cylinder at Re_h = 250.

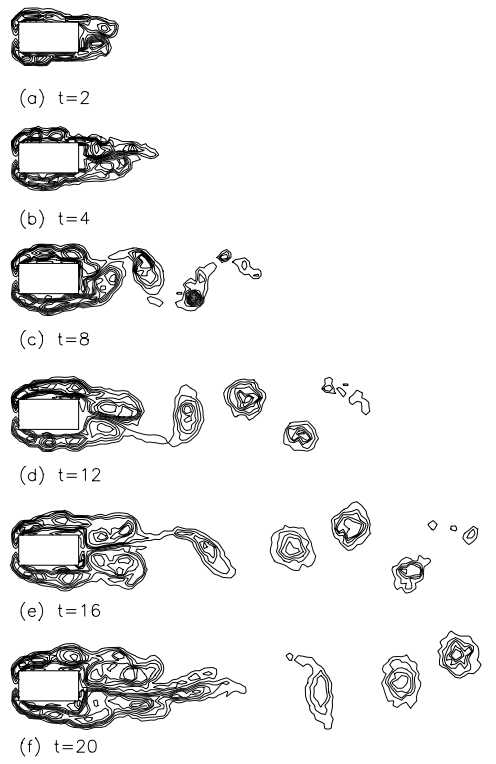

Figure 7.55. Vorticity contours in flow over C = 2 cylinder at Re_h = 500.

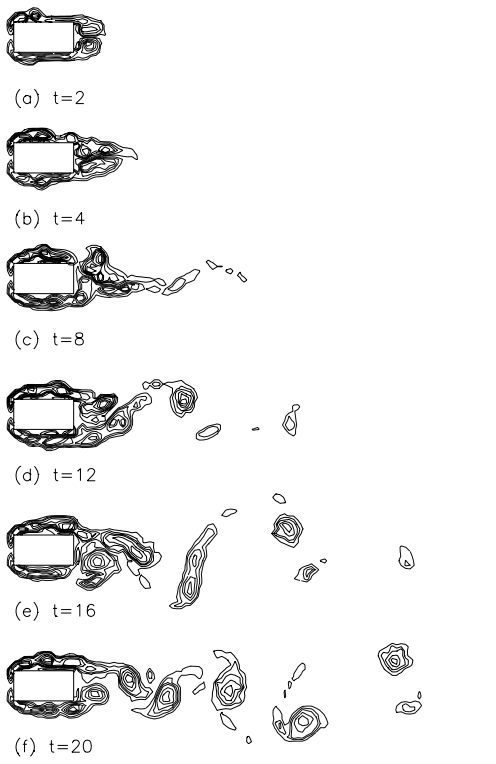

Figure 7.56. Vorticity contours in flow over C = 2 cylinder at Re_h = 1,000.

(a) Re_h = 100, C = 4, t = 2

(b) Re_h = 100, C = 4, t = 4

(c) Re_h = 100, C = 4, t = 8

(d) Re_h = 100, C = 4, t = 12

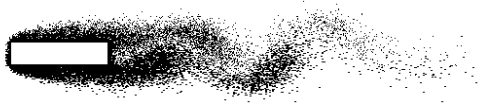

(e) Re_h = 100, C = 4, t = 16

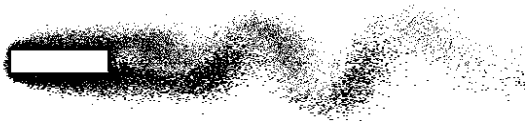

(f) Re_h = 100, C = 4, t = 20

Figure 7.57. Elemental-vortex distributions in flow over C = 4 cylinder at Re_h = 100.

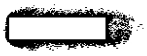

(a) Re_h = 250, C = 4, t = 2

(b) Re_h = 250, C = 4, t = 4

(c) Re_h = 250, C = 4, t = 8

(d) Re_h = 250, C = 4, t = 12

(e) Re_h = 250, C = 4, t = 16

(f) Re_h = 250, C = 4, t = 20

Figure 7.58. Elemental-vortex distributions in flow over C = 4 cylinder at Re_h = 250.

(a) Re_h=500, C=4, t=2

(b) Re_h=500, C=4, t=4

(c) Re_h=500, C=4, t=8

(d) Re_h=500, C=4, t=12

(e) Re_h=500, C=4, t=16

(f) Re_h=500, C=4, t=20

Figure 7.59. Elemental-vortex distributions in flow over C = 4 cylinder at Re_h = 500.

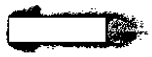

(a) Re_h=1,000, C=4, t=3

(b) Re_h=1,000, C=4, t=6

(c) Re_h=1,000, C=4, t=9

(d) Re_h=1,000, C=4, t=12

(e) Re_h=1,000, C=4, t=15

(f) Re_h=1,000, C=4, t=18

Figure 7.60. Elemental-vortex distributions in flow over C = 4 cylinder at Re_h = 1,000.

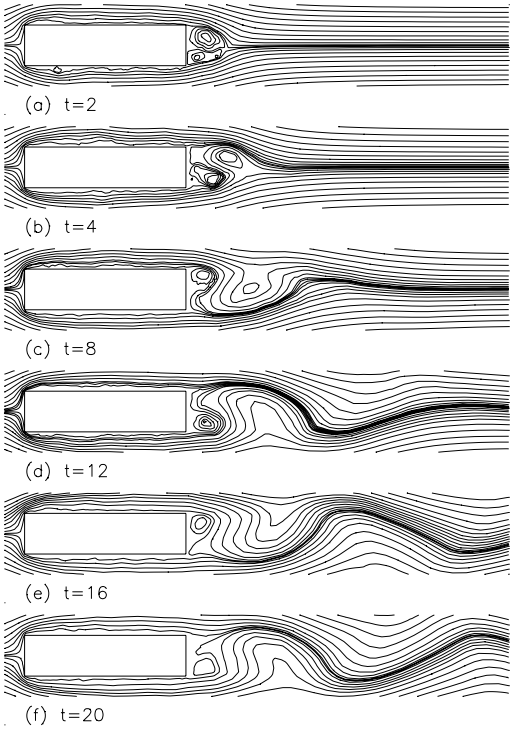

Figure 7.61. Streamline patterns in flow over C = 4 cylinder at Re_h = 100.

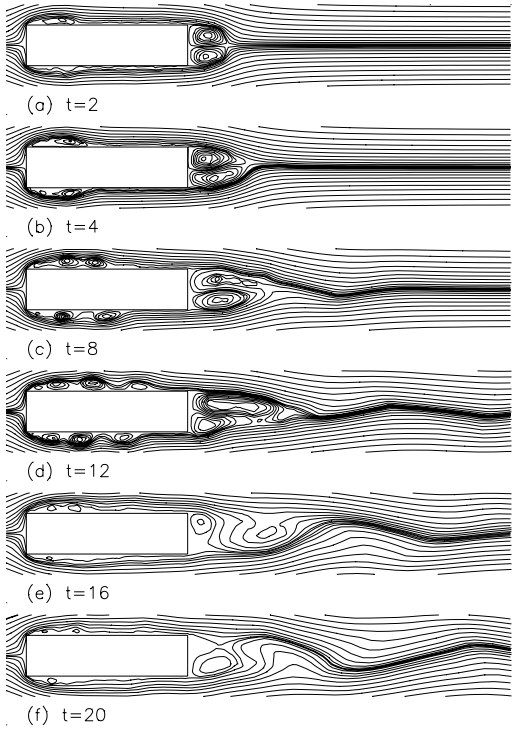

Figure 7.62. Streamline patterns in flow over C = 4 cylinder at Re_h = 250.

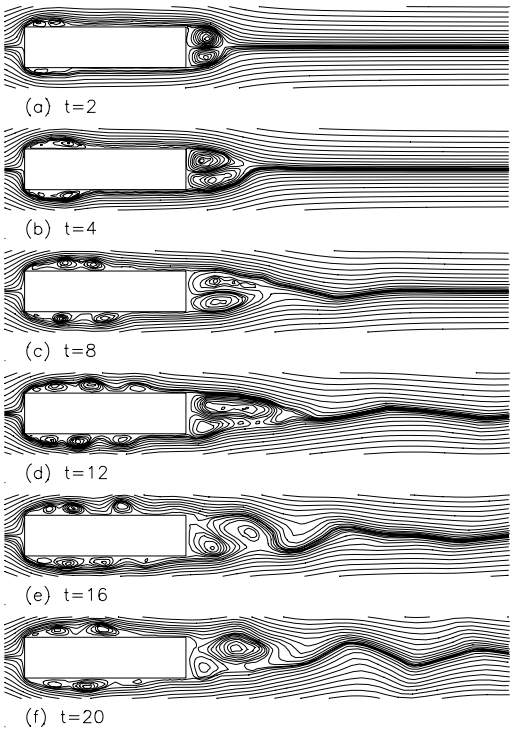

Figure 7.63. Streamline patterns in flow over C = 4 cylinder at Re_h = 500.

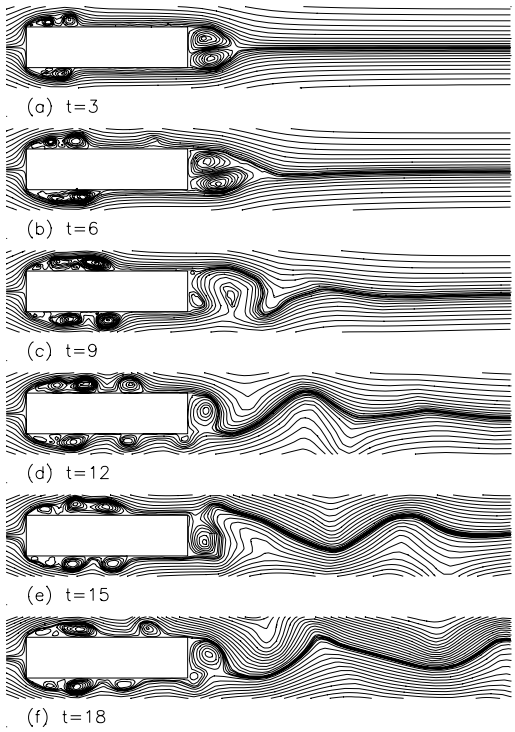

Figure 7.64. Streamline patterns in flow over C = 4 cylinder at Re_h = 1,000.

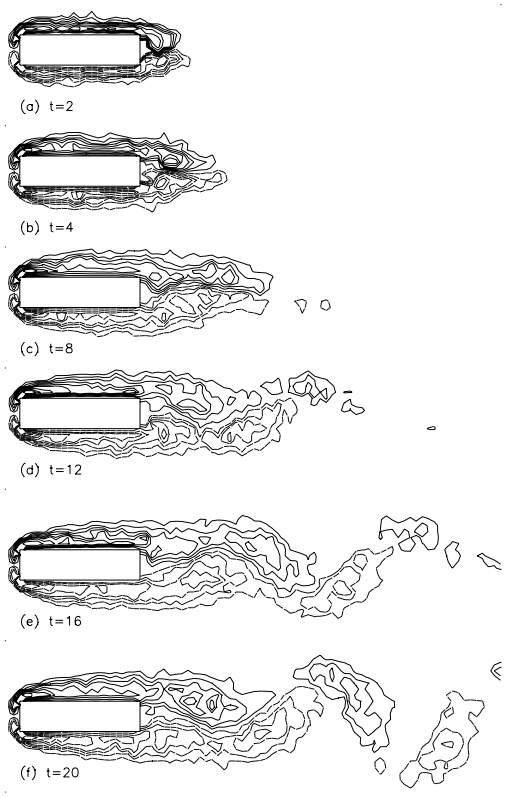

Figure 7.65. Vorticity contours in flow over C = 4 cylinder at Re_h = 100.

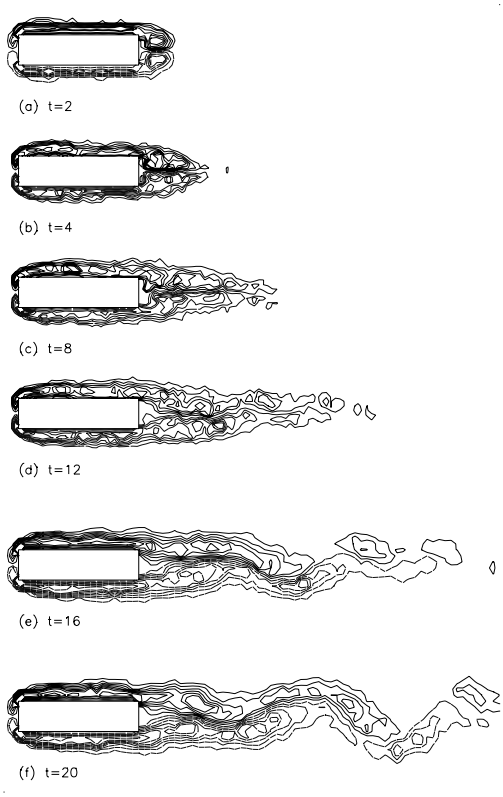

Figure 7.66. Vorticity contours in flow over C = 4 cylinder at Re_h = 250.

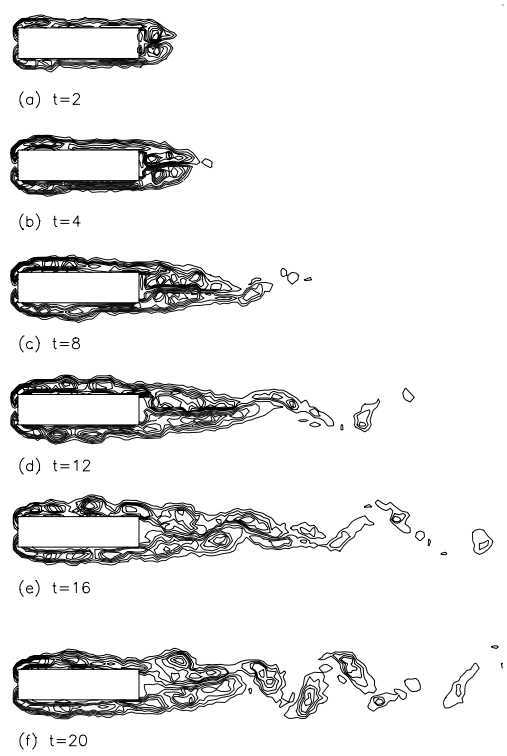

Figure 7.67. Vorticity contours in flow over C = 4 cylinder at Re_h = 500.

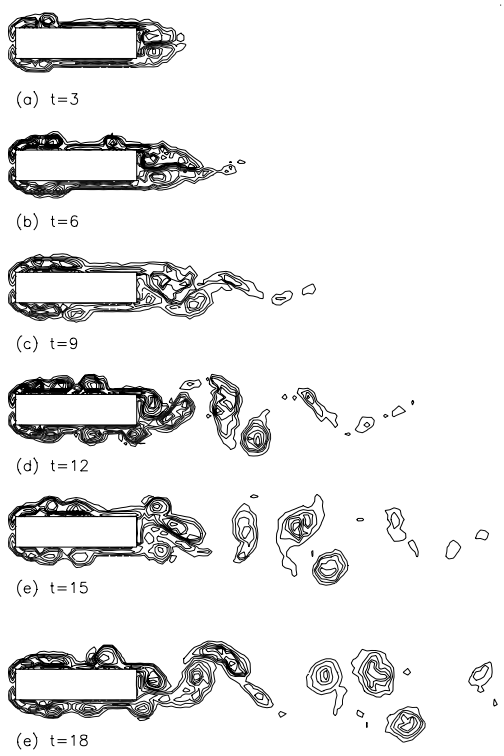

Figure 7.68. Vorticity contours in flow over C = 4 cylinder at Re_h = 1,000.

7.4.2 Fully-Developed Flow Over a Rectangular Plate with $C = 2$

Rectangular plates with $C = 2$ have been extensively investigated: by Lane and Loehrke [1980], Okajima [1982], Okajima [1990], Okajima, Nagahisa and Rokugoh [1990], Okajima, Ueno and Sakai [1992], Norberg [1993] and others. The generalised dependence of the fully-developed flow regime on C and Re_h presented earlier as Fig. 7.1 indicates a sequence of three flow regimes as Re_h increases from 100 to 1000. At the lower end of this range, steady flow with laminar separation from the leading corners and laminar reattachment to the side surfaces is indicated. A change occurs at $Re_h \sim 250$ to a flow with laminar leading-corner separation followed by intermittent turbulent reattachment to the side surfaces, which persists to $Re_h \sim 500$. For $Re_h > 500$, the figure indicates flow with turbulent separation from the leading edges and no reattachment to the side faces.

The computational results of the present study for $Re_h = 100$ are presented in Figs. 7.73 to 7.76: distributions of elemental vortices in Fig. 7.73; streamline patterns in Fig. 7.74; vorticity contours in Fig. 7.75; instantaneous pressure distributions in Fig. 7.76. Corresponding results for Reynolds numbers of 250, 500 and 1000 are presented in Figs. 7.77 to 7.80; Figs. 7.81 to 7.84 and Figs. 7.85 to 7.88 respectively. Calculated time histories of lift and drag for $Re_h = 100$, 250, 500 and 1,000 are shown in Figs. 7.89–92 respectively, and power spectra of lift fluctuations in Fig. 7.94. Calculated Strouhal numbers and surface-pressure distributions as a function of Reynolds number are shown in Fig. 7.72 and Fig. 7.95 respectively.

7.4.2.1 Comparisons of Present Results with Existing Experimental and Numerical Data

The experimental results of Okajima [1982] on the effects of Reynolds number on flow regime are as outlined above in section 7.4.2, having been used in the construction of Fig. 7.1. They also show that the sudden change in flow regime, from one with intermittent separation from and reattachment to the side surfaces of the plate to one with predominantly fully-separated flow and wider wake, which occurs at $Re_h \approx 500$, produces a striking change in the vortex-shedding characteristic of $C = 2$ plates: the Strouhal number rises continuously with increasing Reynolds number at low Reynolds number, but drops sharply, and apparently discontinuously, as the Reynolds number is increased through a value of about 500. Streamline patterns calculated by Okajima [1982] for $Re_h = 250$ and $Re_h = 600$, respectively below and above the critical value, appear to be consistent with the experimental patterns: for $Re_h = 250$, attached

flow (with leading-edge separation bubble) on a side face alternates with fully-detached flow, but the flow is always attached to one or other of the side faces; for Re_h = 600, reattachment on the side faces does sometimes occur, but the dominant pattern is simultaneous fully-separated flow over both side surfaces. The calculations reproduce the Strouhal number discontinuity, although the calculated Strouhal numbers are significantly lower than the measured values for $Re_h \lesssim 500$. It is notable that the calculated flow for Re_h = 600 exhibits both the high and low Strouhal frequencies associated with the discontinuity.

Okajima [1990] presents further calculated flow results for Re_h = 250 and 500. In these results, the spectrum of lift fluctuations at Re_h = 250 shows two distinct peaks, that with the higher Strouhal number predominating at large flow-development times. At Re_h = 500, only one spectral peak, at the lower Strouhal number, is found. Similar calculations by Okajima, Nagahisa and Rokugoh [1990], indicate that the step change in St at $Re_h \approx 500$ results from rapid changes in the relative magnitudes of the two frequency components, the higher characteristic of intermittent reattached and separated flow and the lower characteristic of flow fully-separated from both the cylinder leading edges.

Okajima's [1990] calculations also show the change from intermittently separated and reattached flow to fully-separated flow as being characterised by a significant widening of the cylinder wake and a large change in the amplitude of lift-coefficient fluctuation. Comparisons of the experimental and calculated streamline patterns obtained by Okajima [1982] for C = 2 at Re_h = 250 and the present results (for t = 88 and 91) are made in Fig. 7.69, which shows that there are close similarities in the general characteristics of all three patterns at each of the two stages in the flow. However, the computed results of Okajima and the present work show differences in the fine details of the flow close to the cylinder. The present calculations yield somewhat greater detail near the surface, and in contrast to the Okajima patterns show flow on the side surfaces involving large-scale vortices. For example, the present calculations show formation of vortices within leading-edge-separation bubbles, and their subsequent shedding from the bubble and movement along the side surface in a process similar to that described by Kiya [1989]. The periodic passage of these discrete vortices past the trailing corners of the cylinder influences the alternation between reattached and detached flow on the surface. As a second example, the present results suggest that, in flow fully separated from a side surface, the flow between the surface and the separated shear layer consists of a string of several co-rotating vortices – as can be seen in the lower-surface separation in Fig. 7.78 at t = 83 – rather than one

single large recirculating flow as might be inferred from the Okajima calculation shown in Fig. 7.69(b). Later calculations by Okajima, Nagahisa and Rokugoh [1990], showing fully-separated and large scale reverse flow on one side surface and reattachment on the other at Re_h = 250 and fully-separated flow on both side surfaces at Re_h = 500, are reproduced in Fig. 7.70; streamline patterns from present work are also shown. Again, there are close similarities in the general characteristics of the flow patterns.

Calculated streamline patterns and isovorticity contours for C = 2 at Re_h = 1,000 given by Okajima, Ueno and Sakai [1992] are reproduced in Fig. 7.71. There is obvious similarity between these and results of the present work, which are also shown. The present results clearly indicate intermittent reattachment on the side surface, and the formation of a leading-edge-separation bubble and vortex shedding from it. Although limited fine detail can be seen in the results given by Okajima *et al.*, the lower-surface flow, as for Re_h = 250, could well be interpreted as showing the same process.

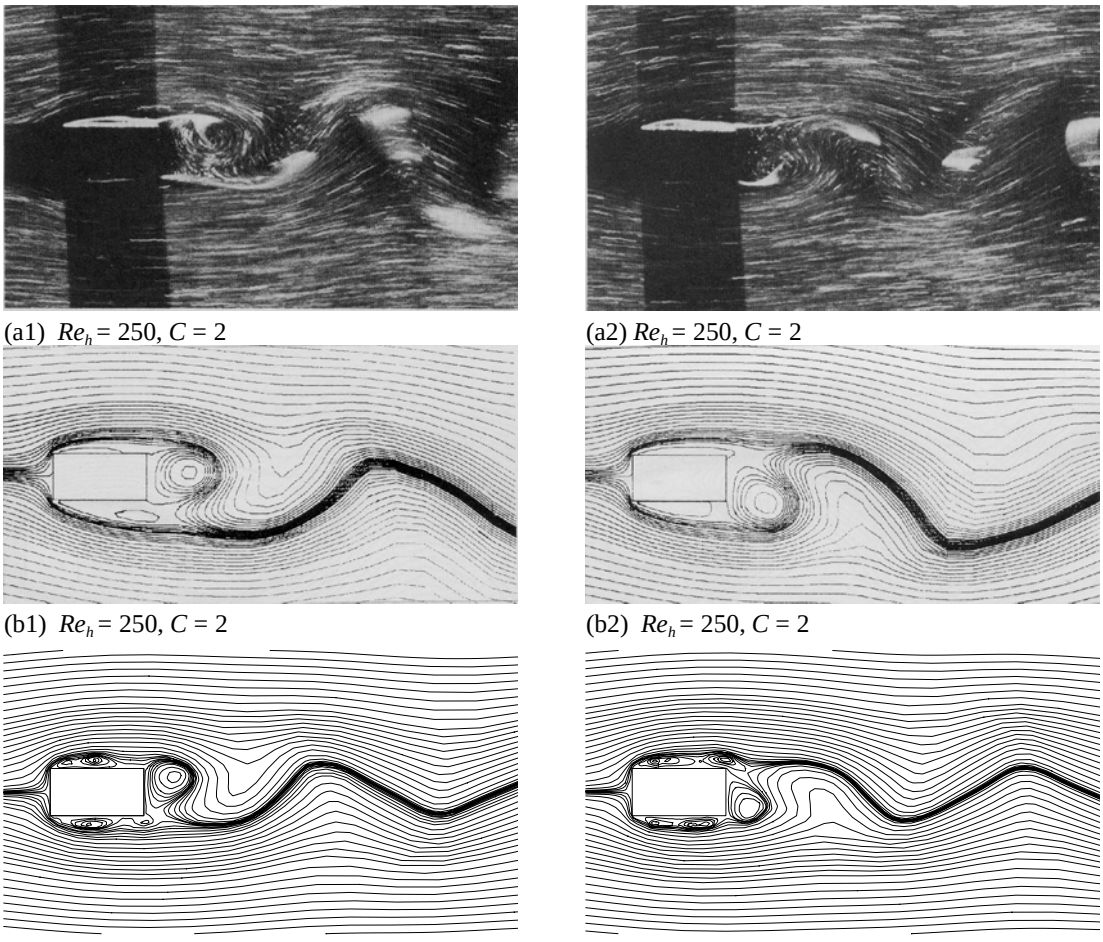

(a1) Re_h = 250, C = 2 (a2) Re_h = 250, C = 2

(b1) Re_h = 250, C = 2 (b2) Re_h = 250, C = 2

(c1) Re_h = 250, C = 2, t = 88 (c2) Re_h = 250, C = 2, t = 91

Figure 7.69. Comparison between visualised flow patterns and numerical calculation for flow over a single rectangular plate with C = 2 at Re_h = 250: (a) experimental results of Okajima [1982], (b) computed flow patterns of Okajima [1982], (c) computed results of this study.

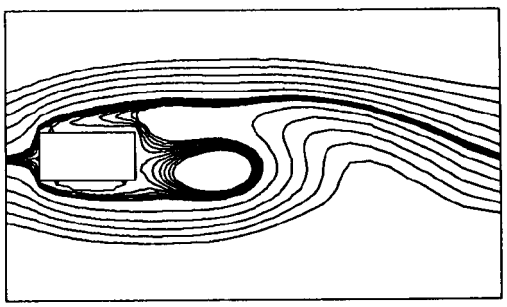

(a) Streamlines for $C = 2$ at $Re_h = 250$

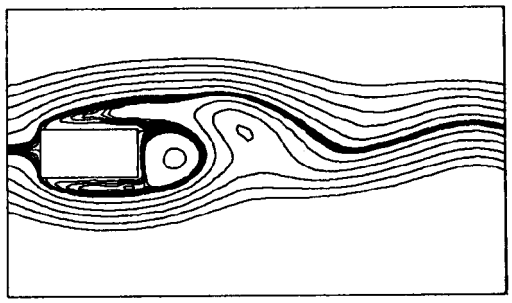

(c) Streamlines for $C = 2$ at $Re_h = 500$.

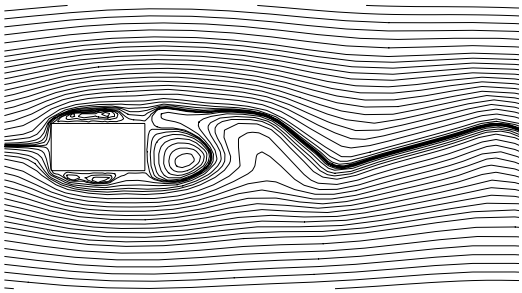

(b) Streamlines for $C = 2$ at $Re_h = 250$, $t = 98$.

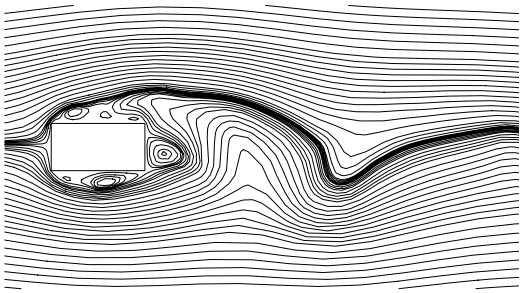

(d) Streamlines for $C = 2$ at $Re_h = 500$, $t = 71$.

Figure 7.70. Streamline patterns for $C = 2$ at $Re_h = 250$ and 500, (a) and (c) calculated results of Okajima, Nagahisa and Rokugoh [1990], (b) and (d) calculated results of this study.

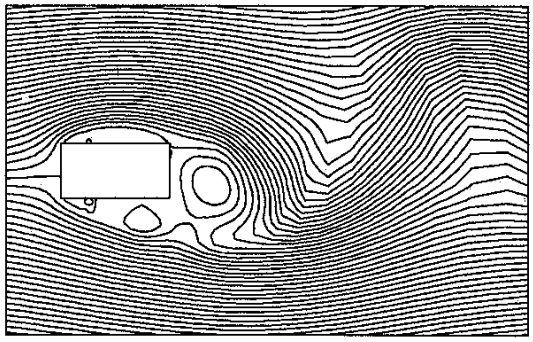

(a) Streamlines for $Re_h = 1{,}000$

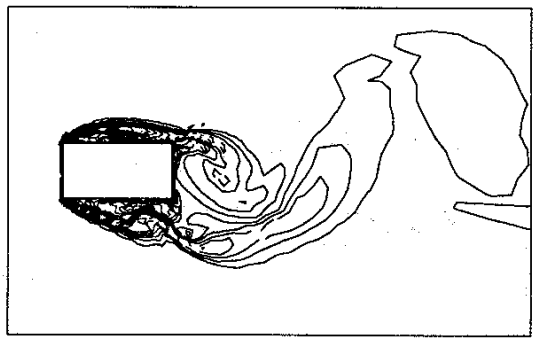

(c) Isovorticity contours for $Re_h = 1{,}000$

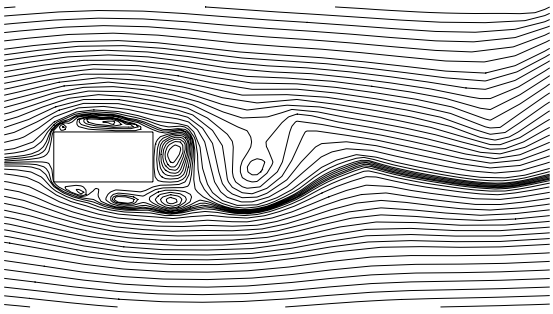

(b) Streamlines for $C = 2$ at $Re_h = 1{,}000$ at $t = 90$.

(d) Isovorticity contours for $Re_h = 1{,}000$ at $t = 90$.

Figure 7.71. Streamlines and isovorticity contours for $C = 2$ at Re_h=1,000, (a) and (c) calculated results of Okajima, Ueno and Sakai [1992], (b) and (d) calculated results of this study.

Comparisons of Strouhal numbers are made in Fig. 7.72, which summarises experimental and calculated results as a function of Reynolds number. It can be seen from this figure that computations are generally able to predict the experimentally-observed step change in Strouhal number at about $Re_h = 500$. But, despite the similarities in numerically predicted flow patterns discussed above, there are quite significant differences in computed Strouhal numbers at some Reynolds numbers. The calculated flow patterns of Okajima [1990] give Strouhal numbers which are generally lower than the experimental values for $Re_h < 500$, while the present results agree quite well with experiment over the whole Reynolds number range of the calculations. It might also be noted that, in the present calculated results, power spectra of lift fluctuations (Figs. 7.94) show two (or sometimes more) peaks, the higher one corresponding to the variation of Strouhal number with Reynolds number at sub-critical Reynolds numbers, and the lower one to the variation at super-critical Reynolds numbers; as found by Okajima *et al*. [1990], the step change in Strouhal number corresponds to a rapid reversal in the relative magnitudes of these two components.

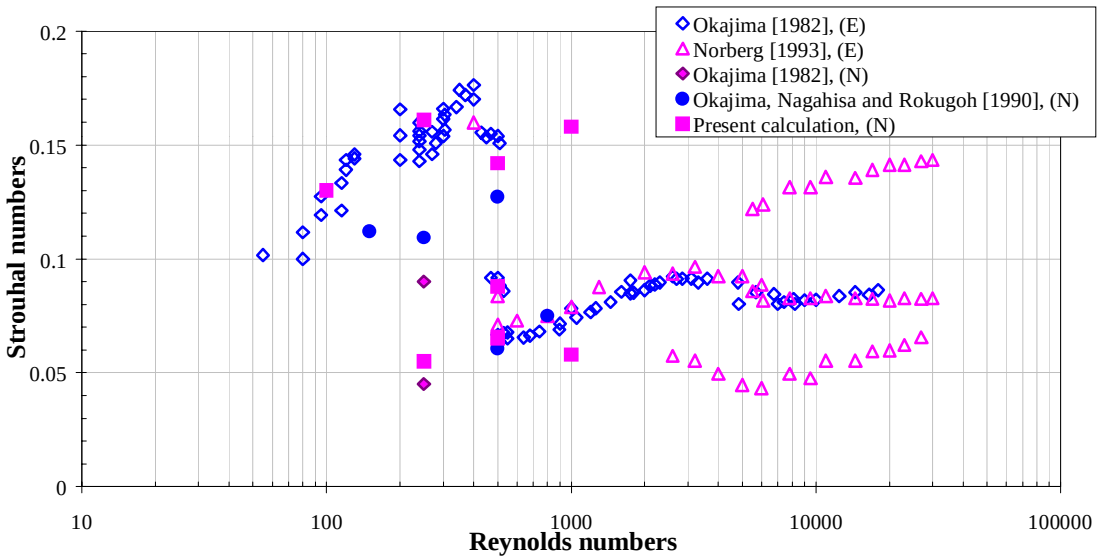

Figure 7.72. Variation of Strouhal number with Reynolds number for $C = 2$ cylinders.

7.4.2.2 Details of Computed Fully-Developed Flow Patterns for C = 2 Cylinders

The computed streamline and isovorticity contours of fully-developed flow over the cylinder with $C = 2$ at $Re_h = 100$ (Figs. 7.74 and 7.75) indicate that flow separation from the leading corners of the cylinder occurs at all times, and is followed by reattachment of the separated shear layers to the side surfaces to form a short leading-edge-separation bubble. As is evident in the isovorticity contours of Fig. 7.75, the dominant process of vorticity transport is continuous convection along the side surfaces, so that thick shear layers are built up at the trailing edges. Vortex formation downstream of the cylinder is due primarily to the rolling up of the shear layers separating from the trailing edge of the cylinder. There is, however, also evidence (Fig. 7.74) of formation of weak discrete vortices in the separation bubble, and their subsequent shedding from the bubble and convection along the side surfaces of the cylinder. The frequency of formation of these discrete vortices is higher than the frequency of the formation of wake vortices. Despite the weakness of the discrete side-surface vortices, the initiation of a wake vortex appears to be in phase with the passage of one of these vortices over the trailing corner. At other times, the convected discrete vortices merge with the wake vortex already forming on the trailing face of the cylinder, before the latter is shed into the wake. A typical sequence of these events, on the lower surface can be seen in Figs. 7.74 and 7.76 from time $t = 80.5$ onwards: side-face vortex formation and convection at $t = 80–82$; arrival of side-face vortex at trailing corner and initiation of trailing-face vortex at $t = 82.5, 83$; and shedding of wake vortex at $t = 87$.

The periodic vortex-shedding, alternately from the upper and lower side surfaces, which is established produces a narrow, regular, vortex-street wake behind the cylinder. The largely attached flow on the side faces results in weak pressure forces on the cylinder (see pressure distributions, Fig. 7.76), a small amplitude of lift variation and very small drag fluctuations about a mean value of $C_D = 1.2$, as shown in Fig. 7.89. The power spectrum of lift variation, Fig. 7.94(a), shows a single dominant sharp spectral peak at the Strouhal number of $St \approx 0.13$. The drag fluctuations are so small that a dominant periodicity cannot be detected in them.

At $Re_h = 250$, the calculations indicate a similar process of formation of leading-edge-separation bubbles and generation of discrete vortices on the side surfaces, but in this case the discrete vortices are stronger and play a more dominant part in wake formation. Movement of discrete vortices along the side surface, following their detachment from the leading-edge bubble, results

in the shear layers separated from the leading corners reattaching to the cylinder intermittently. A typical sequence of events in the flow, as it occurs on the upper surface, can be seen in the streamline patterns of Fig. 7.78 from time t = 70 onwards. Just after an upper trailing-face vortex has been shed into the wake, reattachment of the separated shear layer splits the existing side-face vortices producing a short leading-edge-separation bubble and a convected vortex downstream of it. The latter moves into the wake and merges with the recently-formed upper wake vortex. The bubble increases in length (t = 72, 73), and becomes a full-chord separation bubble; further growth gives rise to a detached shear layer and reverse flow between the shear layer and the side surface (t = 74). Then, about half way along the side face, the separated shear layer deflects towards the side surface and reattaches, again forming a leading-edge-separation bubble with a convected discrete vortex downstream of it (t = 75). The discrete vortex, after passing the trailing corner, takes up a position on the rear face of the cylinder where it becomes a trailing-face vortex (t = 75, 76). The trailing-face vortex grows until it is eventually shed into the wake (t = 76, 77), and the cycle begins again. It can be clearly seen in the streamline patterns that the onset of the formation of a trailing-face vortex coincides with the passage of a discrete vortex over the trailing corner. However, the discrete vortices are generated at a higher frequency than the vortex-shedding frequency, so that not all discrete vortices convected past the trailing corner lead to wake-vortex formation. Those that do not, as in the flow sequence just described, merge with the trailing-face vortex which is already forming.

The streamline patterns show that trailing-face vortices do not grow laterally to any significant extent beyond the width of the cylinder, before being shed into the wake. This leads to a narrow regular vortex street behind the cylinder (as shown in the distribution of the elemental discrete vortices in Fig. 7.77) and lift fluctuations of small amplitude not significantly greater than those for Re_h = 100, even though the pressure gradients on the side faces (Fig. 7.80) are noticeably higher than at Re_h = 100. Although the vortex-shedding process itself is quite regular, the time-histories of lift and drag variation (Fig. 7.90) are somewhat irregular, due apparently to irregularities in the generation and convection of discrete side-surface vortices.

The power spectrum of the time-history of lift variation (Fig. 7.94(b)) at Re_h = 250 has two spectral peaks, at St = 0.06 and St = 0.16. As can be inferred from the variation of Strouhal number with Reynolds number (Fig. 7.72), these two values of Strouhal number correspond to two different classes of flow. The flow with St = 0.16 belongs to the same class as the flow at

Re_h = 100. This indicates that the high-frequency component of St = 0.16 at Re_h = 250 is associated with wake-vortex formation following separation, from the trailing edge, of a boundary layer formed by attached flow on a side surface, while the low-frequency component characterises intermittently-attached flow associated with the movement of discrete vortices along the side surfaces. The calculations indicate that the spectral peak at the higher Strouhal number of St = 0.16 is smaller than that at St = 0.06 in the early stages of flow development but grows, as time progresses, to become the dominant peak in the fully-developed flow. This is similar to the behaviour of the two spectral peaks at St = 0.07 and St = 0.11 found by Okajima [1990] for the C = 2 cylinder at Re_h = 250.

At Re_h = 500, the calculated flow patterns exhibit a complexity which might be expected if they correctly represent the changes in flow regime which, according to experiment and previous numerical simulations, occur at this Reynolds number. In accord with experiment, they show a flow alternating between two regimes: one in which the shear layer, separated from a leading corner of the cylinder, reattaches to the side surface and the other in which the flow is completely detached from the side surface; and they yield Strouhal numbers in good agreement with experimental values at sub- and super-critical Reynolds numbers. The process of formation of large-scale discrete vortices on the side surfaces is similar to that in the previous cases of Re_h = 100 and 250. At the higher Reynolds number of Re_h = 500, however, the discrete vortices on the side surfaces are stronger and larger; at times they become comparable in size to the trailing-face vortices. During times of detached flow, interaction between a developing wake-vortex and a side-surface vortex, near the trailing corner, frequently leads to reverse flow on the side surface (as, for example, on the upper surface at t = 70, 81, 84, Fig. 7.82). The extent of reverse flow and its effect in displacing the separated shear layer is determined by the strength and size of the discrete vortices, which vary from one vortex to the next – for instance, the effect of reverse flow on the upper side at time t = 70 is much greater than that of the corresponding flow occurring at time t = 78.

Furthermore, this interaction, in which the passage of a side-face vortex over the trailing corner may or may not lead to the formation of a trailing-face vortex, depending on the phasing, gives rise to a complicated process of vortex shedding from the cylinder. This is reflected in the presence of several peaks in the power spectrum of lift fluctuations (Fig. 7.94(c)) at Strouhal numbers of St = 0.067, 0.088 and 0.142, and the modulated variation of lift with time (Fig. 7.91). The resulting irregularities in vortex shedding can be clearly seen in the elemental vortex

configurations in Fig. 7.81. A particularly strong irregularity occurs over the times t = 78–82, during which a lower-surface vortex enters the wake; due to the persistence of the large vortex near the upper corner, the lower-surface vortex does not become detached by the simple process of establishment of a down flow between the vortex and the trailing face, as occurs for the previous and succeeding vortices at t = 72 and 85. The complexity of vortex shedding is consistent with a flow in transition.

Despite the complexity of the flow in transition, some basic characteristics of the vortex shedding process at this Reynolds number can be identified. It can be seen from the streamline and vorticity patterns (Figs. 7.83 and 7.85) that the vortices which form in the base region of the cylinder are shed into the wake at roughly regular intervals. Their shedding frequency is essentially the same as that of the high-frequency, low-level, lift variation with a Strouhal number St = 0.142. However, the lift variations of greatest amplitude occur not at this vortex-shedding frequency but at the considerably lower frequency corresponding to St = 0.088. Evaluation of the strengths of a sequence of vortices in the cylinder wake shows that the circulation of vortices shed from the trailing edges of both the upper and lower faces varies more or less periodically at a frequency matching this value. (The result of a similar calculation for Re_h = 1,000 is shown later in Fig. 7.93.) Even though the frequency of formation of side-face vortices is greater than the frequency of shedding of wake vortices (as a result of some amalgamations downstream of the cylinder), it can be inferred that the rate of generation of vorticity, its transport by side-face vortices into the base region of the cylinder, and hence the rate at which it is shed into the wake via trailing-face vortices, all vary periodically at this frequency. Although a quantitative connection has not been established, it appears that this fluctuation is associated with quasi-periodic variation in the size of the leading-edge-separation bubble.

The behaviour of the leading-edge-separation bubble and the formation of side-surface vortices from it, as already described for the flows at Re_h = 100 and 250, can be seen in the streamline patterns of Fig. 7.82 from time t = 70 onwards. Following detached flow over the upper surface (t = 70, 71), the separated shear layers from the leading corner reattach to the side surface to produce a leading-edge-separation bubble (t = 72). The bubble grows, divides and contracts (t = 73). When the bubble divides, a large discrete vortex is released and convected downstream along the side surface, past the trailing corner (t = 74). During this process the leading-edge separation bubble has again grown and divided. The new convected side-face

vortex and its predecessor together form a trailing-face vortex (t = 75, 76), but retain their identities and are shed separately into the wake (t = 78–81). Interaction between this trailing-face vortex-pair and the vortical flow of the next discrete vortex passing over the trailing corner (t = 77, 78) produces reverse flow on the side face. Reattachment occurs at t = 79. Meanwhile, discrete vortices are formed and convected along the lower surface also. Interaction between the wake vortices and a discrete vortex on the lower side gives rise to flow detachment from the lower side (t = 75–77). Following the passage of this large discrete vortex into the wake (t = 78), reattachment on the lower side produces a new, short, leading-edge-separation bubble (t = 79). The intermittent attached and fully-separated flow results in a wider wake than at lower Reynolds numbers.

In line with the increase in size and strength of the discrete side-face vortices with Reynolds number, the discrete vortices at Re_h = 500 are associated with higher pressure gradients and larger pressure forces on the side faces (Fig. 7.84) than at lower Reynolds numbers. This results in an increased amplitude of lift variation (Fig. 7.91). Furthermore, due to the localised high surface-pressure gradients produced by the discrete vortices, convection of these vortices produces large fluctuations in surface pressure, particularly towards the trailing edges ($s \approx 2$–3 and $s \approx 4$–5) as shown in Fig. 7.95. The high r.m.s. pressure fluctuations on the side faces are consistent with the changes in instantaneous pressure distribution around the cylinder over one vortex-shedding cycle shown in Fig. 7.84.

The calculated general characteristics of the flow at Re_h = 1,000 are quite similar to those of the flow at Re_h = 500: the flow is still characterised by the formation of large-scale vortices on the side surfaces and intermittent reattachment of the leading-edge shear layers. There are close similarities in streamline patterns (Figs. 7.82 and 7.86), isovorticity contours (Figs. 7.83 and 7.87) and the time-histories of lift variation (Figs. 7.91 and 7.92). Interaction between convected side-surface vortices and trailing-face vortices leads to irregularity in the vortex street downstream of the cylinder. The spectrum of lift variation has a major spectral peak at St = 0.065 and a minor peak at St = 0.167. From the streamline and isovorticity patterns (Figs. 7.86 and 7.87), the high-frequency component at St = 0.167 can be identified as that of vortex shedding into the wake from the base region of the cylinder, as in the previous case of Re_h = 500, while the low-frequency component can be associated with periodic variation in the strength of the shed vortices, as shown by calculation of the strength of a sequence of wake vortices (Fig. 7.93).

Figure 7.88 shows the change in the instantaneous pressure field around the cylinder over one vortex-shedding cycle at Re_h = 1,000. The pressure gradients associated with flow reattachment and side-surface vortices increase with the increase in Reynolds number from 500 to 1,000. This is reflected in the greater values of r.m.s. pressure coefficient $C_{p'}$ on the side surfaces of the cylinder than at Re_h = 500 (Fig. 7.95).

The distributions of time-averaged pressure coefficient C_p over the surface of the C = 2 cylinders, at the four Reynolds numbers considered, are shown in Fig. 7.95. The pressure distribution on the leading face of the C = 2 cylinders, as in the case of square cylinders described in section 7.3.2.3, is essentially independent of Reynolds number and is very similar to the inviscid-flow pressure distribution. The surface pressure decreases from C_p = 1 at the front stagnation point (s = 0.5) to its lowest value $C_p \approx -2$ on the side surfaces near the leading-edge corners (s = 0, 1); on both the upper and lower surfaces, the pressure then gradually rises to the base pressure on the rear face. However, the general pattern of pressure distribution on the side surfaces changes with Reynolds number: at low Reynolds numbers the pressure rises sharply over the upstream part of the side faces (s = 1–2) and more gradually over the downstream part (s = 2–3); at higher Reynolds numbers this pattern is reversed. This reflects increasing deviation of the pressure distribution on the side surfaces from the inviscid-flow pattern as the Reynolds number increases, as a result of the increasing difference of the flow pattern from that of a fully-attached flow. On the trailing face (s = 3–4), the base pressure is fairly uniform and its value insensitive to Reynolds number: the base pressure coefficient increases from $-C_{pb} \approx 0.5$ at Re_h = 100 to $-C_{pb} \approx 0.7$ at Re_h = 250, and remains fairly constant at $-C_{pb} \approx 0.7$ as the Reynolds number is further increased to 1,000. These values compare quite well with the experimental and computed values given by Okajima, Nagahisa and Rokugoh [1990] as a function of Reynolds number, as shown in Fig. 7.96.

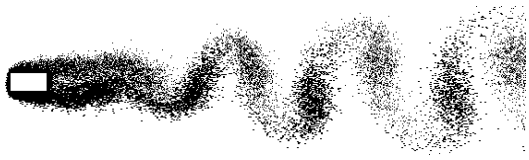

(a) Re_h = 100, C = 2, t = 60

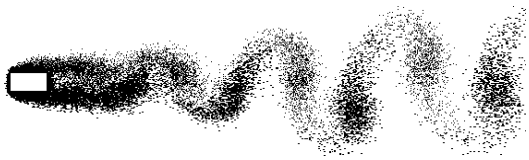

(j) Re_h = 100, C = 2, t = 78

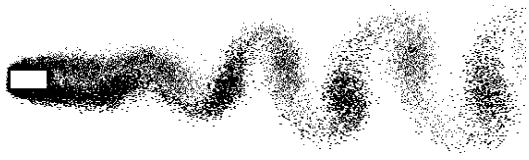

(b) Re_h = 100, C = 2, t = 62

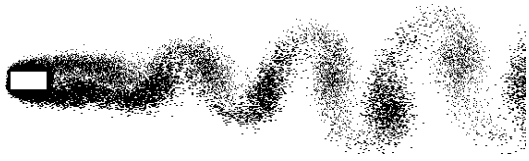

(k) Re_h = 100, C = 2, t = 80

(c) Re_h = 100, C = 2, t = 64

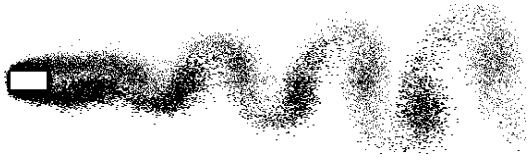

(l) Re_h = 100, C = 2, t = 82

(d) Re_h = 100, C = 2, t = 66

(m) Re_h = 100, C = 2, t = 84

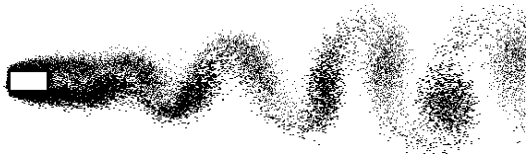

(e) Re_h = 100, C = 2, t = 68

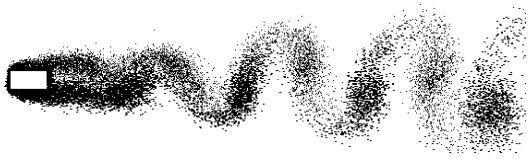

(n) Re_h = 100, C = 2, t = 86

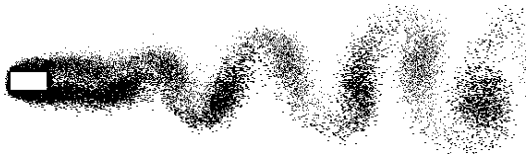

(f) Re_h = 100, C = 2, t = 70

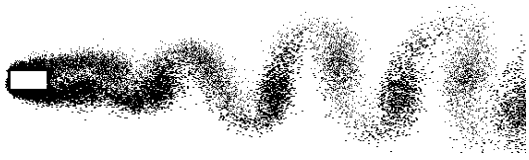

(o) Re_h = 100, C = 2, t = 88

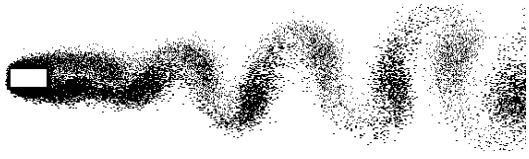

(g) Re_h = 100, C = 2, t = 72

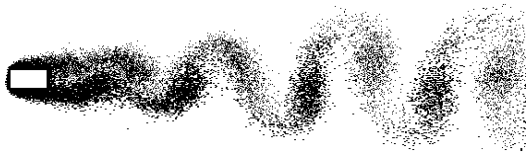

(p) Re_h = 100, C = 2, t = 90

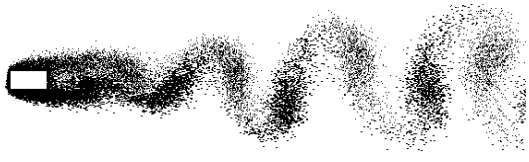

(h) Re_h = 100, C = 2, t = 74

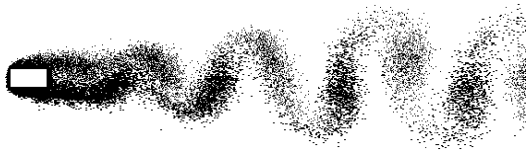

(q) Re_h = 100, C = 2, t = 92

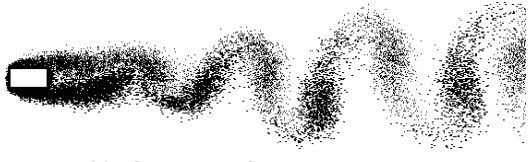

(i) Re_h = 100, C = 2, t = 76

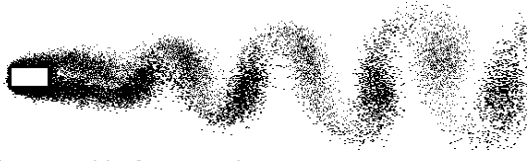

(r) Re_h = 100, C = 2, t = 94

Figure 7.73. Elemental-vortex distributions in fully-developed flow over C = 2 cylinder at Re_h = 100.

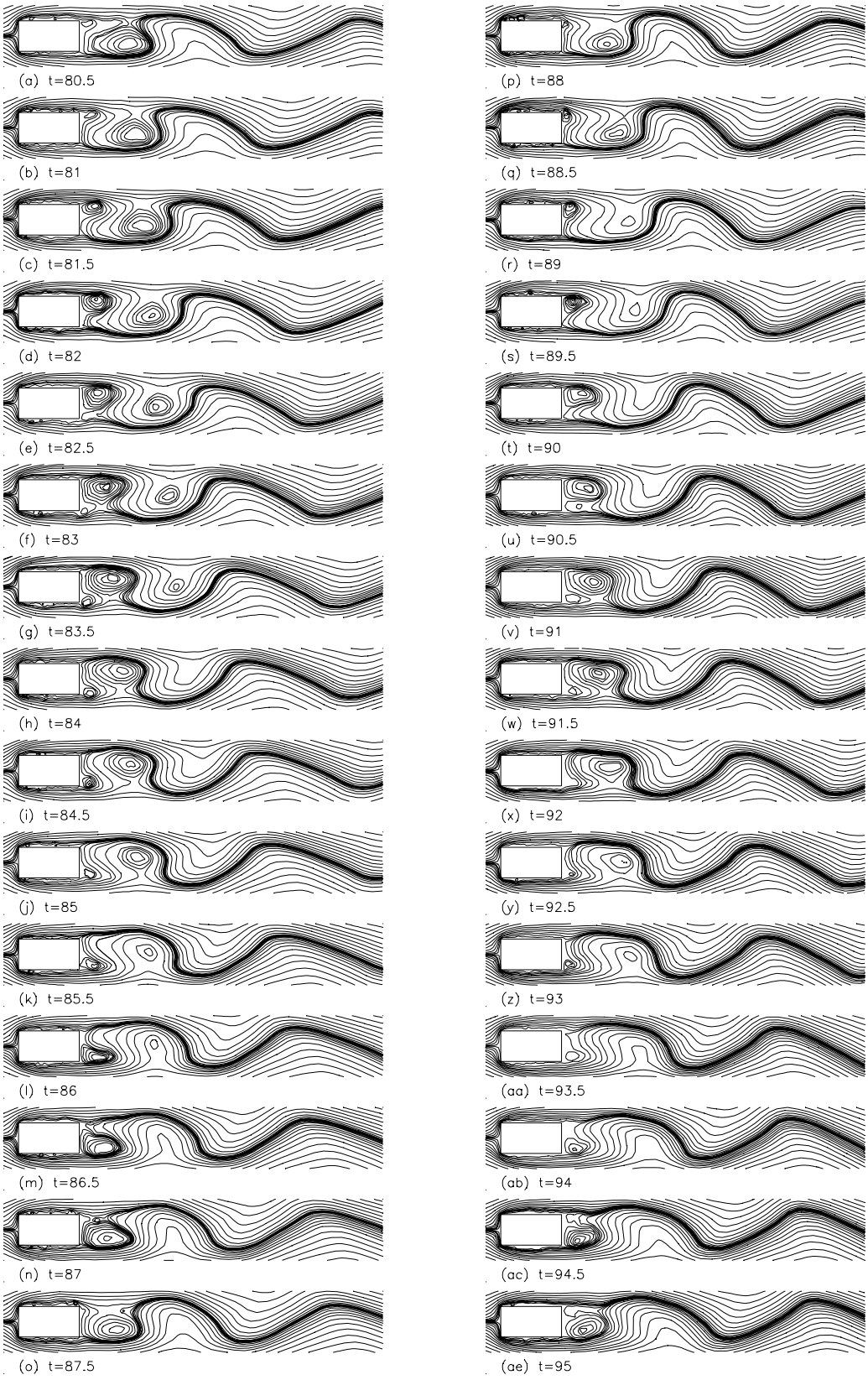

Figure 7.74. Streamline patterns in fully-developed flow over $C = 2$ cylinder at $Re_h = 100$.

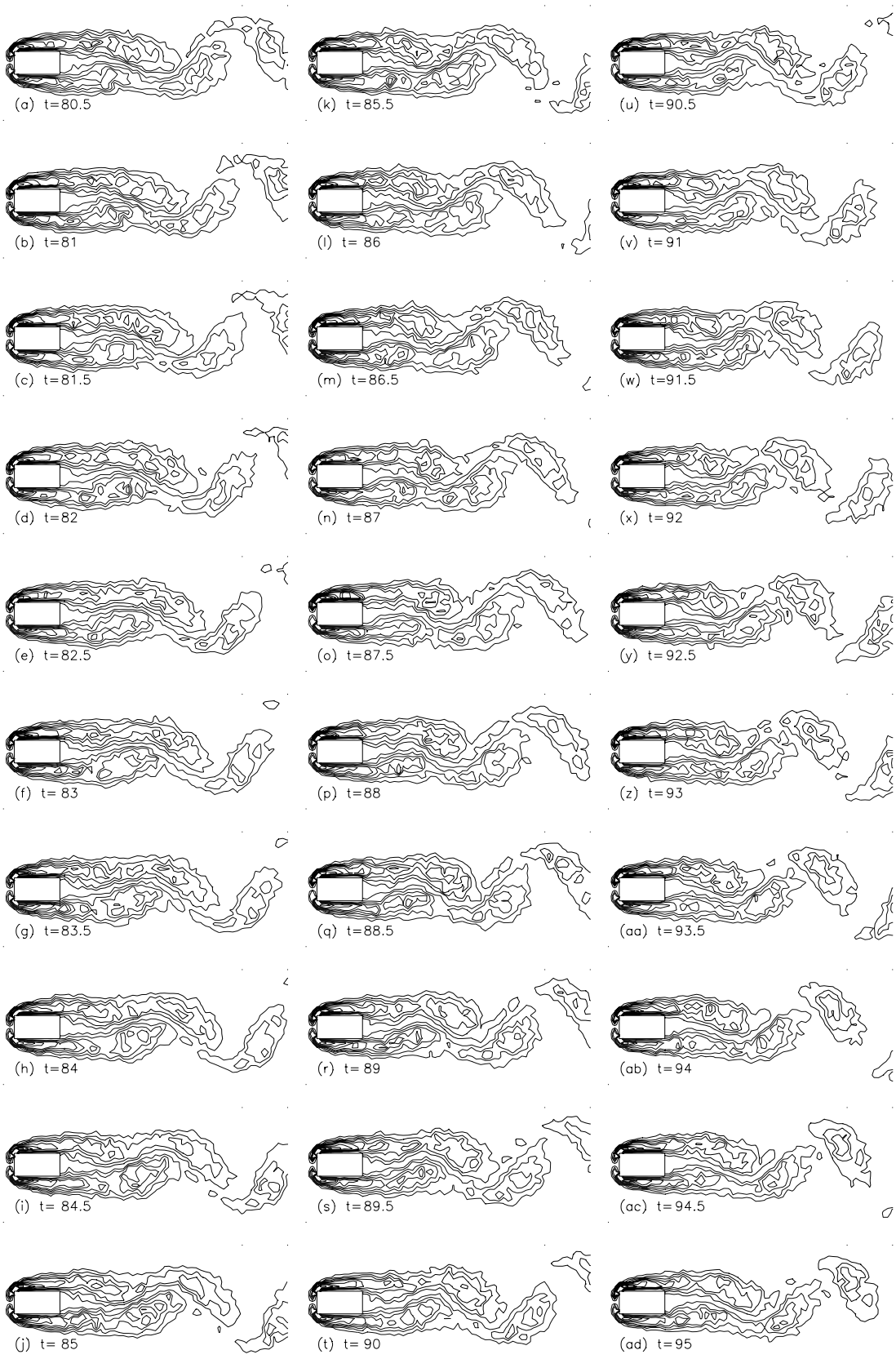

Figure 7.75. Vorticity contours in fully-developed flow over $C = 2$ cylinder at $Re_h = 100$.

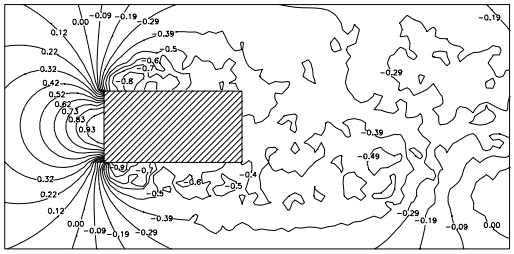

(a1) Re_h = 100, C = 2, t = 80.5

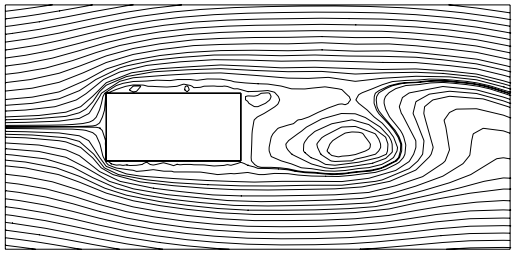

(a2) Re_h = 100, C = 2, t = 80.5

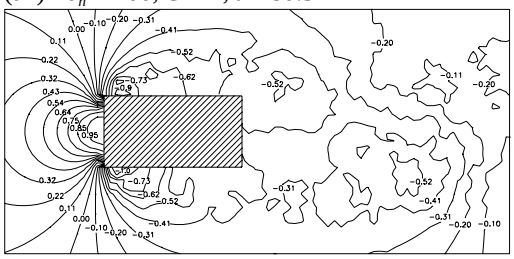

(b1) Re_h = 100, C = 2, t = 82

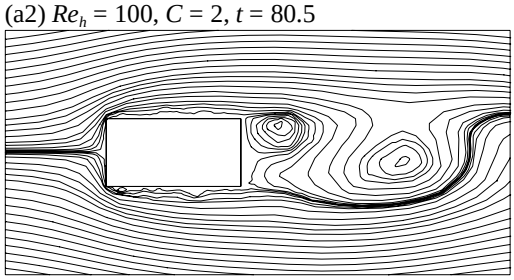

(b2) Re_h = 100, C = 4, t = 82

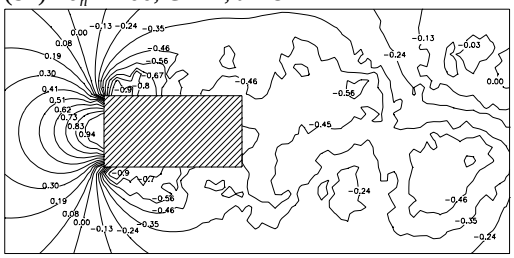

(c1) Re_h = 100, C = 2, t = 83.5

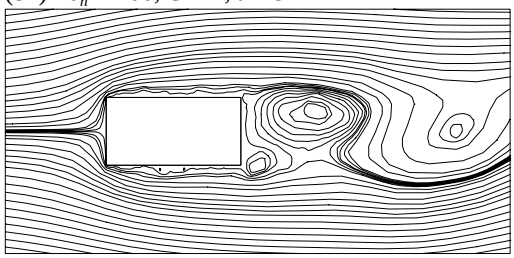

(c2) Re_h = 100, C = 2, t = 83.5

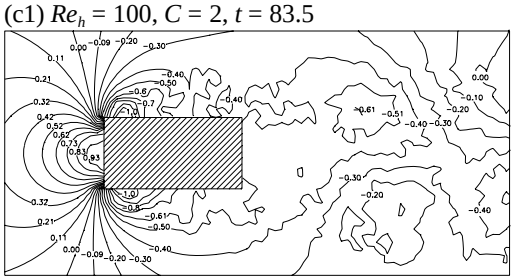

(d1) Re_h = 100, C = 2, t = 85

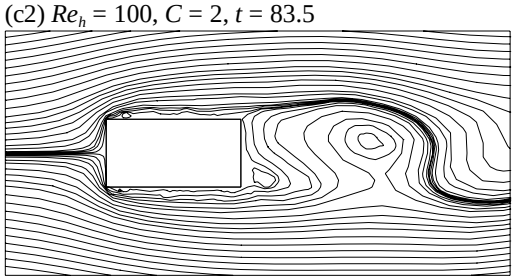

(d2) Re_h = 100, C = 2, t = 85

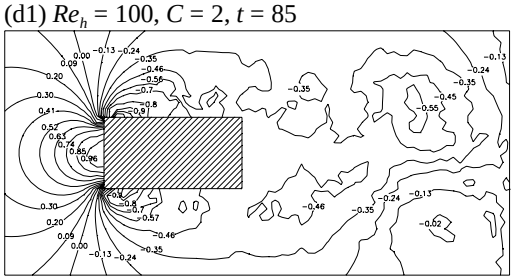

(e1) Re_h = 100, C = 2, t = 86.5

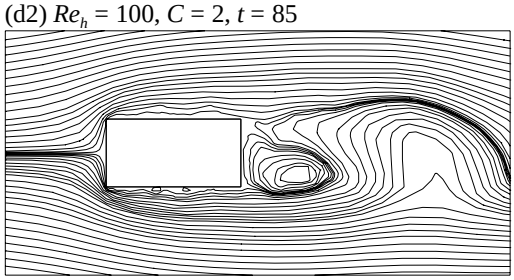

(e2) Re_h = 100, C = 2, t = 86.5

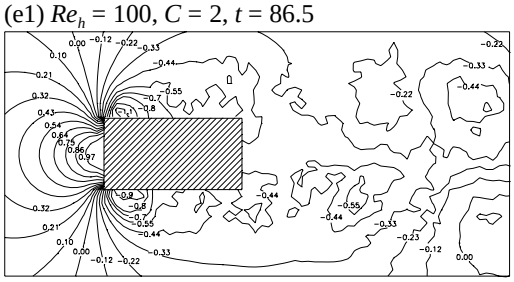

(f1) Re_h = 100, C = 2, t = 88

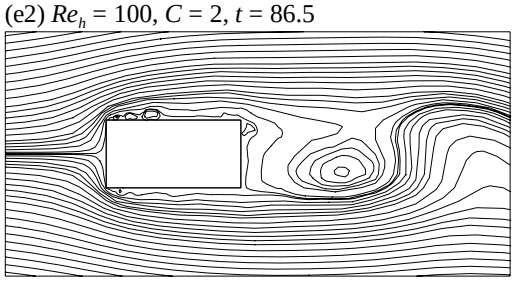

(f2) Re_h = 100, C = 2, t = 88

Figure 7.76. Instantaneous pressure fields and streamline patterns around the C = 2 cylinder at Re_h = 100. Numbers shown are coefficients of static pressure.

(a) Re_h = 250, C = 2, t = 60

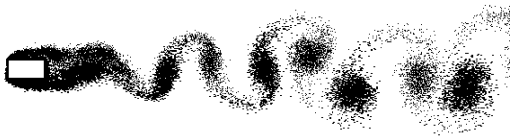

(b) Re_h = 250, C = 2, t = 62

(c) Re_h = 250, C = 2, t = 64

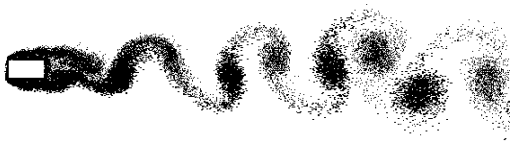

(d) Re_h = 250, C = 2, t = 66

(e) Re_h = 250, C = 2, t = 68

(f) Re_h = 250, C = 2, t = 70

(g) Re_h = 250, C = 2, t = 72

(h) Re_h = 250, C = 2, t = 74

(i) Re_h = 250, C = 2, t = 76

(j) Re_h = 250, C = 2, t = 78

(k) Re_h = 250, C = 2, t = 80

(l) Re_h = 250, C = 2, t = 82

(m) Re_h = 250, C = 2, t = 84

(n) Re_h = 250, C = 2, t = 86

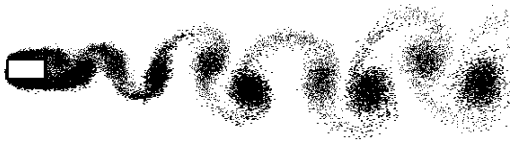

(o) Re_h = 250, C = 2, t = 88

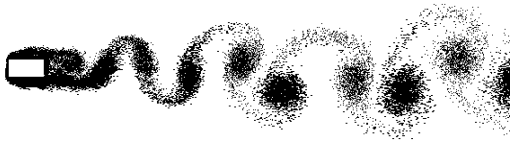

(p) Re_h = 250, C = 2, t = 90

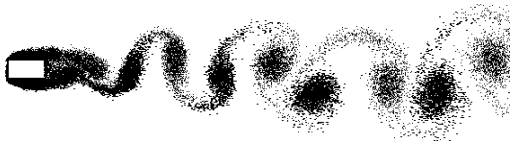

(q) Re_h = 250, C = 2, t = 92

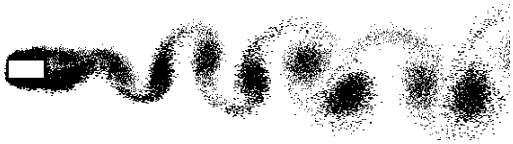

(r) Re_h = 250, C = 2, t = 94

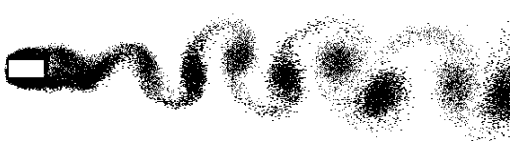

(s) Re_h = 250, C = 2, t = 96

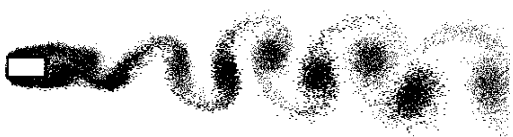

(t) Re_h = 250, C = 2, t = 98

Figure 7.77. Elemental-vortex distributions in fully-developed flow over C = 2 cylinder at Re_h = 250.

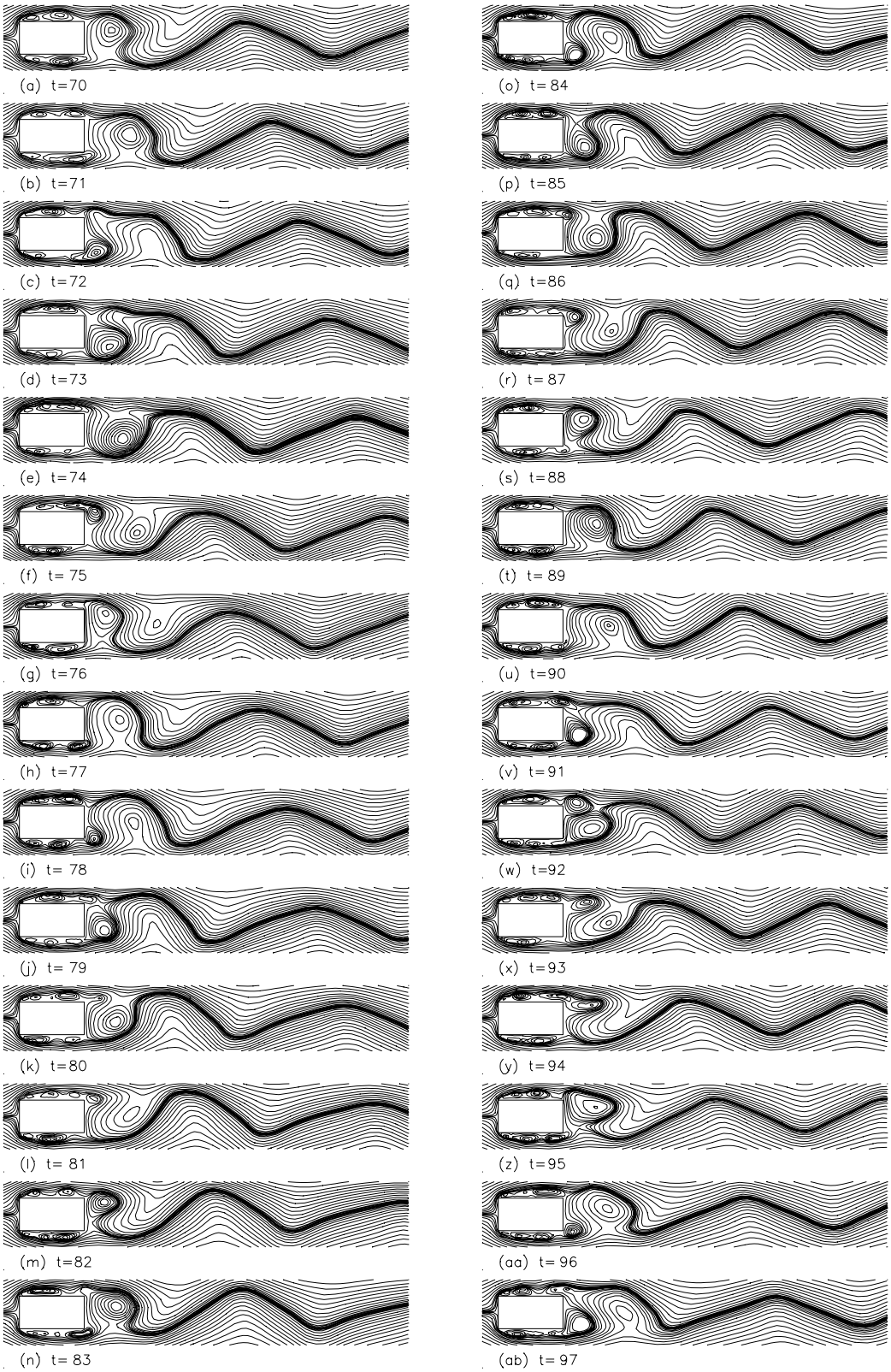

Figure 7.78. Streamline patterns in fully-developed flow over $C = 2$ cylinder at $Re_h = 250$.

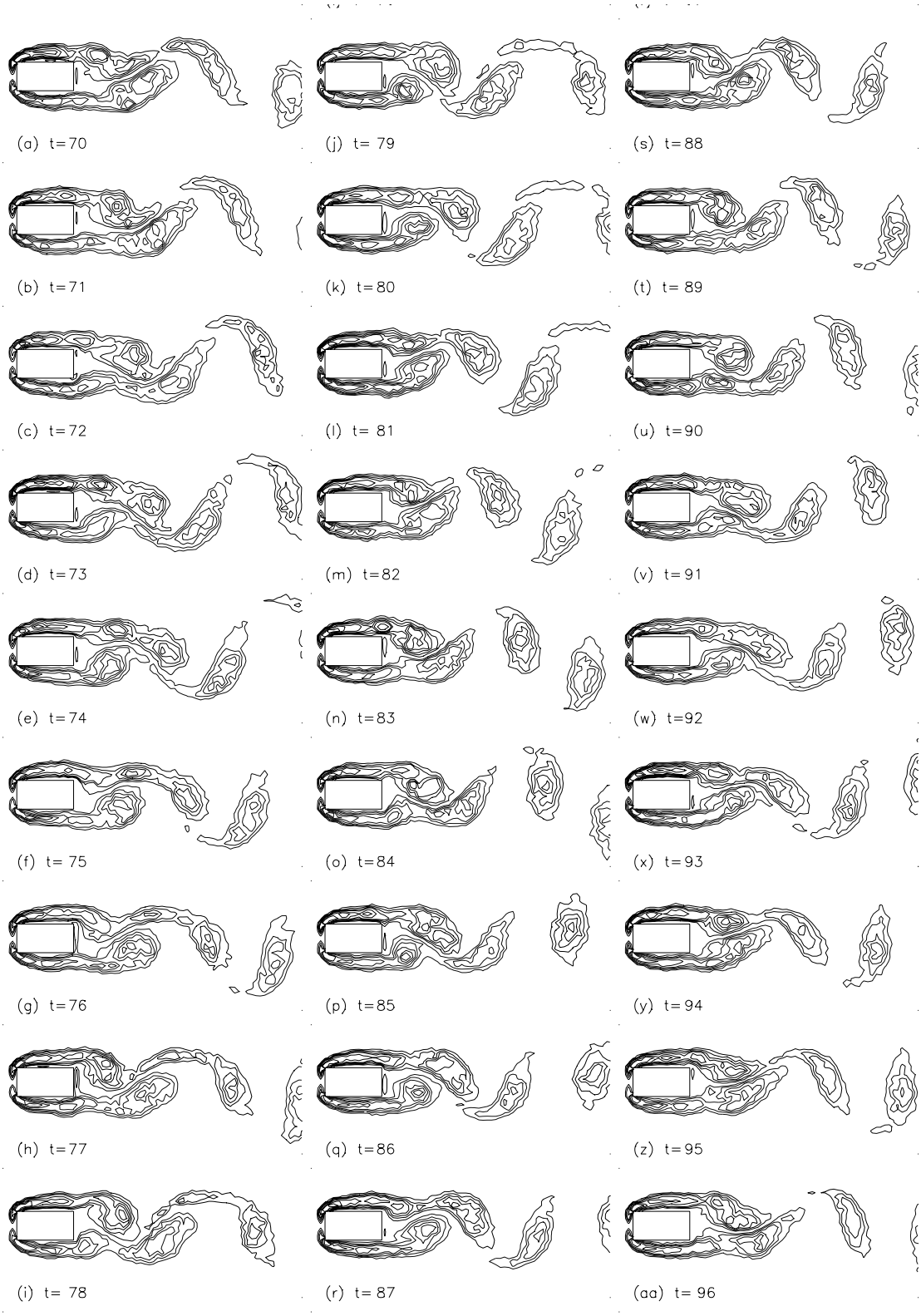

Figure 7.79. Vorticity contours in fully-developed flow over $C = 2$ cylinder at $Re_h = 250$.

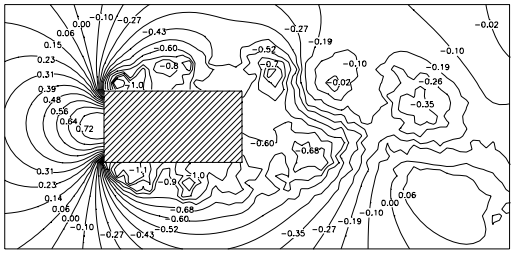

(a1) Re_h = 250, C = 2, t = 92

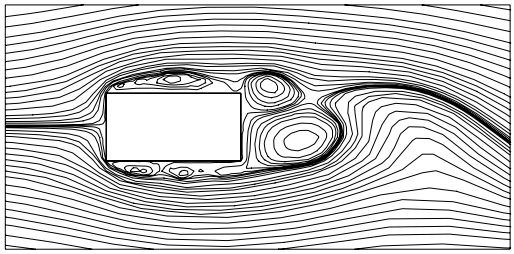

(a2) Re_h = 250, C = 2, t = 92

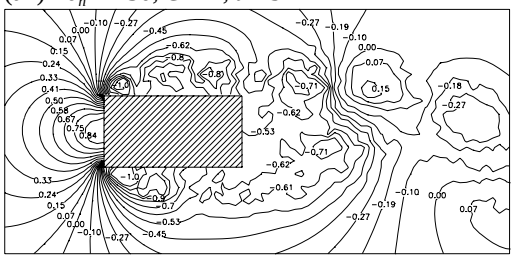

(b1) Re_h = 250, C = 2, t = 93

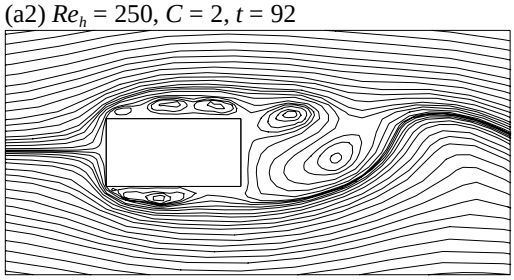

(b2) Re_h = 250, C = 2, t = 93

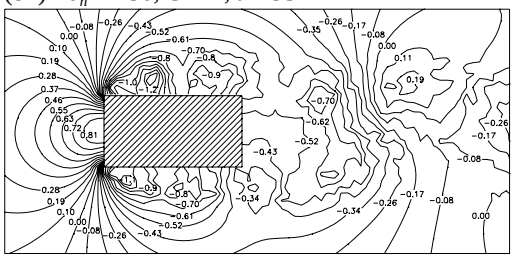

(c1) Re_h = 250, C = 2, t = 94

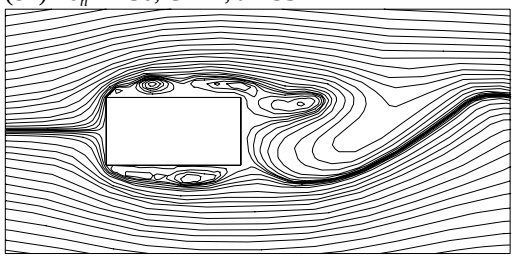

(c2) Re_h = 250, C = 2, t = 94

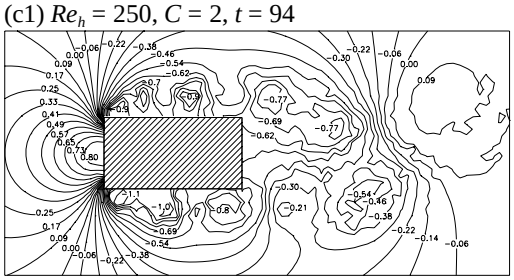

(d1) Re_h = 250, C = 2, t = 95

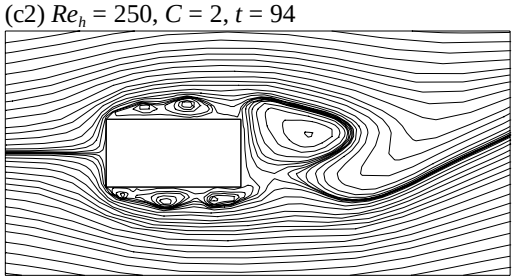

(d2) Re_h = 250, C = 2, t = 95

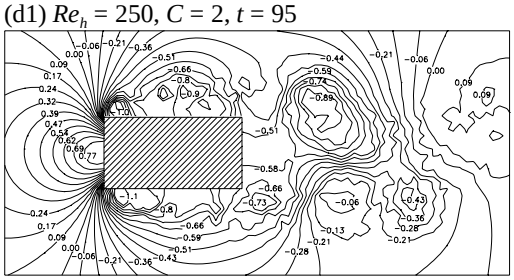

(e1) Re_h = 250, C = 2, t = 96

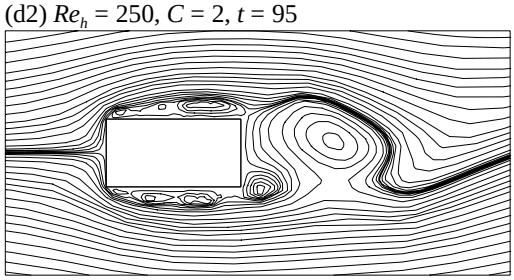

(e2) Re_h = 250, C = 2, t = 96

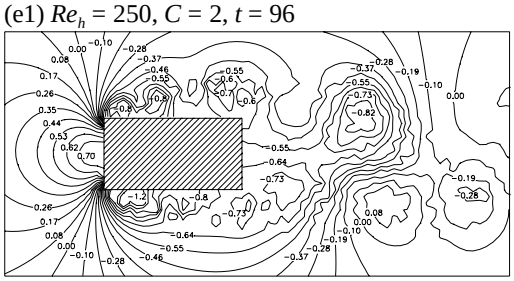

(f1) Re_h = 250, C = 2, t = 97

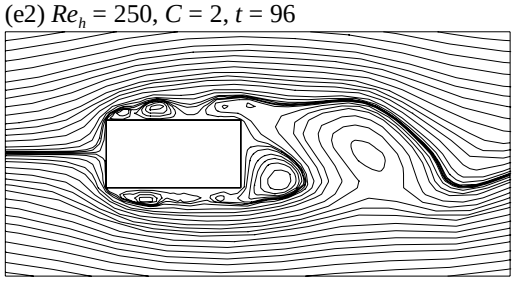

(f2) Re_h = 250, C = 2, t = 97

Figure 7.80. Instantaneous pressure fields and streamline patterns around C = 2 cylinder at Re_h = 250. Numbers shown are coefficients of static pressure.

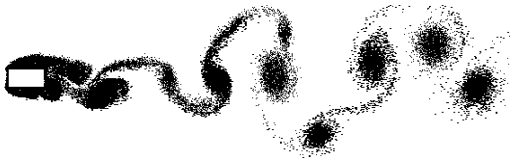

(a) Re_h = 500, C = 2, t = 70

(b) Re_h = 500, C = 2, t = 72

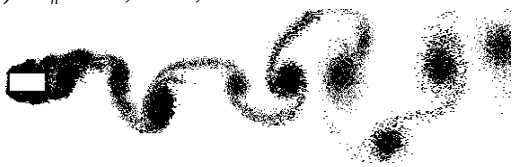

(c) Re_h = 500, C = 2, t = 74

(d) Re_h = 500, C = 2, t = 76

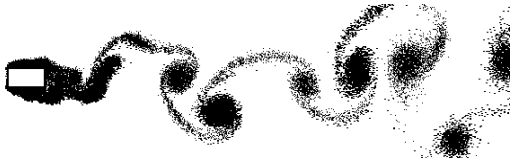

(e) Re_h = 500, C = 2, t = 78

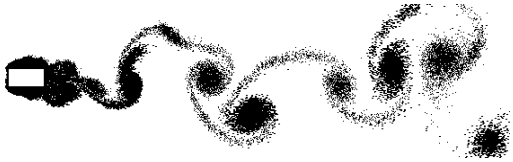

(f) Re_h = 500, C = 2, t = 80

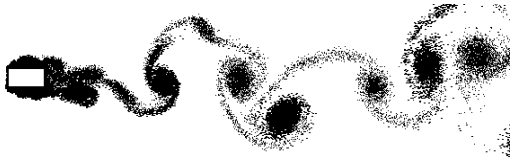

(g) Re_h = 500, C = 2, t = 82

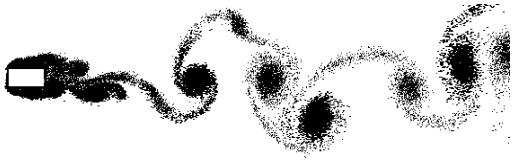

(h) Re_h = 500, C = 2, t = 84

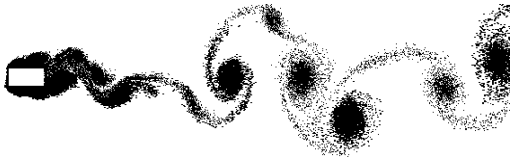

(i) Re_h = 500, C = 2, t = 86

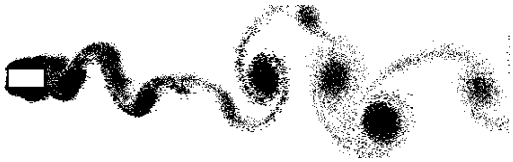

(j) Re_h = 500, C = 2, t = 88

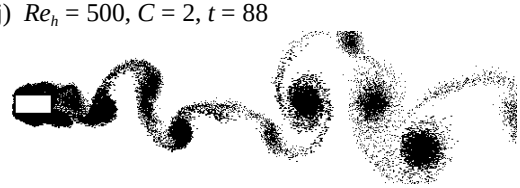

(k) Re_h = 500, C = 2, t = 90

(l) Re_h = 500, C = 2, t = 92

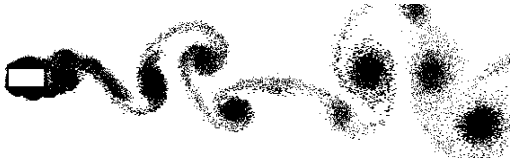

(m) Re_h = 500, C = 2, t = 94

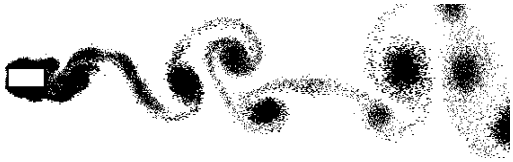

(n) Re_h = 500, C = 2, t = 96

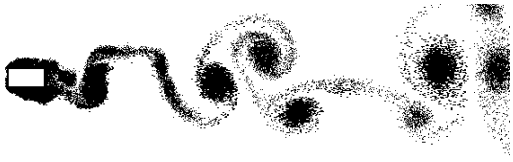

(o) Re_h = 500, C = 2, t = 98

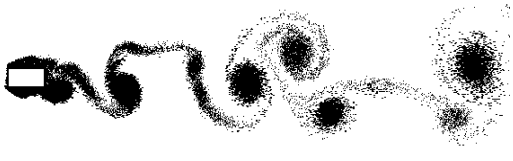

(p) Re_h = 500, C = 2, t = 100

(q) Re_h = 500, C = 2, t = 102

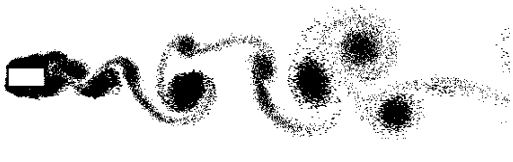

(r) Re_h = 500, C = 2, t = 104

Figure 7.81. Elemental-vortex distributions in fully-developed flow over C = 2 cylinder at Re_h = 500.

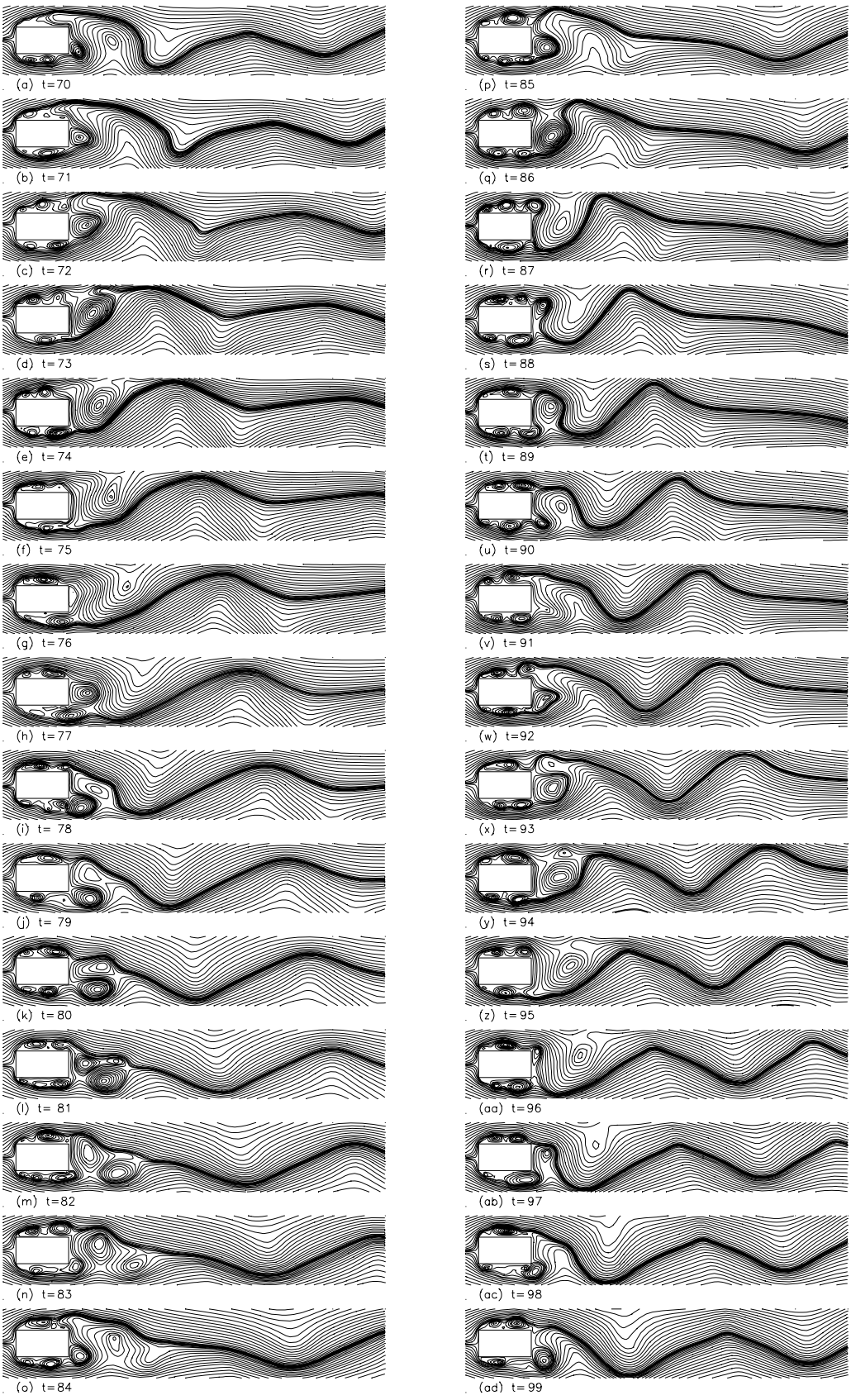

Figure 7.82. Streamline patterns in fully-developed flow over $C = 2$ cylinder at $Re_h = 500$.

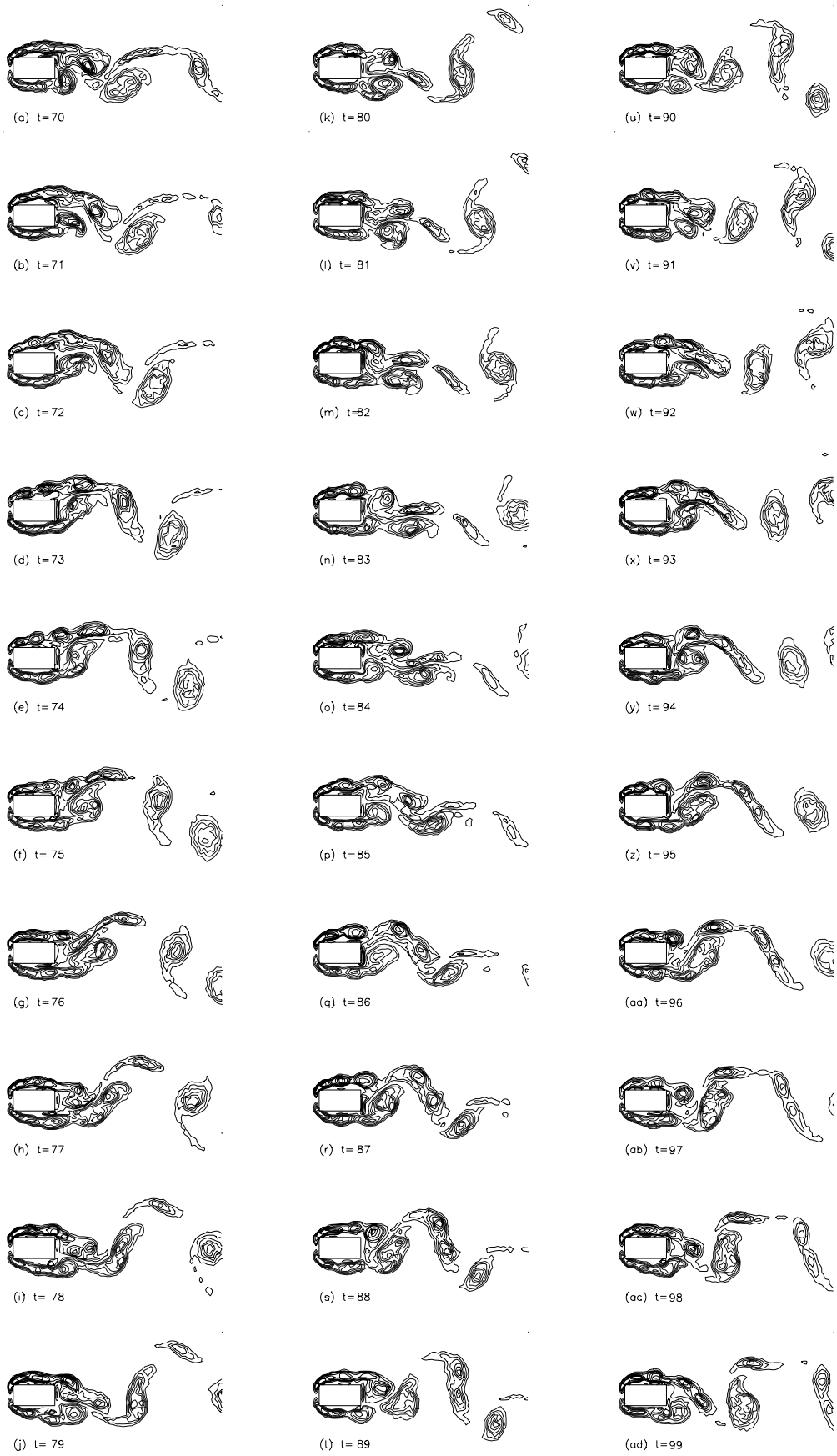

Figure 7.83. Vorticity contours in fully-developed flow over $C = 2$ cylinder at $Re_h = 500$.

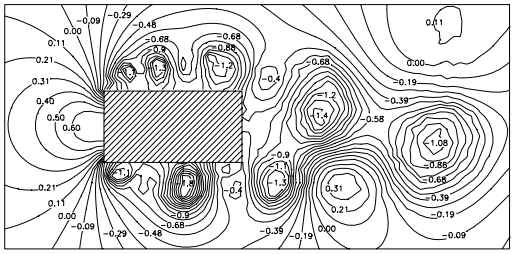

(a1) Re_h = 500, C = 2, t = 90

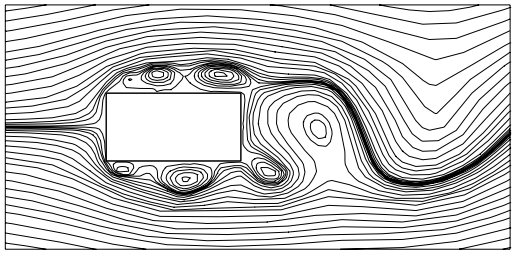

(a2) Re_h = 500, C = 2, t = 90

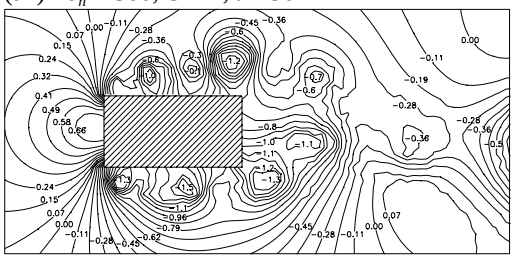

(b1) Re_h = 500, C = 2, t = 92

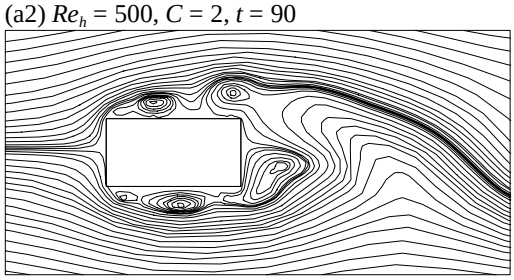

(b2) Re_h = 500, C = 2, t = 92

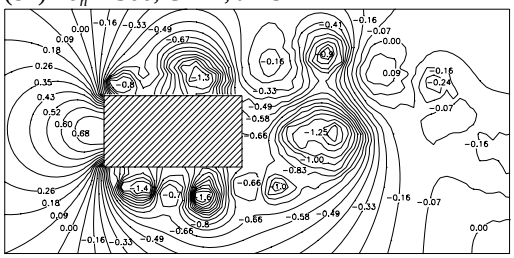

(c1) Re_h = 500, C = 2, t = 94

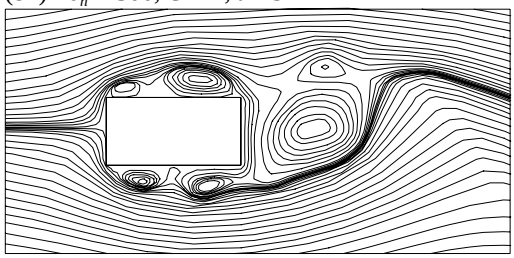

(c2) Re_h = 500, C = 2, t = 94

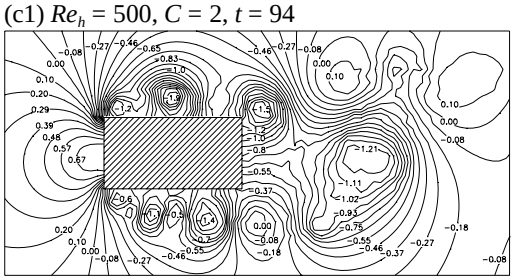

(d1) Re_h = 500, C = 2, t = 96

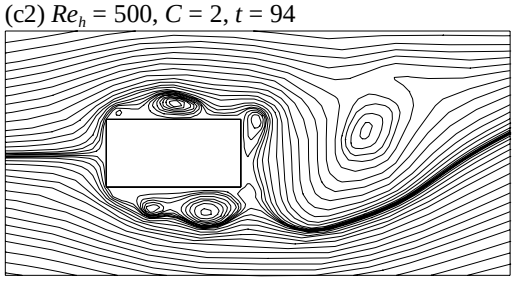

(d2) Re_h = 500, C = 2, t = 96

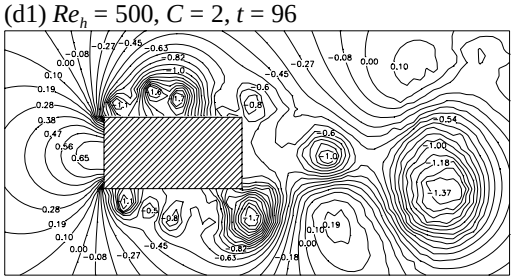

(e1) Re_h = 500, C = 2, t = 98

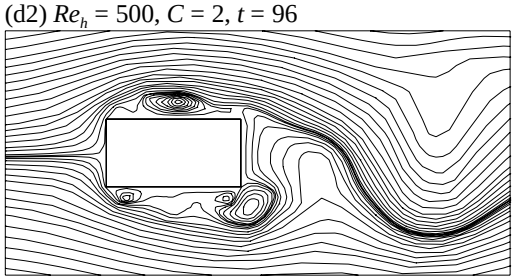

(e2) Re_h = 500, C = 4, t = 98

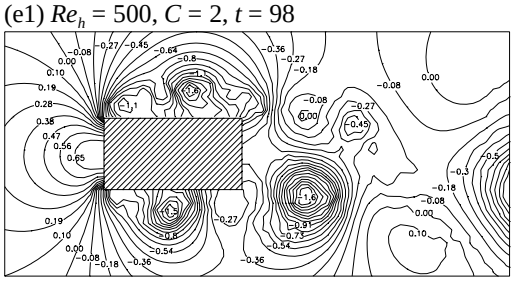

(f1) Re_h = 500, C = 2, t = 100

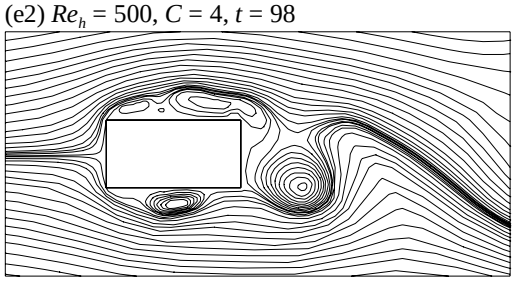

(f2) Re_h = 500, C = 2, t = 100

Figure 7.84. Instantaneous pressure fields and streamline patterns around C = 2 cylinder at Re_h = 500. Numbers shown are coefficients of static pressure.

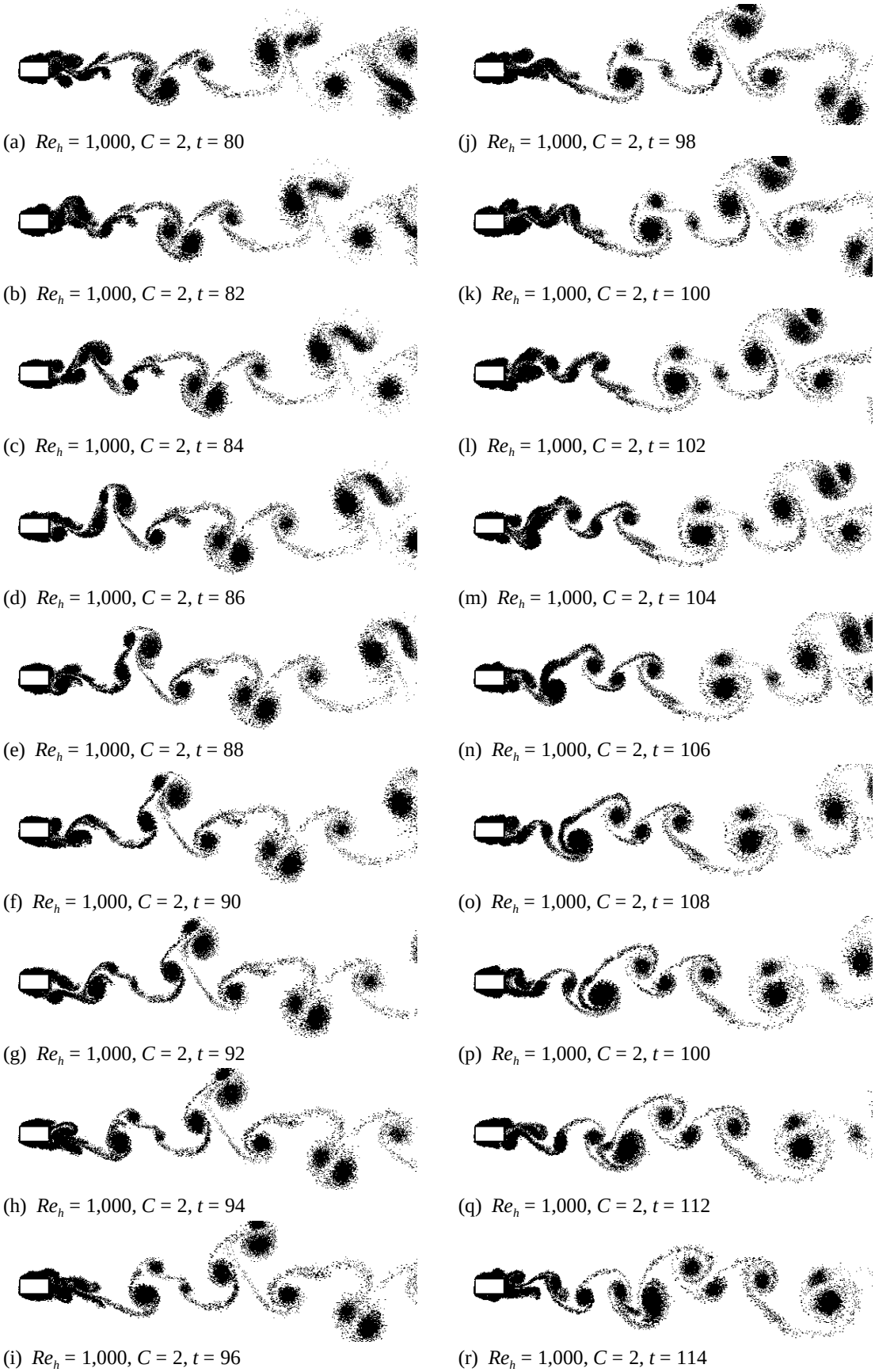

(a) Re_h = 1,000, C = 2, t = 80

(b) Re_h = 1,000, C = 2, t = 82

(c) Re_h = 1,000, C = 2, t = 84

(d) Re_h = 1,000, C = 2, t = 86

(e) Re_h = 1,000, C = 2, t = 88

(f) Re_h = 1,000, C = 2, t = 90

(g) Re_h = 1,000, C = 2, t = 92

(h) Re_h = 1,000, C = 2, t = 94

(i) Re_h = 1,000, C = 2, t = 96

(j) Re_h = 1,000, C = 2, t = 98

(k) Re_h = 1,000, C = 2, t = 100

(l) Re_h = 1,000, C = 2, t = 102

(m) Re_h = 1,000, C = 2, t = 104

(n) Re_h = 1,000, C = 2, t = 106

(o) Re_h = 1,000, C = 2, t = 108

(p) Re_h = 1,000, C = 2, t = 100

(q) Re_h = 1,000, C = 2, t = 112

(r) Re_h = 1,000, C = 2, t = 114

Figure 7.85. Elemental-vortex distributions in fully-developed flow over C = 2 cylinder at Re_h = 1,000.

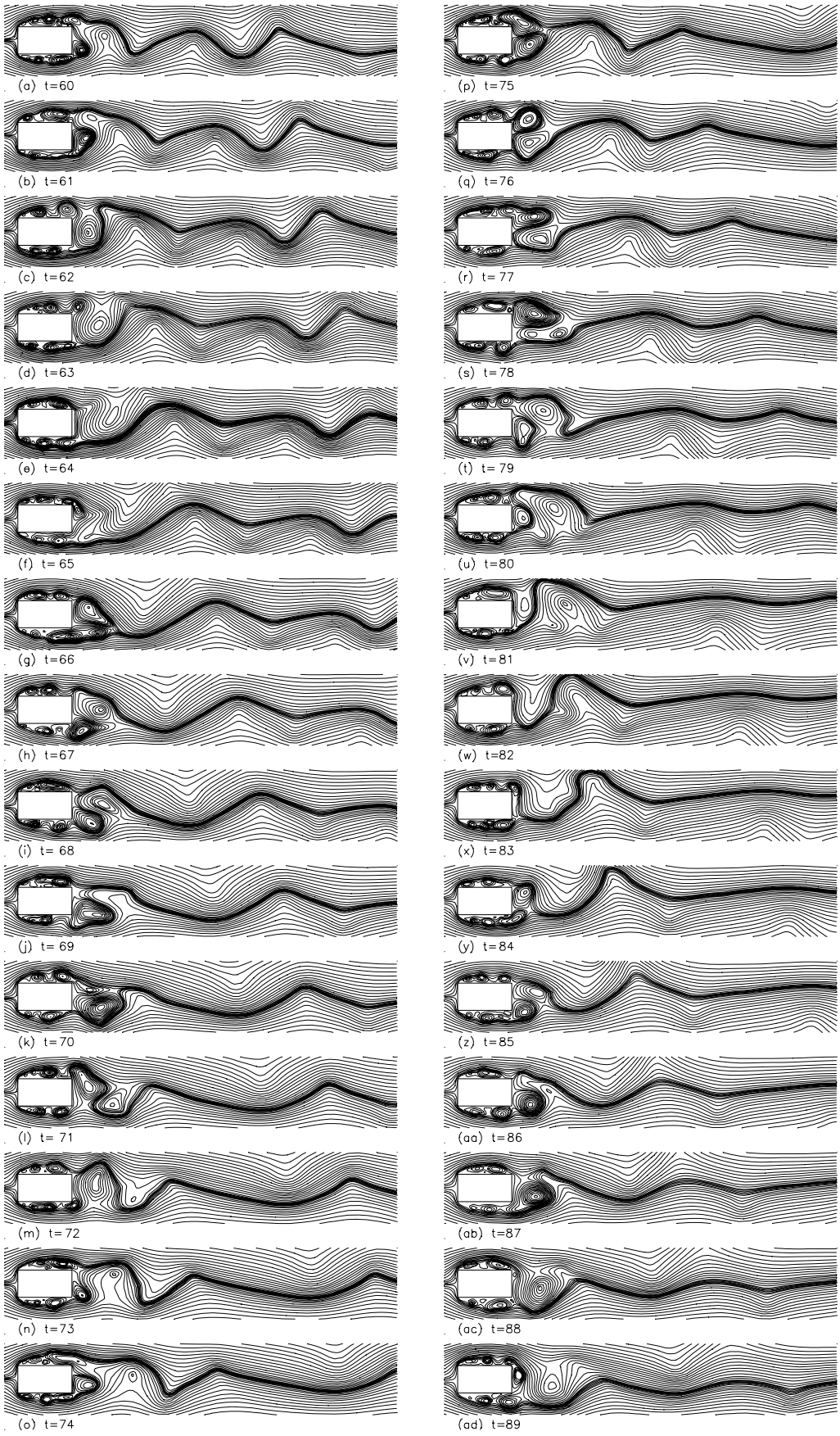

Figure 7.86. Streamline patterns in fully-developed flow over $C = 2$ cylinder at $Re_h = 1{,}000$.

Figure 7.87. Vorticity contours in fully-developed flow over $C = 2$ cylinder at $Re_h = 1{,}000$.

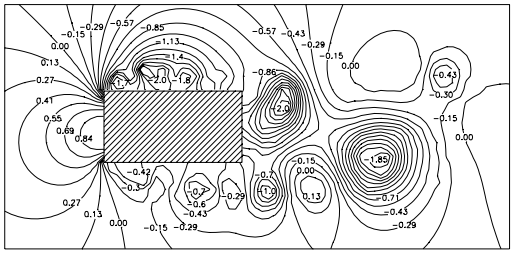

(a1) Re_h = 1,000, C = 2, t = 90

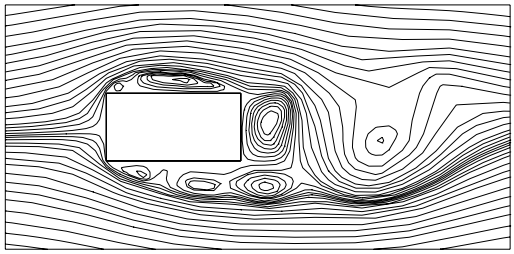

(a2) Re_h = 1,000, C = 2, t = 90

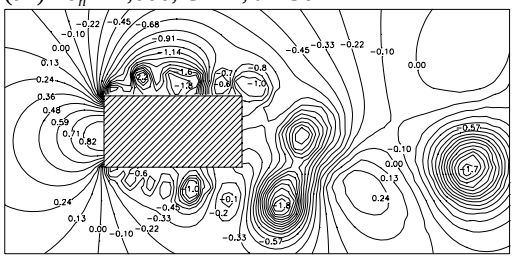

(b1) Re_h = 1,000, C = 2, t = 92

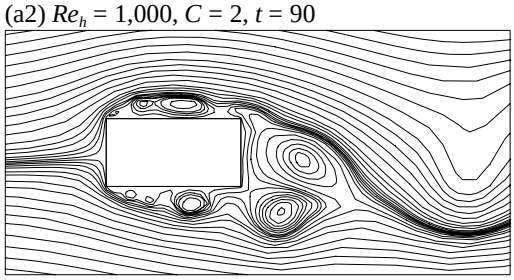

(b2) Re_h = 1,000, C = 2, t = 92

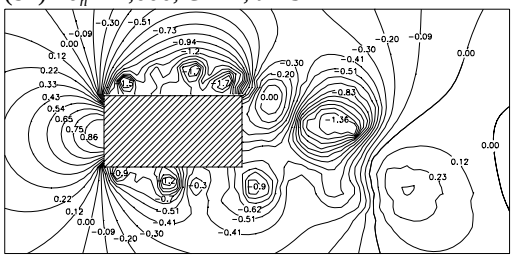

(c1) Re_h = 1,000, C = 2, t = 94

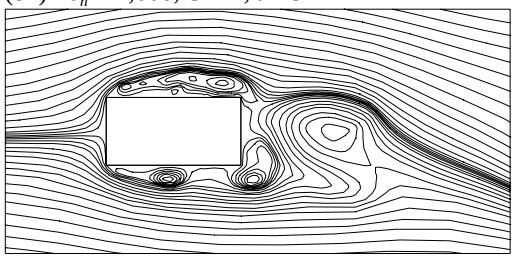

(c2) Re_h = 1,000, C = 2, t = 94

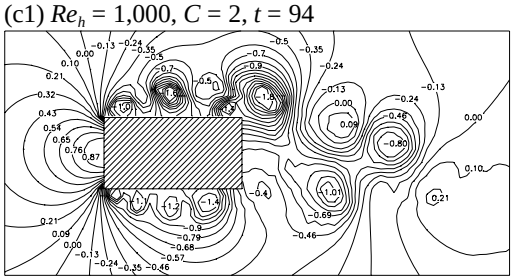

(d1) Re_h = 1,000, C = 2, t = 96

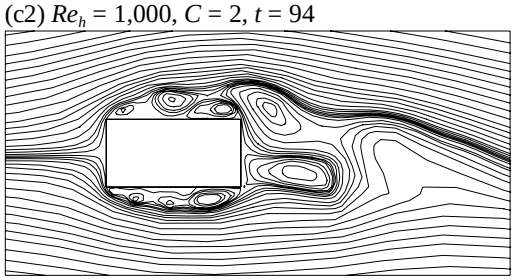

(d2) Re_h = 1,000, C = 2, t = 96

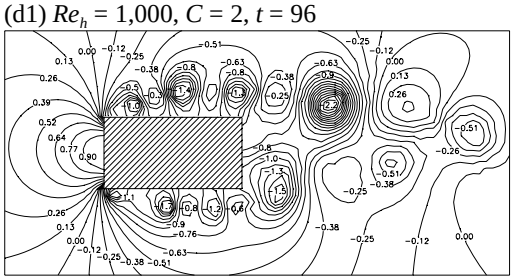

(e1) Re_h = 1,000, C = 2, t = 98

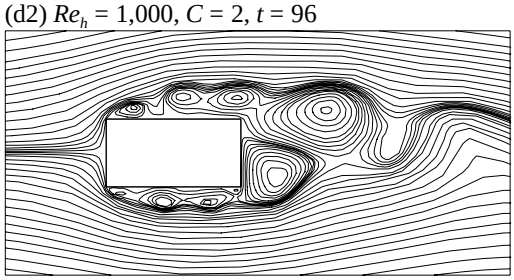

(e2) Re_h = 1,000, C = 2, t = 98

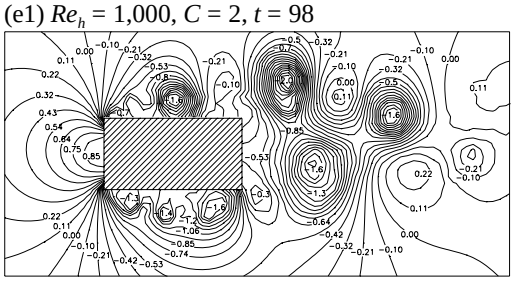

(f1) Re_h = 1,000, C = 2, t = 100

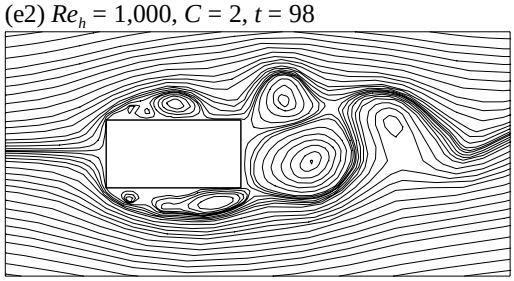

(f2) Re_h = 1,000, C = 2, t = 100

Figure 7.88. Instantaneous pressure fields and streamline patterns around C = 2 cylinder at Re_h = 1,000. Numbers shown are coefficients of static pressure.

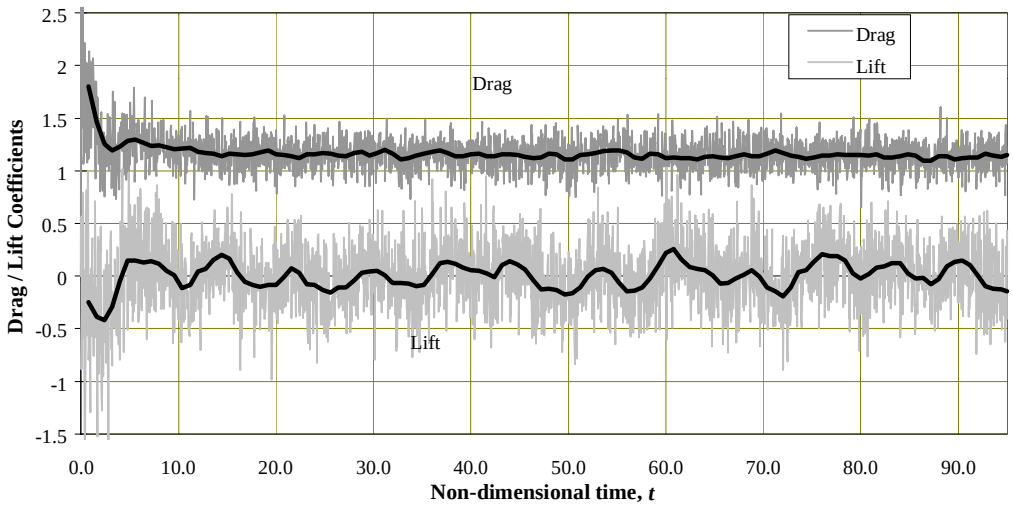

Figure 7.89. Time-histories of drag and lift coefficients on the $C = 2$ cylinder at $Re_h = 100$. Drag and lift are calculated for $\Delta t = 0.02$; highlighted mean drag and lift are averaged over $\Delta t = 0.8$.

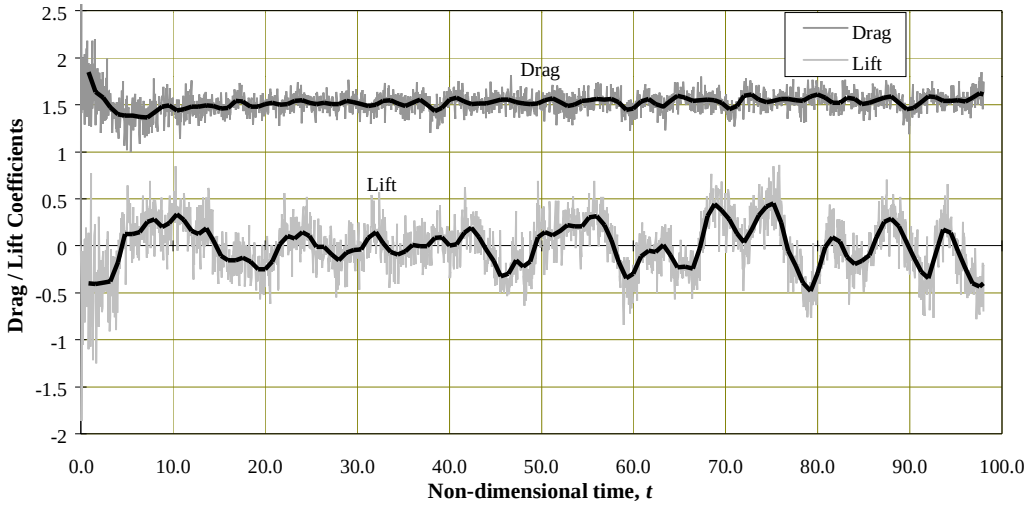

Figure 7.90. Time-histories of drag and lift coefficients on the $C = 2$ cylinder at $Re_h = 250$. Drag and lift are calculated for $\Delta t = 0.02$; highlighted mean drag and lift are averaged over $\Delta t = 0.8$.

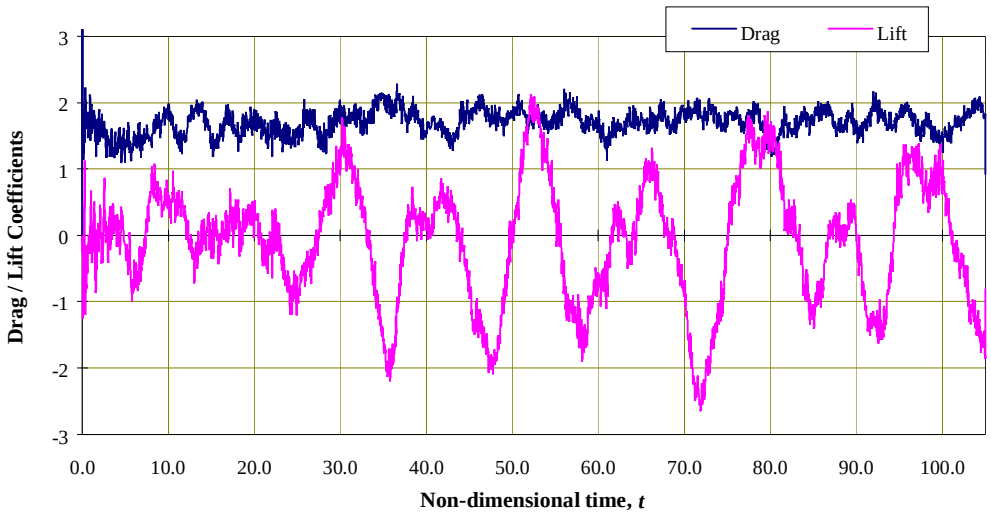

Figure 7.91. Time-histories of drag and lift coefficients on the $C = 2$ cylinder at $Re_h = 500$.

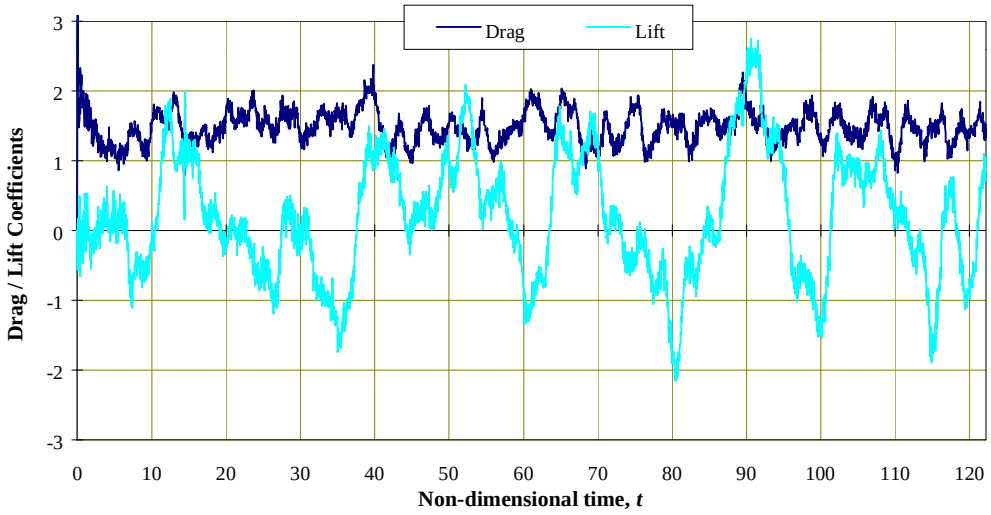

Figure 7.92. Time-histories of drag and lift coefficients on the C = 2 cylinder at Re_h = 1,000.

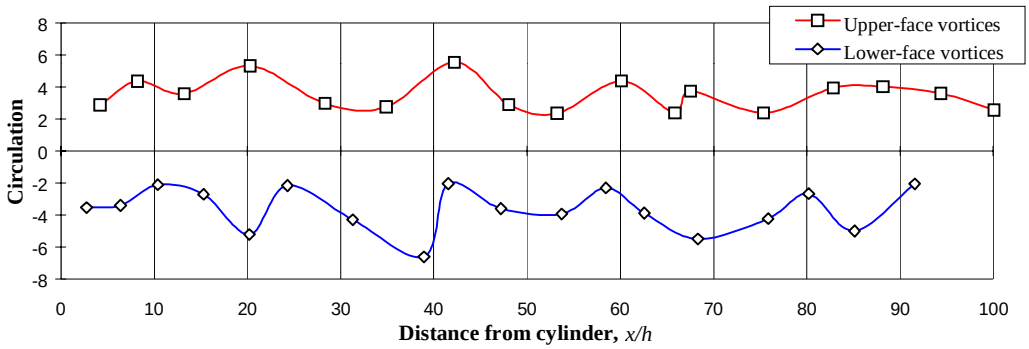

Figure 7.93. Variation of the circulation of vortices in the wake of C = 2 cylinder at Re_h = 1,000.

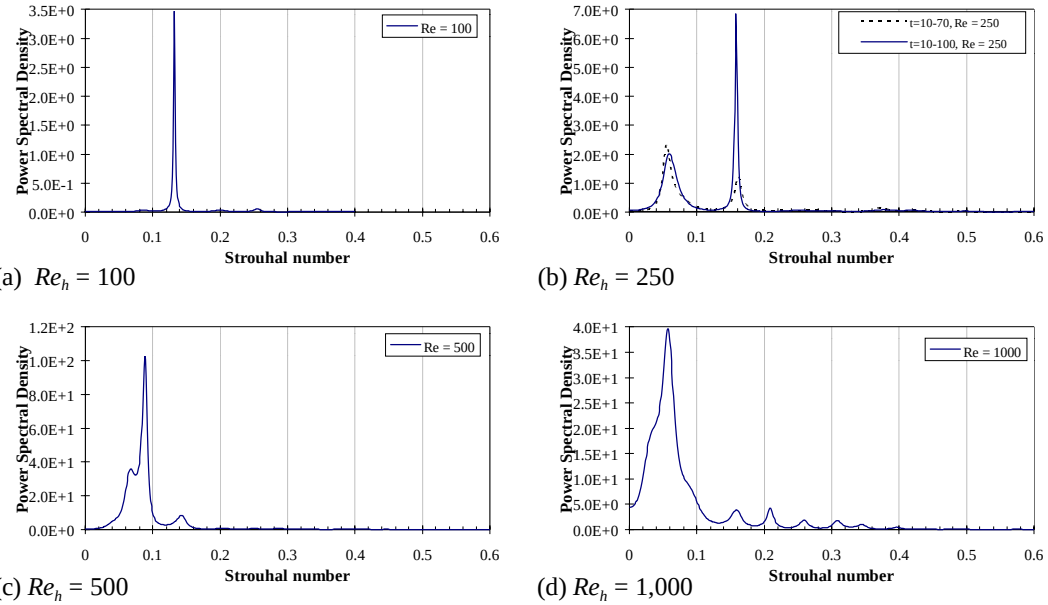

(a) Re_h = 100 (b) Re_h = 250

(c) Re_h = 500 (d) Re_h = 1,000

Figure 7.94. Power spectra of fluctuating lift of the C = 2 cylinder at Re_h = 100, 250, 500 and 1,000.

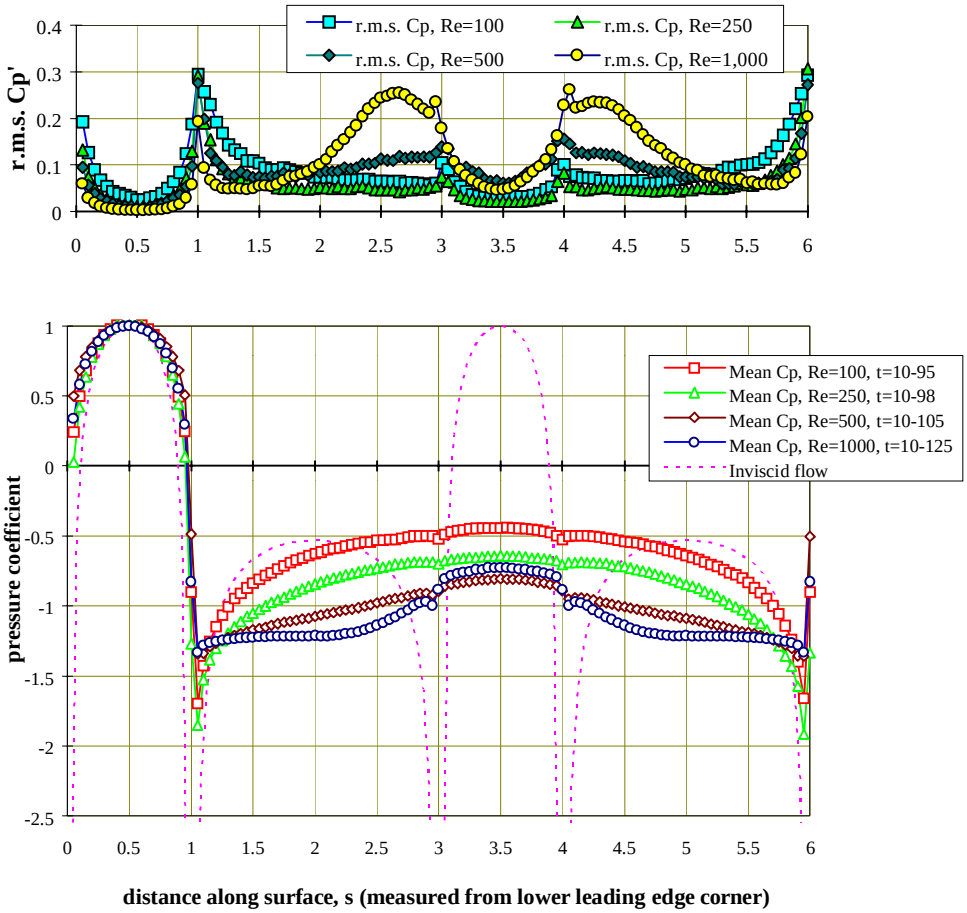

Figure 7.95. Predicted distributions of mean and r.m.s. pressure coefficients along surface of rectangular plate with C = 2 at Re_h = 100, 250, 500 and 1,000.

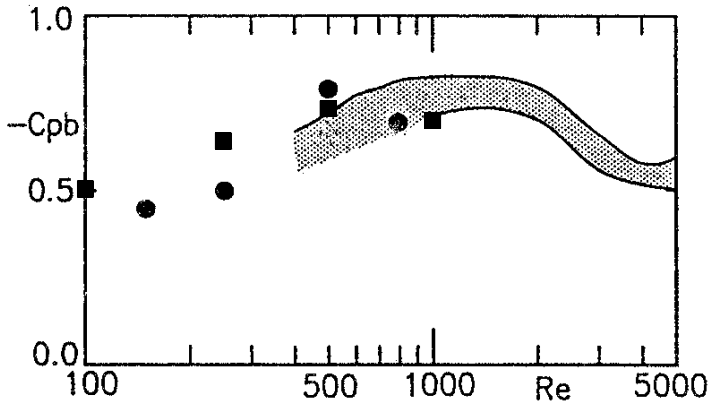

Figure 7.96. Base pressure coefficients $-C_{pb}$ of the C = 2 cylinder; ● : computed values of Okajima *et al.* [1990], ■ : computed results of this study, ▒ : experimental data of Okajima *et al.* [1990].

7.4.3 Fully-Developed Flow Over a Rectangular Plate with $C = 4$

Rectangular cylinders with $C = 4$ have been studied by Lane and Loehrke [1980], Okajima [1982], Okajima [1990], Okajima, Nagahisa and Rokugoh [1990], Nakamura, Ohya and Tsuruta [1991], Ohya, Nakamura, Ozono, Tsuruta and Nakayama [1992], Okajima, Ueno and Sakai [1992], Ozono, Ohya and Nakamura [1992], Norberg [1993] and others.

According to the generalised dependence of the fully-developed flow regime on C and Re_h shown in Fig. 7.1, a sequence of three flow regimes can be expected as Re_h increases from 100 to very high values (in excess of 10^5): steady flow with laminar separation from the leading corners and laminar reattachment to the side surfaces for $100 \leq Re_h \lesssim 400$; laminar leading-corner separation followed by intermittent turbulent reattachment to the side surfaces for $400 \lesssim Re_h \lesssim 1{,}500$, and turbulent separation from the leading corners followed by turbulent reattachment to both side surfaces for $Re_h > 1{,}500$. The flow over $C = 4$ cylinders is subject to impinging-shear-layer instability which, as reported by Nakamura, Ohya and Tsuruta [1991], characterises the vortex-shedding process from long rectangular cylinders with $C \gtrsim 3$.

The present calculated results for $Re_h = 100$ are presented in Figs. 7.101–7.104: distributions of elemental vortices in Fig. 7.101; streamline patterns in Fig. 7.102; vorticity contours in Fig. 7.103; instantaneous pressure distributions in Fig. 7.104. Corresponding results for Reynolds numbers of 250, 500 and 1,000 are presented in Figs. 7.105–7.108; Figs. 7.109–7.112 and Figs. 7.113–7.116 respectively. The time-histories of lift and drag for $Re_h = 100$, 250, 500 and 1,000 are shown in Figs. 7.117–7.120 respectively, and the power spectra of lift fluctuations for these Reynolds numbers in Fig. 7.121. Calculated Strouhal numbers and surface-pressure distributions are shown in Figs. 7.122 and 7.123 as a function of Reynolds number.

7.4.3.1 Comparisons of Present Results with Experimental and Numerical Data of Previous Work

Calculated streamline patterns for $C = 4$ at $Re_h = 500$ given by Okajima [1990] are shown in Fig. 7.97 together with the streamline patterns of the present calculation. There are close similarities between these two sets of calculated flow patterns. Both indicate side-surface reattachment, and the formation of a leading-edge-separation bubble and shedding of large-scale side-face vortices from it. In the present results, convective motion of vortices along the

side face can be seen in (b) and (d) of the figure (and more clearly in the time sequence shown later in Fig. 7.106). A similar process can be inferred from the results given by Okajima [1990]. However, there are differences in the finer details. The flow patterns obtained by Okajima indicate the leading-edge-separation bubble growing to such a size that it takes up most of the side surface, resulting in a flow pattern with the character of a flow detached from the side surface; the flow patterns obtained in the present work show rather short leading-edge-separation bubbles and a rather greater extent of reattached flow towards the trailing corner and in this respect show a stronger similarity to the flows at somewhat higher Reynolds numbers.

Ohya, Nakamura, Ozono, Tsuruta and Nakayama [1992] and Okajima, Ueno and Sakai [1992] present examples of calculated streamline and vorticity patterns for Re_h = 1,000. Comparisons of their calculations and the present results are made in Figs. 7.98 and 7.99 respectively, and there are clearly quite close general similarities. As for Re_h = 500, the present calculations tend to show rather shorter leading-edge-separation bubbles and greater extents of reattached flow. The calculation of Ohya *et al.* show a zero value of the time-averaged C_L in the initial stages of the motion with a later change to non-zero value. The present calculations, while not reproducing this particular behaviour, do show variation in the mean C_L value although not on quite so large a time-scale. As Figs. 7.98(c) and (d) show, the present calculations produce a more irregular vortex wake than that of Ohya *et al.*'s C_L = 0 flow.

Calculated Strouhal numbers of vortex shedding for C = 4, as a function of Reynolds number, are compared with the experimental data of Okajima [1982] and Norberg [1993] in Fig. 7.100. The experimental Strouhal number varies very little with Reynolds number, even though changes in flow regime occur over the Reynolds number range investigated. The values computed by Ohya *et al.* and Okajima *et al.* agree very closely with experimental data. The values from the present study are however noticeably higher over the Reynolds number range $250 \leq Re_h \leq 1{,}000$. This difference appears to be related to the difference in the lengths of reattached flow, already referred to, which are indicated by the present calculations; the significance of this difference is discussed later (in section 7.5).

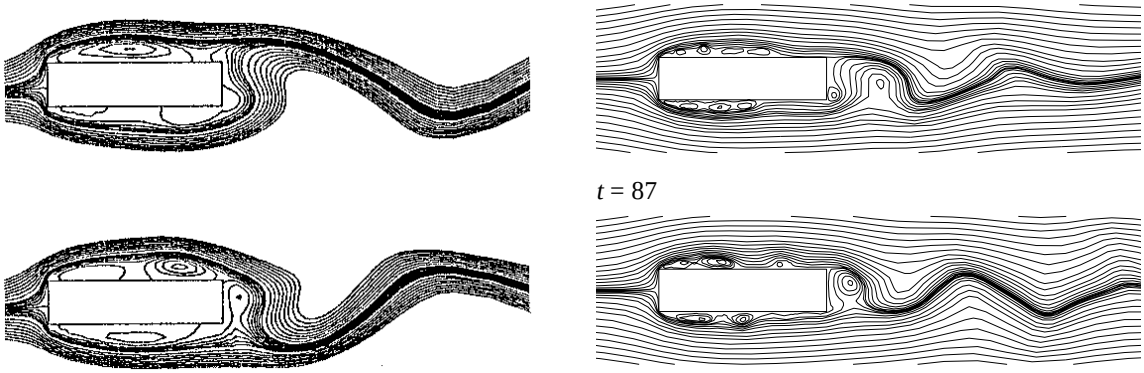

(a) (b)

Figure 7.97. Streamline patterns for $C = 4$ at $Re_h = 500$: (a) calculated results of Okajima [1990], (b) calculated results of this study.

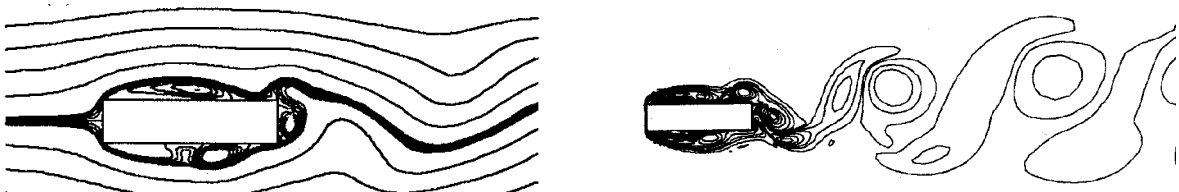

(a) Streamlines for $Re_h = 1{,}000$, $t = 92.9$

(c) Isovorticity contours for $Re_h = 1{,}000$

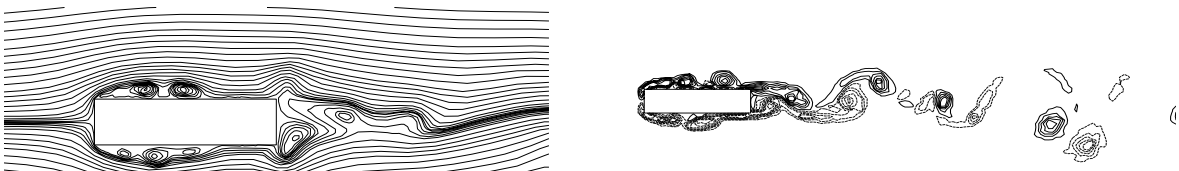

(b) Streamlines for $C = 4$ at $Re_h = 1{,}000$ at $t = 87$.

(d) Isovorticity contours for $Re_h = 1{,}000$ at $t = 90$.

Figure 7.98. Streamlines and isovorticity contours for $C = 4$ at $Re_h = 1{,}000$: (a) and (c) calculated results of Ohya, Nakamura, Ozono, Tsuruta and Nakayama [1992], (b) and (d) calculated results of this study.

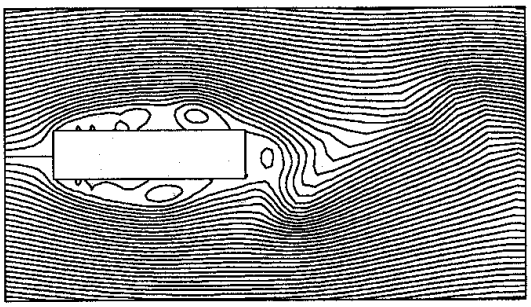

(a) Streamlines for $C = 4$ at $Re_h = 1{,}000$

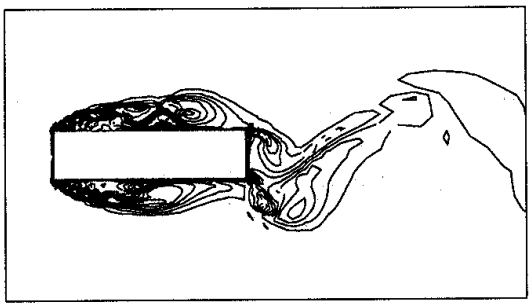

(c) Isovorticity contours for $C = 4$ at $Re_h = 1{,}000$

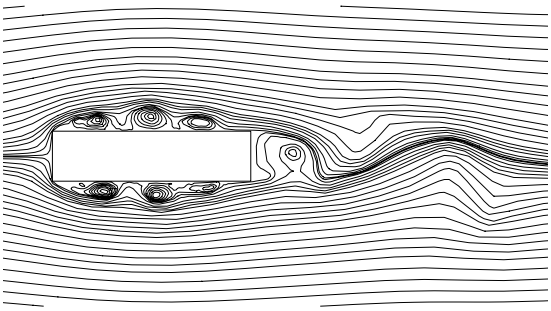

(b) Streamlines for $C = 4$ at $Re_h = 1{,}000$, $t = 75$

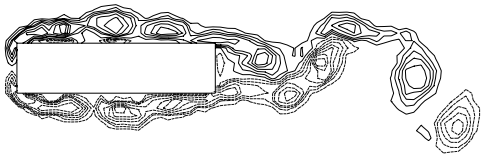

(d) Vorticity contours for $C = 4$ at $Re_h = 1{,}000$, $t = 75$

Figure 7.99. Streamlines and isovorticity contours for $C = 4$ at $Re_h = 1{,}000$: (a) and (c) calculated results of Okajima, Ueno and Sakai [1992], (b) and (d) calculated results of this study.

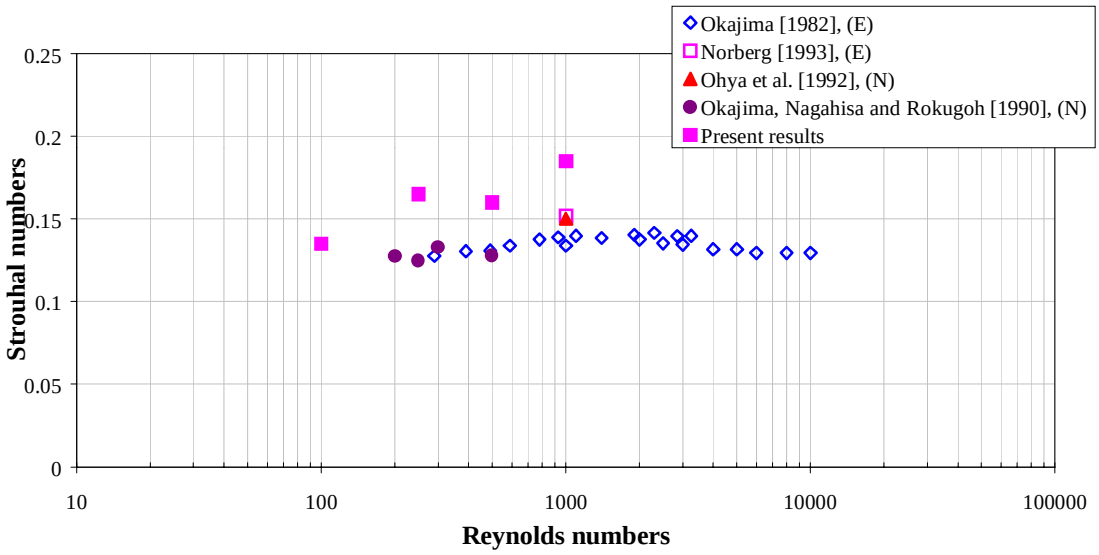

Figure 7.100. Variation of Strouhal number with Reynolds number for flow over $C = 4$ cylinder.

7.4.3.2 Details of Computed Fully-Developed Flow Patterns for C = 4 Cylinders

For the fully-developed flow over the $C = 4$ cylinder at $Re_h = 100$, the calculated streamline patterns (Fig. 7.102) show that the flow along the side surfaces is essentially fully-attached. There are some traces of the formation of very weak discrete vortices on the side faces of the cylinder, but the instantaneous pressure fields (Fig. 7.104) do not show the high pressure gradients associated with the flow reattachment accompanying formation of a leading-edge-separation bubble, and the streamlines remain essentially parallel to the cylinder surface. There is therefore continuous transport of vorticity along the side surfaces of the cylinder in the boundary layers. The dominant process of vortex formation downstream of the cylinder is the rolling up of the shear layers formed by separation of the side-face boundary layers from the trailing corners of the cylinder. The vortex-formation region behind the cylinder, (Figs. 7.102 and 7.103) is quite long, of the order of 10 plate thicknesses. It seems that the flow over the $C = 4$ cylinder at $Re_h = 100$ is in a marginal state between fully attached flow and flow with small leading-edge-separation bubbles in which discrete vortices might form.

The vortex street formed behind the cylinder is narrow and the lift on the cylinder fluctuates with small amplitude (Fig. 7.117). The vortex wake is quite regular (more so than the lift fluctuation might indicate), and the power spectrum of the lift fluctuation (Fig. 7.121(a)) shows a sharp dominant peak at the vortex-shedding frequency $St \approx 0.13$. The drag fluctuations, about the mean value of $C_D = 1.05$, are too small to yield a meaningful spectrum.

At $Re_h = 250$, the streamline, vorticity and instantaneous pressures patterns (Figs. 7.106-7.108) show flow separation at the leading corners of the cylinder, followed by reattachment of the separated shear layers to the side faces, occurring at all times. This results in the formation of leading-edge-separation bubbles and discrete side-face vortices, which are now more prominent than at $Re_h = 100$, but still quite weak, and become quite diffuse before reaching the trailing edge. The flow downstream of reattachment is thus essentially fully-attached along the side faces. As in the previous case of $Re_h = 100$, the dominant process of formation of wake vortices is the rolling up of shear layers formed by boundary layer separation from the trailing edge. Consequently, the vortex-street patterns, the time-histories of lift and drag variations, and the distributions of surface-pressure are very similar to those for $Re_h = 100$. The power spectrum of fluctuating lift (Fig. 7.121(b)) has a single dominant peak at $St \approx 0.16$. The drag on the cylinder varies with very small fluctuation about a mean value of $C_D = 1.3$.

It is apparent, from the time-histories of the elemental-vortex distributions (Fig. 7.105) and lift variations (Fig. 7.118), that the vortex shedding process at $Re_h = 250$ is essentially regular, but subject to a low-frequency modulation. The vortex-shedding frequency ($St \approx 0.16$) appears as the major peak in the power spectrum of lift variation while the modulation frequency appears as the minor peak at $St \approx 0.03$. The modulation can, as previously seen in the case of $C = 2$ cylinders, be related to periodic variation in strength of the vortices shed from the cylinder into the wake. It is also notable that the frequency of formation of side-face vortices from the leading-edge separation bubbles is greater than the wake shedding frequency (owing to amalgamation of side-face vortices in the wake). A small peak in the power spectrum at $St \approx 0.22$ appears to correspond to the frequency of side-vortex formation. It therefore appears that the calculated process of vortex generation and shedding is essentially the same as that observed experimentally (at higher Reynolds number) by Kiya and Sasaki [1983] in their study of the leading-edge-separation bubble on a very long plate with square leading edge. Kiya and Sasaki found that side-face vortices are shed from the bubble at a frequency of about $0.6U_\infty/x_R$, and that, in addition, the bubble undergoes a lower-frequency enlargement and contraction, accompanied by shedding of much larger vortices at a frequency less than about $0.2U_\infty/x_R$ (and typically about $0.12U_\infty/x_R$). (This latter large-scale unsteadiness of the bubble is responsible for the observed "flapping" motion of the separated shear layer near the separation line.) In these frequency relations x_R is the time-mean bubble length. In the present context a value of $x_R/h \sim 2.5$ appears to be consistent with the calculated flow patterns. With Kiya and Sasaki's relations, this would yield Strouhal numbers of $St = 0.24$ and 0.048 respectively, which are similar to the calculated side-face-vortex-shedding and modulation Strouhal numbers of 0.22 and 0.03.

At $Re_h = 500$, the calculated streamline and isobar patterns indicate that the reattached flow persists (in contrast to the expectation from Fig. 7.1 of intermittent separation). The process of formation of discrete side-face vortices by bifurcation of the leading-edge-separation bubble (as in the previous cases of $C = 1$ and $C = 2$) is now much more clearly evident than at the lower Reynolds numbers, but the flow downstream of the bubble remains attached except in so far as it is disturbed by the passing large-scale vortices.

A typical sequence of events in the flow can be seen, for example, on the upper surface from $t = 90$ onwards, as shown in Fig. 7.110. While a discrete vortex is being convected along the side surface, the shear layer separated from the trailing corner rolls up to form a wake vortex

on the trailing face (t = 94 and 94.5). There is some general indication that the initiation of a nascent trailing-face vortex occurs in synchronism with the passage of a discrete vortex over the trailing corner. The resulting wake vortex grows (t = 95) before it is shed into the wake (t = 96). It should be noted that the frequency of formation of discrete vortices on the side surface is higher than the frequency of formation of wake vortices. There are therefore times at which the passage of a discrete vortex over the trailing corner does not coincide with the birth of a wake vortex on the trailing face. In this case, the discrete side-face vortex is shed into the wake without merging with the forming wake vortex. However, when the two vortices are convected further downstream, they merge to form one vortex in the final vortex street (as can be seen, for example, in the flow on the upper surface from t = 91 to 94 and t = 96 to 100, Fig. 7.111).

The frequencies of wake and side-face vortex shedding can be determined from the time-sequences of vorticity contours such as those of Fig. 7.111 to be $St \approx 0.16$ and $St \approx 0.19$. These two values are reflected as peaks in the spectrum of fluctuating lift (Fig. 7.121(c)). The presence of these two frequencies is responsible for the departures from regular vortex shedding which are evident in Fig. 7.109. The increased strength of the side-face vortices, accompanying the increase in Re_h from 250 to 500, results in their becoming more dominant in determining lift fluctuations than the trailing-face vortices: the largest spectral component in the lift spectrum (Fig. 7.121(c)) is now that at St = 0.19 corresponding to side-face-vortex generation. A small low-frequency spectral peak at $St \approx 0.02$ can be identified with modulation of the time-history of the lift coefficient (Fig. 7.119), which is presumably associated with oscillation of the leading-edge-separation bubble and corresponding variation in strength of side-face vortices, as previously seen for the C = 2 cylinder.

When the Reynolds number is increased to Re_h = 1,000, the calculated streamline patterns and instantaneous pressure fields (Figs. 7.114 and 7.116) still show flow with permanent reattachment to both side surfaces and subsequent separation from the trailing edges. There are close similarities between the flows at Reynolds numbers of 500 and 1000. The process of formation of large-scale discrete vortices in the leading-edge-separation bubble and the shedding of side-face vortices from the bubble at Re_h = 1,000, which is similar to all previously described cases, can be seen in the streamline and isovorticity patterns in Figs. 7.114 and 7.115. However, the flow at Re_h = 1,000 exhibits a significant difference from flows at lower Reynolds numbers: the shedding frequencies of side-face vortices and of trailing-face vortices are now synchronised, and side-face and trailing-face vortices are shed into the wake simultaneously.

This appears to be an instance of the effect observed by Rockwell and Naudasher [1978] and Nakamura, Ohya and Tsuruta [1991] of enhancement of an impinging-shear-layer instability by feed-back from the impingement surface. Because of the synchronism of shedding of side-surface and trailing-face vortices, the lift-fluctuation spectrum (Fig. 7.121(d)) no longer exhibits a double peak such as that in the Re_h = 500 spectrum (at $St \approx 0.16$ and 0.19), but, instead, a single sharp peak at $St \approx 0.19$. However, since the mechanism of formation of side-face vortices appears to be unchanged, low-frequency oscillation of the leading-edge-separation bubble and a corresponding periodic variation in the strength of the side-face vortices are still to be expected. The low-frequency modulation of the time-history of lift coefficient (Fig. 7.120) and the minor peak in the lift spectrum at this frequency, $St \approx 0.02$, (Fig. 7.121(d)) are attributed to these effects.

A typical sequence of events in the flow can be seen on the upper surface from t = 77 onwards (Figs. 7.114 and 7.115). While a vortex from the separation bubble is being convected along the side surface (t = 77 and 78), the shear layer separating from the upper trailing corner is rolling up to form a wake vortex on the trailing face of the cylinder. The side-face vortex, after passing the trailing corner, is shed into the wake with the trailing-face vortex (t = 79, 80). As is evident from the isovorticity contours, Fig. 7.115, from time t = 79 to t = 84, the two vortices merge as they are convected downstream. After passage of the side-surface vortex over the trailing corner, the flow on the side surface, downstream of the bubble, again becomes fully-attached, with separation finally occurring at the trailing edge. This leads to the formation of a new nascent trailing-face vortex which gains vorticity from the shear layer separating from the trailing edge. In the mean time, the next side-face vortex is released from the separation bubble, as the latter splits and contracts (t = 80, 81), and convected downstream along the side surface. The forming trailing-face vortex and the side-face vortex are then shed into the wake simultaneously to form the next wake vortex shed from the upper surface (at t = 83).

The comparison between the vortex-shedding frequencies for the plate with C = 4 obtained in the present work and existing numerical and experimental data has been briefly introduced in section 7.4.3.1 and is now considered further. The preceding examination in this section of the results of present work shows that, according to the calculations, the flow in the Reynolds number range $100 \le Re_h \le 1{,}000$ is always attached to the side faces for some distance upstream of the trailing-edge corners and separates at the corners. The mechanism of vortex shedding then involves the interaction of side-face vortices generated from the leading-edge-separation

bubbles and trailing-face vortices generated by trailing corner separation. Each of these two vortex-generation processes has its own characteristic frequency. The frequency of generation of side-face vortices is greater than that of trailing-face vortices; the difference between the two frequencies is greatest at low Reynolds numbers but decreases with increasing Reynolds number until the two frequencies coincide at $Re_h \approx 1{,}000$. The frequency of vortices in the wake, well downstream of the cylinder, is that of the trailing-face vortices, after amalgamation with side-face vortices, either in the process of side-face-vortex formation or during convection in the near-wake of the cylinder. The Strouhal numbers shown previously in Fig. 7.100 are those of the (far-) wake-vortex frequencies. The data are presented again in Fig. 7.122 with the addition of the Strouhal numbers of side-face-vortex formation and the modulation frequency of lift variation. Modulation of the amplitude of lift fluctuation results from periodic variation of side-face-vortex strength in a particular flow, but the general level of this vortex strength increases with Reynolds number. As a result of the latter effect, the largest spectral amplitude of lift fluctuation occurs at the wake-vortex frequency at low Reynolds numbers, but at the side-face-vortex frequency at high Reynolds numbers.

It has already been noted that the present calculated flow patterns always show attached flow upstream of the trailing corners, and do not predict the intermittently attached and detached flow observed experimentally when $Re_h \gtrsim 400$. However, although calculations for $Re_h > 1000$ have not been made, further increases in side-face-vortex strength with increasing Reynolds number could well be expected to lead to flows with intermittent complete detachment. This consideration suggests that the calculations represent a transitional unsteady flow between one of steady laminar leading-edge separation and reattachment and one of intermittent reattachment after leading-edge-separation, but that the effects of increasing Reynolds number are not sufficiently strongly simulated. One possible deficiency in the calculations is the effect of inaccurate simulation of the boundary layer development on the side faces after reattachment on trailing-edge vortex shedding frequency. It should also be remembered that the calculations do not take account of transition toturbulence in the separated shear layer, which according to experimental results occurs for $Re_h \gtrsim 300$.

The instantaneous pressure fields around the cylinder over one vortex-shedding cycle at Re_h = 100, 250, 500 and 1,000 (Figs. 7.104, 7.108, 7.112 and 7.116 respectively) show that the surface pressure gradients associated with flow reattachment and side-face vortices increase with increasing Reynolds number, in accord with the previously noted general increase in

strength of the side-face vortices with increasing Re_h. Consequently, streamwise movement of these pressure-gradient patterns with the convected side-face vortices leads to pressure fluctuations increasing with Reynolds number. The increase in the r.m.s. surface-pressure coefficient $C_{p'}$ (Fig. 7.123) is most dramatic for the increase in Reynolds number from 500 to 1,000. The calculated pressure-fluctuation coefficientsare of similar magnitude and streamwise distribution to those measured in an isolated leading-edge-separation bubble by Cherry, Hillier and Latour [1984]. On both side faces, the highest value of $C_{p'}$ occurs at a distance downstream of the leading edge of $x/h \approx 2.2$ at $Re_h = 500$ and $x/h \approx 2.0$ at $Re_h = 1{,}000$, and from the streamline patterns (Figs. 7.110 and 7.114) it can be seen that these positions are somewhat upstream of the mean positions of flow reattachment on the side surfaces; this is also in accord with Cherry *at al*.'s measurements.

The distributions of the coefficient of time-averaged pressure C_p over the cylinder surface, at the selected Reynolds numbers, are also shown in Fig. 7.123. They are very similar to those for the $C = 2$ cylinders (Fig. 7.95), and show a very similar variation with Reynolds number. As for the $C = 2$ cylinder, the base pressure is fairly uniform: the base pressure coefficient increases from $-C_{pb} \approx 0.35$ at $Re_h = 100$ to $-C_{pb} \approx 0.65$ at $Re_h = 250$, and remains fairly constant at $-C_{pb} \approx 0.65$ as the Reynolds number is further increased to 1,000.

Okajima, Nagahisa and Rokugoh [1990] have computed base pressure coefficients for Reynolds numbers in the range $200 \le Re_h \le 500$, and give a comparison of their results with experimental values. Both calculated and experimental values of $-C_{pb}$ increase with increasing Reynolds number for $Re_h \le 1{,}000$; the computed values are generally rather higher than the experimental values, although the difference decreases as Re_h increases. The present calculated values show a similar variation with Reynolds number, but are generally higher than both the experimental and computed values of Okajima *et al*. This discrepancy is consistent with the difference in flow patterns between present calculations and Okajima *et al.'s* (whose computed flow patterns are the same as the ones given by Okajima [1990] which have been shown earlier in section 7.4.3.1 as Fig. 7.97). In contrast, the calculated $-C_{pb}$ for $Re_h = 1{,}000$ given by Okajima, Ueno and Sakai [1992] is on the low side of experimental data; but the present result is still slightly higher than the experimental values. Further comparisons of base pressure coefficients, as a function of chord-to-thickness ratio for $Re_h = 1{,}000$, are made in the next section.

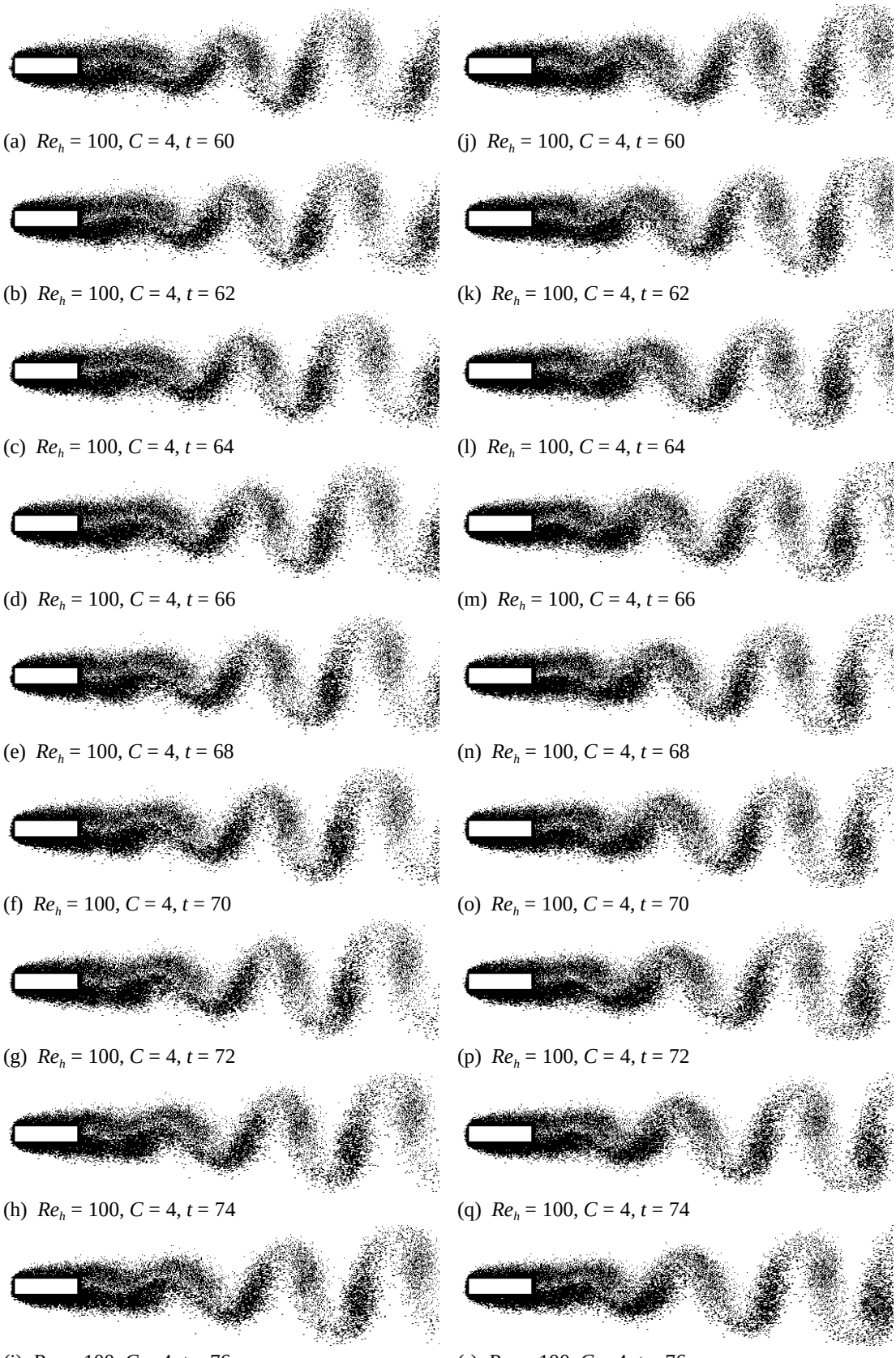

(a) Re_h = 100, C = 4, t = 60

(j) Re_h = 100, C = 4, t = 60

(b) Re_h = 100, C = 4, t = 62

(k) Re_h = 100, C = 4, t = 62

(c) Re_h = 100, C = 4, t = 64

(l) Re_h = 100, C = 4, t = 64

(d) Re_h = 100, C = 4, t = 66

(m) Re_h = 100, C = 4, t = 66

(e) Re_h = 100, C = 4, t = 68

(n) Re_h = 100, C = 4, t = 68

(f) Re_h = 100, C = 4, t = 70

(o) Re_h = 100, C = 4, t = 70

(g) Re_h = 100, C = 4, t = 72

(p) Re_h = 100, C = 4, t = 72

(h) Re_h = 100, C = 4, t = 74

(q) Re_h = 100, C = 4, t = 74

(i) Re_h = 100, C = 4, t = 76

(r) Re_h = 100, C = 4, t = 76

Figure 7.101. Elemental-vortex distributions in fully-developed flow over C = 4 cylinder at Re_h = 100.

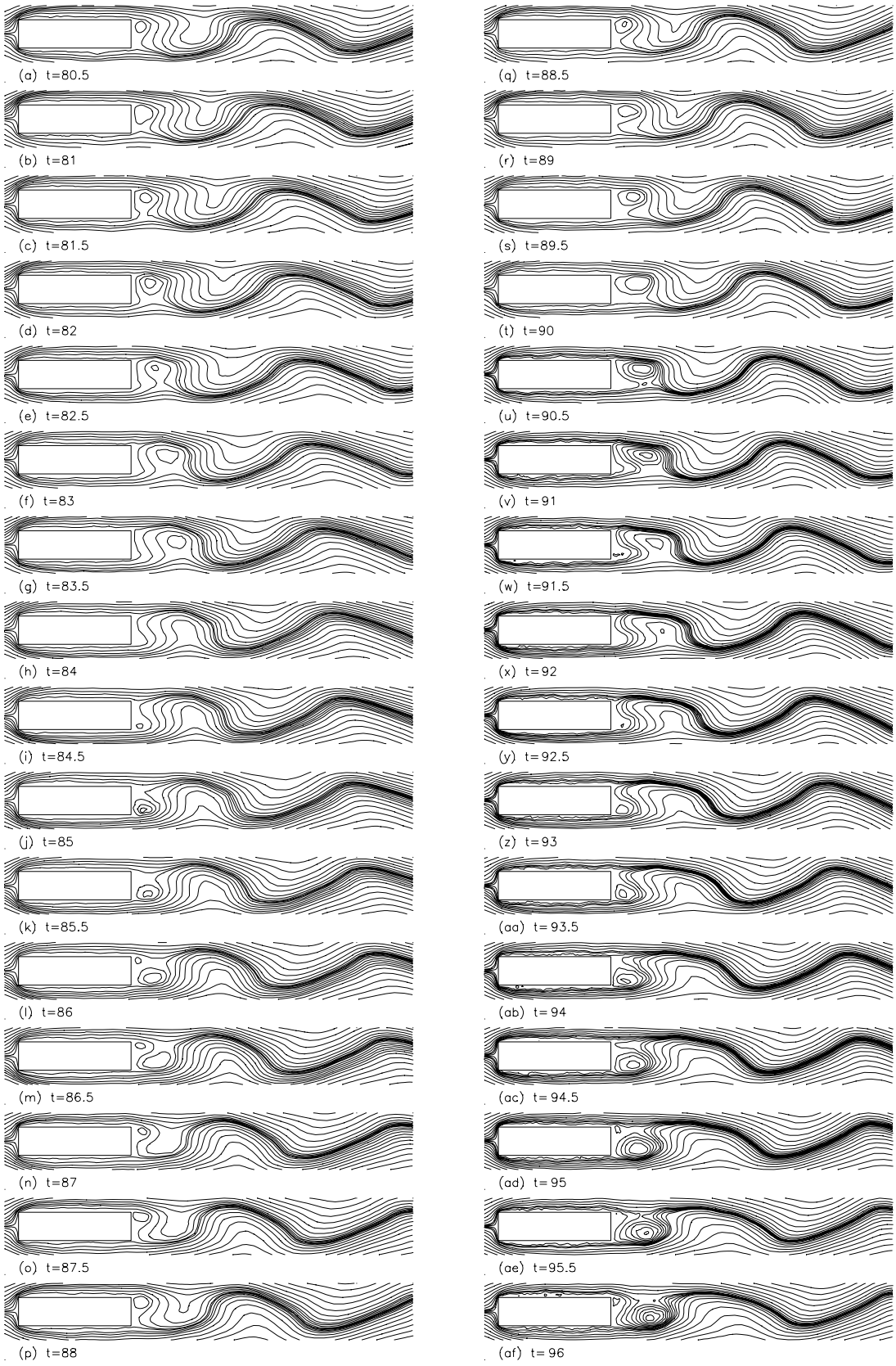

Figure 7.102. Streamline patterns in fully-developed flow over $C = 4$ cylinder at $Re_h = 100$.

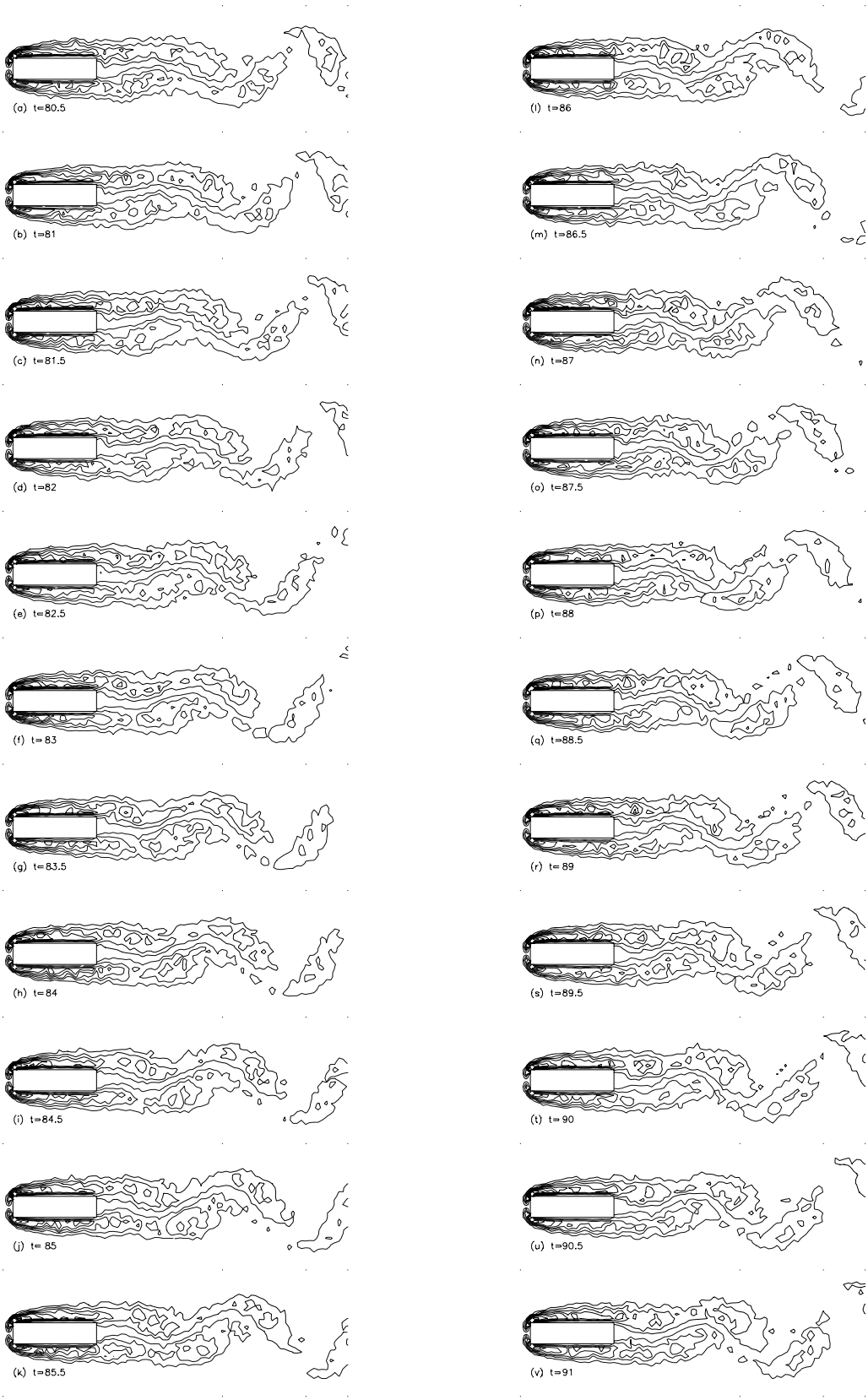

Figure 7.103. Vorticity contours in fully-developed flow over $C = 4$ cylinder at $Re_h = 100$.

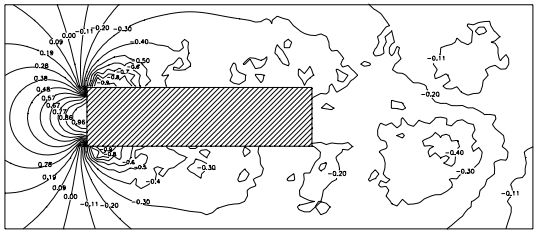

(a1) Re_h = 100, C = 4, t = 80.5

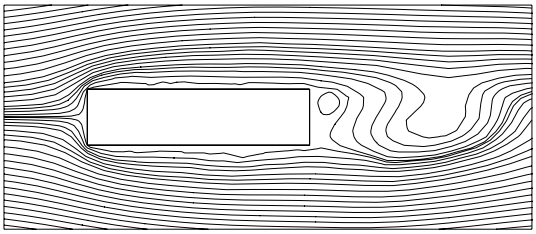

(a2) Re_h = 100, C = 4, t = 80.5

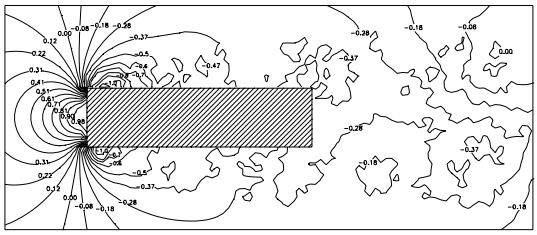

(b1) Re_h = 100, C = 4, t = 82

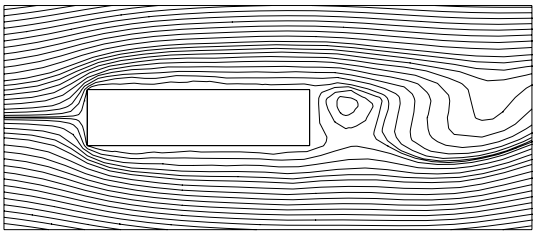

(b2) Re_h = 100, C = 4, t = 82

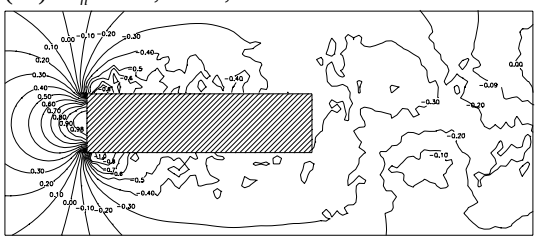

(c1) Re_h = 100, C = 4, t = 83.5

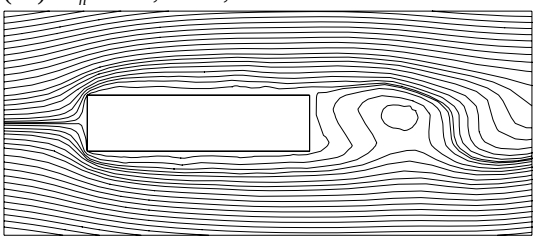

(c2) Re_h = 100, C = 4, t = 83.5

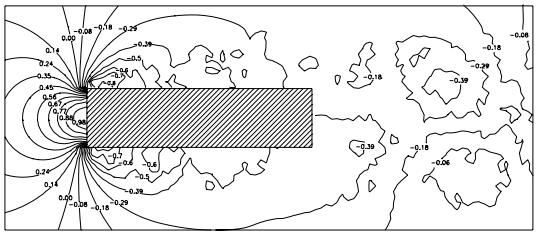

(d1) Re_h = 100, C = 4, t = 85

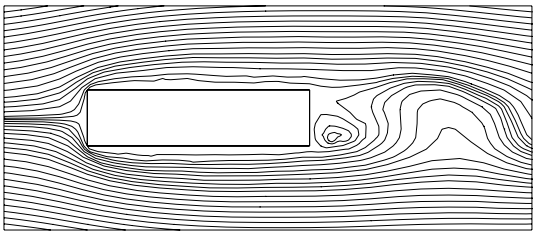

(d2) Re_h = 100, C = 4, t = 85

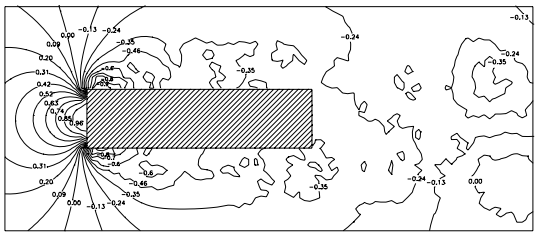

(e1) Re_h = 100, C = 4, t = 86.5

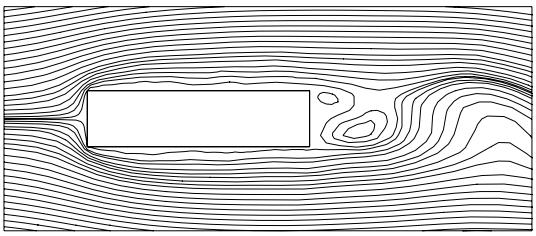

(e2) Re_h = 100, C = 4, t = 86.5

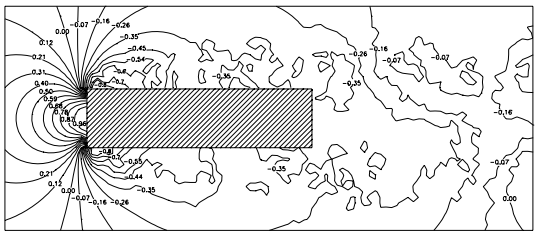

(f1) Re_h = 100, C = 4, t = 88

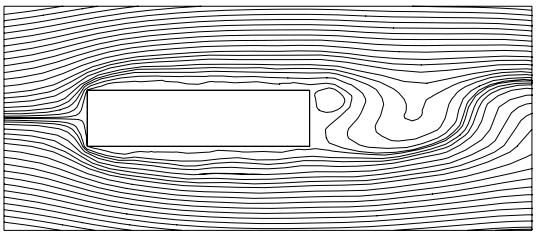

(f2) Re_h = 100, C = 4, t = 88

Figure 7.104. Instantaneous pressure fields and streamline patterns around C = 4 cylinder at Re_h = 100. Numbers shown are coefficients of static pressure.

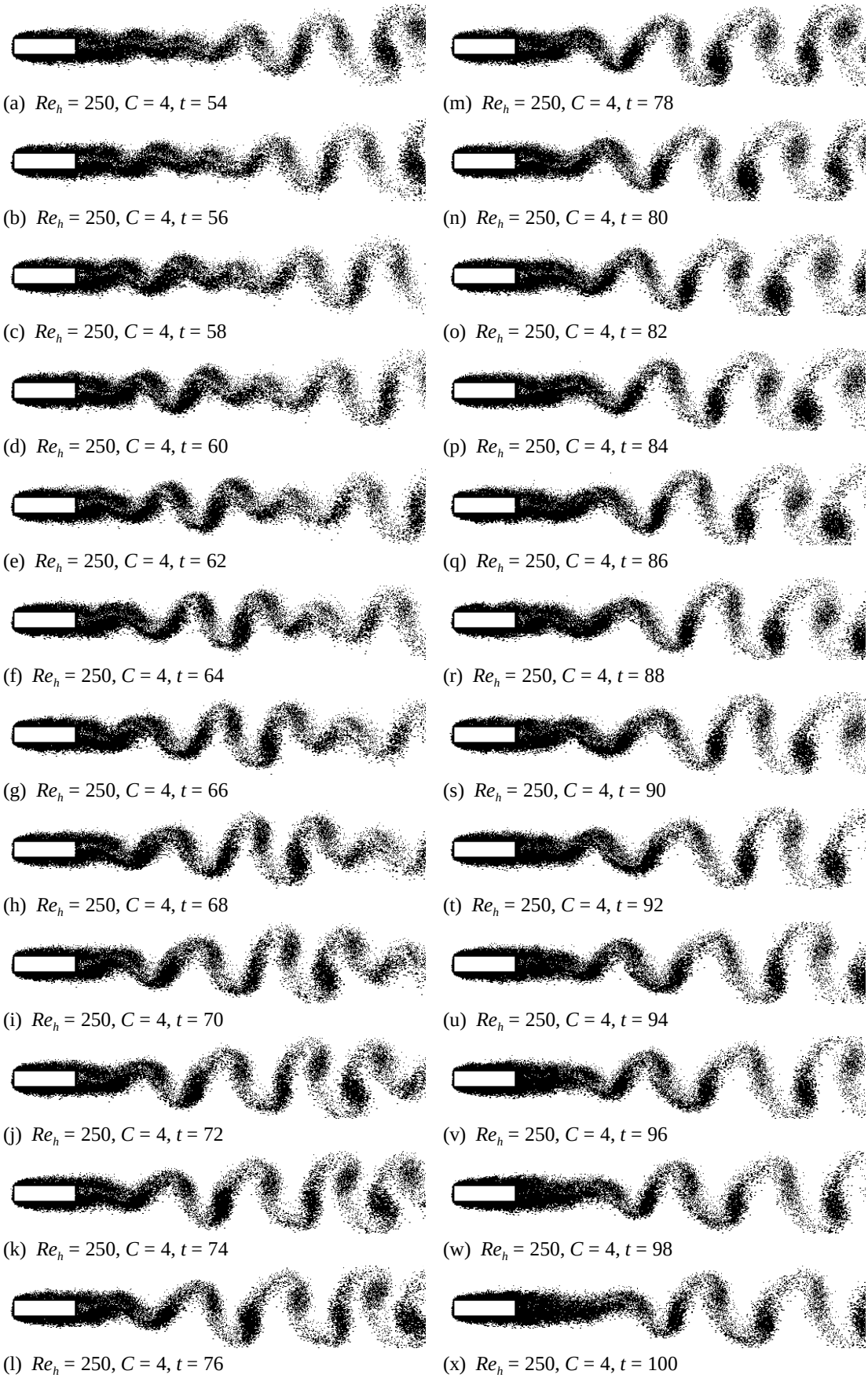

(a) Re_h = 250, C = 4, t = 54
(m) Re_h = 250, C = 4, t = 78
(b) Re_h = 250, C = 4, t = 56
(n) Re_h = 250, C = 4, t = 80
(c) Re_h = 250, C = 4, t = 58
(o) Re_h = 250, C = 4, t = 82
(d) Re_h = 250, C = 4, t = 60
(p) Re_h = 250, C = 4, t = 84
(e) Re_h = 250, C = 4, t = 62
(q) Re_h = 250, C = 4, t = 86
(f) Re_h = 250, C = 4, t = 64
(r) Re_h = 250, C = 4, t = 88
(g) Re_h = 250, C = 4, t = 66
(s) Re_h = 250, C = 4, t = 90
(h) Re_h = 250, C = 4, t = 68
(t) Re_h = 250, C = 4, t = 92
(i) Re_h = 250, C = 4, t = 70
(u) Re_h = 250, C = 4, t = 94
(j) Re_h = 250, C = 4, t = 72
(v) Re_h = 250, C = 4, t = 96
(k) Re_h = 250, C = 4, t = 74
(w) Re_h = 250, C = 4, t = 98
(l) Re_h = 250, C = 4, t = 76
(x) Re_h = 250, C = 4, t = 100

Figure 7.105. Elemental-vortex distributions in fully-developed flow over C = 4 cylinder at Re_h = 250.

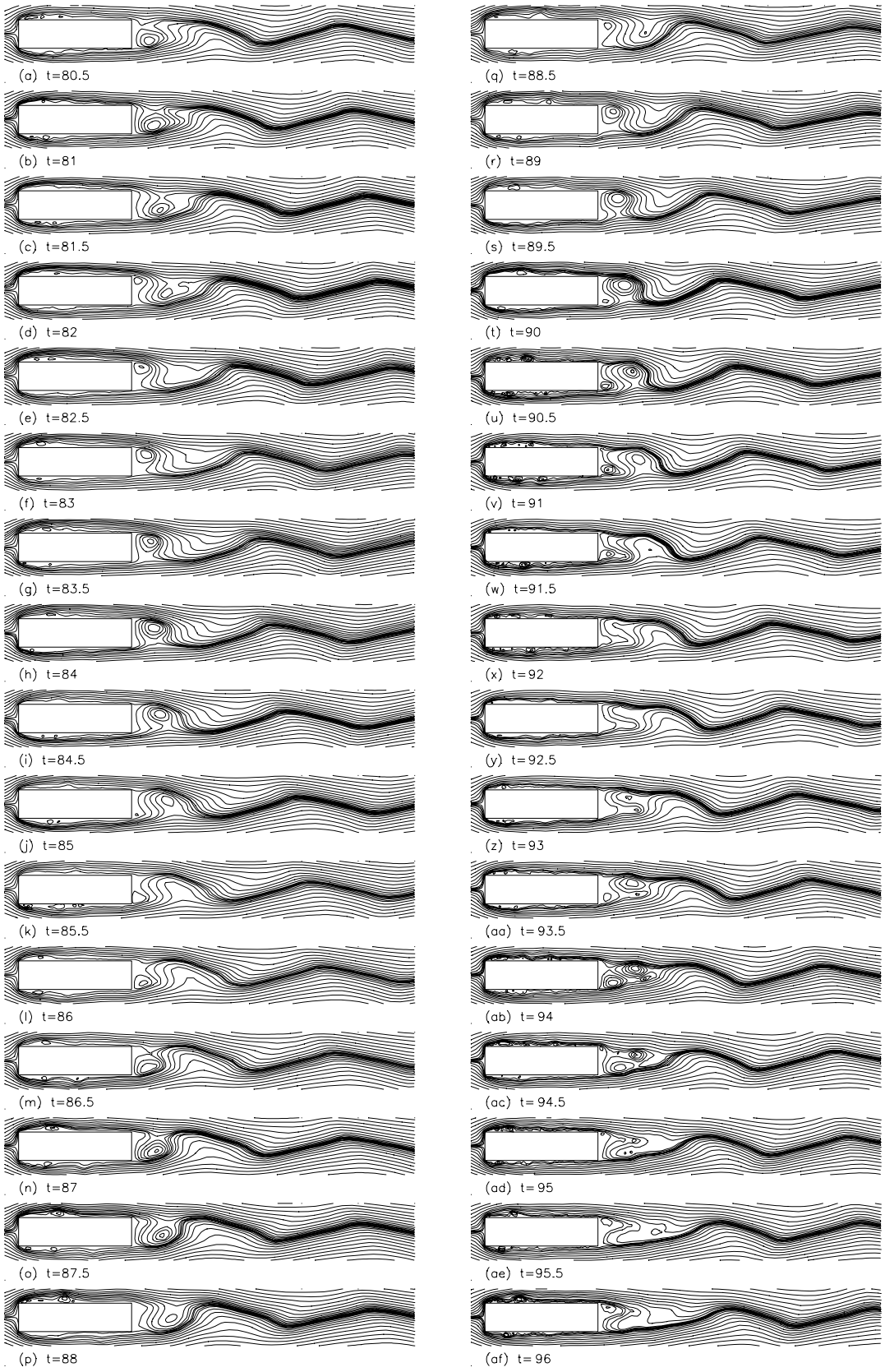

Figure 7.106. Streamline patterns in fully-developed flow over $C = 4$ cylinder at $Re_h = 250$.

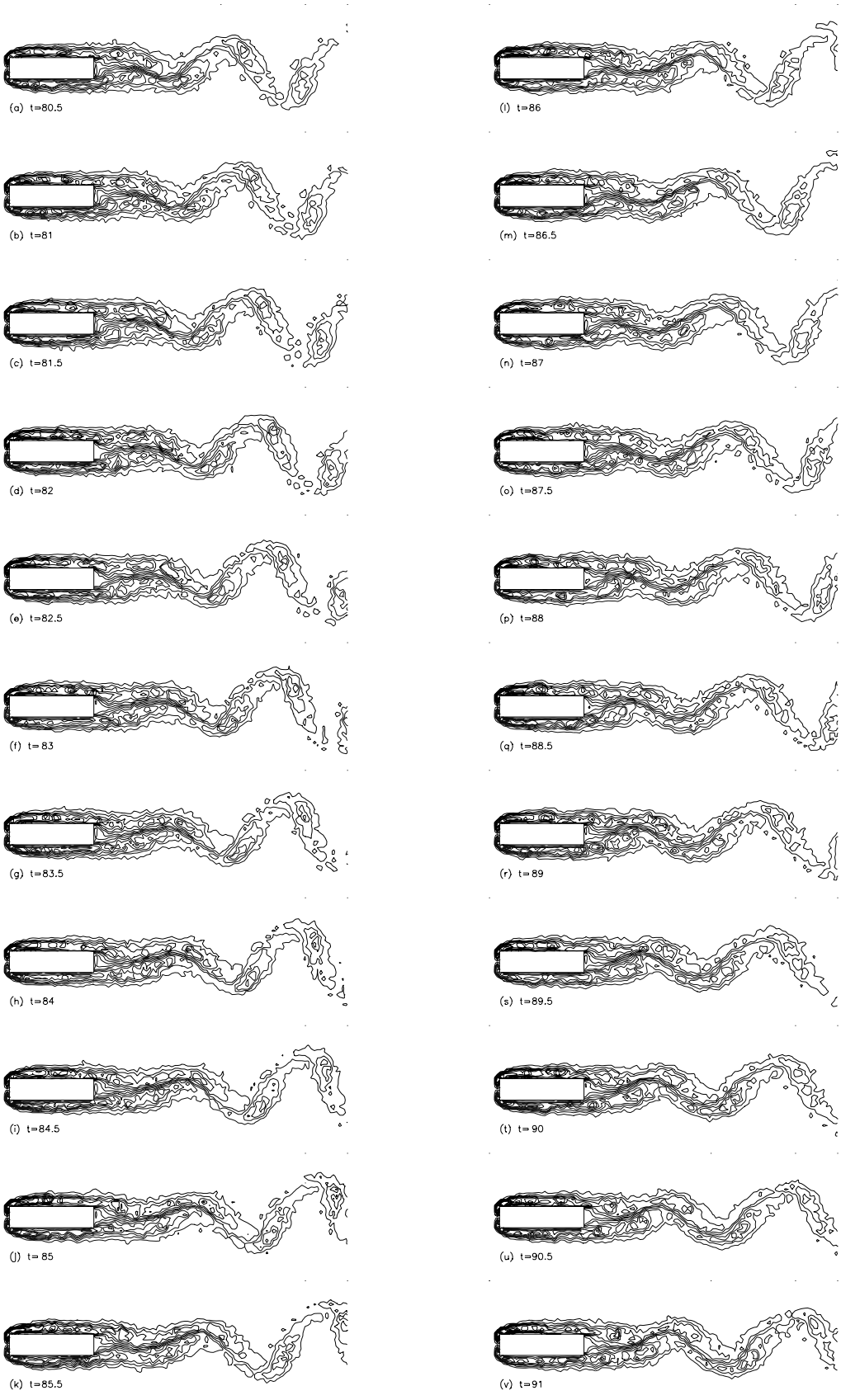

Figure 7.107. Vorticity contours in fully-developed flow over $C = 4$ cylinder at $Re_h = 250$.

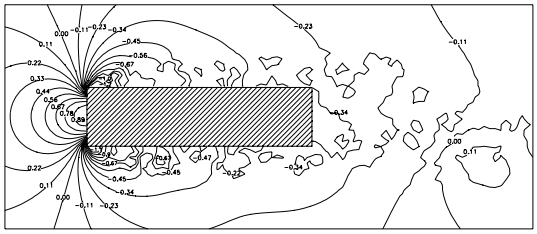

(a1) Re_h = 250, C = 4, t = 80.5

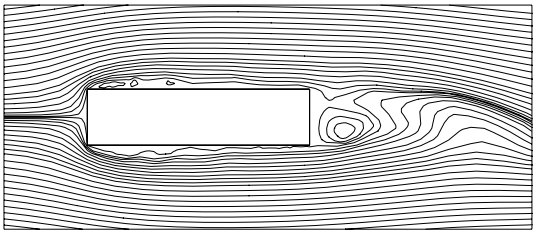

(a2) Re_h = 250, C = 4, t = 80.5

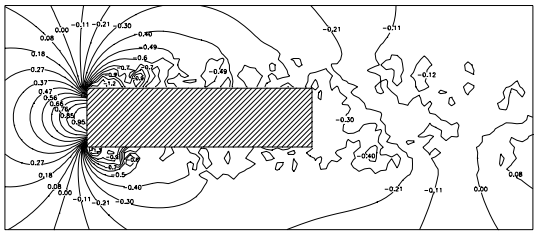

(b1) Re_h = 250, C = 4, t = 82

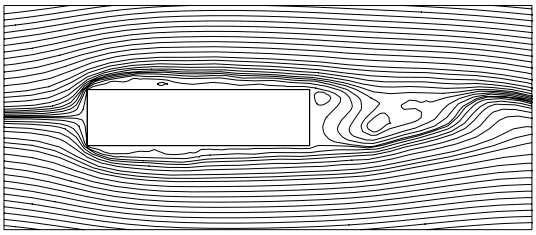

(b2) Re_h = 250, C = 4, t = 82

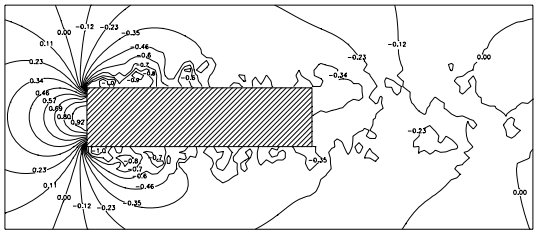

(c1) Re_h = 250, C = 4, t = 83.5

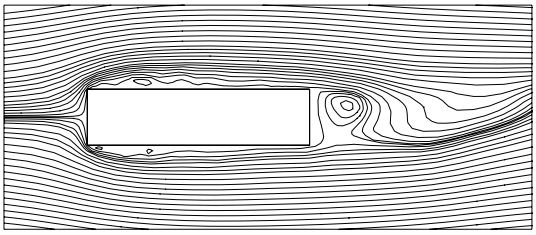

(c2) Re_h = 250, C = 4, t = 83.5

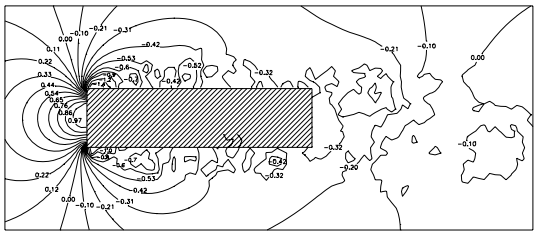

(d1) Re_h = 250, C = 4, t = 85

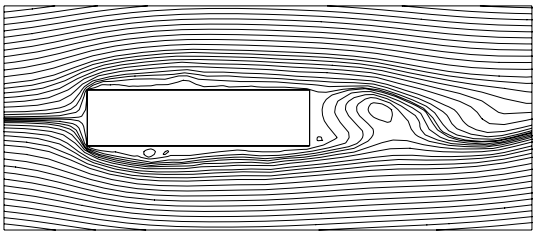

(d2) Re_h = 250, C = 4, t = 85

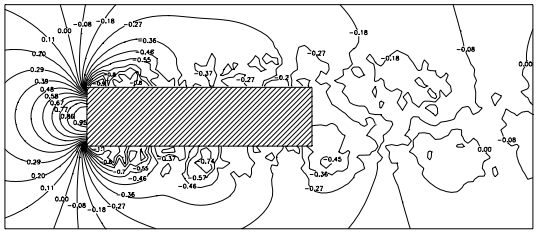

(e1) Re_h = 250, C = 4, t = 86.5

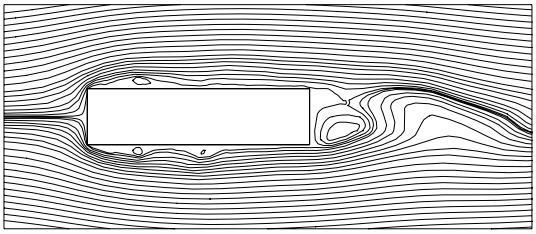

(e2) Re_h = 250, C = 4, t = 86.5

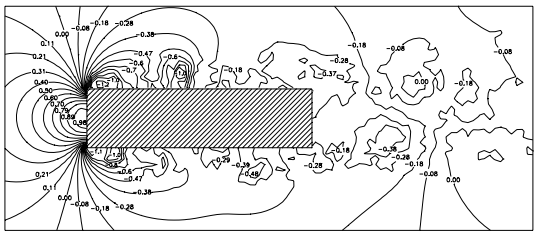

(f1) Re_h = 250, C = 4, t = 88

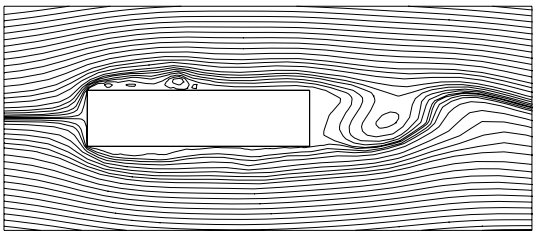

(f2) Re_h = 250, C = 4, t = 88

Figure 7.108. Instantaneous pressure fields and streamline patterns around C = 4 cylinder at Re_h = 250. Numbers shown are coefficients of static pressure.

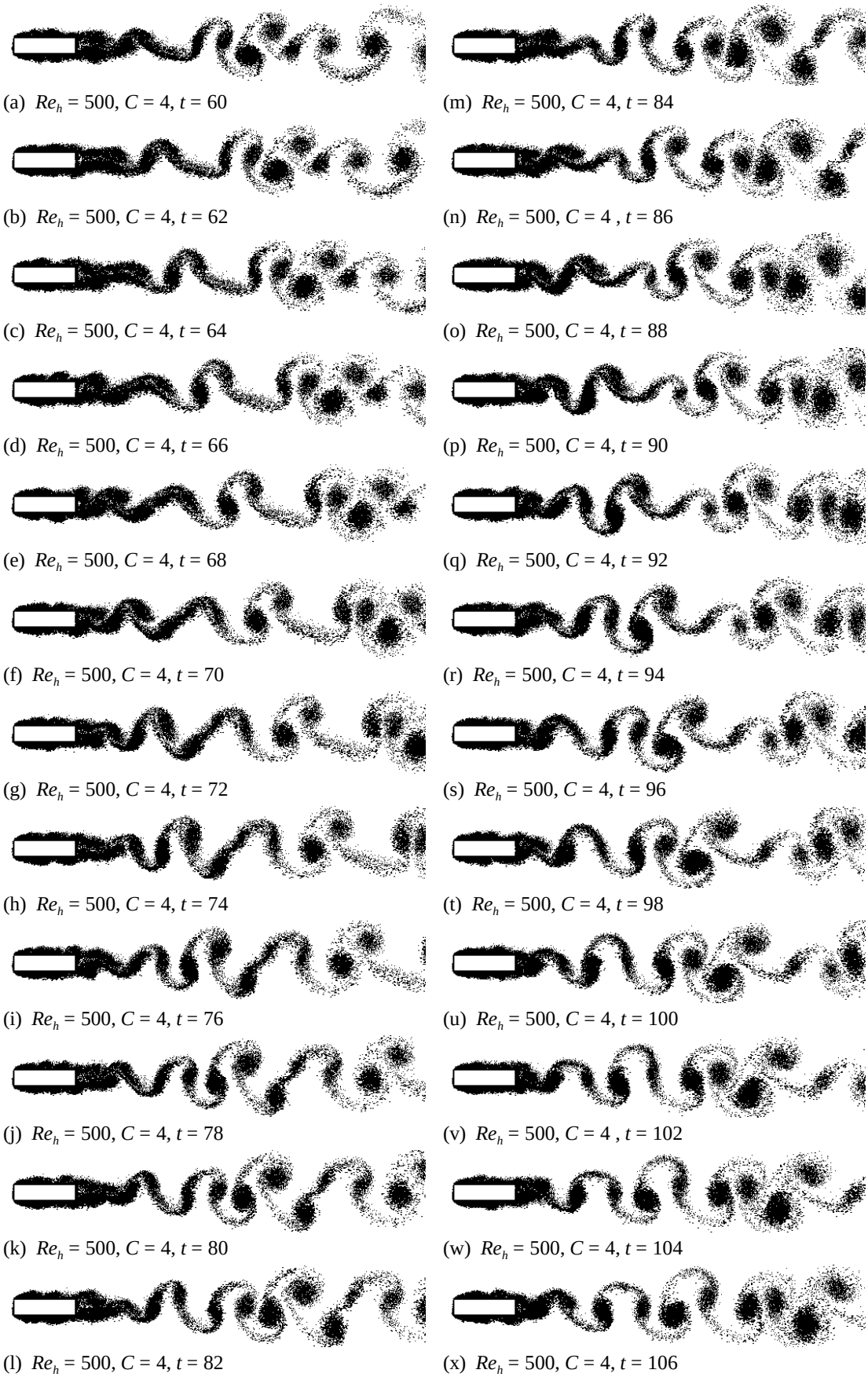

(a) Re_h = 500, C = 4, t = 60

(b) Re_h = 500, C = 4, t = 62

(c) Re_h = 500, C = 4, t = 64

(d) Re_h = 500, C = 4, t = 66

(e) Re_h = 500, C = 4, t = 68

(f) Re_h = 500, C = 4, t = 70

(g) Re_h = 500, C = 4, t = 72

(h) Re_h = 500, C = 4, t = 74

(i) Re_h = 500, C = 4, t = 76

(j) Re_h = 500, C = 4, t = 78

(k) Re_h = 500, C = 4, t = 80

(l) Re_h = 500, C = 4, t = 82

(m) Re_h = 500, C = 4, t = 84

(n) Re_h = 500, C = 4 , t = 86

(o) Re_h = 500, C = 4, t = 88

(p) Re_h = 500, C = 4, t = 90

(q) Re_h = 500, C = 4, t = 92

(r) Re_h = 500, C = 4, t = 94

(s) Re_h = 500, C = 4, t = 96

(t) Re_h = 500, C = 4, t = 98

(u) Re_h = 500, C = 4, t = 100

(v) Re_h = 500, C = 4 , t = 102

(w) Re_h = 500, C = 4, t = 104

(x) Re_h = 500, C = 4, t = 106

Figure 7.109. Elemental-vortex distributions in fully-developed flow over C = 4 cylinder at Re_h = 500.

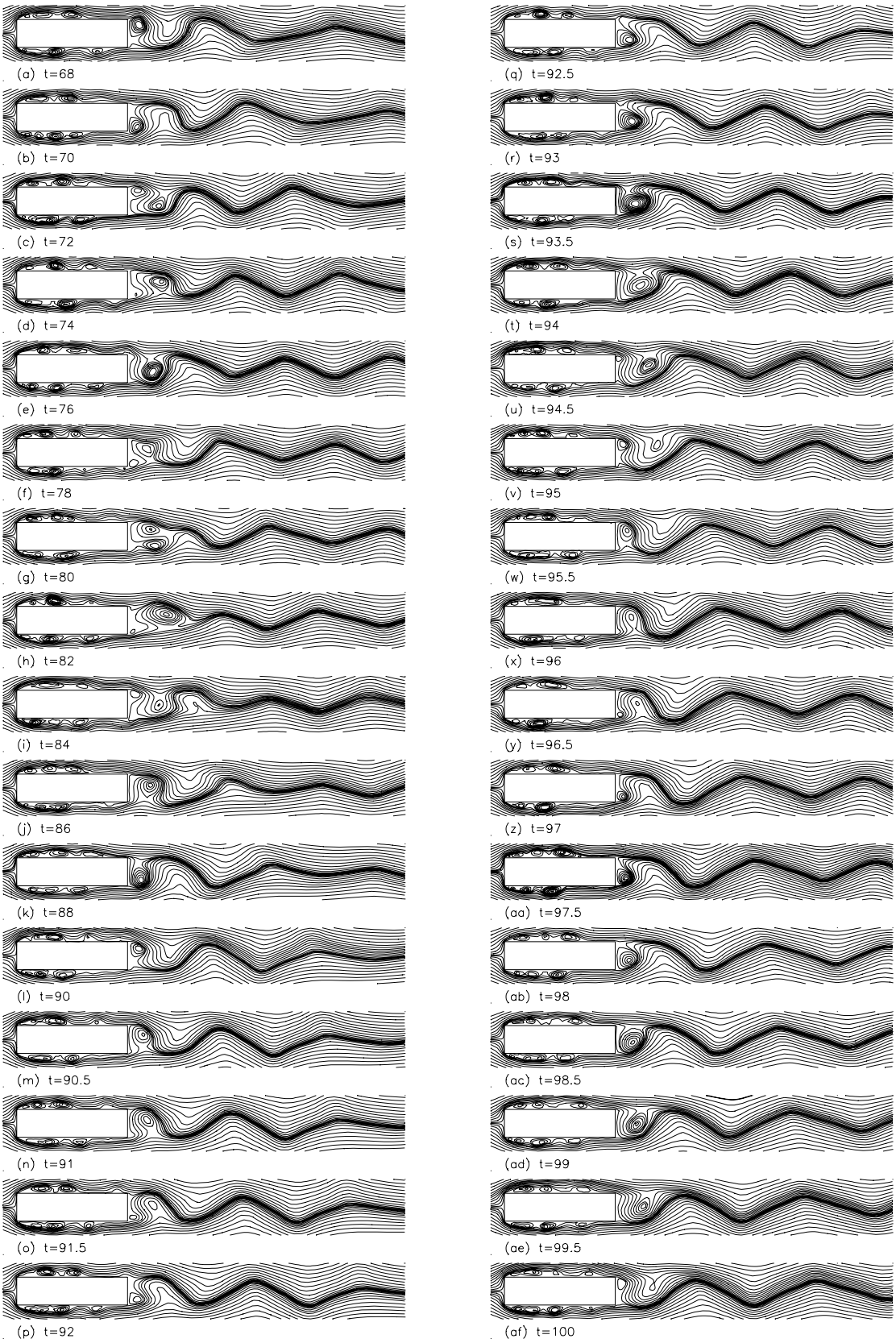

Figure 7.110. Streamline patterns in fully-developed flow over $C = 4$ cylinder at $Re_h = 500$.

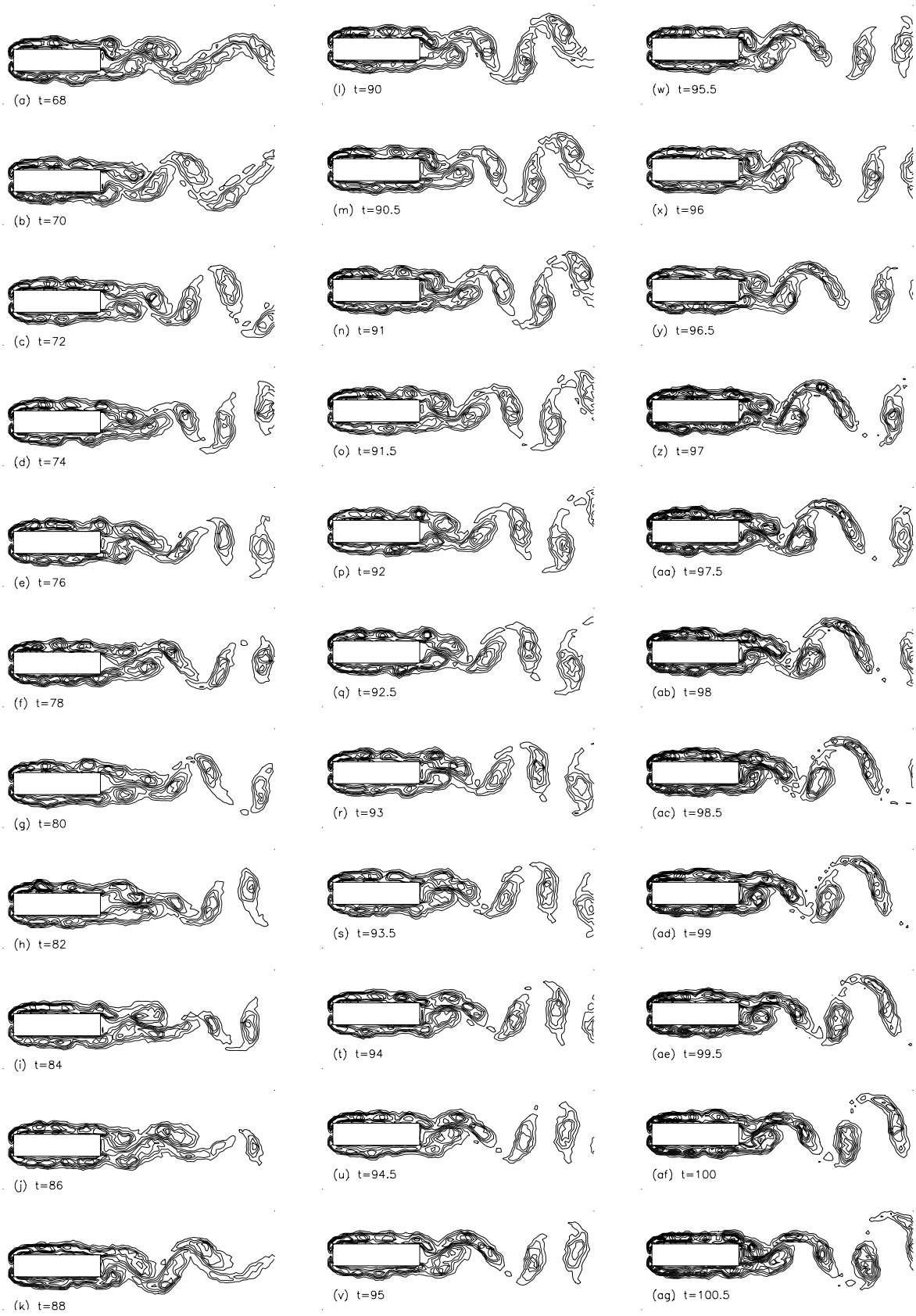

Figure 7.111. Vorticity contours in fully-developed flow over $C = 4$ cylinder at $Re_h = 500$.

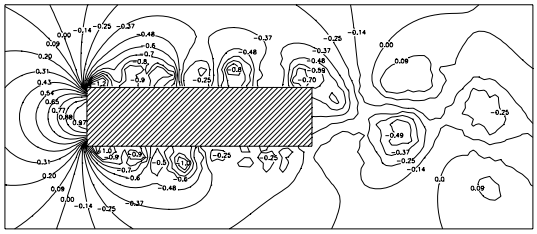

(a1) Re_h = 500, C = 4, t = 90

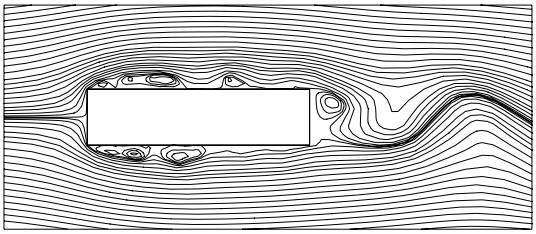

(a2) Re_h = 500, C = 4, t = 90

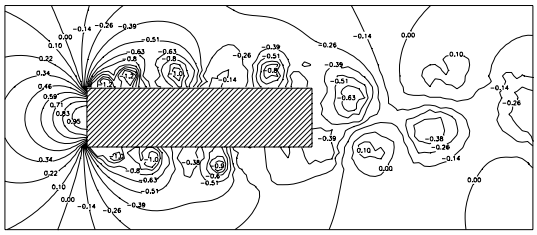

(b1) Re_h = 500, C = 4, t = 91

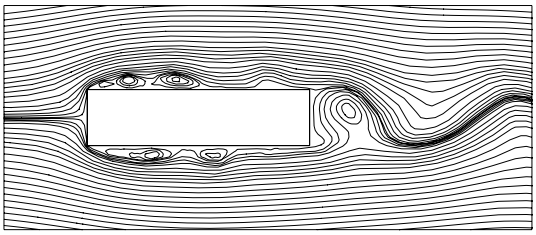

(b2) Re_h = 500, C = 4, t = 91

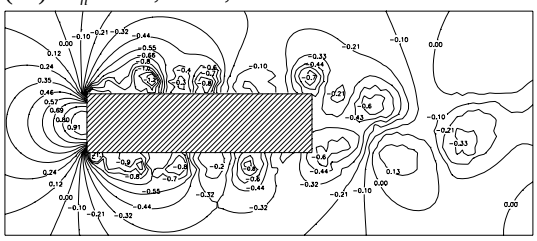

(c1) Re_h = 500, C = 4, t = 92

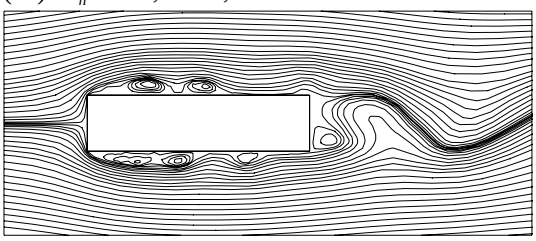

(c2) Re_h = 500, C = 4, t = 92

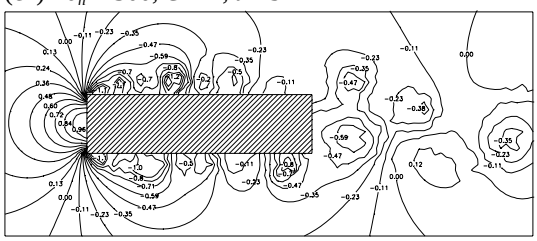

(d1) Re_h = 500, C = 4, t = 93

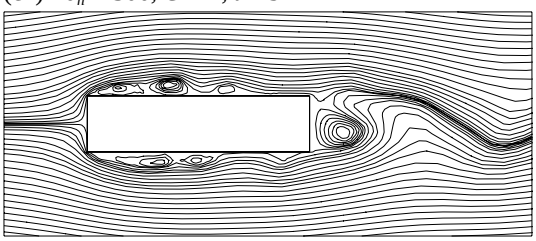

(d2) Re_h = 500, C = 4, t = 93

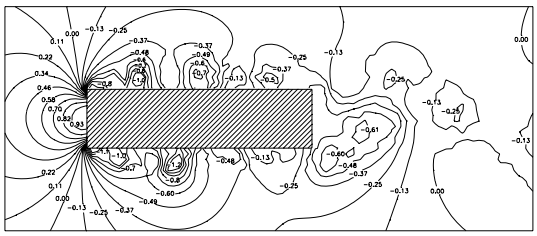

(e1) Re_h = 500, C = 4, t = 94

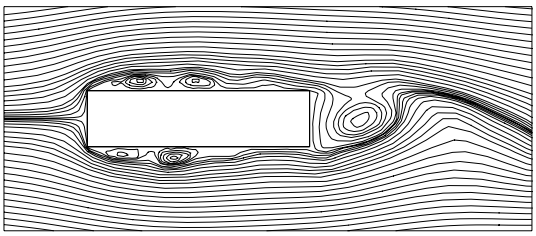

(e2) Re_h = 500, C = 4, t = 94

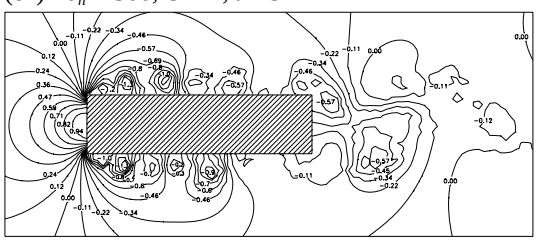

(f1) Re_h = 500, C = 4, t = 95

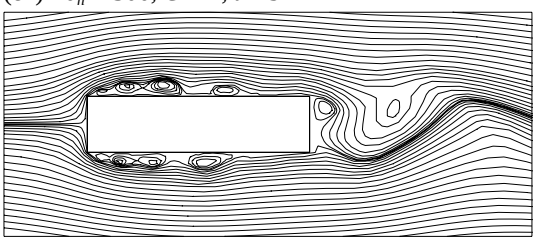

(f2) Re_h = 500, C = 4, t = 95

Figure 7.112. Instantaneous pressure fields and streamline patterns around C = 4 cylinder at Re_h = 500. Numbers shown are coefficients of static pressure.

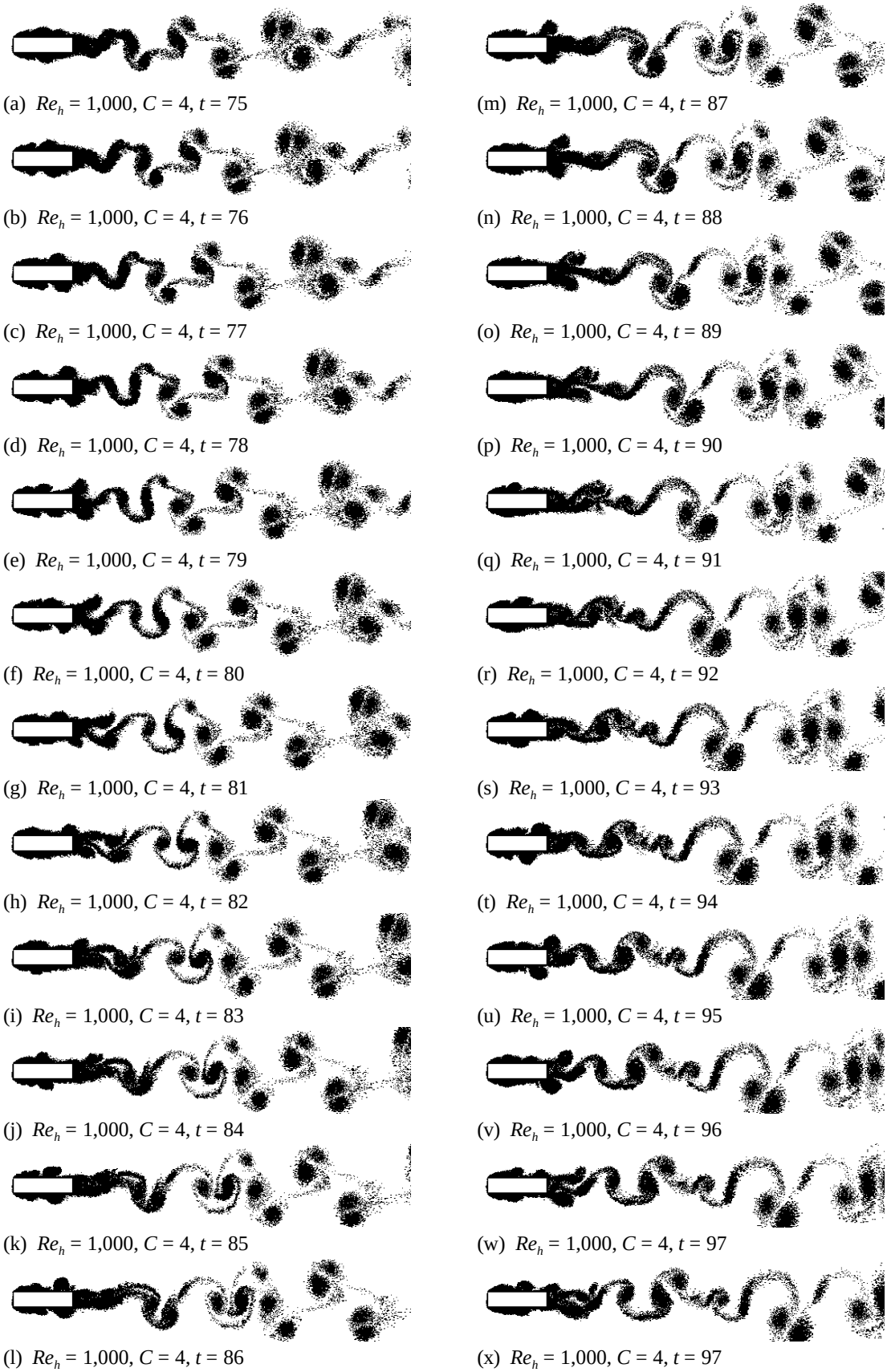

(a) Re_h = 1,000, C = 4, t = 75
(b) Re_h = 1,000, C = 4, t = 76
(c) Re_h = 1,000, C = 4, t = 77
(d) Re_h = 1,000, C = 4, t = 78
(e) Re_h = 1,000, C = 4, t = 79
(f) Re_h = 1,000, C = 4, t = 80
(g) Re_h = 1,000, C = 4, t = 81
(h) Re_h = 1,000, C = 4, t = 82
(i) Re_h = 1,000, C = 4, t = 83
(j) Re_h = 1,000, C = 4, t = 84
(k) Re_h = 1,000, C = 4, t = 85
(l) Re_h = 1,000, C = 4, t = 86
(m) Re_h = 1,000, C = 4, t = 87
(n) Re_h = 1,000, C = 4, t = 88
(o) Re_h = 1,000, C = 4, t = 89
(p) Re_h = 1,000, C = 4, t = 90
(q) Re_h = 1,000, C = 4, t = 91
(r) Re_h = 1,000, C = 4, t = 92
(s) Re_h = 1,000, C = 4, t = 93
(t) Re_h = 1,000, C = 4, t = 94
(u) Re_h = 1,000, C = 4, t = 95
(v) Re_h = 1,000, C = 4, t = 96
(w) Re_h = 1,000, C = 4, t = 97
(x) Re_h = 1,000, C = 4, t = 97

Figure 7.113. Elemental-vortex distributions in fully-developed flow over C = 4 cylinder at Re_h = 1,000.

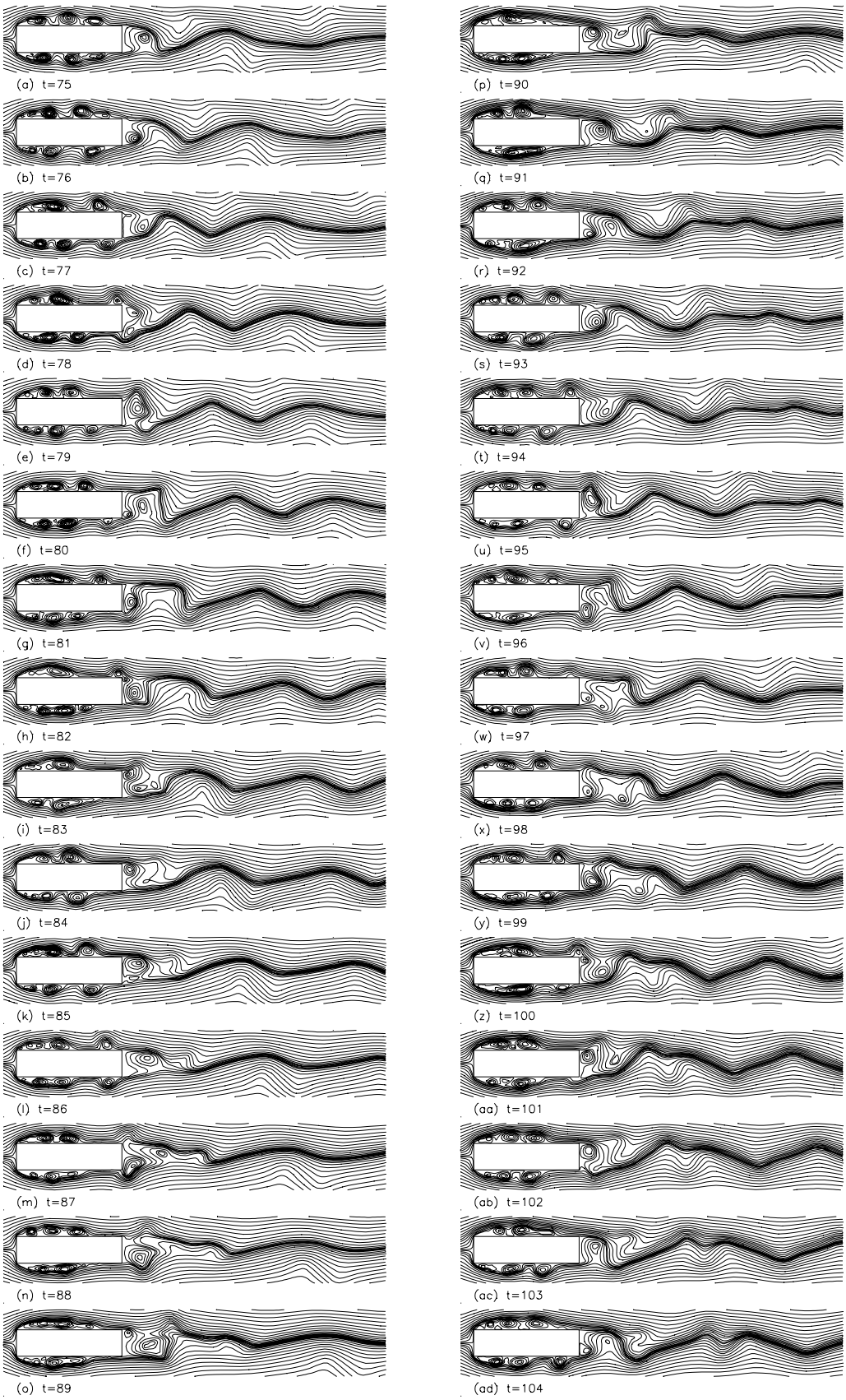

Figure 7.114. Streamline patterns in fully-developed flow over $C = 4$ cylinder at $Re_h = 1{,}000$.

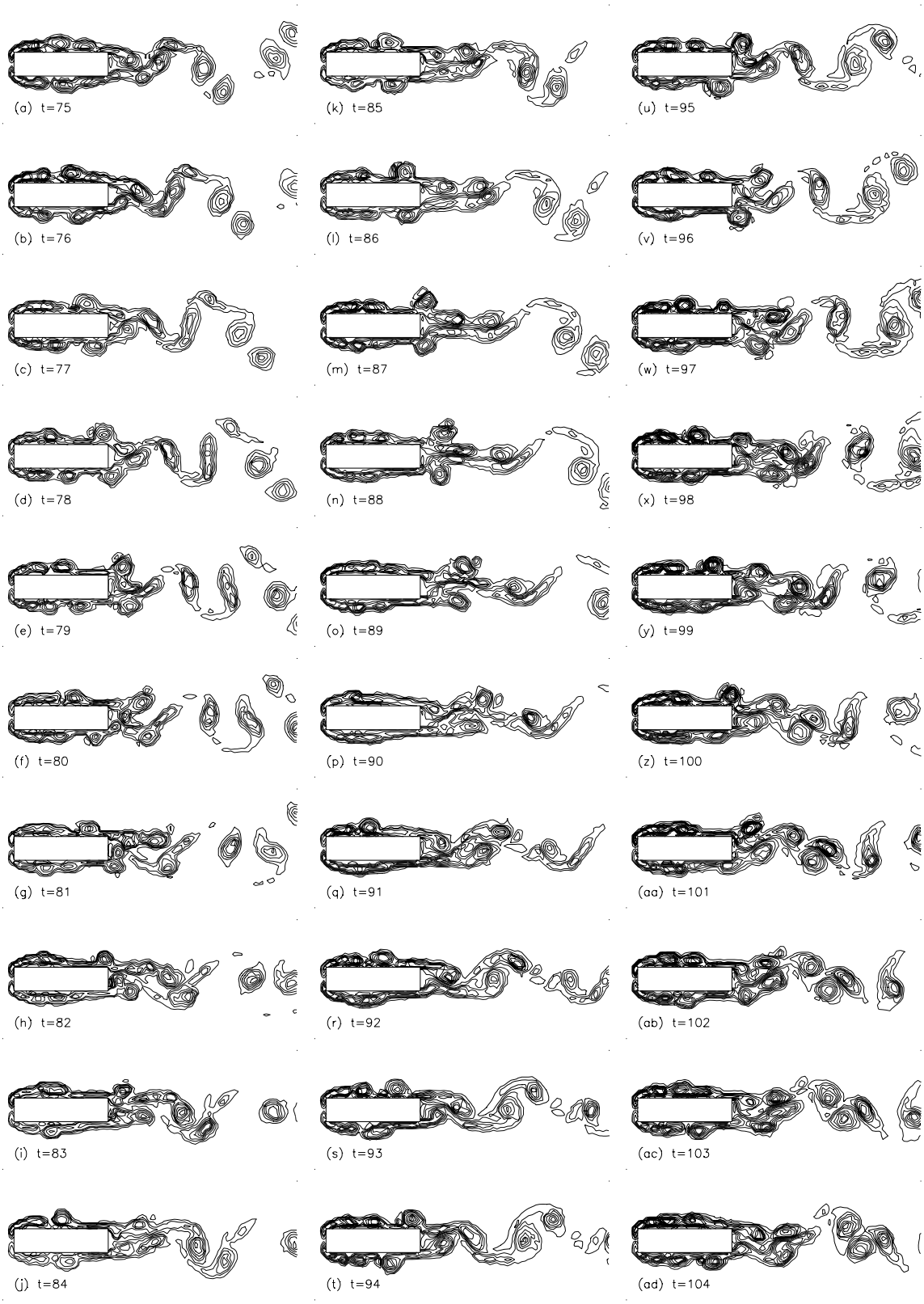

Figure 7.115. Vorticity contours in fully-developed flow over C = 4 cylinder at Re_h = 1,000.

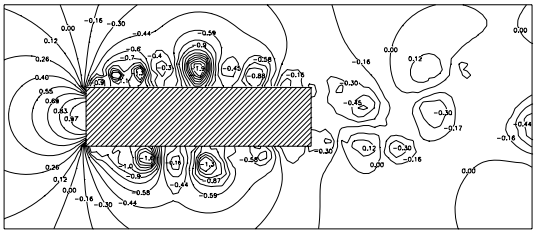

(a1) Re_h = 1,000, C = 4, t = 75

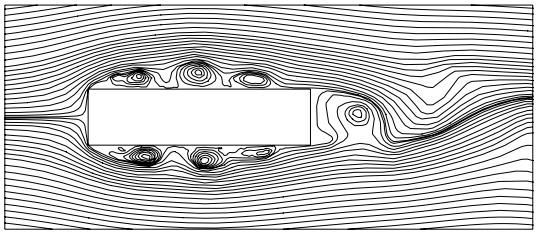

(a2) Re_h = 1,000, C = 4, t = 75

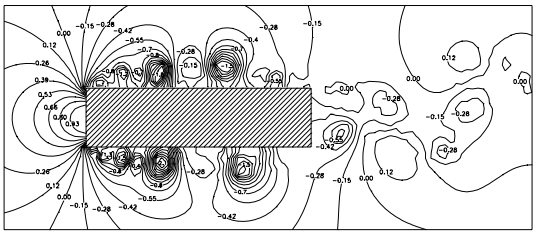

(b1) Re_h = 1,000, C = 4, t = 76

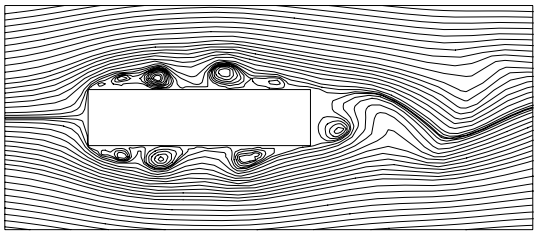

(b2) Re_h = 1,000, C = 4, t = 76

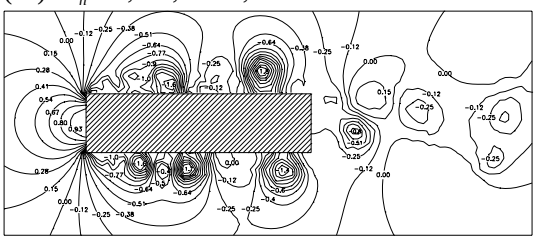

(c1) Re_h = 1,000, C = 4, t = 77

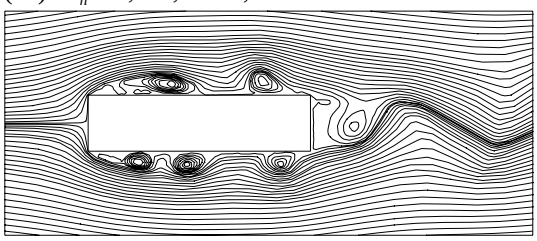

(c2) Re_h = 1,000, C = 4, t = 77

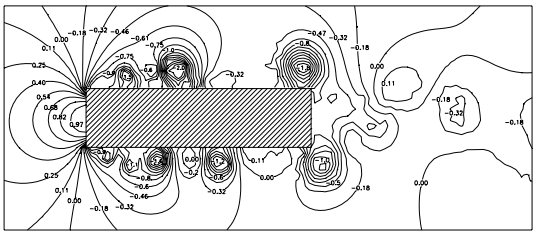

(d1) Re_h = 1,000, C = 4, t = 78

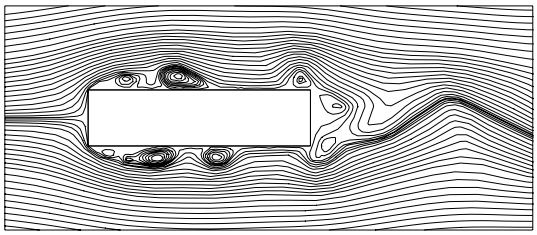

(d2) Re_h = 1,000, C = 4, t = 78

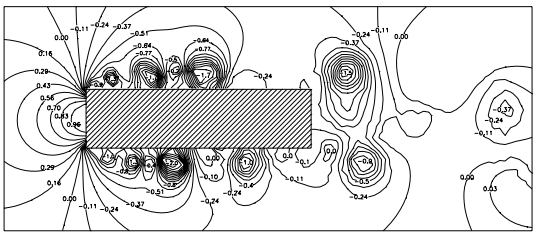

(e1) Re_h = 1,000, C = 4, t = 79

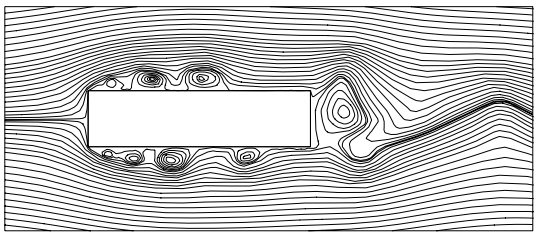

(e2) Re_h = 1,000, C = 4, t = 79

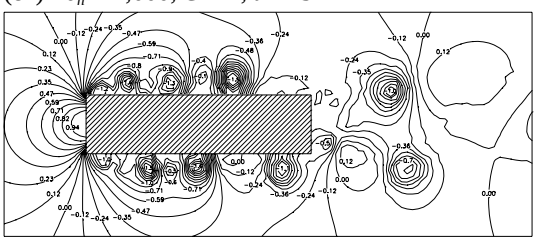

(f1) Re_h = 1,000, C = 4, t = 80

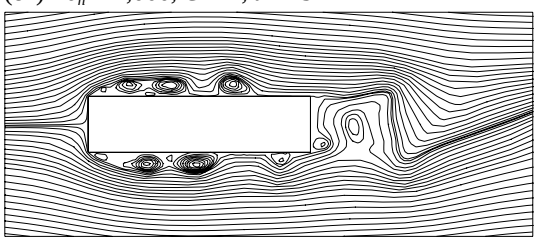

(f2) Re_h = 1,000, C = 4, t = 80

Figure 7.116. Instantaneous pressure fields and streamline patterns around C = 4 cylinder at Re_h = 1,000. Numbers shown are coefficients of static pressure.

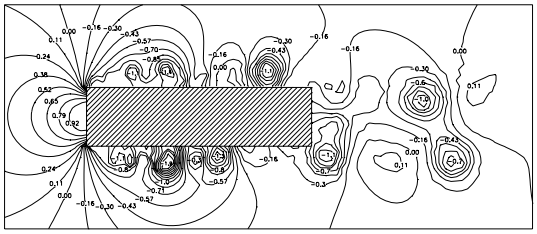

(g1) Re_h = 1,000, C = 4, t = 81

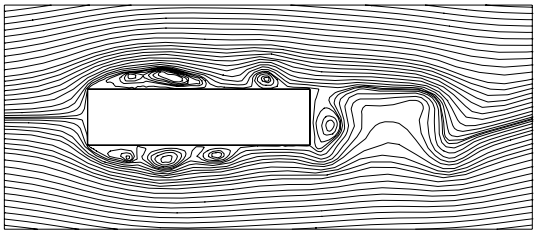

(g2) Re_h = 1,000, C = 4, t = 81

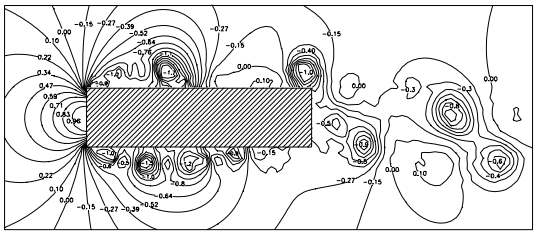

(h1) Re_h = 1,000, C = 4, t = 82

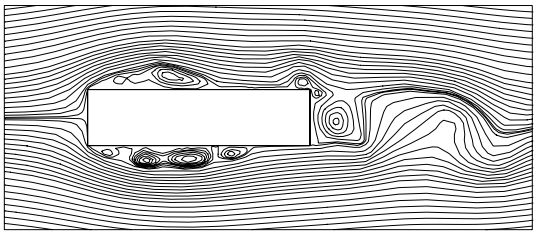

(h2) Re_h = 1,000, C = 4, t = 82

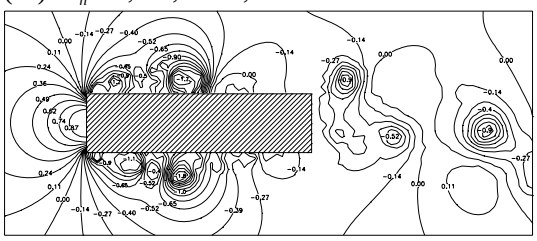

(i1) Re_h = 1,000, C = 4, t = 83

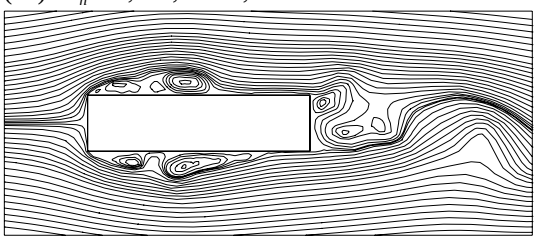

(i2) Re_h = 1,000, C = 4, t = 83

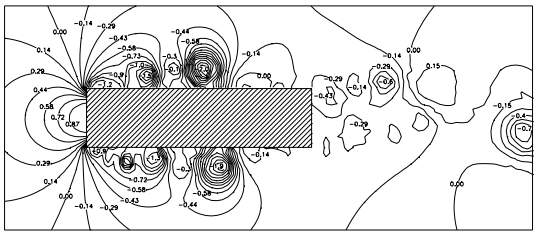

(j1) Re_h = 1,000, C = 4, t = 84

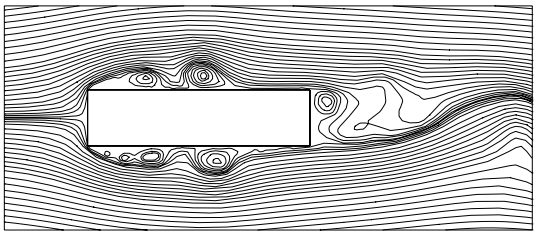

(j2) Re_h = 1,000, C = 4, t = 84

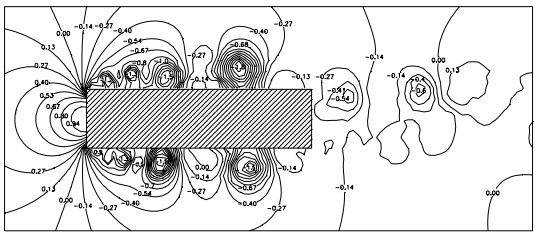

(k1) Re_h = 1,000, C = 4, t = 85

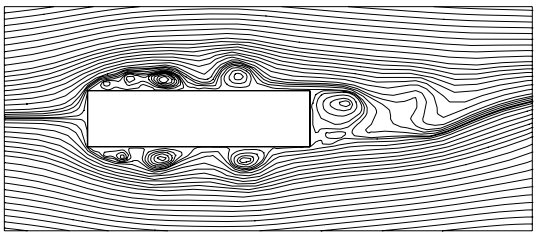

(k2) Re_h = 1,000, C = 4, t = 85

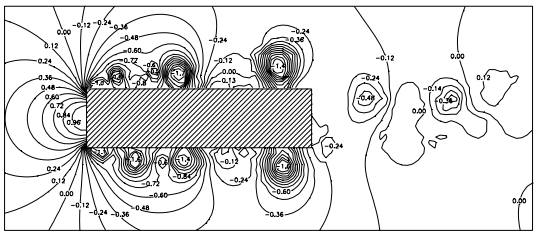

(l1) Re_h = 1,000, C = 4, t = 86

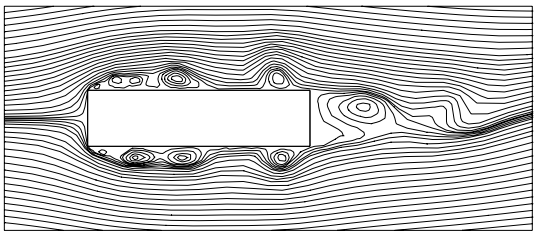

(l2) Re_h = 1,000, C = 4, t = 86

Figure 7.116. Cont'd

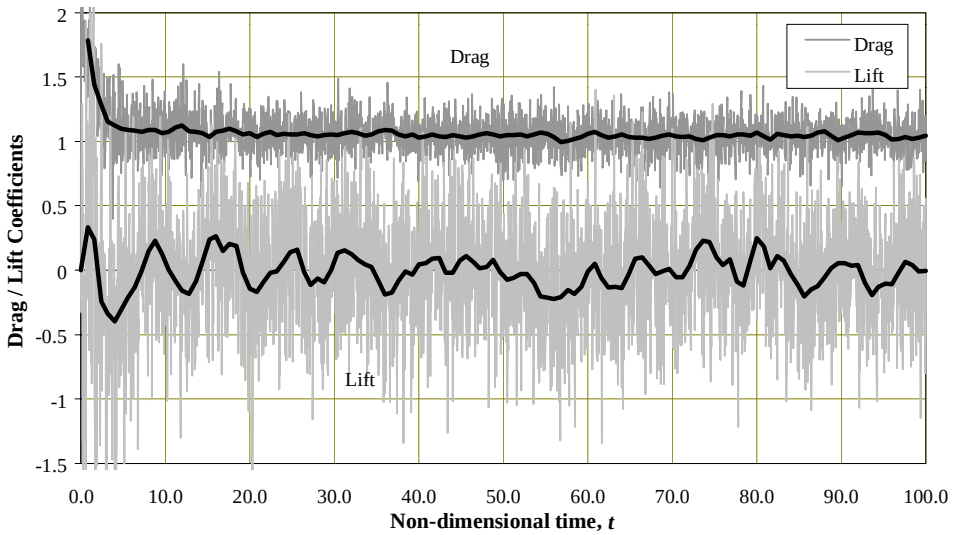

Figure 7.117. Time histories of drag and lift coefficients on $C = 4$ cylinder at $Re_h = 100$. Drag and lift are calculated for $\Delta t = 0.02$; highlighted mean drag and lift are averaged over $\Delta t = 0.4$

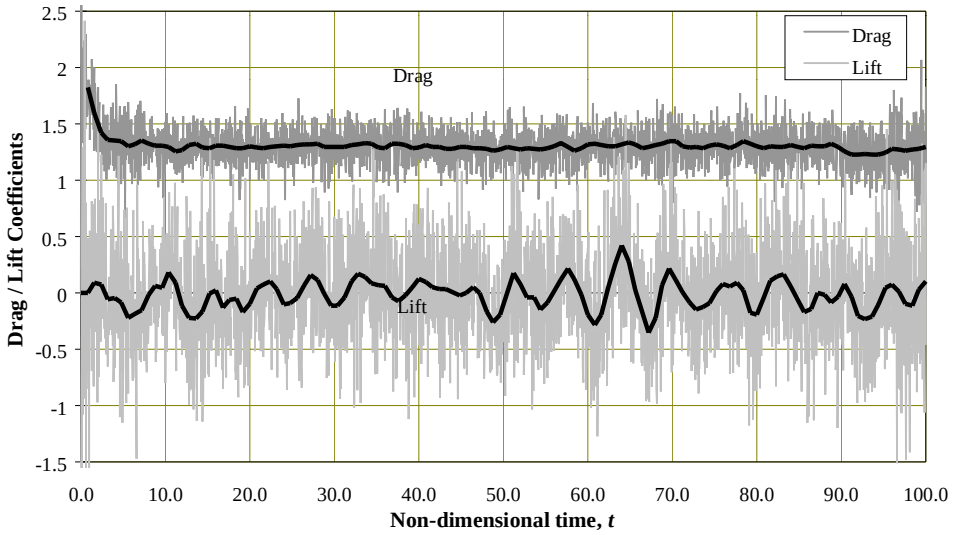

Figure 7.118. Time histories of drag and lift coefficients on $C = 4$ cylinder at $Re_h = 250$. Drag and lift are calculated for $\Delta t = 0.02$; highlighted mean drag and lift are averaged over $\Delta t = 0.4$

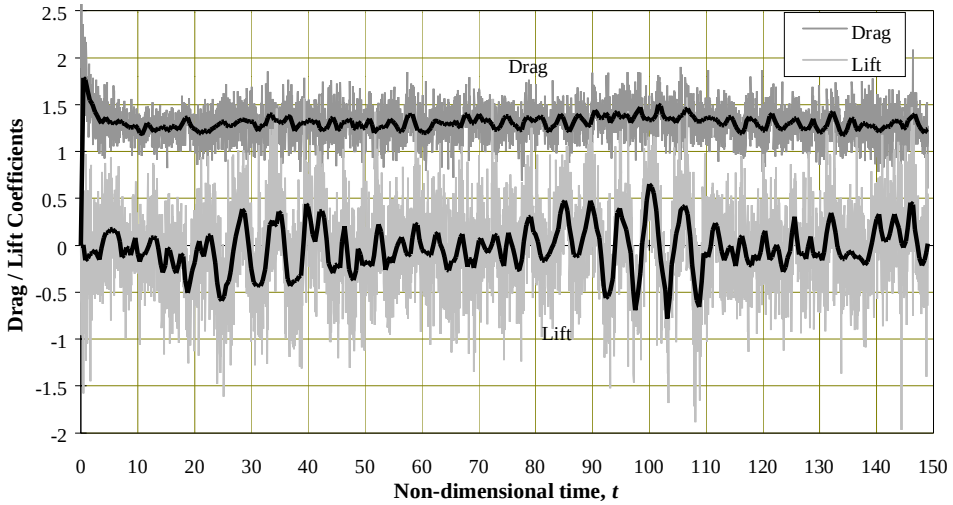

Figure 7.119. Time histories of drag and lift coefficients on $C = 4$ cylinder at $Re_h = 500$. Drag and lift are calculated for $\Delta t = 0.02$; highlighted mean drag and lift are averaged over $\Delta t = 0.4$

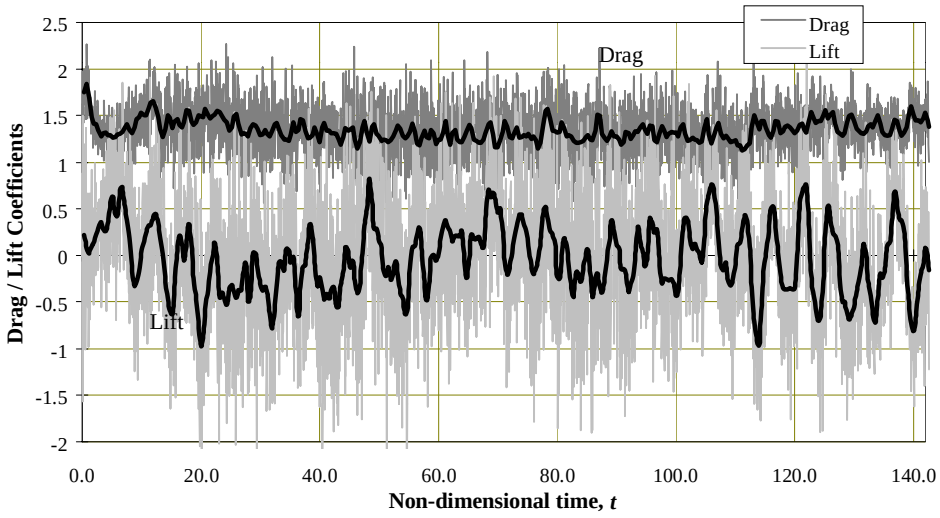

Figure 7.120. Time histories of drag and lift coefficients on $C = 4$ cylinder at $Re_h = 1{,}000$. Drag and lift are calculated for $\Delta t = 0.02$; highlighted mean drag and lift are averaged over $\Delta t = 0.4$

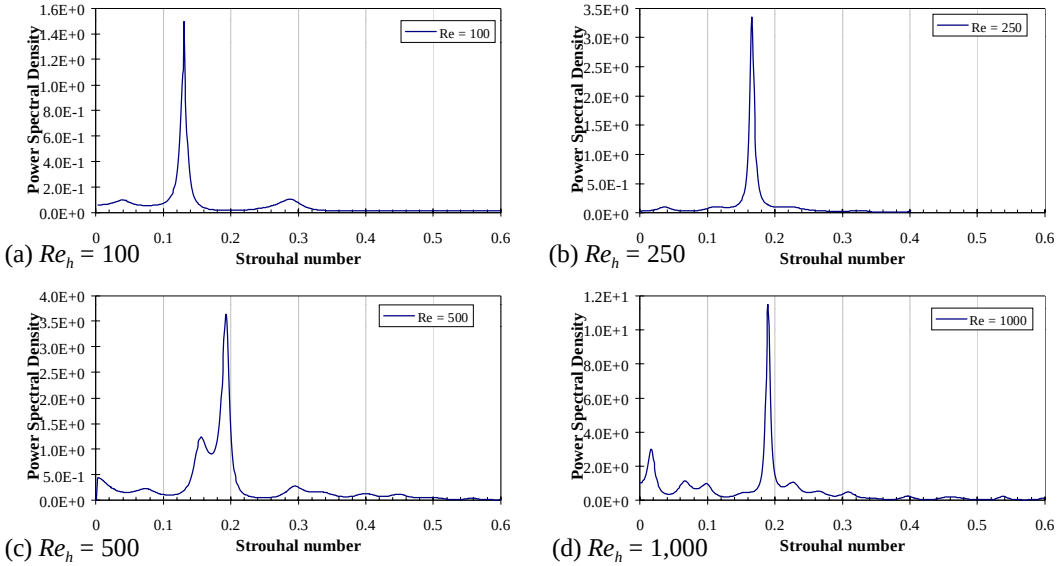

Figure 7.121. Power spectra of fluctuating lift on $C = 4$ cylinder at Reynolds numbers: (a) $Re_h = 100$, (b) 250, (c) 500 and (d) 1,000.

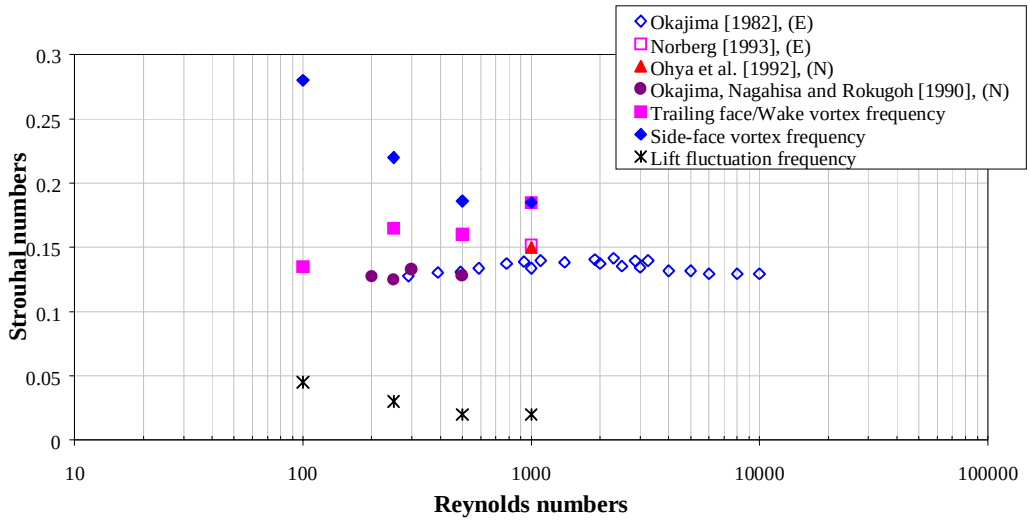

Figure 7.122. Variation of Strouhal number with Reynolds number for flow over rectangular plate with $C = 4$.

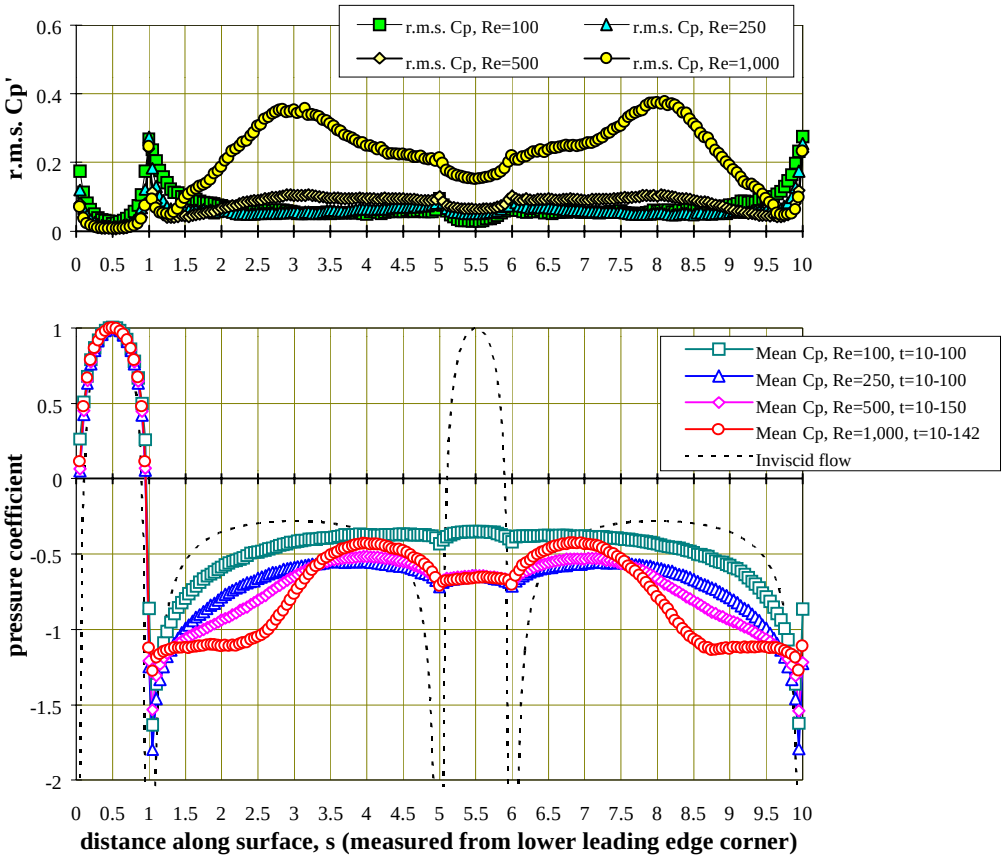

Figure 7.123. Predicted distributions of mean and r.m.s. pressure coefficients along surface of rectangular plate with C = 4 at Re_h = 100, 250, 500 and 1,000.

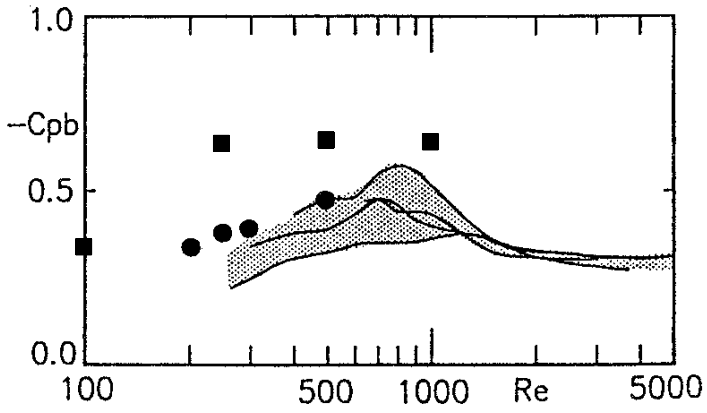

Figure 7.124. Base pressure coefficients $-C_{pb}$ of the C = 4 cylinder; ● : computed values of Okajima *et al.* [1990], ■ : computed results of this study, ▒ : experimental data of Okajima et al. [1990].

7.5 Effects of Chord-to-Thickness Ratio on Flow Parameters at Constant Reynolds Number

In the main, attention in this chapter has been concentrated on details of the flow around cylinders with particular values of C, and on the effects of Reynolds number on the flow and various parameters associated with it. In this section attention is turned to the variation of characteristic flow parameters with C at constant Re_h. The flow parameters considered are base-pressure coefficient, drag coefficient and Strouhal number of vortex shedding.

Okajima, Ueno and Sakai [1992] show comparisons of their calculated values (by a finite volume method) of drag and base pressure coefficients with experiment, for Re_h = 1,000, as a function of chord-to-thickness ratio over the range $0.2 \leq C \leq 10$. Their figure, with values from the present work added, is reproduced as Fig. 7.125. Okajima *et al*.'s calculated values of both C_D and $-C_{pb}$ have maximum values at about $C = 0.6$ and decrease continuously as the value of C is increased beyond 0.6. Experimental values of $-C_{pb}$ (only) decrease in a similar fashion for $C \gtrsim 1$. The calculated values of $-C_{pb}$ for C = 1, 2 and 4 of the present study agree quite well with the experimental data and the general character of their variation with C is also in accord with experiment. The calculated drag coefficients C_D are in very good agreement with the results obtained by Okajima *et al*. using their different numerical scheme.

The variation of Strouhal number with C at Re_h = 1,000 is summarised in Fig. 7.126, which is reproduced from Okajima *et al.* [1992], again with the addition of present results. While the values of C_D and $-C_{pb}$ vary continuously with C, there are discontinuities in the variation of Strouhal number, which undergoes abrupt stepwise increases at certain C values. Nakamura, Ohya and Tsuruta [1991] attribute vortex formation to impinging-shear-layer instability (in the shear layer reattaching to the side surfaces after leading-edge-separation) enhanced by feedback control from the impingement surface, with the wavelength of vortex shedding locked to the plate chord: stepwise increases in Strouhal number correspond to changes from one allowed vortex-shedding wavelength to the next. The shedding frequency therefore generally decreases with increase of C, but jumps to a higher value at certain critical values of C at which either of the two characteristic frequencies may exist intermittently. The experimental results obtained by Okajima *et al*. for Re_h = 1,000 indicate that the stepwise increases in Strouhal number occur at C = 3 and 6; the Strouhal number $St_c = fc/U_\infty$ (based on plate chord) is approximately constant at St_c = 0.15 for $C < 3$ and St_c = 0.6 for C = 3 to 6.

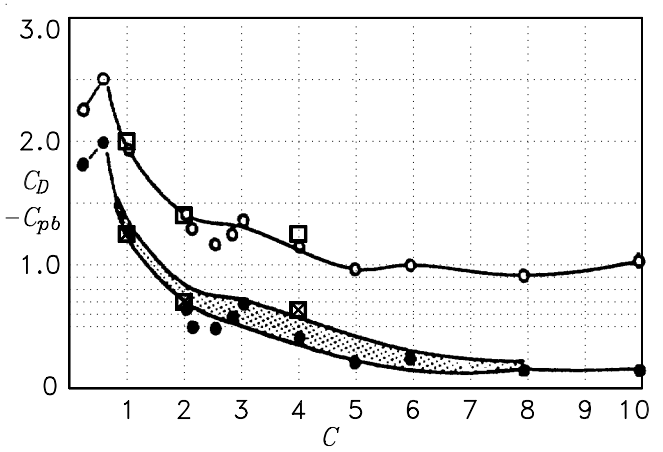

Figure 7.125. Drag coefficient C_D and base-pressure coefficient $-C_{pb}$ on rectangular cylinder at Re_h = 1,000; (a) Okajima *et al.* [1992]: ○ computed C_D, ● computed $-C_{pb}$, ▒ experimental $-C_{pb}$; (b) this study: □, computed C_D, ⊠ computed $-C_{pb}$.

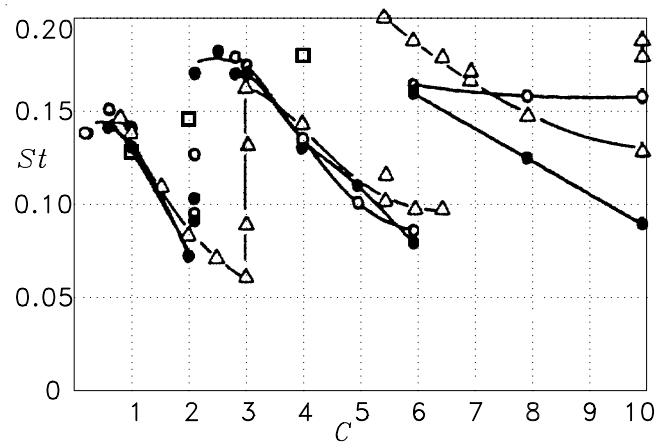

Figure 7.126. Strouhal numbers of wake-vortex frequency *St* for rectangular plate at Re_h=1,000; (a) Okajima *et al.* [1992]: ○ computed *St* in wake; △ experimental *St* in wake; ● computed *St* at trailing edge; (b) this study: □ computed *St*.

The points shown in Fig. 7.126 from the present work are only those corresponding to wake-vortex frequencies; other characteristic frequencies associated with the vortex-shedding process are not shown. The present calculations for the C = 1 cylinders yield a Strouhal number of St = 0.125 at Re_h = 1,000, which characterises intermittent fully-detached flow in which the process of vortex shedding is primarily the rolling up of shear layers separated from the leading corners of the cylinder. For the C = 2 cylinders, the wake-vortex frequency corresponds to a characteristic Strouhal number of 0.16. This Strouhal number apparently belongs to the class for cylinders with $C \approx 3$ to $C \approx 6$, which have intermittently attached flow on their side faces,

as do the present calculated flows for $C = 2$. Similarly, for the $C = 4$ cylinders the present calculations yield a wake-vortex frequency of $St = 0.18$ which appears to correspond with the flow regime characterising cylinders with $C = 6$ to 10 for which the flow is always reattached to both side faces, as in the present calculations for $C = 4$ and in the calculated flow patterns for long rectangular cylinders ($C > 6$) by Ohya, Nakamura, Ozono, Tsuruta and Nakayama [1992] and Ozono, Ohya and Nakamura [1992].

Thus the present calculations, like those of Okajima *et al.*, predict an increase in Strouhal number at $C = 2$ rather than at the experimental value of $C = 3$; and they predict the next step increase at $C = 4$, whereas both the calculations and experiment of Okajima *et al*. give a value of $C = 6$. These discrepancies, although observed at $Re_h = 1{,}000$, quite probably result from the effect shown, at the higher Reynolds number of $Re_h = 10{,}000$, in the two- and three-dimensional calculations of Tamura *et al*. [1993], the former predicting an earlier roll-up of the separated shear layer, a shorter leading-edge separation bubble, and convected vortices located closer to the side surfaces than the latter. These considerations indicate that while the present calculation procedures do produce realistic flow patterns and do predict the step changes in Strouhal number, they require some modification to correctly represent the effects of chord-to-thickness ratio for $C = 4$.

7.6 Concluding Remarks for Flow Over Thick Plates with Sharp Corners

As stated in the introduction, the main purpose of the work presented in this chapter was to establish the validity of the calculation procedure for bluff bodies with sharp edges. To this end, calculations of flow over single rectangular cylinders with $C = 1$, $C = 2$ and $C = 4$, for Reynolds number in the range 100 to 1,000, have been carried out. The calculated flow patterns, pressure forces and Strouhal numbers obtained have been compared with experimental and computational data of previous work. On the basis of previous experimental and numerical data, a general classification of the regimes of flow over rectangular cylinders as determined by chord-to-thickness ratio and Reynolds number, has been made (Fig. 7.1); this forms a framework for the comparison.

The flow patterns – streamlines and vorticity distributions – obtained for the $C = 1$ and $C = 2$ cylinders accord well with the general classification of flow regimes for the Reynolds number

range of calculation; and the variation of Strouhal number with Reynolds number and the coefficients of pressure forces (C_D, C_L and $-C_{pb}$) obtained are in good agreement with previous experimental and numerical results. Of particular note is that for the $C = 2$ cylinder, the sudden change in flow regime and accompanying Strouhal-number discontinuity at $Re_h \approx 500$, observed in experiments, is reproduced in the present calculations.

For the $C = 4$ cylinders, the predicted flow of steady laminar separation and laminar reattachment for low Reynolds numbers, $Re_h \leq 250$, is in accord with the general classification given in Fig. 7.1. However, apparently because of the differences between two- and three-dimensional calculations, similar to those found at higher Reynolds numbers by Tamura *et al*. [1993] referred to in the previous section, the flow patterns obtained for $Re_h = 500$ and 1,000 show permanent rather than the expected intermittent reattachment to the side faces. They therefore correspond with the calculated flow patterns given by Okajima [1990], Ohya *et al*. [1992] and Okajima, Ueno and Sakai [1992] for longer plates with, typically, $C > 6$; and the predicted Strouhal numbers are consistent with an extrapolation of the Okajima et al. [1992] data for $C \geq 6$ back to $C = 4$.

Comparisons of the present calculated flow patterns with existing numerical results show that the present calculations give significantly greater detail of the flow around the cylinder; they can therefore provide greater insight into the behaviour of real flow. In particular, the present calculations reproduce the process of formation of leading-edge-separation bubbles, and the generation and shedding of side-face vortices from the bubble, after the manner described by Kiya [1989]. They bring out the important role of this mechanism in determining the main vortex-shedding frequencies and the low-frequency variation in the strength of side-face vortices which leads to amplitude modulation of the lift on the cylinder.

From the calculations of flow over rectangular plates presented in this chapter, and also the calculations of flow on circular cylinders presented in chapter 6, it is concluded that, apart from the discrepancies noted for $C = 4$ plates, the numerical procedure followed does lead to a valid representation of the behaviour of real flows. On this basis, application of the method to arrays of rectangular plates, which have not been nearly so extensively studied experimentally as have single rectangular cylinders, can be expected to yield valid detailed insights into the mechanisms of real flows over these configurations.

Chapter 8

Flow Over Tandem Arrays of Two Rectangular Plates

When bluff bodies are placed together to form a multi-body system, in close enough proximity to interact with each other, their aerodynamic characteristics can be very different from those of the isolated individual bodies. Tandem arrays of two circular cylinders have been quite extensively studied but other combinations less so. In this chapter, attention is focused on tandem arrays of two plates of the same thickness, both rectangular in cross-section. The two-plate array, shown schematically in Fig. 8.1, consists of an upstream plate $P1$ and downstream plate $P2$, aligned in the streamwise direction. The chord-to-thickness ratios $C1$ (= $c1/h$) and $C2$ (= $c2/h$) of the plates and the gap-to-thickness ratio G (= g/h) define the configuration of the array.

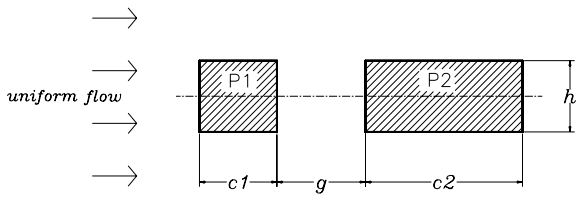

Figure 8.1. Schematic representation of a tandem array of two rectangular plates

8.1 Previous Studies

Although studies of the flow over tandem arrays of two rectangular plates are not numerous, there have been several experimental investigations which are relevant to the present work. Sakamoto, Haniu and Obata [1987] made wind-tunnel measurements of the fluctuating forces acting on a tandem array of two square cylinders and of vortex-shedding frequencies, at Re_h = 2.76×10^4. They identified three main flow regimes as a function of G. For $G < 3$, the plates act like one body connected by a quasi-steady vortex region in the gap and Karman vortices are shed only from the downstream plate. In this range of G, the Strouhal number of vortex

shedding decreases as the gap is increased, reaching a minimum value at $G = 3$. For $3 < G < 27$, the separated shear layers from the upstream plate roll up to form vortices in the gap. The vortices shed from the upstream plate trigger vortex shedding from the downstream plate, resulting in synchronised vortex-shedding from the two plates. The Strouhal number increases as the gap is lengthened, approaching the value for a single square cylinder. For $20 < G < 27$, two different states of vortex shedding are possible, one of synchronous shedding and the other characterised by the plates shedding vortices at different frequencies. For $G > 27$, only asynchronous shedding occurs. Then the upstream plate behaves essentially as a single plate, while the downstream plate, because it is subject to wake flow with a velocity less than the mainstream velocity, sheds vortices at a lower frequency. The experiments also show a discontinuity in the variation of drag coefficient with G accompanying the change in flow regime which occurs at $G \sim 3$. The change of flow regime on an array of two square cylinders, from one without to one with a vortex street between the cylinders, at a critical gap width, was also observed by Takeuchi and Matsumoto [1992] (at $G \sim 2$ in their experiments).

Experiments conducted by Bull, Pickles, Blazewicz and Bies [1992] and Blazewicz, Pickles and Bull [1993] show that for an array of two rectangular plates ($C1 = 1$, $C2 = 6.5$) there exist two distinct flow regimes as a function of the combined length ($C1 + G$). For $(C1 + G) \leq 4.5$, separated shear layers from the leading edge of the upstream plate reattach on the streamwise surface of the downstream plate, resulting in the formation of a separation bubble bridging the gap between the plates. For $(C1 + G) \geq 3$ (there is some overlap between the two regimes), the shear layers separated from the leading edge of the upstream plate form a vortex street in the gap between the plates, which impinges on the downstream plate. An investigation of acoustic radiation from plate arrays by Bull and Pickles [1991] and wind-tunnel measurements of surface pressure fluctuations by Bull, Pickles and Li [1992] show that, in this latter flow regime, impingement of vortices on the leading edges of the downstream plate is the dominant source of surface pressure fluctuations on the downstream plate. The results of Blazewicz *et al*. [1993] also show that the transition from one flow regime to the other is accompanied by a discontinuous change in the Strouhal number of the vortex wake of the array.

The flow regimes which can occur on tandem arrays of two rectangular plates have been classified by Bull, Blazewicz and Pickles [1997] in terms of the position at which the shear layers separated from the leading corners of the upstream plate impinge on the array further downstream. The flow regime established will depend on whether impingement occurs on the

upstream plate, within the gap, on the downstream plate, or beyond the downstream plate. Let 'impingement length' denote the distance from a leading corner of the upstream plate to the impingement position. The regime established will depend on the chordwise lengths of the two plates and the streamwise gap between them, in relation to the impingement length. It will also depend on any fluctuation of the impingement length with time, which can result in impingement occurring entirely on one or other of the plates, entirely within the gap, entirely downstream of the array, or intermittently on the plates.

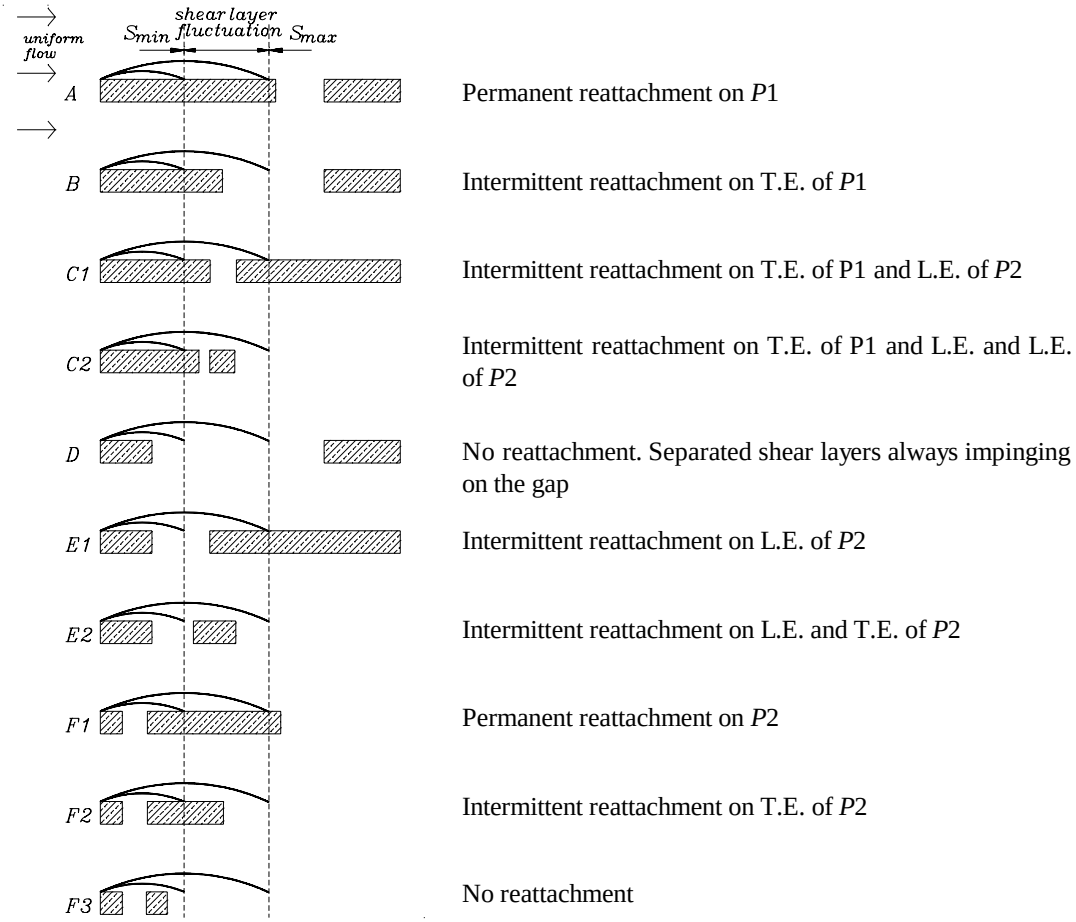

Figure 8.2. Schematic representation of possible flow regimes according to plate configuration in relation to separation bubble length, extracted from Bull, Blazewicz and Pickles [1997]. L.E. and T.E. stand for Leading Edge and Trailing Edge respectively.

Notionally, the impingement length can be regarded as the length of a separation bubble which forms on a long single plate with a square leading edge; consequently, it can be taken to be primarily dependent on the plate thickness. Hence, the parameters determining the flow regime are the main array parameters – the chord-to-thickness ratios of the two plates $C1$ and $C2$ and the gap-to-thickness ratio G – together with the ratio S of impingement length to plate thickness

and its minimum and maximum fluctuation values S_{min} and S_{max}. It appears that, for an array with specified values of $C1$ and $C2$, the values of S, S_{min} and S_{max} are essentially constant and independent of the gap parameter G; although the effective mean value S may in some cases differ considerably from the single-plate value, typically about 6. The schematic representation of the possible flow regimes for tandem arrays of two rectangular plates according to plate configuration in relation to impingement/separation-bubble length is shown in Fig. 8.2, which is reproduced from Bull *et al.* [1997].

Bull *et al*. [1997] show that the various flow regimes can be identified experimentally from changes in the character of the variation of surface pressure p (or the coefficient $C_p = (p-p_\infty)/\frac{1}{2}U_\infty^2$) and vortex shedding frequency f (or Strouhal number $St = fh/U_\infty$) with G. It was found experimentally that the flow within the gap can take a number of different forms including periodic reversal of transverse flow, trapped vortex flow, and vortex street formation.

8.2 Numerical Parameters in the Present Calculations

In the present study, calculations of flow over arrays of two rectangular plates have been performed for three different plate combinations: ($C1 = 1$, $C2 = 1$), ($C1 = 1$, $C2 = 4$) and ($C1 = 4$, $C2 = 4$). Gaps between the plates in the range $0.2 \le G \le 8$ have been considered, so as to embrace all the flow regimes identified by experiment. In order to be consistent with the calculations of flow over single rectangular plates made in previous chapter, all calculated results presented are for a Reynolds number of $Re_h = 500$. The flow is started impulsively from rest at time $t = 0$, and its subsequent development calculated at time t, advancing by intervals of $\Delta t = 0.02$ until a fully-developed state is reached. In the numerical representation, the boundaries of the plates are approximated by uniform straight segments with $\Delta s = 0.05$, 80 for the plates with $C = 1$ and 200 for the plates with $C = 4$. The value of ϵ is $1.15\sqrt{(\Delta t/Re_h)}$ throughout. The general numerical procedures for the formulation of the **[*K*]** matrix, convection and diffusion of discrete vortices, merging of discrete vortices, introduction of vorticity into the flow domain from the solid boundaries, calculation of fluid pressures and surface pressures on the body have been carried out according to the scheme described in Chapter 4.

8.3 Calculations of Flow Over Tandem Arrays of Two Square Cylinders

In the case of a tandem array with $C1 = 1$, the chord of the leading cylinder is less than the minimum length of a leading-edge-separation bubble, i.e. in terms of the classification of Bull *et al*. [1997] referred to above $C1 < S_{min}$, and the shear layers separating from the leading corners of the upstream cylinder never reattach to the cylinder itself. The flow regimes for an array of two square cylinders are then (in the notation of the classification):

(i) *F2* when $(C1 + G) < S_{min} < (C1 + G + C2) < S_{max}$, corresponding to intermittent reattachment and trailing-edge separation on the downstream cylinder;

(ii) *E2* when $S_{min} < (C1 + G) < (C1 + G + C2) < S_{max}$, corresponding to intermittent reattachment and leading-edge or trailing-edge separation on the downstream cylinder;

(iii) *E1* when $S_{min} < (C1 + G) < S_{max} < (C1 + G + C2)$, corresponding to intermittent reattachment and leading-edge separation on the downstream cylinder; and

(iv) *D* when $(C1 + G) > S_{max}$, corresponding to impingement within the gap at all times and no reattachment to the downstream cylinder.

For the array of two square cylinders, experimental results of Bull *et al.* [1997] are in accord with the above classification and show that a vortex street is formed downstream of the second cylinder at all values of G. At very small G values, the two cylinders behave very much like a single plate, with the exception that, in this case, there is a periodic transverse flow through the gap in phase with the vortex-shedding cycle (regime *F*2). With an increase of G, stationary vortices form in the gap (regimes *E*1 and *E*2, which seem to be indistinguishable experimentally). As the gap is further lengthened, a vortex street forms in the gap from the shear layers separating from the leading edges of the upstream plate (regime *D*); these vortices impinge on the downstream plate. The experimental results for Strouhal numbers of vortex shedding and surface pressure coefficients given by Bull *et al.* [1997] (reproduced here as Figs. 8.70) indicate a change from the *F*2 to the *E*1/*E*2 regime at $G \sim 0.5$, with little change in the

form of variation of pressure coefficients with G, but with a change in Strouhal number variation – from increasing to decreasing – as G increases through the change-over value; they also indicate a change from the $E1/E2$ to the D regime at $G \sim 2.5$, accompanied by discontinuity in both surface-pressure-coefficient and Strouhal-number variation. The values of G at the observed changes in flow regime, which were confirmed by flow visualisation, imply values of $S_{min} = 1.5$ and $S_{max} = 3.5$. These experimental results provide a frame of reference for the results of the numerical simulations which are presented in following sections, even though the experimental data were obtained at a very much higher Reynolds number ($Re_h \sim 1.7\times10^4$) than that of the numerical simulations.

8.3.1 Flow Regimes for Very Small Gaps, $G \leq 0.5$

Calculations of flow over a tandem array of two square cylinders with very small streamwise gap have been made at $G = 0.1$, $G = 0.2$ and $G = 0.5$. The gaps of $G = 0.1$ and $G = 0.2$ are expected to produce an $F2$ flow regime, and $G = 0.5$ an $F2$ or $E2$ regime. Flow development from an impulsive start from rest to fully-developed flow for these arrays is shown in the elemental-vortex distributions, streamline patterns and vorticity patterns in Figs. 8.3–8.13. In all these cases, flow development is essentially complete at $t \sim 10$. Apart from details of the flow in the gap between the cylinders, the flow, both in the developing and fully-developed state, is very similar on the three arrays. The flow separates from the leading corners of the upstream cylinder at all times, followed by intermittent reattachment and trailing-edge separation on the downstream cylinder. Reattachment on the downstream cylinder produces a leading-edge-separation bubble which bridges the gap between the cylinders. The process of vortex formation downstream of the array involves both formation of side-face vortices in the leading-edge-separation bubble and their subsequent convection and the rolling up of shear layers separating from the trailing edge of the downstream cylinder. In fact, according to the calculations, the flow regime on these three arrays is $F2$. Consequently there is similarity of elemental-vortex distributions (Figs. 8.4, 8.9 and 8.12), vortex-street patterns in both a fixed frame of reference (Figs. 8.4, 8.9 and 8.12) and a frame of reference moving at a velocity of $U_{ref} = 0.8U_\infty$, equal to the translational velocity of vortex centres (Figs. 8.62(a), 8.62(b) and 8.62(c)); pressure distributions (Figs. 8.12 and 8.14); and periodicities of force fluctuation (Figs. 8.13 and 8.15).

There are also strong similarities between the flows over these three arrays and the flow over a single plate with $C = 2$ (Figs. 7.44 and 7.48); although it appears that side-face vortices on the arrays are relatively weaker than on the single $C = 2$ plate, with the result that flow separation with flow reversal is not so evident in the array flows. The similarity can be seen in greater detail for $G = 0.1$ by comparison of the streamline patterns of Fig. 8.6 over times $t = 70–81$ with corresponding patterns for the single $C = 2$ plate at $t = 84–89$ or $90–97$ in Figs. 7.82 and 7.84; by comparison of the vorticity patterns of Fig. 8.7 with Fig. 7.83; and by comparison of the instantaneous pressure fields of Fig. 8.6 with those for $C = 2$ (Fig. 7.84). It is clear that the flow around arrays of two square cylinders with very small gaps behaves very much like the flow around a single plate with $C = 2$ at the same Reynolds number.

On the other hand, the presence of the gap in the array does produce some modification of the single-plate flow. For the arrays, there is transverse flow through the gap between the cylinders which, as the streamline patterns of Figs. 8.6, 8.9 and 8.12 show, reverses periodically. This feature of the flow is in accord with experimental flow visualisation (Blazewicz [1998]). Figs. 8.14(a)–(c) show the variation with time of the net (upward) transverse flow through the gap Q and the corresponding variation of lift coefficient C_{L2} on the downstream cylinder. The Q values, normalised by the free-stream velocity U_∞ and cylinder thickness h, are calculated at time intervals of $\Delta t = 1$, which is too long to avoid aliasing; so that the true periodicity is not correctly represented. However, the figure clearly shows periodic reversals of the flow through the gap, that are synchronised with the variations of lift coefficient, and, therefore, in phase with the vortex shedding cycle.

Further, although, in terms of broad similarity of flow over the arrays and a single plate, the mean pressure distributions are similar (and in particular there is similarity of pressure distribution on the front faces, C_{pf1}, and the base pressure coefficients $C_{pb2} \approx -0.65$ for $G = 0.1$, -0.6 for $G = 0.2$, -0.5 for $G = 0.5$ and -0.7 for the single $C = 2$ cylinder), when they are considered in detail they show that the gap also has a significant effect on pressure distribution and on the drag coefficient of the array. The distributions of mean pressure coefficient C_p and the coefficient of r.m.s. pressure fluctuation over the surface of the cylinders in the $G = 0.1$ array are shown in Fig. 8.15. The two cylinders have quite different pressure distributions over their front faces, but quite similar distributions over the other three faces. On the upstream cylinder, the distribution of surface-pressure is very similar to that on a single square cylinder at the same Reynolds number (see Fig. 7.35), despite the presence of the second cylinder

immediately downstream: the pressure decreases from $C_{pf1} = 1$ at the front stagnation point ($s = 0.5$) to the lowest pressure overall ($C_p \approx -1.5$) on the side surfaces near the leading edge corners, and gradually rises along the side faces to the almost uniform base pressure $C_{pb1} \approx -1.06$. The mean pressure in the gap is essentially constant, and the pressure on the front face of the downstream cylinder is uniform at $C_{pf2} \approx -1.03$, essentially equal to the base pressure on the upstream cylinder. On the upper and lower faces of the downstream cylinder, the pressure gradually increases to the virtually-constant $C_{pb2} \approx -0.65$ on the base surface. Since $C_{pb2} > C_{pf2}$, the downstream cylinder experiences a negative drag (in the direction against the main stream), the mean value of which is $C_{D2} = -0.38$ while the upstream cylinder is subject to positive drag of mean value $C_{D1} = 1.8$, as is evident from the time-histories of drag coefficient in Fig. 8.13. The resultant drag coefficient for the array, $C_D = 1.42$, is therefore, as a result of the effect of the gap, significantly lower than the value of $C_D = 1.7$ for a single plate with $C = 2$ (Fig. 7.91). The effect is similar on the $G = 0.2$ and $G = 0.5$ arrays, the surface-pressure distributions for which are shown in Figs. 8.17 and 8.19. In these cases, we have for the $G = 0.2$ array $C_{pf2} \approx -0.98$, $C_{pb2} \approx -0.6$, and $C_{D2} = -0.4$ which with $C_{D1} = 1.75$ gives an overall drag coefficient of $C_D = 1.35$, while for the $G = 0.5$ array $C_{pf2} \approx -0.9$, $C_{pb2} \approx -0.5$, $C_{D2} = -0.42$, $C_{D1} = 1.64$ and $C_D = 1.22$. (A summary of the calculated flow parameters in the present study is given in Table 8.1 in section 8.3.5.)

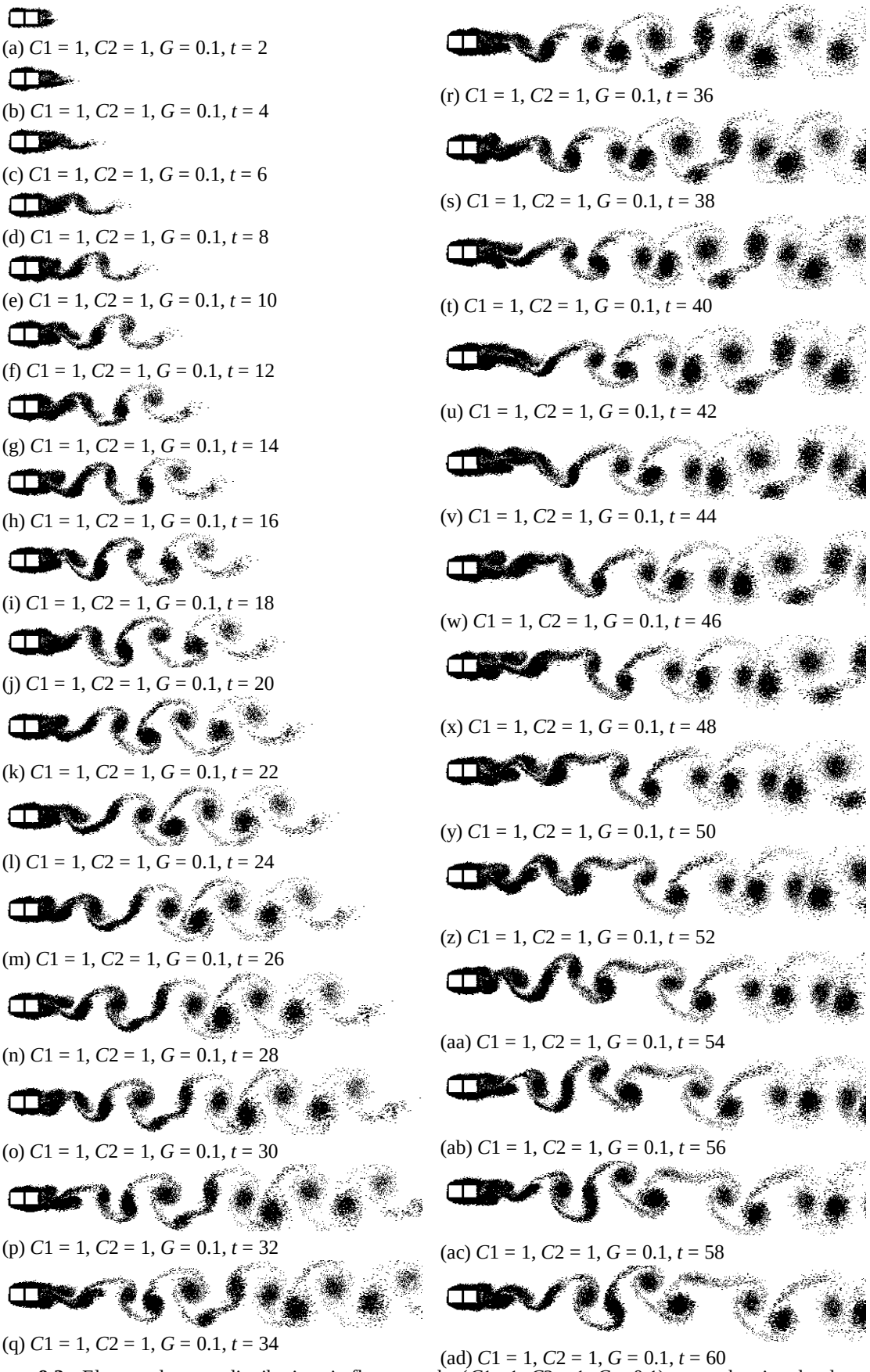

(a) $C1 = 1$, $C2 = 1$, $G = 0.1$, $t = 2$

(b) $C1 = 1$, $C2 = 1$, $G = 0.1$, $t = 4$

(c) $C1 = 1$, $C2 = 1$, $G = 0.1$, $t = 6$

(d) $C1 = 1$, $C2 = 1$, $G = 0.1$, $t = 8$

(e) $C1 = 1$, $C2 = 1$, $G = 0.1$, $t = 10$

(f) $C1 = 1$, $C2 = 1$, $G = 0.1$, $t = 12$

(g) $C1 = 1$, $C2 = 1$, $G = 0.1$, $t = 14$

(h) $C1 = 1$, $C2 = 1$, $G = 0.1$, $t = 16$

(i) $C1 = 1$, $C2 = 1$, $G = 0.1$, $t = 18$

(j) $C1 = 1$, $C2 = 1$, $G = 0.1$, $t = 20$

(k) $C1 = 1$, $C2 = 1$, $G = 0.1$, $t = 22$

(l) $C1 = 1$, $C2 = 1$, $G = 0.1$, $t = 24$

(m) $C1 = 1$, $C2 = 1$, $G = 0.1$, $t = 26$

(n) $C1 = 1$, $C2 = 1$, $G = 0.1$, $t = 28$

(o) $C1 = 1$, $C2 = 1$, $G = 0.1$, $t = 30$

(p) $C1 = 1$, $C2 = 1$, $G = 0.1$, $t = 32$

(q) $C1 = 1$, $C2 = 1$, $G = 0.1$, $t = 34$

(r) $C1 = 1$, $C2 = 1$, $G = 0.1$, $t = 36$

(s) $C1 = 1$, $C2 = 1$, $G = 0.1$, $t = 38$

(t) $C1 = 1$, $C2 = 1$, $G = 0.1$, $t = 40$

(u) $C1 = 1$, $C2 = 1$, $G = 0.1$, $t = 42$

(v) $C1 = 1$, $C2 = 1$, $G = 0.1$, $t = 44$

(w) $C1 = 1$, $C2 = 1$, $G = 0.1$, $t = 46$

(x) $C1 = 1$, $C2 = 1$, $G = 0.1$, $t = 48$

(y) $C1 = 1$, $C2 = 1$, $G = 0.1$, $t = 50$

(z) $C1 = 1$, $C2 = 1$, $G = 0.1$, $t = 52$

(aa) $C1 = 1$, $C2 = 1$, $G = 0.1$, $t = 54$

(ab) $C1 = 1$, $C2 = 1$, $G = 0.1$, $t = 56$

(ac) $C1 = 1$, $C2 = 1$, $G = 0.1$, $t = 58$

(ad) $C1 = 1$, $C2 = 1$, $G = 0.1$, $t = 60$

Figure 8.3. Elemental-vortex distributions in flow over the ($C1 = 1$, $C2 = 1$, $G = 0.1$) array, showing development from the impulsive start to the fully-developed flow; $\epsilon = 1.7\sqrt{(\Delta t/Re_h)}$.

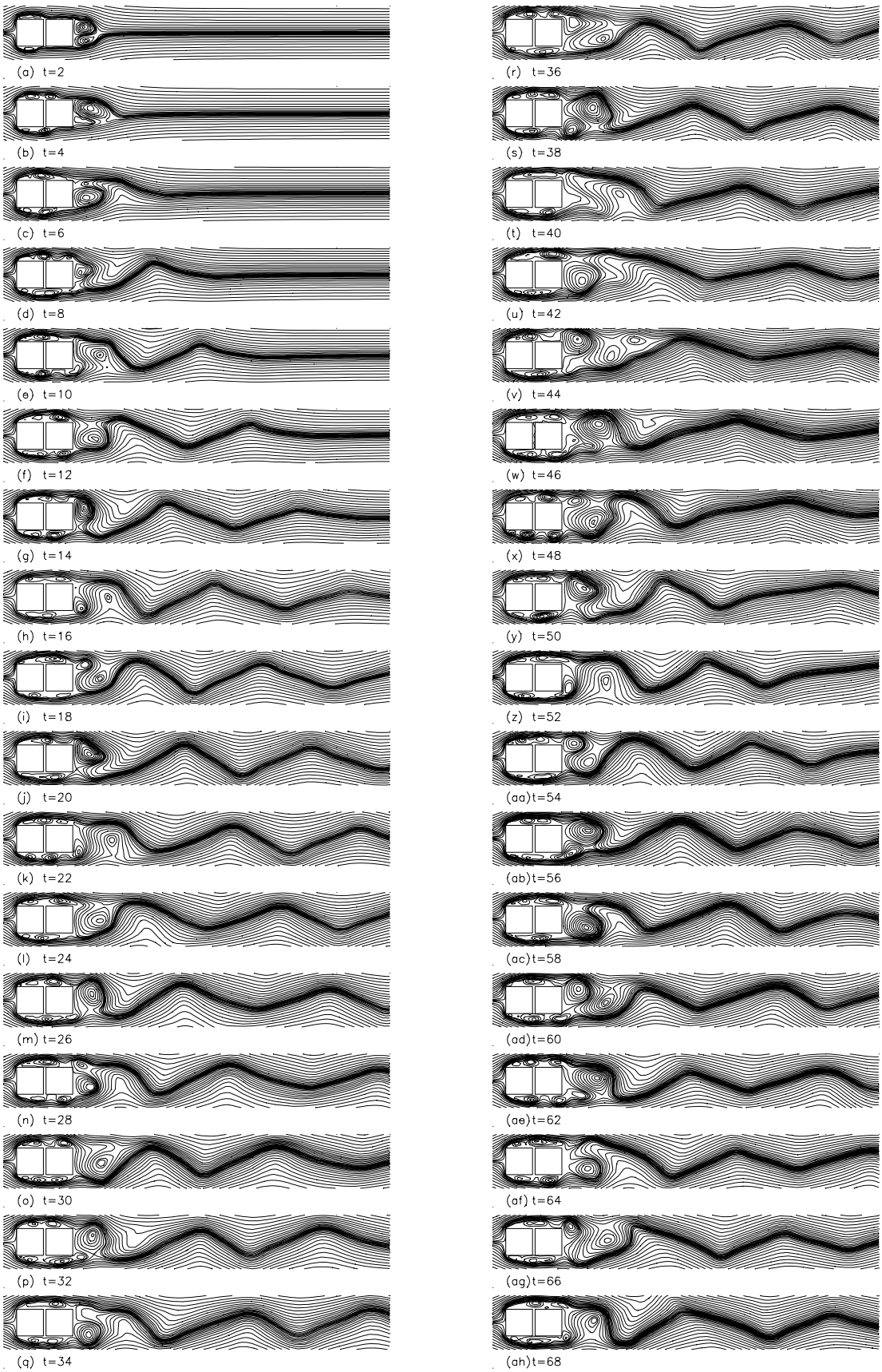

Figure 8.4. Calculated streamline patterns in flow over the ($C1$ =1, $C2$ = 1, G = 0.1) array, showing development from the impulsive start to the fully-developed flow; $\epsilon = 1.7\sqrt{(\Delta t/Re_h)}$.

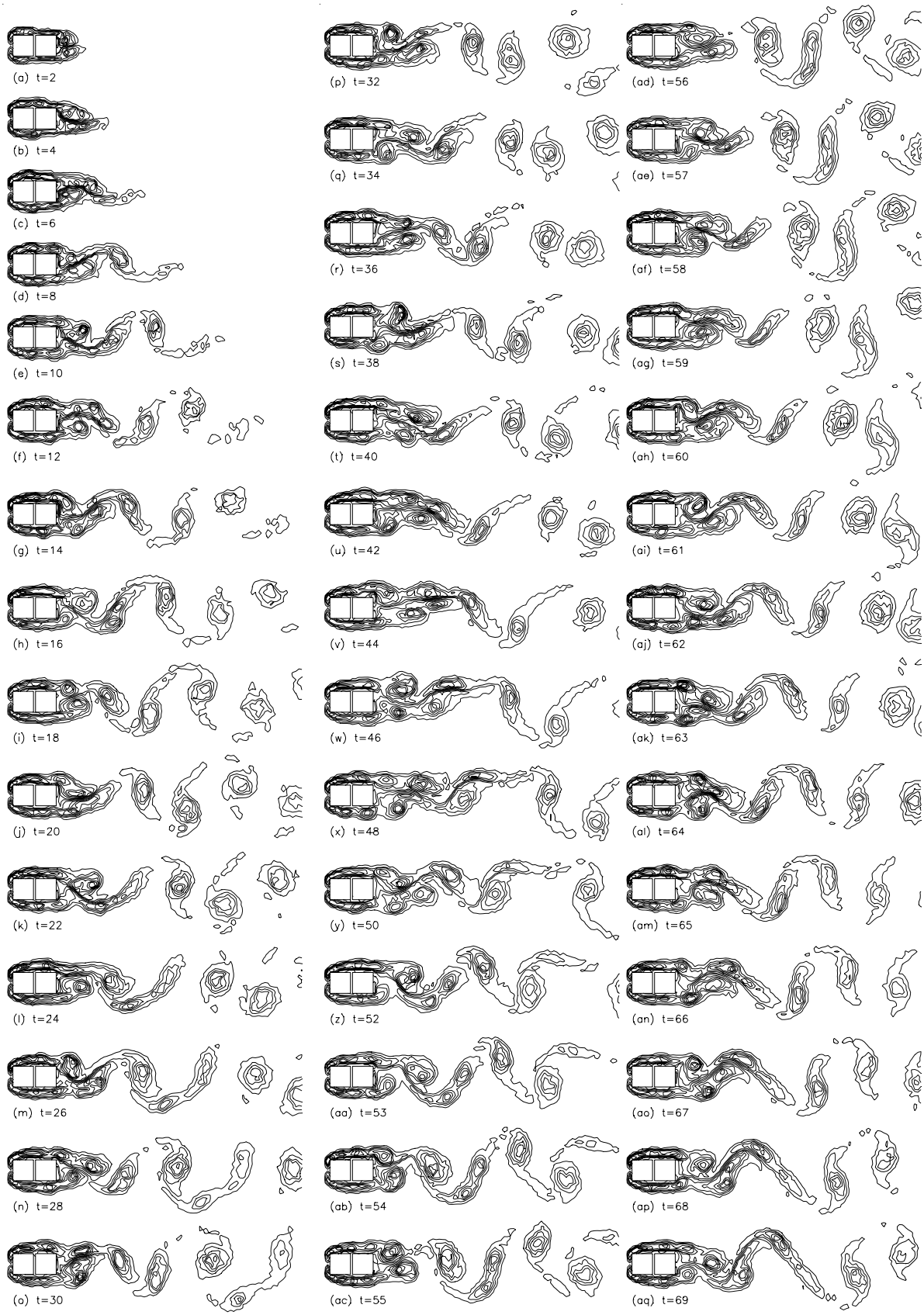

Figure 8.5. Calculated vorticity contours in flow over the ($C1$ =1, $C2$ = 1, G = 0.1) array, showing development from the impulsive start to the fully-developed flow; $\epsilon = 1.7\sqrt{(\Delta t/Re_h)}$.

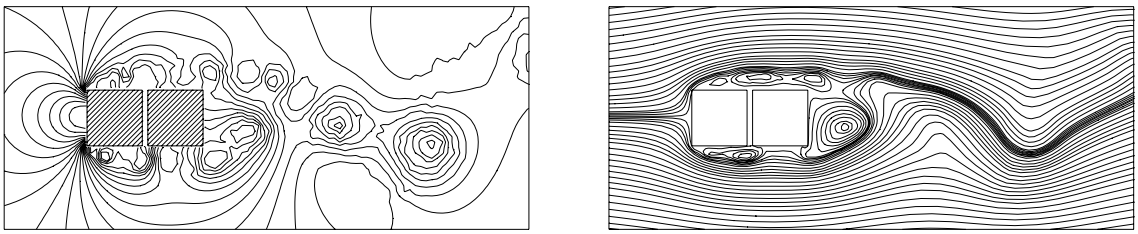

(a1) $G = 0.1$, $t = 70$ (a2) $G = 0.1$, $t = 70$

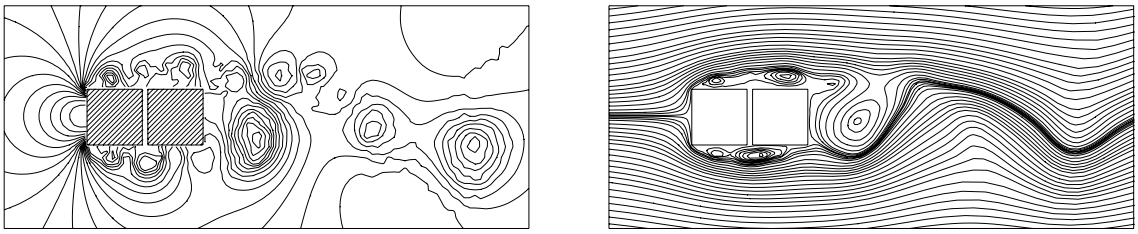

(b1) $G = 0.1$, $t = 71$ (b2) $G = 0.1$, $t = 71$

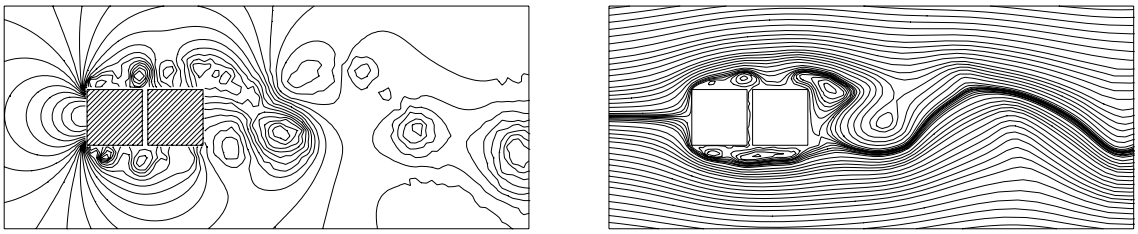

(c1) $G = 0.1$, $t = 72$ (c2) $G = 0.1$, $t = 72$

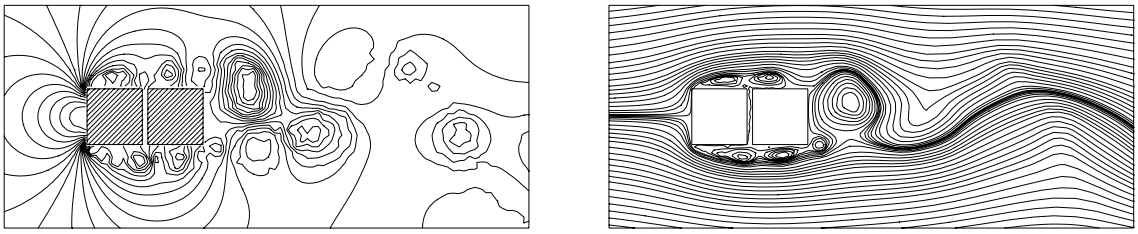

(d1) $G = 0.1$, $t = 73$ (d2) $G = 0.1$, $t = 73$

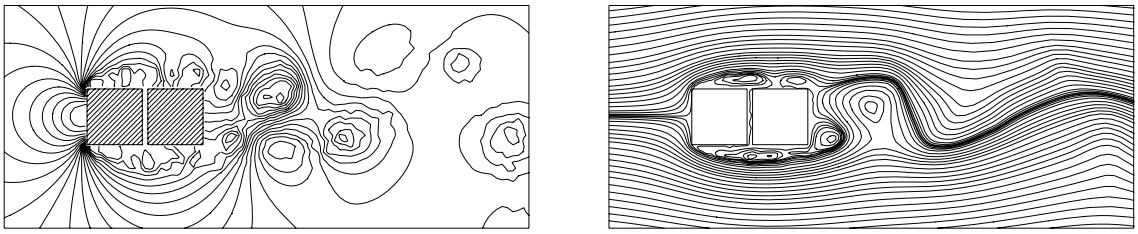

(e1) $G = 0.1$, $t = 74$ (e2) $G = 0.1$, $t = 74$

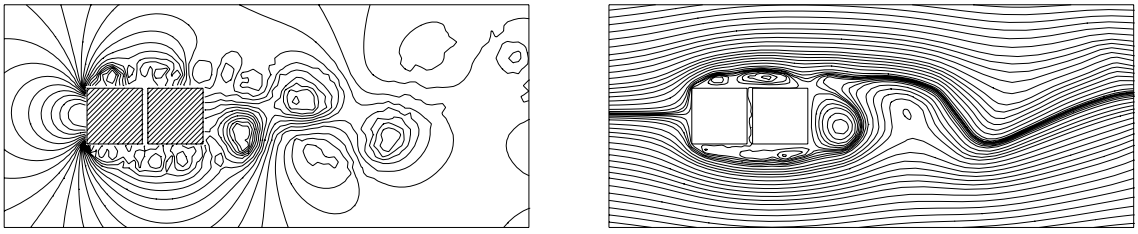

(f1) $G = 0.1$, $t = 75$ (f2) $G = 0.1$, $t = 75$

Figure 8.6. Instantaneous pressure fields and streamline patterns in fully-developed flow around the ($C1 = 1$, $C2 = 1$, $G = 0.1$) array; $\epsilon = 1.7\sqrt{(\Delta t/Re_h)}$.

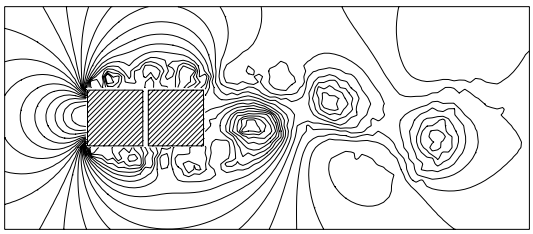

(g1) $G = 0.1$, $t = 76$

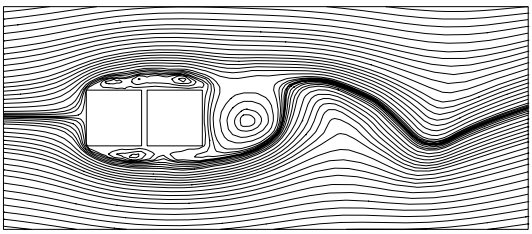

(g2) $G = 0.1$, $t = 76$

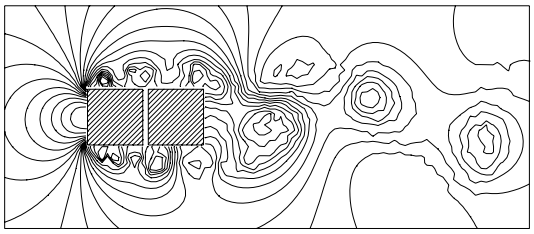

(h1) $G = 0.1$, $t = 77$

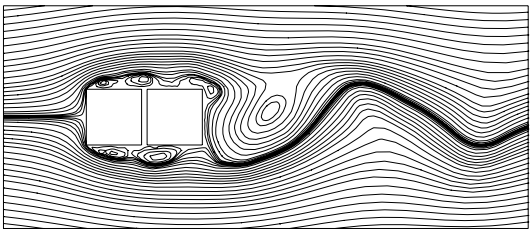

(h2) $G = 0.1$, $t = 77$

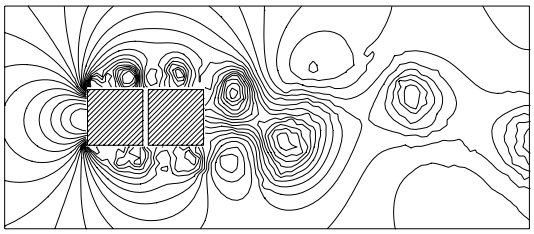

(i1) $G = 0.1$, $t = 78$

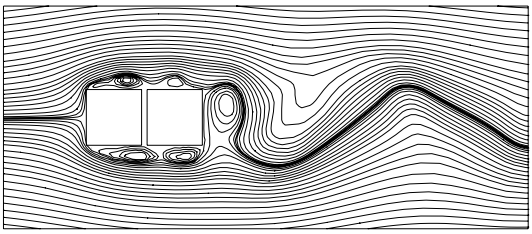

(i2) $G = 0.1$, $t = 78$

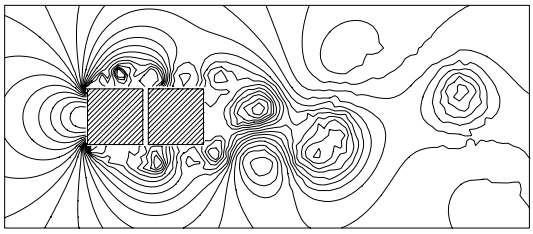

(j1) $G = 0.1$, $t = 79$

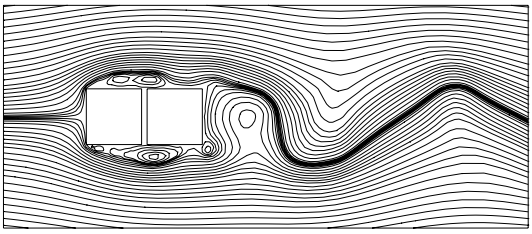

(j2) $G = 0.1$, $t = 79$

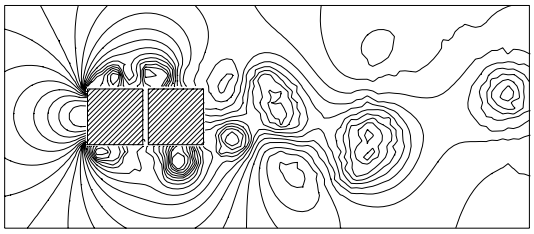

(k1) $G = 0.1$, $t = 80$

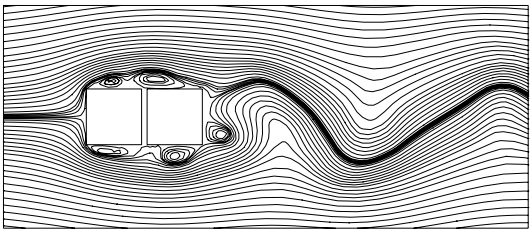

(k2) $G = 0.1$, $t = 80$

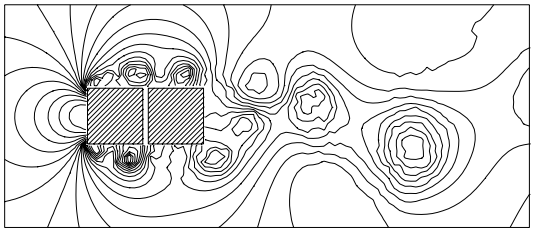

(l1) $G = 0.1$, $t = 81$

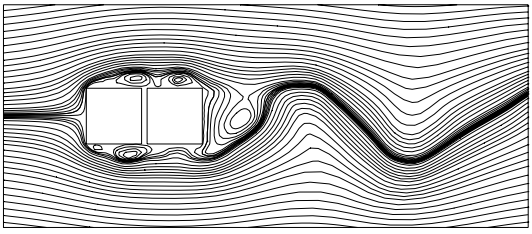

(l2) $G = 0.1$, $t = 81$

Figure 8.6. Cont'd.

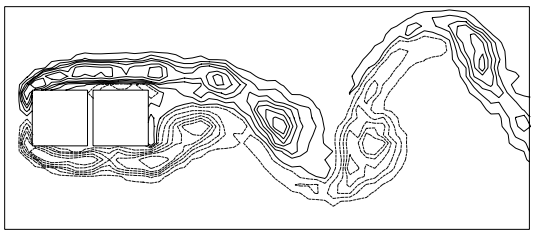

(a) $G = 0.1$, $t = 70$

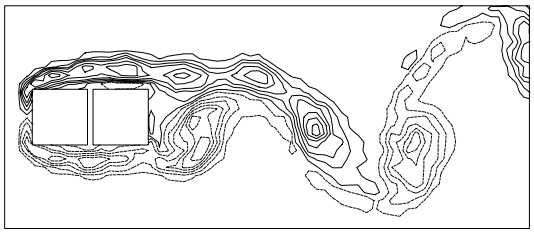

(b) $G = 0.1$, $t = 71$

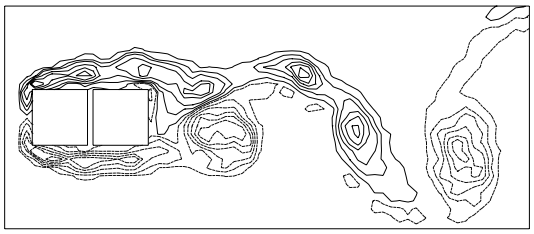

(c) $G = 0.1$, $t = 72$

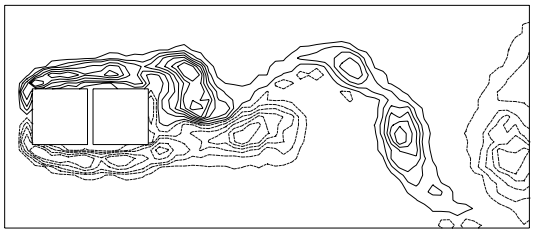

(d) $G = 0.1$, $t = 73$

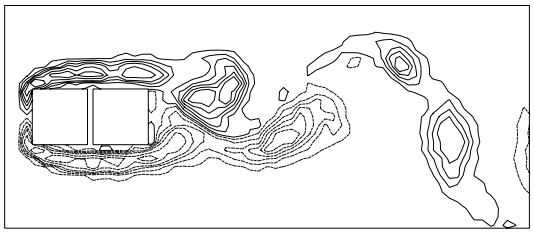

(e) $G = 0.1$, $t = 74$

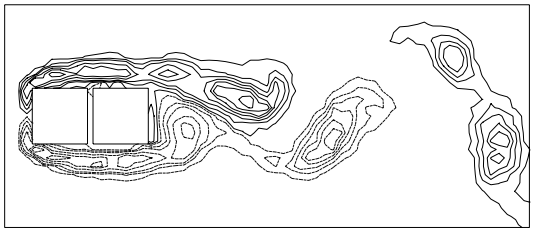

(f) $G = 0.1$, $t = 75$

(g) $G = 0.1$, $t = 76$

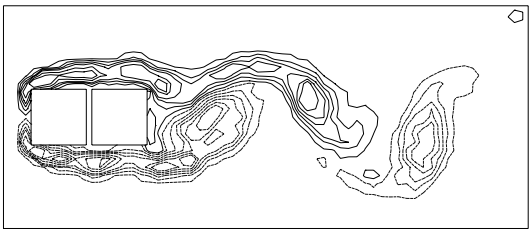

(h) $G = 0.1$, $t = 77$

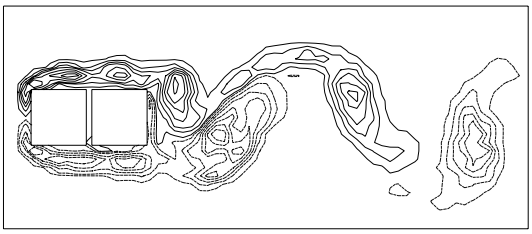

(i) $G = 0.1$, $t = 78$

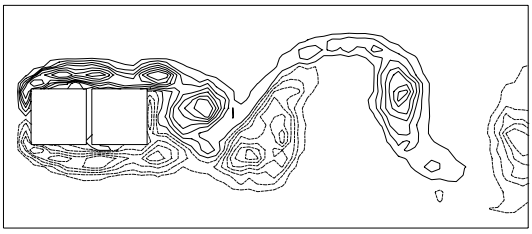

(j) $G = 0.1$, $t = 79$

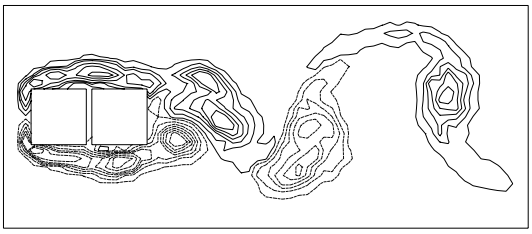

(k) $G = 0.1$, $t = 80$

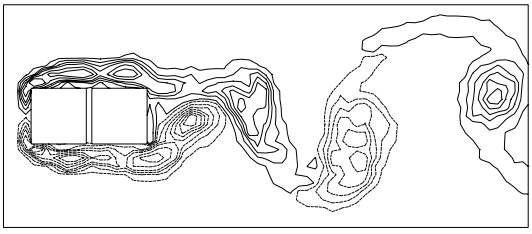

(l) $G = 0.1$, $t = 81$

Figure 8.7. Vorticity contours in fully-developed flow over the ($C1 = 1$, $C2 = 1$, $G = 0.1$) array; $\epsilon = 1.7\sqrt{(\Delta t/Re_h)}$.

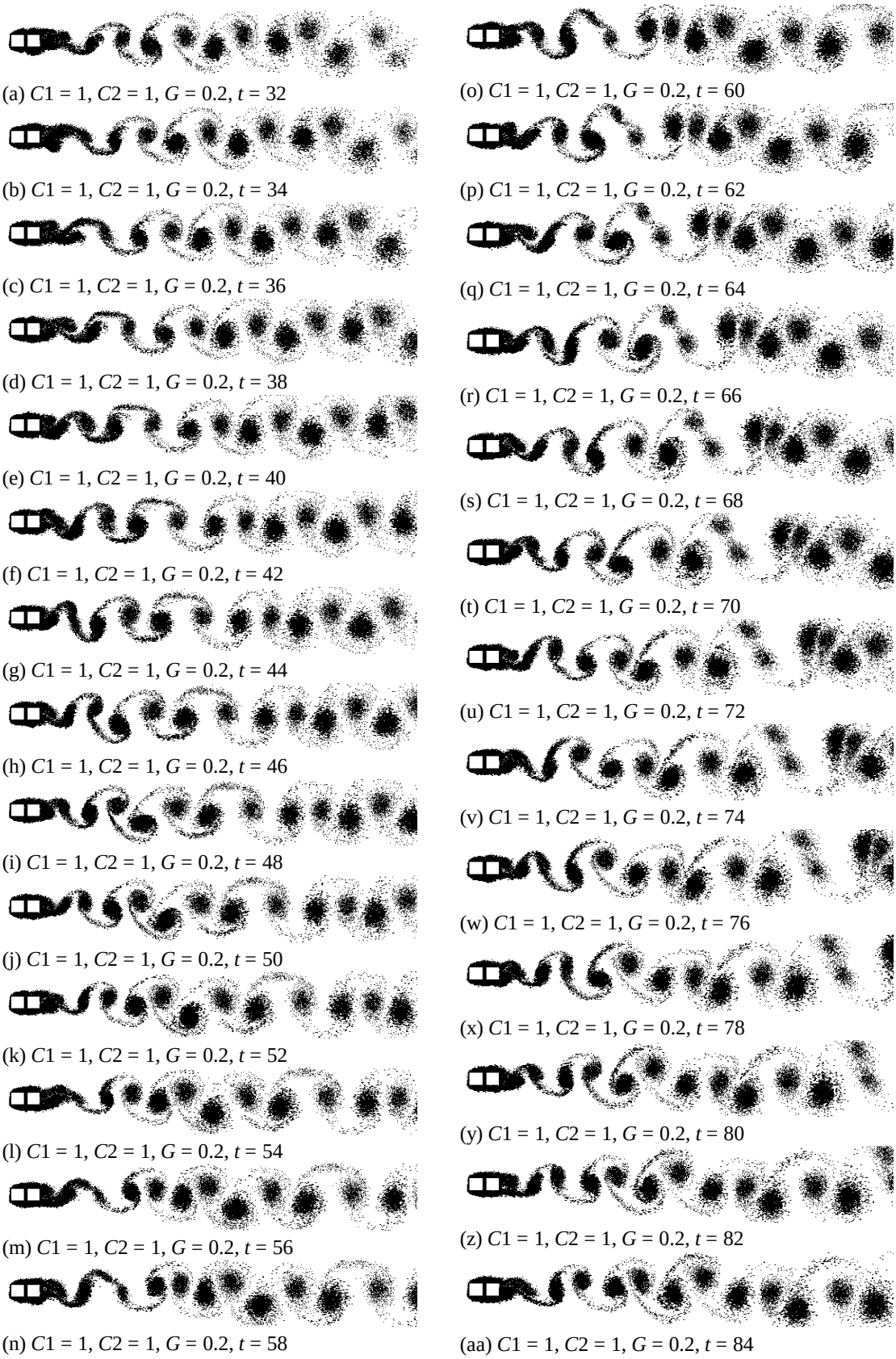

(a) $C1 = 1$, $C2 = 1$, $G = 0.2$, $t = 32$

(b) $C1 = 1$, $C2 = 1$, $G = 0.2$, $t = 34$

(c) $C1 = 1$, $C2 = 1$, $G = 0.2$, $t = 36$

(d) $C1 = 1$, $C2 = 1$, $G = 0.2$, $t = 38$

(e) $C1 = 1$, $C2 = 1$, $G = 0.2$, $t = 40$

(f) $C1 = 1$, $C2 = 1$, $G = 0.2$, $t = 42$

(g) $C1 = 1$, $C2 = 1$, $G = 0.2$, $t = 44$

(h) $C1 = 1$, $C2 = 1$, $G = 0.2$, $t = 46$

(i) $C1 = 1$, $C2 = 1$, $G = 0.2$, $t = 48$

(j) $C1 = 1$, $C2 = 1$, $G = 0.2$, $t = 50$

(k) $C1 = 1$, $C2 = 1$, $G = 0.2$, $t = 52$

(l) $C1 = 1$, $C2 = 1$, $G = 0.2$, $t = 54$

(m) $C1 = 1$, $C2 = 1$, $G = 0.2$, $t = 56$

(n) $C1 = 1$, $C2 = 1$, $G = 0.2$, $t = 58$

(o) $C1 = 1$, $C2 = 1$, $G = 0.2$, $t = 60$

(p) $C1 = 1$, $C2 = 1$, $G = 0.2$, $t = 62$

(q) $C1 = 1$, $C2 = 1$, $G = 0.2$, $t = 64$

(r) $C1 = 1$, $C2 = 1$, $G = 0.2$, $t = 66$

(s) $C1 = 1$, $C2 = 1$, $G = 0.2$, $t = 68$

(t) $C1 = 1$, $C2 = 1$, $G = 0.2$, $t = 70$

(u) $C1 = 1$, $C2 = 1$, $G = 0.2$, $t = 72$

(v) $C1 = 1$, $C2 = 1$, $G = 0.2$, $t = 74$

(w) $C1 = 1$, $C2 = 1$, $G = 0.2$, $t = 76$

(x) $C1 = 1$, $C2 = 1$, $G = 0.2$, $t = 78$

(y) $C1 = 1$, $C2 = 1$, $G = 0.2$, $t = 80$

(z) $C1 = 1$, $C2 = 1$, $G = 0.2$, $t = 82$

(aa) $C1 = 1$, $C2 = 1$, $G = 0.2$, $t = 84$

Figure 8.8. Elemental-vortex distributions over a couple of vortex-shedding periods in flow over the ($C1 = 1$, $C2 = 1$, $G = 0.2$) array; $\epsilon = 1.7\sqrt{(\Delta t/Re_h)}$.

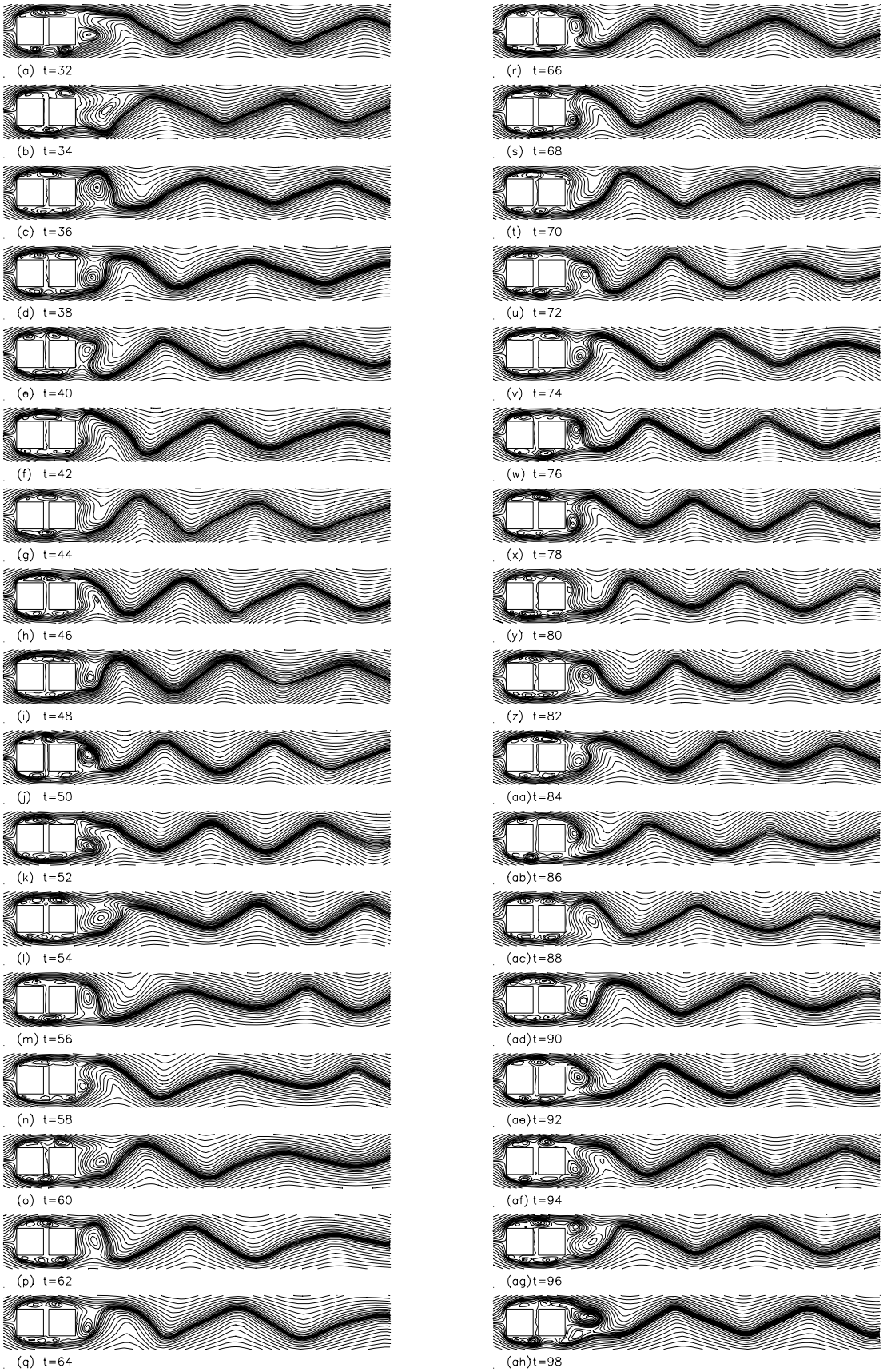

Figure 8.9. Calculated streamline patterns in fully-developed flow over the ($C1$ =1, $C2$ = 1, G = 0.2) array; $\epsilon = 1.7\sqrt{(\Delta t/Re_h)}$.

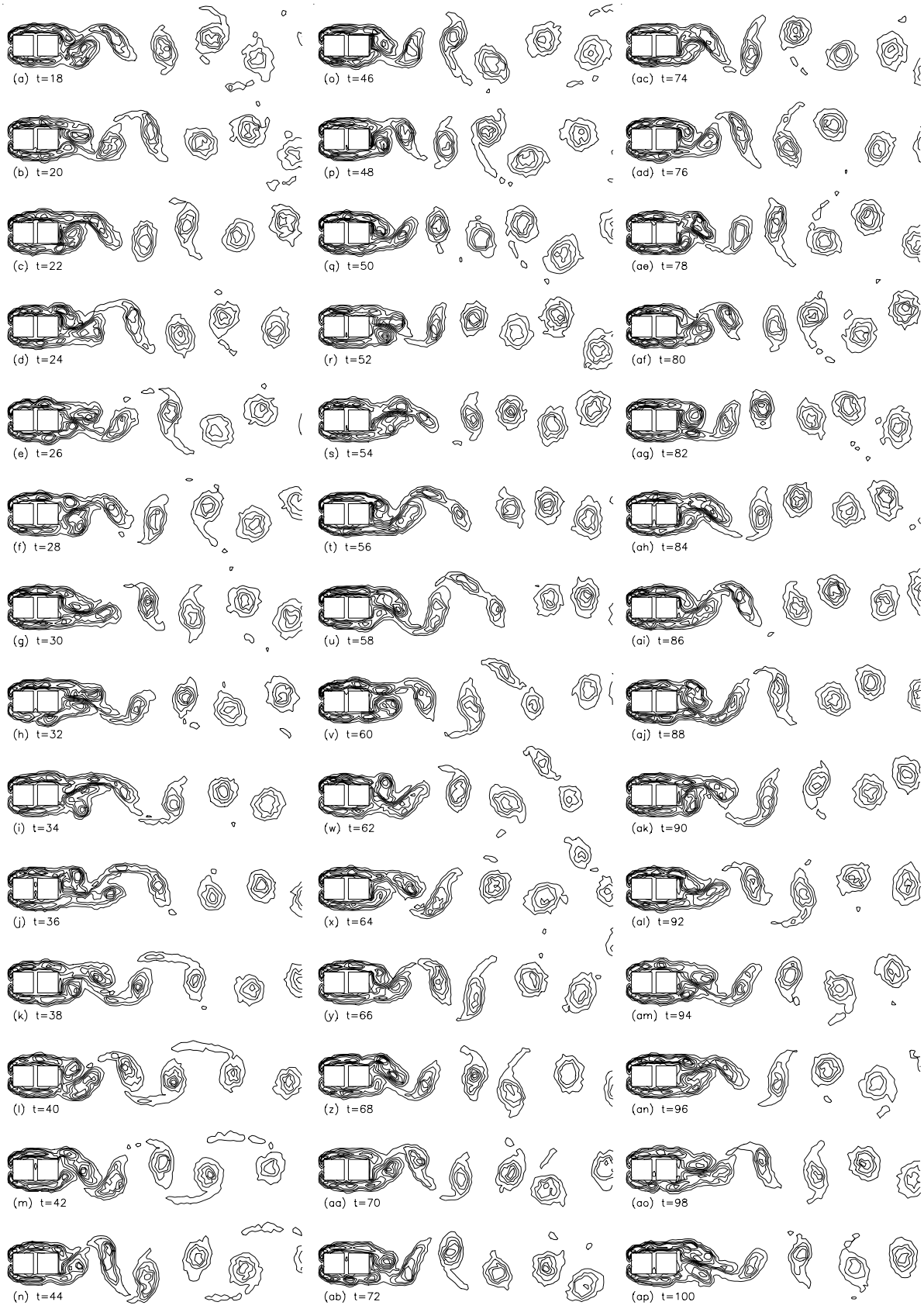

Figure 8.10. Variation of vorticity contours over a couple of vortex-shedding periods in flow over the ($C1$ =1, $C2$ = 1, G = 0.2) array; $\epsilon = 1.7\sqrt{(\Delta t/Re_h)}$.

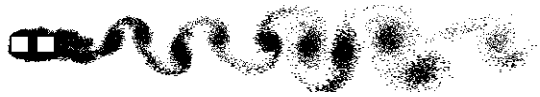

(a) $C1 = 1$, $C2 = 1$, $G = 0.5$, $t = 32$

(b) $C1 = 1$, $C2 = 1$, $G = 0.5$, $t = 34$

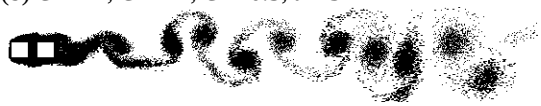

(c) $C1 = 1$, $C2 = 1$, $G = 0.5$, $t = 36$

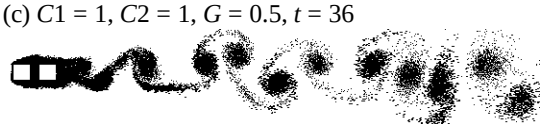

(d) $C1 = 1$, $C2 = 1$, $G = 0.5$, $t = 38$

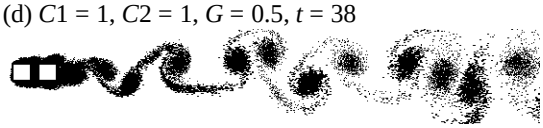

(e) $C1 = 1$, $C2 = 1$, $G = 0.5$, $t = 40$

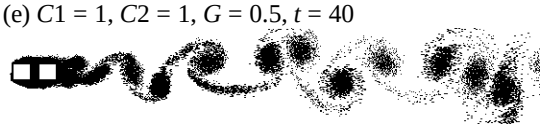

(f) $C1 = 1$, $C2 = 1$, $G = 0.5$, $t = 42$

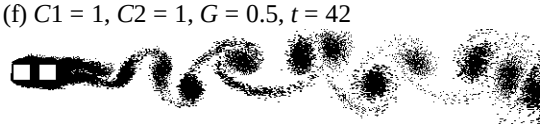

(g) $C1 = 1$, $C2 = 1$, $G = 0.5$, $t = 44$

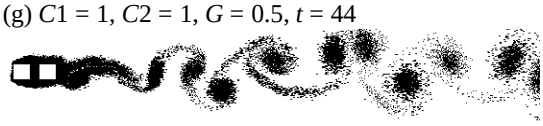

(h) $C1 = 1$, $C2 = 1$, $G = 0.5$, $t = 46$

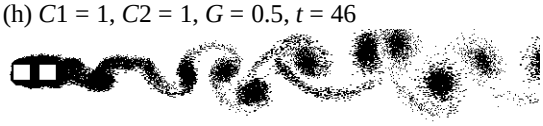

(i) $C1 = 1$, $C2 = 1$, $G = 0.5$, $t = 48$

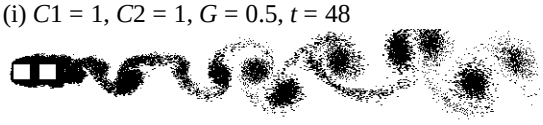

(j) $C1 = 1$, $C2 = 1$, $G = 0.5$, $t = 50$

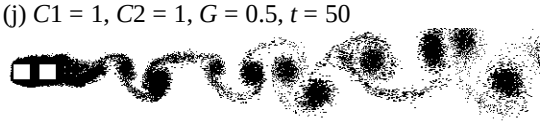

(k) $C1 = 1$, $C2 = 1$, $G = 0.5$, $t = 52$

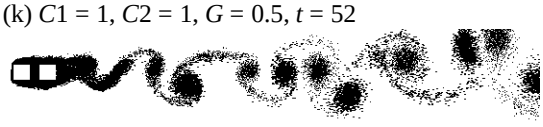

(l) $C1 = 1$, $C2 = 1$, $G = 0.5$, $t = 54$

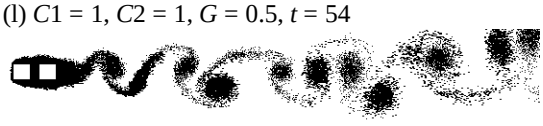

(m) $C1 = 1$, $C2 = 1$, $G = 0.5$, $t = 56$

(n) $C1 = 1$, $C2 = 1$, $G = 0.5$, $t = 58$

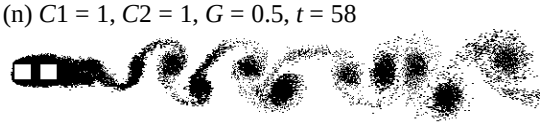

(o) $C1 = 1$, $C2 = 1$, $G = 0.5$, $t = 60$

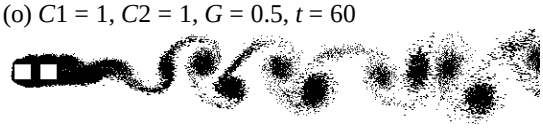

(p) $C1 = 1$, $C2 = 1$, $G = 0.5$, $t = 62$

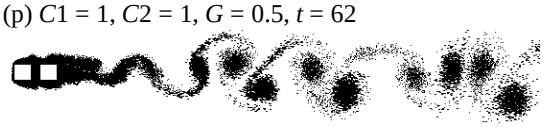

(q) $C1 = 1$, $C2 = 1$, $G = 0.5$, $t = 64$

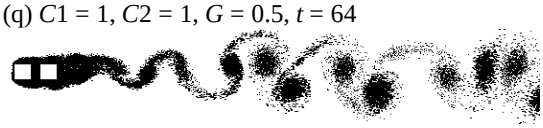

(r) $C1 = 1$, $C2 = 1$, $G = 0.5$, $t = 66$

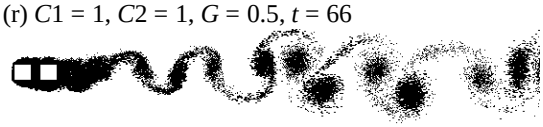

(s) $C1 = 1$, $C2 = 1$, $G = 0.5$, $t = 68$

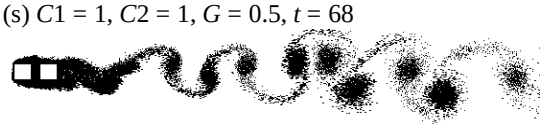

(t) $C1 = 1$, $C2 = 1$, $G = 0.5$, $t = 70$

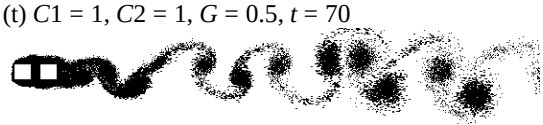

(u) $C1 = 1$, $C2 = 1$, $G = 0.5$, $t = 72$

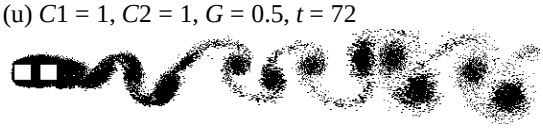

(v) $C1 = 1$, $C2 = 1$, $G = 0.5$, $t = 74$

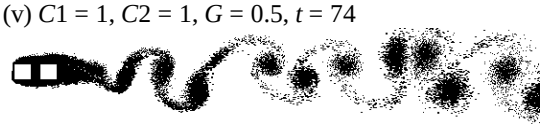

(w) $C1 = 1$, $C2 = 1$, $G = 0.5$, $t = 76$

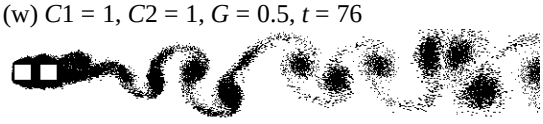

(x) $C1 = 1$, $C2 = 1$, $G = 0.5$, $t = 78$

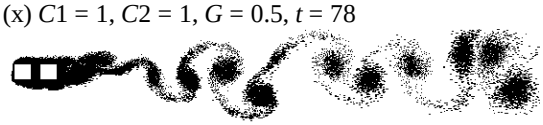

(y) $C1 = 1$, $C2 = 1$, $G = 0.5$, $t = 80$

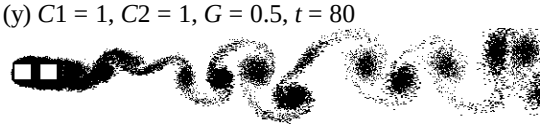

(z) $C1 = 1$, $C2 = 1$, $G = 0.5$, $t = 82$

Figure 8.11. Elemental-vortex distributions over a couple of vortex-shedding periods in flow over the ($C1 = 1$, $C2 = 1$, $G = 0.5$) array; $\epsilon = 1.7\sqrt{(\Delta t/Re_h)}$.

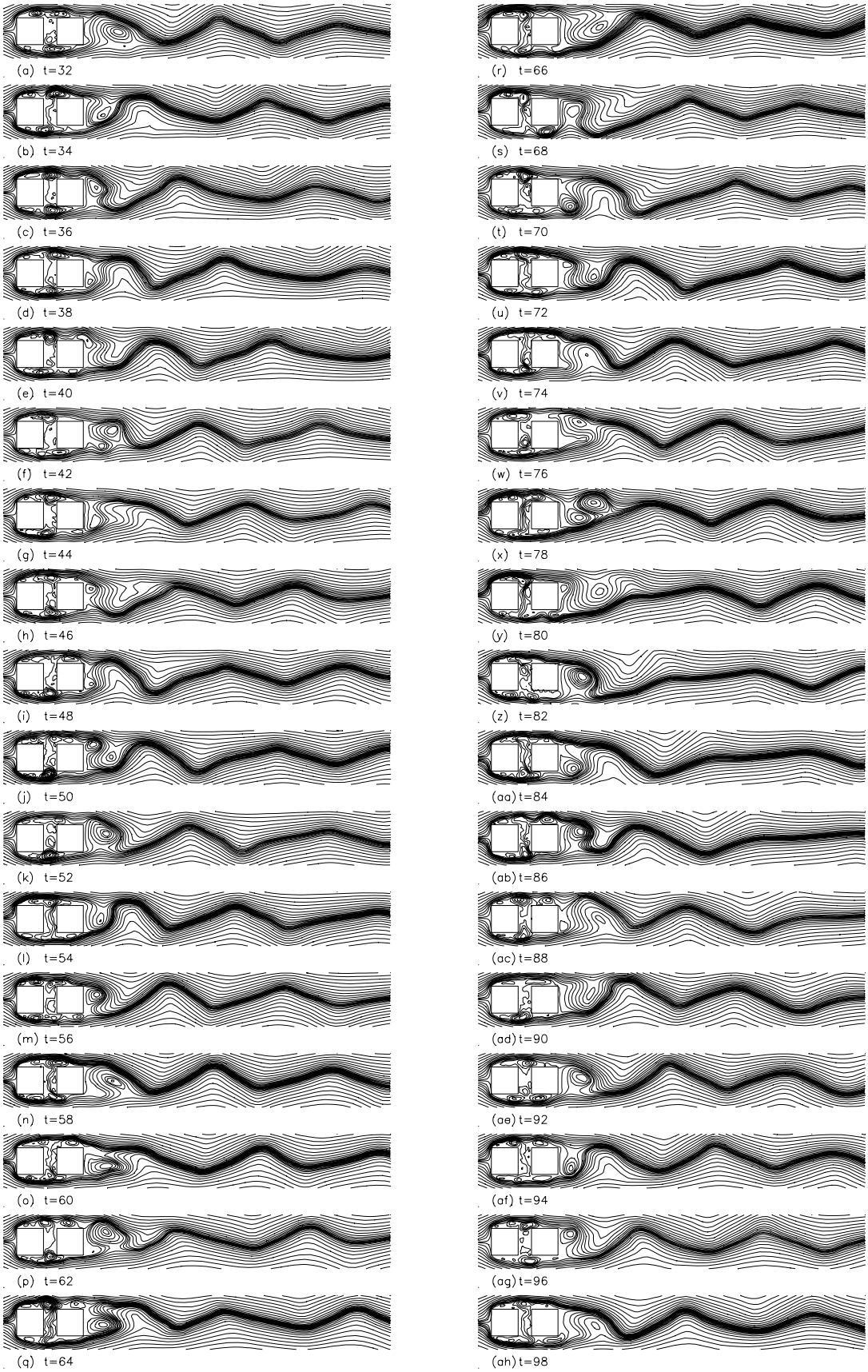

Figure 8.12. Calculated streamline patterns in fully-developed flow over the ($C1$ =1, $C2$ = 1, G = 0.5) array; $\epsilon = 1.7\sqrt{(\Delta t/Re_h)}$.

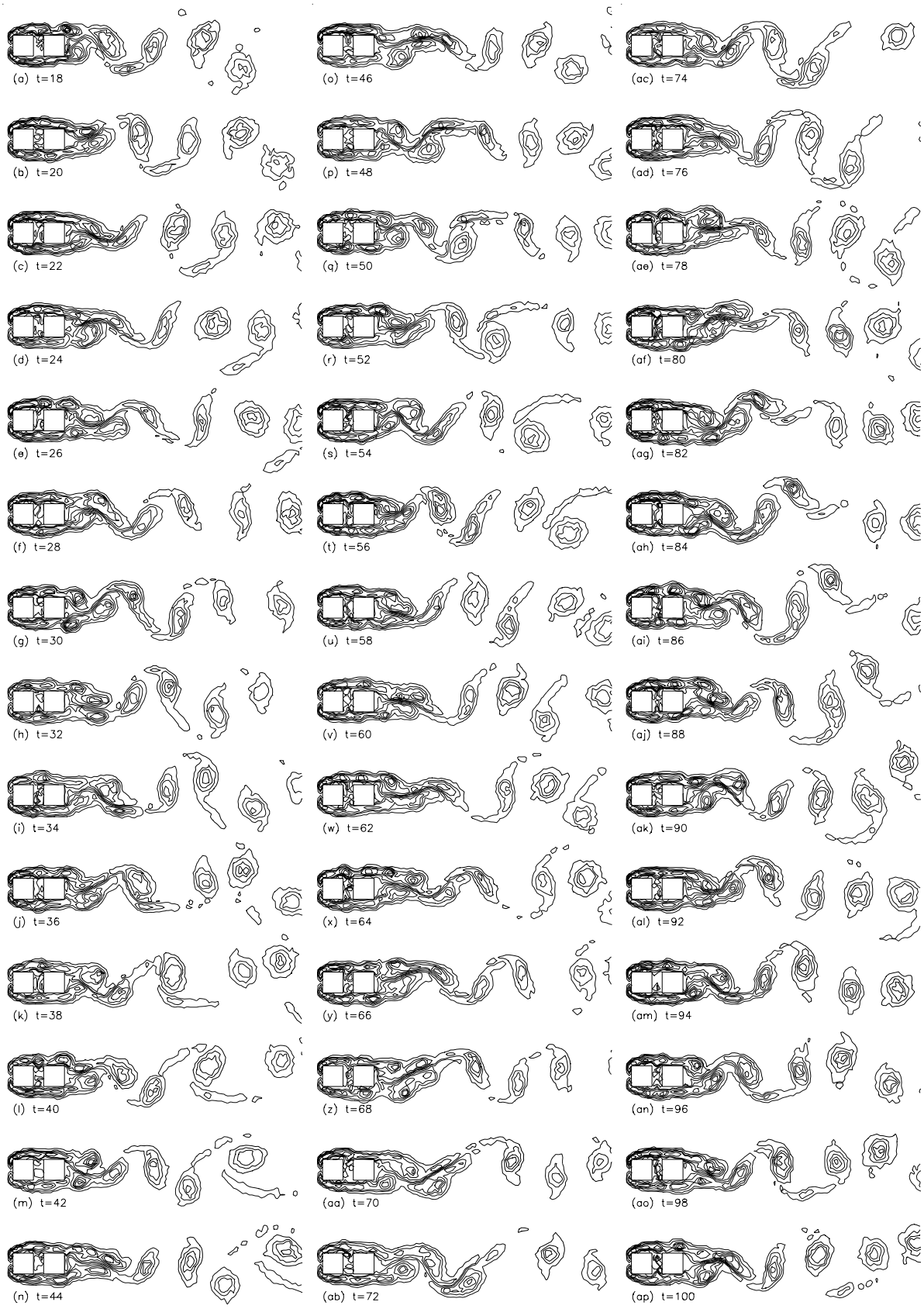

Figure 8.13. Variation of vorticity contours over a couple of vortex-shedding periods in flow over the ($C1$ =1, $C2$ = 1, G = 0.5) array; $\epsilon = 1.7\sqrt{(\Delta t/Re_h)}$.

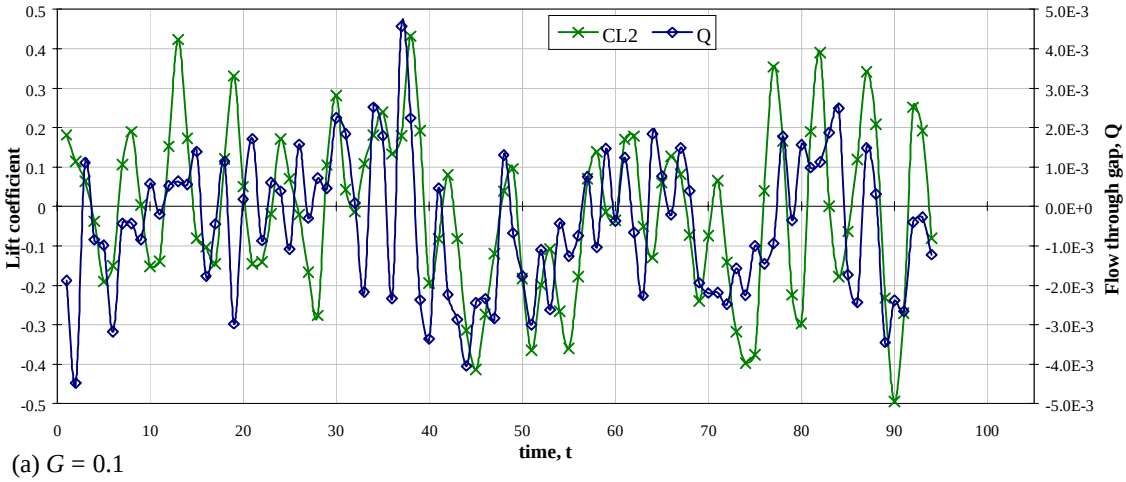

(a) $G = 0.1$

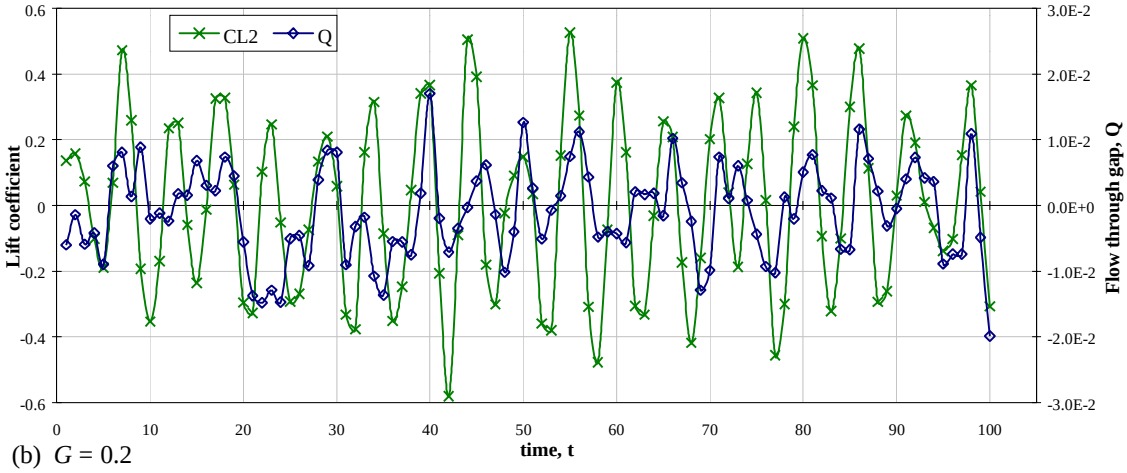

(b) $G = 0.2$

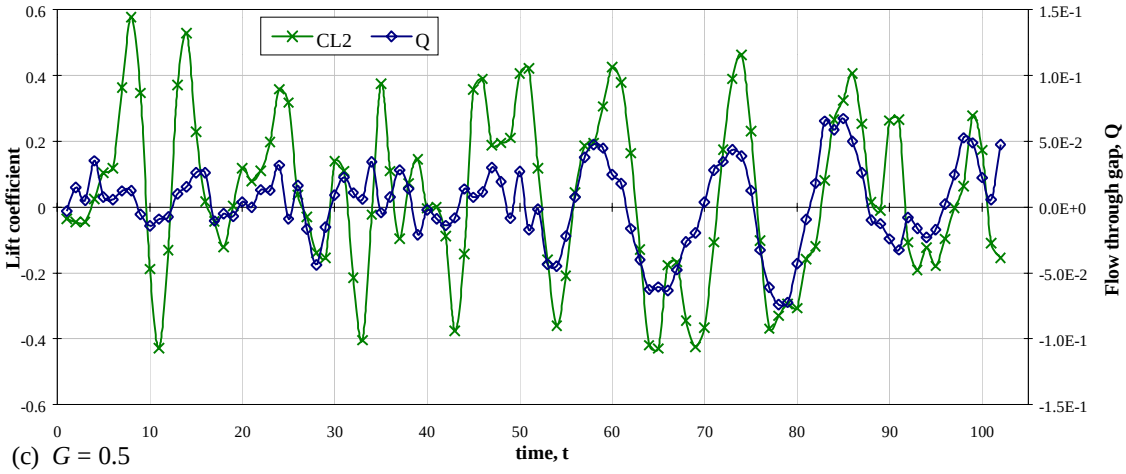

(c) $G = 0.5$

Figure 8.14. Time-histories of the lift coefficient of the downstream cylinder and the flow through the gap in an array of two square cylinders: (a) $G = 0.1$, (b) $G = 0.2$ and (c) $G = 0.5$

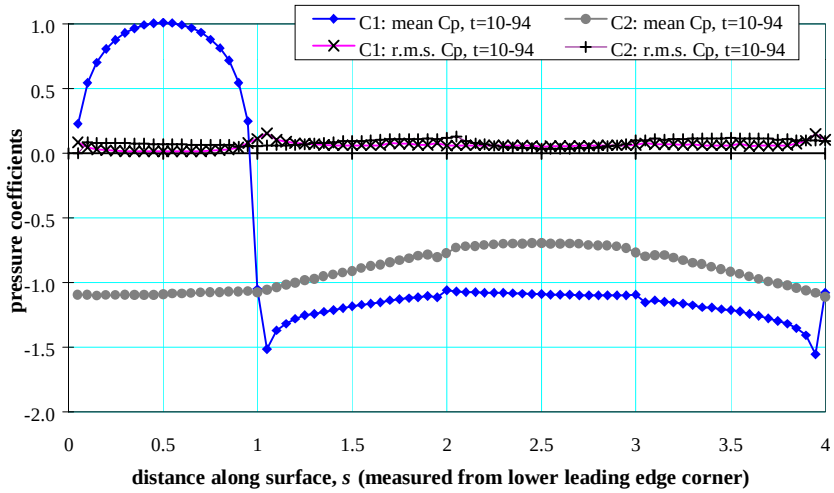

Figure 8.15. Calculated distributions of mean and r.m.s. pressure coefficients on the cylinders in the ($C1 = 1$, $C2 = 1$, $G = 0.1$) array.

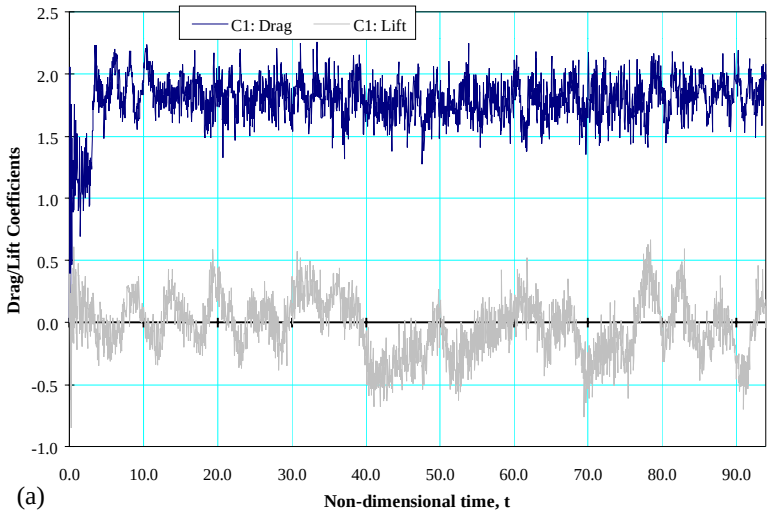

(a)

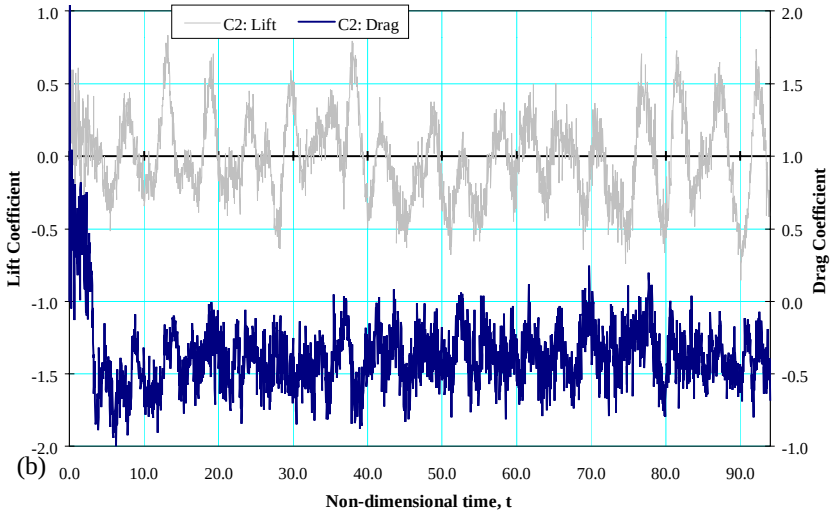

(b)

Figure 8.16. Time-histories of drag and lift on the ($C1 = 1$, $C2 = 1$, $G = 0.1$) array, (a) upstream plate, (b) downstream plate.

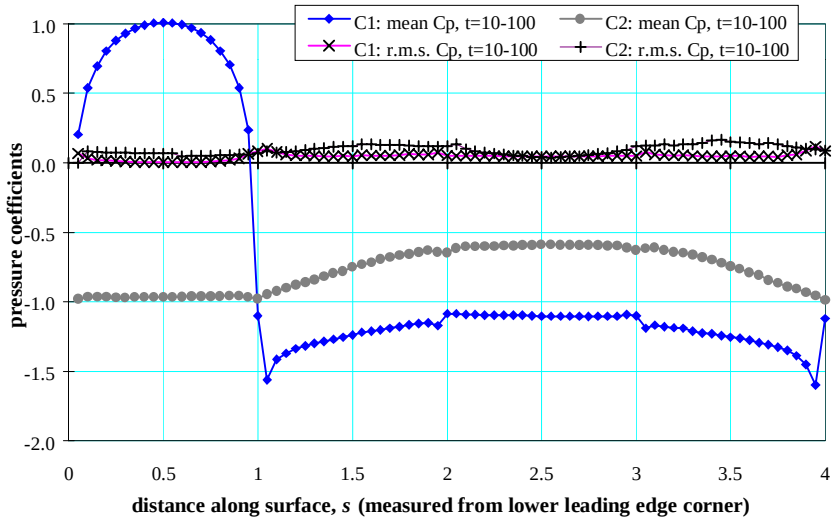

Figure 8.17. Calculated distributions of mean and r.m.s. pressure coefficients on the cylinders in the ($C1 = 1$, $C2 = 1$, $G = 0.2$) array.

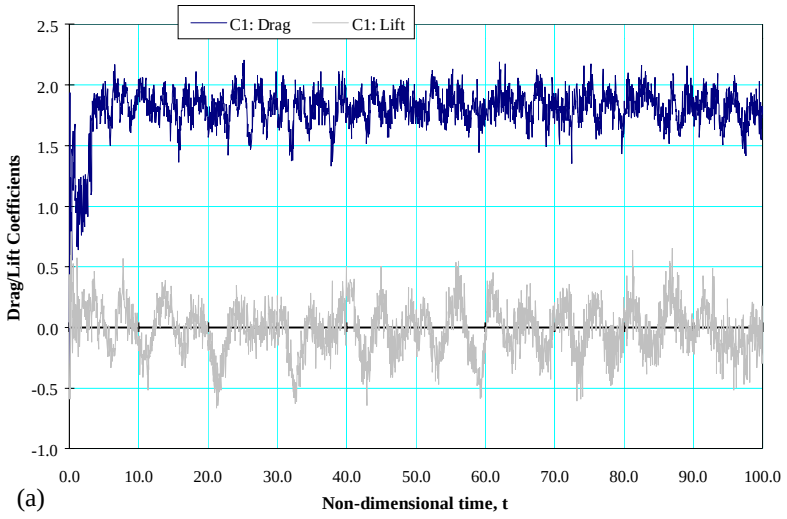

(a)

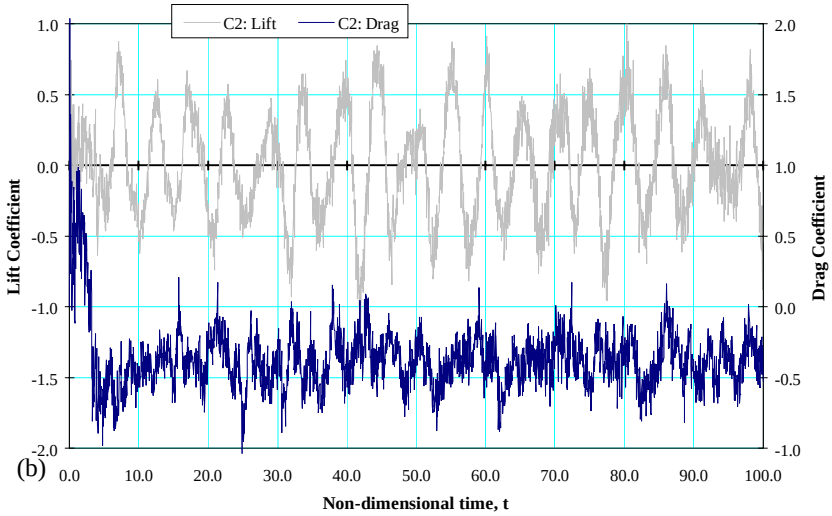

(b)

Figure 8.18. Time-histories of drag and lift on the ($C1 = 1$, $C2 = 1$, $G = 0.2$) array, (a) upstream plate, (b) downstream plate.

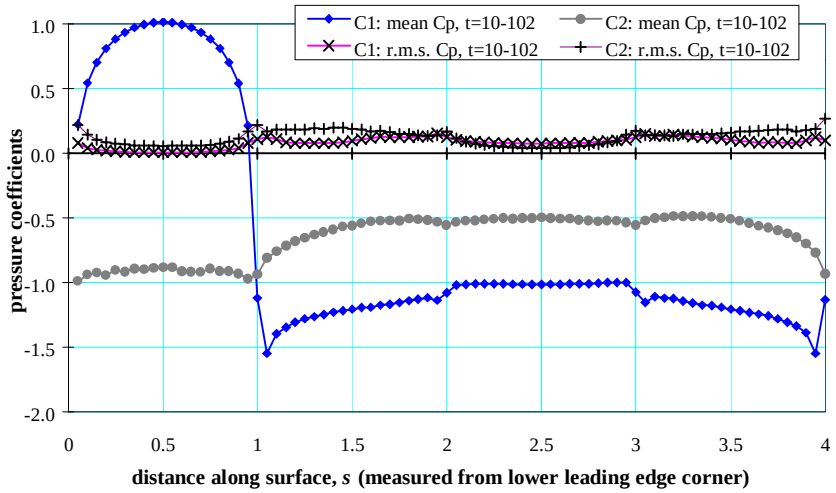

Figure 8.19. Calculated distributions of mean and r.m.s. pressure coefficients on the cylinders in the ($C1 = 1$, $C2 = 1$, $G = 0.5$) array.

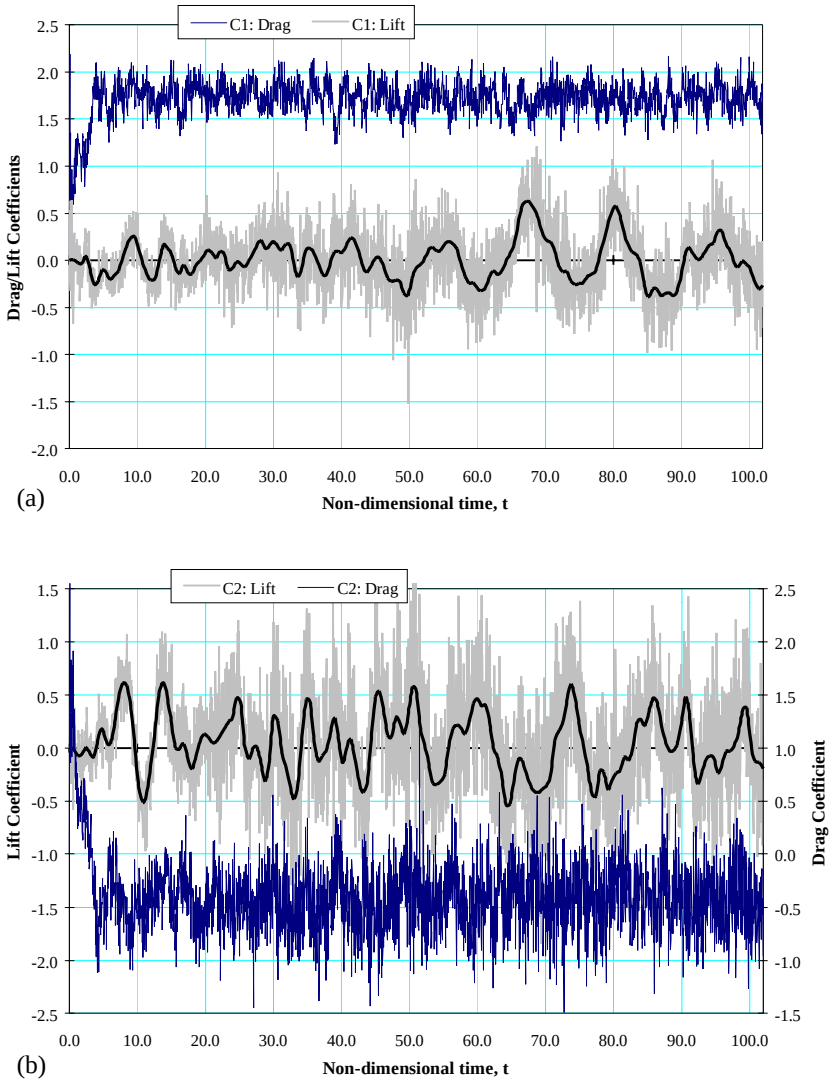

Figure 8.20. Time-histories of drag and lift on the ($C1 = 1$, $C2 = 1$, $G = 0.5$) array, (a) upstream plate, (b) downstream plate. Drag and lift are calculated for $\Delta t = 0.02$; highlighted values are averaged over $\Delta t = 0.4$.

8.3.2 Flow Regimes for Small Gaps, $0.5 < G < 2$

As the gap between the cylinders is widened from $G < 0.5$, the transverse flow through the gap ceases, at least in the early stages of flow development, and a flow with vortices trapped in the gap is established. The calculations indicate that arrays with $G = 0.8$, $G = 1.0$ and $G = 1.5$ exhibit this type of flow, and that the trapped-vortex flow between the cylinders is increasingly well-defined as G increases in this regime of flow.

The evolution of flow from its impulsive start from rest to the fully-developed state for the $G = 0.8$ array is shown in the elemental-vortex distributions in Fig. 8.21, the streamline patterns in Fig. 8.22 and the vorticity patterns in Fig 8.23. In the early stages of flow development ($t \leq 2$), the separated shear layers from the leading corners of the upstream cylinder roll into the gap to produce a pair of symmetric, counter-rotating vortices between the cylinders. During the same time, a closed recirculation region consisting of a pair of counter-rotating vortices forms behind the downstream cylinder. The overall flow pattern is essentially symmetrical about the centre-line of the array. As time progresses, instability of this flow regime leads to vortex shedding from the downstream cylinder and asymmetry of the trapped vortices in the gap, one becoming smaller while the other becomes larger. At the extreme of the disparity in size of the two vortices, the larger one occupies virtually the whole of the space in the gap (as, for example, at $t = 10$). The streamline patterns show that the large vortex so formed decreases in size while the smaller vortex grows again, and that, over a number of vortex-shedding periods, the growing vortex becomes dominant and takes up most of the space in the gap ($t = 22$). The growing and shrinking of the trapped vortices in the gap take place periodically and continuously, resulting in an oscillating trapped-vortex flow between the cylinders in which the vortices gain dominance alternately.

For the flow in its fully-developed state, the calculated streamline patterns (Fig. 8.22) indicate intermittent reattachment to the side faces of the downstream cylinder and intermittent separation from its leading and trailing edges. The flow around the array can be more clearly seen in the enlarged streamline patterns in Fig. 8.24, which also shows the corresponding instantaneous pressure fields around the array. The flow regime is *E1/E2* of the classification of Bull *et al*. [1997]. The process of vortex formation downstream of the array is predominantly the rolling up of the shear layers separated from the trailing edges of the downstream cylinder. As is evident from the instantaneous pressure fields in Fig. 8.24 and the

vorticity contours in Figs. 8.23 and 8.25, small-scale side-face vortices form on the upstream cylinder. These side-face vortices retain their identities in the presence of the trapped vortices in the gap, are convected across the gap, to some extent impinge on the downstream cylinder, and continue to be convected along the side faces of the downstream cylinder. They become quite diffuse before they reach the trailing edge of the downstream cylinder, where they are shed into the wake of the array together with the trailing-face vortices of the downstream cylinder. The side-face vortices and the trailing-face vortices interact and merge in the near wake to form the final Karman vortex street of the array, the regularity of which can be seen in the elemental-vortex distributions in Fig. 8.21.

It should be noted that the frequency at which the side-face vortices form on the upstream cylinder is higher than the frequency of vortex shedding into the wake from the downstream cylinder. The power spectrum of the fluctuating lift of the upstream cylinder (Fig. 8.69) shows a sharp peak at $St = 0.21$, while the power spectrum of the fluctuating lift of the downstream cylinder indicates sharp peaks at $St = 0.175$ and $St = 0.21$. As can be inferred from the time-histories of the vorticity contours shown in Fig. 8.23, the frequency $St = 0.175$ is associated with the vortex-shedding into the wake of the array. Because the side-face vortices formed on the upstream cylinder impinge on the downstream cylinder and are then convected along the side faces of the downstream cylinder, their characteristic frequency is also registered in the fluctuating lift of the downstream cylinder.

When the gap is widened from $G = 0.8$ to $G = 1$ and $G = 1.5$, the trapped-vortex flow continues to exist but now a more strongly defined, symmetrical trapped-vortex configuration characterises the fully-developed flow. The sequence of events in the flow development over the $G = 1.0$ array is shown in the elemental-vortex distributions, streamline patterns and vorticity contours in Figs. 8.26, 8.27 and 8.28 respectively, while the corresponding figures for the $G = 1.5$ array are shown in Figs. 8.31, 8.32 and 8.33. The calculations show that the evolution of the flow in the early development stages for the $G = 1.0$ and $G = 1.5$ arrays is very similar to that for the $G = 0.8$ array: a pair of symmetrical, counter-rotating vortices initially forming in the gap ($t < 2$) and taking up an asymmetrical configuration (with one vortex becoming larger while the other becomes smaller) at the onset of vortex shedding from the array ($t \approx 6$). Dominance of the larger trapped-vortex persists for a period of time, but eventually the gap flow reverts to a symmetrical configuration ($t \gtrsim 40$).

The mechanism of transition from the asymmetric to symmetric trapped-vortex flow in the gap is similar for the G = 1.0 and G = 1.5 arrays. However, the G = 1.5 array exhibits greater dominance of the larger vortex in the gap and therefore shows more clearly the sequence of events of the flow transition. Consider the flow over the G = 1.5 array during the transitional period ($8 < t \lesssim 40$). In the presence of a dominant (anti-clockwise) trapped-vortex in the gap, the (clockwise) side-face vortices formed on the upper side of the array appears to be considerably stronger than those on the lower side. Their merging with the smaller (upper) of the trapped vortices results in equalisation of the trapped vortices and restoration of the symmetry of the gap flow; the pair of similar counter-rotating vortices then persists in the gap throughout the fully-developed state of the flow ($t > 40$). The flow in the gap is now in a quasi-steady state in which the pair of trapped vortices oscillate slightly in size, at the frequency of vortex shedding into the wake of the array. There is therefore transverse oscillation of flow in the gap in the *E1*/*E2* regime also, but of a different form from that seen previously in very small gaps (G = 0.1, 0.2 and 0.5).

The variation of the flow about the G = 1.0 and G = 1.5 arrays in the final fully-developed state, over one vortex-shedding period, can be seen in the streamline patterns and the instantaneous pressure fields in Figs. 8.29 and 8.34 respectively. The shear layer separated from the leading corner of the upstream cylinder intermittently reattaches on the leading edge of the downstream cylinder. Side-face vortices form on the streamwise surfaces of the upstream cylinder. These side-face vortices are clearly identifiable in the instantaneous pressure fields and the vorticity patterns of Figs. 8.30 and 8.35 (but not obvious in the streamline patterns). As in the case of the G = 0.8 array, the side-face vortices are convected across the gap and impinge on the downstream cylinder. With increasing G , the strength of the interaction between the impinging side-face vortices and the downstream cylinder increases. The vorticity patterns (e.g. t = 75–76 in Fig. 8.30 for G = 1.0, t = 61.4–62.4 in Fig. 8.35 for G = 1.5) indicate that on impingement the vortical structure is (in the terminology of Rockwell and Naudascher, 1979) "clipped" by the sharp corner of the downstream cylinder. The portion of the impinging vortex that ends up on the side face of the downstream cylinder is convected downstream and eventually shed into the wake of the array. As a result, the flow on the side faces of the downstream cylinder is mostly fully-attached towards the trailing edge, but with intermittent passage of weak side-face vortices. The vortices in the final vortex street therefore effectively originate from shedding from the downstream cylinder only, by rolling up of the shear layers separating from the trailing corner.

The portion of the impinging vortex that is deflected down the leading face of the downstream cylinder interacts with the vortex flow in the gap. Details of this type of interaction have been investigated experimentally by Tang and Rockwell [1983]. Their work shows that the process involves flow separation from the front face of the downstream cylinder and the generation of secondary vorticity of opposite sign to that of the impinging vortex. Some indication of this type of motion in the gap can be seen in the streamline patterns of Figs. 8.29 and 8.34. Due to the impingement on them of small scale vortices, the leading and side faces of the downstream cylinder are subject to greater pressure fluctuations than those of the upstream cylinder, as is evident from the distributions of r.m.s. pressure fluctuation (Figs. 8.38 and 8.40).

The G = 0.8, G = 1.0 and G = 1.5 arrays have similar trapped-vortex flows, and the wake patterns for the arrays are broadly similar to each other. The wake similarity can be most clearly seen by comparison of streamlines for the three arrays as observed from a frame of reference moving at $U_{ref} = 0.8U_{\infty}$, which are shown in Fig. 8.71. It is largely a consequence of vorticity shedding into the wake being dominated by trailing-edge separation of attached side-face flow on the downstream cylinder.

The distribution of surface-pressure on the upstream cylinder for G = 0.8, 1.0 and 1.5 (Figs. 8.36, 8.38 and 8.40), as in the previous cases of G = 0.1, 0.2 and 0.5, is very similar to the pressure on a single square cylinder. On the downstream cylinder, however, the distribution does differ from those for the G = 0.2 and 0.5 arrays (and also from those for arrays with large gaps $G > 3$ which are discussed later): the pressure is lowest on the leading face, where it is fairly uniform, and increases sharply to its highest overall value near the leading corner; it then gradually decreases on the streamwise surface to the base pressure, in contrast to the rising pressure on the side-faces of the G = 0.1, G = 0.2 and G = 0.5 arrays. As G increases from 0.8 to 1.5, the pressure rise across the leading corner becomes sharper and the position of highest pressure on the side face moves towards the leading corner. The pressure on the leading face is lower than the base pressure; so there is a negative drag on the cylinder. The time-histories of drag coefficient for the G = 0.8 array (Fig. 8.37) indicate that the mean drag coefficient on upstream cylinder over the time period $10 < t < 107$ is C_{D1} = 1.72 while the mean drag coefficient on the downstream cylinder for the same time period is C_{D2} = −0.47, giving an overall drag coefficient for the array of C_D = 1.25. For the G = 1.0 array, the time-histories (Fig. 8.39) indicate a mean drag coefficient of the upstream cylinder over the time $10 < t < 110$ of C_{D1} = 1.70, while the corresponding value for the downstream cylinder is C_{D2} = −0.44, and the

overall $C_D = 1.26$. For the $G = 1.5$ array (Fig. 8.41), the mean drag coefficient of the upstream cylinder over the time $10 < t < 68$ is $C_{D1} = 1.57$ while the corresponding value for the downstream cylinder is $C_{D2} = -0.3$, and the overall $C_D = 1.27$. Thus, in all these cases, the overall drag coefficient is significantly lower than the value of $C_D = 1.72$ for a single plate with $C = 2$.

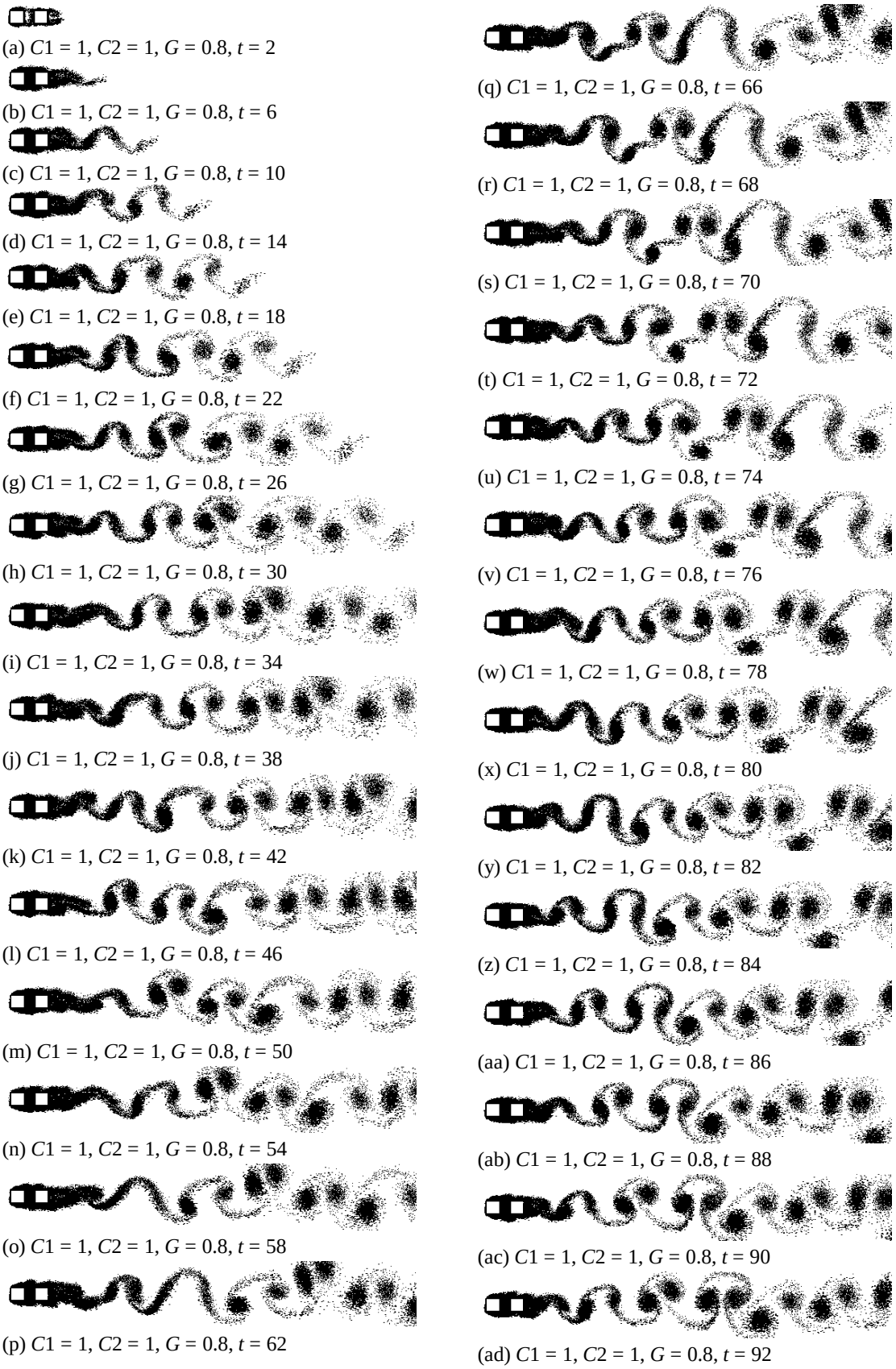

(a) $C1 = 1$, $C2 = 1$, $G = 0.8$, $t = 2$

(b) $C1 = 1$, $C2 = 1$, $G = 0.8$, $t = 6$

(c) $C1 = 1$, $C2 = 1$, $G = 0.8$, $t = 10$

(d) $C1 = 1$, $C2 = 1$, $G = 0.8$, $t = 14$

(e) $C1 = 1$, $C2 = 1$, $G = 0.8$, $t = 18$

(f) $C1 = 1$, $C2 = 1$, $G = 0.8$, $t = 22$

(g) $C1 = 1$, $C2 = 1$, $G = 0.8$, $t = 26$

(h) $C1 = 1$, $C2 = 1$, $G = 0.8$, $t = 30$

(i) $C1 = 1$, $C2 = 1$, $G = 0.8$, $t = 34$

(j) $C1 = 1$, $C2 = 1$, $G = 0.8$, $t = 38$

(k) $C1 = 1$, $C2 = 1$, $G = 0.8$, $t = 42$

(l) $C1 = 1$, $C2 = 1$, $G = 0.8$, $t = 46$

(m) $C1 = 1$, $C2 = 1$, $G = 0.8$, $t = 50$

(n) $C1 = 1$, $C2 = 1$, $G = 0.8$, $t = 54$

(o) $C1 = 1$, $C2 = 1$, $G = 0.8$, $t = 58$

(p) $C1 = 1$, $C2 = 1$, $G = 0.8$, $t = 62$

(q) $C1 = 1$, $C2 = 1$, $G = 0.8$, $t = 66$

(r) $C1 = 1$, $C2 = 1$, $G = 0.8$, $t = 68$

(s) $C1 = 1$, $C2 = 1$, $G = 0.8$, $t = 70$

(t) $C1 = 1$, $C2 = 1$, $G = 0.8$, $t = 72$

(u) $C1 = 1$, $C2 = 1$, $G = 0.8$, $t = 74$

(v) $C1 = 1$, $C2 = 1$, $G = 0.8$, $t = 76$

(w) $C1 = 1$, $C2 = 1$, $G = 0.8$, $t = 78$

(x) $C1 = 1$, $C2 = 1$, $G = 0.8$, $t = 80$

(y) $C1 = 1$, $C2 = 1$, $G = 0.8$, $t = 82$

(z) $C1 = 1$, $C2 = 1$, $G = 0.8$, $t = 84$

(aa) $C1 = 1$, $C2 = 1$, $G = 0.8$, $t = 86$

(ab) $C1 = 1$, $C2 = 1$, $G = 0.8$, $t = 88$

(ac) $C1 = 1$, $C2 = 1$, $G = 0.8$, $t = 90$

(ad) $C1 = 1$, $C2 = 1$, $G = 0.8$, $t = 92$

Figure 8.21. Elemental-vortex distributions in flow over the ($C1 = 1$, $C2 = 1$, $G = 0.8$) array, showing sequence of flow development from the impulsive start to the fully-developed state.

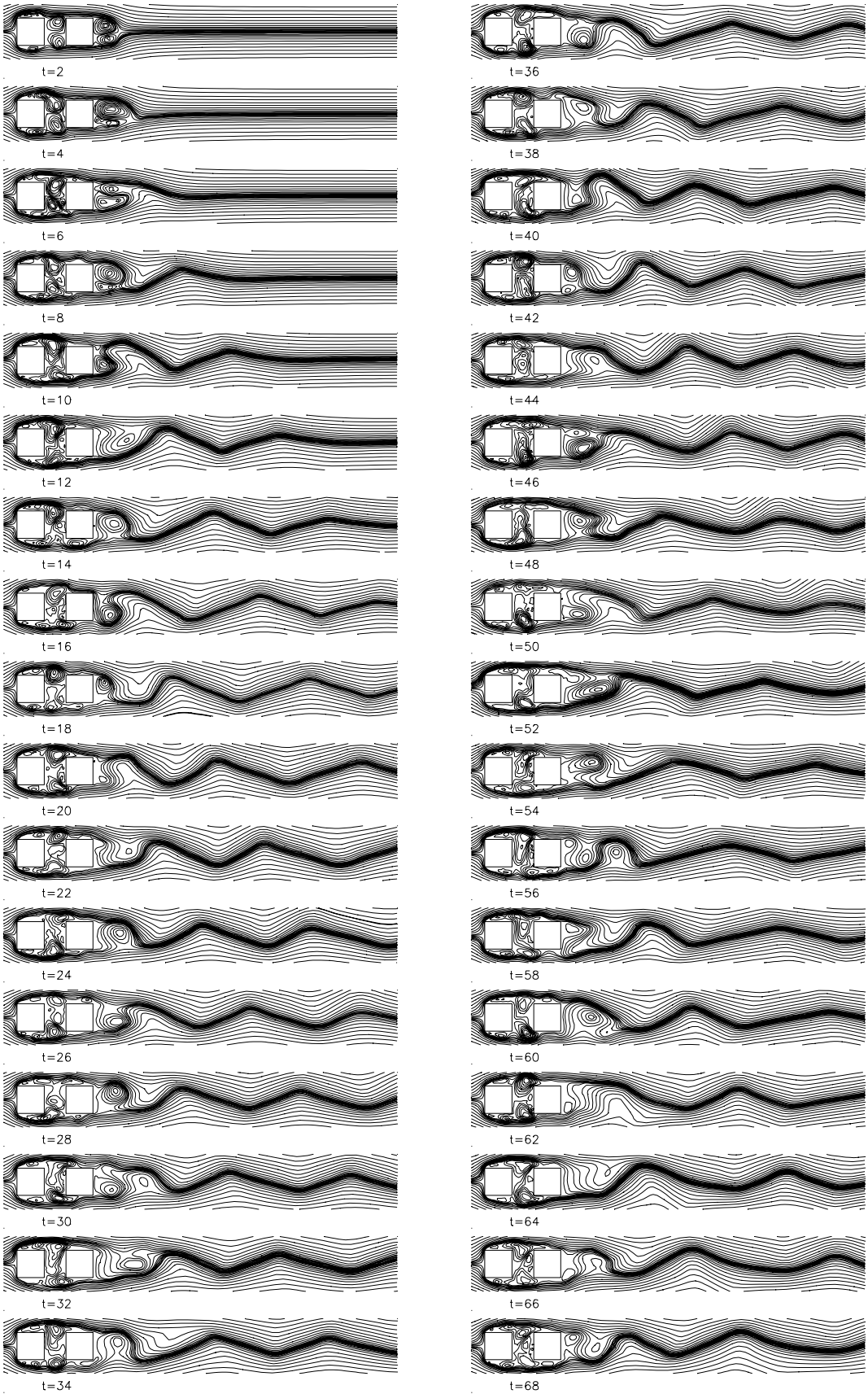

Figure 8.22. Calculated streamline patterns in flow over the ($C1$ =1, $C2$ = 1, G = 0.8) array, showing sequence of flow development from the impulsive start to the fully-developed state.

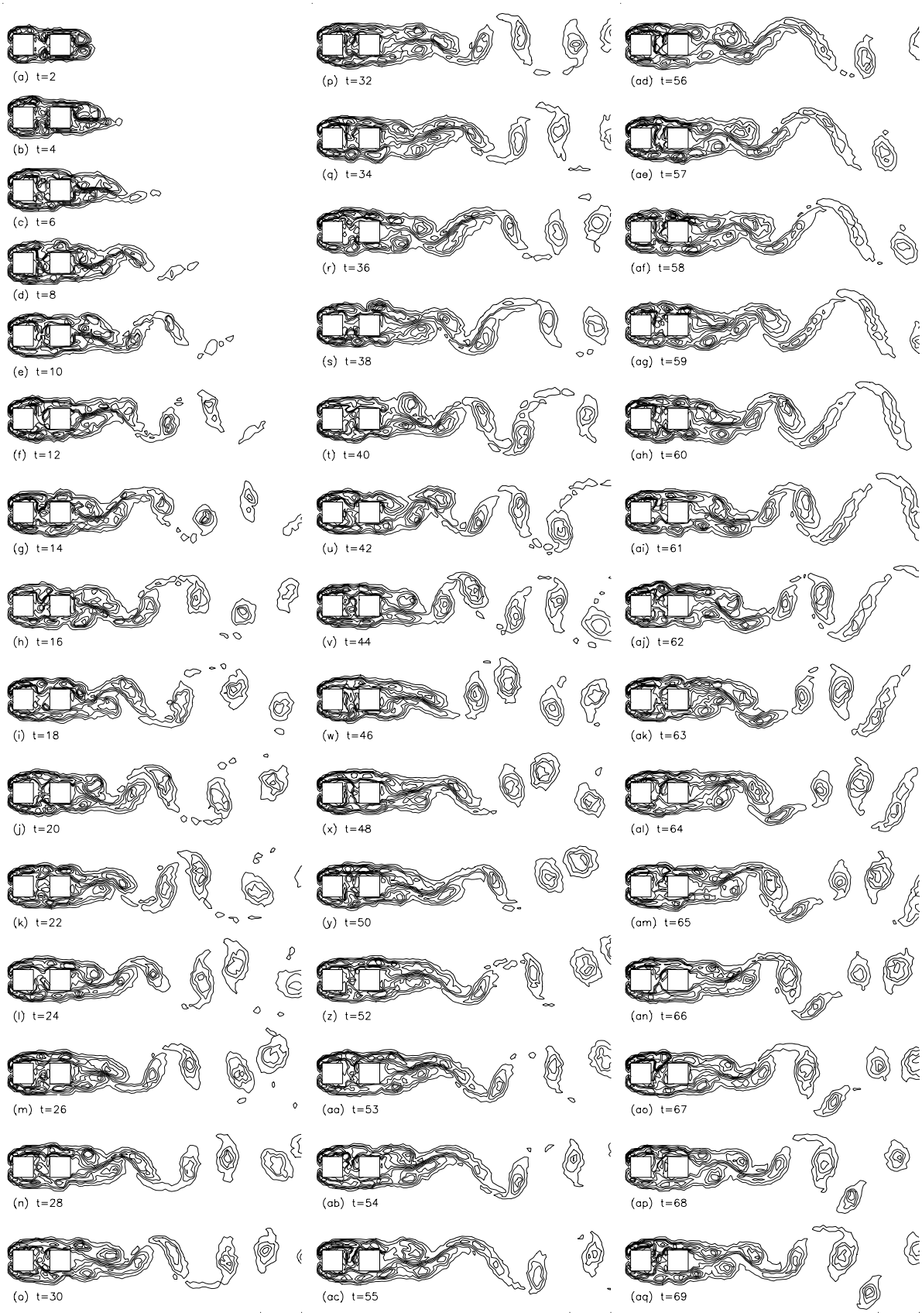

Figure 8.23. Calculated vorticity contours in flow over the ($C1$ =1, $C2$ = 1, G = 0.8) array, showing sequence of flow development from the impulsive start to the fully-developed state.

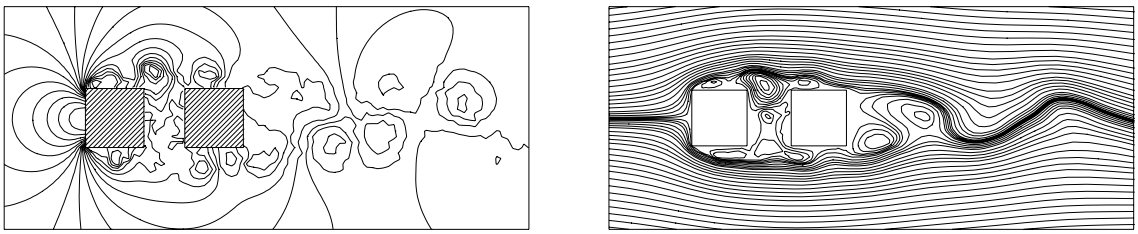

(a1) $G = 0.8$, $t = 70$ (a2) $G = 0.8$, $t = 70$

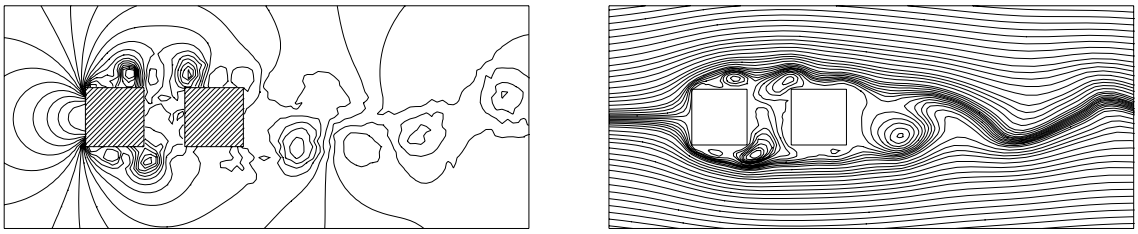

(b1) $G = 0.8$, $t = 71$ (b2) $G = 0.8$, $t = 71$

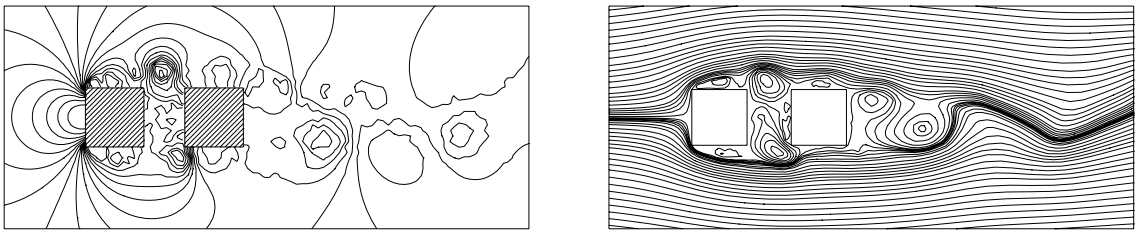

(c1) $G = 0.8$, $t = 72$ (c2) $G = 0.8$, $t = 72$

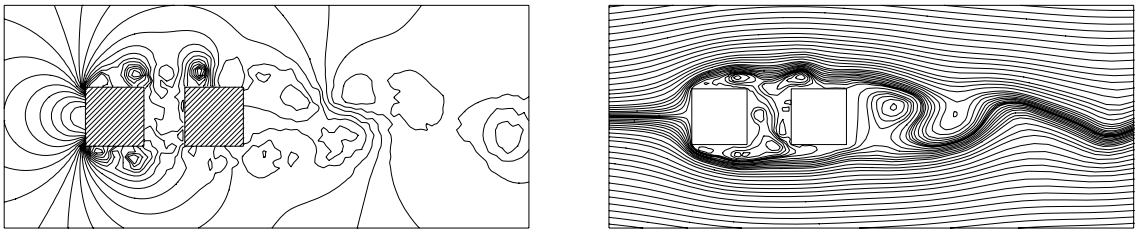

(d1) $G = 0.8$, $t = 73$ (d2) $G = 0.8$, $t = 73$

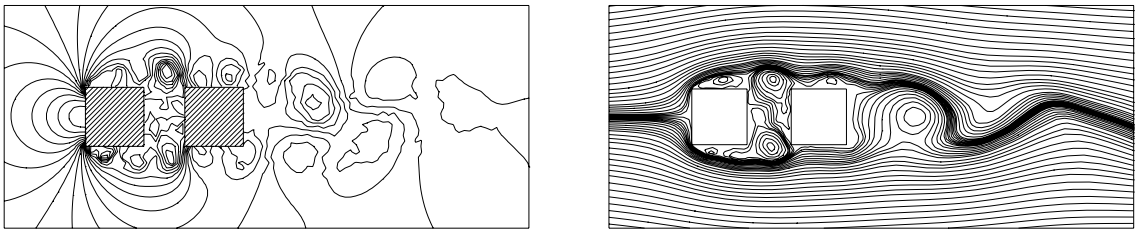

(e1) $G = 0.8$, $t = 74$ (e2) $G = 0.8$, $t = 74$

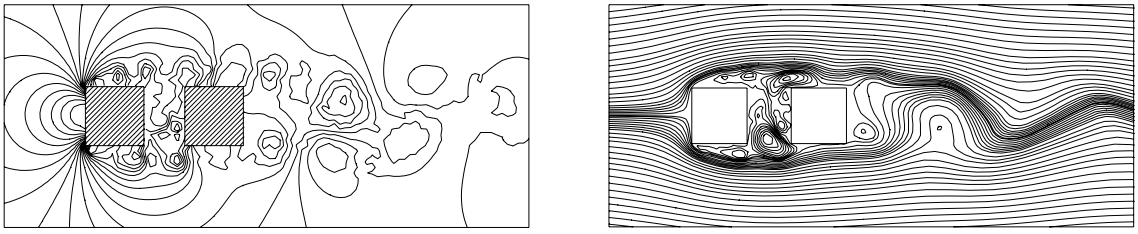

(f1) $G = 0.8$, $t = 75$ (f2) $G = 0.8$, $t = 75$

Figure 8.24. Instantaneous pressure fields and streamline patterns in fully-developed flow over the ($C1 = 1$, $C2 = 1$, $G = 0.8$) array.

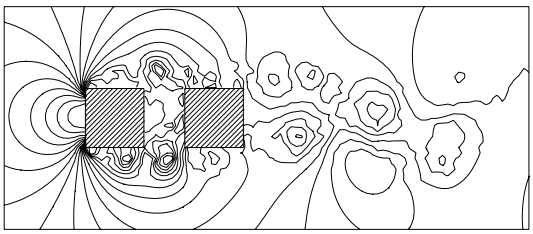

(g1) G = 0.8, t = 76

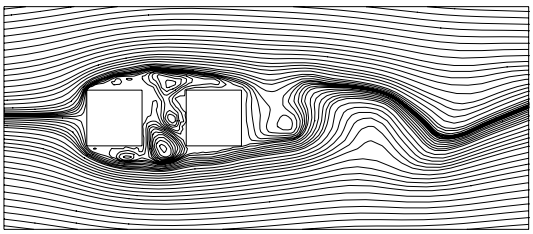

(g2) G = 0.8, t = 76

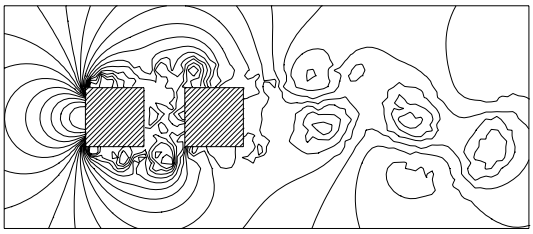

(h1) G = 0.8, t = 77

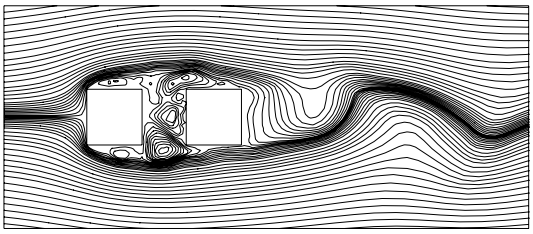

(h2) G = 0.8, t = 77

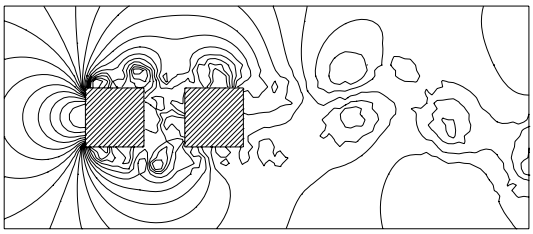

(i1) G = 0.8, t = 78

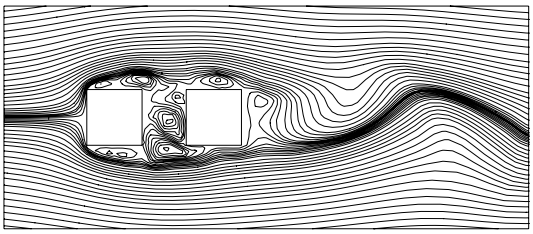

(i2) G = 0.8, t = 78

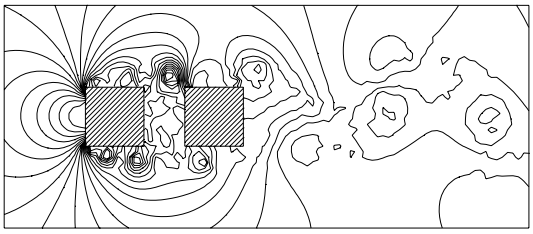

(j1) G = 0.8, t = 79

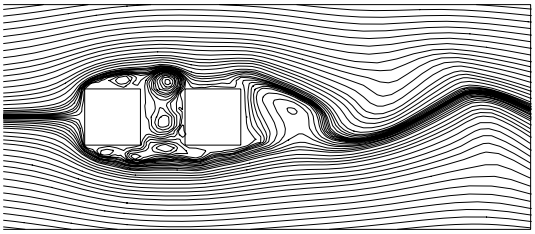

(j2) G = 0.8, t = 79

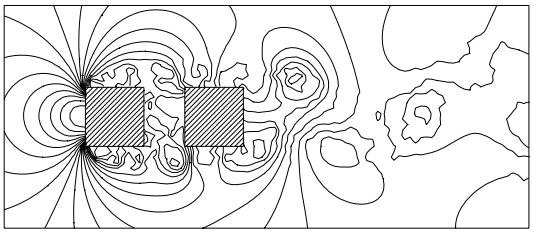

(k1) G = 0.8, t = 80

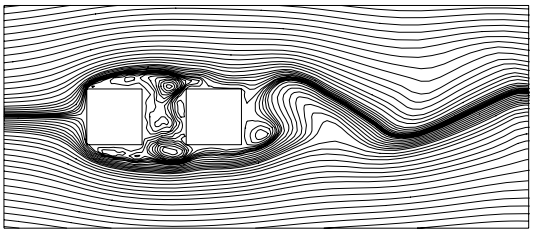

(k2) G = 0.8, t = 80

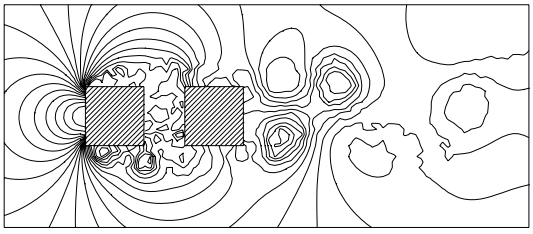

(l1) G = 0.8, t = 81

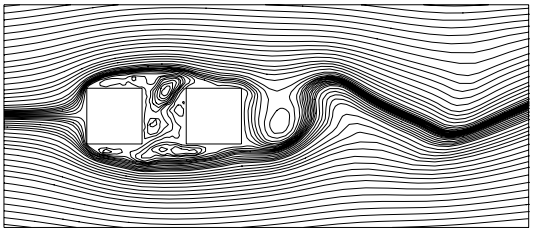

(l2) G = 0.8, t = 81

Figure 8.24. Cont'd.

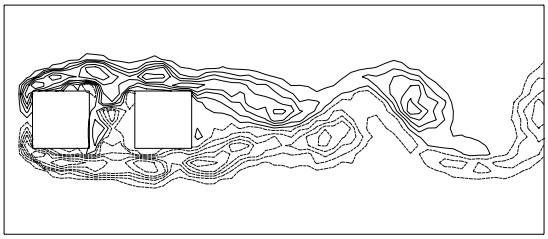

(a) $G = 0.8$, $t = 70$

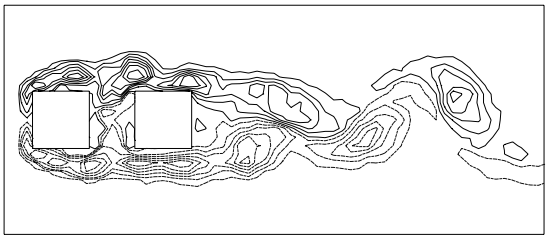

(b) $G = 0.8$, $t = 71$

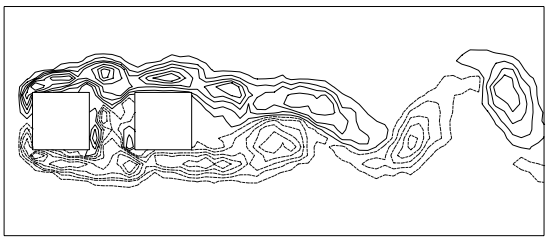

(c) $G = 0.8$, $t = 72$

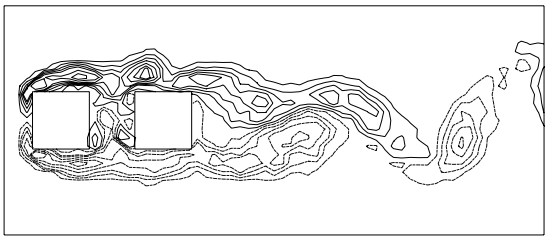

(d) $G = 0.8$, $t = 73$

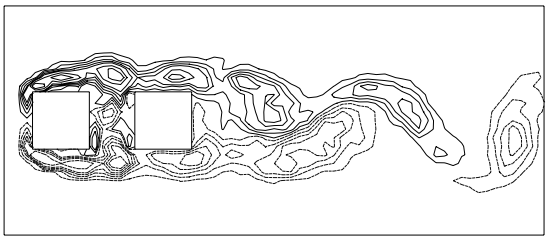

(e) $G = 0.8$, $t = 74$

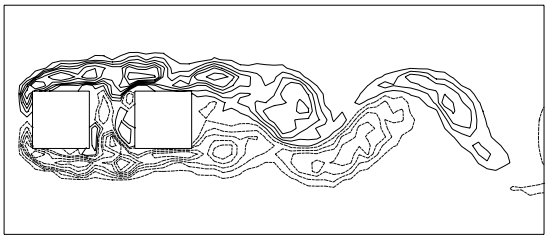

(f) $G = 0.8$, $t = 75$

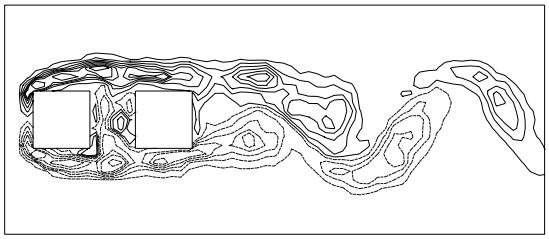

(g) $G = 0.8$, $t = 76$

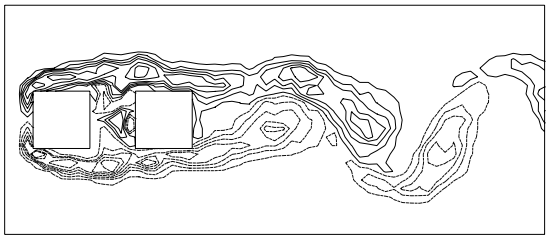

(h) $G = 0.8$, $t = 77$

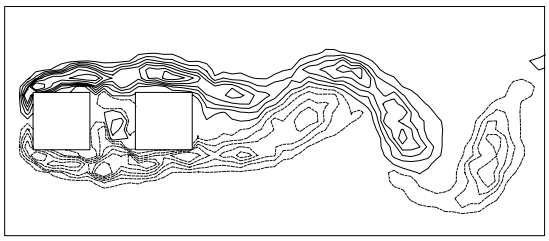

(i) $G = 0.8$, $t = 78$

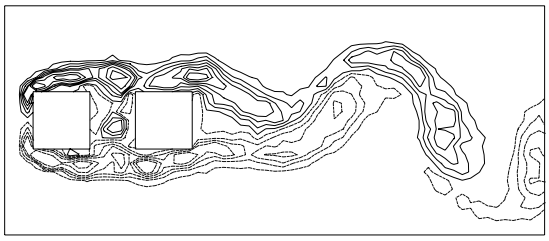

(j) $G = 0.8$, $t = 79$

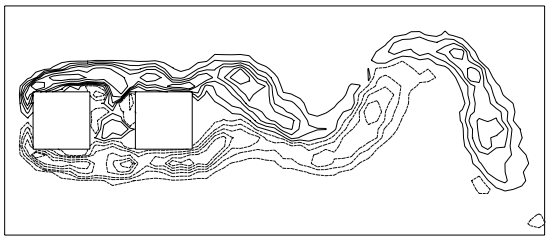

(k) $G = 0.8$, $t = 80$

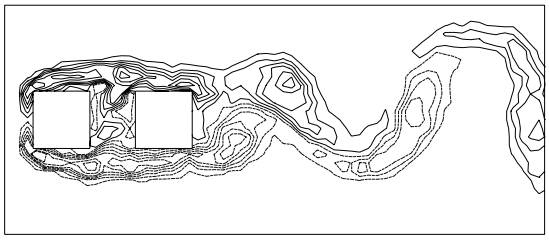

(l) $G = 0.8$, $t = 81$

Figure 8.25. Vorticity contours in fully-developed flow over the ($C1 = 1$, $C2 = 1$, $G = 0.8$).

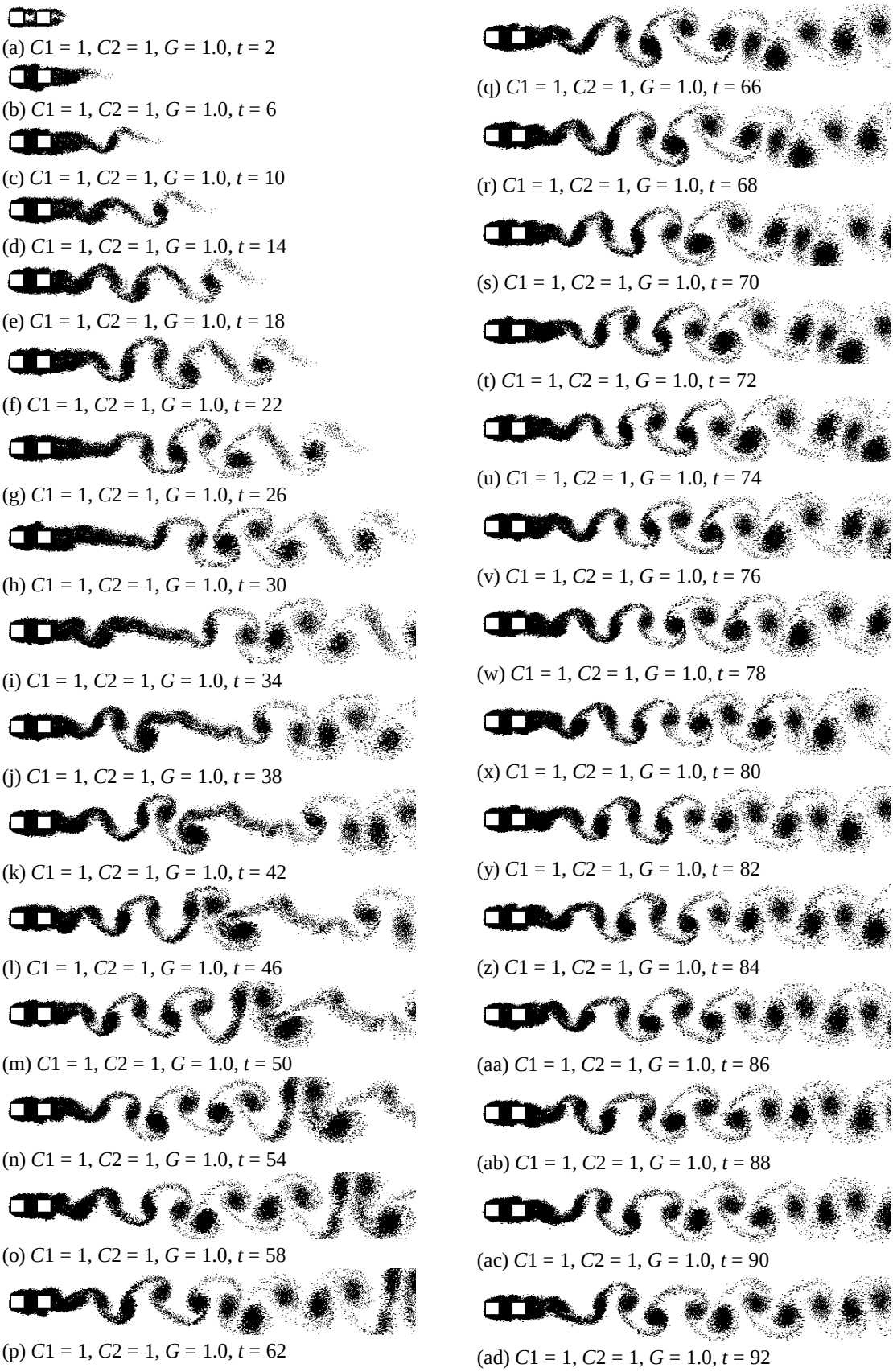

(a) $C1 = 1$, $C2 = 1$, $G = 1.0$, $t = 2$

(b) $C1 = 1$, $C2 = 1$, $G = 1.0$, $t = 6$

(c) $C1 = 1$, $C2 = 1$, $G = 1.0$, $t = 10$

(d) $C1 = 1$, $C2 = 1$, $G = 1.0$, $t = 14$

(e) $C1 = 1$, $C2 = 1$, $G = 1.0$, $t = 18$

(f) $C1 = 1$, $C2 = 1$, $G = 1.0$, $t = 22$

(g) $C1 = 1$, $C2 = 1$, $G = 1.0$, $t = 26$

(h) $C1 = 1$, $C2 = 1$, $G = 1.0$, $t = 30$

(i) $C1 = 1$, $C2 = 1$, $G = 1.0$, $t = 34$

(j) $C1 = 1$, $C2 = 1$, $G = 1.0$, $t = 38$

(k) $C1 = 1$, $C2 = 1$, $G = 1.0$, $t = 42$

(l) $C1 = 1$, $C2 = 1$, $G = 1.0$, $t = 46$

(m) $C1 = 1$, $C2 = 1$, $G = 1.0$, $t = 50$

(n) $C1 = 1$, $C2 = 1$, $G = 1.0$, $t = 54$

(o) $C1 = 1$, $C2 = 1$, $G = 1.0$, $t = 58$

(p) $C1 = 1$, $C2 = 1$, $G = 1.0$, $t = 62$

(q) $C1 = 1$, $C2 = 1$, $G = 1.0$, $t = 66$

(r) $C1 = 1$, $C2 = 1$, $G = 1.0$, $t = 68$

(s) $C1 = 1$, $C2 = 1$, $G = 1.0$, $t = 70$

(t) $C1 = 1$, $C2 = 1$, $G = 1.0$, $t = 72$

(u) $C1 = 1$, $C2 = 1$, $G = 1.0$, $t = 74$

(v) $C1 = 1$, $C2 = 1$, $G = 1.0$, $t = 76$

(w) $C1 = 1$, $C2 = 1$, $G = 1.0$, $t = 78$

(x) $C1 = 1$, $C2 = 1$, $G = 1.0$, $t = 80$

(y) $C1 = 1$, $C2 = 1$, $G = 1.0$, $t = 82$

(z) $C1 = 1$, $C2 = 1$, $G = 1.0$, $t = 84$

(aa) $C1 = 1$, $C2 = 1$, $G = 1.0$, $t = 86$

(ab) $C1 = 1$, $C2 = 1$, $G = 1.0$, $t = 88$

(ac) $C1 = 1$, $C2 = 1$, $G = 1.0$, $t = 90$

(ad) $C1 = 1$, $C2 = 1$, $G = 1.0$, $t = 92$

Figure 8.26. Elemental-vortex distributions in flow over the ($C1 = 1$, $C2 = 1$, $G = 1.0$) array, showing flow evolution from the impulsive start to the fully-developed state.

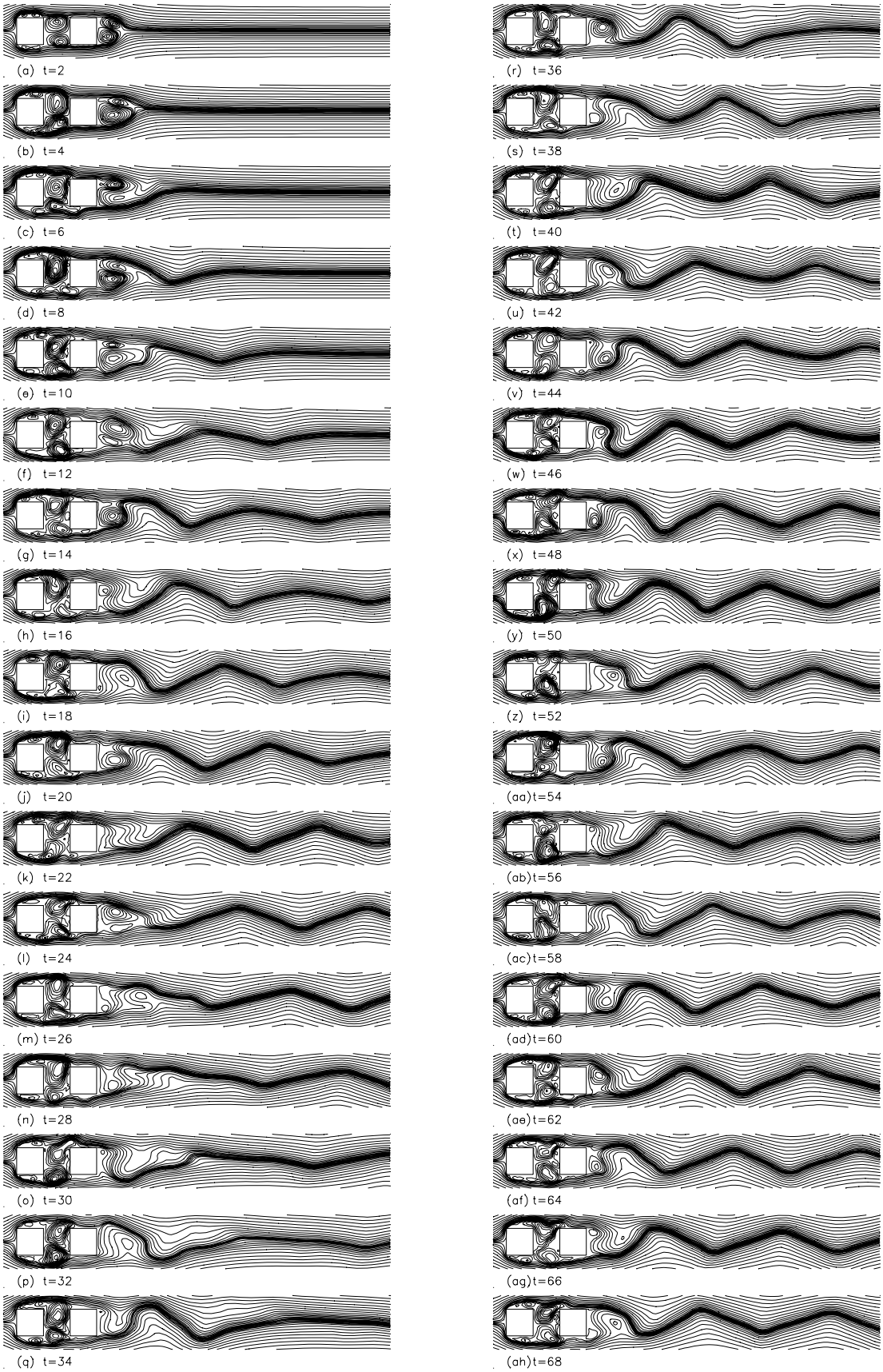

Figure 8.27. Calculated streamline patterns in flow over the ($C1$ =1, $C2$ = 1, G = 1.0) array, showing flow evolution from the impulsive start to the fully-developed state.

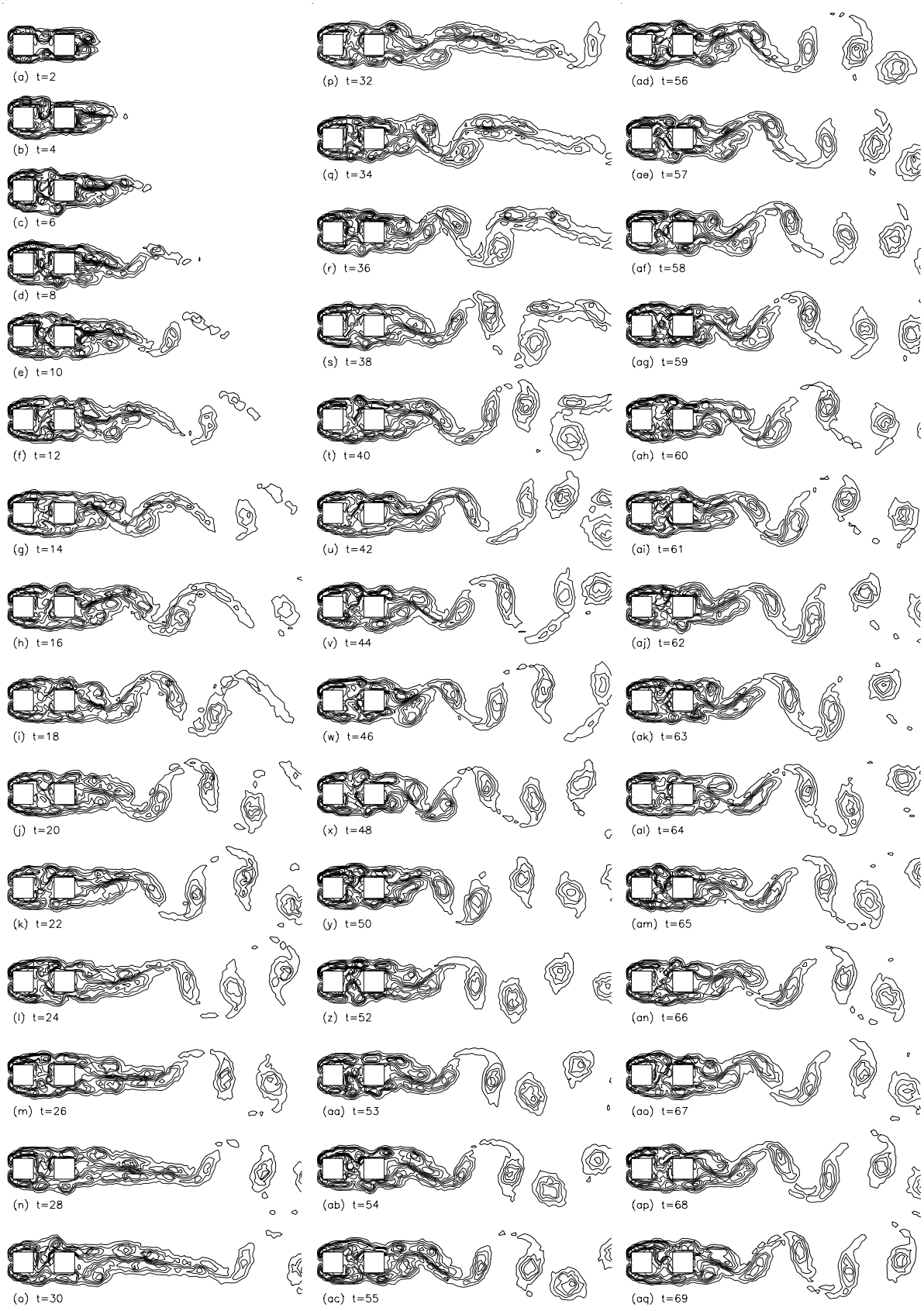

Figure 8.28. Calculated vorticity contours in flow over the ($C1$ =1, $C2$ = 1, G = 1.0) array, showing flow evolution from the impulsive start to the fully-developed state.

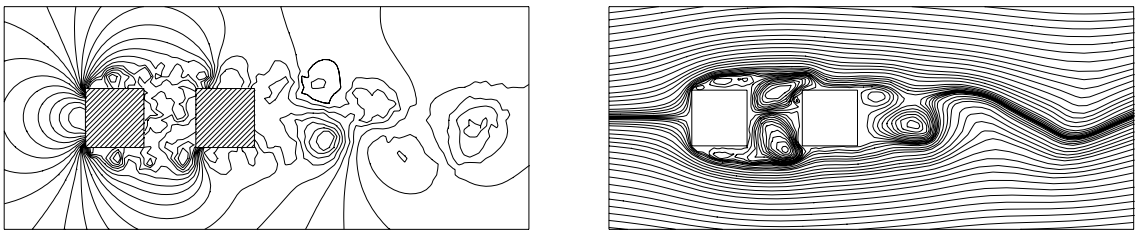

(a1) $G = 1.0$, $t = 70$ (a2) $G = 1.0$, $t = 70$

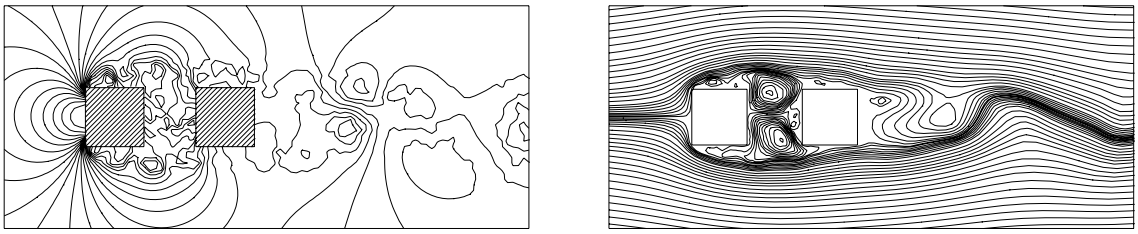

(b1) $G = 1.0$, $t = 71$ (b2) $G = 1.0$, $t = 71$

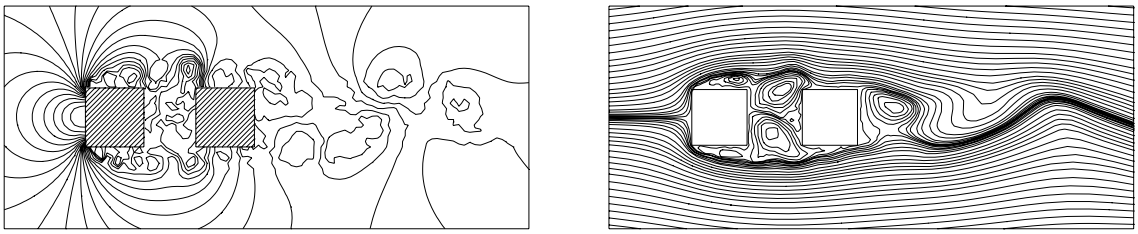

(c1) $G = 1.0$, $t = 72$ (c2) $G = 1.0$, $t = 72$

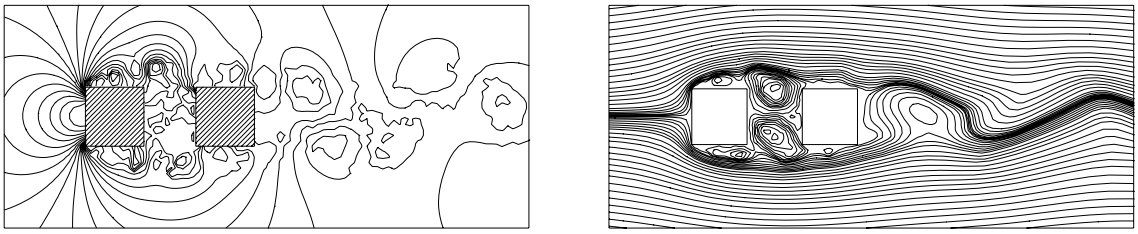

(d1) $G = 1.0$, $t = 73$ (d2) $G = 1.0$, $t = 73$

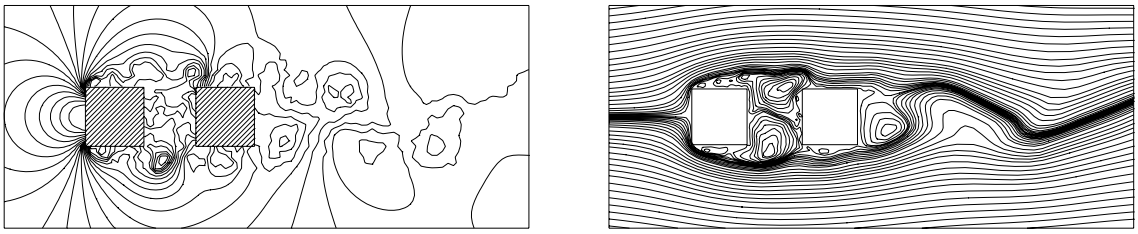

(e1) $G = 1.0$, $t = 74$ (e2) $G = 1.0$, $t = 74$

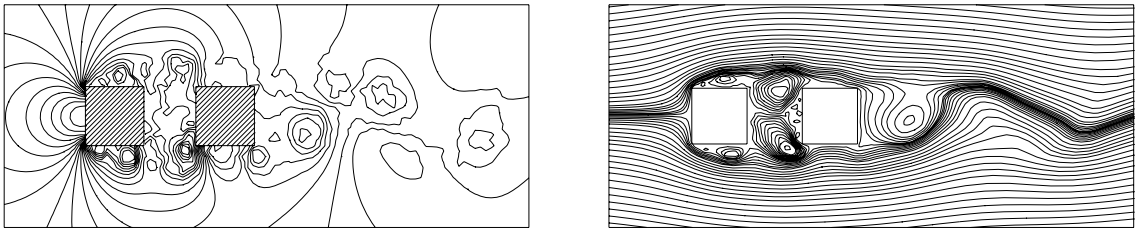

(f1) $G = 1.0$, $t = 75$ (f2) $G = 1.0$, $t = 75$

Figure 8.29. Instantaneous pressure fields and streamline patterns in fully-developed flow over the ($C1 = 1$, $C2 = 1$, $G = 1.0$) array.

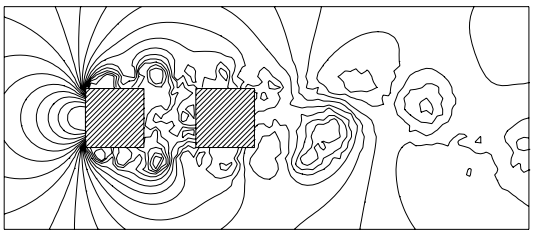

(g1) G = 1.0, t = 76

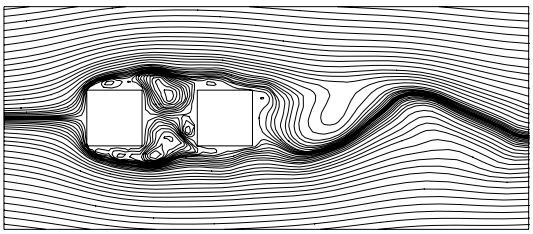

(g2) G = 1.0, t = 76

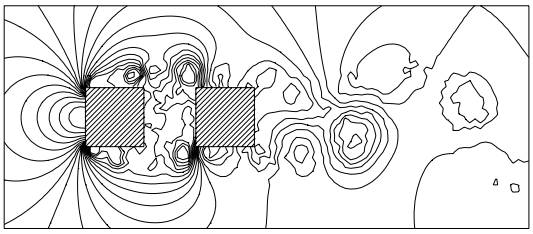

(h1) G = 1.0, t = 77

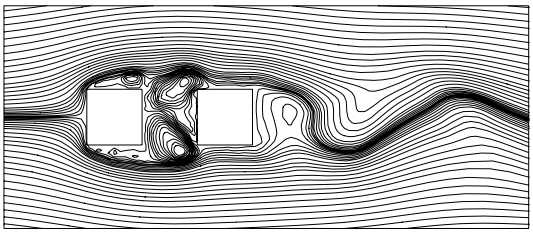

(h2) G = 1.0, t = 77

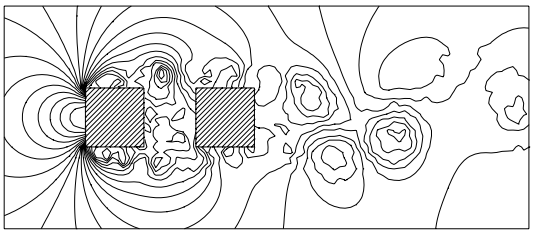

(i1) G = 1.0, t = 78

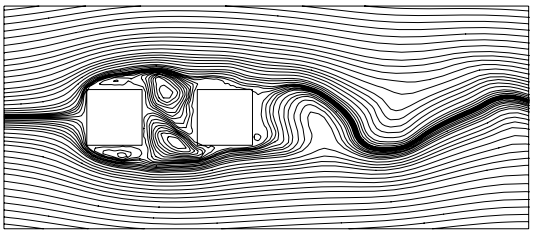

(i2) G = 1.0, t = 78

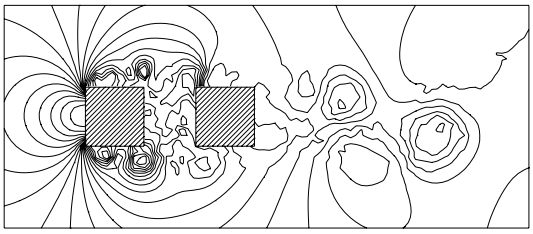

(j1) G = 1.0, t = 79

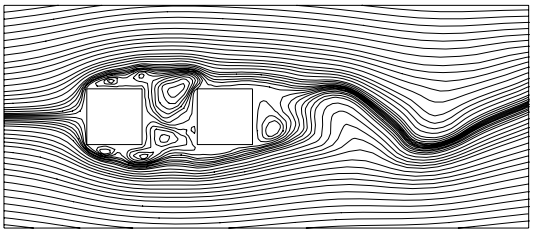

(j2) G = 1.0, t = 79

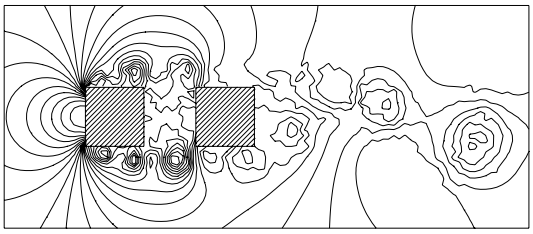

(k1) G = 1.0, t = 80

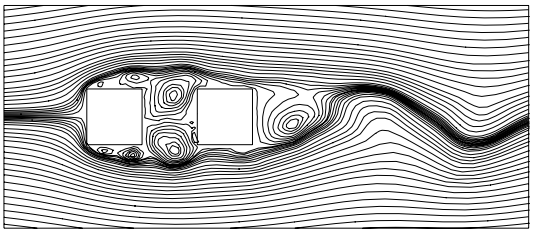

(k2) G = 1.0, t = 80

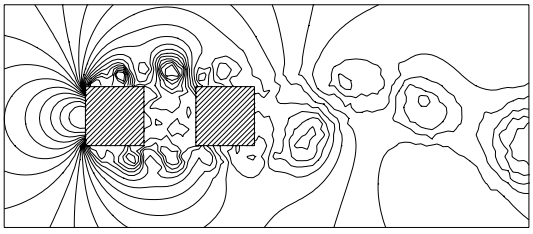

(l1) G = 1.0, t = 81

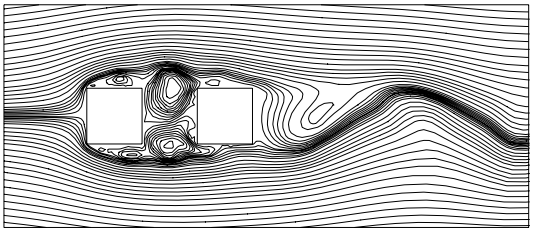

(l2) G = 1.0, t = 81

Figure 8.29. Cont'd.

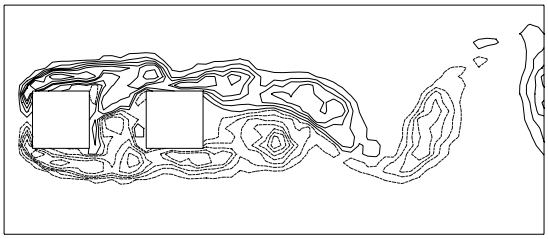

(a) G = 1.0, t = 70

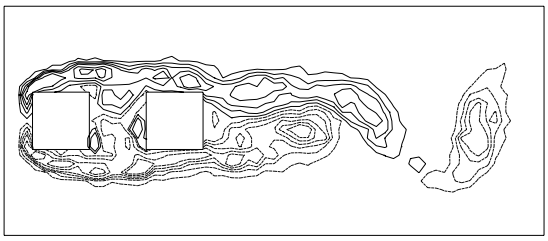

(b) G = 1.0, t = 71

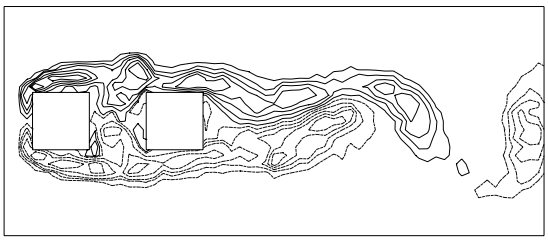

(c) G = 1.0, t = 72

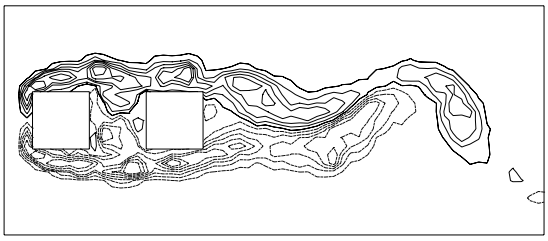

(d) G = 1.0, t = 73

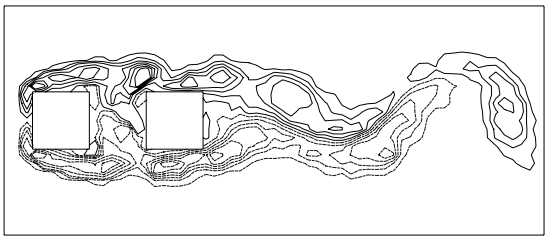

(e) G = 1.0, t = 74

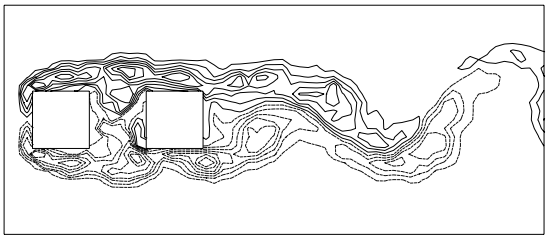

(f) G = 1.0, t = 75

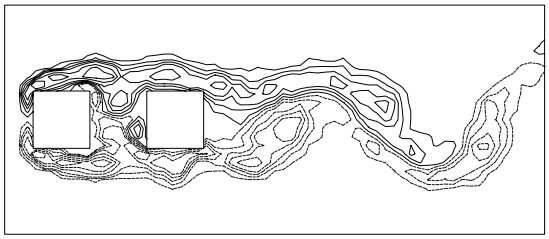

(g) G = 1.0, t = 76

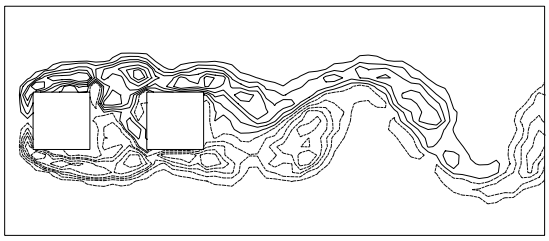

(h) G = 1.0, t = 77

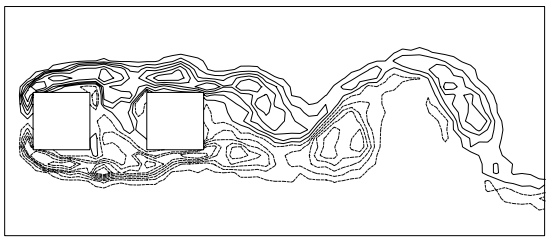

(i) G = 1.0, t = 78

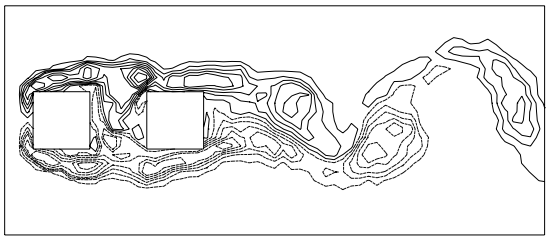

(j) G = 1.0, t = 79

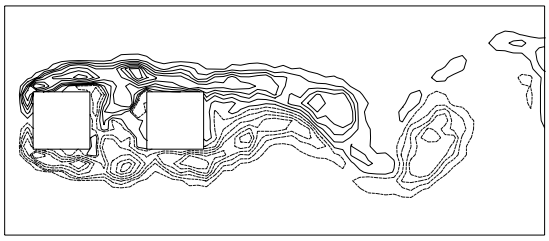

(k) G = 1.0, t = 80

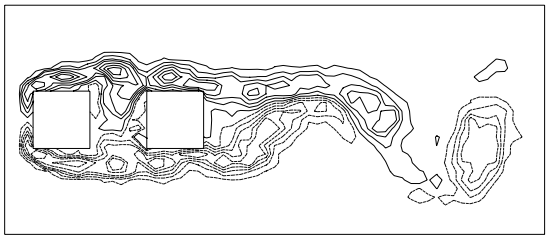

(l) G = 1.0, t = 81

Figure 8.30. Vorticity contours in fully-developed flow over the ($C1$ = 1, $C2$ = 1, G = 1.0) array.

(a) $C1 = 1$, $C2 = 1$, $G = 1.5$, $t = 2$

(b) $C1 = 1$, $C2 = 1$, $G = 1.5$, $t = 4$

(c) $C1 = 1$, $C2 = 1$, $G = 1.5$, $t = 6$

(d) $C1 = 1$, $C2 = 1$, $G = 1.5$, $t = 8$

(e) $C1 = 1$, $C2 = 1$, $G = 1.5$, $t = 10$

(f) $C1 = 1$, $C2 = 1$, $G = 1.5$, $t = 12$

(g) $C1 = 1$, $C2 = 1$, $G = 1.5$, $t = 14$

(h) $C1 = 1$, $C2 = 1$, $G = 1.5$, $t = 16$

(i) $C1 = 1$, $C2 = 1$, $G = 1.5$, $t = 18$

(l) $C1 = 1$, $C2 = 1$, $G = 1.5$, $t = 20$

(k) $C1 = 1$, $C2 = 1$, $G = 1.5$, $t = 22$

(l) $C1 = 1$, $C2 = 1$, $G = 1.5$, $t = 24$

(m) $C1 = 1$, $C2 = 1$, $G = 1.5$, $t = 26$

(n) $C1 = 1$, $C2 = 1$, $G = 1.5$, $t = 28.5$

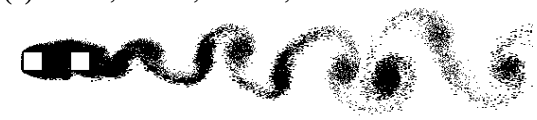

(o) $C1 = 1$, $C2 = 1$, $G = 1.5$, $t = 30.5$

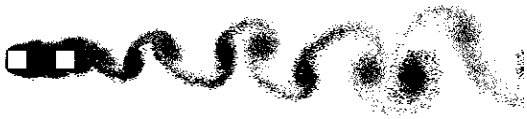

(p) $C1 = 1$, $C2 = 1$, $G = 1.5$, $t = 32.5$

(q) $C1 = 1$, $C2 = 1$, $G = 1.5$, $t = 34.5$

(r) $C1 = 1$, $C2 = 1$, $G = 1.5$, $t = 36.5$

(s) $C1 = 1$, $C2 = 1$, $G = 1.5$, $t = 40.5$

(t) $C1 = 1$, $C2 = 1$, $G = 1.5$, $t = 44.5$

(u) $C1 = 1$, $C2 = 1$, $G = 1.5$, $t = 48.5$

(v) $C1 = 1$, $C2 = 1$, $G = 1.5$, $t = 52.5$

(w) $C1 = 1$, $C2 = 1$, $G = 1.5$, $t = 56.5$

(x) $C1 = 1$, $C2 = 1$, $G = 1.5$, $t = 59.4$

(y) $C1 = 1$, $C2 = 1$, $G = 1.5$, $t = 62.4$

(z) $C1 = 1$, $C2 = 1$, $G = 1.5$, $t = 65.4$

(aa) $C1 = 1$, $C2 = 1$, $G = 1.5$, $t = 68.4$

Figure 8.31. Elemental-vortex distributions in flow over the ($C1 = 1$, $C2 = 1$, $G = 1.5$) array, showing flow development from the impulsive start to the fully-developed state.

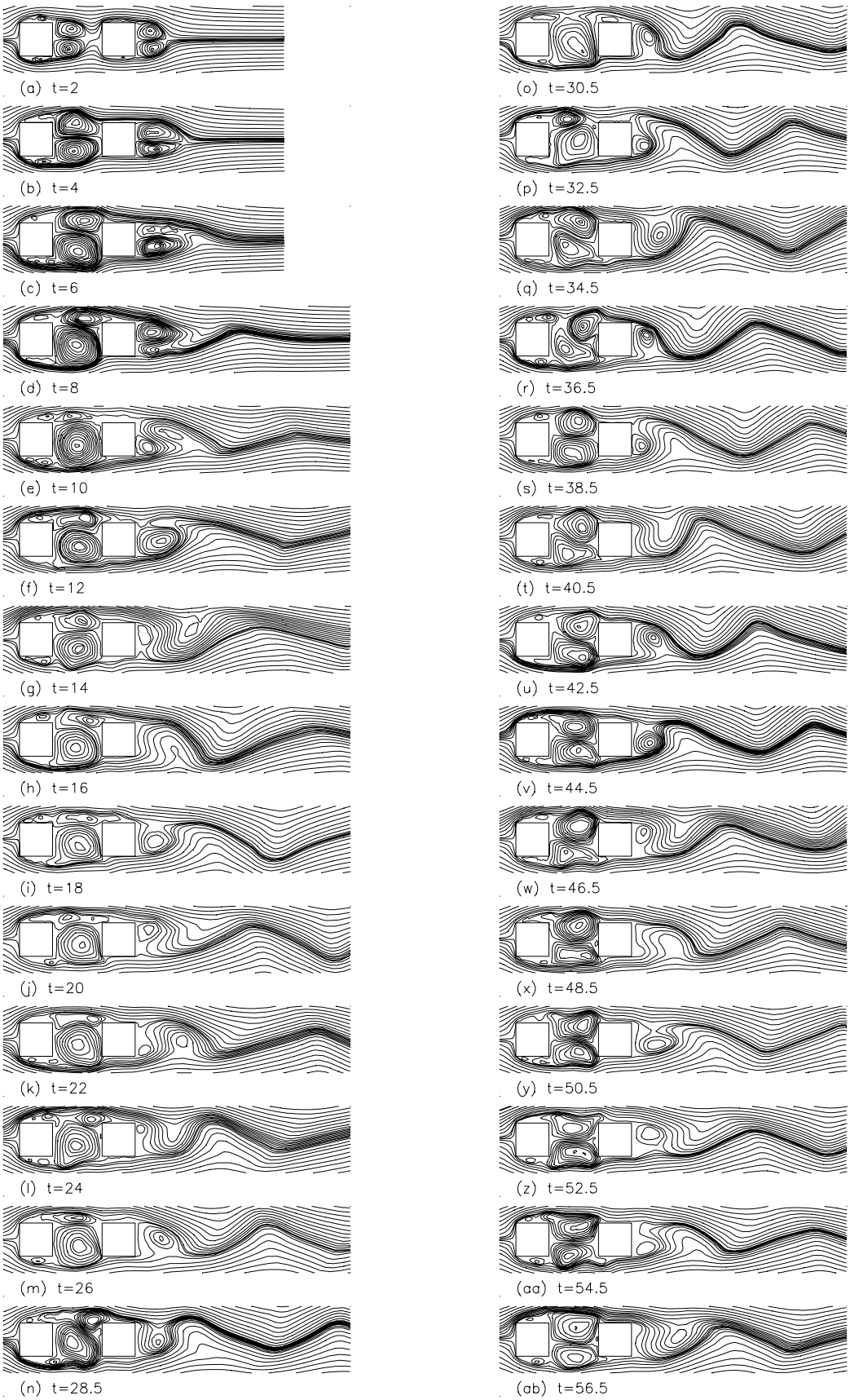

Figure 8.32. Streamline patterns in flow over the ($C1 = 1$, $C2 = 1$, $G = 1.5$) array, showing flow development from the impulsive start to the fully-developed state in which a pair of counter-rotating vortices are trapped in the gap.

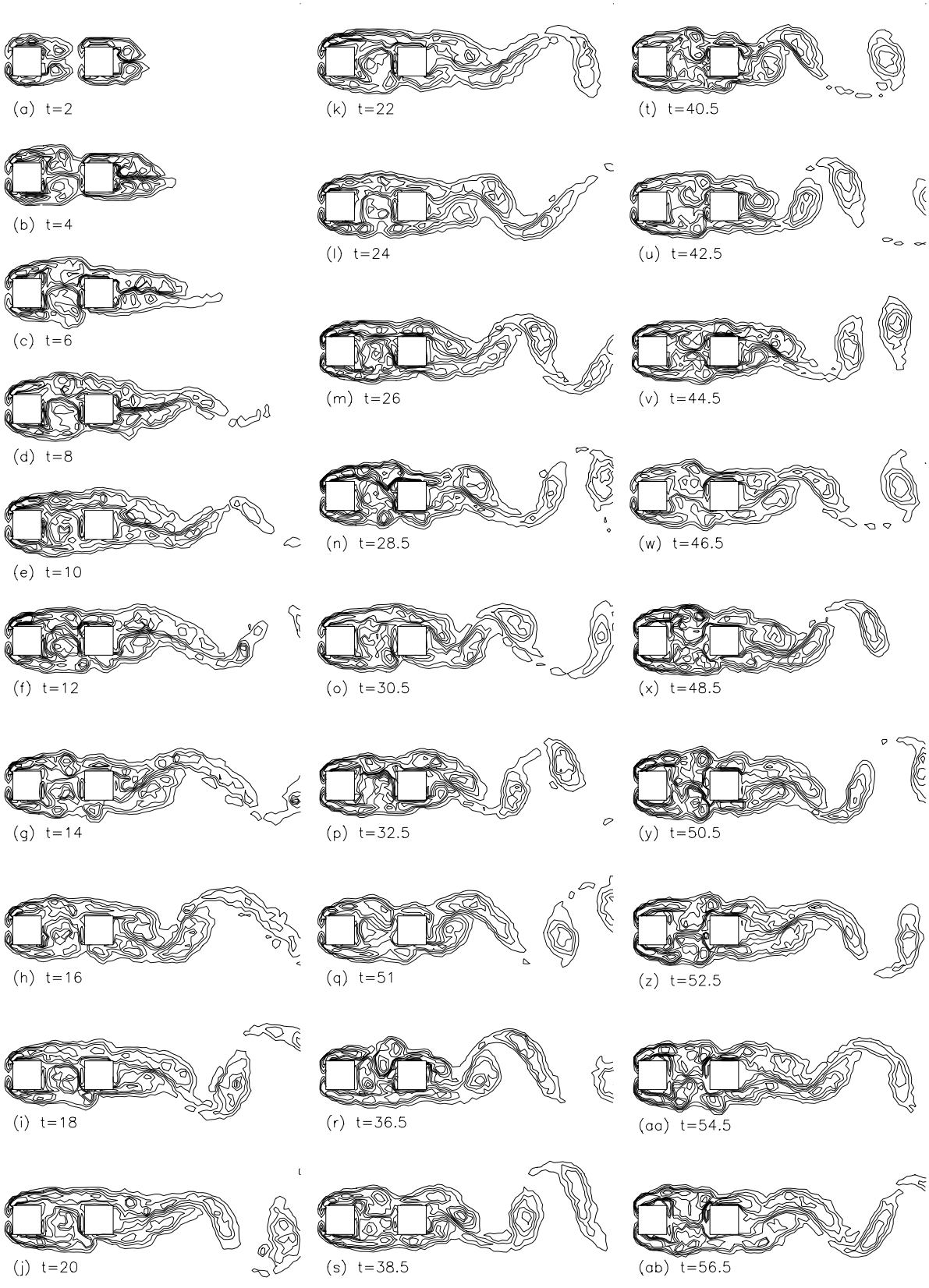

Figure 8.33. Vorticity contours in flow over the ($C1 = 1$, $C2 = 1$, $G = 1.5$) array, showing flow development from the impulsive start to the fully-developed state.

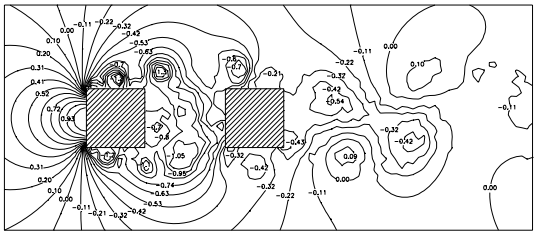

(a1) G = 1.5, t = 58.4

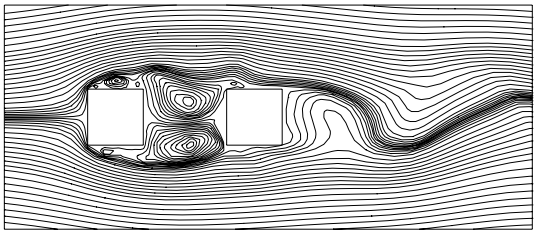

(a2) G = 1.5, t = 58.4

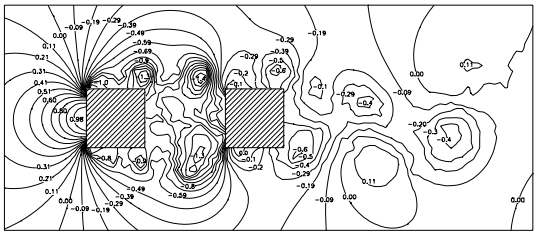

(b1) G = 1.5, t = 59.4

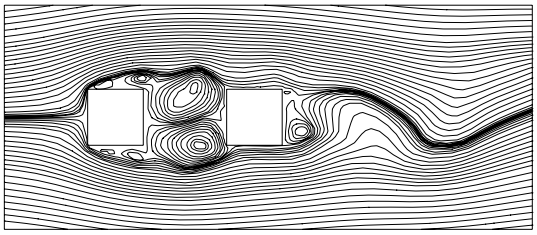

(b2) G = 1.5, t = 59.4

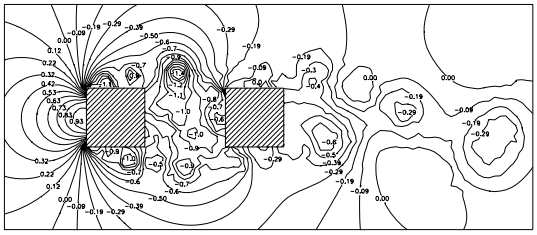

(c1) G = 1.5, t = 60.4

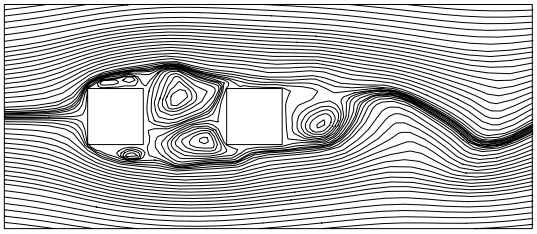

(c2) G = 1.5, t = 60.4

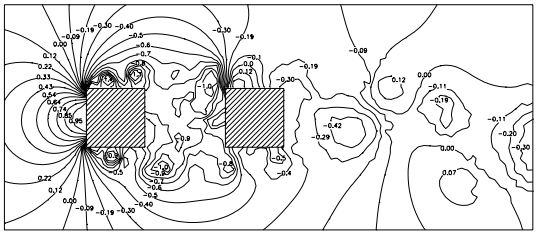

(d1) G = 1.5, t = 61.4

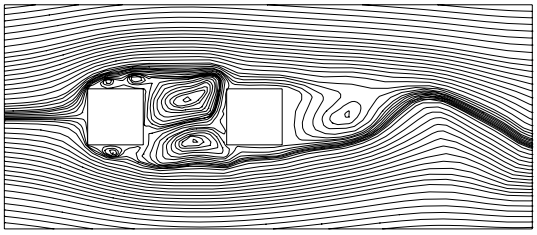

(d2) G = 1.5, t = 61.4

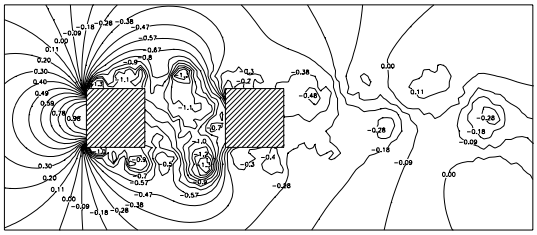

(e1) G = 1.5, t = 62.4

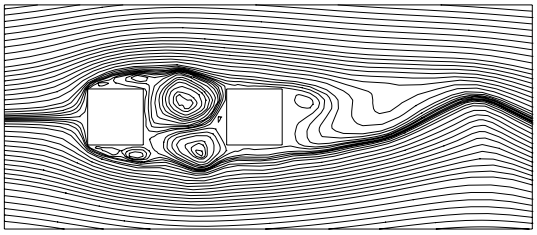

(e2) G = 1.5, t = 62.4

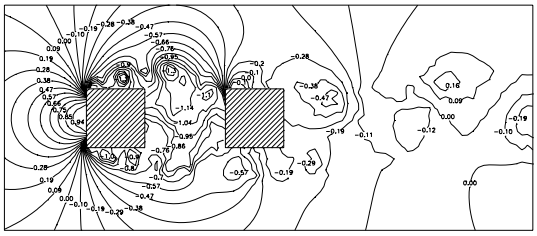

(f1) G = 1.5, t = 63.4

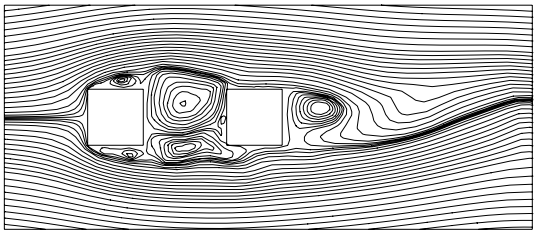

(f2) G = 1.5, t = 63.4

Figure 8.34. Instantaneous pressure fields and streamline patterns in fully-developed flow over the ($C1$ = 1, $C2$ = 1, G = 1.5) array. Numbers shown are coefficients of static pressure.

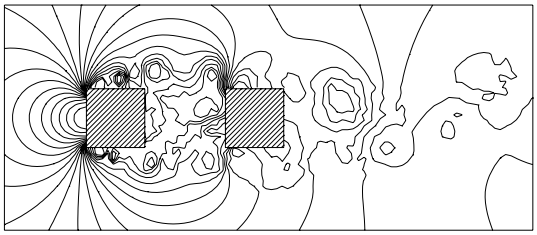

(g1) G = 1.5, t = 64.4

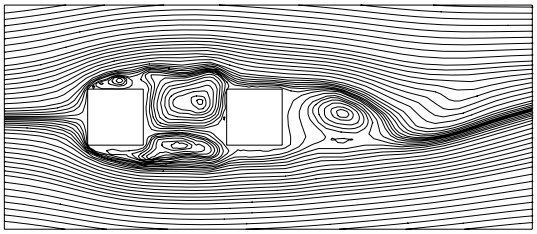

(g2) G = 1.5, t = 64.4

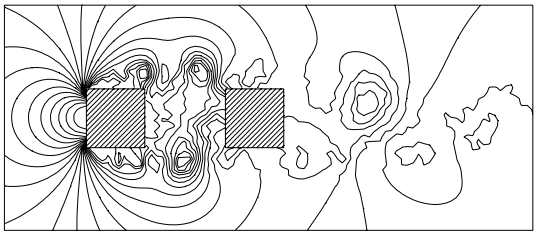

(h1) G = 1.5, t = 65.4

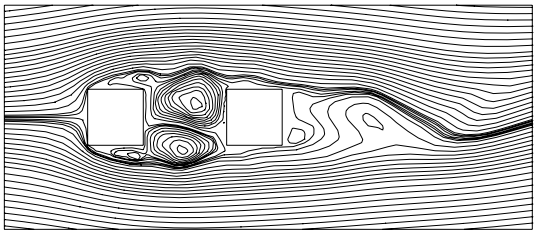

(h2) G = 1.5, t = 65.4

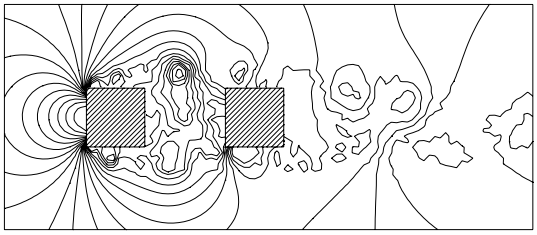

(i1) G = 1.5, t = 66.4

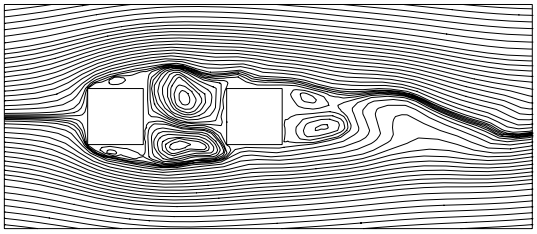

(i2) G = 1.5, t = 66.4

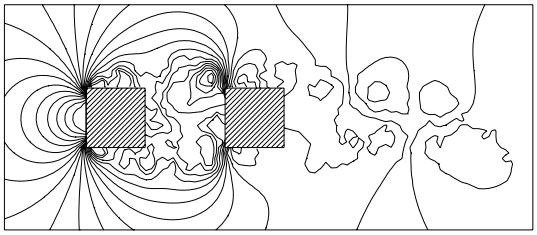

(j1) G = 1.5, t = 67.4

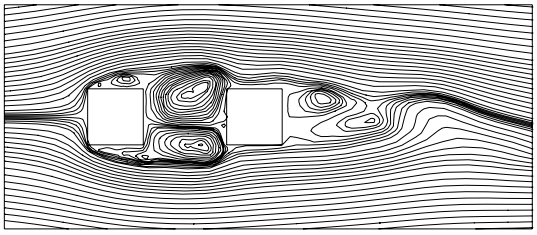

(j2) G = 1.5, t = 67.4

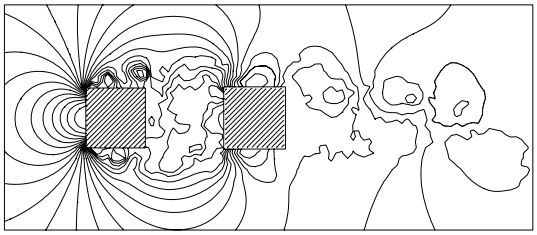

(k1) G = 1.5, t = 67.9

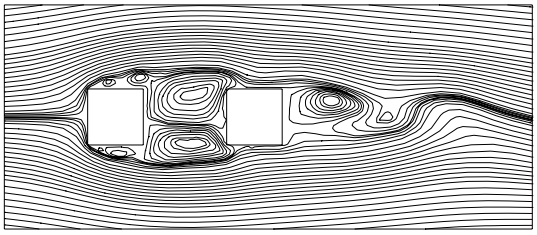

(k2) G = 1.5, t = 67.9

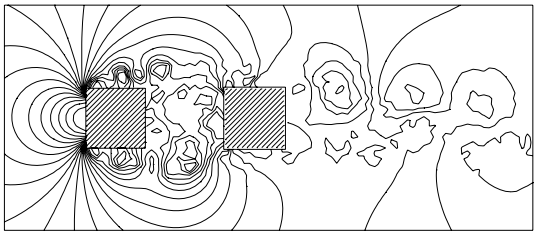

(l1) G = 1.5, t = 68.4

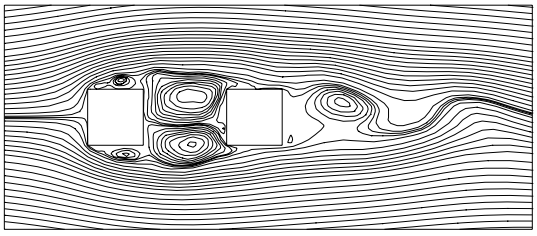

(l2) G = 1.5, t = 68.4

Figure 8.34. Cont'd.

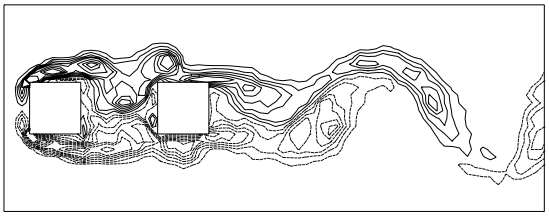

(a) G = 1.5, t = 58.4

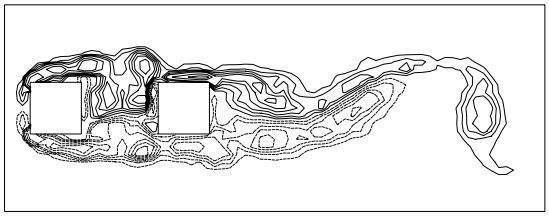

(g) G = 1.5, t = 64.4

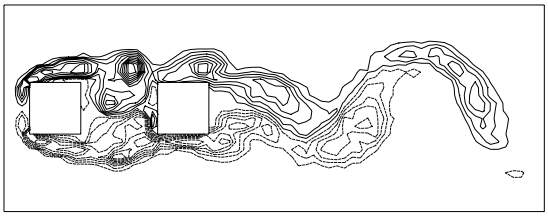

(b) G = 1.5, t = 59.4

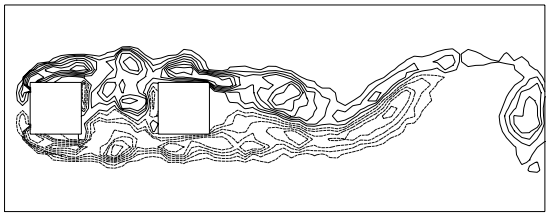

(h) G = 1.5, t = 65.4

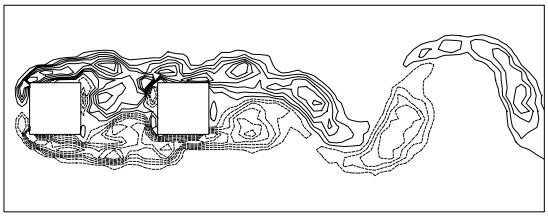

(c) G = 1.5, t = 60.4

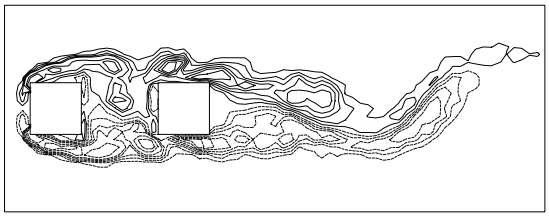

(i) G = 1.5, t = 66.4

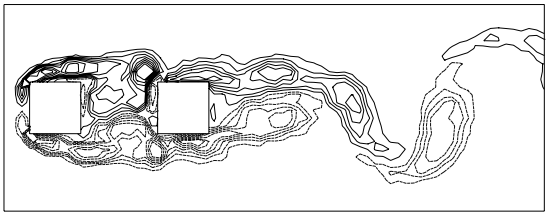

(d) G = 1.5, t = 61.4

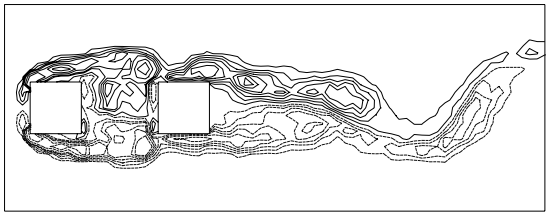

(j) G = 1.5, t = 67.4

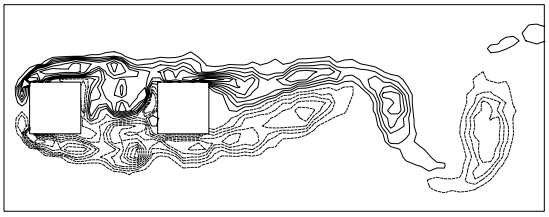

(e) G = 1.5, t = 62.4

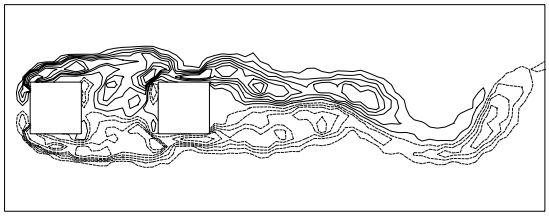

(k) G = 1.5, t = 67.9

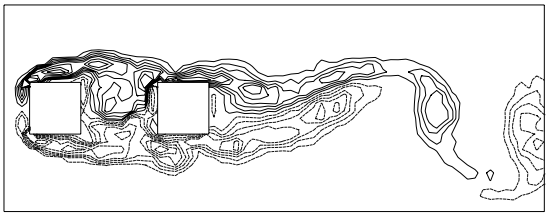

(f) G = 1.5, t = 63.4

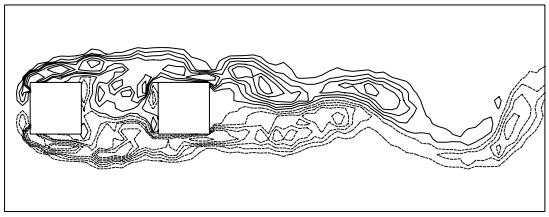

(l) G = 1.5, t = 68.4

Figure 8.35. Vorticity contours in fully-developed flow over the ($C1$ = 1, $C2$ = 1, G = 1.5) array.

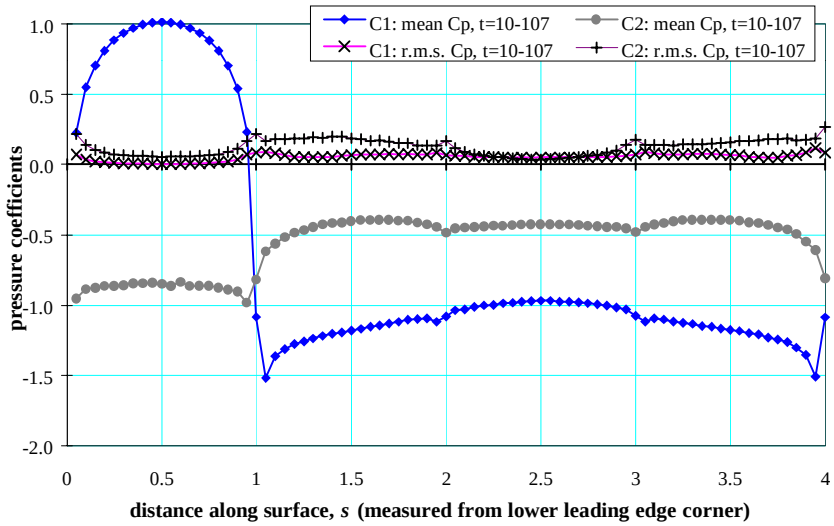

Figure 8.36. Calculated distributions of mean and r.m.s. pressure coefficients on the cylinders in the ($C1 = 1$, $C2 = 1$, $G = 0.8$) array.

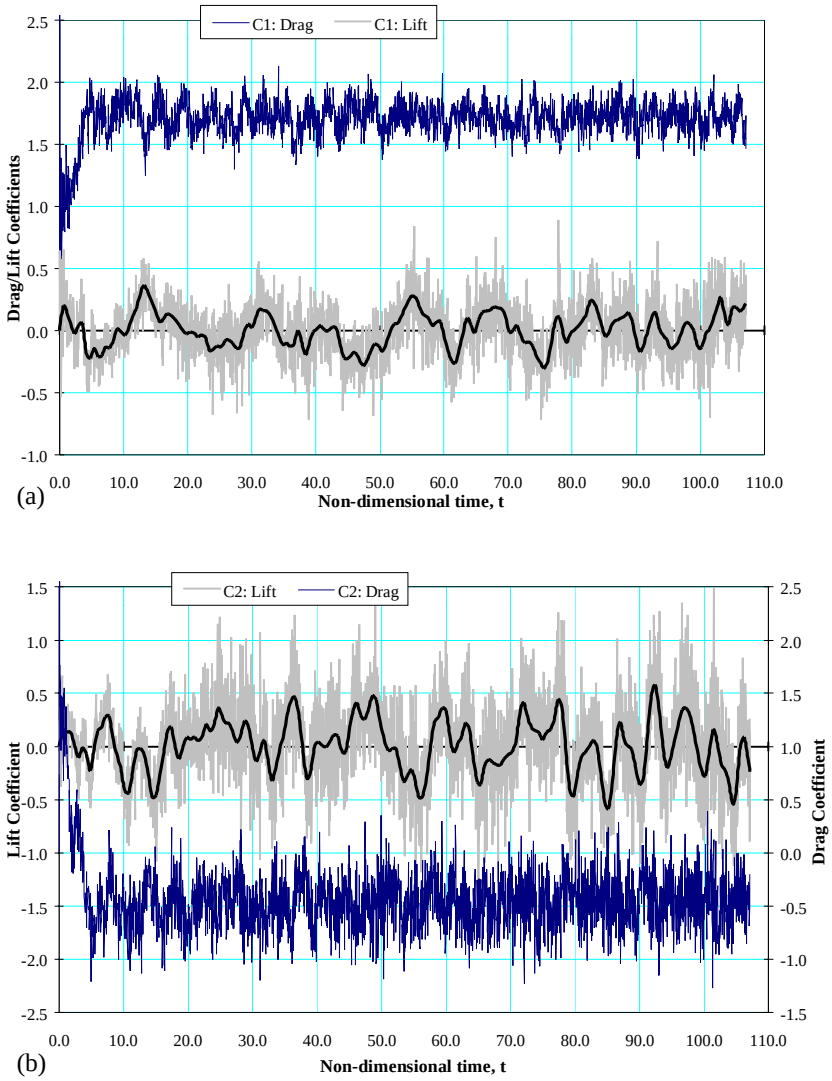

Figure 8.37. Time-histories of drag and lift on the ($C1 = 1$, $C2 = 1$, $G = 0.8$) array, (a) upstream plate, (b) downstream plate. Drag and lift are calculated for $\Delta t = 0.02$; highlighted values are averaged over $\Delta t = 0.4$.

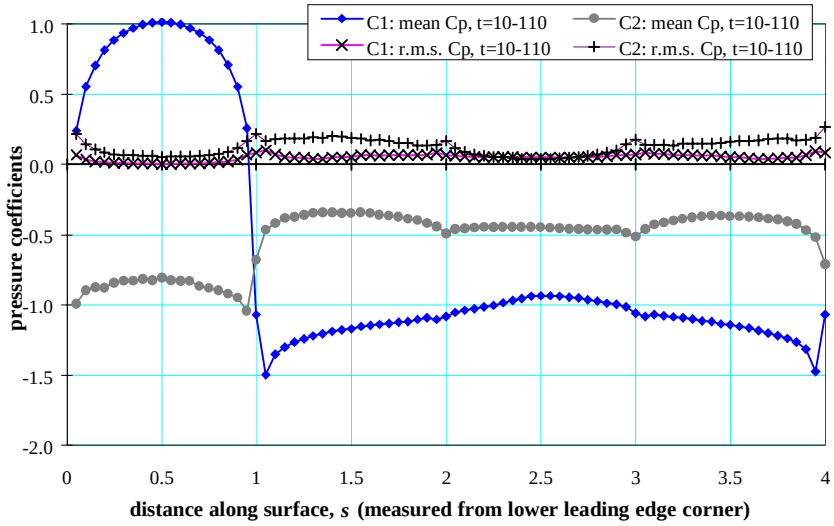

Figure 8.38. Calculated distributions of mean and r.m.s. pressure coefficients on the cylinders in the ($C1 = 1$, $C2 = 1$, $G = 1.0$) array.

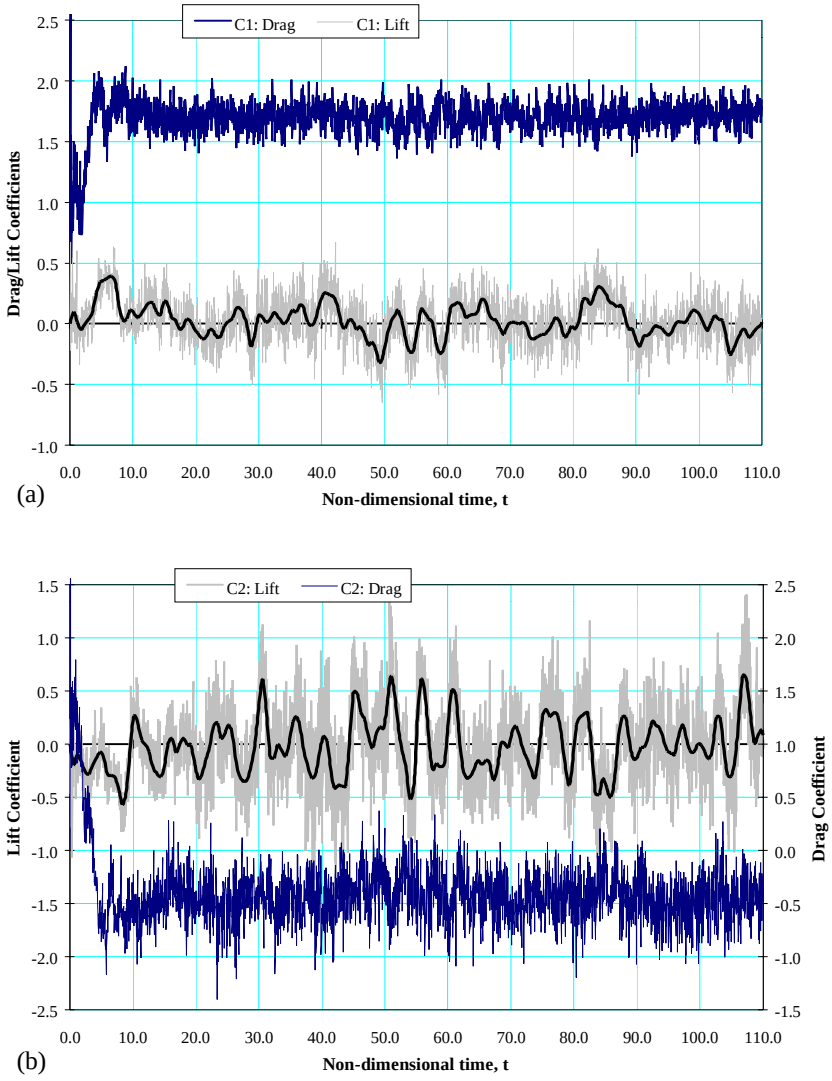

Figure 8.39. Time-histories of drag and lift on the ($C1 = 1$, $C2 = 1$, $G = 1.0$) array, (a) upstream plate, (b) downstream plate. Drag and lift are calculated for $\Delta t = 0.02$; highlighted values are averaged over $\Delta t = 0.4$.

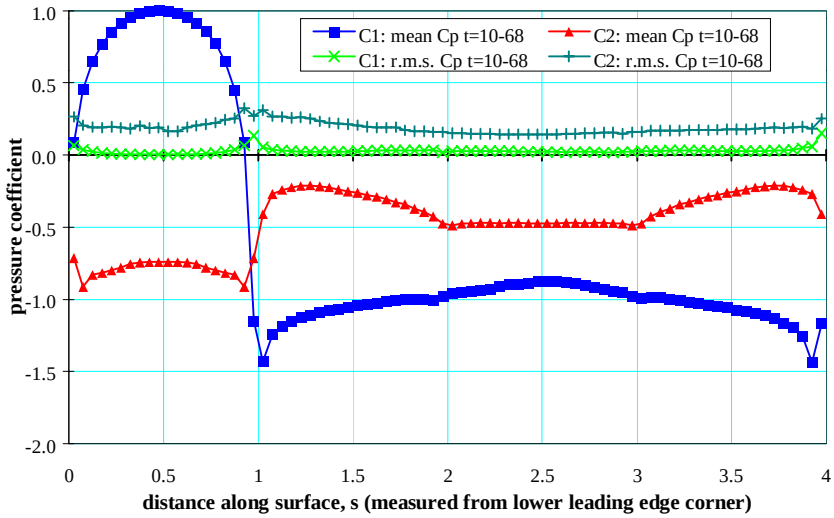

Figure 8.40. Calculated distributions of mean and r.m.s. pressure coefficients on the cylinders in the ($C1$ = 1, $C2$ = 1, G = 1.5) array.

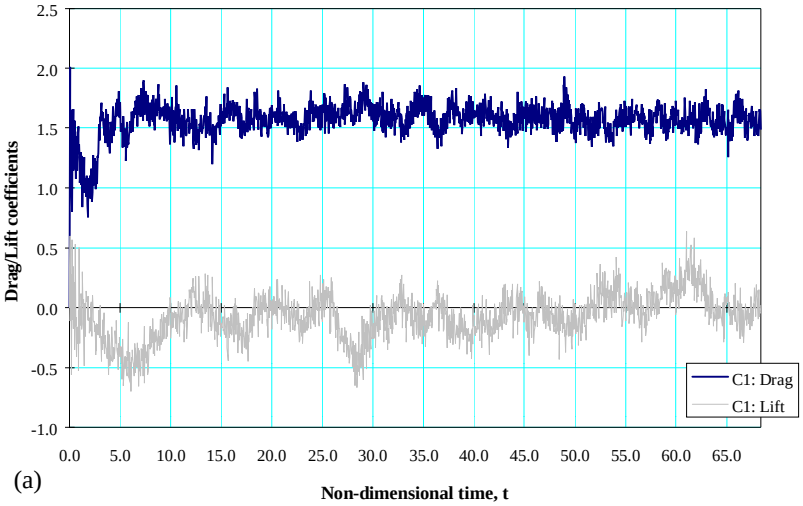

(a)

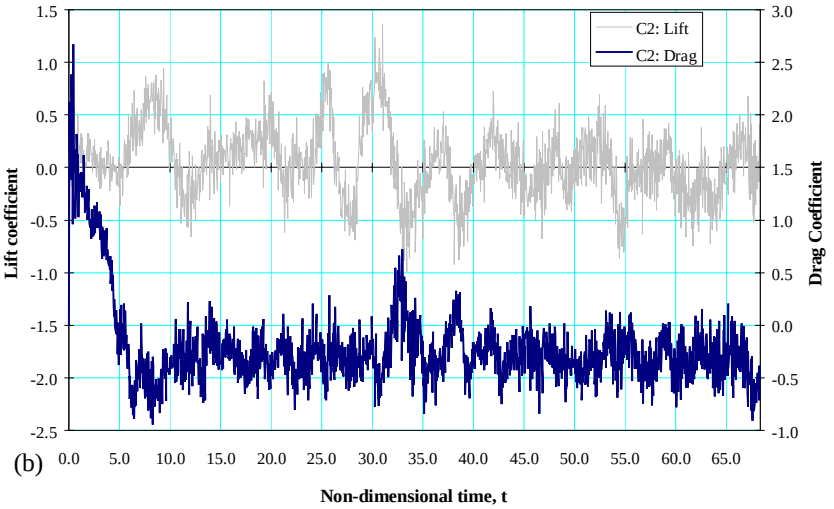

(b)

Figure 8.41. Time-histories of drag and lift on the ($C1$ = 1, $C2$ = 1, G = 1.5) array, (a) upstream plate, (b) downstream plate.

8.3.3 Flow Regimes for Large Gaps, $G \geq 3$

When the two cylinders are separated by a large streamwise gap, there is no longer a trapped, stationary, vortex system in the gap. Instead, the shear layers shed from the upstream cylinder form a vortex street between the cylinders. The flow is now in the *B* regime of the classification of Bull *et al.* [1997], a regime in which the interaction of the vortex street in the gap with the downstream cylinder has a critical influence on the character of the flow established. Simulations have been made for $G = 3$, 4 and 6. The mechanism is similar in all cases and the $G = 4$ array will be used later as a specific example for identifying the details of it.

Consider first the flow development from impulsive start on the cylinders of the $G = 3$ array. The calculated elemental-vortex distributions, streamlines and vorticity patterns presented in Figs. 8.42–8.44 show the early stages of flow evolution. The initial flow over both cylinders ($t \leq 3$) is very much like the flow over a single square cylinder (see section 7.2.1): in all cases, a closed recirculation region comprising two counter-rotating vortices forms behind the cylinder. Initially, the overall flow is symmetrical about the streamwise centre-line of the array, but quickly becomes asymmetric. The recirculation region behind the downstream cylinder develops into a vortex street ($t = 12$), as in the case of a single square cylinder. Vortex-street formation on the upstream cylinder is delayed to a later time: a large stationary vortex is first formed between the cylinders ($t = 12$) before a vortex street is finally established behind the upstream cylinder ($t = 15$). The flow is then in the fully-developed state ($t > 15$) in which vortex streets form behind both cylinders.

In the state of fully-developed flow, the calculated streamline patterns for $G = 3$, 4 and 6 (Figs. 8.43, 8.46 and 8.51) indicate that the shear layers separating from the upstream cylinder impinge either on the side faces of the upstream cylinder itself or on the array at a position within the gap; no direct reattachment occurs on the downstream cylinder. This corresponds with regime *B* of Bull *et al.* [1997]. The fully-developed flow on the upstream cylinder is virtually identical to the flow over a single square cylinder as described earlier in section 7.2.2: the separated shear layers reattach to the side surfaces intermittently, alternating with completely detached flow in which there is reversed flow over the side surface. On the downstream cylinder, however, the flow is significantly different and very much affected by the wake-edge interaction associated with impingement of the vortex-street shed from the upstream cylinder.

8.3.3.1 Mechanisms of Wake-Edge Interaction

Extensive experimental investigations of wake-edge interactions have been made by Rockwell and Knisely [1979], Ziada and Rockwell [1982], Tang and Rockwell [1983], Kaykayoglu and Rockwell [1985], Rockwell, Kaykayoglu, Sohn and Kuo [1985] and Gursul and Rockwell [1990]. Numerical studies have also been made. These follow developments, such as those by Smith and Stansby [1987, 1989] and Graham [1988], of inviscid discrete vortex methods to incorporate the effects of viscous diffusion. They include those by Kaya, Kaykayoglu, Bayar and Graham [1991], Kaykayoglu [1992] and Mook and Dong [1994]. However, while these numerical works include diffusive effects on the impinging vortex street and the boundary layers on the downstream body, which undoubtedly play an important role in the wake-edge interaction, they do not model the evolution of the boundary layer on the upstream body to a fully-developed state. In the present calculations for tandem arrays of finite bluff bodies, diffusive effects on boundary-layer development and separation on both upstream and downstream bodies and on the vortex flow in the gap between the bodies are taken into account. The fine details of flow patterns obtained can then reveal differences in the flow characteristics of impingement of the vortical gap-flow on the downstream blunt edge in the array from those of the impingement models previously considered in the literature.

As a typical case of the interaction of the vortex street in the gap with the downstream cylinder in the array, the details of flow over the $G = 4$ array will be considered. The calculated streamline, isobar and vorticity patterns are presented in Figs. 8.48 and 8.49. A typical sequence of events in the vortex-street impingement can be seen from $t = 58.6$ onwards. At this time, a vortex (of positive circulation) is impinging on the downstream cylinder, while the next vortex (of negative circulation), shed from the lower side of the upstream cylinder and located about midway along the gap, is being convected towards the downstream cylinder ($t = 58.6$, 59.6). As the vortex approaches the downstream cylinder ($t = 59.6$–61.6), the stagnation point on the leading face of the downstream cylinder takes a position near the lower leading corner, and the flow on the entire lower surface of the cylinder is fully-attached. The attached flow on the leading face sweeps upwards and separates from the upper leading corner, forming a leading-edge-separation bubble on the upper surface. When the incident vortex impinges on the downstream cylinder ($t = 61.6$–63.6), it is distorted and partially clipped by the blunt leading edge. The major portion climbs over the lower leading corner and continues to move along the lower side of the downstream cylinder, while the smaller portion is deflected to the front face

where it remains for some time (t = 63.6–65.6). Under the influence of the next, approaching, upper (positive) vortex, the stagnation point on the leading edge of the downstream cylinder rapidly shifts upwards to a position near the upper leading corner (t = 61.6–63.6), as a result of rapid reversal of flow direction on the leading face. The separated flow on the upper surface then changes to fully-attached flow on the entire surface. The fully-attached flow on the lower face of the downstream cylinder gives way to flow separation at the leading corner and reattachment on the side face; a short leading-edge-separation bubble thus forms on the lower face (t = 63.6). As this separation bubble develops, the small vortex on the front face of the cylinder, previously formed by clipping of the impinging vortex, is convected around the lower leading-edge corner and merges with the separation bubble (t = 65.6, 66.5) to form a secondary vortex. During the process of impingement, clipping, and secondary vortex formation, flow separation from the lower trailing edge leads to the formation of a trailing-face vortex which grows over times t = 60.6–63.6. This trailing-face vortex and the secondary vortex on the lower face are shed simultaneously into the wake ($t \approx 67.6$). It appears that generally the shedding of the trailing-face vortex is synchronised with the passage of the major part of the clipped impinging vortex over the trailing edge of the downstream cylinder. The vortical structures associated with the major part of the incident vortex, secondary vortex and trailing-face vortex can be clearly identified in the isobar and vorticity contours ($t \approx 67.6$). These vortices merge (t = 68.6, 69.6) as they move downstream, to form a vortex in the final Karman street of the array. (The G = 3 and G = 6 arrays exhibit similar behaviour: in almost all cases merging occurs, but occasionally the clipped impinging vortex and the vortex formed by combination of the secondary and trailing-face vortices persist as separate vortices.)

As the next vortex (of positive vorticity) shed from the upstream cylinder impinges on the downstream cylinder (t = 65.6), the flow on the leading edge, due to the effect of the following (negative) vortex from the upstream cylinder, again rapidly reverses direction; and the stagnation point shifts from near the upper leading corner to near the lower leading corner (t = 65.6, 66.6). As a result, the fully-attached flow on the upper side changes to one separating at the leading corner and accompanied by the formation of a leading-edge-separation bubble; at the same time the flow on the lower side changes from separated flow to fully-attached flow. The separation bubble formed on the upper side combined with the smaller part of the clipped impinging vortex is later shed into the flow (t = 67.6) and convected downstream together with the main portion of the incident vortex (t = 68.6 – 69.6). The upper trailing-face vortex formed on the downstream cylinder is also shed into the flow at t = 67.6. The incident vortex,

secondary vortex and the trailing-face vortex merge during downstream convection to form a wake vortex (t = 69.6). While the formation and shedding of the secondary vortex and upper trailing-face vortex are taking place, a vortex (of negative vorticity) shed from the lower side of the upstream cylinder is approaching the leading face of the downstream cylinder. The impingement cycle is then repeated. However, the calculations indicate that the impingement cycle is not exactly repeated each time. Successive vortices in the vortex street in the gap are not identical, but vary somewhat in strength, spatial scale, and regularity of shedding from the upstream cylinder, and do not follow identical paths. The degree of distortion and redistribution of the incident vortical structure which occurs upon impingement on the downstream blunt edge is primarily determined by the spatial scale of the vortex and the extent to which the vortex trajectory is laterally offset with respect to the side face of the downstream cylinder. Significant differences in these parameters from one impingement to another can be seen by comparing the vorticity patterns of the impingements at t = 62.6 and t = 68.6. Consequently, the proportion of the incident vortex clipped by the downstream blunt edge varies, and so does the intensity of the secondary vortex. Irregularities of this type in the vortex-impingement pattern are also observed experimentally (Tang and Rockwell, 1983).

Vortex formation on the trailing face of the downstream cylinder is also affected by variations in the scale and lateral offset of the impinging vortices. Consequently, the irregularities in the impingement flow give rise to irregularity in the final vortex street, as can be seen in the elemental-vortex distributions of Fig. 8.33. There are indications that the trailing-face vortices on the downstream cylinder are formed mainly by rolling up of the shear layers separating from the trailing edges (as, for example, in the formation of the lower trailing-face vortex at t = 60.6), but there are also occasions when a side-face vortex convected past the trailing corner becomes the seed of a trailing-face vortex (as in the formation of the upper trailing-face vortex at t = 61.6); it appears that both processes make a contribution. However, despite the variations in the vortex-impingement patterns, the trailing-face vortex formation is always coupled with vortex impingement and the associated shedding of the secondary vortex.

The onset of impingement of a vortex on the downstream cylinder is therefore closely associated with the shedding of a vortex of the opposite sign (formed from the previous impingement) from the cylinder into the wake. It is also closely associated with the shedding of a vortex opposite sign from the upstream cylinder. Thus, vortices of the same sign are shed from corresponding corners of the upstream and downstream cylinders, at times close to that at which a convected

vortex in the gap, of the opposite sign, arrives at the downstream cylinder. All three events occur at the same frequency, but, because of the irregularities in the impingement cycle, their precise relative phasing is difficult to determine from the streamline or vorticity patterns. The phase difference between the lift fluctuations on the upstream and downstream cylinders, discussed later, can however be readily determined.

8.3.3.2 Effects of Gap Width on Flow for $G \geq 3$

As a result of the irregularities in the impingement flow, already referred to for $G = 4$, the final vortex street in the *B* regime is not regular; this can be seen in the elemental-vortex distributions of Figs. 8.42, 8.45 and 8.50 for $G = 3$, 4 and 6 respectively. Further illustration of the irregularity, for all three gaps, is provided by the streamlines of the flows observed from a frame of reference moving at $U_{ref} = 0.8U_{\infty}$, depicted in Figs. 8.71(i)–8.71(k): the final vortex street is less regular and the wake wider than in the *F*2 and *E*1/*E*2 regimes for smaller gaps (Figs. 8.71(a)–8.71(f)).

Calculated distributions of surface-pressure on the $G = 3$, 4 and 6 arrays (Figs. 8.53, 8.55 and 8.57) show that the pressure on the upstream cylinder is again very similar to the pressure on a single square cylinder: in all cases the base-pressure coefficient is close to $C_{pb1} \approx -1$, and the mean drag coefficients are virtually the same at $C_{D1} \approx 1.7$. These parameters are comparable to the corresponding values $C_{pb} \approx -1.1$ and $C_D \approx 1.8$ for a single square cylinder at $Re_h = 500$ (see section 7.2). On the downstream cylinder, however, the pressure distribution is more sensitive to the *G* value. Most noticeable are the increase of pressure on the leading face with increasing *G* ($C_{pf2} = 0.1$, 0.3 and 0.7 for $G = 3$, 4 and 6 respectively) and the increasing similarity of the distribution on the other faces to the corresponding distributions on the upstream cylinder. Thus, the overall pressure distribution on the downstream cylinder approaches that on the upstream cylinder, and both approach the pressure distribution on a single square cylinder, as *G* increases.

It is evident from the distributions of r.m.s. pressure coefficient (Figs. 8.53, 8.55 and 8.57) that, due to vortex-street impingement, the pressure fluctuations on the downstream cylinder are significantly greater than on the upstream cylinder. The largest pressure fluctuations on the downstream cylinder occur near its leading edges. This is in accord with the experimental findings of Bull and Pickles [1991] and Bull, Pickles and Li [1992] that interaction with the

impinging vortex-street from the upstream cylinder makes the most significant contribution to the surface-pressure fluctuation. (It might be noted that the character of the pressure and force fluctuations – see particularly the drag on the downstream cylinder – is such that rather larger averaging times would be required to produce steady r.m.s. values. Small deviations from symmetry of the pressure-fluctuation distributions are evident in the figures.)

Calculated time-histories of the drag and lift coefficients on the cylinders of the G = 3, 4 and 6 arrays are shown in Figs. 8.54, 8.56 and 8.58 respectively. They indicate that, when the flow becomes fully-developed at large time, $t \gtrsim 15$, the pressure forces on the cylinders vary periodically with time at the vortex-shedding frequency, but with a phase difference depending on G. As indicated above, the flow over the upstream cylinder is very similar to that over an isolated cylinder. This conclusion is reinforced by the insensitivity to the value of G of the Strouhal numbers for the arrays, determined from lift-coefficient fluctuations (St = 0.12, 0.125 and 0.13 for G = 3, 4 and 6 respectively) and their similarity to the value for an isolated square cylinder (St = 0.132 at Re_h = 500). This suggests that vortex shedding from the upstream cylinder is essentially uninfluenced by the presence of the downstream cylinder when $G \geq 3$. In that case, the phase difference between lift fluctuations on the two cylinders should be proportional to the time taken for vortices shed from the upstream cylinder to traverse the gap; the phase difference should then vary linearly with G, as found experimentally by Sakamoto, Haniu and Obata [1987]. Calcualated values for the phase lag of the downstream cylinder are 0.06π, 0.2π and 1.05π for G = 3, 4 and 6 respectively, or if the reference value is taken as 2π for G = 3 (as Sakamoto *et al.*) 2.06π, 2.2π and 3.05π. These values agree quite well with the empirical linear relation obtained by Sakamoto *et al*. to fit their experimental data, which can be expressed with sufficient accuracy as $(1 + G/3)\pi$. Note that, as the calculated streamline patterns show, in the case of G = 3, impingement of a vortex on the downstream cylinder is synchronised with simultaneous shedding of vortices of the opposite sign from both upstream and downstream cylinders, while for G = 6 impingement is synchronised with shedding of a vortex of the same sign as the impinging vortex from the upstream cylinder and the shedding of a vortex of the opposite sign from the downstream cylinder.

The drag on the upstream cylinder is insensitive to the value of G over the range being considered: in each case the drag coefficient has a mean value of $C_{D1} \approx 1.7$. The mean drag coefficient C_{D2} on the downstream cylinder increases with increasing G, having values of $C_{D2} \approx 1.4$, 1.5 and 1.6 for G = 3, 4 and 6 respectively. The corresponding values of the coefficients

of total drag on the array are therefore 3.1, 3.2 and 3.3. Thus, as G increases the drag of each cylinder in the array approaches that of an isolated square cylinder, and the total drag of the array approaches twice that of an isolated square cylinder.

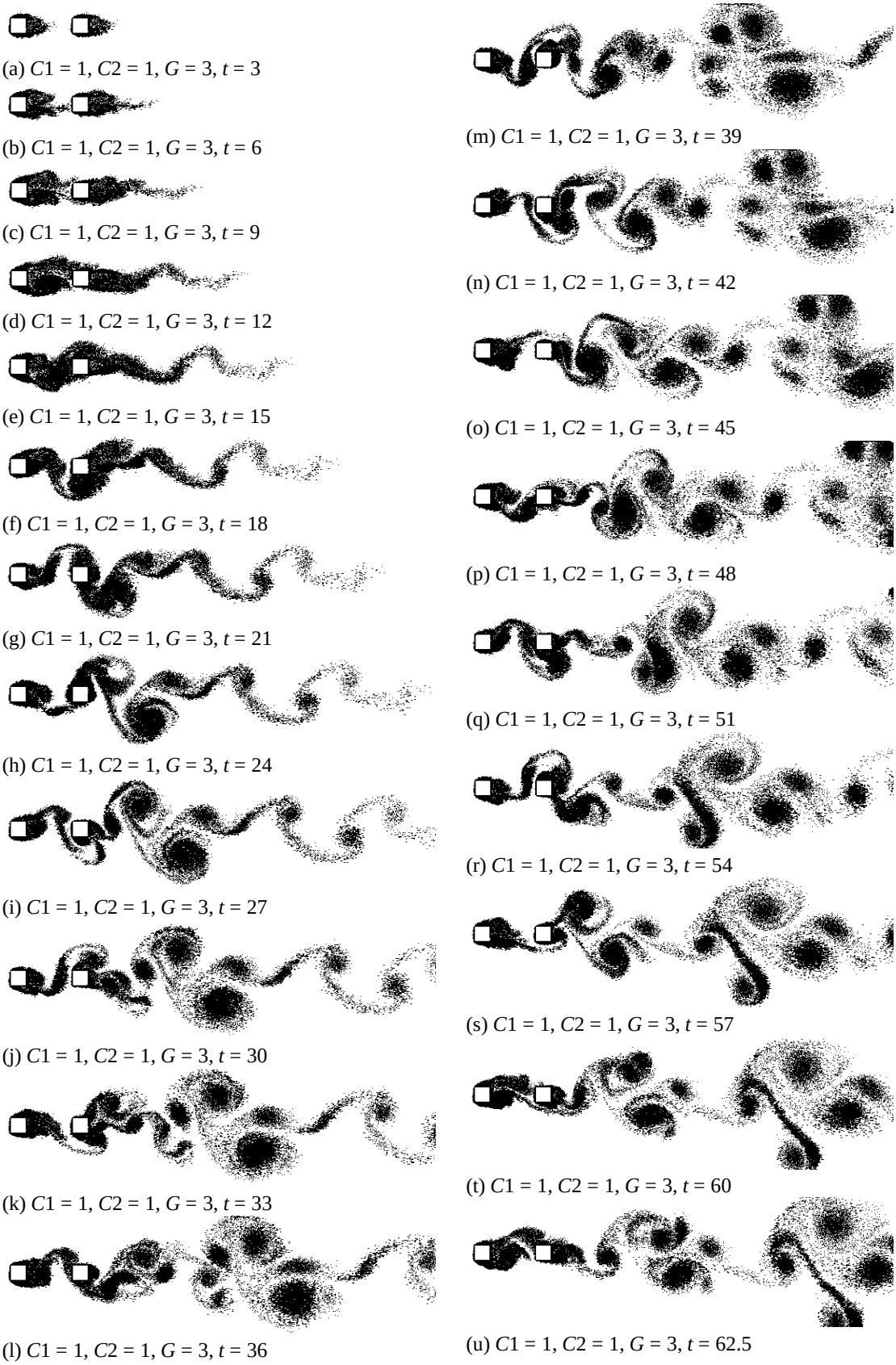

(a) $C1 = 1$, $C2 = 1$, $G = 3$, $t = 3$

(b) $C1 = 1$, $C2 = 1$, $G = 3$, $t = 6$

(c) $C1 = 1$, $C2 = 1$, $G = 3$, $t = 9$

(d) $C1 = 1$, $C2 = 1$, $G = 3$, $t = 12$

(e) $C1 = 1$, $C2 = 1$, $G = 3$, $t = 15$

(f) $C1 = 1$, $C2 = 1$, $G = 3$, $t = 18$

(g) $C1 = 1$, $C2 = 1$, $G = 3$, $t = 21$

(h) $C1 = 1$, $C2 = 1$, $G = 3$, $t = 24$

(i) $C1 = 1$, $C2 = 1$, $G = 3$, $t = 27$

(j) $C1 = 1$, $C2 = 1$, $G = 3$, $t = 30$

(k) $C1 = 1$, $C2 = 1$, $G = 3$, $t = 33$

(l) $C1 = 1$, $C2 = 1$, $G = 3$, $t = 36$

(m) $C1 = 1$, $C2 = 1$, $G = 3$, $t = 39$

(n) $C1 = 1$, $C2 = 1$, $G = 3$, $t = 42$

(o) $C1 = 1$, $C2 = 1$, $G = 3$, $t = 45$

(p) $C1 = 1$, $C2 = 1$, $G = 3$, $t = 48$

(q) $C1 = 1$, $C2 = 1$, $G = 3$, $t = 51$

(r) $C1 = 1$, $C2 = 1$, $G = 3$, $t = 54$

(s) $C1 = 1$, $C2 = 1$, $G = 3$, $t = 57$

(t) $C1 = 1$, $C2 = 1$, $G = 3$, $t = 60$

(u) $C1 = 1$, $C2 = 1$, $G = 3$, $t = 62.5$

Figure 8.42. Elemental-vortex distributions in flow over the ($C1 = 1$, $C2 = 1$, $G = 3$) array, showing flow development from an impulsive start from rest to the state of fully-developed flow.

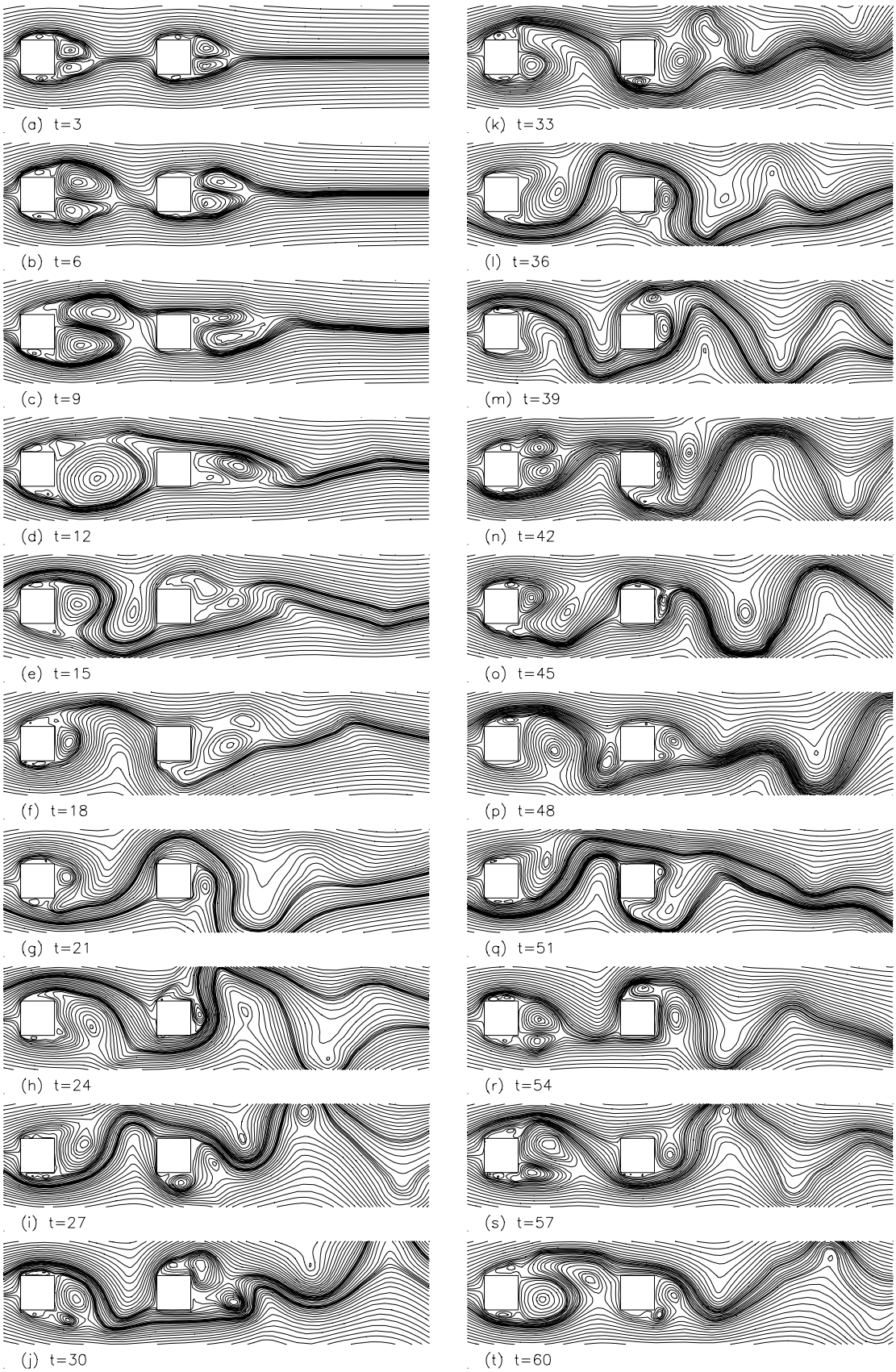

Figure 8.43. Calculated streamline patterns in flow over the ($C1$ = 1, $C2$ = 1, G = 3) array, showing flow development from an impulsive start to the fully-developed flow in the *B* regime.

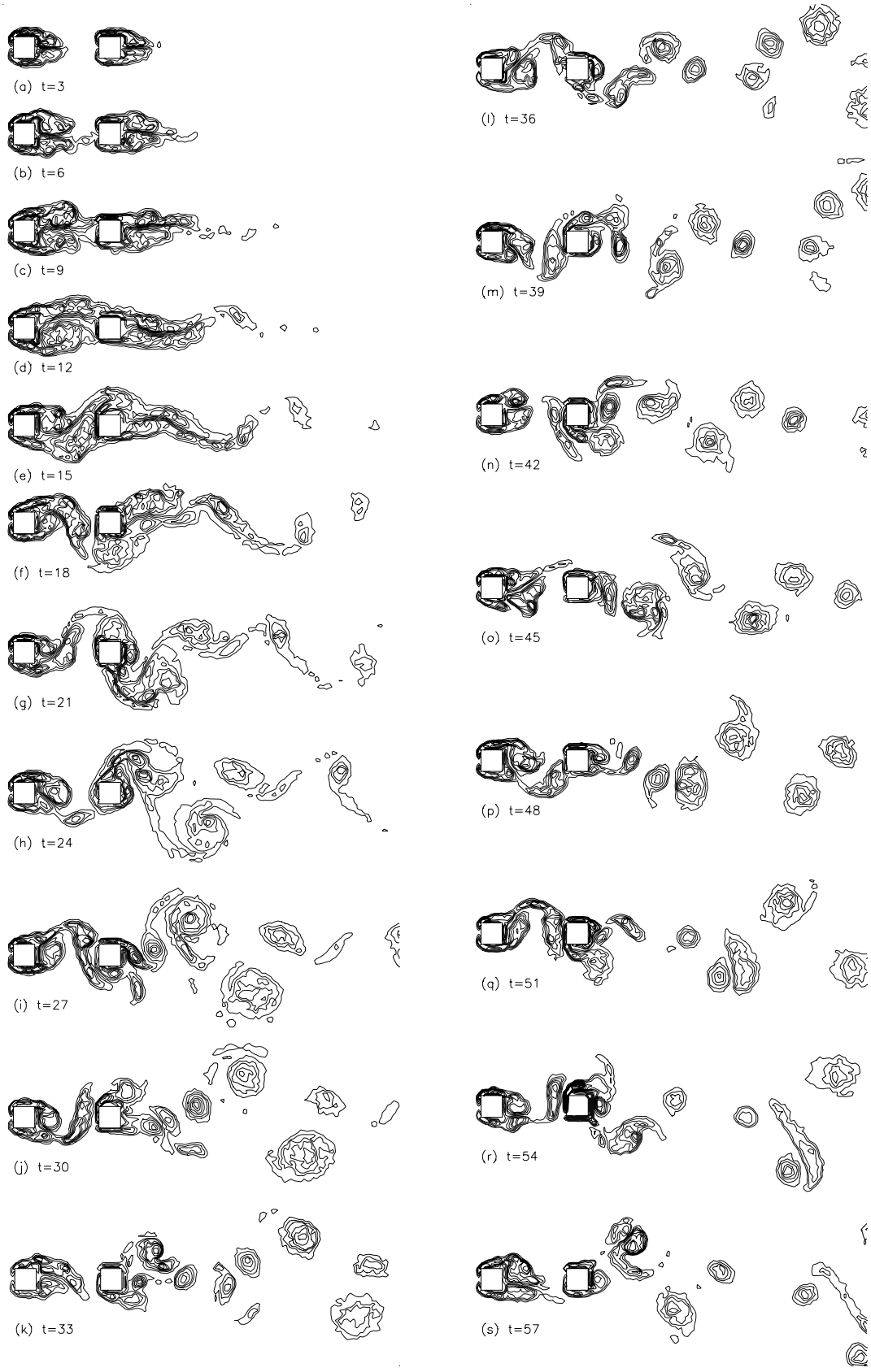

Figure 8.44. Vorticity contours in flow over the ($C1 = 1$, $C2 = 1$, $G = 3$) array, showing flow development from an impulsive start from rest to the fully-developed flow.

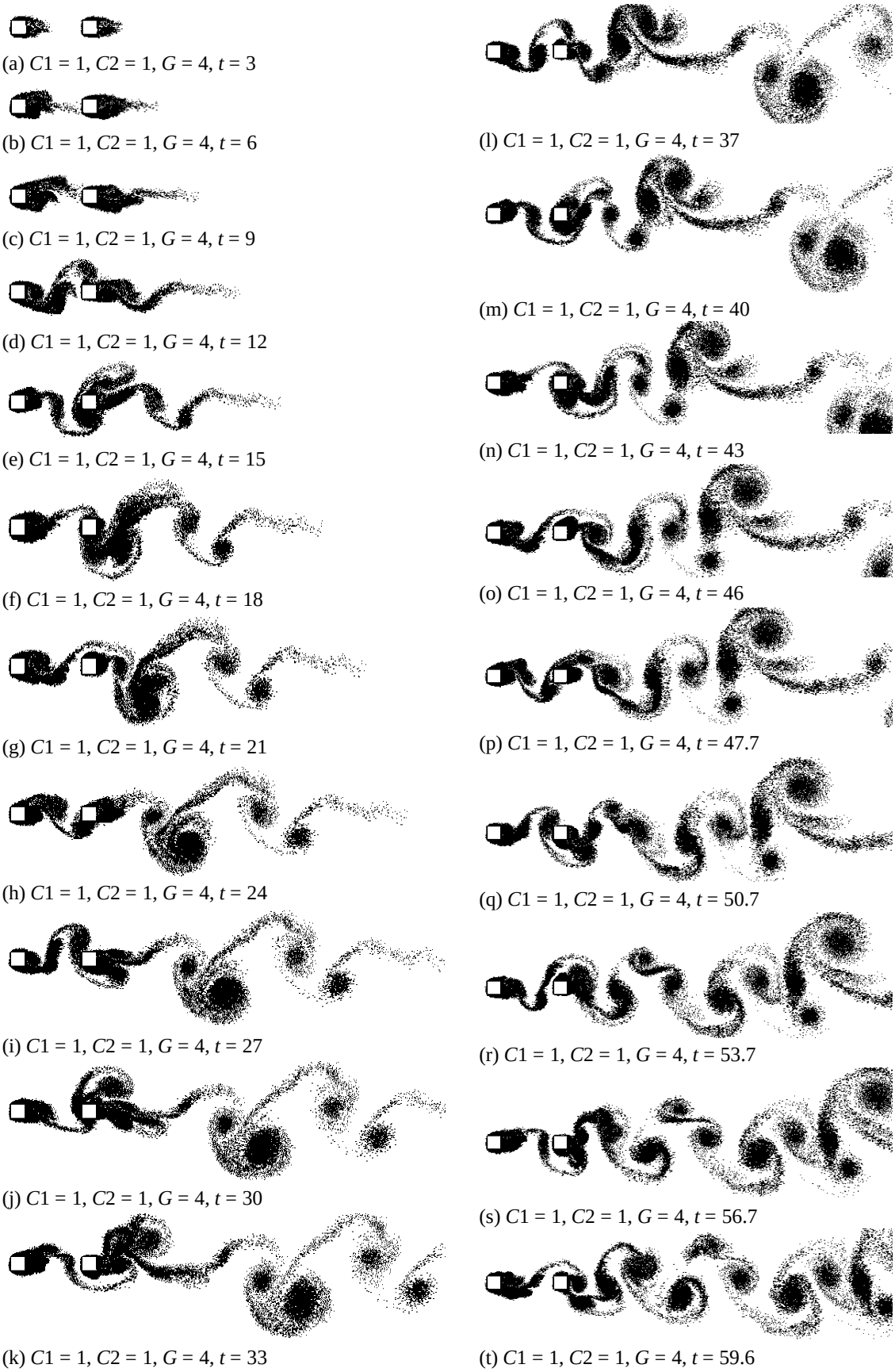

(a) $C1 = 1$, $C2 = 1$, $G = 4$, $t = 3$

(b) $C1 = 1$, $C2 = 1$, $G = 4$, $t = 6$

(c) $C1 = 1$, $C2 = 1$, $G = 4$, $t = 9$

(d) $C1 = 1$, $C2 = 1$, $G = 4$, $t = 12$

(e) $C1 = 1$, $C2 = 1$, $G = 4$, $t = 15$

(f) $C1 = 1$, $C2 = 1$, $G = 4$, $t = 18$

(g) $C1 = 1$, $C2 = 1$, $G = 4$, $t = 21$

(h) $C1 = 1$, $C2 = 1$, $G = 4$, $t = 24$

(i) $C1 = 1$, $C2 = 1$, $G = 4$, $t = 27$

(j) $C1 = 1$, $C2 = 1$, $G = 4$, $t = 30$

(k) $C1 = 1$, $C2 = 1$, $G = 4$, $t = 33$

(l) $C1 = 1$, $C2 = 1$, $G = 4$, $t = 37$

(m) $C1 = 1$, $C2 = 1$, $G = 4$, $t = 40$

(n) $C1 = 1$, $C2 = 1$, $G = 4$, $t = 43$

(o) $C1 = 1$, $C2 = 1$, $G = 4$, $t = 46$

(p) $C1 = 1$, $C2 = 1$, $G = 4$, $t = 47.7$

(q) $C1 = 1$, $C2 = 1$, $G = 4$, $t = 50.7$

(r) $C1 = 1$, $C2 = 1$, $G = 4$, $t = 53.7$

(s) $C1 = 1$, $C2 = 1$, $G = 4$, $t = 56.7$

(t) $C1 = 1$, $C2 = 1$, $G = 4$, $t = 59.6$

Figure 8.45. Elemental-vortex distributions in flow over the ($C1 = 1$, $C2 = 1$, $G = 4$) array, showing flow development from an impulsive start from rest to the state of fully-developed flow.

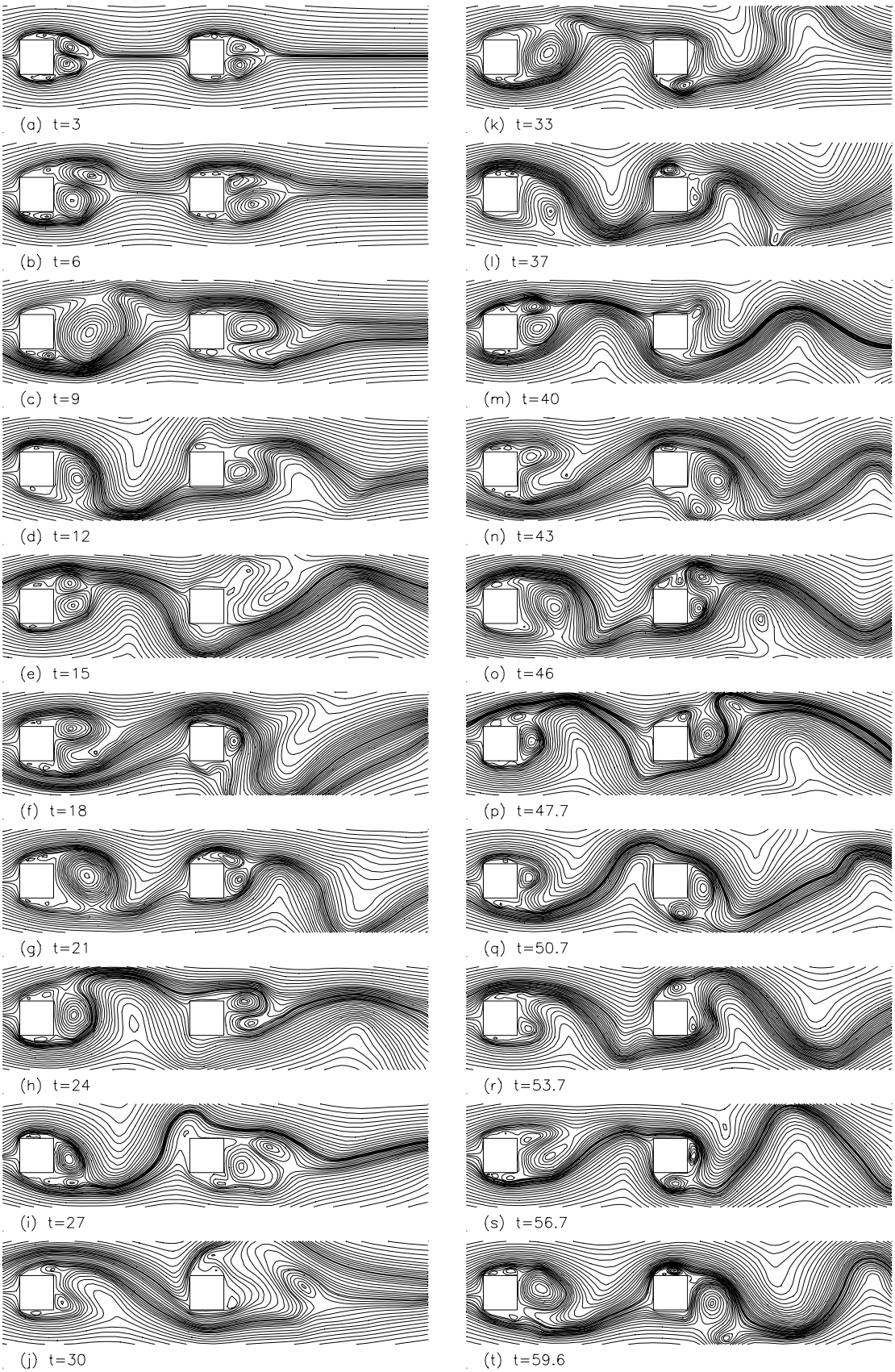

Figure 8.46. Calculated streamline patterns in flow over the ($C1 = 1$, $C2 = 1$, $G = 4$) array, showing development from the impulsive start to the fully-developed flow.

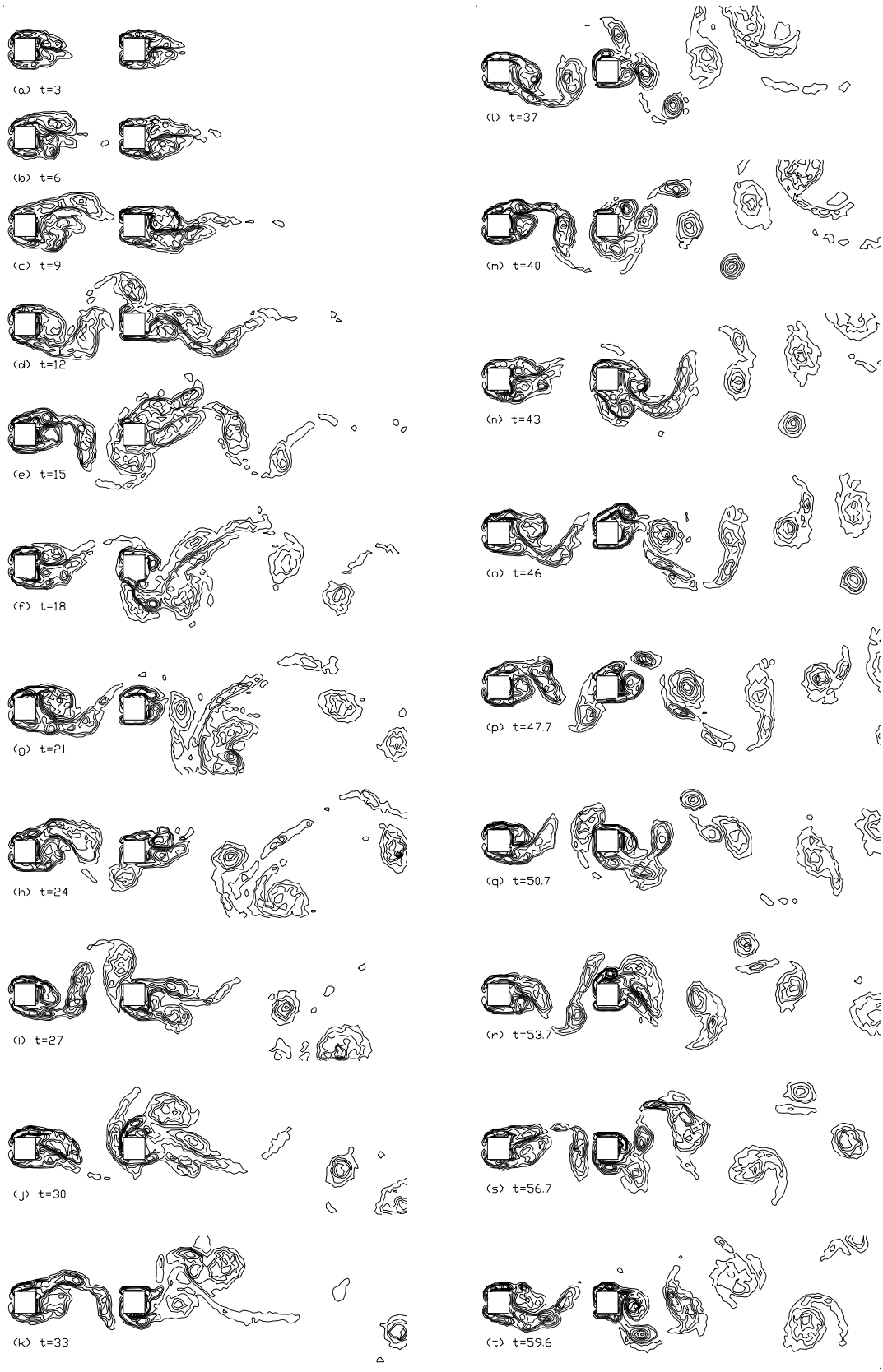

Figure 8.47. Vorticity contours in flow over the ($C1 = 1$, $C2 = 1$, $G = 4$) array, showing development from the impulsive start to the fully-developed flow.

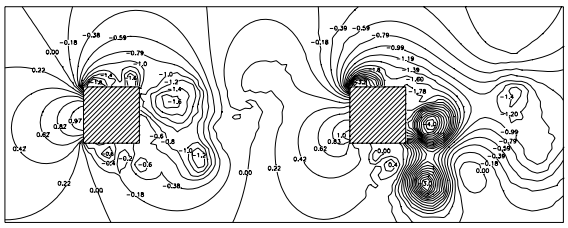

(a1) G = 4.0, t = 58.6

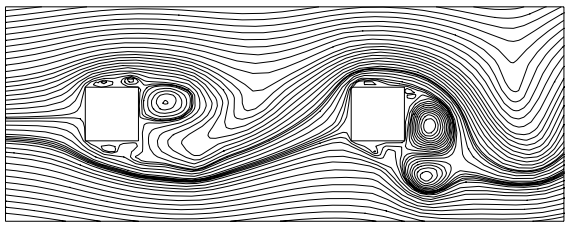

(a2) G = 4.0, t = 58.6

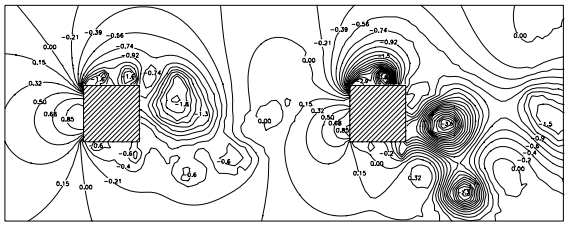

(b1) G = 4.0, t = 59.6

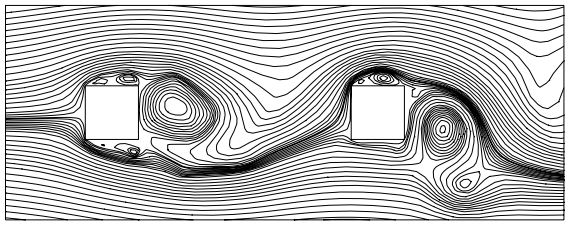

(b2) G = 4.0, t = 59.6

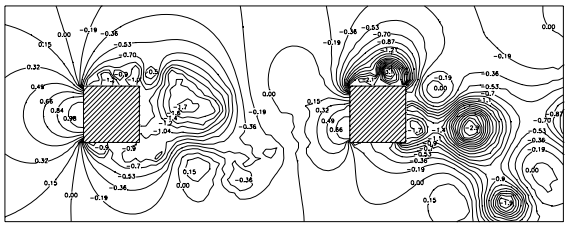

(c1) G = 4.0, t = 60.6

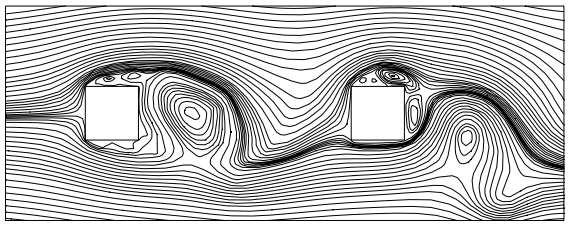

(c2) G = 4.0, t = 60.6

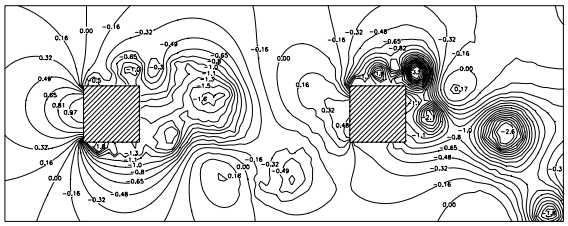

(d1) G = 4.0, t = 61.6

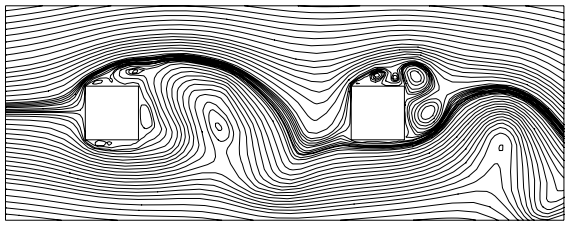

(d2) G = 4.0, t = 61.6

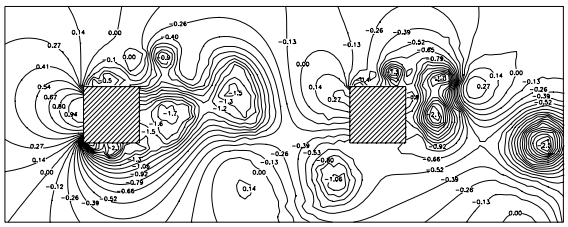

(e1) G = 4.0, t = 62.6

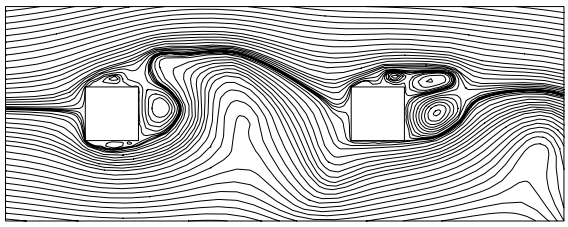

(e2) G = 4.0, t = 62.6

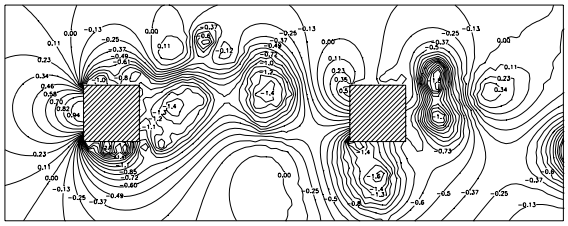

(f1) G = 4.0, t = 63.6

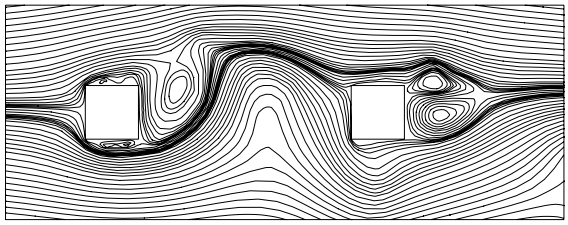

(f2) G = 4.0, t = 63.6

Figure 8.48. Instantaneous pressure fields and streamline patterns in fully-developed flow over the ($C1$ = 1, $C2$ = 1, G = 4.0) array. Numbers shown are coefficients of static pressure.

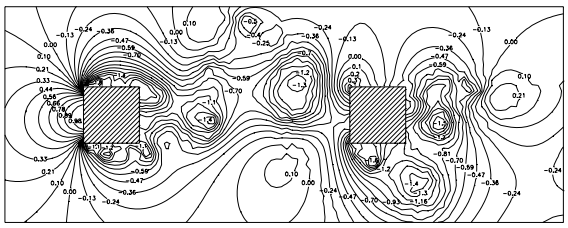

(g1) G = 4.0, t = 64.6

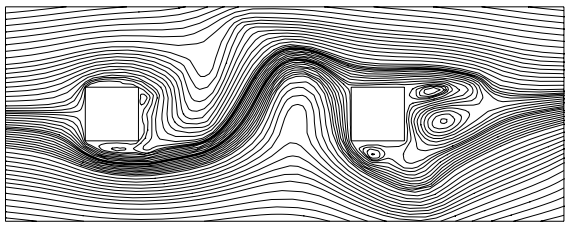

(g2) G = 4.0, t = 64.6

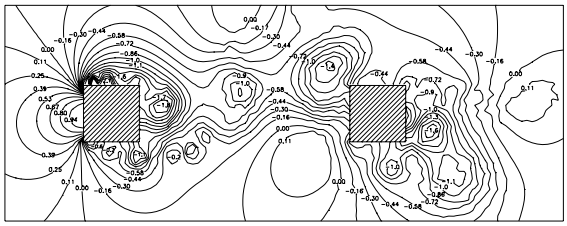

(h1) G = 4.0, t = 65.6

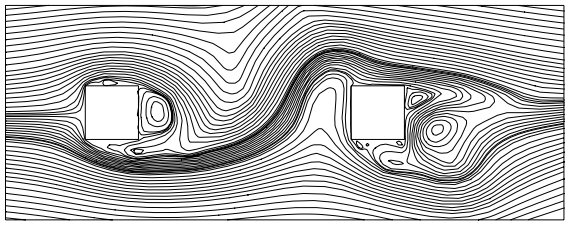

(h2) G = 4.0, t = 65.6

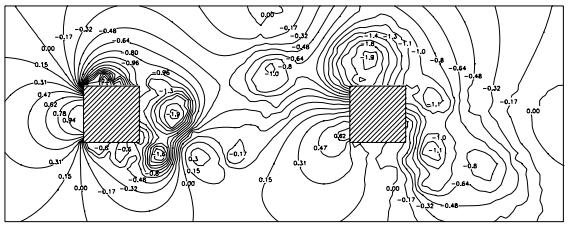

(i1) G = 4.0, t = 66.6

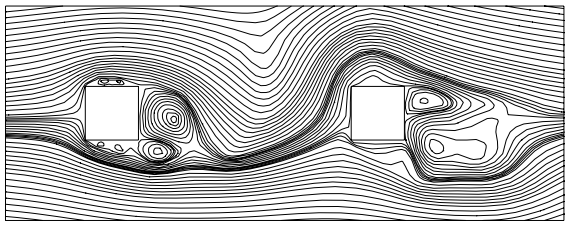

(i2) G = 4.0, t = 66.6

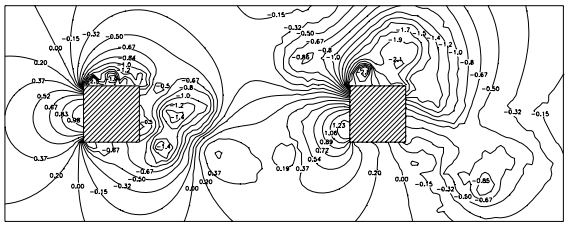

(j1) G = 4.0, t = 67.6

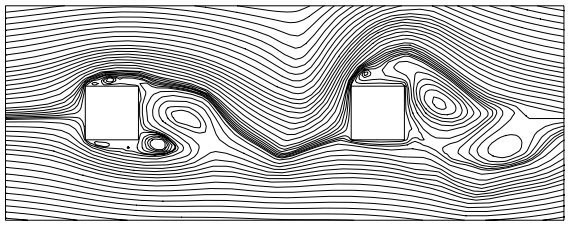

(j2) G = 4.0, t = 67.6

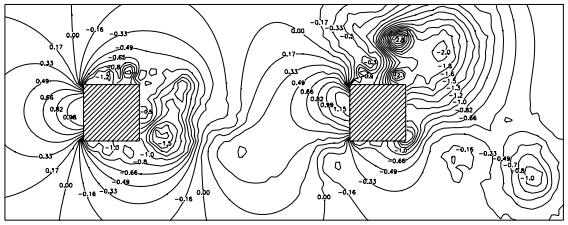

(k1) G = 4.0, t = 68.6

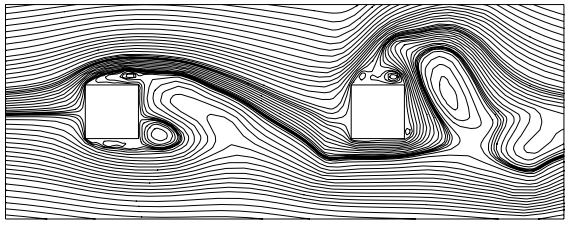

(k2) G = 4.0, t = 68.6

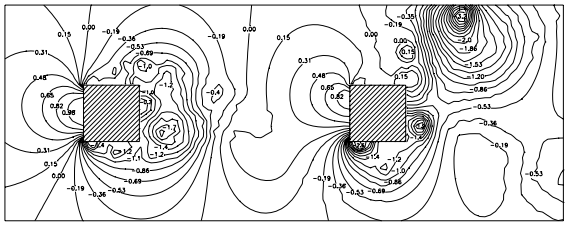

(l1) G = 4.0, t = 69.6

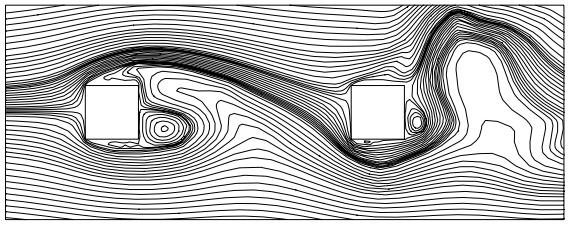

(l2) G = 4.0, t = 69.6

Figure 8.48. Cont'd.

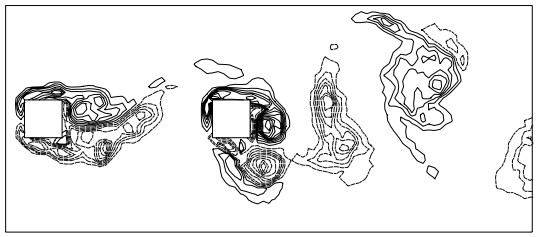

(a) G = 4.0, t = 58.6

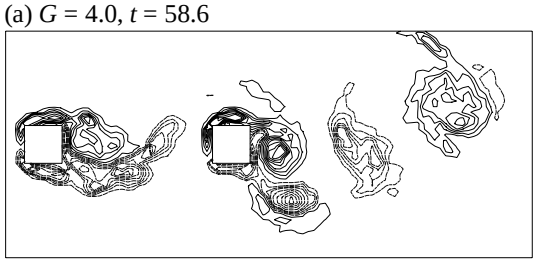

(b) G = 4.0, t = 59.6

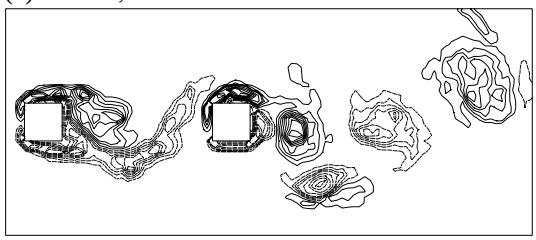

(c) G = 4.0, t = 60.6

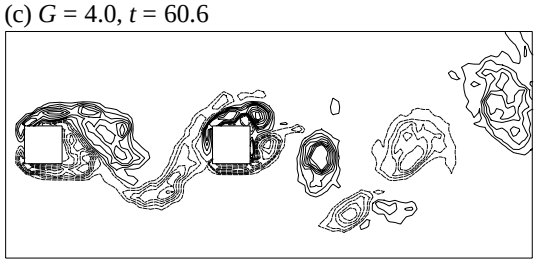

(d) G = 4.0, t = 61.6

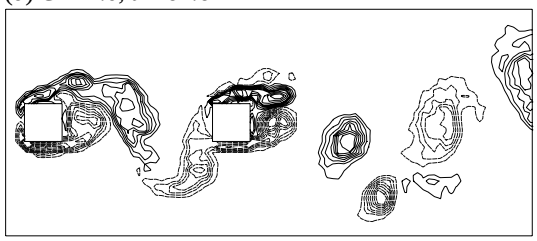

(e) G = 4.0, t = 62.6

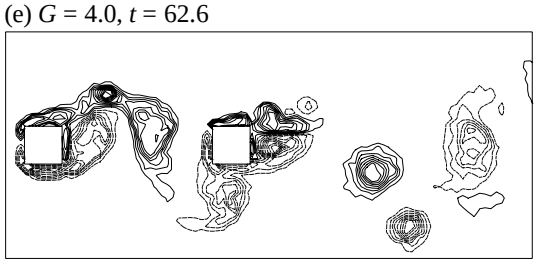

(f) G = 4.0, t = 63.6

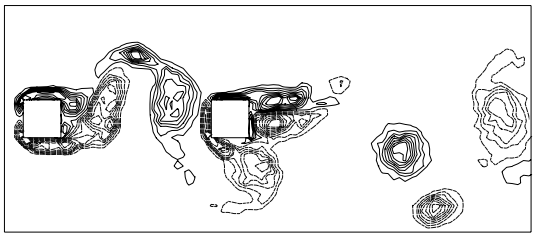

(g) G = 4.0, t = 64.6

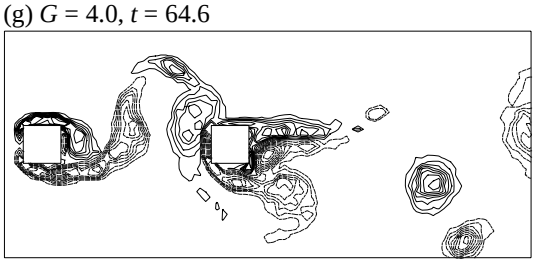

(h) G = 4.0, t = 65.6

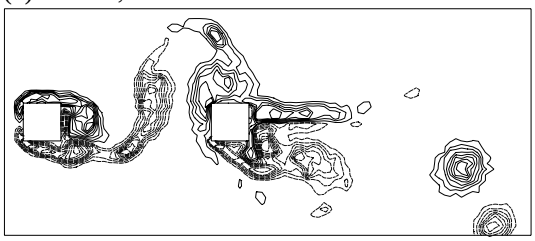

(i) G = 4.0, t = 66.6

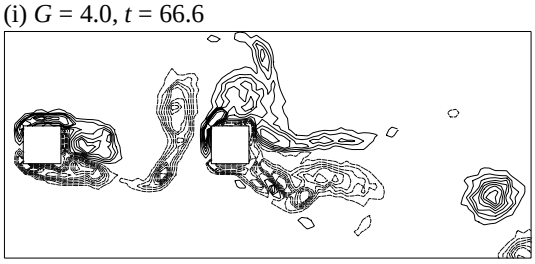

(j) G = 4.0, t = 67.6

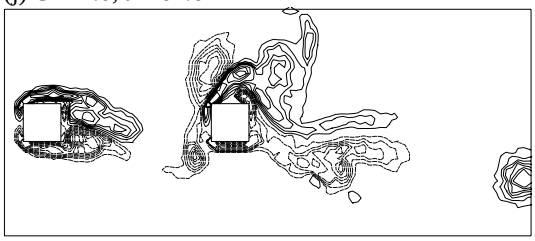

(k) G = 4.0, t = 68.6

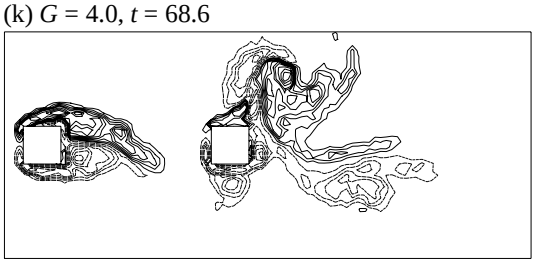

(l) G = 4.0, t = 69.6

Figure 8.49. Vorticity contours in fully-developed flow over the ($C1$ = 1, $C2$ = 1, G = 4.0) array.

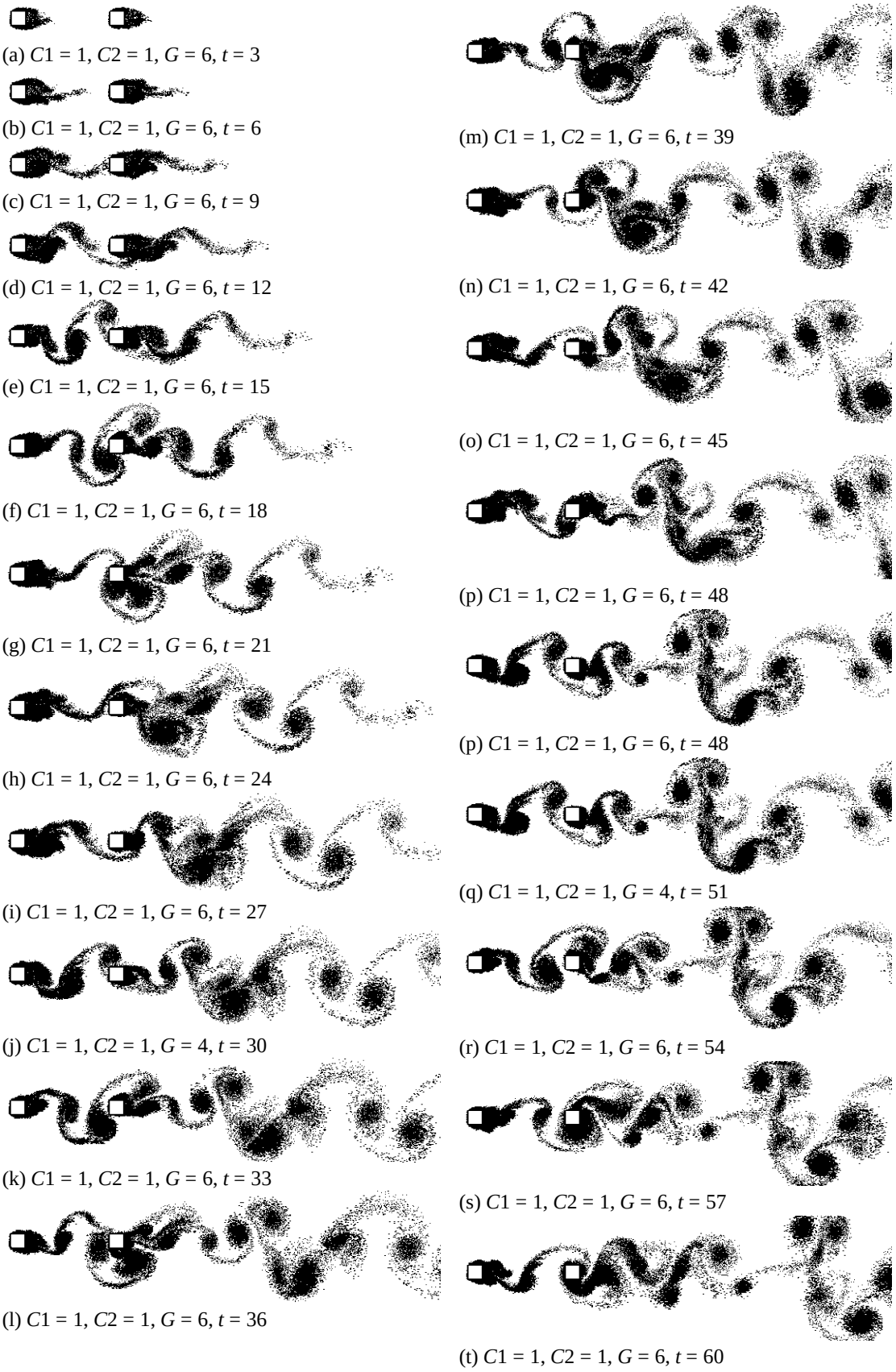

(a) $C1 = 1$, $C2 = 1$, $G = 6$, $t = 3$

(b) $C1 = 1$, $C2 = 1$, $G = 6$, $t = 6$

(c) $C1 = 1$, $C2 = 1$, $G = 6$, $t = 9$

(d) $C1 = 1$, $C2 = 1$, $G = 6$, $t = 12$

(e) $C1 = 1$, $C2 = 1$, $G = 6$, $t = 15$

(f) $C1 = 1$, $C2 = 1$, $G = 6$, $t = 18$

(g) $C1 = 1$, $C2 = 1$, $G = 6$, $t = 21$

(h) $C1 = 1$, $C2 = 1$, $G = 6$, $t = 24$

(i) $C1 = 1$, $C2 = 1$, $G = 6$, $t = 27$

(j) $C1 = 1$, $C2 = 1$, $G = 4$, $t = 30$

(k) $C1 = 1$, $C2 = 1$, $G = 6$, $t = 33$

(l) $C1 = 1$, $C2 = 1$, $G = 6$, $t = 36$

(m) $C1 = 1$, $C2 = 1$, $G = 6$, $t = 39$

(n) $C1 = 1$, $C2 = 1$, $G = 6$, $t = 42$

(o) $C1 = 1$, $C2 = 1$, $G = 6$, $t = 45$

(p) $C1 = 1$, $C2 = 1$, $G = 6$, $t = 48$

(p) $C1 = 1$, $C2 = 1$, $G = 6$, $t = 48$

(q) $C1 = 1$, $C2 = 1$, $G = 4$, $t = 51$

(r) $C1 = 1$, $C2 = 1$, $G = 6$, $t = 54$

(s) $C1 = 1$, $C2 = 1$, $G = 6$, $t = 57$

(t) $C1 = 1$, $C2 = 1$, $G = 6$, $t = 60$

Figure 8.50. Elemental-vortex distributions in flow over the ($C1 = 1$, $C2 = 1$, $G = 6$) array, showing sequence of flow development from the impulsive start to the fully-developed state.

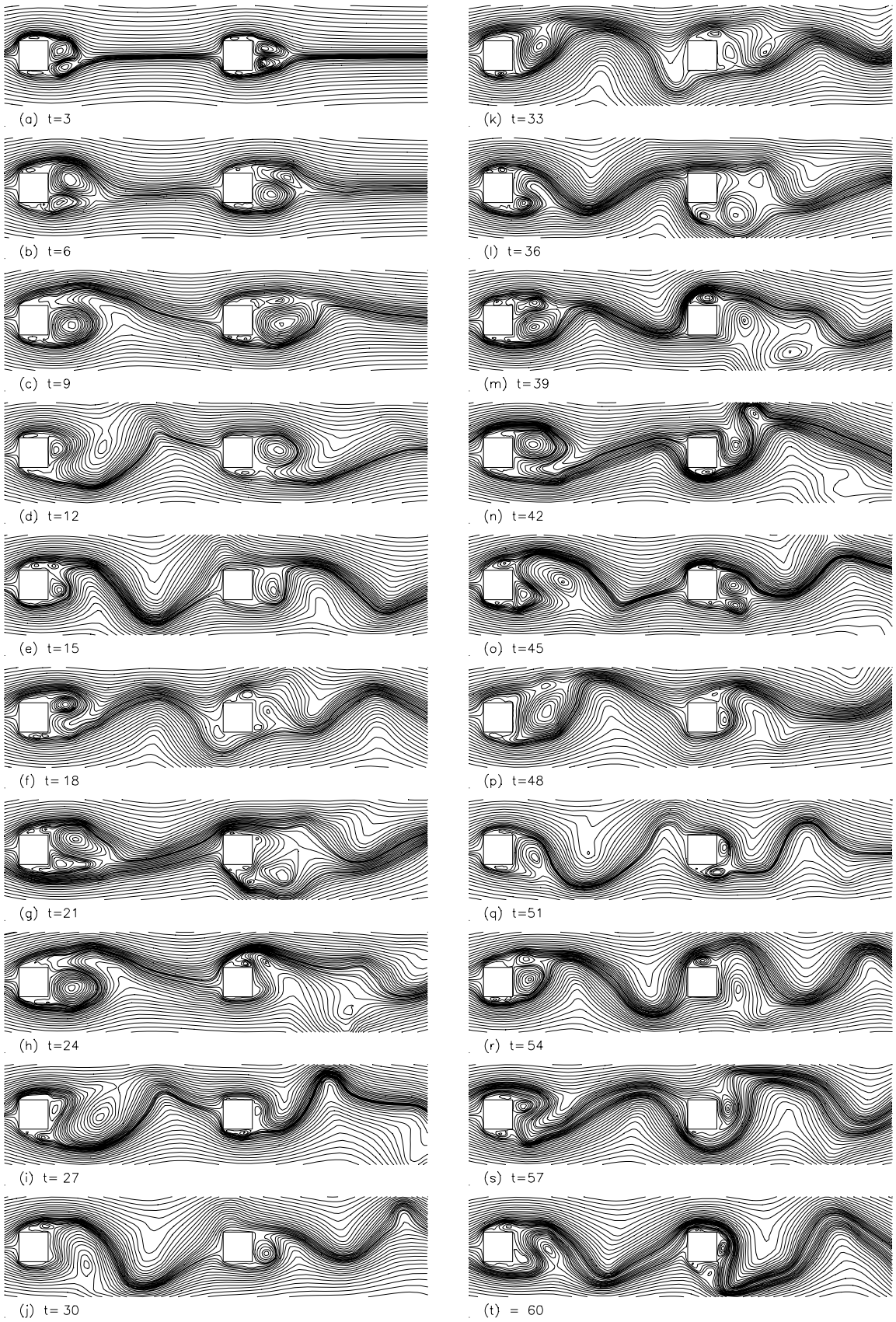

Figure 8.51. Streamline patterns in flow over the ($C1$ = 1, $C2$ = 1, G = 6) array, showing sequence of flow development from the impulsive start to the fully-developed state.

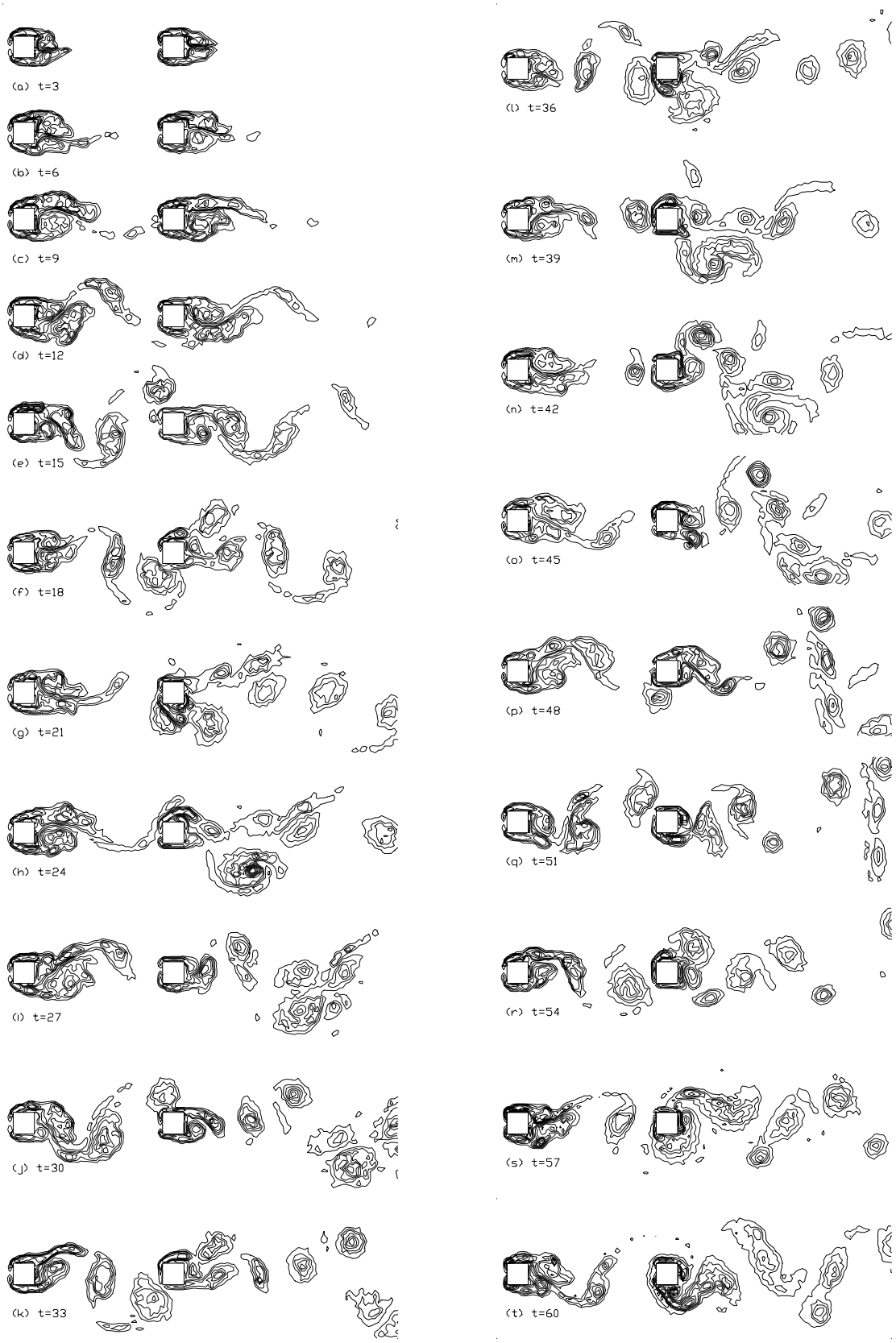

Figure 8.52. Vorticity contours in flow over the ($C1 = 1$, $C2 = 1$, $G = 6$) array, showing sequence of flow development from the impulsive start to the fully-developed state.

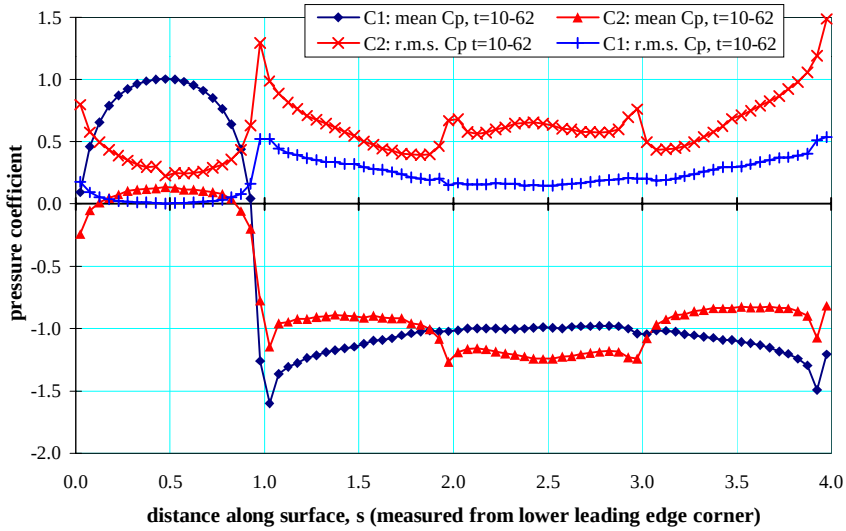

Figure 8.53. Calculated distributions of mean and r.m.s. pressure coefficients on the cylinders in the ($C1 = 1$, $C2 = 1$, $G = 3.0$) array.

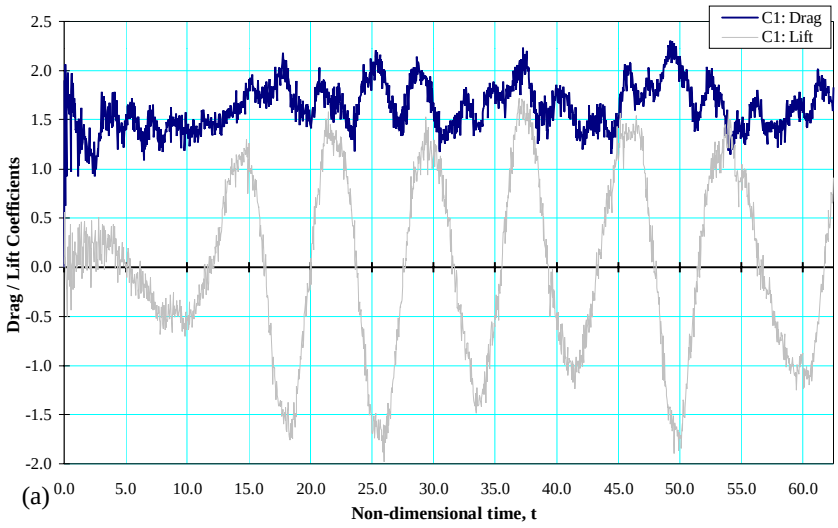

(a)

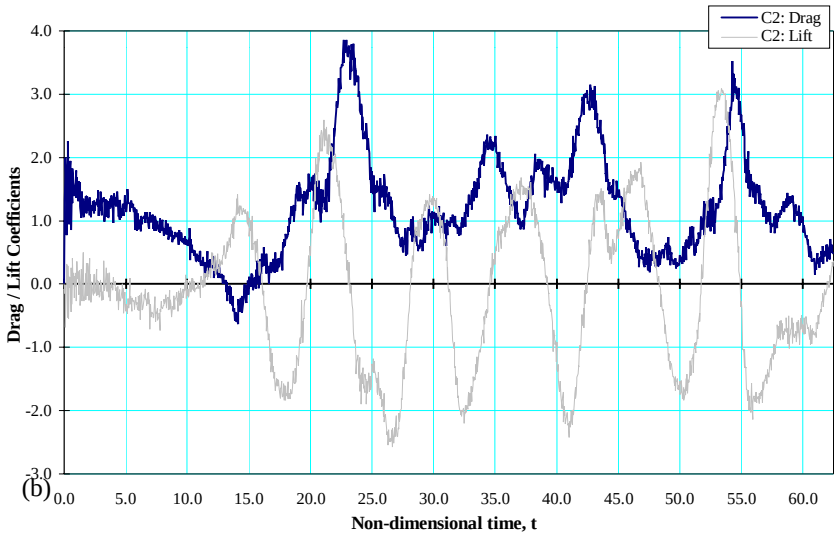

(b)

Figure 8.54. Time-histories of drag and lift on the ($C1 = 1$, $C2 = 1$, $G = 3.0$) array, (a) upstream plate, (b) downstream plate.

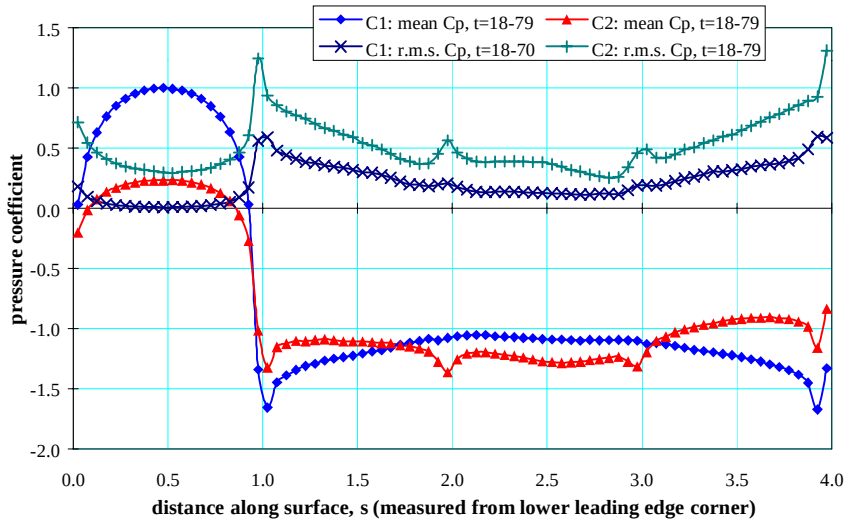

Figure 8.55. Calculated distributions of mean and r.m.s. pressure coefficients on the cylinders in the ($C1 = 1$, $C2 = 1$, $G = 4.0$) array.

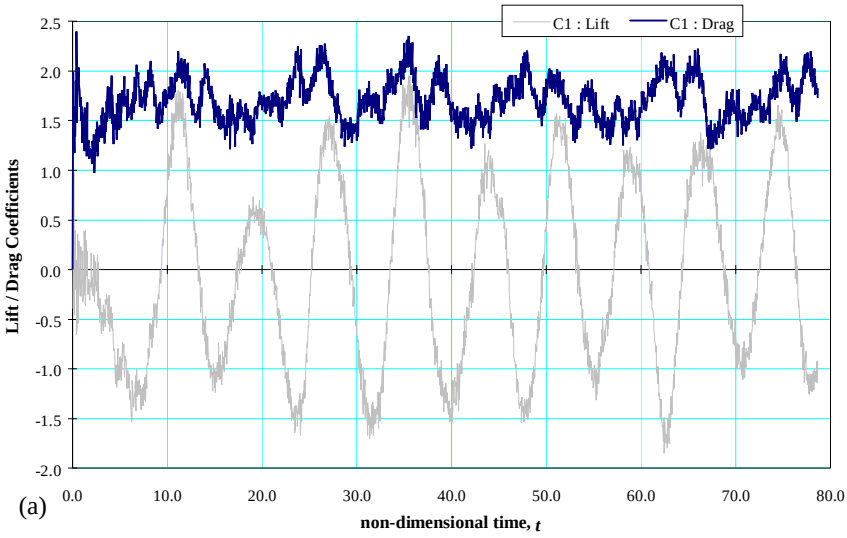

(a)

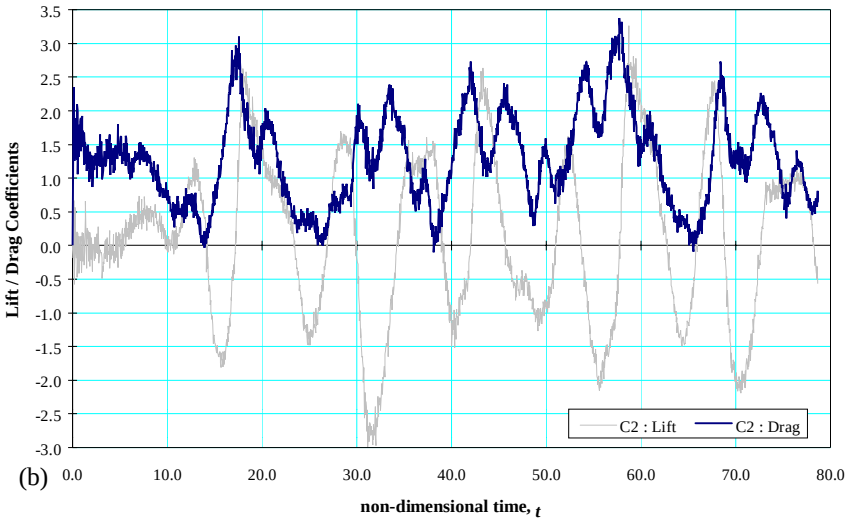

(b)

Figure 8.56. Time-histories of drag and lift on the ($C1 = 1$, $C2 = 1$, $G = 4.0$) array, (a) upstream plate, (b) downstream plate.

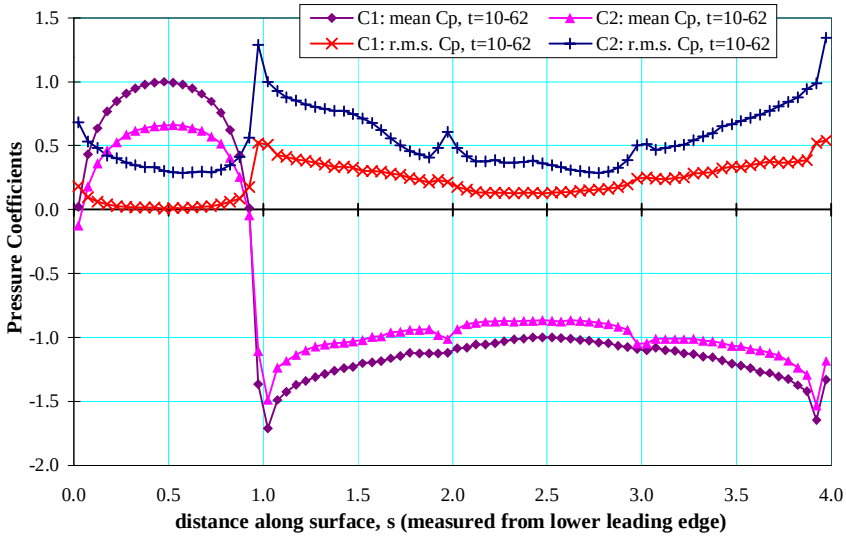

Figure 8.57. Calculated distributions of mean and r.m.s. pressure coefficients on the cylinders in the ($C1$ = 1, $C2$ = 1, G = 6.0) array.

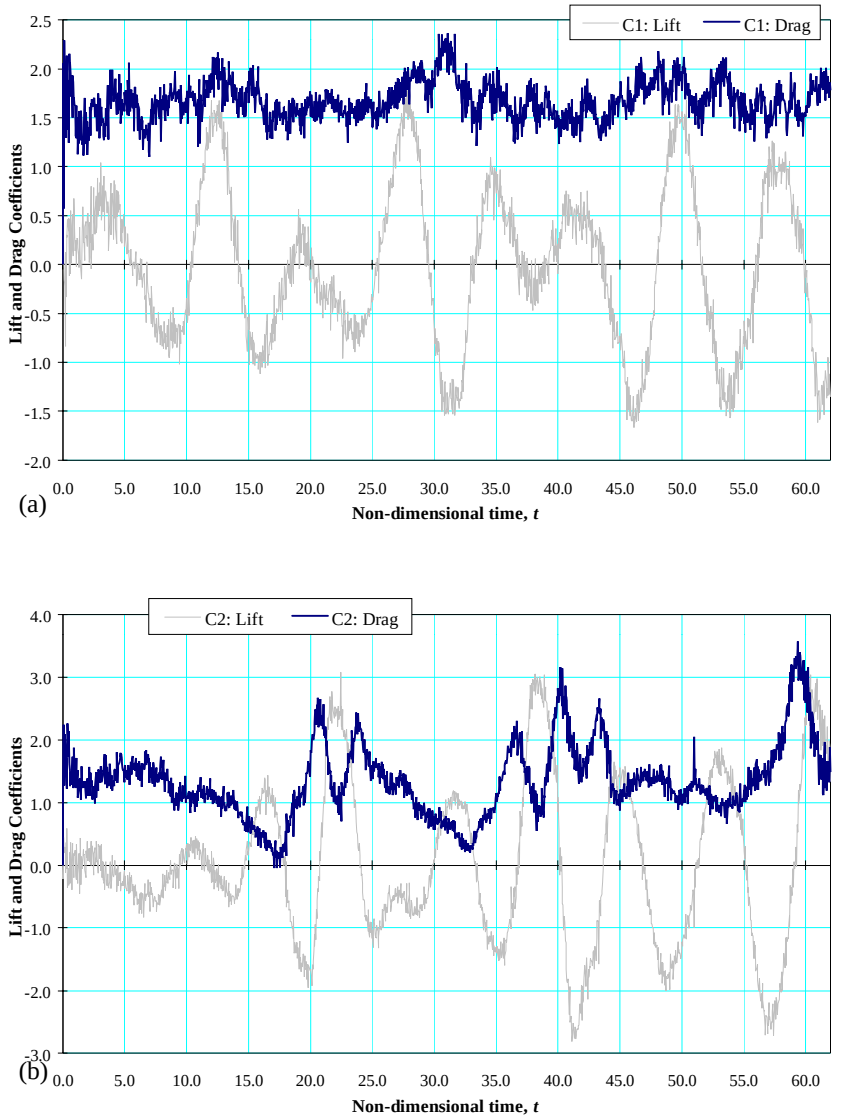

Figure 8.58. Time-histories of drag and lift on the ($C1$ = 1, $C2$ = 1, G = 6.0) array, (a) upstream plate, (b) downstream plate.

8.3.4 Flow in Transitional State, $2 < G < 3$

For gaps in the range $2 \leq G < 3$, the flow experiences transition from regime *E*1/*E*2 through regime *D*, and finally to regime *B*, as it develops. Calculations have been made for the arrays with $G = 2$ and $G = 2.5$. The elemental-vortex distributions, streamlines and vorticity patterns for these arrays are shown in Figs. 8.59–8.64.

The sequence of events through the transitional stage can be seen in the elemental-vortex, streamline patterns and vorticity contours for the $G = 2$ array. In the early stage of flow development ($t < 9$), a pair of counter-rotating vortices forms between the two cylinders. The process of formation of these trapped vortices in the gap is similar to the previous cases of flow in the *E*1/*E*2 regime ($G = 0.8$, 1.0 and 1.5). When periodic vortex-shedding becomes established on the downstream cylinder, the vortices in the gap oscillate in size at the frequency of the vortex shedding cycle ($9 < t \lesssim 33$). As is evident from the streamline patterns (Fig. 8.60), intermittent reattachment of separated shear layers from the upstream cylinder on the downstream cylinder is characteristic of the flow at this stage. The flow therefore exhibits similar characteristics to the trapped-vortex flow of the $G = 1.5$ array. The trapped-vortex configuration becomes unstable as the flow further evolves, and at $t = 18$–21, vortex shedding from the upstream cylinder begins. Immediately, following the onset of vortex shedding, the shed vortex occupies almost the whole of the space between the cylinders ($t = 30$, 33) but becomes rather smaller as time progresses. Transition to vortex-street flow in the gap becomes complete at $t \sim 42$. From this time onward, the streamline and vortex patterns clearly show vortex shedding from the upstream cylinder and vortex impingement on the downstream cylinder. The separated shear layers from the upstream cylinder, reattaching intermittently to the cylinder itself, impinge on the array at a position within the gap without reattaching to the downstream cylinder. The flow is now in the *B* regime, and remains so throughout the subsequent flow evolution.

A similar process of flow transition from the *E*1/*E*2 to *B* regime, with the same sequence of events, can be seen in the elemental-vortex, streamline and vorticity patterns (Figs. 8.48–8.50) for the $G = 2.5$ array. However, the onset of vortex shedding from the upstream cylinder and the completion of transition occur earlier on the $G = 2.5$ array, at $t = 9$–12 and $t \approx 24$ respectively compared with $t = 18$–21 and $t \approx 42$ for the $G = 2$ array. This reflects the fact that an entirely *B*-regime flow is being approached as *G* increases. The transition of gap flow from

trapped-vortex to vortex-street formation in the G = 2 and 2.5 arrays is highlighted in Figs. 8.71(g) and 8.71(h), which shows the streamlines as observed from a frame of reference moving at $U_{ref} = 0.8U_{\infty}$. The rotating flow associated with the vortex street in the gap when the flow is fully established can be clearly seen.

Surface-pressure distributions and time-histories of drag and lift coefficients are shown in Figs. 8.65–8.68. The variation of the force-coefficients on the cylinders with time reflects the flow development through the transition from the *E*1/*E*2 to the *B* regime. Shortly after the flow is started ($t \gtrsim 10$), the G = 2 array has a drag coefficient and an amplitude of lift and drag fluctuation on the upstream and downstream cylinders typical of the *E*1/*E*2 regime and similar to those of the G = 1.0 and G = 1.5 arrays. This is followed by a progressive increase of mean drag and force fluctuations to values typical of the *B* regime of flow. The behaviour of the G = 2.5 array is similar but with a much less extended period where the same parameters have the values of the *E*1/*E*2 regime. The mean pressure distribution on the upstream cylinder remains very much unchanged through the transition, except for a slight decrease in base pressure; this results in the drag on the upstream cylinder increasing from $C_{D1} \approx 1.5$ to about 1.7. The corresponding variation of pressure forces on the downstream cylinder is more dramatic: the pressure on the front face increases considerably while the base pressure decreases. Consequently, the drag on the downstream cylinder increases from a low (or even slightly negative) value to a high value with increased amplitude of fluctuation about the mean value of $C_{D2} \approx 1.5$.

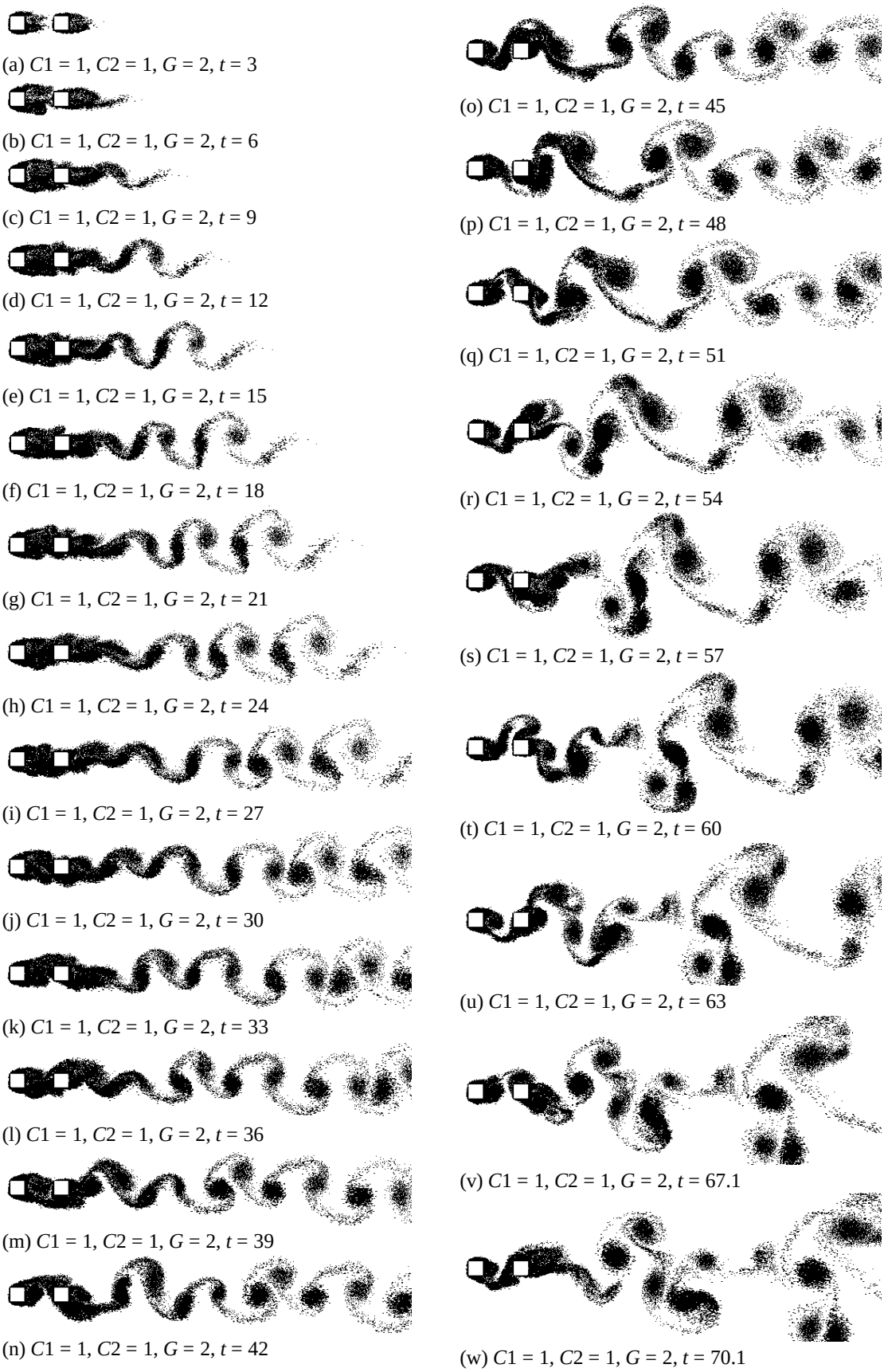

(a) $C1 = 1$, $C2 = 1$, $G = 2$, $t = 3$

(b) $C1 = 1$, $C2 = 1$, $G = 2$, $t = 6$

(c) $C1 = 1$, $C2 = 1$, $G = 2$, $t = 9$

(d) $C1 = 1$, $C2 = 1$, $G = 2$, $t = 12$

(e) $C1 = 1$, $C2 = 1$, $G = 2$, $t = 15$

(f) $C1 = 1$, $C2 = 1$, $G = 2$, $t = 18$

(g) $C1 = 1$, $C2 = 1$, $G = 2$, $t = 21$

(h) $C1 = 1$, $C2 = 1$, $G = 2$, $t = 24$

(i) $C1 = 1$, $C2 = 1$, $G = 2$, $t = 27$

(j) $C1 = 1$, $C2 = 1$, $G = 2$, $t = 30$

(k) $C1 = 1$, $C2 = 1$, $G = 2$, $t = 33$

(l) $C1 = 1$, $C2 = 1$, $G = 2$, $t = 36$

(m) $C1 = 1$, $C2 = 1$, $G = 2$, $t = 39$

(n) $C1 = 1$, $C2 = 1$, $G = 2$, $t = 42$

(o) $C1 = 1$, $C2 = 1$, $G = 2$, $t = 45$

(p) $C1 = 1$, $C2 = 1$, $G = 2$, $t = 48$

(q) $C1 = 1$, $C2 = 1$, $G = 2$, $t = 51$

(r) $C1 = 1$, $C2 = 1$, $G = 2$, $t = 54$

(s) $C1 = 1$, $C2 = 1$, $G = 2$, $t = 57$

(t) $C1 = 1$, $C2 = 1$, $G = 2$, $t = 60$

(u) $C1 = 1$, $C2 = 1$, $G = 2$, $t = 63$

(v) $C1 = 1$, $C2 = 1$, $G = 2$, $t = 67.1$

(w) $C1 = 1$, $C2 = 1$, $G = 2$, $t = 70.1$

Figure 8.59. Elemental-vortex distributions in flow over the ($C1 = 1$, $C2 = 1$, $G = 2$) array, showing flow development through the transition from the $E1/E2$, to D, and finally to the B regime.

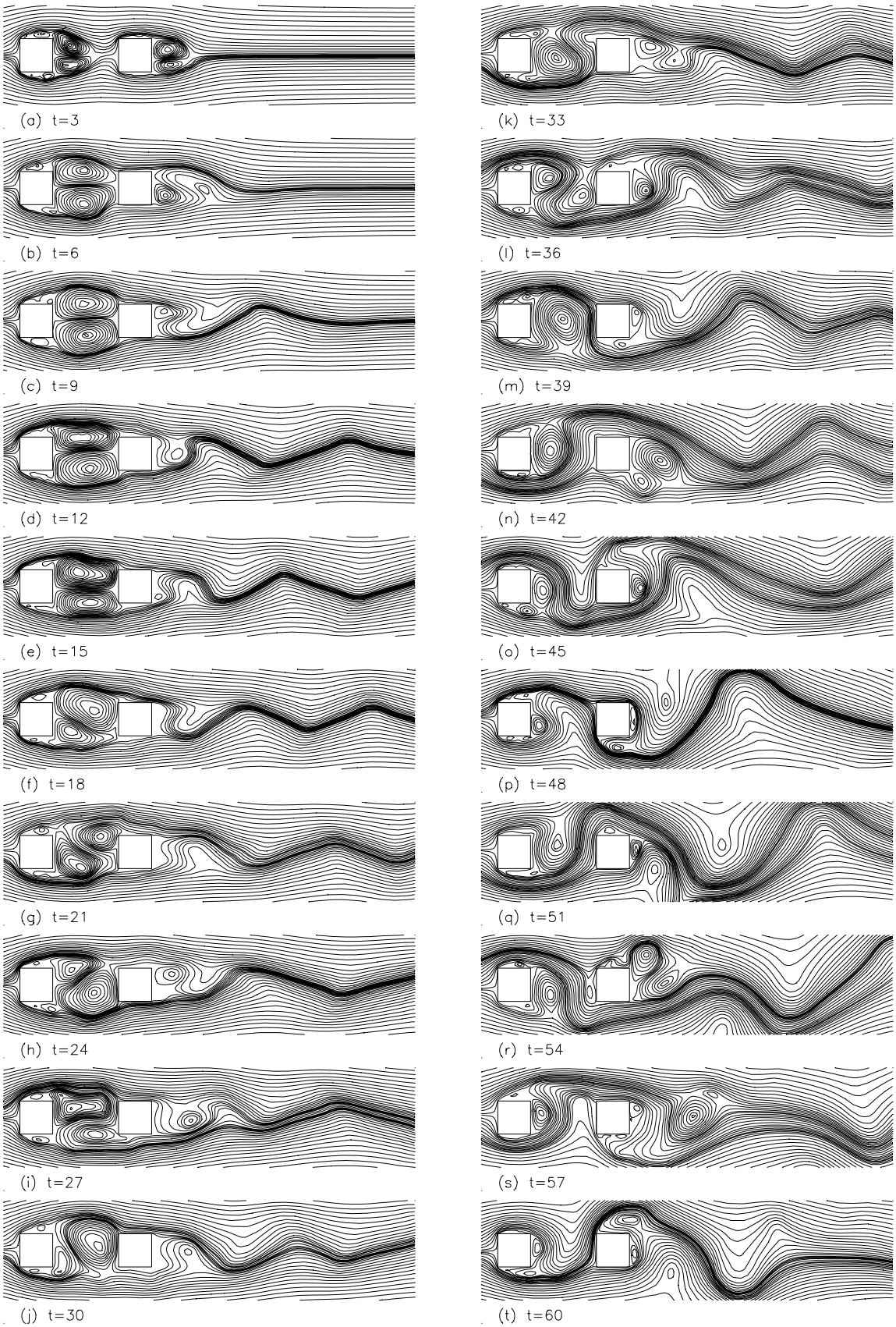

Figure 8.60. Streamline patterns in flow over the ($C1 = 1$, $C2 = 1$, $G = 2$) array, showing flow development through the transition from the $E1/E2$, to D, and finally to the B regime.

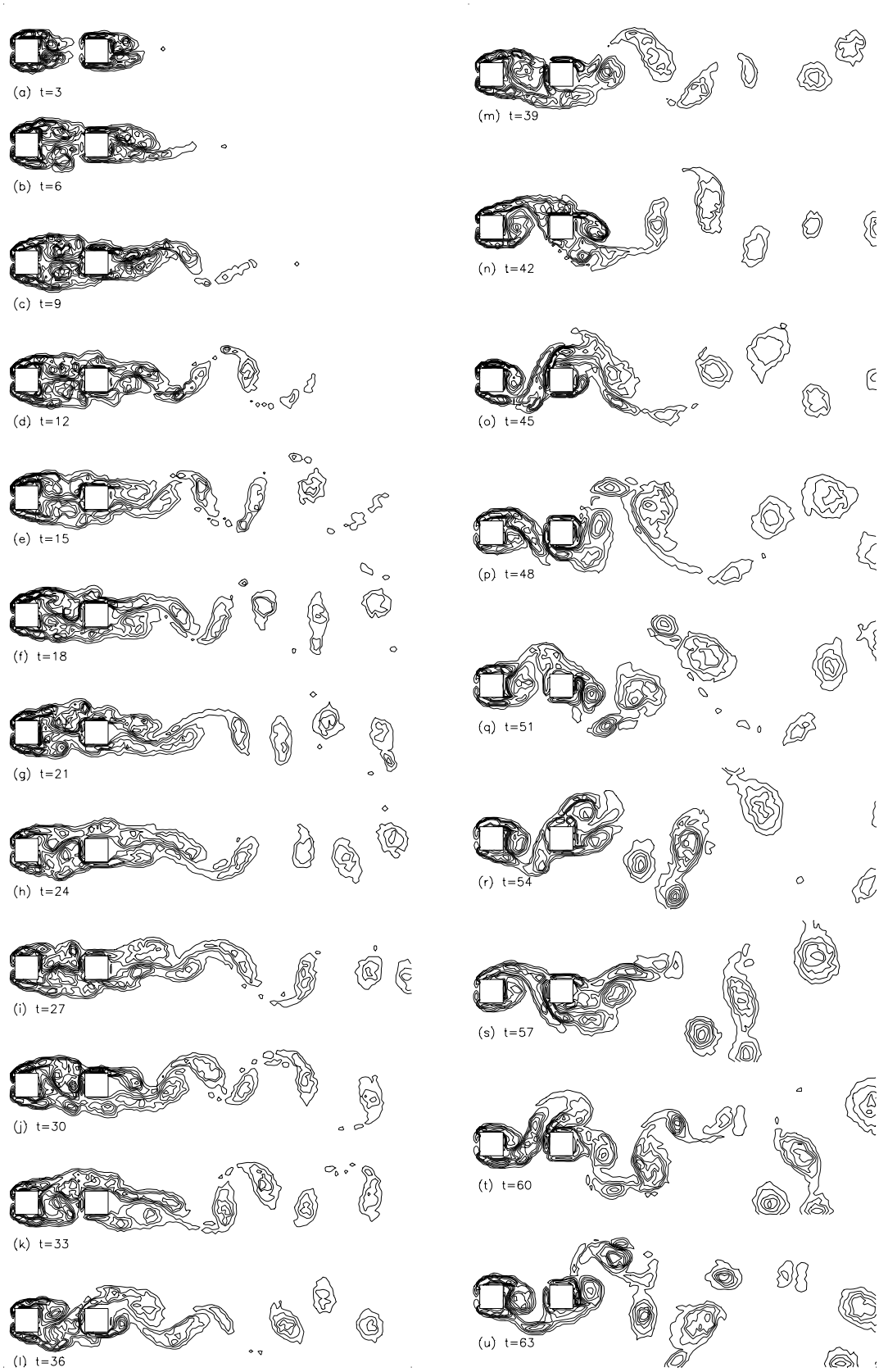

Figure 8.61. Vorticity contours in flow over the ($C1 = 1$, $C2 = 1$, $G = 2$) array, showing flow development through the transition from the *E*1/*E*2, to *D*, and finally to the *B* regime.

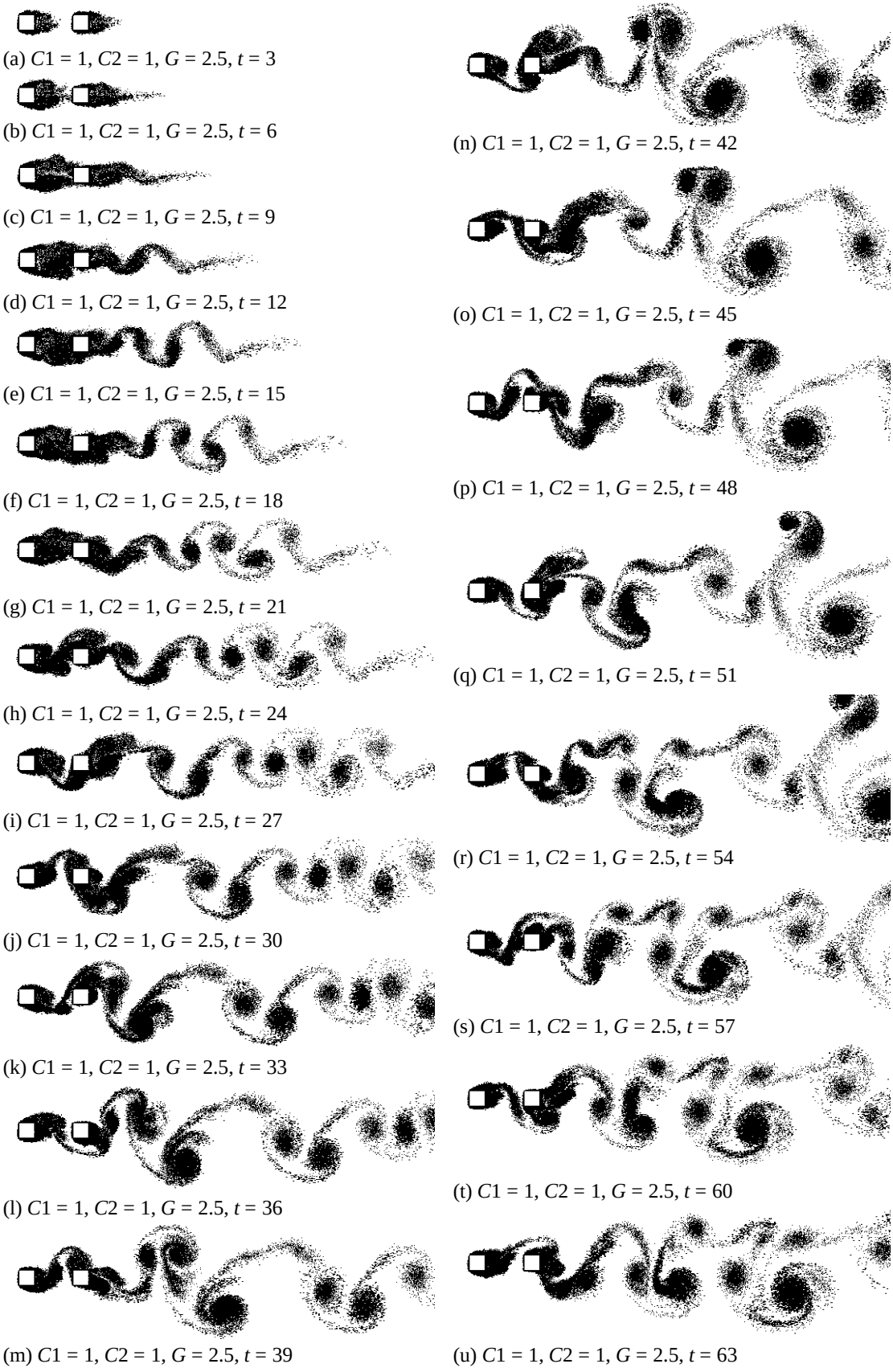

(a) $C1 = 1$, $C2 = 1$, $G = 2.5$, $t = 3$

(b) $C1 = 1$, $C2 = 1$, $G = 2.5$, $t = 6$

(c) $C1 = 1$, $C2 = 1$, $G = 2.5$, $t = 9$

(d) $C1 = 1$, $C2 = 1$, $G = 2.5$, $t = 12$

(e) $C1 = 1$, $C2 = 1$, $G = 2.5$, $t = 15$

(f) $C1 = 1$, $C2 = 1$, $G = 2.5$, $t = 18$

(g) $C1 = 1$, $C2 = 1$, $G = 2.5$, $t = 21$

(h) $C1 = 1$, $C2 = 1$, $G = 2.5$, $t = 24$

(i) $C1 = 1$, $C2 = 1$, $G = 2.5$, $t = 27$

(j) $C1 = 1$, $C2 = 1$, $G = 2.5$, $t = 30$

(k) $C1 = 1$, $C2 = 1$, $G = 2.5$, $t = 33$

(l) $C1 = 1$, $C2 = 1$, $G = 2.5$, $t = 36$

(m) $C1 = 1$, $C2 = 1$, $G = 2.5$, $t = 39$

(n) $C1 = 1$, $C2 = 1$, $G = 2.5$, $t = 42$

(o) $C1 = 1$, $C2 = 1$, $G = 2.5$, $t = 45$

(p) $C1 = 1$, $C2 = 1$, $G = 2.5$, $t = 48$

(q) $C1 = 1$, $C2 = 1$, $G = 2.5$, $t = 51$

(r) $C1 = 1$, $C2 = 1$, $G = 2.5$, $t = 54$

(s) $C1 = 1$, $C2 = 1$, $G = 2.5$, $t = 57$

(t) $C1 = 1$, $C2 = 1$, $G = 2.5$, $t = 60$

(u) $C1 = 1$, $C2 = 1$, $G = 2.5$, $t = 63$

Figure 8.62. Elemental-vortex distributions in flow over the ($C1 = 1$, $C2 = 1$, $G = 2.5$) array, showing flow development through the transition from the $E1/E2$, to D, and finally to the B regime.

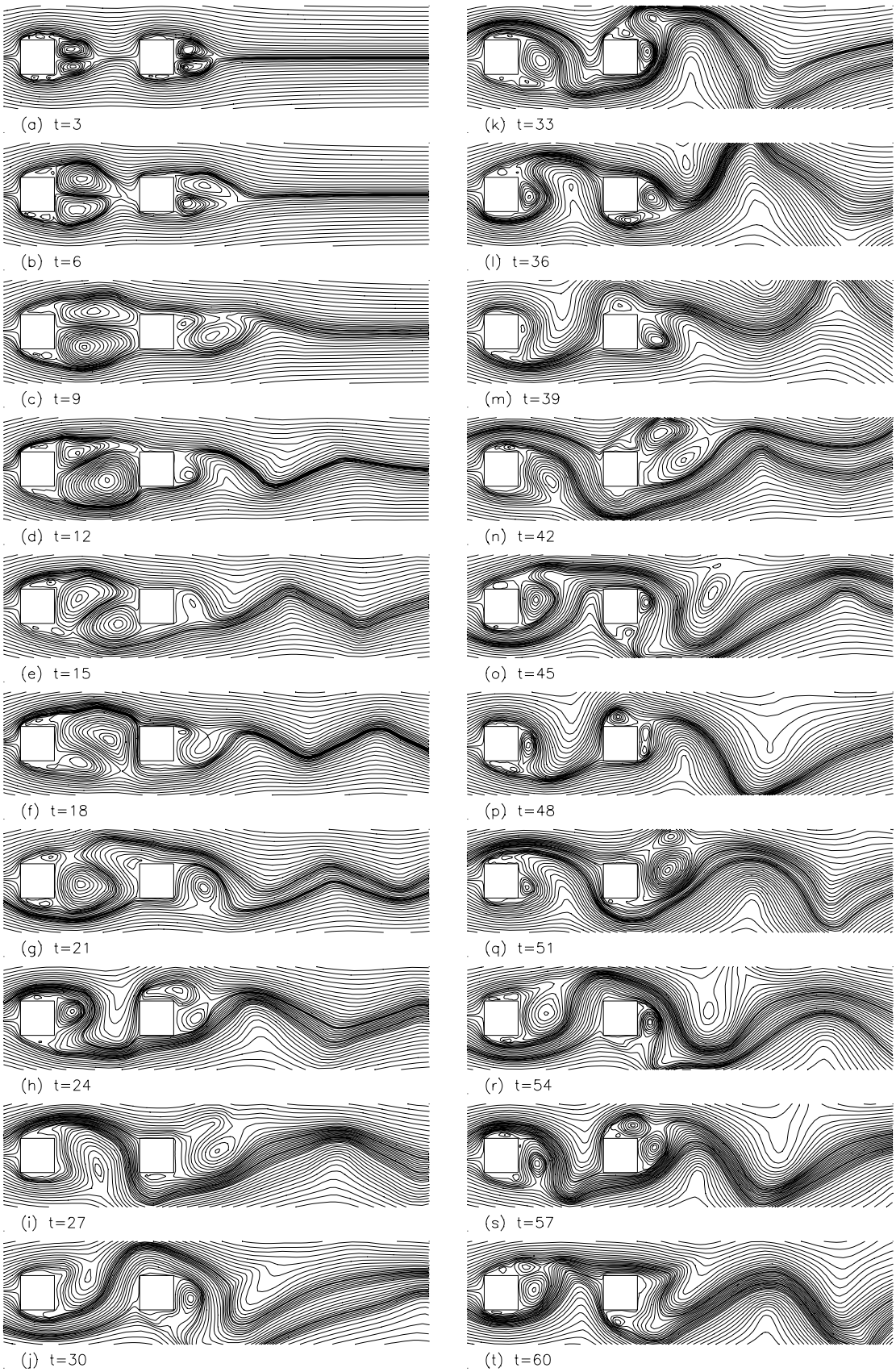

Figure 8.63. Streamline patterns in flow over the ($C1 = 1$, $C2 = 1$, $G = 2.5$) array, showing flow development through the transition from the *E*1/*E*2, to *D*, and finally to the *B* regime.

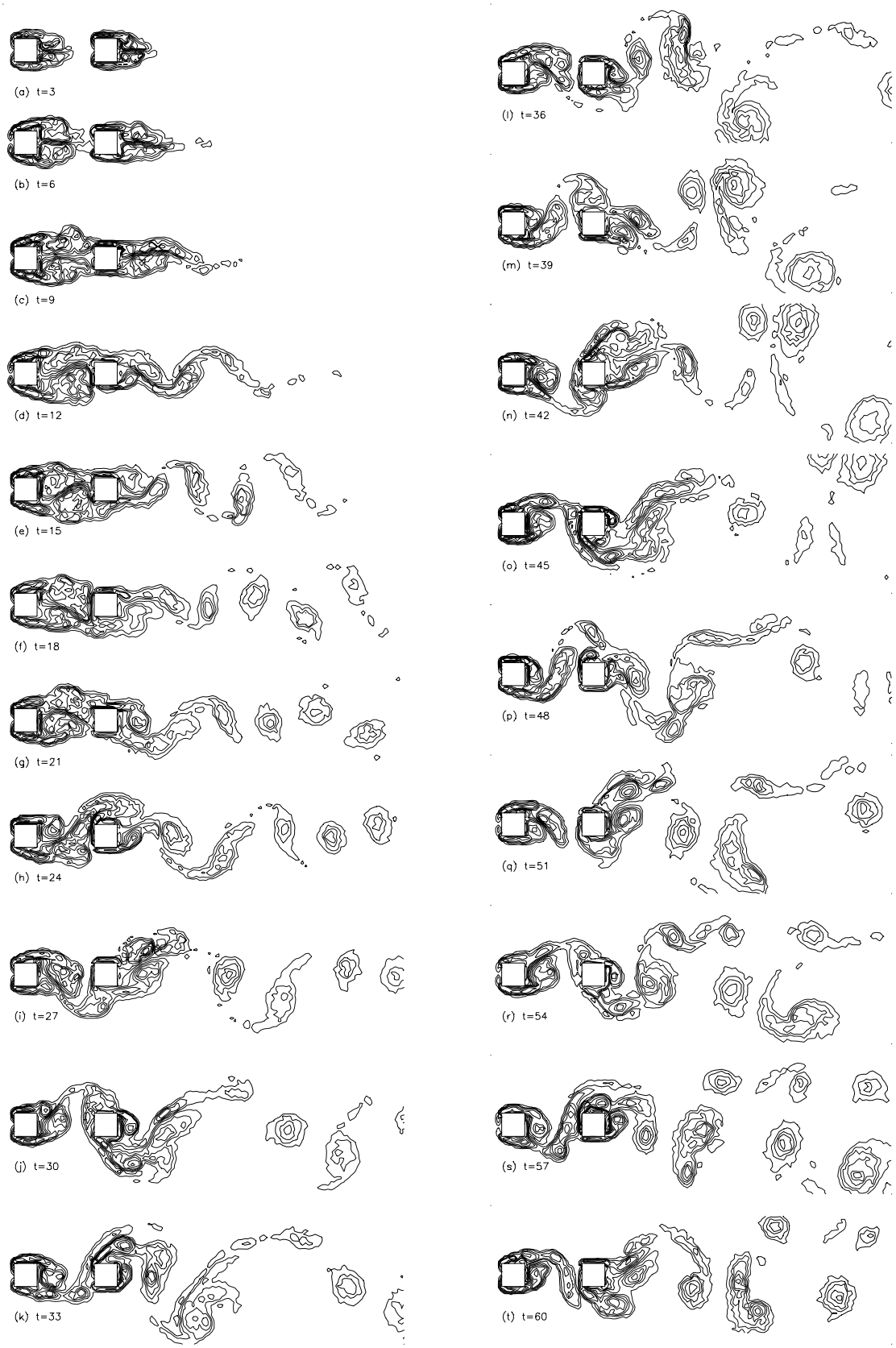

Figure 8.64. Vorticity contours in flow over the ($C1 = 1$, $C2 = 1$, $G = 2.5$) array, showing flow development through the transition from the *E*1/*E*2, to *D*, and finally to the *B* regime.

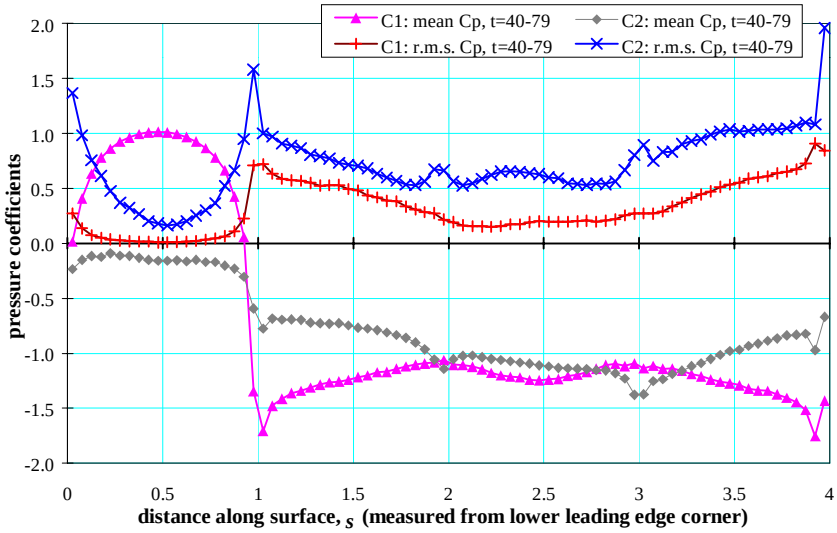

Figure 8.65. Calculated distributions of mean and r.m.s. pressure coefficients on the cylinders in the ($C1 = 1$, $C2 = 1$, $G = 2.0$) array.

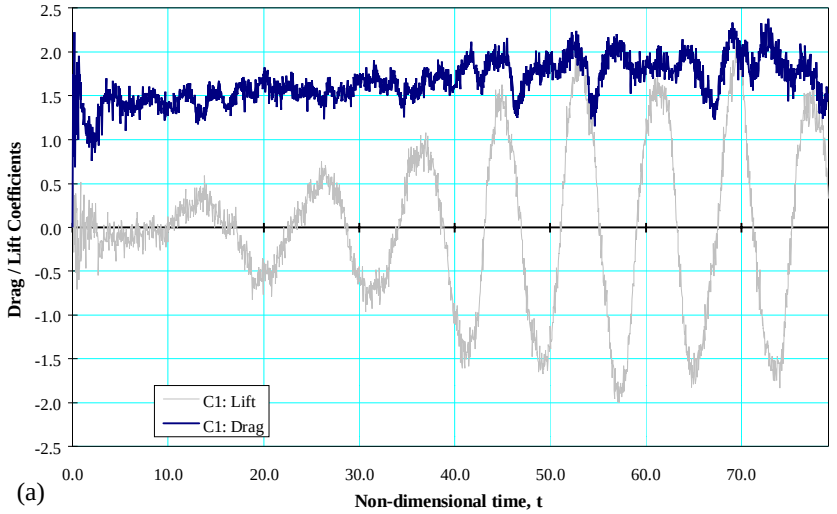

(a)

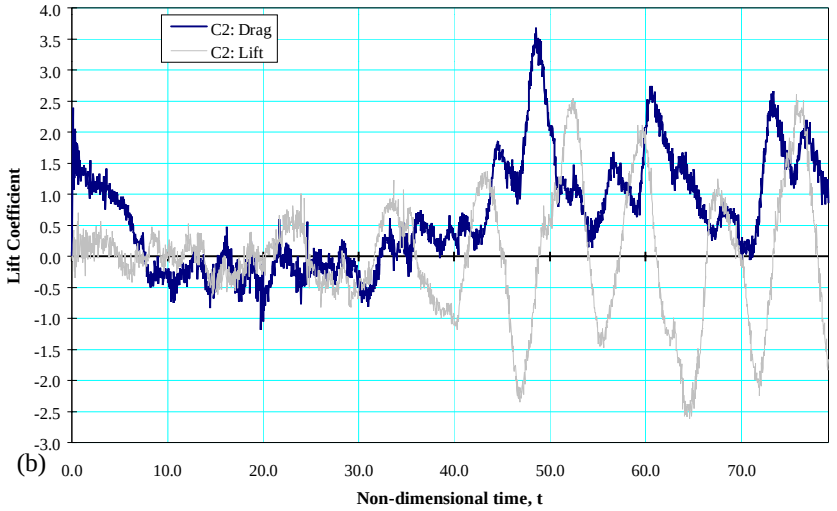

(b)

Figure 8.66. Time-histories of drag and lift on the ($C1 = 1$, $C2 = 1$, $G = 2.0$) array, (a) upstream plate, (b) downstream plate.

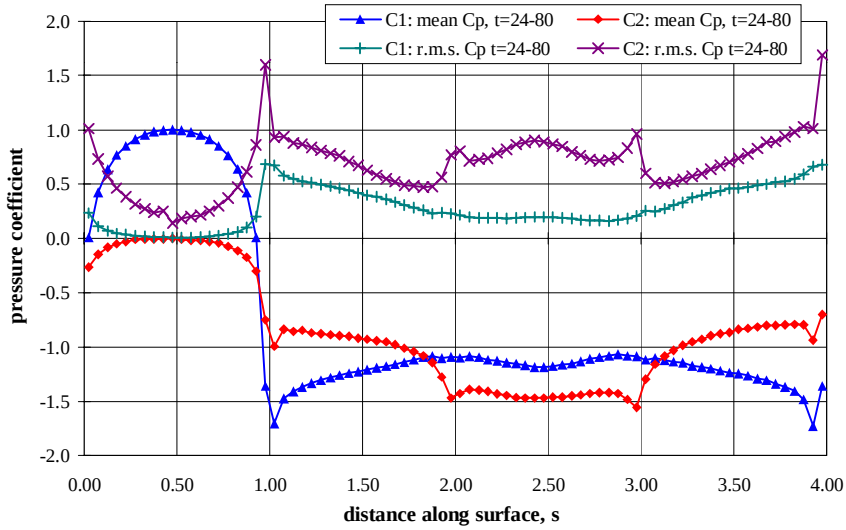

Figure 8.67. Calculated distributions of mean and r.m.s. pressure coefficients on the cylinders in the ($C1$ = 1, $C2$ = 1, G = 2.5) array.

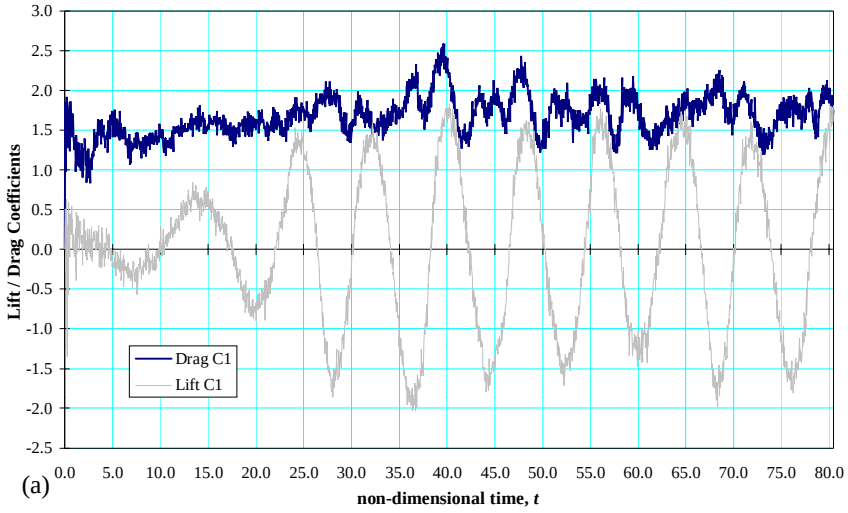

(a)

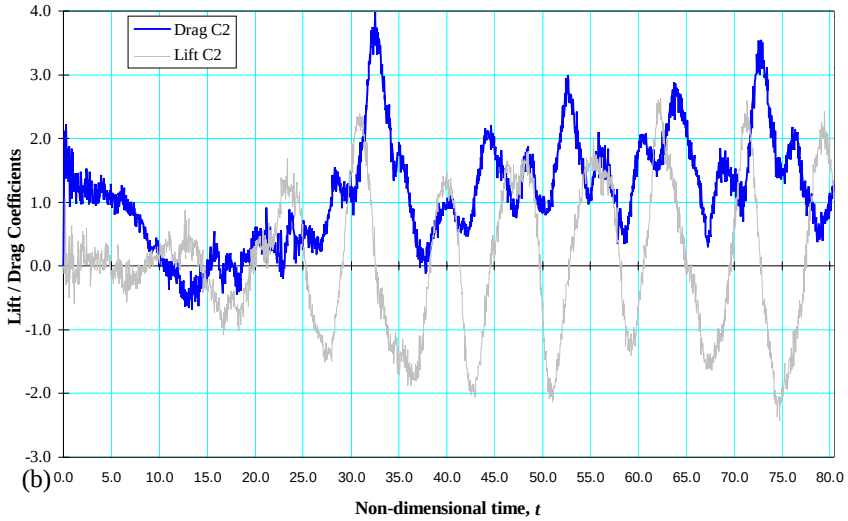

(b)

Figure 8.68. Time-histories of drag and lift on the ($C1$ = 1, $C2$ = 1, G = 2.5) array, (a) upstream plate, (b) downstream plate.

8.3.5 Dependence of Flow Parameters on the Gap-to-Thickness Ratio

The characteristic flow patterns and pressure forces associated with the various possible flow regimes on arrays of two square cylinders have been given in previous sections for particular values of the gap-to-thickness ratio G. In this section, the variation of flow parameters – base-pressure coefficients, drag coefficients and Strouhal numbers – for fully-developed flow with gap-to-thickness ratio over the range $0 \le G \le 6$ will be considered. Comparisons will be made with the experimental data of Sakamoto, Haniu and Obata [1987] and of Bull, Blazewicz and Pickles [1997]. However, it should be borne in mind that the Reynolds number of these tests Re_h was either 2.76×10^4 or 5.52×10^4 for the former and $Re_h \sim 1.7\times10^4$ for the latter. Hence, because of the dependence of these flow parameters on Reynolds number in some flow regimes, strict comparisons between calculation and experiment are not always possible. For example, the numerical simulation at $Re_h = 500$ predicts flow in regime B at large gaps ($G \gtrsim 3$) while the experiments of Bull *et al*. indicate flow in regime D. Calculated flow parameters are summarised in Table 8.1.

The effects of gap length on the flow as G increases from 0 to 6.0, are summarised in the streamline patterns viewed in a frame of reference moving at a velocity $U_{ref} = 0.8U_\infty$ shown in Fig. 8.71. In this frame of reference the progression of the flow in the gap, from cross-flow at $G = 0.1$, to trapped-vortex flow at $G \sim 0.5$, to a vortex street for $G \gtrsim 2.5$, and the accompanying changes in the vortex patterns in the wake of the array can be clearly seen.

Strouhal numbers of vortex-shedding, as determined from power spectra of lift fluctuations on the downstream cylinder (Fig. 8.69) and inspection of vorticity contours, are shown in Fig. 8.70(a). The general form of the numerically-predicted dependence of Strouhal number on G is similar to that found in both sets of experiments, and there is quite close agreement between calculated and experimental values for gaps with $G \gtrsim 2$. For $G < 2$, there are significant differences between prediction and experiment for the flow regime *F2* and for the smaller gaps in regime *E1/E2*. Whether the difference in this range of G values is a consequence of Reynolds number differences is of course not known. However, both calculation and experiment indicate rapid variation of Strouhal number with G in this range, particularly for G between zero and 0.2. The experimental data of both Sakamoto *et al*. [1987] and Bull *et al*. [1997] show a small discontinuity in Strouhal number at G between 2 and 3, accompanying the change of flow regime from $E1/E2$ (which corresponds to Sakamoto *et al*.'s

Region I, in which vortices are shed only from the downstream cylinder) to *B* (which corresponds to Sakamoto *et al.*'s Region II of synchronised vortex shedding from both cylinders). The calculations smooth out this discontinuity even though they correctly identify the change in flow regime from *E1*/*E2* to *B*.

As might be expected, the calculations show very little effect of changes in *G* and the flow regime on the pressure distribution on the leading and side faces of the upstream cylinder, and the base-pressure coefficient (Fig. 8.70(b)) does not vary greatly from the value $C_{pb1} \approx -1$; the overall distribution is essentially similar to the pressure distribution on a single square cylinder. The calculations predict a variation of base pressure with *G* that is similar to experiment in both magnitude and character, and correctly predict a discontinuity in the value of C_{pb1} for a gap in the range $2 < G < 3$. The surface-pressure distribution on the downstream cylinder is very much more dependent on flow regime, and the pressure on the leading face C_{pf2} is fairly uniform, departing significantly from the distribution on a single cylinder. The predicted variation of both C_{pf2} and C_{pb2} (Fig. 8.70(b)), which determine the drag on the cylinder, is again of a similar character to that observed experimentally, including the discontinuity for *G* between 2 and 3. Notable is the change in C_{pf2} from a negative to a positive value at the discontinuity, which is associated with the change from the *E*1/*E*2 to the *B* regime of flow.

The drag coefficients of the individual cylinders and the overall value for the array resulting from the numerical analysis, together with the experimental data of Sakamoto *et al*. [1987] are shown in Fig. 8.70(c). The calculated drag coefficients are determined by the pressures on the front and back faces of the cylinders, and so follow closely from the values shown in Fig. 8.70(b). The upstream cylinder, which has a pressure distribution resembling that on a single cylinder at all *G*, has a mean drag coefficient of $C_{D1} = 1.65–1.8$ (compared with $C_D \approx 1.8$ calculated for a single square cylinder at $Re_h = 500$, as in section 7.3). The mean drag coefficient C_{D2} of the downstream cylinder, as a consequence of the behaviour of C_{pb2}, increases from negative values in regimes *F*2 and *E*1/*E*2 to positive values in regime *B* as the streamwise gap is lengthened. Furthermore, again as a result of C_{pb2} behaviour, the overall C_D in the *F*2 and *E*1/*E*2 regimes decreases with increasing *G* and is lower than that of a single cylinder with either $C = 1$ or $C = 2$. As the mutual influence between the cylinders diminishes, for large *G* values, each of the two cylinders behaves like a separate single cylinder, and the overall C_D approaches twice the value for a single square cylinder.

There are discontinuities in the drag coefficient values in the range $2 < G < 3$, corresponding to those in the base-pressure coefficients. The experimental values of Sakamoto *et al*. [1987] have similar discontinuities, even though, presumably due to differences in Reynolds number, the calculated and experimental drag coefficients themselves have significantly different values.

The rapid variation of Strouhal number with G for $G < 0.2$ has been remarked on previously. Table 8.1 indicates a similar sensitivity of the total drag coefficient to the establishment of a very small gap – a decrease in C_D from 1.72 to 1.41 as G is increased from zero to 0.1. The small gap produces apparently minor changes in the pressure distributions on the leading face of the upstream cylinder and the base of the downstream cylinder, which nevertheless result in a significant change in drag coefficient despite the broad similarity of the $G = 0$ and $G = 0.1$ pressure distributions.

G	C_{pb1}	C_{pf2}	C_{pb2}	C_{D1}	C_{D2}	C_D	St [b]
0 [a]	—	—	-0.78	1.80	—	1.72	0.14
0.1	-1.09	-1.08	-0.69	1.80	-0.39	1.41	0.193
0.2	-1.10	-0.97	-0.59	1.75	-0.40	1.35	0.195
0.5	-1.02	-0.88	-0.49	1.73	-0.43	1.30	0.19
0.8	-0.97	-0.85	-0.43	1.72	-0.47	1.24	0.175
1.0	-0.94	-0.82	-0.45	1.71	-0.44	1.26	0.16
1.5	-0.93	-0.75	-0.50	1.57	-0.35	1.22	0.135
2.0	-1.05	-0.10	-0.50	1.78	1.23	3.01	0.125
2.5	-1.12	0.01	-0.45	1.76	1.45	3.21	0.122
3.0	-1.0	0.18	-1.20	1.75	1.40	3.15	0.12
4.0	-1.0	0.31	-1.05	1.76	1.45	3.21	0.125
6.0	-1.0	0.70	-0.90	1.78	1.60	3.38	0.13

a Values quoted for $G = 0$ refer to flow parameters of single plate with $C = 2$, except that C_{D1} at $G = 0$ is the drag coefficient of a single square cylinder.

b Strouhal number of vortex shedding into the wake of the array.

Table 8.1. Computed results of pressure coefficients, drag coefficients and Strouhal numbers for flow over tandem array of two square cylinders, at the G values considerd in the present calculations. Note that the C_p values are those at the mid-points of the relevant faces.

8.3.6 Concluding Remarks on the Calculations of Flow Over Arrays of Two Square Cylinders

Numerical simulations of the flow over tandem arrays of two square cylinders at Re_h = 500, for gap-to-thickness ratios of G = 0.1, 0.2, 0.5, 0.8, 1.0, 1.5, 2.0, 2.5, 3.0, 4.0 and 6.0, lead to the identification of several different flow regimes determined by the gap-to-thickness ratio. They provide details of the different interactions between the gap flow and the downstream cylinder in the various flow regimes, and the influence of the interaction on the character of the vortex wake of the whole array. The dependence of the calculated flow regimes, flow patterns and flow parameters on gap-to-thickness ratio is in general accord with the experimental results obtained by Sakamoto, Haniu and Obata [1987] and of Bull, Blazewicz and Pickles [1997], even though the experiments were made at considerably higher Reynolds numbers.

At very small gaps, $G < 0.5$, the flow (in the *F*2 regime) features intermittent trailing-edge separation and reattachment on the downstream cylinder, and the formation of a regular Karman street behind the array. There is flow through the gap which undergoes periodic reversal in phase with the vortex shedding cycle. For gaps in the range $0.5 < G < 2$, the flow (in the *E*1/*E*2 regime) is characterised by intermittent reattachment on the downstream cylinder and intermittent separation from the leading and trailing edges of the downstream cylinder. A pair of counter-rotating vortices forms in the gap; these vortices oscillate in size at the frequency of vortex shedding of the array.

For arrays with $G > 3$, the flow (in regime *B*) is one in which the shear layers separating from the leading corners of the upstream cylinder reattach to the side-faces of the upstream cylinder or impinge on the array at a position within the gap, and a vortex street is formed in the gap. Impingement of the vortex street on the downstream cylinder is responsible for the formation of secondary vortices on that cylinder, and also for the greater pressure fluctuation on its leading face than at smaller gaps. For $2 < G < 3$, the flow is in a transitional state between regimes *E*1/*E*2 and *B*. In general, significant changes in flow parameters are associated with the change in flow regime; some flow parameters – in particular the pressure coefficients and drag coefficients – exhibit a discontinuity at a gap in this range.

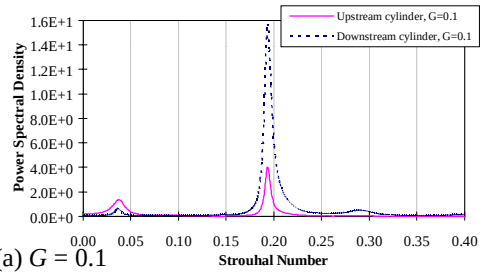

(a) G = 0.1

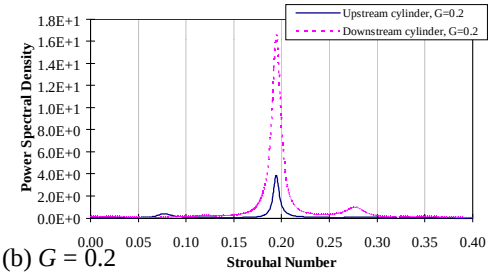

(b) G = 0.2

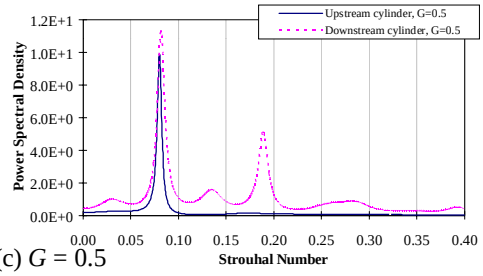

(c) G = 0.5

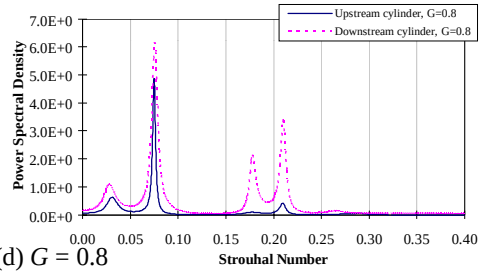

(d) G = 0.8

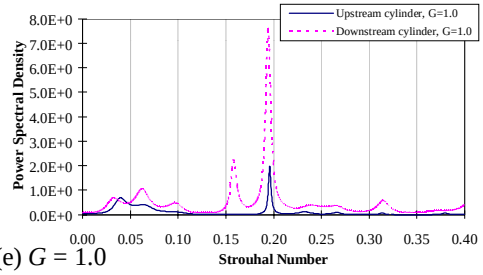

(e) G = 1.0

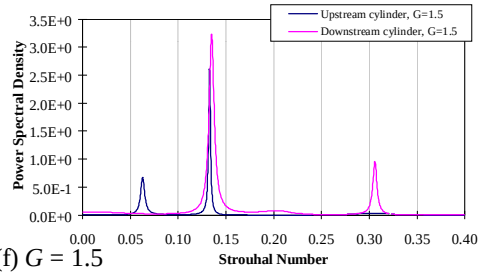

(f) G = 1.5

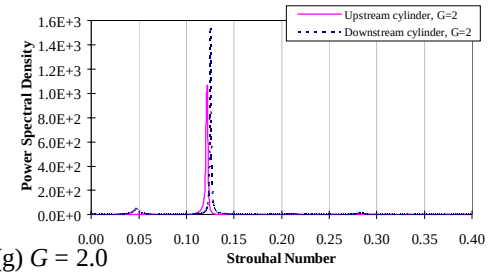

(g) G = 2.0

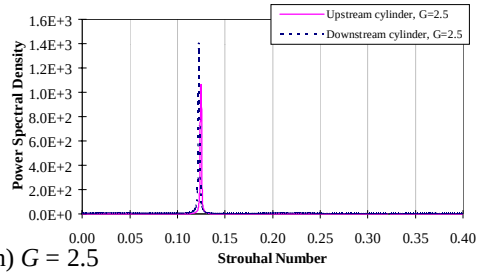

(h) G = 2.5

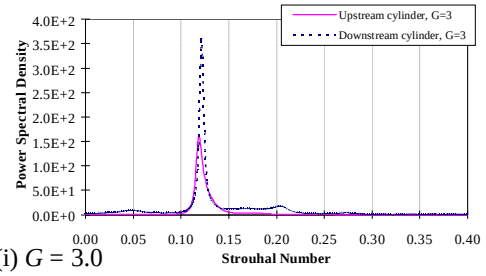

(i) G = 3.0

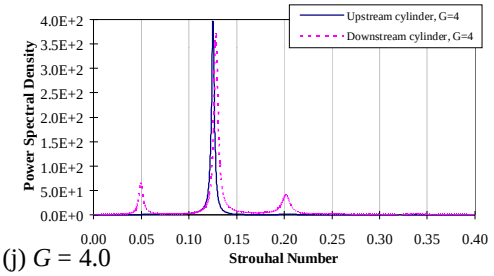

(j) G = 4.0

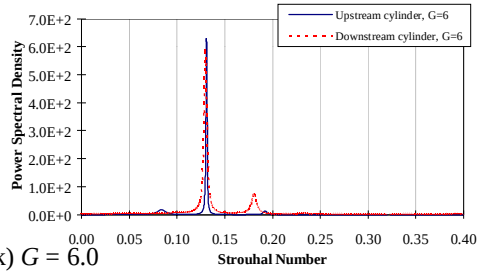

(k) G = 6.0

Figure 8.69. Power spectra of fluctuating lift of tandem arrays of two square cylinders with various gap-to-thickness ratio in the range $0.1 \leq G \leq 6.0$.

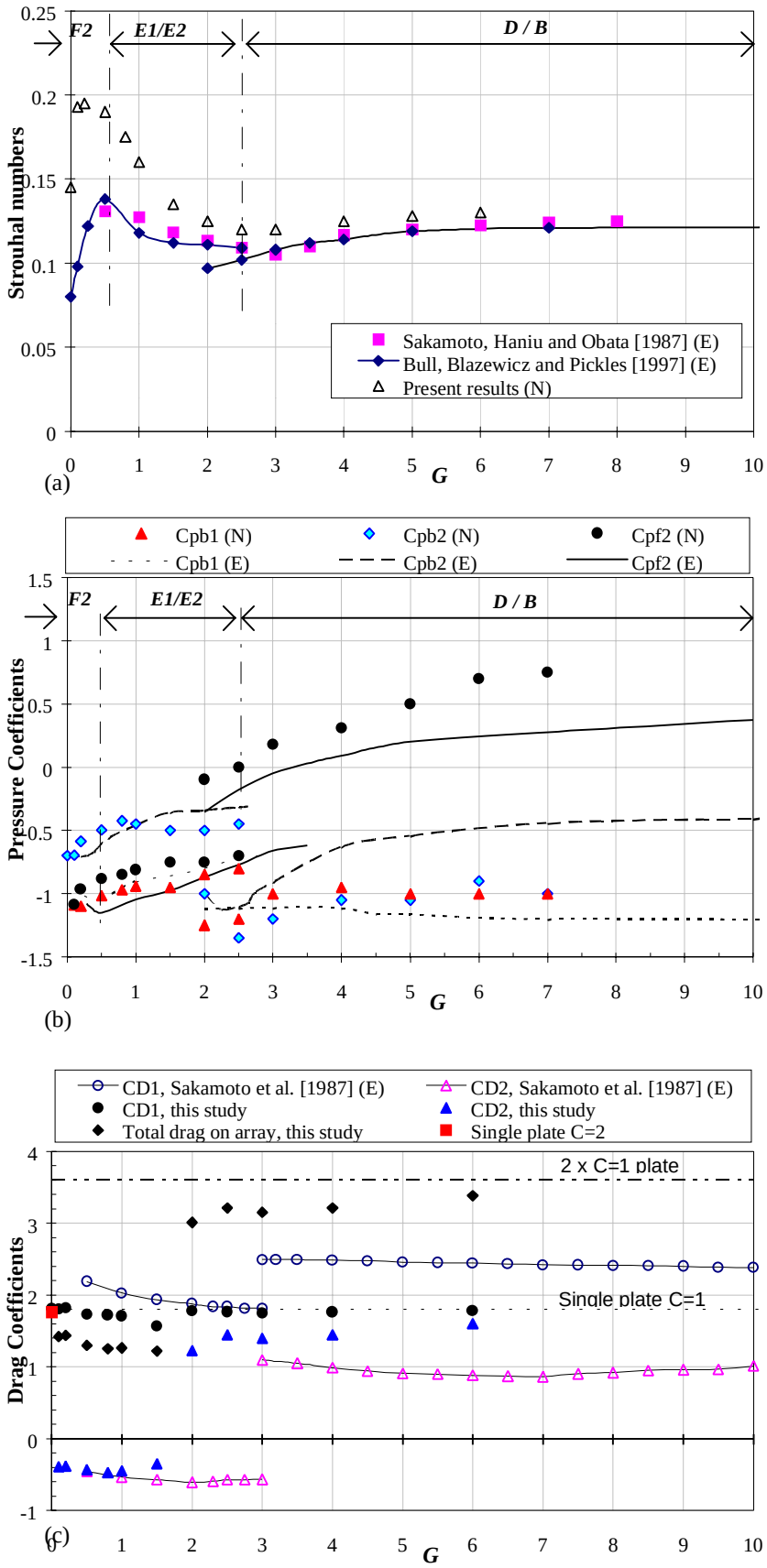

Figure 8.70. Variation of flow parameters with gap-to-thickness ratio of tandem array of two square cylinders: (a) Strouhal numbers of vortex shedding into the wake of the array, (b) pressure coefficients and (c) drag coefficients.

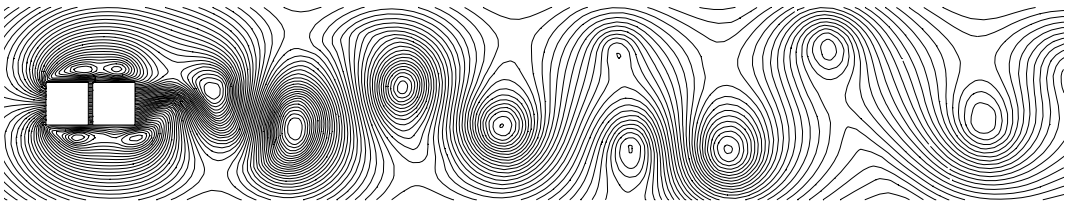

(a) G = 0.1, t = 81, flow regime $F2$.

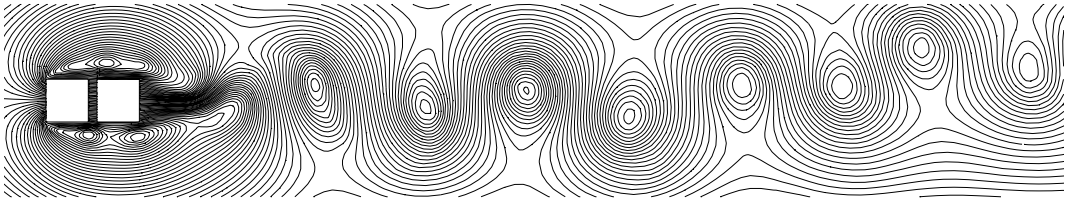

(b) G = 0.2, t = 98, flow regime $F2$.

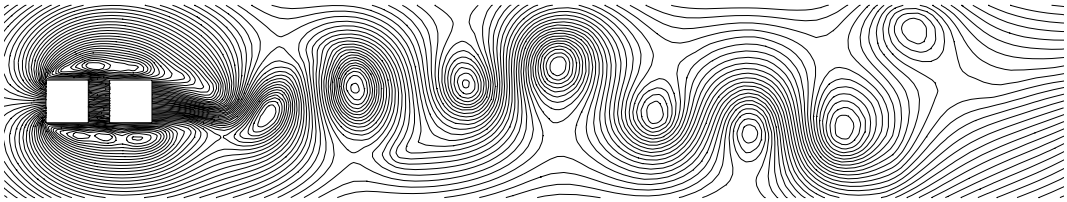

(c) G = 0.5, t = 98, flow regime $E1/E2$.

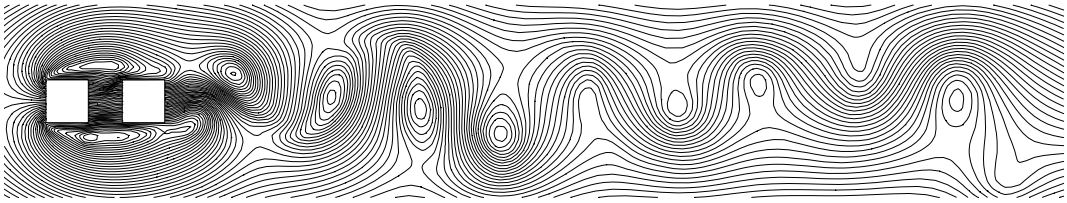

(d) G = 0.8, t = 81, flow regime $E1/E2$.

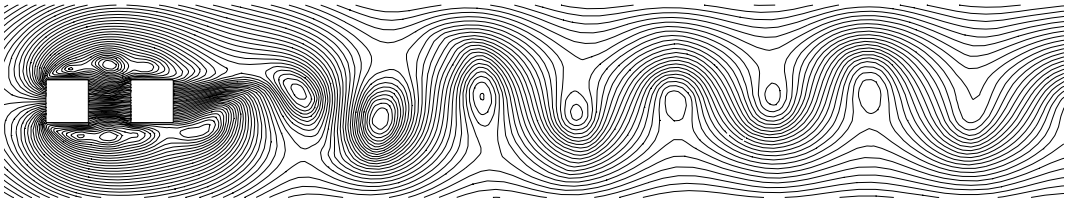

(e) G = 1.0, t = 81, flow regime $E1/E2$.

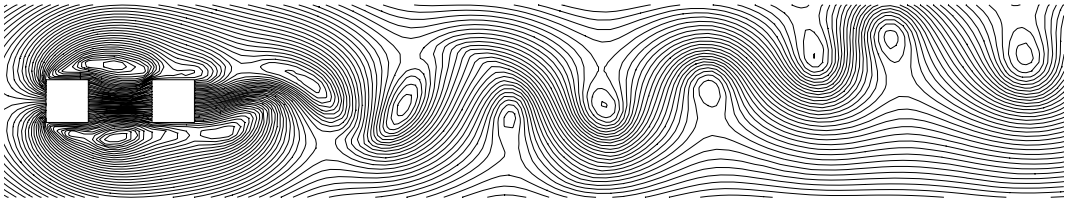

(f) G = 1.5, t = 56.5, flow regime $E1/E2$.

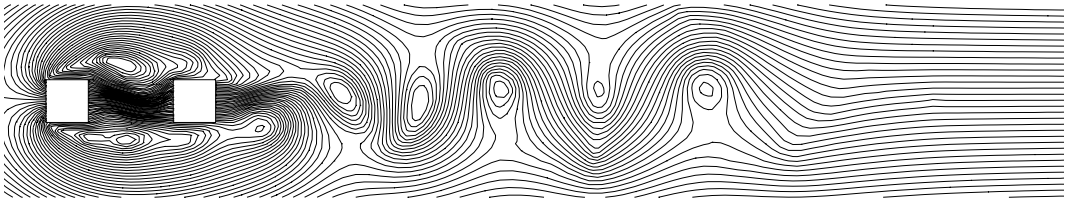

(g1) G = 2.0, t = 18, in transition from regime $E1/E2$ to regime B.

Figure 8.71. Streamline patterns in flow over tandem array of two square cylinders in various flow regimes; calculated in a reference frame moving at a velocity of $U_{ref} = 0.8U_{\infty}$.

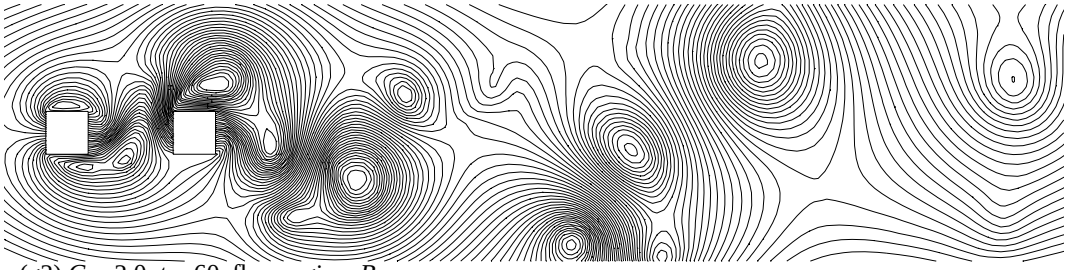

(g2) G = 2.0, t = 60, flow regime *B*.

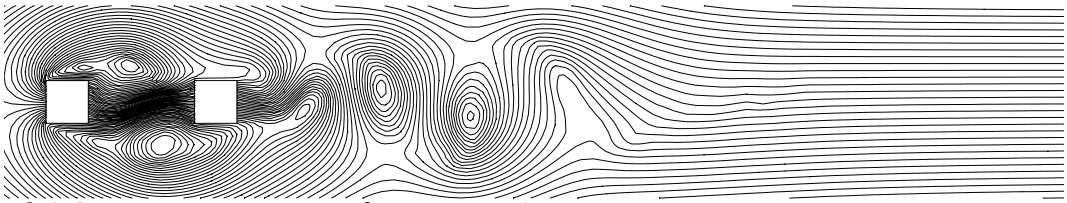

(h1) G = 2.5, t = 15, in transition from regime *E*1/*E*2 to regime *B*.

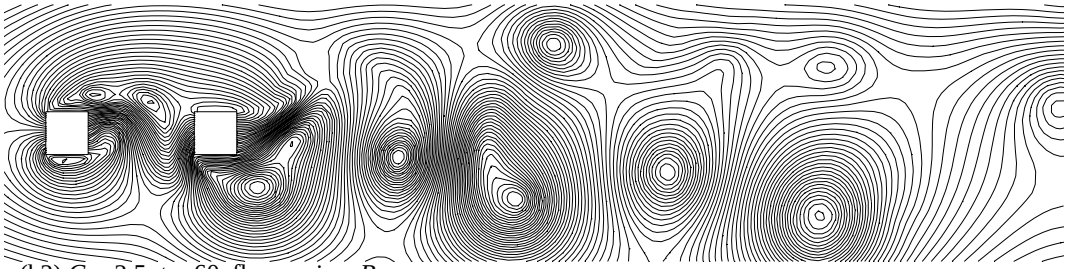

(h2) G = 2.5, t = 60, flow regime *B*.

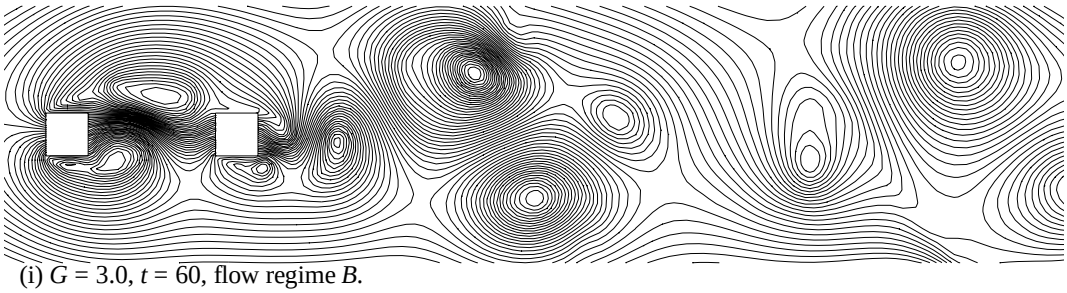

(i) G = 3.0, t = 60, flow regime *B*.

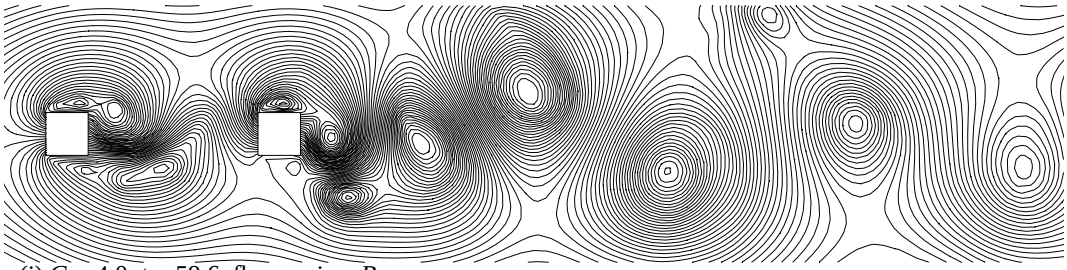

(j) G = 4.0, t = 59.6, flow regime *B*.

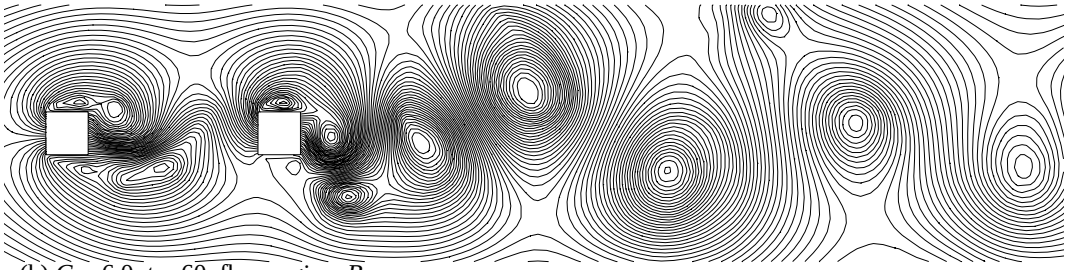

(k) G = 6.0, t = 60, flow regime *B*.

Figure 8.71. Cont'd.

8.4 Arrays with a Square Upstream Cylinder and a Long Downstream Plate

Calculations of flow over tandem arrays with an upstream square cylinder $C1 = 1$ and a downstream rectangular plate with chord-to-thickness ratio $C2 = 4$, have been made, also for $Re_h = 500$, to investigate the effects on the flow characteristics of the length of the downstream cylinder. Particular attention is given to the trapped-vortex flow in small gaps (in the $E1/E2$ regime) and the vortex-street flow in large gaps (in the B regime), and to the change-over between these two regimes of flow. From the calculations of flow over arrays of two square cylinders, it is known that the flow undergoes transition from regime $E1/E2$ to regime B over gaps in the range $2 < G < 3$. Based on this consideration, calculations made in this section are confined to gaps in the range $1.5 \leq G \leq 6$. For very small gaps $G < 0.5$, the flow is expected to be characterised by periodically-reversing flow through the gap (in the $F2$ regime), as for the ($C1 = 1$, $C2 = 1$) array with $G < 0.5$.

8.4.1 Flow Regimes for Small Gaps, $G \leq 2$

Calculations of flow for small gaps have been performed for the gap-to-thickness ratios of $G = 1.5$ and $G = 2.0$. The computational results of elemental-vortex distributions, streamline patterns and vorticity patterns for $G = 1.5$ are presented in Figs. 8.72–8.74. Corresponding results for $G = 2.0$ are presented in Figs. 8.76–8.78.

Consider specifically the flow development on the $G = 1.5$ array, from impulsive start to the fully-developed state. There are, as to be expected, strong similarities between this flow and that over the ($C1 = 1$, $C2 = 1$) array, particularly in relation to the flow in the gap. The similarity in gap flow is greatest to that for the ($C1 = 1$, $C2 = 1$) array with $G = 0.8$; the marked asymmetries which occur in the development phase of the flow over the ($C1 = 1$, $C2 = 1$) array with $G = 1.5$ are not in evidence in the present case. Thus, at the very beginning of the motion ($t < 2$), the shear layers separated from the leading corners of the upstream cylinder roll into the gap to produce a closed recirculation region immediately behind the cylinder, containing a pair of counter-rotating vortices. A similar recirculation region is produced in the near-wake of the array by separation from the trailing edge of the downstream plate. The initial flow pattern is essentially symmetrical about the centre-line of the array. Both recirculation regions then elongate in the streamwise direction. The vortices behind the upstream cylinder grow until they

occupy the whole of the space between the plates, and remain trapped in the gap throughout the later course of flow development. At the same time, instability in the elongated recirculation region behind the downstream plate leads to vortex shedding into the wake of the array (t = 6). From this time onwards, mild asymmetry develops in the trapped-vortices in the gap which then undergo an oscillation in size: one vortex grows bigger by progressive acquisition of vorticity from the separated shear layer and side-face vortices of the upstream cylinder while the other becomes smaller by progressive loss of vorticity to the side-face boundary layer on the downstream plate. The oscillation appears to be periodic, but in this case is not synchronised with trailing-edge vortex shedding, having a very much greater period. The power spectrum of fluctuating lift of the upstream cylinder (Fig. 8.99) shows large sharp peaks at St = 0.06 and St = 0.1 and smaller peaks at St = 0.176 and St = 0.31. The time-histories of streamline patterns (Figs. 8.73 and 8.75) and vorticity contours (Fig. 8.74) show that the frequency St = 0.176 is that of vortex-shedding into the wake of the array, while the frequency St = 0.31 appears to be that of vortex generation and passage on the side faces of the upstream cylinder. The variation in the size of the trapped vortices and the amplitude of their oscillation are quite small, and so the frequency of oscillation cannot be precisely determined; it is estimated to be in the order of St = 0.1. The origin of the other large spectral peak, at St = 0.06, has not been positively identified; it is possibly due to variation of the strength of side-face vortices on the upstream cylinder, as previously observed in the flow over single plates.

The variation of flow pattern around the array over about one vortex-shedding period can be clearly seen in the streamline patterns and the instantaneous pressure fields in Fig. 8.60. The shear layers separating from the upstream cylinder reattach to the leading edge of the downstream plate intermittently. The flow is in the E1 regime in the classification given by Bull *et al*. [1997] (Fig. 8.2). The flow on the downstream plate, after reattachment in the vicinity of the leading edge, remains fully-attached down to the trailing edge on both the upper and lower side-faces. Formation of vortices downstream of the array is due primarily to rolling up of the side-face boundary layers which separate from the trailing edges of the downstream plate. This results in the formation of a narrow regular wake behind the array (Fig. 8.72) and the lift on the downstream plate fluctuating with very small amplitude (Fig. 8.80).

There is evidence in the vorticity distributions (Fig. 8.74) and the instantaneous pressure fields (Fig. 8.75) of impingement on the leading end of the downstream plate of small-scale vortical structures, formed earlier on the side-face of the upstream cylinder. The process is similar to

the impingement described in the cases of the ($C1 = 1$, $C2 = 1$) array with $G = 0.8$, 1.0 and 1.5, but in this case the impinging vortices appear to be very much weaker; as a result of this weakness and the effects of diffusion during convection along the side face of the downstream plate, the presence of these vortices is scarcely discernible in the streamline patterns on the downstream plate (Fig. 8.73). Likewise, the surface-pressure fluctuations on the leading end of the downstream plate appear to be very little affected by the vortex impingement, showing no significant divergence there from the general, almost uniform, level prevailing over the whole plate (Fig. 8.79). The power spectrum of the fluctuating lift on the downstream plate (Fig. 8.99) has large peaks at $St = 0.04$ and $St = 0.09$, and small peaks at $St = 0.176$ and $St = 0.31$ with a number of additional minor peaks at higher frequencies. The frequencies $St = 0.176$ and 0.31, are, as for the upstream plate, associated with the vortex shedding into the wake of the array, and side-face vortex formation on the upstream cylinder. The frequencies $St = 0.04$ and $St = 0.09$, even though slightly different from those of the peaks in the spectrum of the upstream cylinder, are taken to result from the same flow process.

For the array with $G = 2$, the elemental-vortex distributions, streamline patterns and vorticity contours (Figs. 8.76–8.78) show an apparently similar sequence of flow development to that of the $G = 1.5$ array: symmetric recirculation regions initially forming behind both plates ($t < 2$); formation of vortices in the gap; establishment of fully-developed flow ($t > 10$) with detached shear layers from the upstream cylinder reattaching intermittently to the leading edge of the downstream plate; largely fully-attached flow on the side faces of the downstream plate; and formation of a narrow regular vortex-street wake behind the array (Fig. 8.76) following trailing-edge separation of side-face boundary layers.

However, the streamline and vorticity patterns (Figs. 8.77 and 8.78) show that the vortex flow between the plates differs significantly from that in the $G = 1.5$ array. In fact, the flow is in the transitional state between trapped-vortex flow and vortex-street flow in the gap. It is similar to, but at a slightly earlier stage of transition than, the transitional flow previously found for the ($C1 = 1$, $C2 = 1$) array with $G = 2$. In the early development ($t < 8$) a pair of trapped counter-rotating vortices forms in the gap, but, later, these vortices give way to a form of vortex shedding, alternately from the upper and lower sides of the upstream cylinder. The vortices formed by this process do not however form a recognisable vortex street in the gap.

A typical sequence of events in the flow can be seen in the streamline patterns from about t = 28 onwards (Fig. 8.77). The shear layers separated from the leading corners of the upstream cylinder impinge on the downstream plate intermittently. When they impinge on the gap rather than the downstream plate itself, they roll up to form vortices between the plates, and vortex formation occurs alternately on the upper and lower sides of the array. At t = 28 and 29, the lower vortex in the gap is shrinking by losing vorticity to the downstream flow. Between t = 29 and 30, a nascent vortex forms on the lower trailing-face of the upstream plate; it grows gradually by gaining vorticity from the impinging free shear layer and convected side-face vortices which form on the upstream cylinder beneath the separated shear layer. During this process the upper separated shear layer is diverted around the gap to reattach on the upper surface of the downstream plate. Growth of the lower vortex, within the gap, displaces the already-formed large vortex out of the gap (t = 30–35); in this process the upper vortex gradually loses its vorticity to the downstream flow, shrinks, and disappears (t = 35). At this point the growing lower vortex almost completely fills the gap. At t = 34–35, the next nascent vortex forms on the upper trailing-face of the upstream cylinder. As this vortex grows, the onset of downward flow through the gap (t = 36) indicates the "shedding" of the large lower vortex from the upstream cylinder. Further growth of the upper vortex forces the lower vortex out of the gap and brings about its disappearance by vorticity loss ($t \approx 42$). At t = 41–42, the next lower nascent lower vortex forms, and the cycle of formation, growth, shrinkage and disappearance of gap vortices is repeated. The power spectra of fluctuating lift on both the upstream and downstream cylinders feature a large peak at St = 0.085, and a very much smaller, scarcely discernible, peak at St = 0.172. The frequency St = 0.172 is that of the vortex shedding into the wake from the downstream plate. The frequency of vortex-shedding from the upstream cylinder, St = 0.085, is very close to that of vortex oscillation in the gap at G = 1.5, from which it clearly evolves.

There are indications that nascent trailing-face vortices on the upstream cylinder originate from side-face vortices on the cylinder. This can be seen, for example, over times t = 33 to 36 in Fig. 8.77: a side-face vortex on the upstream cylinder convected past the upper trailing-corner takes up a position on the trailing face where it grows into an upper trailing-face vortex. This sequence is similar to that in the flow over a single square cylinder described in section 7.3.2.

The calculated distributions of surface-pressure on the arrays with $G = 1.5$ and $G = 2.0$ exhibits similar characteristics, as is evident in Figs. 8.79 and 8.81. The surface-pressure distribution on the upstream cylinder is, as in the previous cases of the ($C1 = 1$, $C2 = 1$) array, very similar to that of a single square cylinder. The base-pressure and mean drag coefficients obtained for the upstream plate are, respectively, $-C_{pb1} \approx 0.8$ and $C_{D1} \approx 1.5$ for both the $G = 1.5$ and $G = 2.0$ arrays. It is notable that the surface-pressure distributions on the downstream plate exhibit similar characteristics to those of the ($C1 = 1$, $C2 = 1$) arrays in the trapped-vortex regime (Figs. 8.36, 8.38 and 8.40): the pressure rises sharply across the leading corners of the plate, then decreases along the streamwise surface to the base pressure on the trailing face. The leading-face pressure-coefficient on the downstream plate is $C_{pf2} = -0.6$ and the base-pressure coefficient $C_{pb2} \approx -0.65$ for $G = 1.5$; for the $G = 2$ array $C_{pf2} = -0.5$ and $C_{pb2} \approx -0.65$. For both gaps, the drag coefficient C_{D2} on the downstream plate fluctuates about a mean value very close to zero (Figs. 8.80 and 8.82).

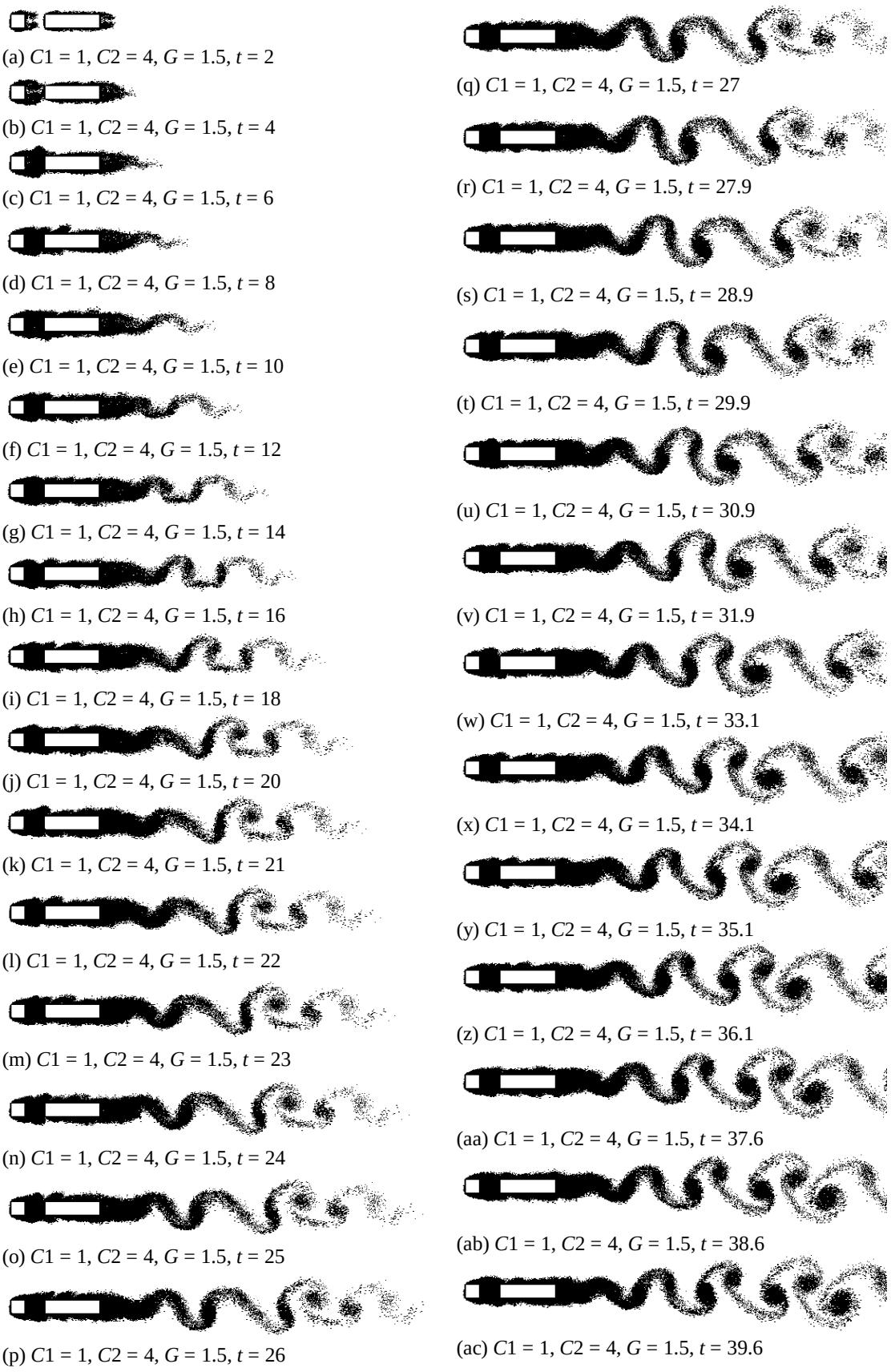

(a) $C1 = 1$, $C2 = 4$, $G = 1.5$, $t = 2$

(b) $C1 = 1$, $C2 = 4$, $G = 1.5$, $t = 4$

(c) $C1 = 1$, $C2 = 4$, $G = 1.5$, $t = 6$

(d) $C1 = 1$, $C2 = 4$, $G = 1.5$, $t = 8$

(e) $C1 = 1$, $C2 = 4$, $G = 1.5$, $t = 10$

(f) $C1 = 1$, $C2 = 4$, $G = 1.5$, $t = 12$

(g) $C1 = 1$, $C2 = 4$, $G = 1.5$, $t = 14$

(h) $C1 = 1$, $C2 = 4$, $G = 1.5$, $t = 16$

(i) $C1 = 1$, $C2 = 4$, $G = 1.5$, $t = 18$

(j) $C1 = 1$, $C2 = 4$, $G = 1.5$, $t = 20$

(k) $C1 = 1$, $C2 = 4$, $G = 1.5$, $t = 21$

(l) $C1 = 1$, $C2 = 4$, $G = 1.5$, $t = 22$

(m) $C1 = 1$, $C2 = 4$, $G = 1.5$, $t = 23$

(n) $C1 = 1$, $C2 = 4$, $G = 1.5$, $t = 24$

(o) $C1 = 1$, $C2 = 4$, $G = 1.5$, $t = 25$

(p) $C1 = 1$, $C2 = 4$, $G = 1.5$, $t = 26$

(q) $C1 = 1$, $C2 = 4$, $G = 1.5$, $t = 27$

(r) $C1 = 1$, $C2 = 4$, $G = 1.5$, $t = 27.9$

(s) $C1 = 1$, $C2 = 4$, $G = 1.5$, $t = 28.9$

(t) $C1 = 1$, $C2 = 4$, $G = 1.5$, $t = 29.9$

(u) $C1 = 1$, $C2 = 4$, $G = 1.5$, $t = 30.9$

(v) $C1 = 1$, $C2 = 4$, $G = 1.5$, $t = 31.9$

(w) $C1 = 1$, $C2 = 4$, $G = 1.5$, $t = 33.1$

(x) $C1 = 1$, $C2 = 4$, $G = 1.5$, $t = 34.1$

(y) $C1 = 1$, $C2 = 4$, $G = 1.5$, $t = 35.1$

(z) $C1 = 1$, $C2 = 4$, $G = 1.5$, $t = 36.1$

(aa) $C1 = 1$, $C2 = 4$, $G = 1.5$, $t = 37.6$

(ab) $C1 = 1$, $C2 = 4$, $G = 1.5$, $t = 38.6$

(ac) $C1 = 1$, $C2 = 4$, $G = 1.5$, $t = 39.6$

Figure 8.72. Elemental-vortex distributions in flow over the ($C1 = 1$, $C2 = 4$, $G = 1.5$) array, showing flow development from an impulsive start from rest to the fully-developed flow.

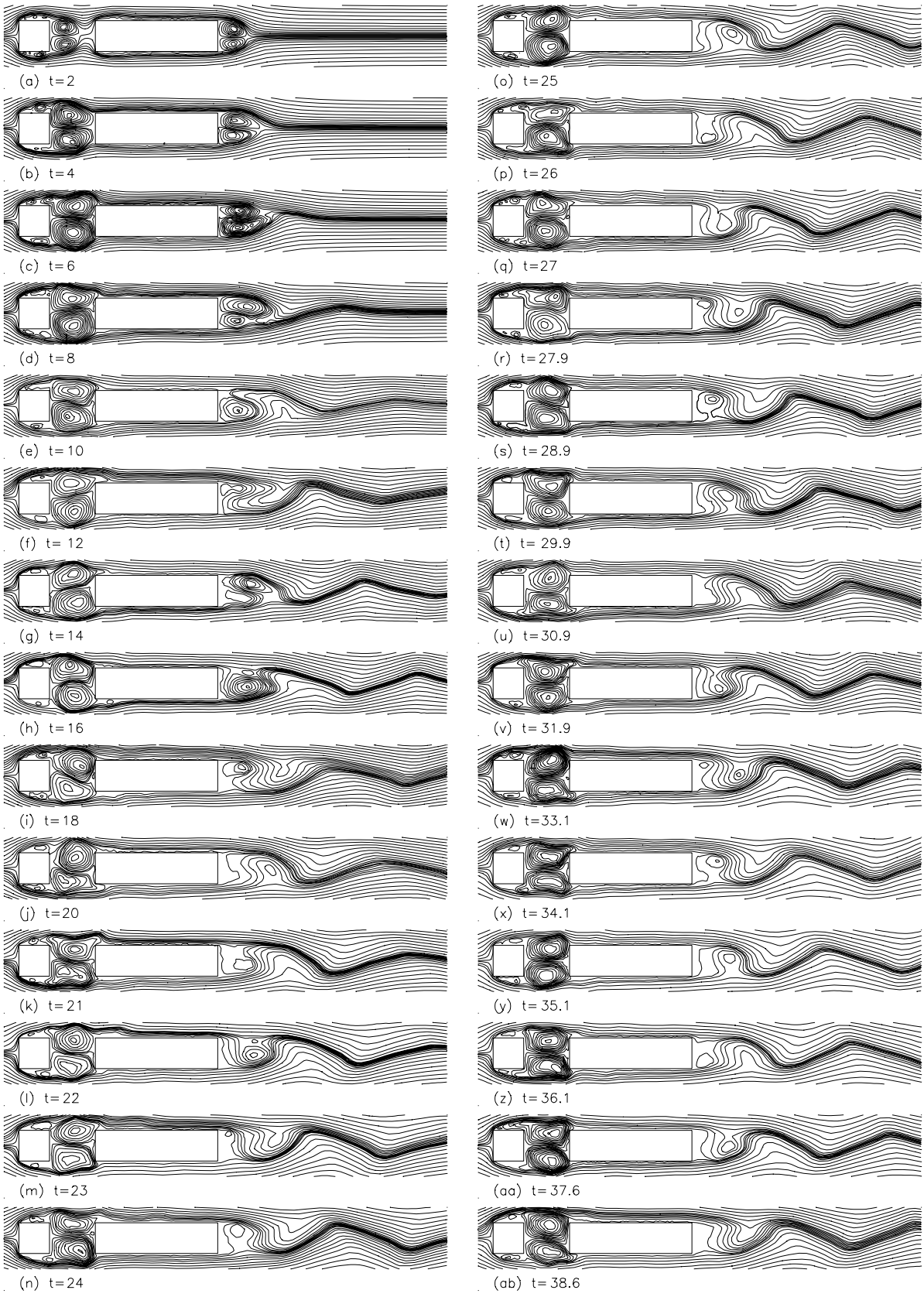

Figure 8.73. Calculated streamline patterns in flow over the ($C1$ =1, $C2$ = 4, G = 1.5) array, showing flow development from an impulsive start from rest to the fully-developed flow.

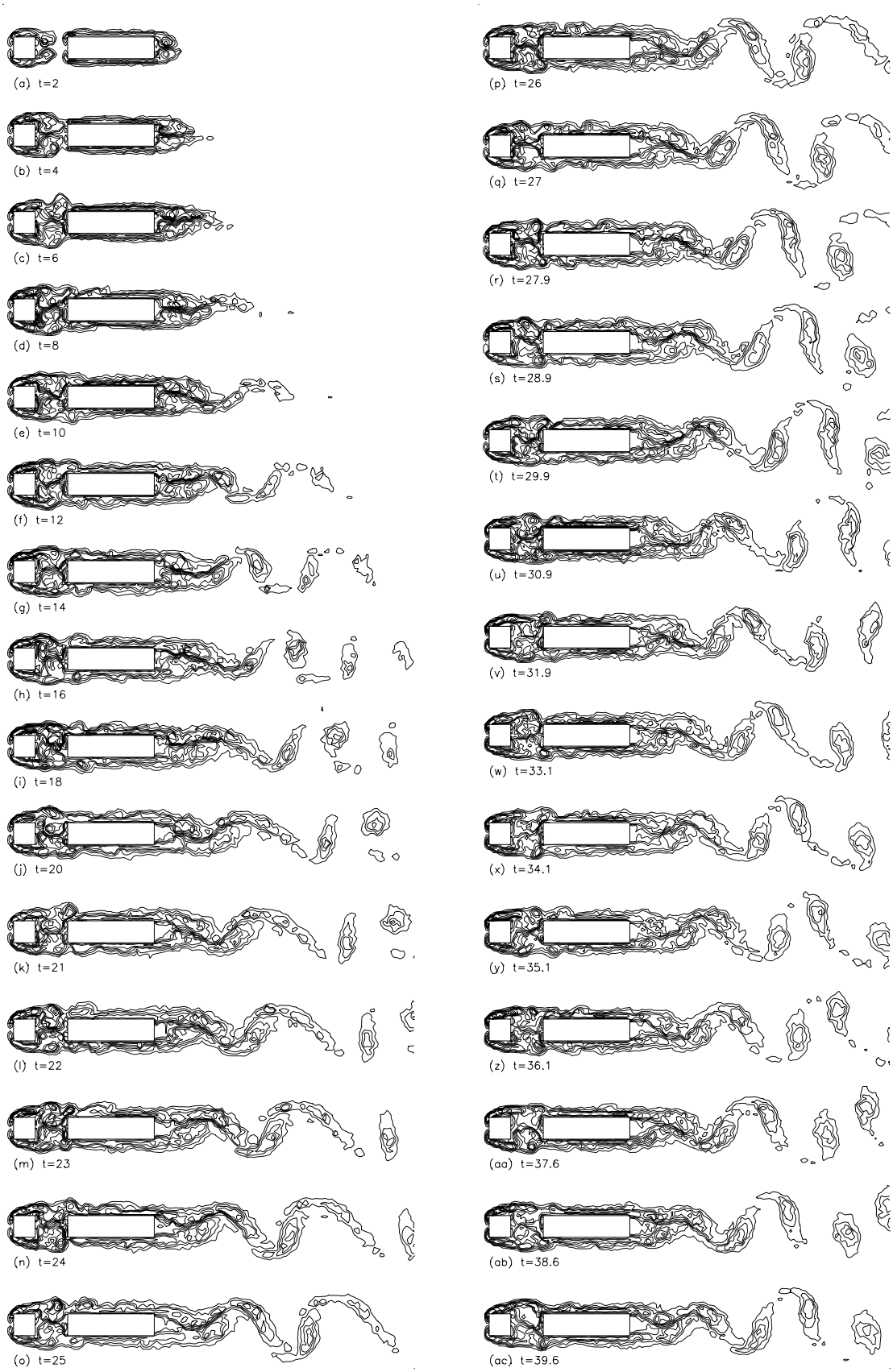

Figure 8.74. Vorticity contours in flow over the ($C1 = 1$, $C2 = 4$, $G = 1.5$) array, showing flow development from an impulsive start from rest to the fully-developed flow.

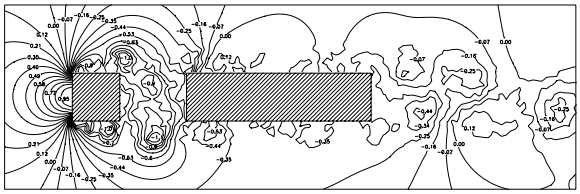

(a1) G = 1.5, t = 31.9

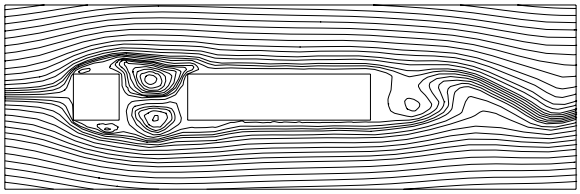

(a2) G = 1.5, t = 31.9

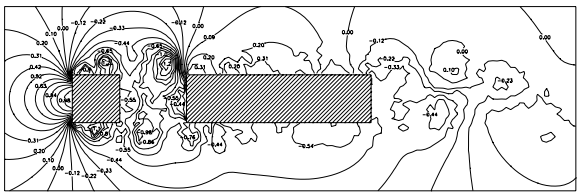

(b1) G = 1.5, t = 33.1

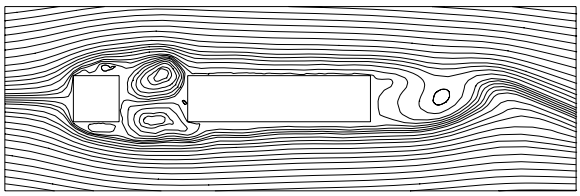

(b2) G = 1.5, t = 33.1

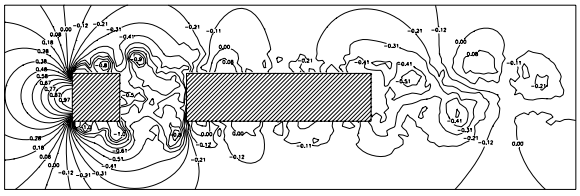

(c1) G = 1.5, t = 34.1

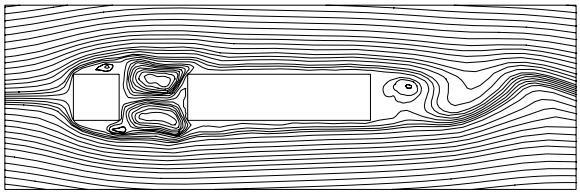

(c2) G = 1.5, t = 34.1

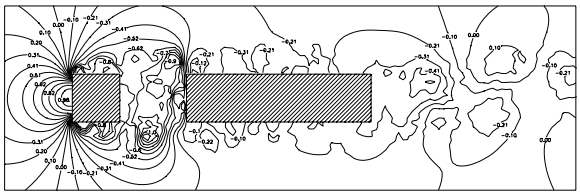

(d1) G = 1.5, t = 35.1

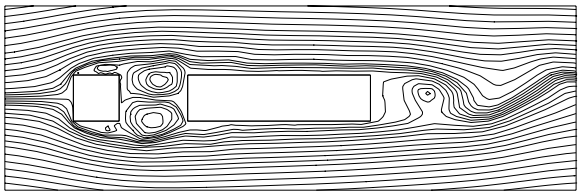

(d2) G = 1.5, t = 35.1

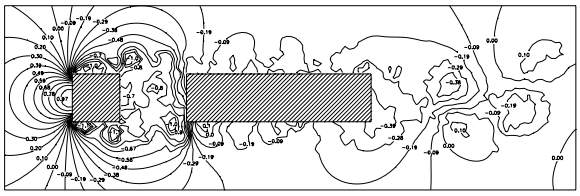

(e1) G = 1.5, t = 36.1

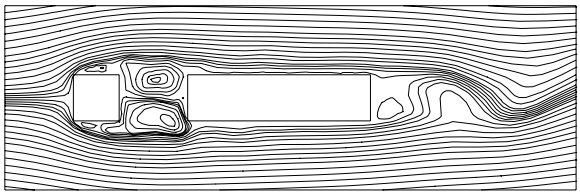

(e2) G = 1.5, t = 36.1

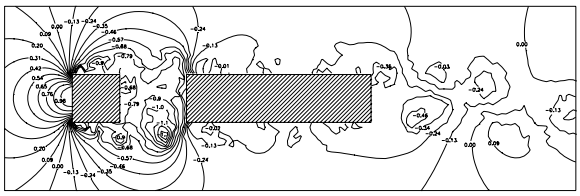

(f1) G = 1.5, t = 37.6

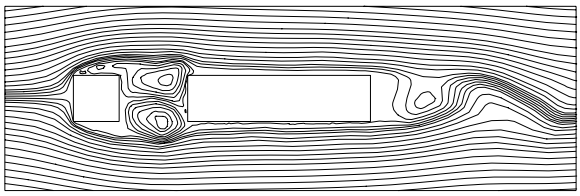

(f2) G = 1.5, t = 37.6

Figure 8.75. Instantaneous pressure fields and streamline patterns in fully-developed flow over the ($C1$ = 1, $C2$ = 4, G = 1.5) array. Numbers shown are coefficients of static pressure.

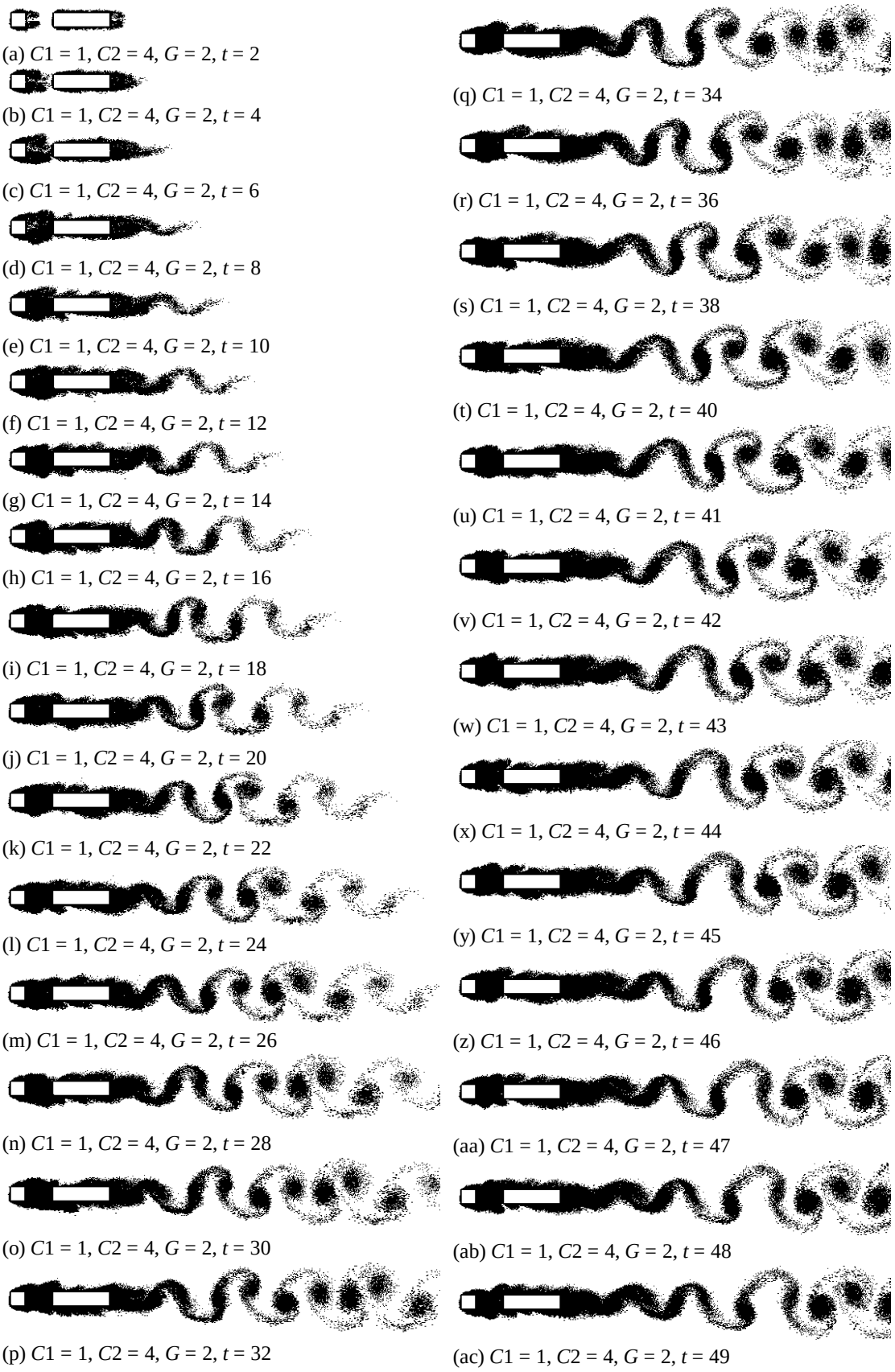

(a) $C1 = 1$, $C2 = 4$, $G = 2$, $t = 2$

(b) $C1 = 1$, $C2 = 4$, $G = 2$, $t = 4$

(c) $C1 = 1$, $C2 = 4$, $G = 2$, $t = 6$

(d) $C1 = 1$, $C2 = 4$, $G = 2$, $t = 8$

(e) $C1 = 1$, $C2 = 4$, $G = 2$, $t = 10$

(f) $C1 = 1$, $C2 = 4$, $G = 2$, $t = 12$

(g) $C1 = 1$, $C2 = 4$, $G = 2$, $t = 14$

(h) $C1 = 1$, $C2 = 4$, $G = 2$, $t = 16$

(i) $C1 = 1$, $C2 = 4$, $G = 2$, $t = 18$

(j) $C1 = 1$, $C2 = 4$, $G = 2$, $t = 20$

(k) $C1 = 1$, $C2 = 4$, $G = 2$, $t = 22$

(l) $C1 = 1$, $C2 = 4$, $G = 2$, $t = 24$

(m) $C1 = 1$, $C2 = 4$, $G = 2$, $t = 26$

(n) $C1 = 1$, $C2 = 4$, $G = 2$, $t = 28$

(o) $C1 = 1$, $C2 = 4$, $G = 2$, $t = 30$

(p) $C1 = 1$, $C2 = 4$, $G = 2$, $t = 32$

(q) $C1 = 1$, $C2 = 4$, $G = 2$, $t = 34$

(r) $C1 = 1$, $C2 = 4$, $G = 2$, $t = 36$

(s) $C1 = 1$, $C2 = 4$, $G = 2$, $t = 38$

(t) $C1 = 1$, $C2 = 4$, $G = 2$, $t = 40$

(u) $C1 = 1$, $C2 = 4$, $G = 2$, $t = 41$

(v) $C1 = 1$, $C2 = 4$, $G = 2$, $t = 42$

(w) $C1 = 1$, $C2 = 4$, $G = 2$, $t = 43$

(x) $C1 = 1$, $C2 = 4$, $G = 2$, $t = 44$

(y) $C1 = 1$, $C2 = 4$, $G = 2$, $t = 45$

(z) $C1 = 1$, $C2 = 4$, $G = 2$, $t = 46$

(aa) $C1 = 1$, $C2 = 4$, $G = 2$, $t = 47$

(ab) $C1 = 1$, $C2 = 4$, $G = 2$, $t = 48$

(ac) $C1 = 1$, $C2 = 4$, $G = 2$, $t = 49$

Figure 8.76. Elemental-vortex distributions in flow over the ($C1 = 1$, $C2 = 4$, $G = 2$) array, showing sequence of flow evolution from the impulsive start to the fully-developed state.

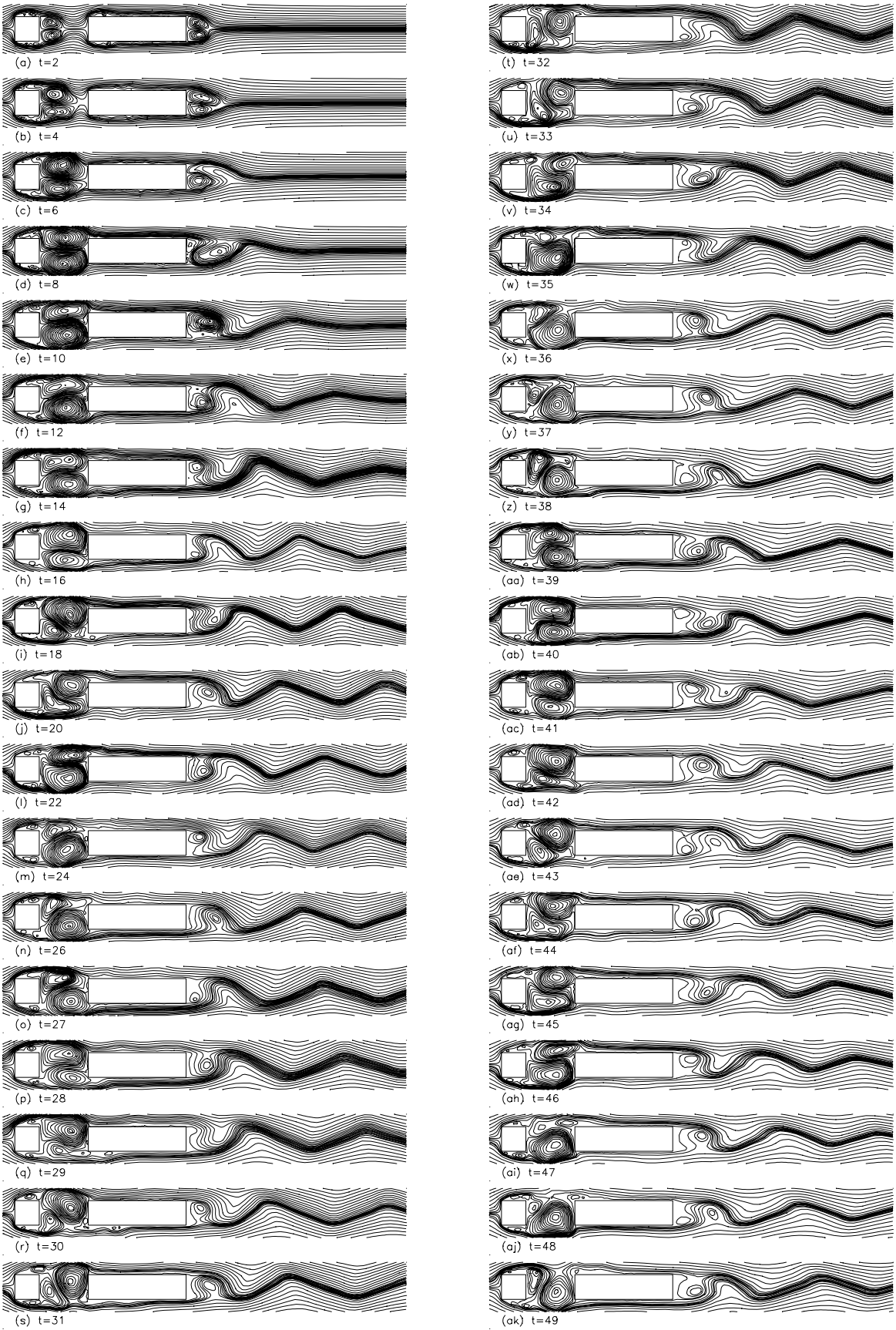

Figure 8.77. Streamline patterns in flow over the ($C1$ =1, $C2$ = 4, G = 2) array, showing sequence of flow evolution from the impulsive start to the fully-developed state.

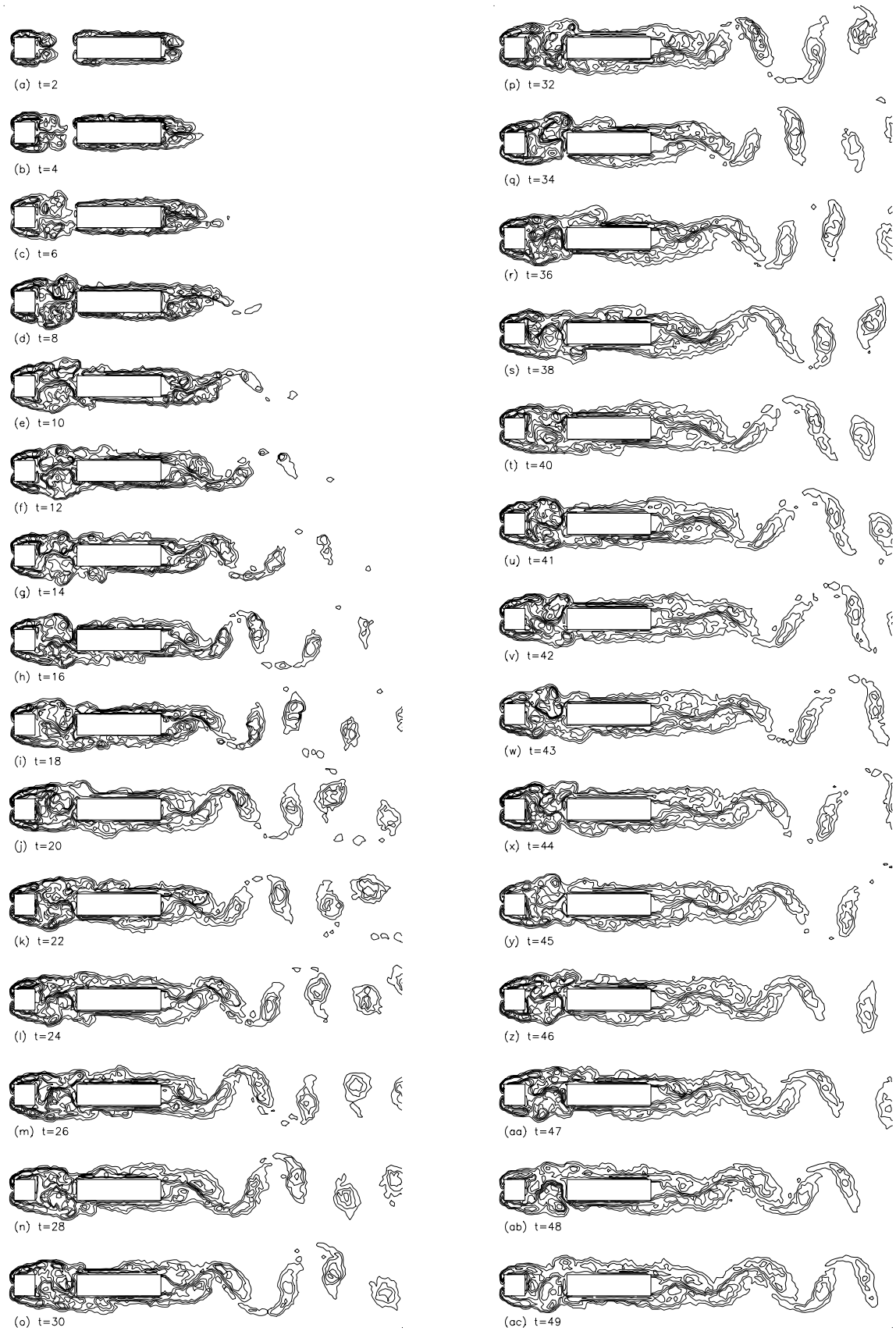

Figure 8.78. Vorticity contours in flow over the ($C1 = 1$, $C2 = 4$, $G = 2$) array, showing sequence of flow evolution from the impulsive start to the fully-developed state.

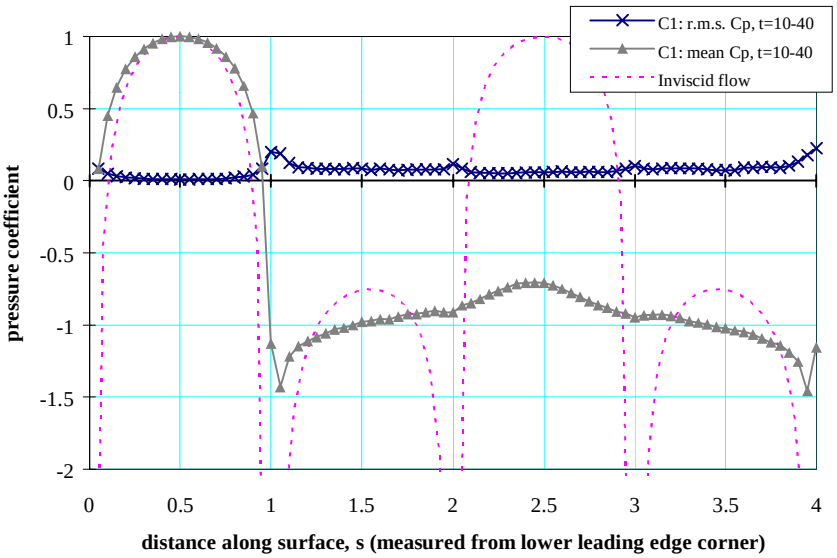

(a)

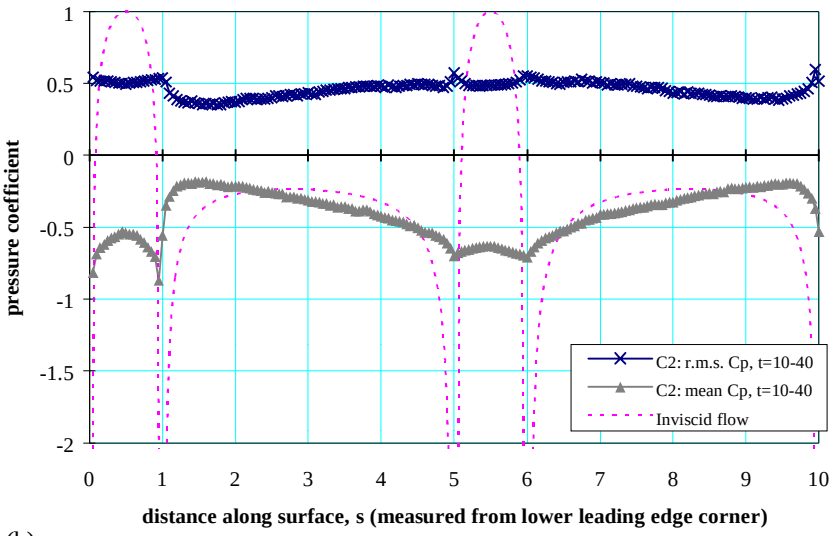

(b)

Figure 8.79. Calculated distributions of mean and r.m.s. pressure coefficients on the cylinders in the ($C1 = 1$, $C2 = 4$, $G = 1.5$) array.

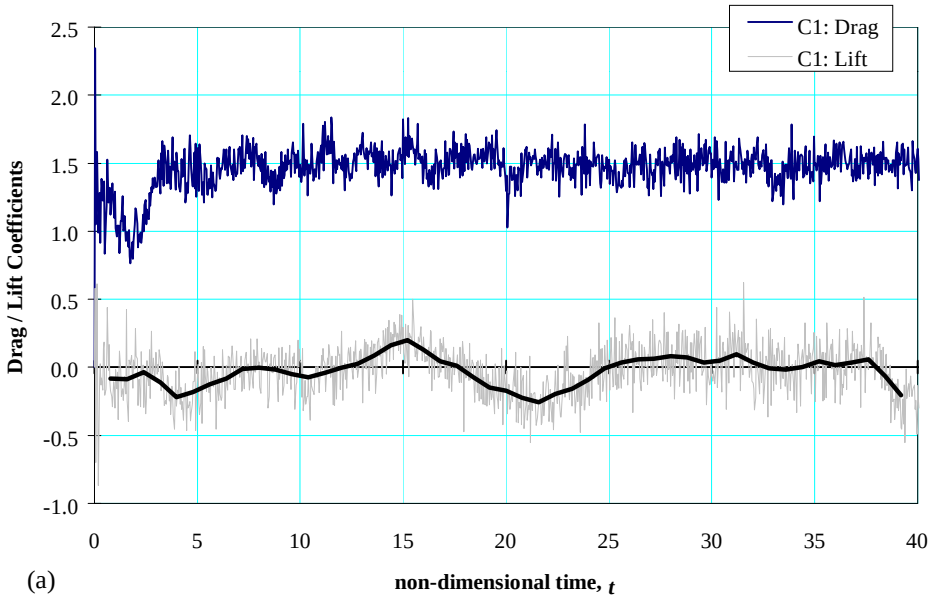

(a)

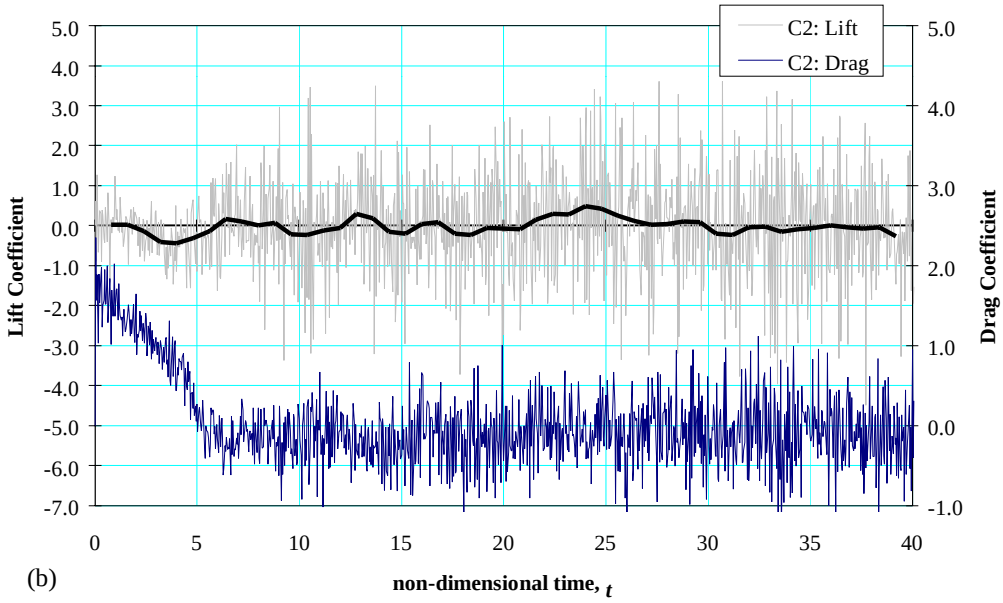

(b)

Figure 8.80. Time-histories of drag and lift on the ($C1 = 1$, $C2 = 4$, $G = 1.5$) array, (a) upstream plate, (b) downstream plate. Drag and lift are calculated for $\Delta t = 0.02$; highlighted values are averaged over $\Delta t = 0.4$.

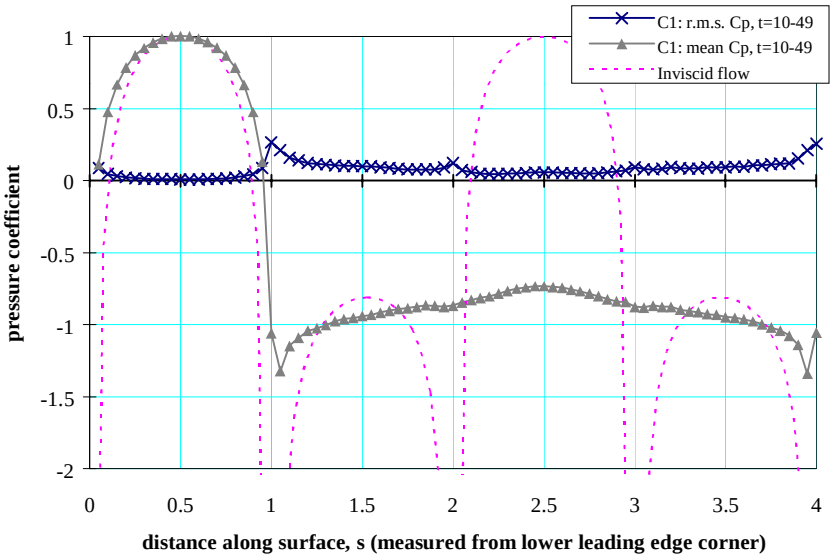

(a)

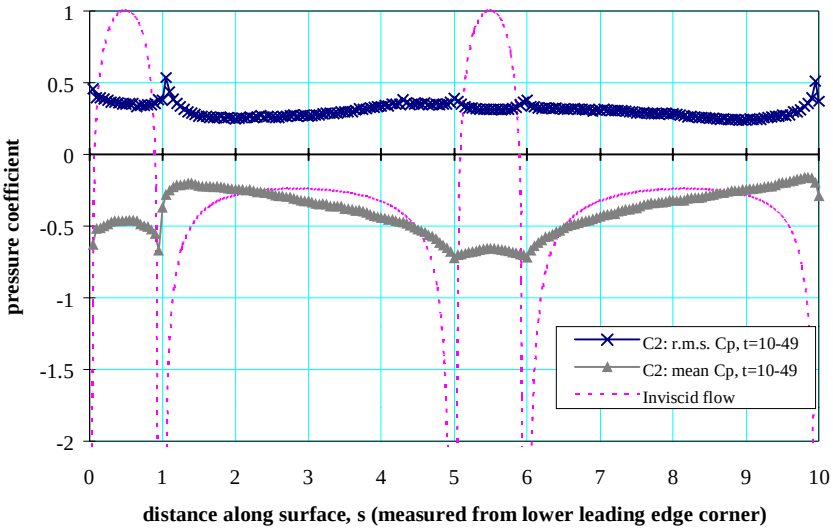

(b)

Figure 8.81. Calculated distributions of mean and r.m.s. pressure coefficients on the cylinders in the ($C1$ = 1, $C2$ = 4, G = 2.0) array.

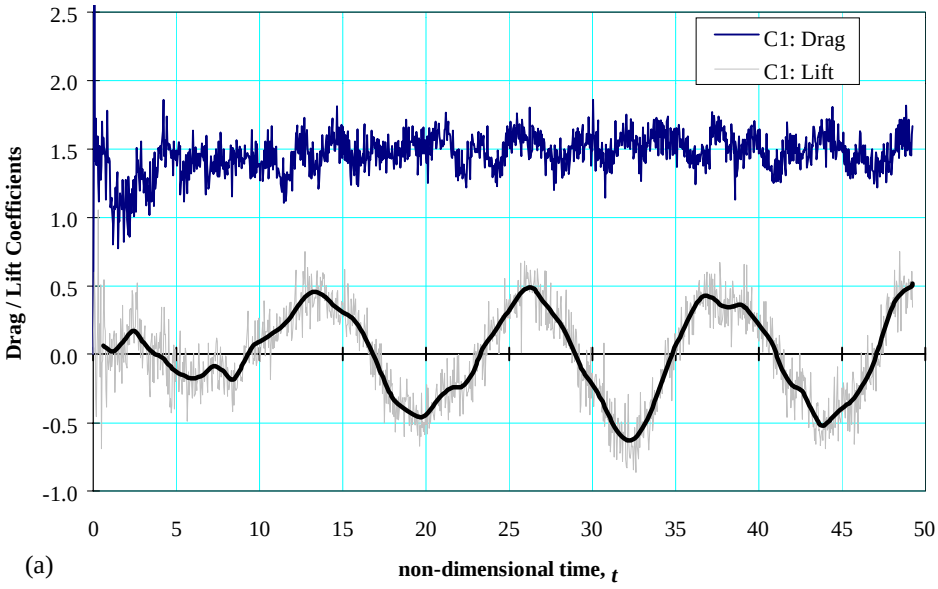

(a)

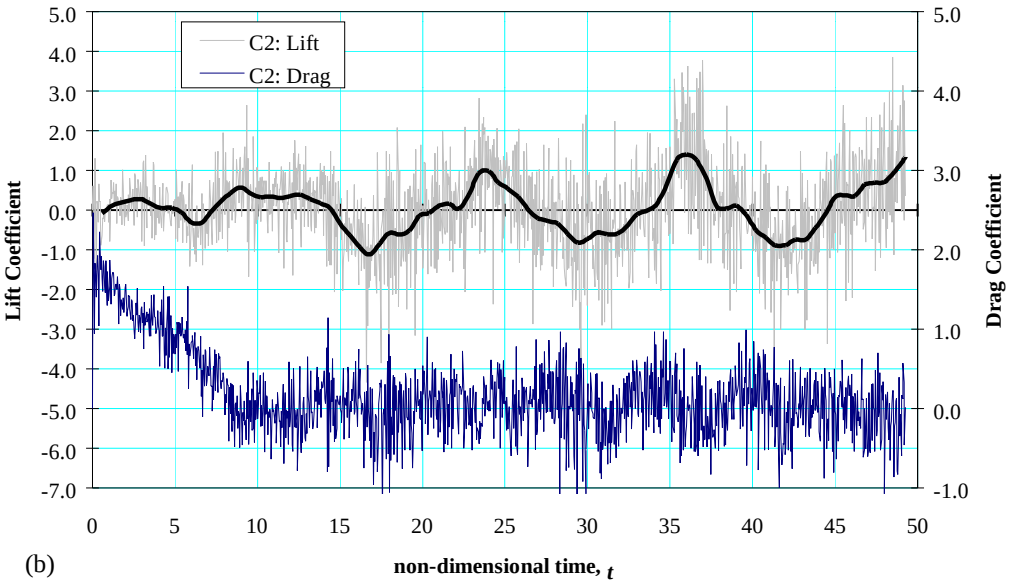

(b)

Figure 8.82. Time-histories of drag and lift on the ($C1 = 1$, $C2 = 4$, $G = 2.0$) array, (a) upstream plate, (b) downstream plate. Drag and lift are calculated for $\Delta t = 0.02$; highlighted values are averaged over $\Delta t = 0.4$.

8.4.2 Flow Regimes for Large Gaps, $G > 2$

As the gap increases beyond $G = 2$, the flow enters completely the regime with vortex-street flow in the gap. Calculations of flow in this regime have been performed on the arrays with $G = 3$, $G = 4$ and $G = 6$. The elemental-vortex distributions, streamline and vorticity patterns for the $G = 3$ array are shown in Figs. 8.83–8.85; the corresponding results for $G = 4$ and $G = 6$ are presented in Figs. 8.86–8.88 and Figs. 8.90–8.92 respectively. The flows over these arrays exhibit similar characteristics to each other in both the developing stages and the fully-developed state.

Consider first the flow development on the array from the impulsive start. A typical sequence of events in the developing flow can be seen, for example, on the $G = 3$ array. The initial flow ($t < 4$) is essentially symmetrical about the centre-line of the array, in which a closed recirculation region forms behind both the upstream and downstream plates. The recirculation region behind the upstream plate extends but, even while it does so, vortex shedding is developing. By $t = 6$, there is already flow upwards through the gap, and the upper vortex in the gap has effectively been shed from the upstream cylinder. It is then forced out of the gap by the growing lower vortex ($t = 8–12$) and becomes a side-face vortex near the upper leading edge of the downstream plate. The large lower vortex which fills the gap at $t = 12$ is then itself shed and vortex-street flow in the gap with periodic vortex-shedding from the upstream cylinder becomes established ($t > 14$). During the same time, instability in the extended recirculation region behind the downstream plate leads to vortex shedding into the wake of the array ($t \approx 8$). For $t > 14$, the flow is in its fully-developed state, in which vortices are shed from both the upstream and downstream plates.

The fully-developed flow over the array exhibits the characteristics of a flow in the *B* regime in the classification of Bull *et al*. [1997]. The flow on the upstream cylinder is very similar to the flow over the upstream cylinder in the ($C1 = 1$, $C2 = 1$) array and to the flow over a single square cylinder. In all three cases, reattachment on a side face of the square cylinder of the shear layer separated from the leading corner alternates with completely detached flow with side-face flow reversal; the vortex street in the gap is formed by rolling up of separated shear layers. The frequencies of vortex-shedding of the upstream cylinder ($St_1 = 0.118$, 0.127 and 0.131 for $G = 3$, 4 and 6 respectively), as determined from the power spectrum of lift fluctuation (Fig. 8.99), are similar to the value for a single square cylinder at the same Reynolds

number (St = 0.132 at Re_h = 500), increasing and approaching the single-cylinder value with increasing gap-to-thickness ratio. The similarity between the flow on the upstream cylinder and the flow over a single square cylinder extends to the surface-pressure distribution (Figs. 8.93, 8.95 and 8.97 for array flow, and Fig. 7.35 for square-cylinder flow), time-histories of drag and lift coefficients (Figs. 8.94, 8.96 and 8.98 for array flow, and Fig. 7 .39 for square-cylinder flow). These similarities indicate that the vortex shedding from the upstream cylinder is essentially uninfluenced by the presence of the downstream plate for $G > 3$, as for the ($C1 = 1$, $C2 = 1$) array with $G > 3$.

The vortex-street flow in the gap impinges on the leading end of the downstream plate, where each impinging vortex is clipped to form, generally, a still-large primary vortex and a smaller secondary vortex. The larger vortex moves onto the side-face of the downstream plate, followed by the secondary vortex. Both vortices are then convected along the side face of the downstream plate and eventually shed into wake of the array. The flow on both the upper and lower side-faces of the downstream plate is largely fully-attached, except in so far as it is disturbed by the passage of these vortices. Vortex formation downstream of the array involves the shedding of side-face vortices and, to a lesser extent, the rolling up of the shear layers resulting from separation of the attached-flow boundary layers, at the trailing edge of the downstream plate. These two sets of vortices interact in the near-wake to form the final Karman vortex street of the array. The vortex-shedding frequency of the downstream plate, obtained from the power spectrum of fluctuating lift, is essentially equal to the frequency of vortex-shedding from the upstream cylinder (having values St_2 = 0.121, 0.125 and 0.129 for G = 3, 4 and 6 respectively), indicating coupling of the vortex motion on the two plates and control of the process by shedding from the upstream cylinder.

8.4.2.1 Interaction of Vortex-Street with a Long Downstream Plate

The sequence of events associated with impingement of the vortex-street in the gap on the leading face of the downstream plate is essentially identical with that previously seen on the ($C1$ = 1, $C2$ = 1) array with the same gap. The same processes of impingement, alternation of the stagnation point between upper and lower leading corners, alternation of flow direction over the leading face, alternation of fully attached flow and leading-edge separation bubble on the side-faces of the downstream plate, vortex clipping, formation of a large and a secondary vortex at each impingement, and the movement of the main and secondary vortices formed by clipping

to the side-face of the downstream plate, as previously described, occur on both arrays. The similarity can be seen clearly for the two arrays with $G = 4$ by comparing the flow patterns for the present case for time $t = 36$ to 44.5 (Fig. 8.89), with the corresponding patterns for the ($C1 = 1$, $C2 = 1$) array over time $t = 59.6$ to 67.6 (Fig. 8.48).

Thus, in effect, differences between the flow over the ($C1 = 1$, $C2 = 1$) and ($C1 = 1$, $C2 = 4$) arrays arise only in the flow over the downstream plate itself, from the point where the main and secondary vortices resulting from impingement move onto a side-face of the downstream plate. In the case of the ($C1 = 1$, $C2 = 4$) array, these two vortices are convected along the side-face, and in most instances, but not all, they merge before reaching the trailing edge of the downstream plate – for example, the vorticity contours (Fig. 8.88) and the instantaneous pressure fields (Fig. 8.89) show that the secondary vortex formed on the lower side at time $t \approx 37$ merges with the main vortex before they are shed into the wake at $t \approx 40.5$ while the secondary vortex formed on the lower side at time $t \approx 43.5$ remains distinct from the main vortex which precedes it.

Although the streamline patterns indicate attached flow over the greater part of the downstream plate at most times, the formation of wake vortices appears to the dominated by side-face vortices formed by impingement of the vortex street in the gap on the downstream plate. In general, these vortices form trailing-face vortices before being shed into the wake. In isolated cases, such as at $t = 26.3–30.3$ for $G = 4$ (Fig. 8.87), a trailing-face vortex does appear to be formed and shed by rolling up of the side face boundary layers separating from the trailing edge. However, such vortices are apparently very weak and merge with the convected side-face vortices which dominate in the wake. There is, therefore, clearly synchronism of vortex shedding from the upstream cylinder, impingement of the gap vortex-street on the downstream plate, and shedding of vortices from the trailing edge to form the Karman street of the array. Irregularities are evident in the final vortex streets, similar to those found on the ($C1 = 1$, $C2 = 1$) array. They arise from the same source: irregularities in the size, strength and the lateral location of gap vortices impinging on the downstream plate.

The time-histories of drag and lift coefficients on the $G = 3$, $G = 4$ and $G = 6$ arrays (Figs. 8.94, 8.96 and 8.98) show that, when fully-developed flow becomes established at $t \gtrsim 15$, the pressure forces on the upstream and downstream plates both fluctuate at the same frequency as the vortex-shedding frequency of the array, but with a phase difference dependent on G. The

calculated values of phase lags between lift fluctuations on the downstream and upstream plates are 0.1π, 0.4π and 1.1π for G = 3, 4 and 6 respectively. If a reference datum of 2π is taken, as for the ($C1$ = 1, $C2$ = 1) array, these satisfy quite well the linear relationship $(1.1 + G/3)\pi$.

On the upstream cylinders of the G = 3, 4 and 6 arrays, as on their counterparts in the ($C1$ = 1, $C2$ = 1) arrays, the surface-pressure distributions are very similar to that on a single square cylinder: the base-pressure and drag coefficients almost all the same at $C_{pb1} \approx -1$ and $C_{D1} \approx 1.6$ respectively, compared with $C_{pb1} = -1.1$ and $C_D \approx 1.8$ for a single square cylinder at the same Reynolds number. Again, the pressure distribution on the downstream plate is dependent on G, but approaches that of a single rectangular plate with increasing gap-to-thickness ratio. C_{pf2} takes on the values 0.15, 0.35 and 0.5, and C_{D2} the values 0.75, 0.8 and 1, for G = 3, 4, and 6 respectively. Compared with arrays with smaller gaps $G \leq 2$, the r.m.s. pressure fluctuation on the leading end of the downstream plate of the arrays with G = 3, 4, and 6 is significantly increased by vortex-street impingement (Fig. 8.93, 8.95 and 8.97).

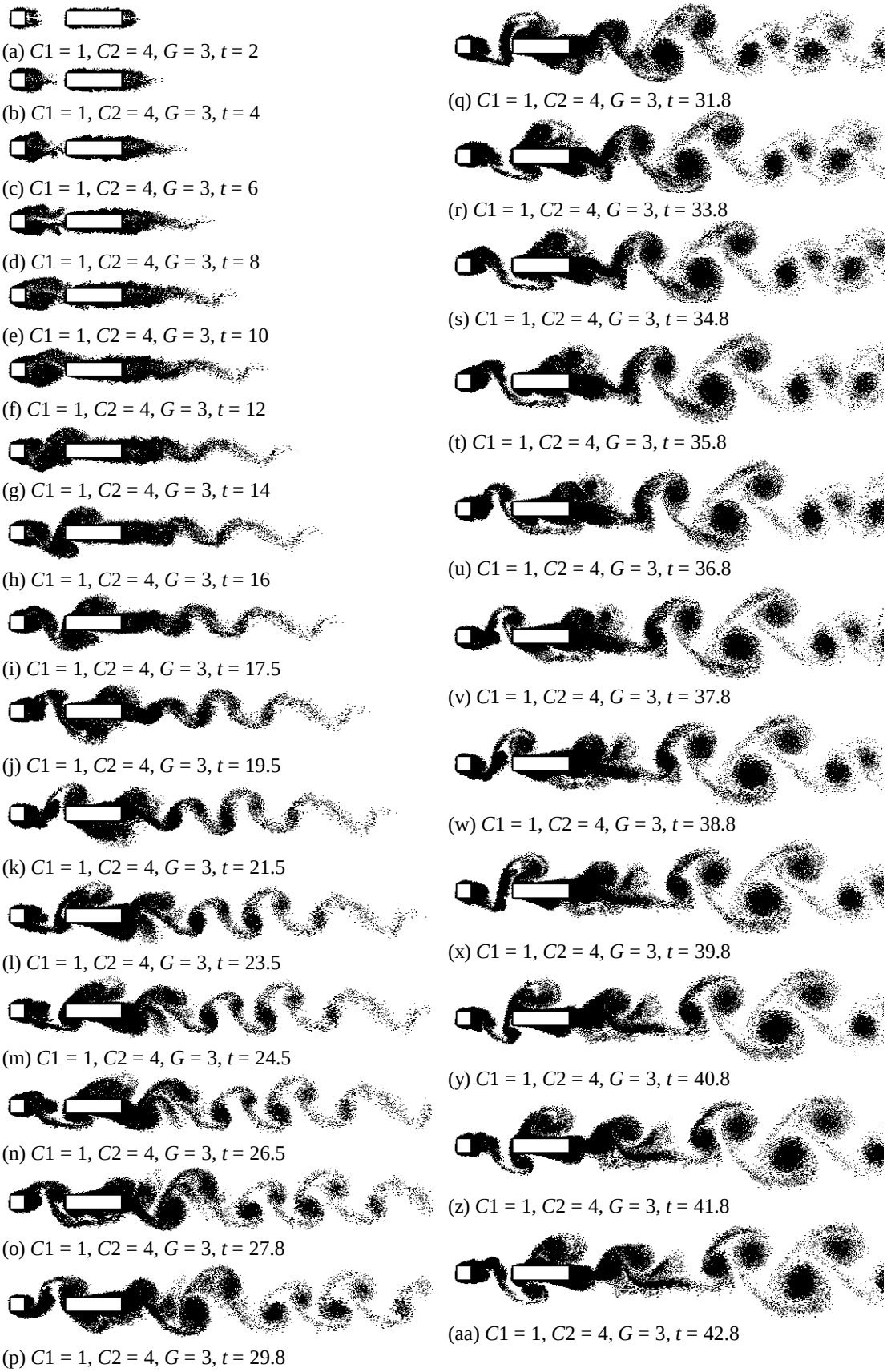

(a) $C1 = 1$, $C2 = 4$, $G = 3$, $t = 2$

(b) $C1 = 1$, $C2 = 4$, $G = 3$, $t = 4$

(c) $C1 = 1$, $C2 = 4$, $G = 3$, $t = 6$

(d) $C1 = 1$, $C2 = 4$, $G = 3$, $t = 8$

(e) $C1 = 1$, $C2 = 4$, $G = 3$, $t = 10$

(f) $C1 = 1$, $C2 = 4$, $G = 3$, $t = 12$

(g) $C1 = 1$, $C2 = 4$, $G = 3$, $t = 14$

(h) $C1 = 1$, $C2 = 4$, $G = 3$, $t = 16$

(i) $C1 = 1$, $C2 = 4$, $G = 3$, $t = 17.5$

(j) $C1 = 1$, $C2 = 4$, $G = 3$, $t = 19.5$

(k) $C1 = 1$, $C2 = 4$, $G = 3$, $t = 21.5$

(l) $C1 = 1$, $C2 = 4$, $G = 3$, $t = 23.5$

(m) $C1 = 1$, $C2 = 4$, $G = 3$, $t = 24.5$

(n) $C1 = 1$, $C2 = 4$, $G = 3$, $t = 26.5$

(o) $C1 = 1$, $C2 = 4$, $G = 3$, $t = 27.8$

(p) $C1 = 1$, $C2 = 4$, $G = 3$, $t = 29.8$

(q) $C1 = 1$, $C2 = 4$, $G = 3$, $t = 31.8$

(r) $C1 = 1$, $C2 = 4$, $G = 3$, $t = 33.8$

(s) $C1 = 1$, $C2 = 4$, $G = 3$, $t = 34.8$

(t) $C1 = 1$, $C2 = 4$, $G = 3$, $t = 35.8$

(u) $C1 = 1$, $C2 = 4$, $G = 3$, $t = 36.8$

(v) $C1 = 1$, $C2 = 4$, $G = 3$, $t = 37.8$

(w) $C1 = 1$, $C2 = 4$, $G = 3$, $t = 38.8$

(x) $C1 = 1$, $C2 = 4$, $G = 3$, $t = 39.8$

(y) $C1 = 1$, $C2 = 4$, $G = 3$, $t = 40.8$

(z) $C1 = 1$, $C2 = 4$, $G = 3$, $t = 41.8$

(aa) $C1 = 1$, $C2 = 4$, $G = 3$, $t = 42.8$

Figure 8.83. Elemental-vortex distributions in flow over the ($C1 = 1$, $C2 = 4$, $G = 3$) array, showing flow development from an impulsive start to the fully-developed flow.

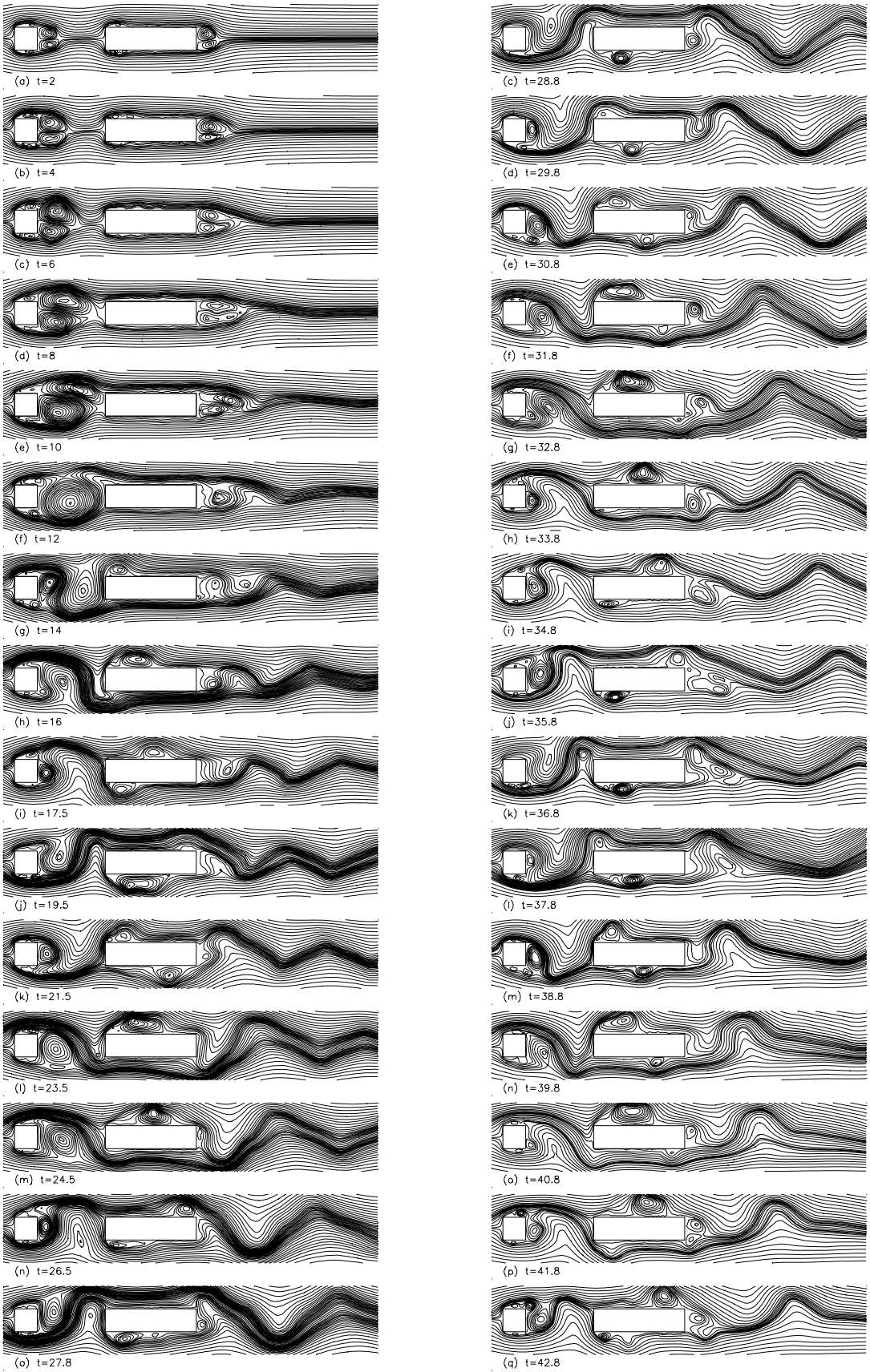

Figure 8.84. Calculated streamline patterns in flow over the ($C1$ = 1, $C2$ = 4, G = 3) array, showing flow development from the impulsive start to the fully-developed flow in which a vortex street forms in the gap.

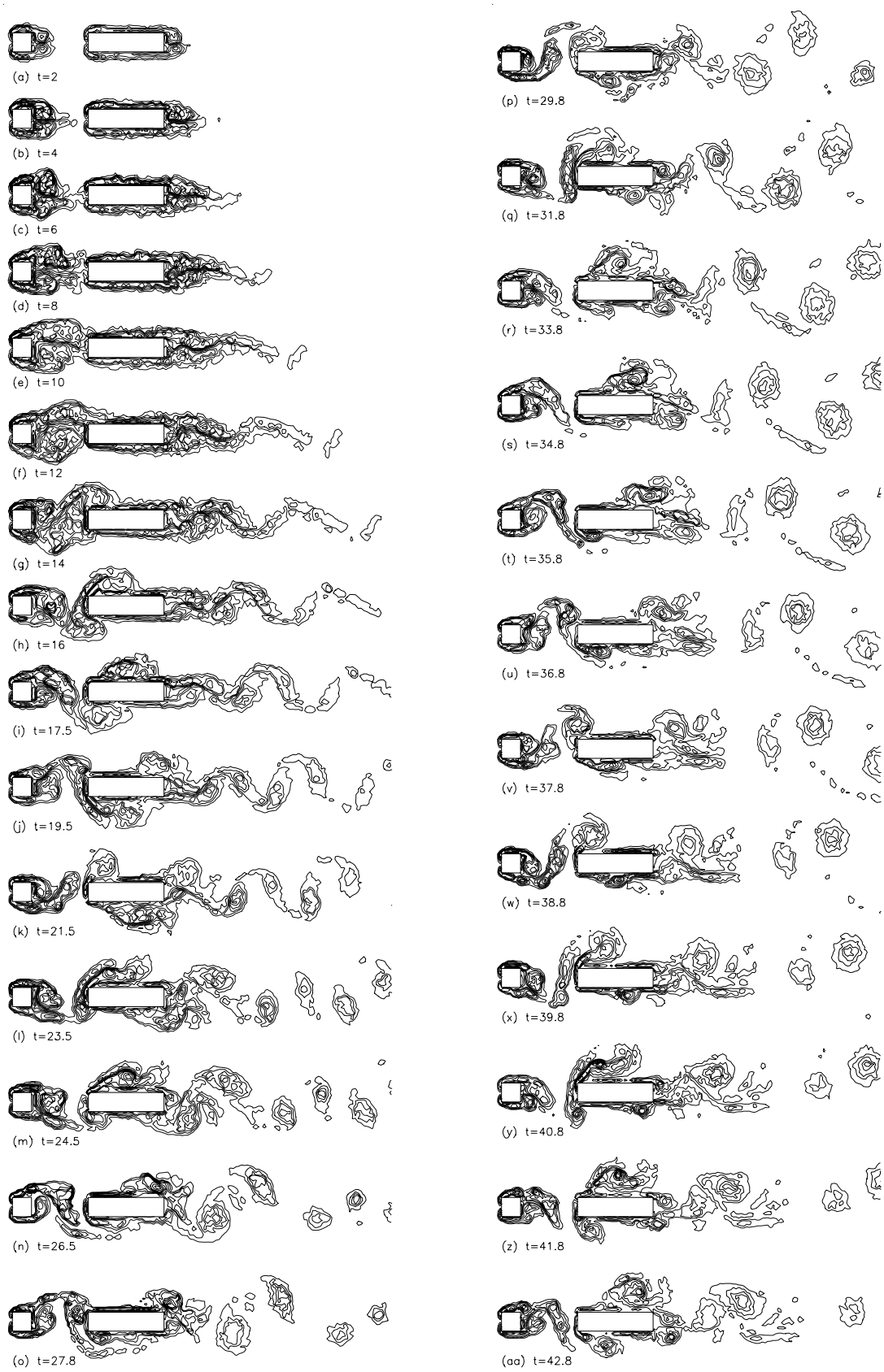

Figure 8.85. Calculated vorticity contours in flow over the ($C1 = 1$, $C2 = 4$, $G = 3$) array, showing flow development from an impulsive start to the fully-developed flow.

(a) $C1 = 1$, $C2 = 4$, $G = 4$, $t = 2$

(b) $C1 = 1$, $C2 = 4$, $G = 4$, $t = 4$

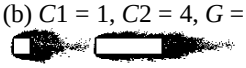

(c) $C1 = 1$, $C2 = 4$, $G = 4$, $t = 6$

(d) $C1 = 1$, $C2 = 4$, $G = 4$, $t = 8$

(e) $C1 = 1$, $C2 = 4$, $G = 4$, $t = 10$

(f) $C1 = 1$, $C2 = 4$, $G = 4$, $t = 12$

(g) $C1 = 1$, $C2 = 4$, $G = 4$, $t = 14.3$

(h) $C1 = 1$, $C2 = 4$, $G = 4$, $t = 16.3$

(i) $C1 = 1$, $C2 = 4$, $G = 4$, $t = 18.3$

(j) $C1 = 1$, $C2 = 4$, $G = 4$, $t = 20.3$

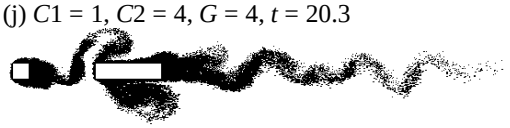

(k) $C1 = 1$, $C2 = 4$, $G = 4$, $t = 22.3$

(l) $C1 = 1$, $C2 = 4$, $G = 4$, $t = 24.3$

(m) $C1 = 1$, $C2 = 4$, $G = 4$, $t = 26.3$

(n) $C1 = 1$, $C2 = 4$, $G = 4$, $t = 28.3$

(o) $C1 = 1$, $C2 = 4$, $G = 4$, $t = 30.3$

(p) $C1 = 1$, $C2 = 4$, $G = 4$, $t = 32.3$

(q) $C1 = 1$, $C2 = 4$, $G = 4$, $t = 34.3$

(r) $C1 = 1$, $C2 = 4$, $G = 4$, $t = 36$

(s) $C1 = 1$, $C2 = 4$, $G = 4$, $t = 38$

(t) $C1 = 1$, $C2 = 4$, $G = 4$, $t = 39$

(u) $C1 = 1$, $C2 = 4$, $G = 4$, $t = 40.5$

(v) $C1 = 1$, $C2 = 4$, $G = 4$, $t = 41.5$

(w) $C1 = 1$, $C2 = 4$, $G = 4$, $t = 42.5$

(x) $C1 = 1$, $C2 = 4$, $G = 4$, $t = 43.5$

(y) $C1 = 1$, $C2 = 4$, $G = 4$, $t = 44.5$

(z) $C1 = 1$, $C2 = 4$, $G = 4$, $t = 45.5$

(aa) $C1 = 1$, $C2 = 4$, $G = 4$, $t = 46.5$

Figure 8.86. Elemental-vortex distributions in flow over the ($C1 = 1$, $C2 = 4$, $G = 4$) array, showing sequence of flow development from the impulsive start to the fully-developed state.

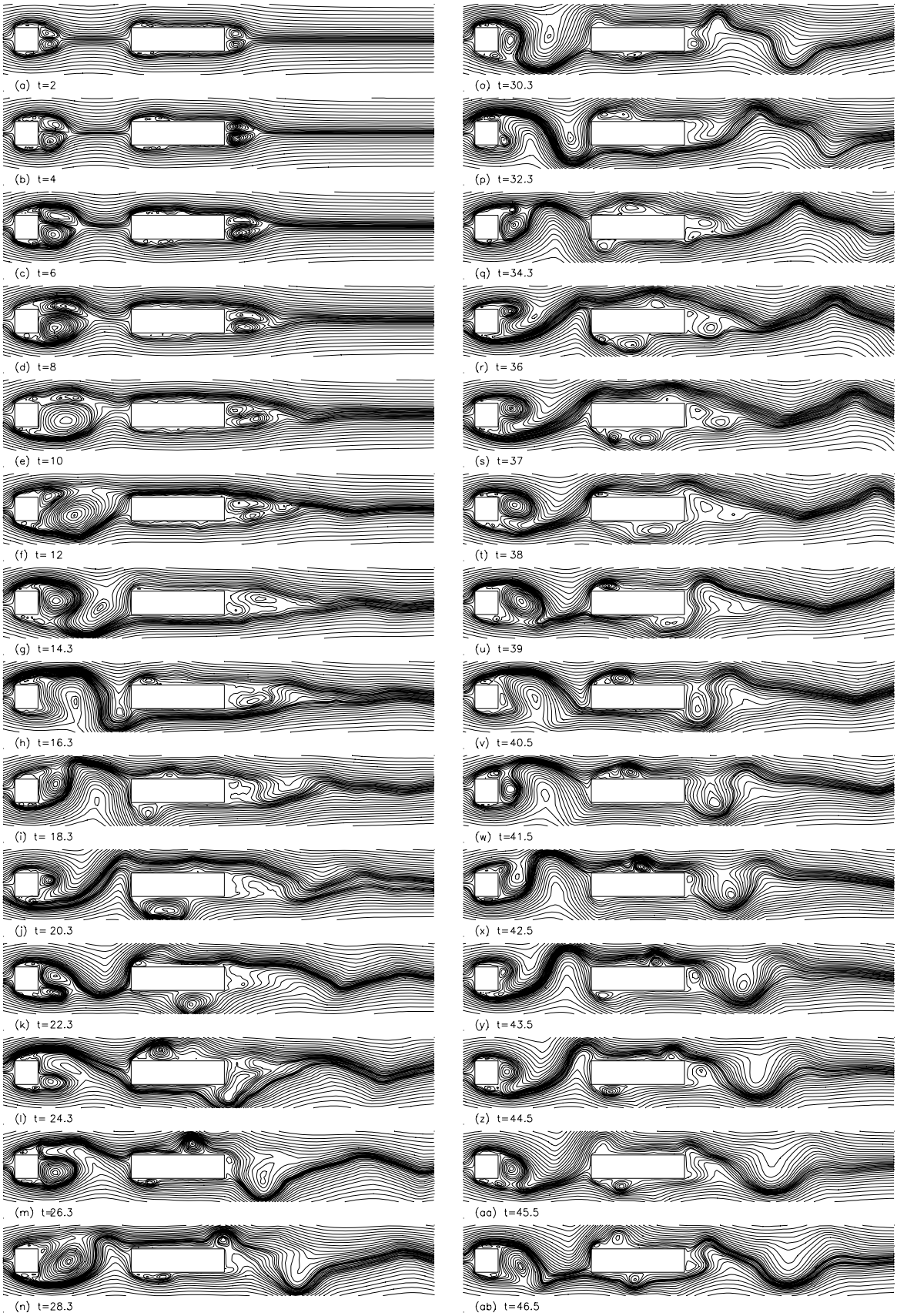

Figure 8.87. Streamline patterns in flow over the ($C1$ = 1, $C2$ = 4, G = 4) array, showing sequence of flow development from the impulsive start to the fully-developed state.

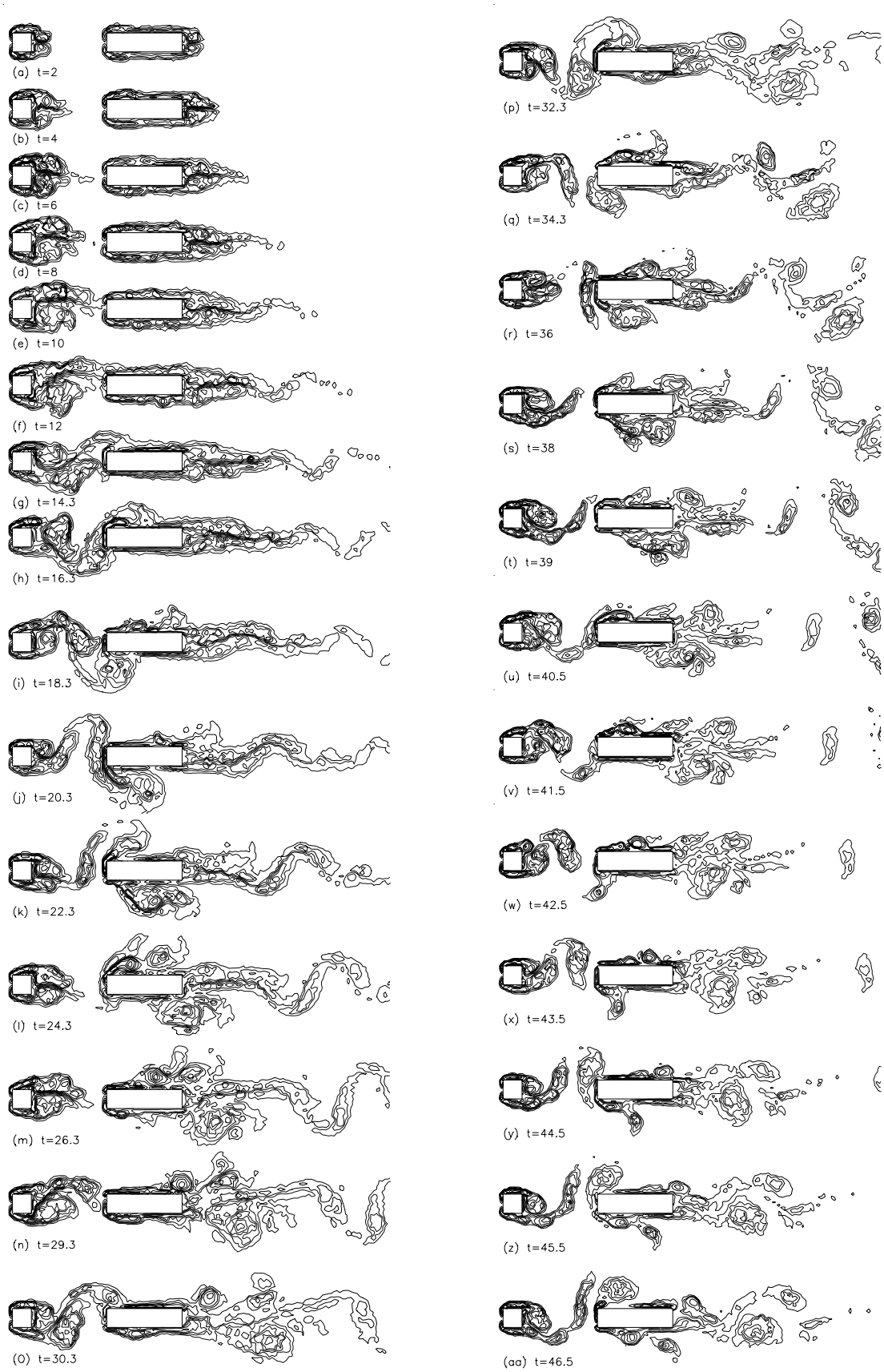

Figure 8.88. Calculated vorticity contours in flow over the ($C1 = 1$, $C2 = 4$, $G = 4$) array, showing sequence of flow development from the impulsive start to the fully-developed state.

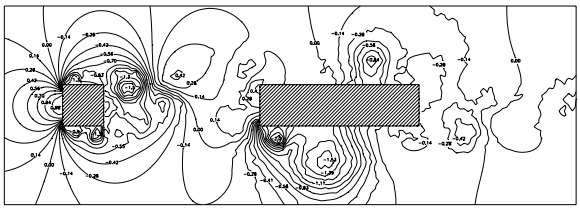

(a1) $G = 4$, $t = 36$

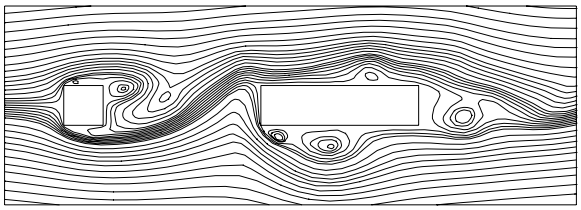

(a2) $G = 4$, $t = 36$

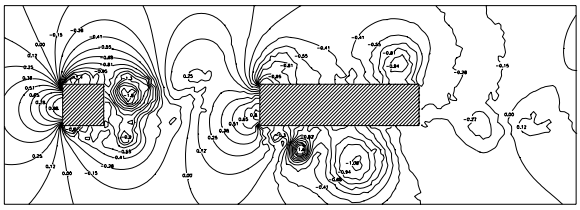

(b1) $G = 4$, $t = 37$

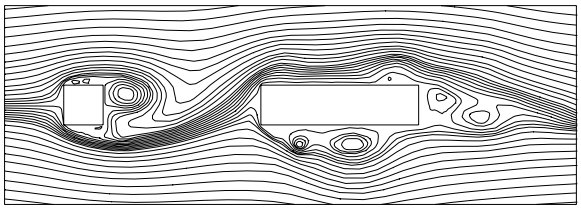

(b2) $G = 4$, $t = 37$

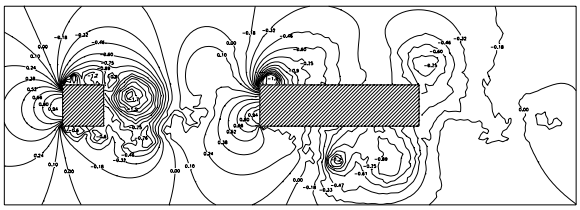

(c1) $G = 4$, $t = 38$

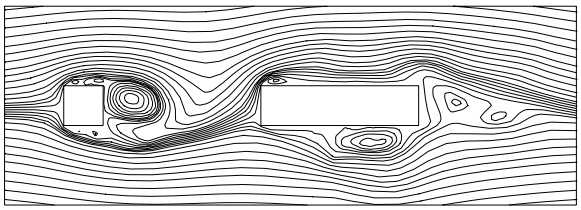

(c2) $G = 4$, $t = 38$

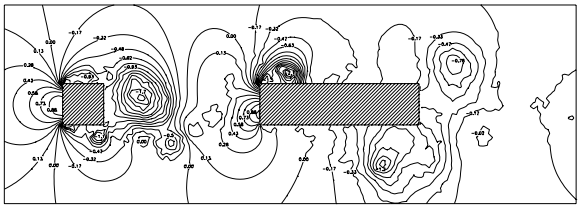

(d1) $G = 4$, $t = 39$

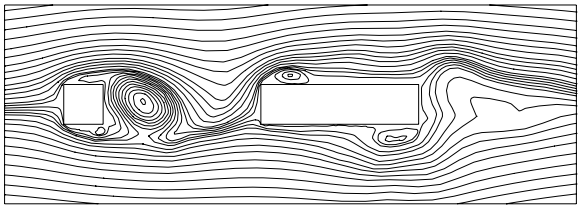

(d2) $G = 4$, $t = 39$

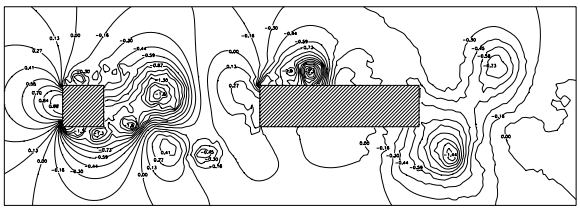

(e1) $G = 4$, $t = 40.5$

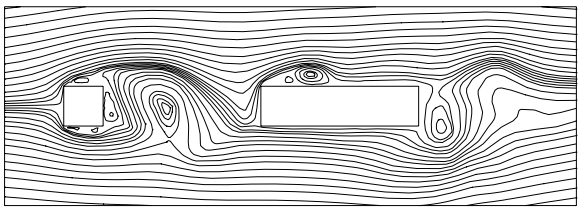

(e2) $G = 4$, $t = 40.5$

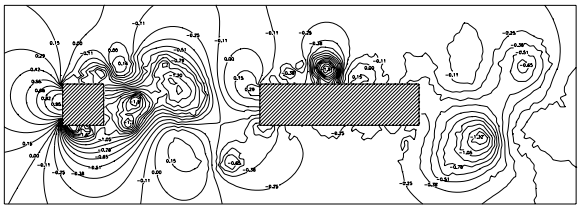

(f1) $G = 4$, $t = 41.5$

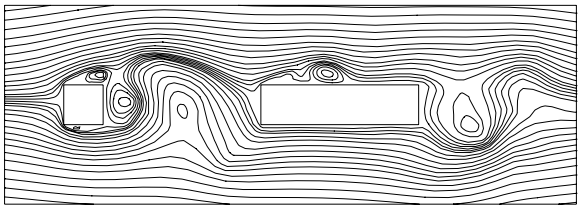

(f2) $G = 4$, $t = 41.5$

Figure 8.89. Instantaneous pressure fields and streamline patterns in fully-developed flow over the ($C1 = 1$, $C2 = 4$, $G = 4$) array, showing sequence of vortex-street impingement on the downstream plate. Numbers shown are coefficients of static pressure.

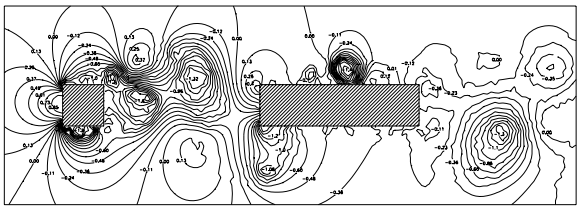

(g1) G = 4, t = 42.5

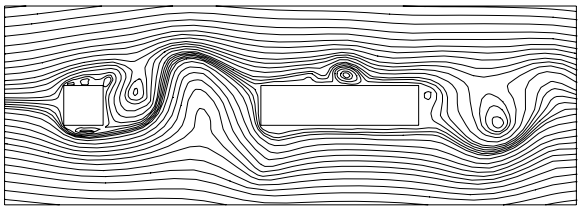

(g2) G = 4, t = 42.5

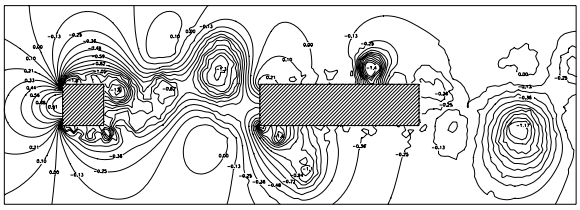

(h1) G = 4, t = 43.5

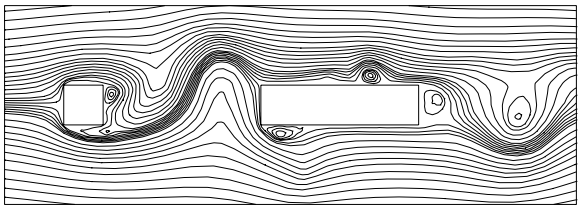

(h2) G = 4, t = 43.5

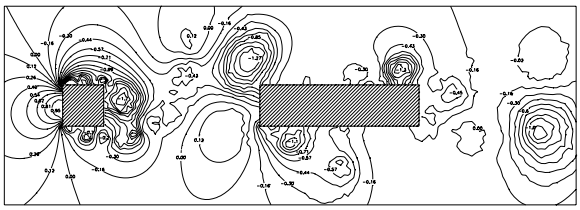

(i1) G = 4, t = 44.5

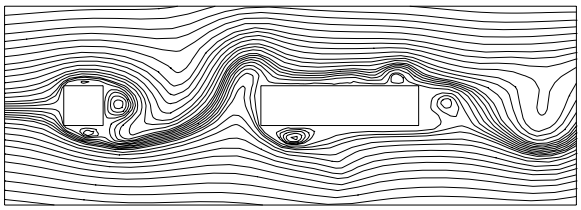

(i2) G = 4, t = 44.5

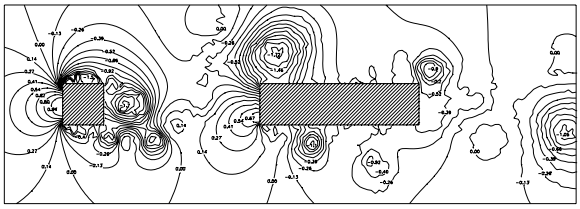

(j1) G = 4, t = 45.5

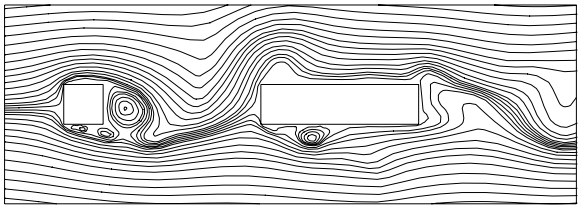

(j2) G = 4, t = 45.5

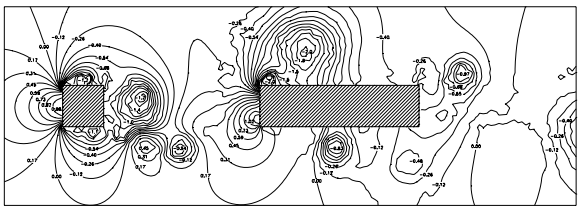

(k1) G = 4, t = 46.5

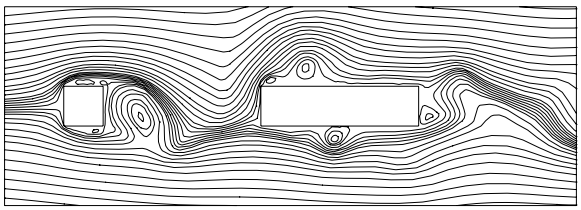

(k2) G = 4, t = 46.5

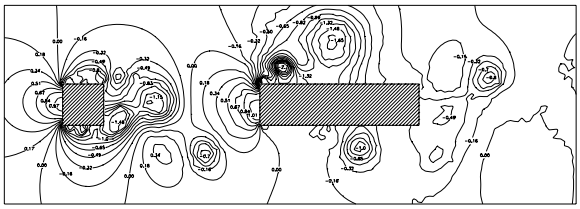

(l1) G = 4, t = 47.4

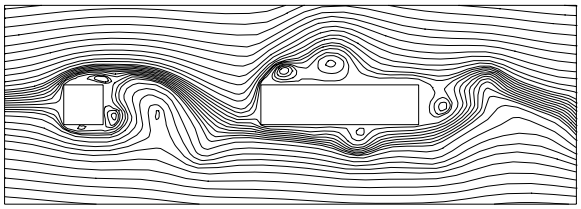

(l2) G = 4, t = 47.4

Figure 8.89. Cont'd.

(a) $C1 = 1$, $C2 = 4$, $G = 6$, $t = 4$

(b) $C1 = 1$, $C2 = 4$, $G = 6$, $t = 6$

(c) $C1 = 1$, $C2 = 4$, $G = 6$, $t = 8$

(d) $C1 = 1$, $C2 = 4$, $G = 6$, $t = 10$

(e) $C1 = 1$, $C2 = 4$, $G = 6$, $t = 12$

(f) $C1 = 1$, $C2 = 4$, $G = 6$, $t = 14$

(g) $C1 = 1$, $C2 = 4$, $G = 6$, $t = 16$

(h) $C1 = 1$, $C2 = 4$, $G = 6$, $t = 18$

(i) $C1 = 1$, $C2 = 4$, $G = 6$, $t = 20$

(j) $C1 = 1$, $C2 = 4$, $G = 6$, $t = 22$

(k) $C1 = 1$, $C2 = 4$, $G = 6$, $t = 24$

(l) $C1 = 1$, $C2 = 4$, $G = 6$, $t = 26$

(m) $C1 = 1$, $C2 = 4$, $G = 6$, $t = 28$

(n) $C1 = 1$, $C2 = 4$, $G = 6$, $t = 30$

(o) $C1 = 1$, $C2 = 4$, $G = 6$, $t = 32$

(p) $C1 = 1$, $C2 = 4$, $G = 6$, $t = 34$

(q) $C1 = 1$, $C2 = 4$, $G = 6$, $t = 36$

(r) $C1 = 1$, $C2 = 4$, $G = 6$, $t = 38$

(s) $C1 = 1$, $C2 = 4$, $G = 6$, $t = 40$

(t) $C1 = 1$, $C2 = 4$, $G = 6$, $t = 42$

(u) $C1 = 1$, $C2 = 4$, $G = 6$, $t = 44$

(v) $C1 = 1$, $C2 = 4$, $G = 6$, $t = 46$

(w) $C1 = 1$, $C2 = 4$, $G = 6$, $t = 47$

(x) $C1 = 1$, $C2 = 4$, $G = 6$, $t = 48$

(y) $C1 = 1$, $C2 = 4$, $G = 6$, $t = 49$

Figure 8.90. Elemental-vortex distributions in flow over the ($C1 = 1$, $C2 = 4$, $G = 6$) array, showing flow development from an impulsive start to the fully-developed flow.

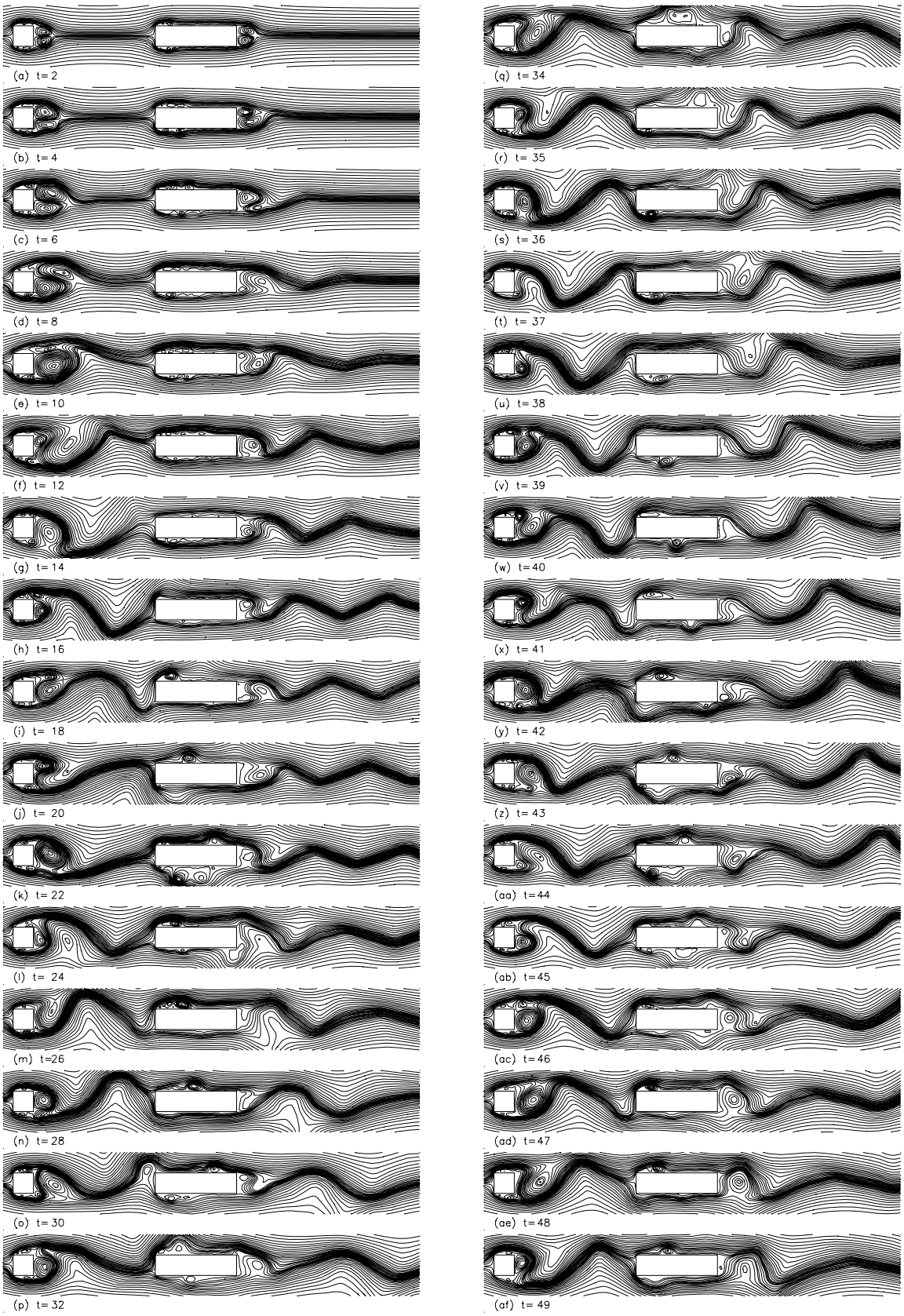

Figure 8.91. Streamline patterns in flow over the ($C1$ = 1, $C2$ = 4, G = 6) array, showing flow development from the impulsive start to the fully-developed flow in which a vortex street forms in the gap.

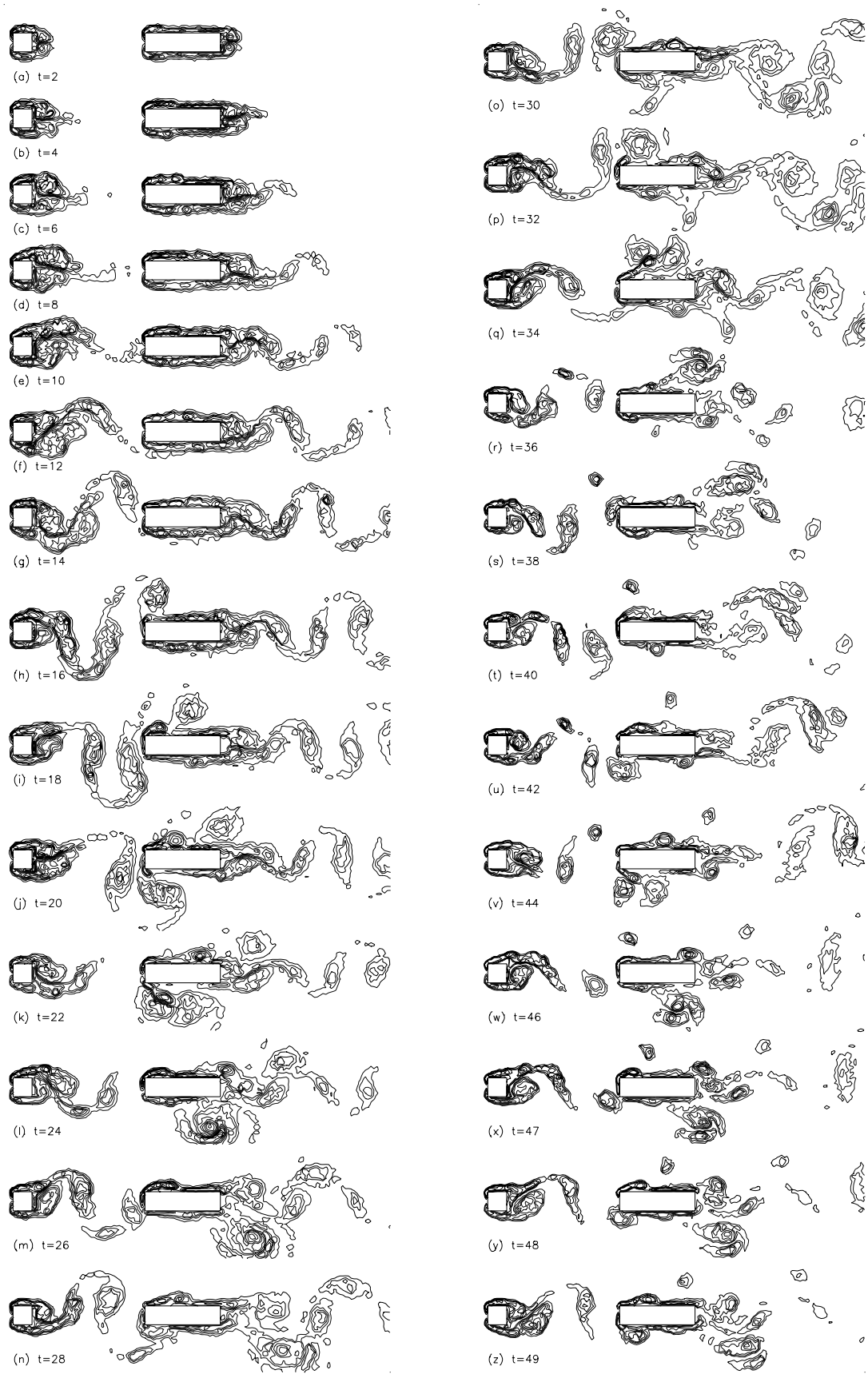

Figure 8.92. Calculated vorticity contours in flow over the ($C1 = 1$, $C2 = 4$, $G = 6$) array, showing flow development from the impulsive start to the fully-developed flow in which a vortex street forms in the gap.

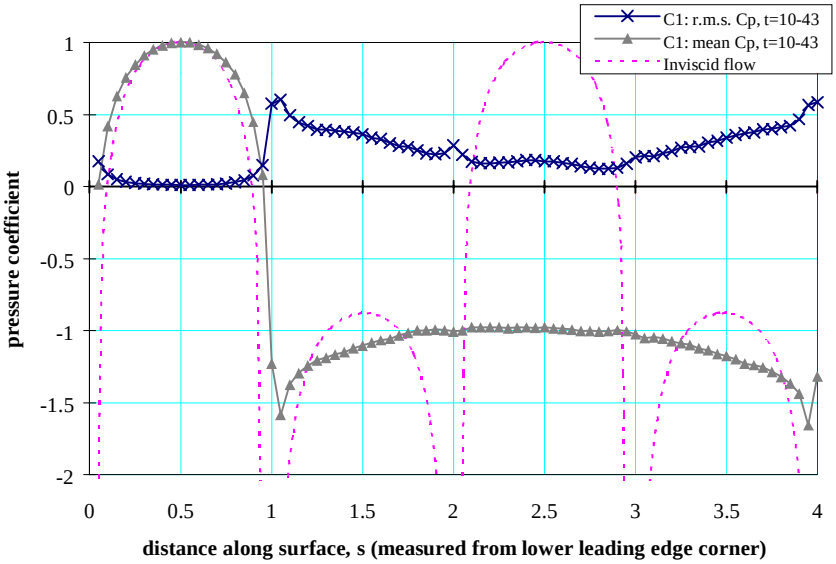

(a)

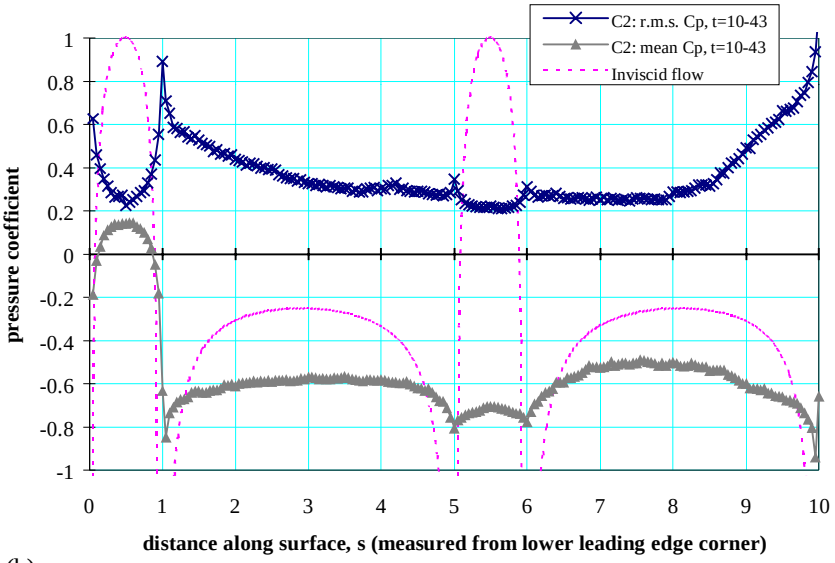

(b)

Figure 8.93. Calculated distributions of mean and r.m.s. pressure coefficients on the cylinders in the ($C1 = 1$, $C2 = 4$, $G = 3.0$) array.

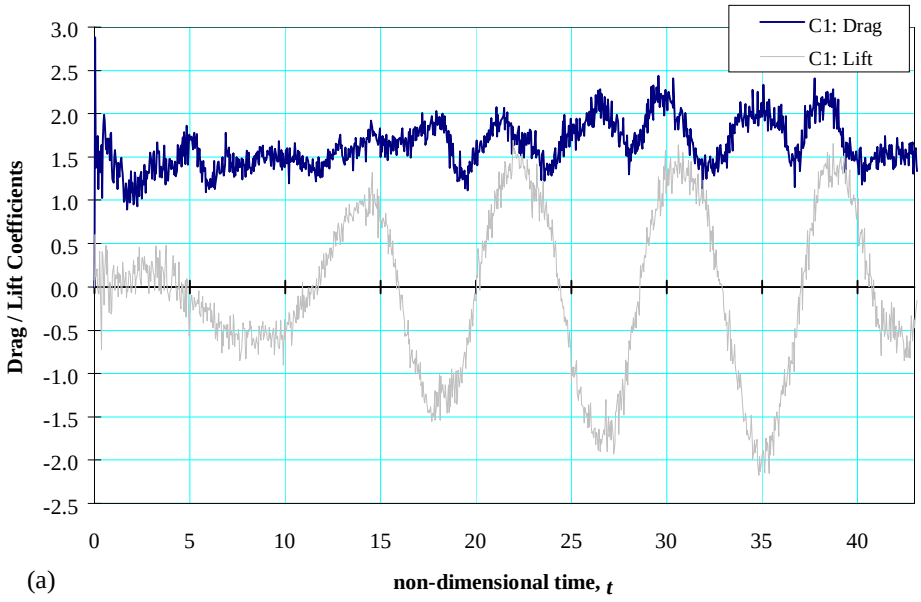

(a)

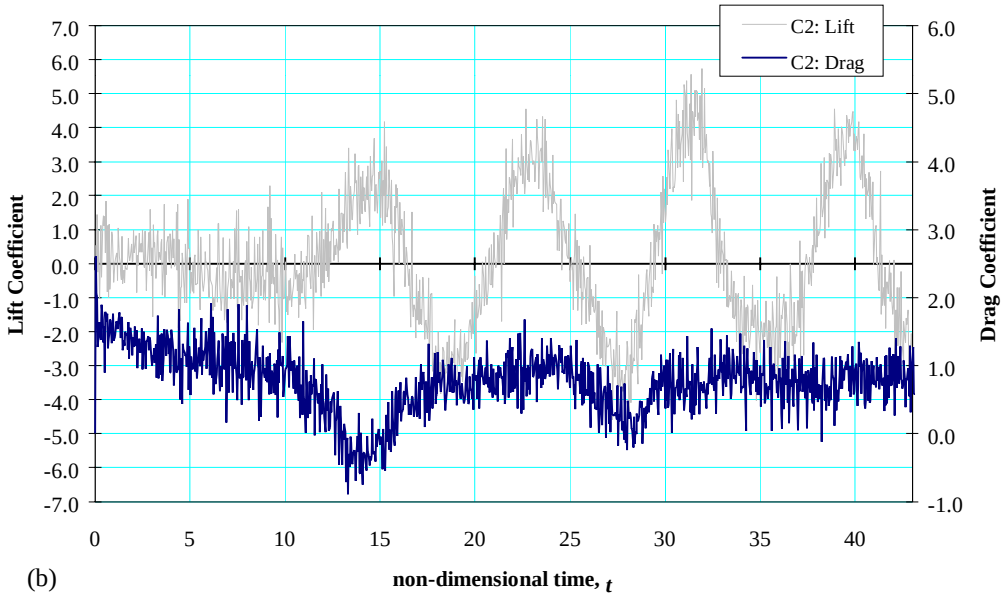

(b)

Figure 8.94. Time-histories of drag and lift on the ($C1$ = 1, $C2$ = 4, G = 3.0) array, (a) upstream plate, (b) downstream plate.

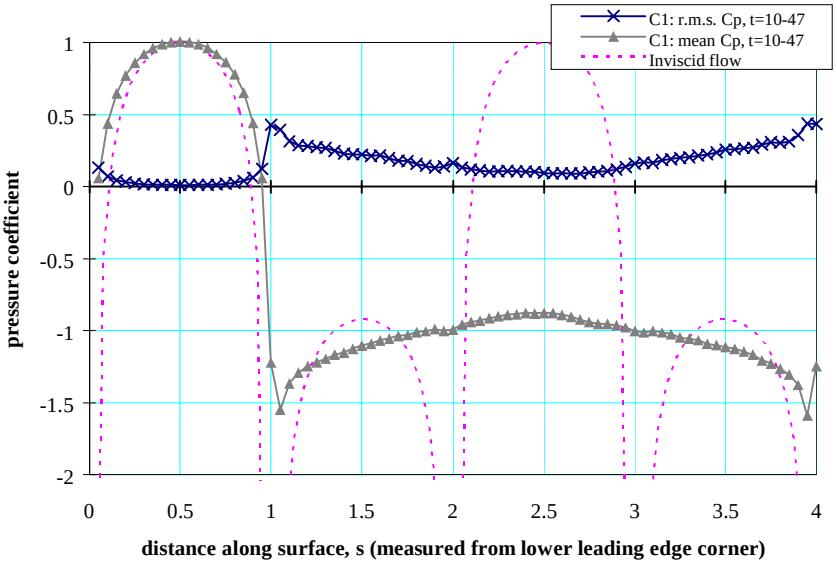

(a)

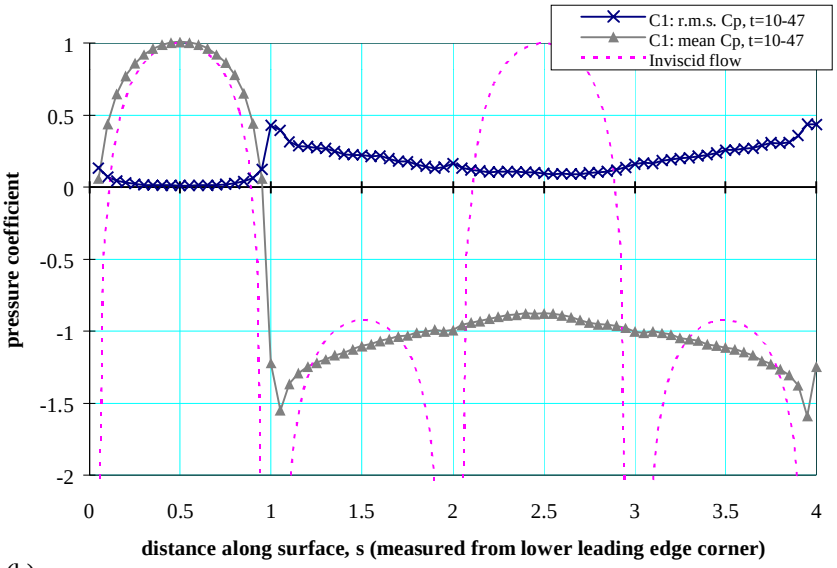

(b)

Figure 8.95. Calculated distributions of mean and r.m.s. pressure coefficients on the cylinders in the ($C1 = 1$, $C2 = 4$, $G = 4.0$) array.

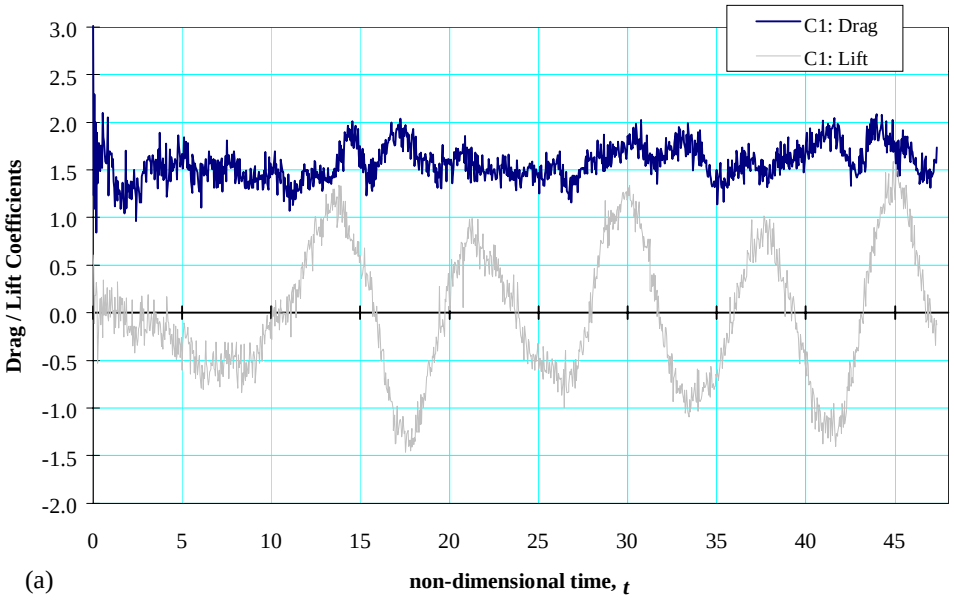

(a)

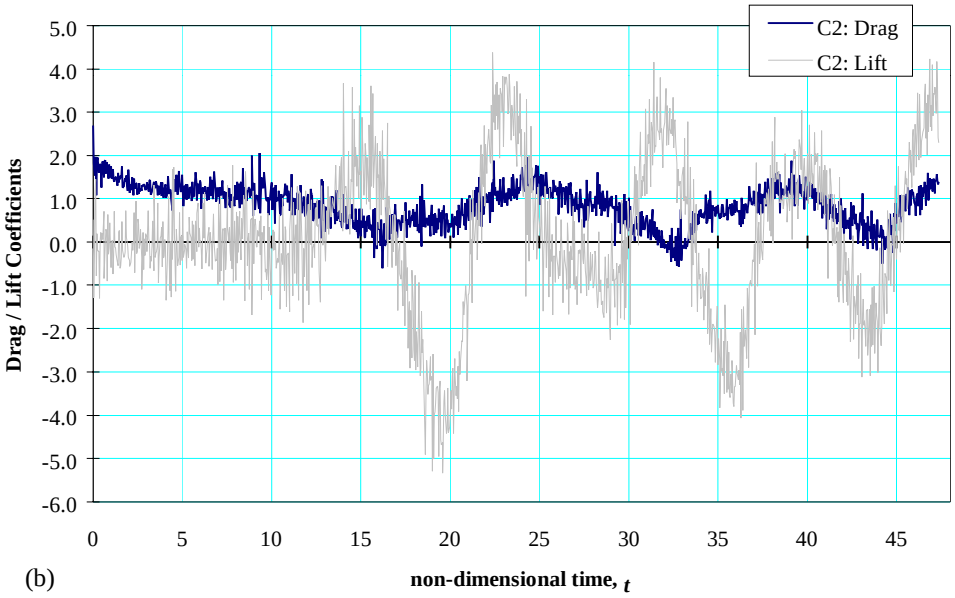

(b)

Figure 8.96. Time-histories of drag and lift on the ($C1 = 1$, $C2 = 4$, $G = 4.0$) array, (a) upstream plate, (b) downstream plate.

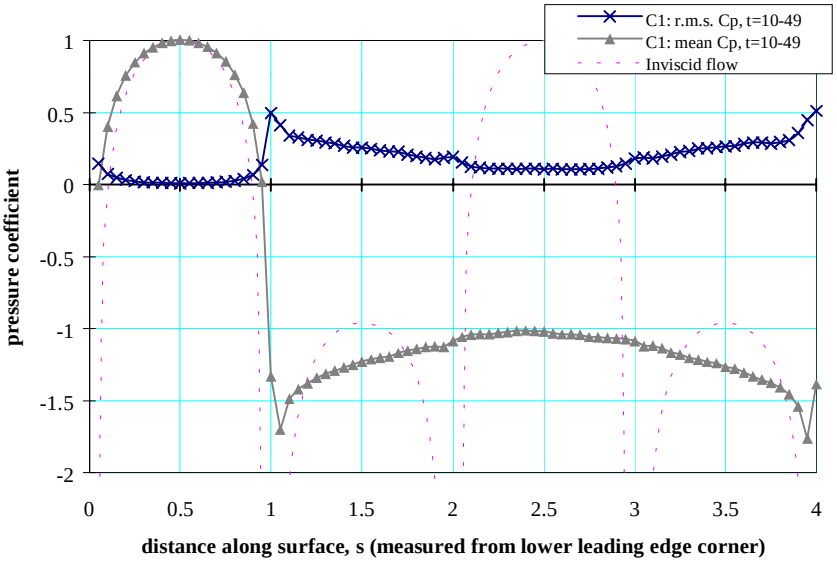

(a)

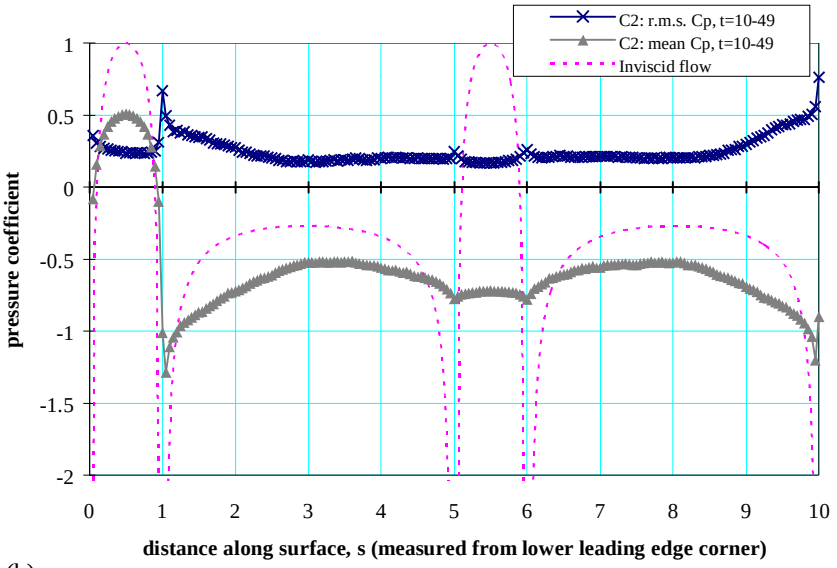

(b)

Figure 8.97. Calculated distributions of mean and r.m.s. pressure coefficients on the cylinders in the ($C1 = 1$, $C2 = 4$, $G = 6.0$) array.

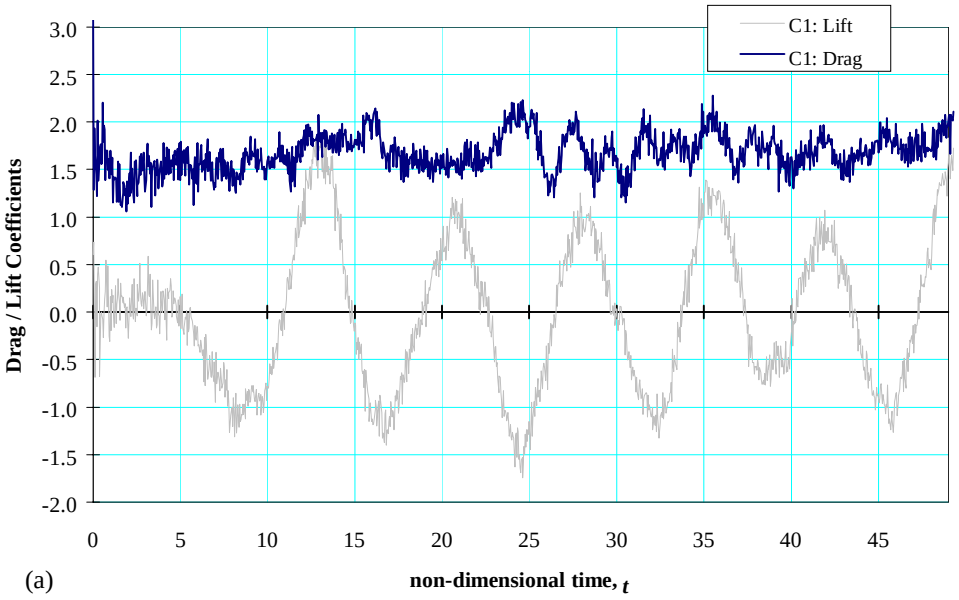

(a)

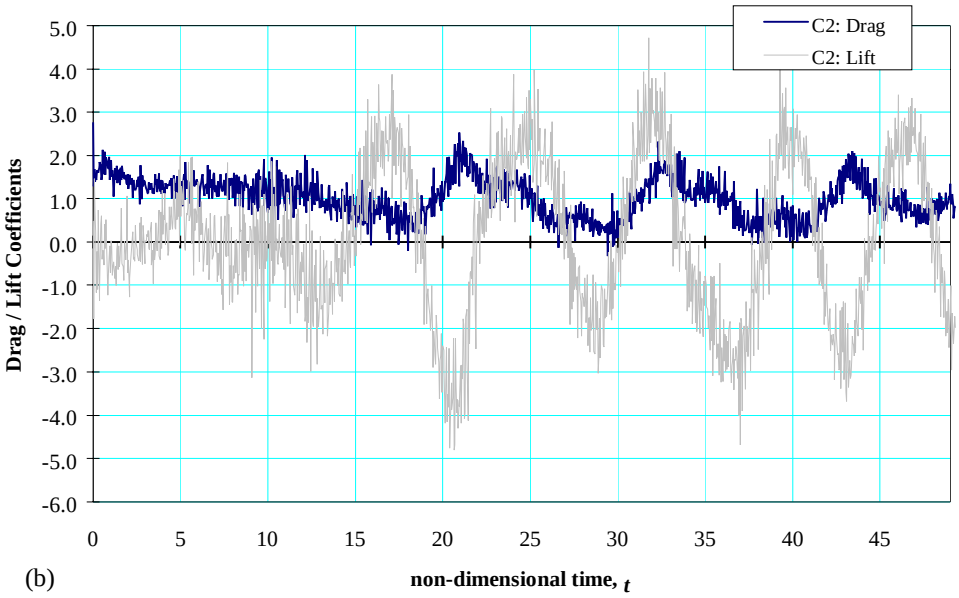

(b)

Figure 8.98. Time-histories of drag and lift on the ($C1 = 1$, $C2 = 4$, $G = 6.0$) array, (a) upstream plate, (b) downstream plate.

8.4.3 Effects of the Gap-to-Thickness Ratio on the Flow Parameters

Calculated results for the Strouhal number of vortex shedding into the wake *St* derived from vorticity patterns and the power spectra of fluctuating lift on the downstream plate, the base-pressure coefficients C_{pb1} and C_{pb2} on the upstream and downstream plates, the pressure coefficient C_{pf2} on the leading face of the downstream plate, the drag coefficient on both the upstream and downstream plates and the coefficient of total drag of the array, at $Re_h = 500$, are displayed in Fig. 8.100 as a function of gap-to-thickness ratio. The experimental data of Bull *et al.* [1997], for the ($C1 = 1$, $C2 = 6$) array at $Re_h \sim 17{,}000$, are also shown in Figs. 8.100(a) and 8.100(b). Again, because of dependence of these flow parameters on Reynolds number and plate configuration in some flow regimes, strict comparisons between calculation and experiment are not always possible. Computational results indicate that the flow changes from the *E*1 to the *B* regime at about $G = 3$, with an accompanying discontinuous change in the pressure coefficients and Strouhal number.

Streamline patterns given previously for the array in the flow regimes with trapped-vortex flow in the gap and vortex-street formation in the gap have been as seen from a fixed reference frame. The characteristic streamline patterns of these flow regimes and their development as gap-to-thickness ratio is increased through the range $G = 1.5$ to 6.0 can be usefully viewed from another perspective, namely that of a frame of reference moving at the velocity of convected vortices. In the patterns viewed from a frame of reference moving at a velocity $U_{ref} = 0.8U_\infty$ (Fig. 8.101), the vortical structures are highlighted and the effects of increasing gap length on the flow structure in the gap and the wake of the array can be clearly seen.

The predicted Strouhal numbers of vortex-shedding into the wake from the downstream plate are shown in Fig. 8.100(a). The general trend of their variation with *G* follows quite closely that shown by the experimental data of Bull *et al*. [1997]. There are generally only small differences between the calculated and experimental values of *St*. As previously remarked on for the ($C1 = 1$, $C2 = 1$) array, whether these differences are a consequence of Reynolds number differences is not known. Both calculation and experiment indicate a change from the trapped-vortex regime to the vortex-street in the gap regime at $G \sim 3$; and both indicate a change in the Strouhal-number variation, from decreasing to increasing, as *G* increases through this change-over value. The experimental data also show that these changes are accompanied by a discontinuity in *St*; it appears that the simulations would also predict the discontinuity.

The characteristics of surface-pressure distributions on the plates in the specific regimes have been described in previous sections 8.4.1 and 8.4.2. The general trend of the variation of surface-pressure with gap-to-thickness ratio is that, as the gap is lengthened, the mutual influence between the plates decreases and they behave more like two isolated single plates. The surface-pressure distribution on the upstream cylinder remains virtually unchanged with G and is very similar to that on a single square cylinder throughout, even though changes in flow regime occur over the range of G values considered. As the gap is increased from $G = 1.5$ to 6, the base-pressure on the upstream cylinder increases from $C_{pb1} \approx -0.8$ to -1.0 towards the single-cylinder value $C_{pb} \approx -1.1$. Similarly, the drag coefficient increases from $C_{D1} \approx 1.5$ to 1.7, approaching the value $C_D \approx 1.8$ for a single square cylinder at $Re_h = 500$ (Fig. 7.39).

The surface-pressure distribution on the down stream plate is very much dependent on the flow regime. The leading-face pressure increases from $C_{pf2} \approx -0.5$ at small gaps in the $E1$ regime to $C_{pf2} \approx 0.5$ in the B regime, while the base-pressure changes very little, from $C_{pb2} \approx -0.65$ to -0.75 as the gap is increased from $G = 1.5$ to 6. Consequently, the drag on the downstream plate increases from negative to positive values as the gap-to-thickness ratio is increased through the value at which the change from the $E1$ to the B regime occurs. As the mutual influence between the plates diminishes for large value of G, the base-pressure coefficient approaches the value $C_{pb2} = -0.8$ calculated for a single plate, and the leading-face pressure coefficient C_{pf2} tends to the stagnation value of unity.

In general, the variation of pressure coefficients with G predicted by the numerical simulations has the same form as found experimentally. There is fairly close quantitative agreement between calculation and experiment for the base pressure on the upstream cylinder, rather less close agreement for the leading-face pressure on the downstream plate, and greater disparity for the base pressure on the downstream plate. As in previous comparisons for the ($C1 = 1$, $C2 = 1$) array, the relative effects of the large Reynolds number differences and possible shortcomings in the simulation procedures are not known.

8.4.4 Concluding Remarks for the ($C1 = 1$, $C2 = 4$) Arrays

Calculations of flow over an array with an upstream plate with $C = 1$ and a downstream plate with $C = 4$ have been made for gap-to-thickness ratios of $G = 1.5$, 2, 3, 4 and 6 and a Reynolds number of $Re_h = 500$. From the calculated flow patterns, two flow regimes within this range of gap-to-thickness ratio can be identified and are of similar character to those found in experimental flow visualisation by Bull *et al.* [1997] at higher Reynolds number. There is also some measure of quantitative agreement between calculated and experimental data.

For arrays with small gaps $G \leq 2$, the flow is characterised by intermittent reattachment at the leading edge of the downstream plate, and permanent trailing-edge separation on the downstream plate (regime $E1$). At $G = 1.5$, the gap flow is characterised by an oscillating trapped-vortex flow, in which a pair of counter-rotating vortices oscillate periodically in size and configuration but at a lower frequency than that of the cycle of vortex-shedding into the wake from the downstream plate. At $G = 2$, transition to vortex-street flow in the gap is just beginning, and periodic vortex shedding from the upstream cylinder can be identified. The shedding frequency is, however, significantly lower than the wake-vortex frequency; it appears that this frequency increases with increasing G until vortex shedding from the two plates becomes synchronised when a vortex-street flow becomes established in the gap at larger G.

For arrays with large gaps, $G > 3$, the shear layers separating from the leading corners of the upstream cylinder either reattach on the u pstream cylinder or impinge on the array at a position within the gap (regime B). The flow is characterised by the formation of a vortex street in the gap and its subsequent impingement on the downstream plate. As a result of clipping in the impingement process, each vortex in the street is transformed into a primary vortex (which usually comprises the greater part of the incident vortex) and a secondary vortex which both move onto a side face of the downstream plate. After convection along the side face, both are shed into the wake of the array, together with any, usually very weak, trailing-face vortex present at the same time. The final vortex street of the whole array is less regular than that of an array in the trapped-vortex regime. The characteristic vortex-shedding frequencies of the upstream and downstream plate are the same.

From the variation of flow patterns and flow parameters with the gap-to-thickness ratio (Fig. 8.100), it is evident that transition from the *E*1 to the *B* regime occurs at $G \approx 3$, accompanied by sharp changes in both pressure-coefficient and Strouhal-number variation. With increased chord-length of the downstream plate, the transition from regime *E*1 to regime *B* is delayed to a higher value of *G* – from $G \approx 2$ for the ($C1 = 1$, $C2 = 1$) array to $G \approx 3$ for the ($C1 = 1$, $C2 = 4$) array. This appears to reflect the diminished influence exerted on the gap flow by the near-wake flow of the array as the downstream plate is lengthened, resulting in the persistence of quasi-steady trapped-vortex flow to larger gaps.

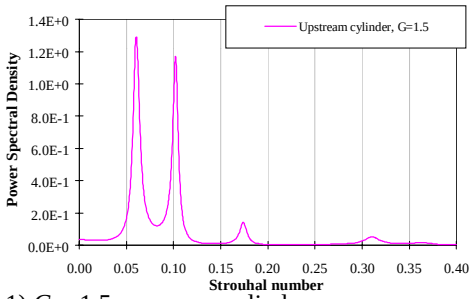

(a1) G = 1.5, upsrream cylinder

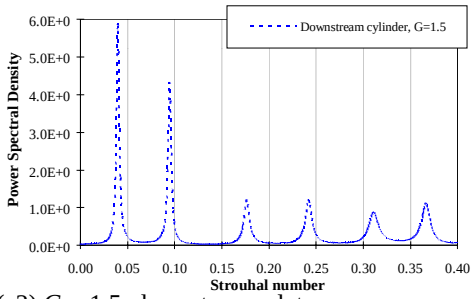

(a2) G = 1.5, downstream plate

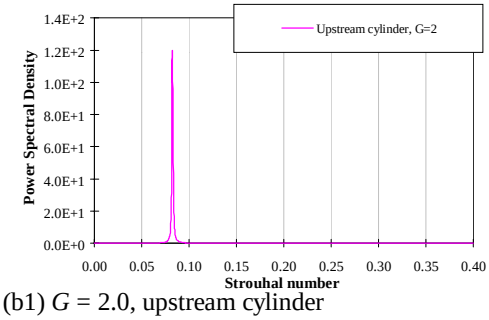

(b1) G = 2.0, upstream cylinder

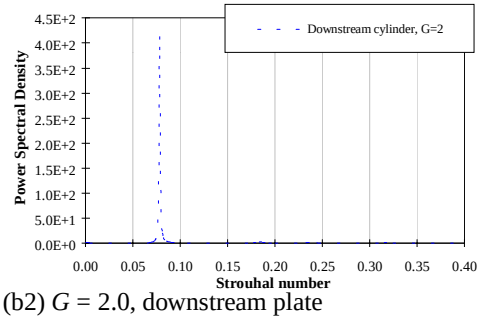

(b2) G = 2.0, downstream plate

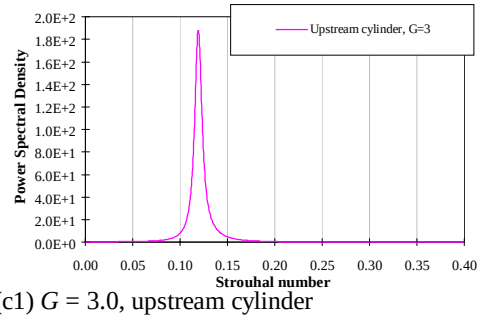

(c1) G = 3.0, upstream cylinder

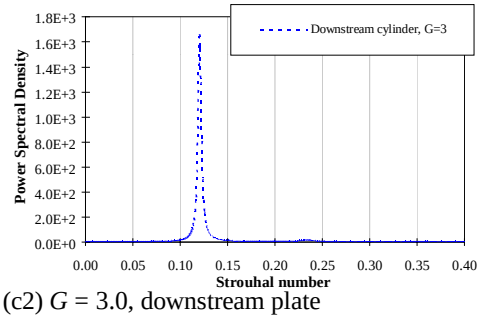

(c2) G = 3.0, downstream plate

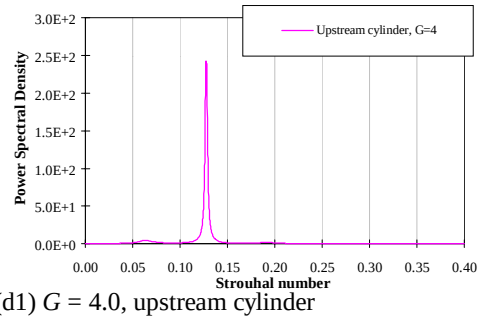

(d1) G = 4.0, upstream cylinder

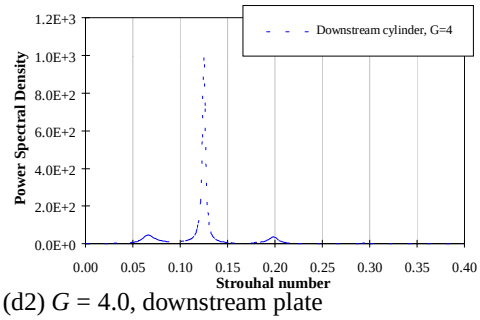

(d2) G = 4.0, downstream plate

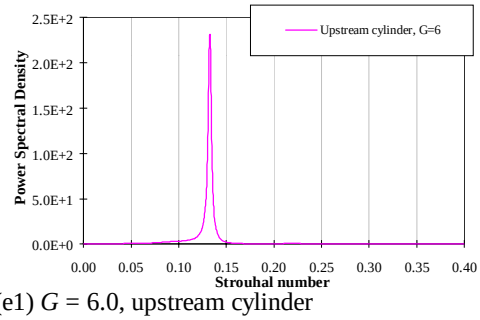

(e1) G = 6.0, upstream cylinder

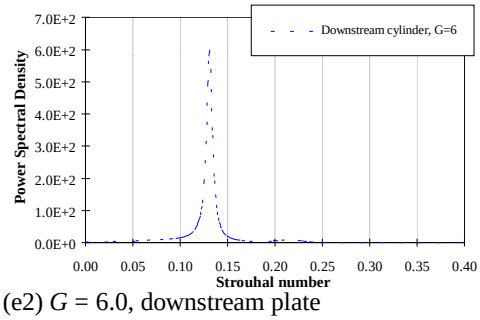

(e2) G = 6.0, downstream plate

Figure 8.99. Power spectra of fluctuating lift of the ($C1$ = 1, $C2$ = 4) array with various gap-to-thickness ratio in the range $1.5 \leq G \leq 6.0$.

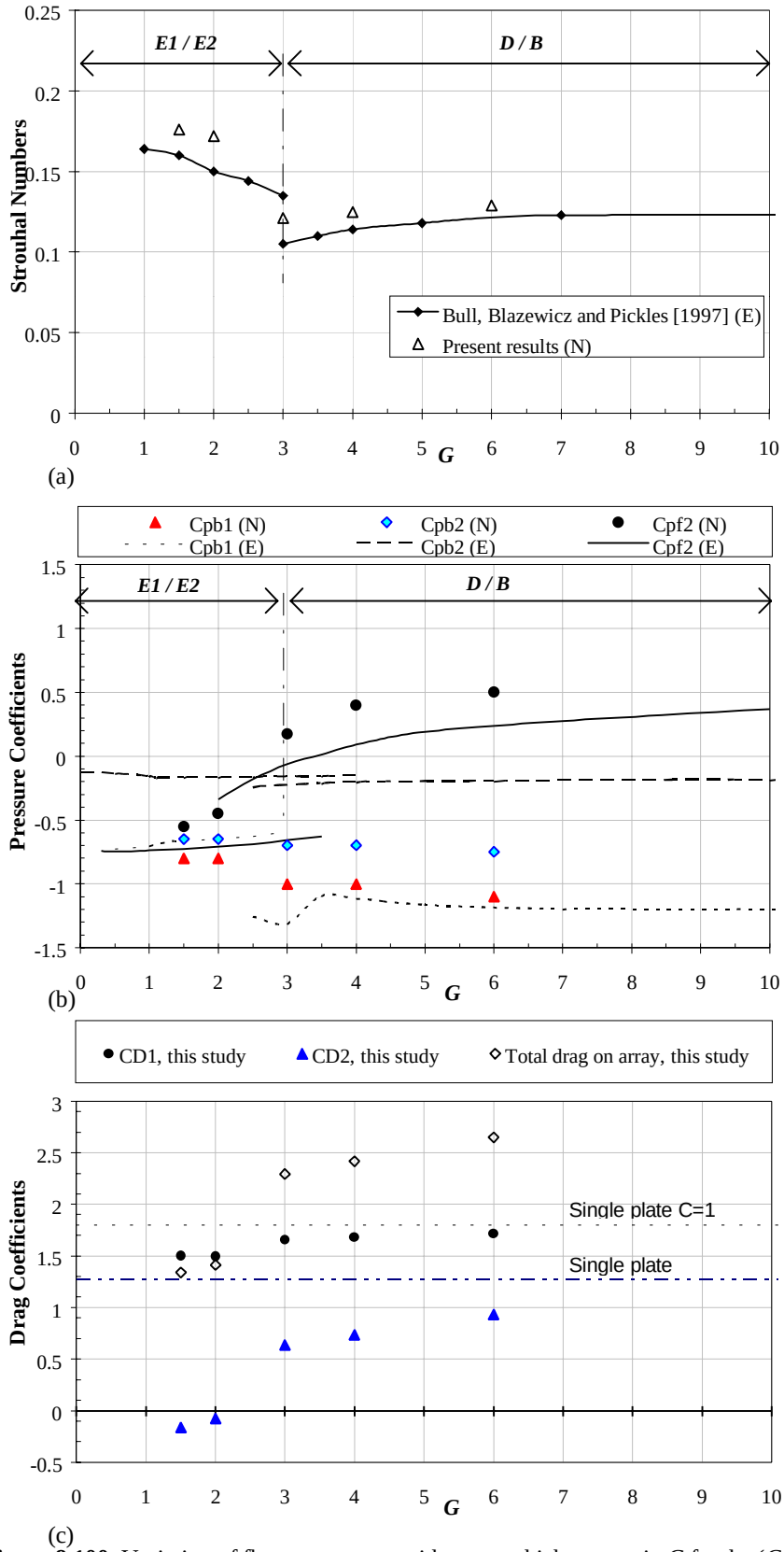

Figure 8.100. Variation of flow parameters with gap-to-thickness ratio G for the ($C1$ = 1, $C2$ = 4) array: (a) Strouhal numbers of vortex shedding into the wake of the array, (b) pressure coefficients and (c) drag coefficients. Experimental data (E) are those of Bull, Blazewicz and Pickles [1997] for the ($C1$ = 1, $C2$ = 6) array at Re_h ~ 17,000; Strouhal numbers St (E) are frequencies of vortex shedding from the upstream plate.

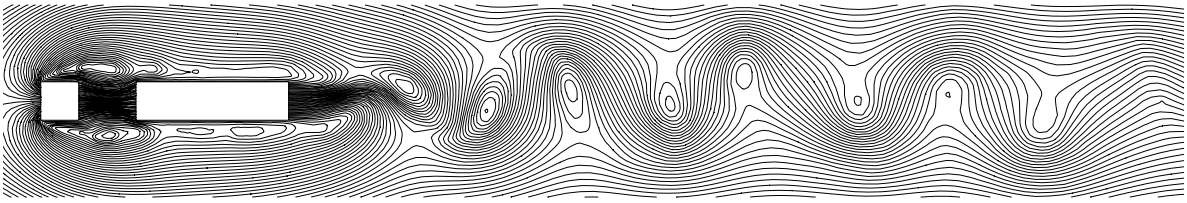

(a) G = 1.5, t = 38.6

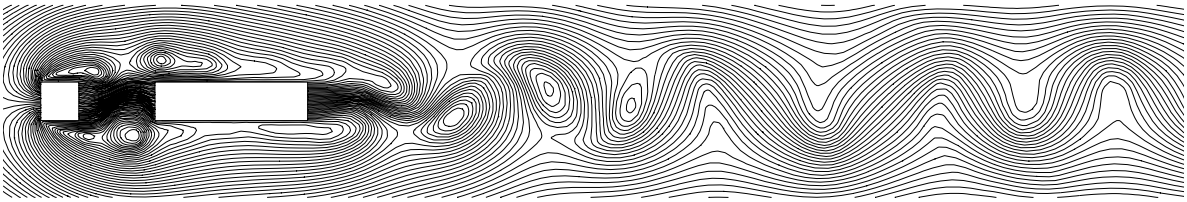

(b) G = 2.0, t = 49.3

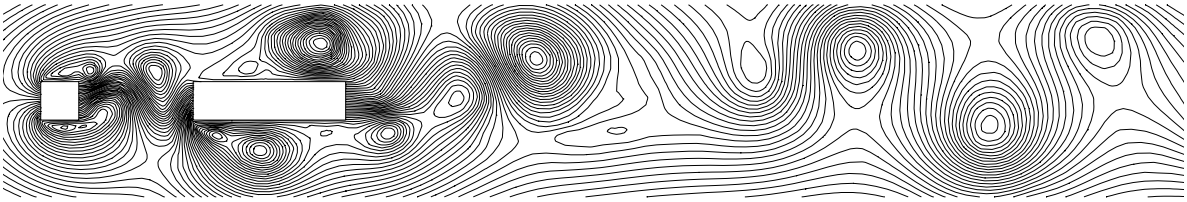

(c) G = 2.0, t = 43.1

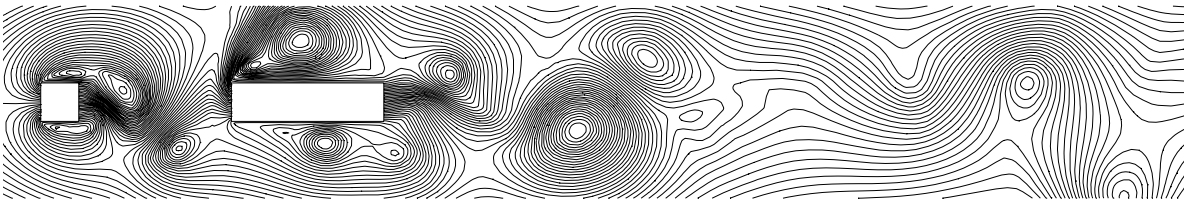

(d) G = 4.0, t = 47.4

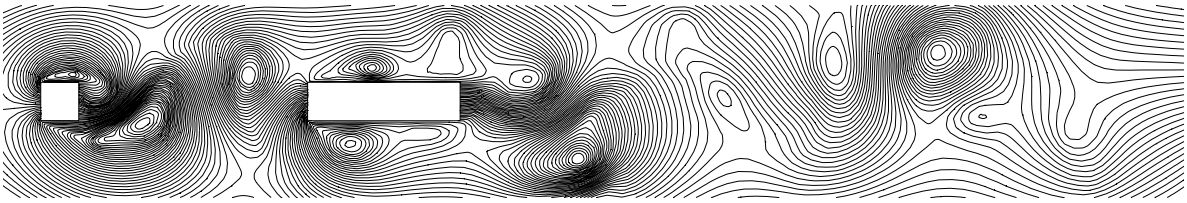

(e) G = 6.0, t = 49.3

Figure 8.101. Predicted streamline patterns in flow over the ($C1$ = 1, $C2$ = 4) array: (a) G = 1.5, (b) G = 2, (c) G = 3, (d) G = 4 and (e) G = 6; calculated in a reference frame moving at a velocity of $U_{ref} = 0.8U_{\infty}$.

8.5 Arrays with Long Upstream and Downstream Plates

Calculations presented in previous sections 8.2 and 8.3 have been focused on arrays with a square upstream cylinder at $Re_h = 500$. The flow regimes which have been identified are *F*2, *E*1, *E*2, and *B*, in which impingement of the shear layers separated from the leading corners of the upstream cylinder occurs intermittently on or beyond the downstream plate, intermittently on the gap or the downstream plate, or intermittently on the upstream cylinder itself or the gap. Attention in this section is given to arrays with an upstream plate with sufficiently long chord ($C1 > S_{max}$) to ensure permanent reattachment of the shear layers from the leading corners to the upstream plate, and the formation of a leading-edge-separation bubble. The flow is then in the regime *A* of Bull *et al*. [1997]. It has been noted for single rectangular plates that the process of vortex shedding from a long plate (with, for example, $C = 4$) is different from the vortex formation on a short plate (with, for example, $C = 1$). For long plates, the formation of vortices downstream of the plate results from a combination of boundary-layer separation from the trailing edge and the shedding of convected side-face vortices originally formed in the leading-edge-separation bubble on the plate. Increasing the chord-to-thickness ratio *C*1 of the upstream plate, to such an extent as to switch the mechanism of vortex-shedding on the upstream plate to this form, gives rise to differences in the details of the flow between the plates although the general characteristics remain unchanged, as will be seen in following sections.

The calculation results presented here are for arrays with the upstream and downstream plates of the same chord-to-thickness ratio $C1 = C2 = 4$, and, as in all cases of tandem array previously considered, at the Reynolds number $Re_h = 500$. The gap-to-thickness ratios considered are in the range $1.0 \le G \le 8.0$, intended to cover both flow regimes with trapped-vortex flow in the gap and the flow regimes with a vortex-street flow in the gap.

8.5.1 Previous Studies of Flow over Tandem Arrays with a Long Upstream Plate

Tandem arrays of two rectangular cylinders with a long upstream plate, $C1 = 12.7$, and downstream plates with $C2 \sim 6$ and 16 have been studied by Blazewicz, Bull and Pickles [1995]. They found the general flow patterns for these arrays to be similar to those found in earlier studies of an array of an upstream plate with $C1 = 6.1$ and an elliptically-faired leading edge and a rectangular downstream plate with $C2 = 6.1$ by Bull, Pickles, Martin and Welsh

[1989] and Bull and Pickles [1991], even though flow separation and leading-edge bubble formation did not occur on the upstream plates with faired leading edges. On the arrays with faired upstream plate, vo rtices shed from that plate into the gap are formed from the boundary layer separating from the trailing edge. It appears that this is also the dominant process of vortex shedding from the upstream plate when that plate is rectangular with $C1 = 12.7$, the leading-edge separation bubble and vortices associated with it then apparently having little influence on vortex formation at the trailing edge. However, the present numerical simulations for $C1 = 4$ indicate that this situation may change if the length of the upstream plate is not so great. For their faired arrays, tested over the Reynolds number range $Re_h = 430$ to 2.9×10^4, Bull *et al*. [1989] and Bull and Pickles [1991] found that for arrays with large gaps the frequency of vortex-shedding from the trailing edge of the upstream plate decreases as the gap is reduced, that the frequency of vortex shedding from the downstream plate does not become locked to it, being in general lower, and that when the gap between the plates is reduced below a critical value G_c (in the range $2 < G_c < 2.5$), vortex shedding from the upstream plate is suppressed. Bull, Bies and Pickles [1990] and Bull and Pickles [1991] established that for $G < G_c$ the gap contains two trapped counter-rotating vortices while for $G > G_c$ shedding from the trailing edge of the upstream plate forms a vortex street which interacts with the leading edge of the downstream plate. The similar flow regimes for arrays with a long rectangular upstream plate, identified by Blazewicz *et al*. [1995] from measurements made in a wind tunnel at Reynolds number in the range $8.1\times10^3 < Re_h < 5.3\times10^4$, are

(i) for $C1 \geq 4.5$ and $G \leq 2$, trapped-vortex flow in the gap, consisting of a pair of stationary counter-rotating vortices (their *Regime 3*), and

(ii) for $C1 \geq 4.5$ and $G \geq 3$, vortex-street flow in the gap (their *Regime 4*).

These two flow regimes are subsets of the regime *A* of Bull *et al*. [1997], which can be considered as a general regime in which $C1 > S_{max}$ and the shear layers separating from the leading corners of upstream plate reattach on the plate itself.

8.5.2 Flow Regime for Small Gaps, $G \leq 2$

Simulations of flow over the ($C1 = 4$, $C2 = 4$) array with small gaps have been made for the gap-to-thickness ratios of $G = 1$, 1.5 and 2. The developing flows on these arrays are all similar to each other, and it is found that the fully-developed flows on all three arrays are in the transitional state between trapped-vortex flow and vortex-street flow in the gap. The onset of vortex shedding from the upstream plate has already occurred at $G = 1$ although in such a short gap vortex-street flow cannot be established; there is a clear approach to vortex-street flow in the gap with increasing G in this range. The calculated distributions of elemental vortices, streamline patterns and vorticity contours for $G = 1$ are shown in Figs. 8.102–8.104; the corresponding results for $G = 1.5$ and $G = 2$ are shown in Figs. 8.105–8.107 and Figs. 8.108–8.110 respectively.

As a representative case of flow development on the array with small gaps, consider the developing flow over the $G = 1.5$ array. In the early part of development ($t < 2$), the flow on both the upstream and downstream plates features separation from the leading corners and subsequent reattachment to the side faces. Short leading-edge-separation bubbles form on both the upper and lower side-faces of each of the plates. The side-face flow downstream of reattachment is fully-attached all the way to the trailing edge where it separates from the plate; in association with this separation, a pair of counter-rotating vortices forms within a closed recirculation region behind each of the plates. (The leading-edge-separation bubbles on the downstream plate are more pronounced on the $G = 2.0$ array and less so on the $G = 1.0$ array, reflecting the smaller proportion of the gap occupied by the recirculation region behind the upstream plate as the gap length increases). Up to this point, the initial flow is symmetrical about the centre-line of the array.

The (trapped) vortices between the plates grow until they fill up the entire space in the gap. In the presence of these large vortices in the gap, the side-face shear layers from the upstream plate are diverted across the gap to reattach on the side face of the downstream plate, where the leading-edge separation bubble gives way to fully-attached flow which prevails along the entire length of the side face ($t = 4$). This time also marks the disappearance of the closed recirculation region behind the array and the onset of vortex shedding into the wake from the downstream plate. Trapped vortex flow in the gap persists for only a short time before giving way to a process of vortex shedding from the upstream plate, of the same type as previously

found on the ($C1 = 1$, $C2 = 4$) array with a gap of $G = 2$ ($t = 8$). Vortices form from the shear layers separating from the trailing corners, alternately from the upper and lower side-faces. As one vortex grows (until it almost completely fills the gap), the previous vortex is displaced from the gap and shrinks and disappears as it loses vorticity to the downstream flow. The process is then repeated periodically; vortex shedding is occurring, but the gap is not long enough to allow establishment of a vortex street within it.

At the same time as this shedding process develops in the gap, the separation bubbles on the upstream plate, which have been growing since the inception of the flow, begin to shed side-face vortices and this process becomes established at $t \gtrsim 8$. Downstream convection of side-face vortices then provides a source of vorticity for vortices growing within the gap, (as at $t = 26$ and 33.8 on the upper surface and $t = 37.8$ and 47.7 on the lower sur face). A similar pattern of flow development can be seen, somewhat less sharply defined and somewhat asymmetric about the array centre-line, on the $G = 1.0$ array, and on the $G = 2.0$ array where it is much more clearly apparent.

For the flow in its fully-developed state, the flow on the upstream plate continues to feature leading-edge separation and reattachment on the side face, followed by fully-attached flow downstream of reattachment with intermittent passage of side-face vortices. In fact, the fully-developed flows on the upstream plates of the $G = 1.0$, $G = 1.5$ and $G = 2$ arrays are similar to each other and to the flow over a single $C = 4$ plate at the same Reynolds number. Further, the pressure distributions of the upstream plates of these arrays (Figs. 8.113, 8.115 and 8.117 for $G = 1.0$, 1.5 and 2.0 respectively) exhibit strong similarities to each other and also to the pressure distribution on a single $C = 4$ plate at $Re_h = 500$ (Fig. 7.124). However, for all three arrays, vortex formation from the upstream plate is due primarily to separation of the attached-flow boundary layer from the trailing edge and, to a lesser extent, the shedding of convected side-face vortices, whereas in the single-plate case side-face vortices play the more dominant role. The process in the gap of vortex formation, growth, and shedding follows the same pattern as in the latter stages of the developing flow. In this respect the flow regime differs from that with trapped-vortex flow in the gap as observed experimentally by Blazewicz *et al.* [1995] for $G < 2$ at much higher Reynolds numbers, in the range $8.1\times10^3 < Re_h < 5.3\times10^4$.

Greater detail of the vortex flow in the gap in the $G = 2.0$ array can be seen in the enlarged views of streamline patterns, instantaneous pressure fields and vorticity contours over about one vortex-shedding period, from time $t = 55.7 - 68.9$, presented in Figs. 8.111 and 8.112. Comparison of the ($C1 = 1$, $C2 = 4$) and ($C1 = 4$, $C2 = 4$) arrays with $G = 2$ shows that, while they exhibit similar sequences of vortex formation and shedding in the gap, the differences in the process of gap-vortex formation – from leading-edge separation in the former case, but from trailing-edge separation in the latter – give rise to differences in the scale of the vortices and the fine details of the flow in the gap. The gap vortices in the ($C1 = 4$, $C2 = 4$) array are very much confined within gap whereas those in the ($C1 = 1$, $C2 = 4$) array noticeably extend laterally outside the gap.

The fully-developed flow on the downstream plate, over the range of G values considered, is characterised by attached flow on the side faces with intermittent passage of side-face vortices. Although gap-vortex formation and shedding is dominated by trailing-edge separation from the upstream plate, the smaller-scale vortices shed from the upstream plate do to some extent retain their own identity, and impinge on the leading edge of the downstream plate, as is evident in the instantaneous pressure fields of the $G = 2$ array (Fig. 8.111). The vorticity contours (such as those for $G = 2$, Fig. 8.112) indicate that these impinging vortices and the vorticity transferred out of the gap by progressive displacement of large gap-vortices constitute the source of the vorticity of the weak side-face vortices which can be seen in the streamline patterns (e.g. Figs. 8.109 and 8.111). These side-face vortices, which are convected along the downstream plate, become quite diffuse before reaching the trailing edge and being shed into the wake. The formation of vortices downstream of the array is primarily from the boundary layer separating from the trailing edge of the downstream plate, with some contribution from these weak side-face vortices. The final vortex streets of the arrays with small gap are therefore similar to each other, as can be seen in the elemental-vortex distributions (Figs. 8.102, 8.105 and 8.108), although the establishment of the final pattern is less regular at the larger values of G.

The time-histories of lift and drag of the upstream and downstream plates of the $G = 1.0$, 1.5 and 2.0 arrays are presented in Figs. 8.114, 8.116 and 8.118. The power spectra of lift fluctuation on the upstream plate of all three arrays (Fig. 8.135) have a large peak at $St \sim 0.15$ ($St = 0.155$, 0.145, 0.134 for $G = 1.0$, 1.5, 2.0 respectively). Inspection of the streamline patterns (Fig. 8.103) and vorticity contours (Fig. 8.104) shows that this peak is associated with vortex formation in the gap following flow separation from the trailing edge of the upstream

plate, and subsequent shedding from the gap. This frequency can therefore be compared to the frequency of shedding of wake vortices, $St = 0.16$, from a single $C = 4$ plate (section 7.4.3.2). The spectra for the upstream plate of the $G = 1.0$ and 1.5 arrays both have smaller peaks at $St \sim 0.19$ (0.195 and 0.197) and $St \sim 0.27$ (0.27 and 0.265) which can be respectively identified with the wake shedding frequency from the downstream plate and the frequency of shedding of side-face vortices into the gap from the upstream plate. (The frequency of side-face vortex shedding from the upstream plate in the array is significantly greater than the value $St = 0.19$ found for an isolated plate with $C = 4$.) The spectra show that the strength of vortices shed from the gap (at $St \sim 0.15$) increases significantly as G increases from 1.0 to 2.0. Further, in the case of the $G = 2.0$ array, the wake shedding frequency has become locked to the frequency of vortex shedding from the gap (at $St = 0.132$).

The spectra for the downstream plate show that the lift fluctuations on that plate in the $G = 1.0$ array are dominated by the wake shedding ($St \sim 0.2$) with minor influences of side-face vortex shedding on the upstream plate ($St \sim 0.27$) and gap shedding ($St \sim 0.15$). However, with increasing strength of vortices shed from the gap as G increases, the lift fluctuations become dominated by variation at this frequency ($St \sim 0.15$) at $G = 1.5$ and completely so at $G = 2.0$ when phase-locking between upstream and downstream plates occurs. For all three arrays the spectra for the downstream plate have a minor peak at the frequency $St = 0.27$ of formation of side-face vortices on the upstream plate.

(a) $C1 = 4$, $C2 = 4$, $G = 1$, $t = 2$

(b) $C1 = 4$, $C2 = 4$, $G = 1$, $t = 4$

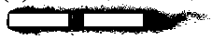

(c) $C1 = 4$, $C2 = 4$, $G = 1$, $t = 6$

(d) $C1 = 4$, $C2 = 4$, $G = 1$, $t = 8$

(e) $C1 = 4$, $C2 = 4$, $G = 1$, $t = 10$

(f) $C1 = 4$, $C2 = 4$, $G = 1$, $t = 12$

(g) $C1 = 4$, $C2 = 4$, $G = 1$, $t = 14$

(h) $C1 = 4$, $C2 = 4$, $G = 1$, $t = 16$

(i) $C1 = 4$, $C2 = 4$, $G = 1$, $t = 18$

(j) $C1 = 4$, $C2 = 4$, $G = 1$, $t = 20$

(k) $C1 = 4$, $C2 = 4$, $G = 1$, $t = 22$

(l) $C1 = 4$, $C2 = 4$, $G = 1$, $t = 24$

(m) $C1 = 4$, $C2 = 4$, $G = 1$, $t = 26$

(n) $C1 = 4$, $C2 = 4$, $G = 1$, $t = 28$

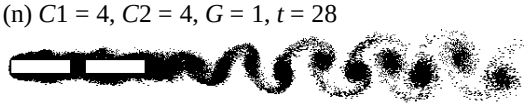

(o) $C1 = 4$, $C2 = 4$, $G = 1$, $t = 30$

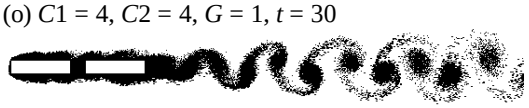

(p) $C1 = 4$, $C2 = 4$, $G = 1$, $t = 32$

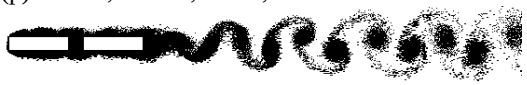

(q) $C1 = 4$, $C2 = 4$, $G = 1$, $t = 34$

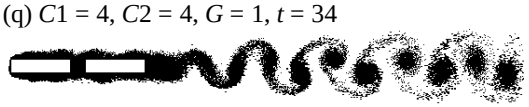

(r) $C1 = 4$, $C2 = 4$, $G = 1$, $t = 36$

(s) $C1 = 4$, $C2 = 4$, $G = 1$, $t = 37$

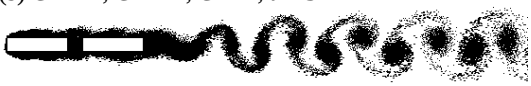

(t) $C1 = 4$, $C2 = 4$, $G = 1$, $t = 38$

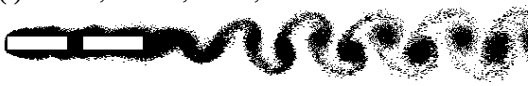

(u) $C1 = 4$, $C2 = 4$, $G = 1$, $t = 39.7$

(v) $C1 = 4$, $C2 = 4$, $G = 1$, $t = 40.7$

(w) $C1 = 4$, $C2 = 4$, $G = 1$, $t = 41.7$

(x) $C1 = 4$, $C2 = 4$, $G = 1$, $t = 42.7$

(y) $C1 = 4$, $C2 = 4$, $G = 1$, $t = 43.7$

(z) $C1 = 4$, $C2 = 4$, $G = 1$, $t = 44.7$

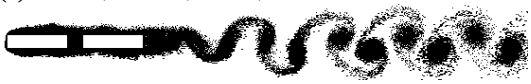

(aa) $C1 = 4$, $C2 = 4$, $G = 1$, $t = 45.9$

(ab) $C1 = 4$, $C2 = 4$, $G = 1$, $t = 46.9$

(ac) $C1 = 4$, $C2 = 4$, $G = 1$, $t = 47.9$

(ad) $C1 = 4$, $C2 = 4$, $G = 1$, $t = 48.9$

(ae) $C1 = 4$, $C2 = 4$, $G = 1$, $t = 49.9$

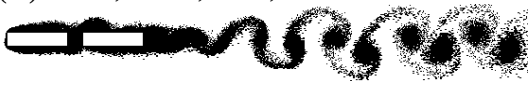

(af) $C1 = 4$, $C2 = 4$, $G = 1$, $t = 50.9$

(ag) $C1 = 4$, $C2 = 4$, $G = 1$, $t = 51.7$

Figure 8.102. Elemental-vortex distributions in flow over the ($C1 = 4$, $C2 = 4$, $G = 1$) array, showing flow development from an impulsive start to the fully-developed state.

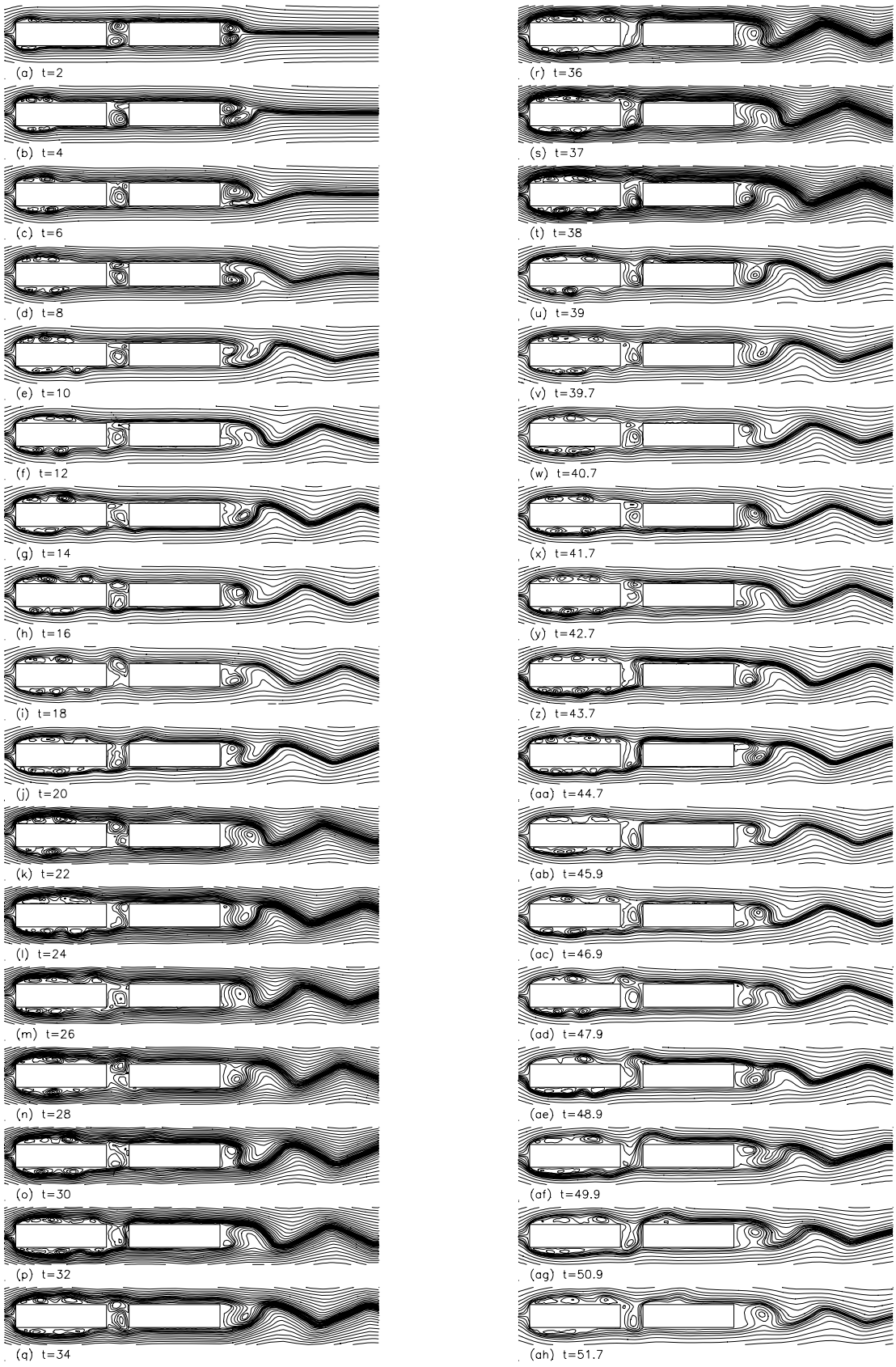

Figure 8.103. Calculated streamline patterns in flow over the ($C1$ = 4, $C2$ = 4, G = 1) array, showing flow development from an impulsive start to the fully-developed flow.

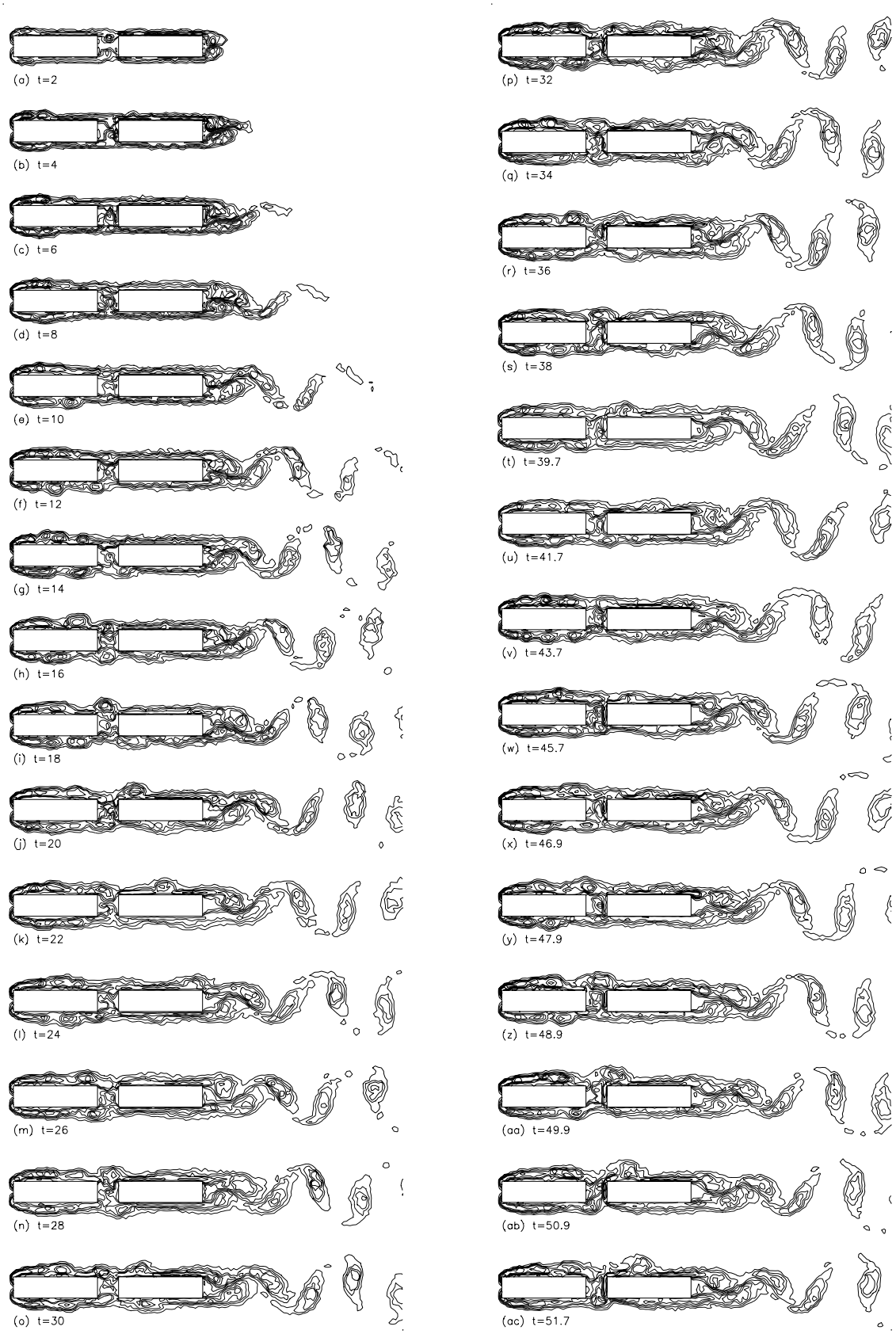

Figure 8.104. Vorticity contours in flow over the ($C1 = 4$, $C2 = 4$, $G = 1$) array, showing flow development from an impulsive start to the fully-developed flow.

(a) $C1 = 4$, $C2 = 4$, $G = 1.5$, $t = 2$

(b) $C1 = 4$, $C2 = 4$, $G = 1.5$, $t = 4$

(c) $C1 = 4$, $C2 = 4$, $G = 1.5$, $t = 6$

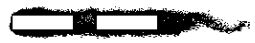

(d) $C1 = 4$, $C2 = 4$, $G = 1.5$, $t = 8$

(e) $C1 = 4$, $C2 = 4$, $G = 1.5$, $t = 10$

(f) $C1 = 4$, $C2 = 4$, $G = 1.5$, $t = 12$

(g) $C1 = 4$, $C2 = 4$, $G = 1.5$, $t = 14$

(h) $C1 = 4$, $C2 = 4$, $G = 1.5$, $t = 16$

(i) $C1 = 4$, $C2 = 4$, $G = 1.5$, $t = 18$

(j) $C1 = 4$, $C2 = 4$, $G = 1.5$, $t = 20$

(k) $C1 = 4$, $C2 = 4$, $G = 1.5$, $t = 22$

(l) $C1 = 4$, $C2 = 4$, $G = 1.5$, $t = 24$

(m) $C1 = 4$, $C2 = 4$, $G = 1.5$, $t = 26$

(n) $C1 = 4$, $C2 = 4$, $G = 1.5$, $t = 28.2$

(o) $C1 = 4$, $C2 = 4$, $G = 1.5$, $t = 30.2$

(p) $C1 = 4$, $C2 = 4$, $G = 1.5$, $t = 32.2$

(q) $C1 = 4$, $C2 = 4$, $G = 1.5$, $t = 33.8$

(r) $C1 = 4$, $C2 = 4$, $G = 1.5$, $t = 35.8$

(s) $C1 = 4$, $C2 = 4$, $G = 1.5$, $t = 37.8$

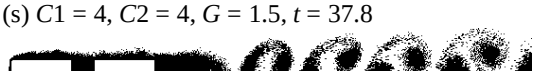

(t) $C1 = 4$, $C2 = 4$, $G = 1.5$, $t = 39.8$

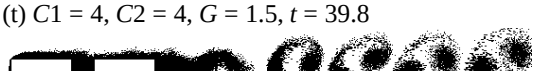

(u) $C1 = 4$, $C2 = 4$, $G = 1.5$, $t = 41.8$

(v) $C1 = 4$, $C2 = 4$, $G = 1.5$, $t = 43.7$

(w) $C1 = 4$, $C2 = 4$, $G = 1.5$, $t = 45.7$

(x) $C1 = 4$, $C2 = 4$, $G = 1.5$, $t = 47.7$

(y) $C1 = 4$, $C2 = 4$, $G = 1.5$, $t = 48.7$

(z) $C1 = 4$, $C2 = 4$, $G = 1.5$, $t = 49.7$

(aa) $C1 = 4$, $C2 = 4$, $G = 1.5$, $t = 50.7$

(ab) $C1 = 4$, $C2 = 4$, $G = 1.5$, $t = 51.7$

(ac) $C1 = 4$, $C2 = 4$, $G = 1.5$, $t = 52.7$

(ad) $C1 = 4$, $C2 = 4$, $G = 1.5$, $t = 53.7$

(ae) $C1 = 4$, $C2 = 4$, $G = 1.5$, $t = 54.7$

(af) $C1 = 4$, $C2 = 4$, $G = 1.5$, $t = 55.7$

(ag) $C1 = 4$, $C2 = 4$, $G = 1.5$, $t = 56.7$

Figure 8.105. Elemental-vortex distributions in flow over the ($C1 = 4$, $C2 = 4$, $G = 1.5$) array, showing flow development from an impulsive start from rest to the fully-developed flow.

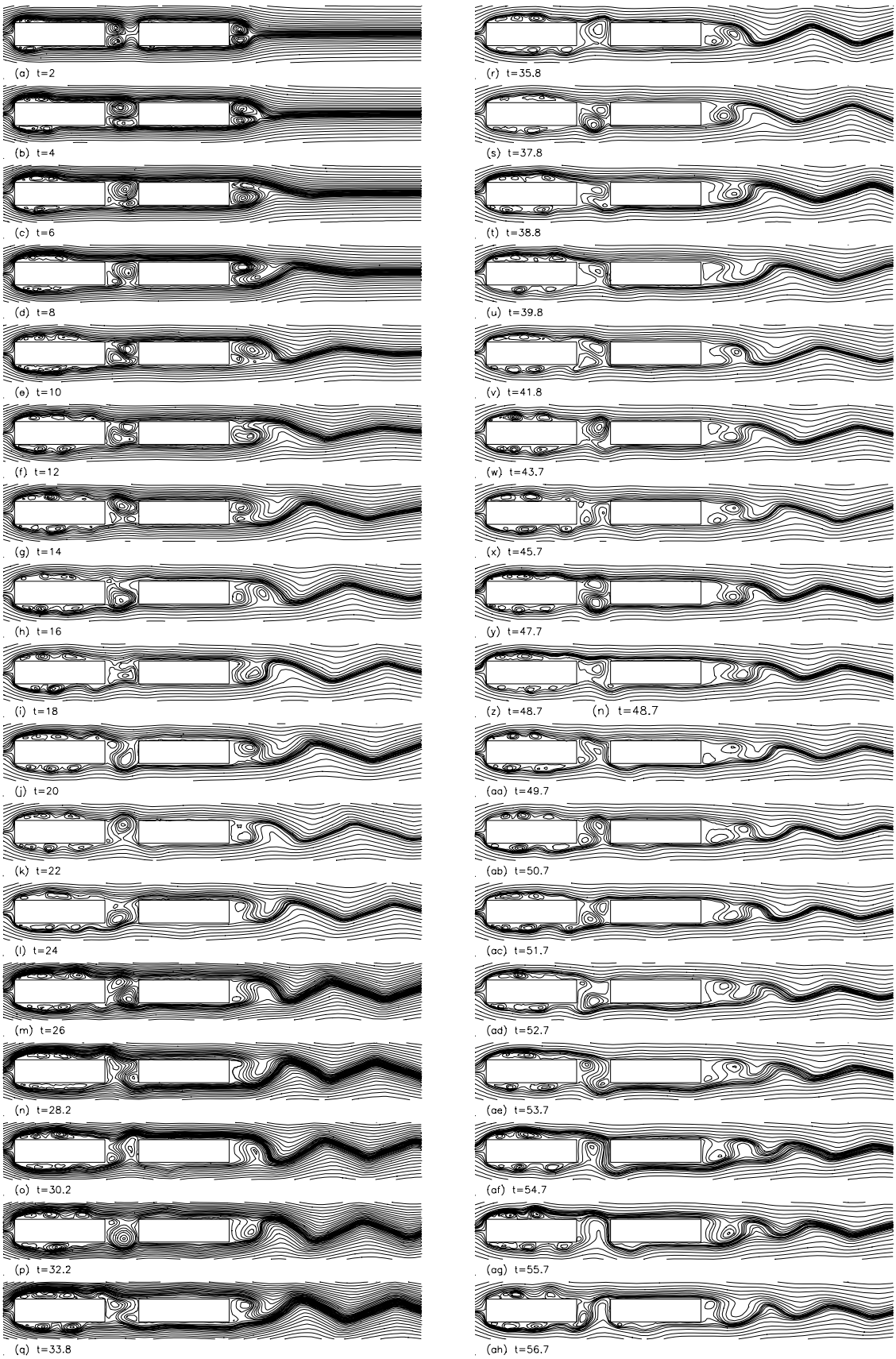

Figure 8.106. Calculated streamline patterns in flow over the ($C1 = 4$, $C2 = 4$, $G = 1.5$) array from an impulsive start from rest to the fully-developed flow.

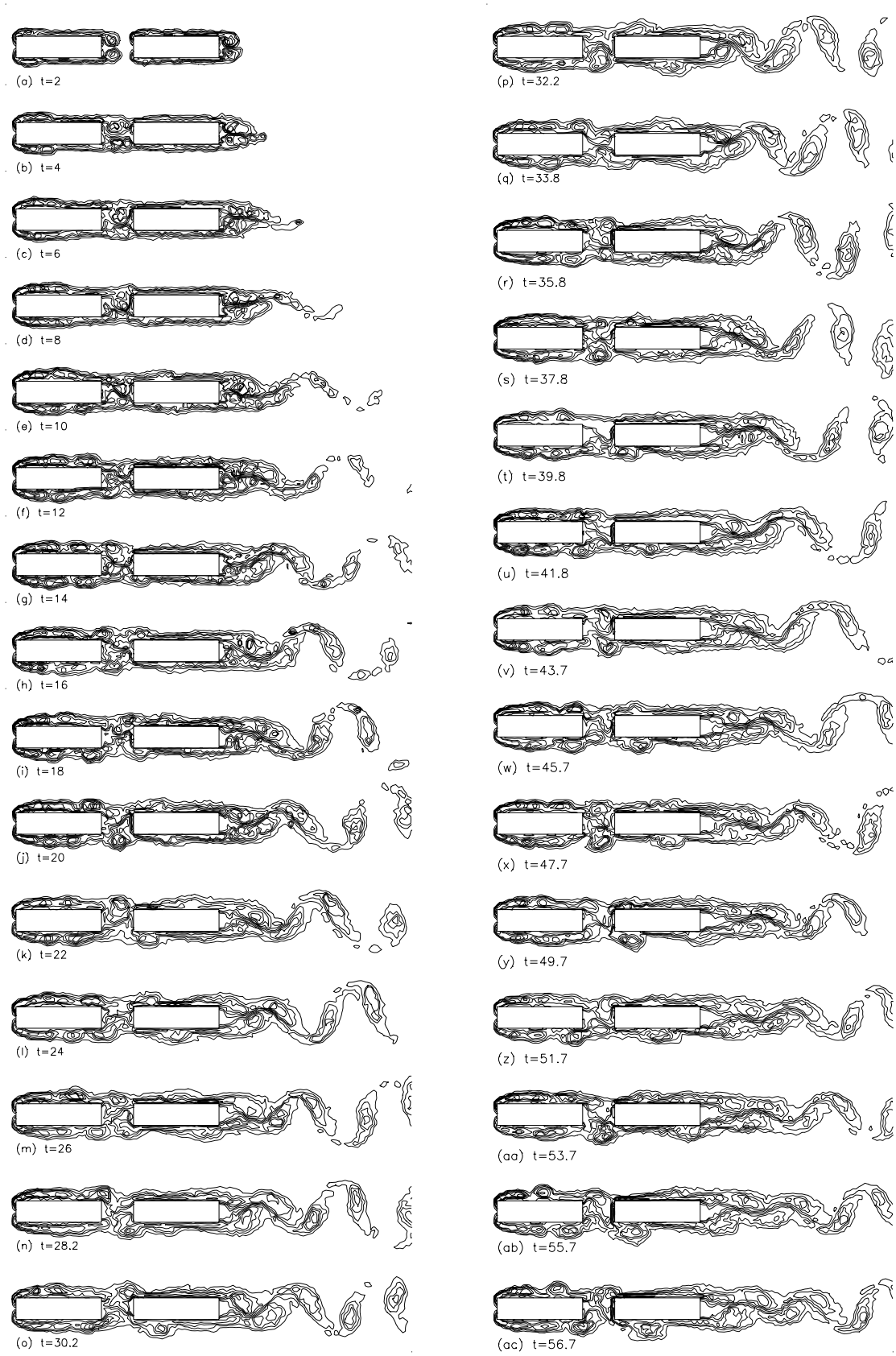

Figure 8.107. Vorticity contours in flow over the ($C1 = 4$, $C2 = 4$, $G = 1.5$) array, showing flow development from an impulsive start from rest to the fully-developed flow.

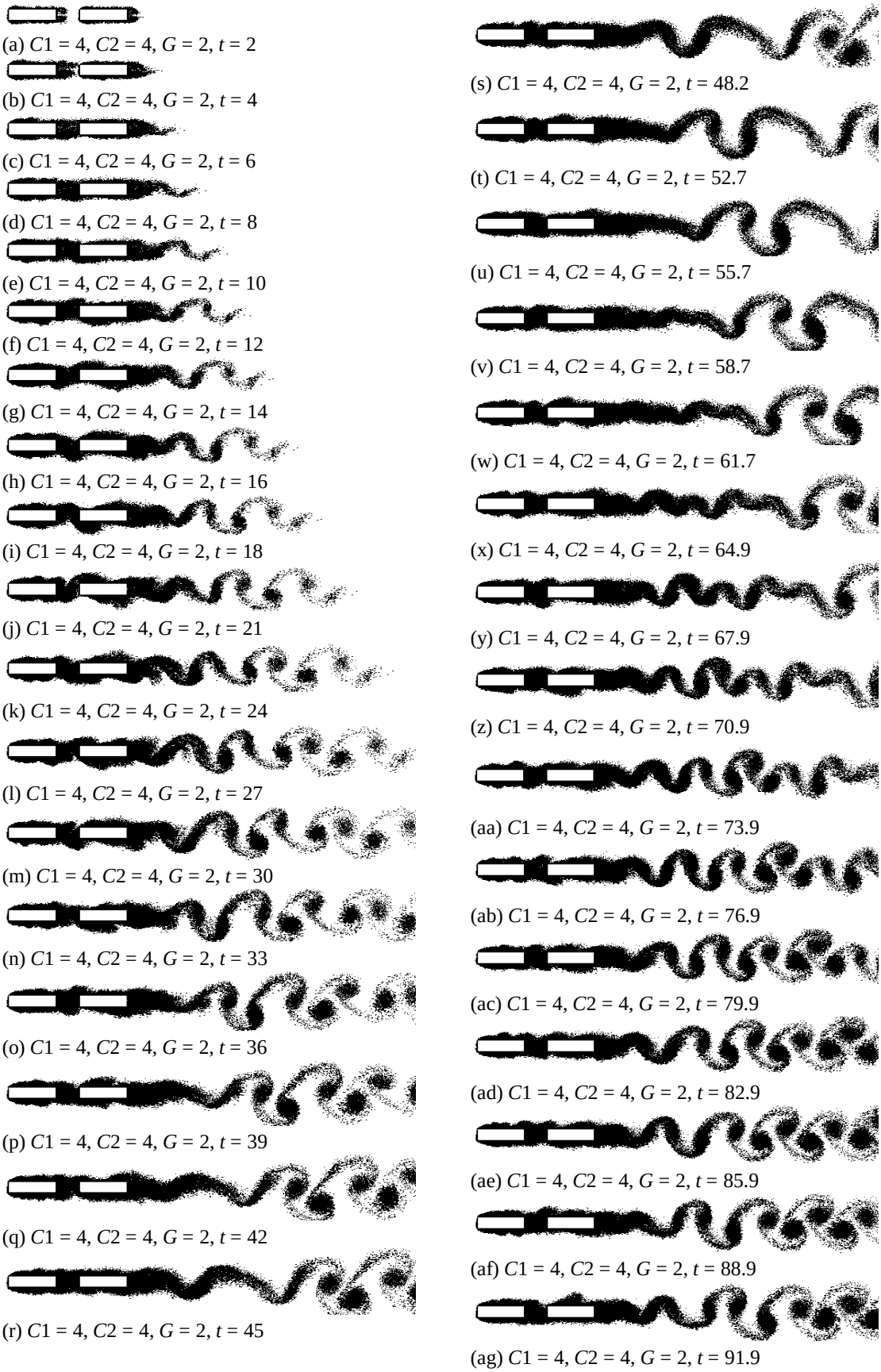

Figure 8.108. Elemental-vortex distributions in flow over the ($C1$ = 4, $C2$ = 4, G = 2) array, showing flow development from an impulsive start from rest to the fully-developed flow.

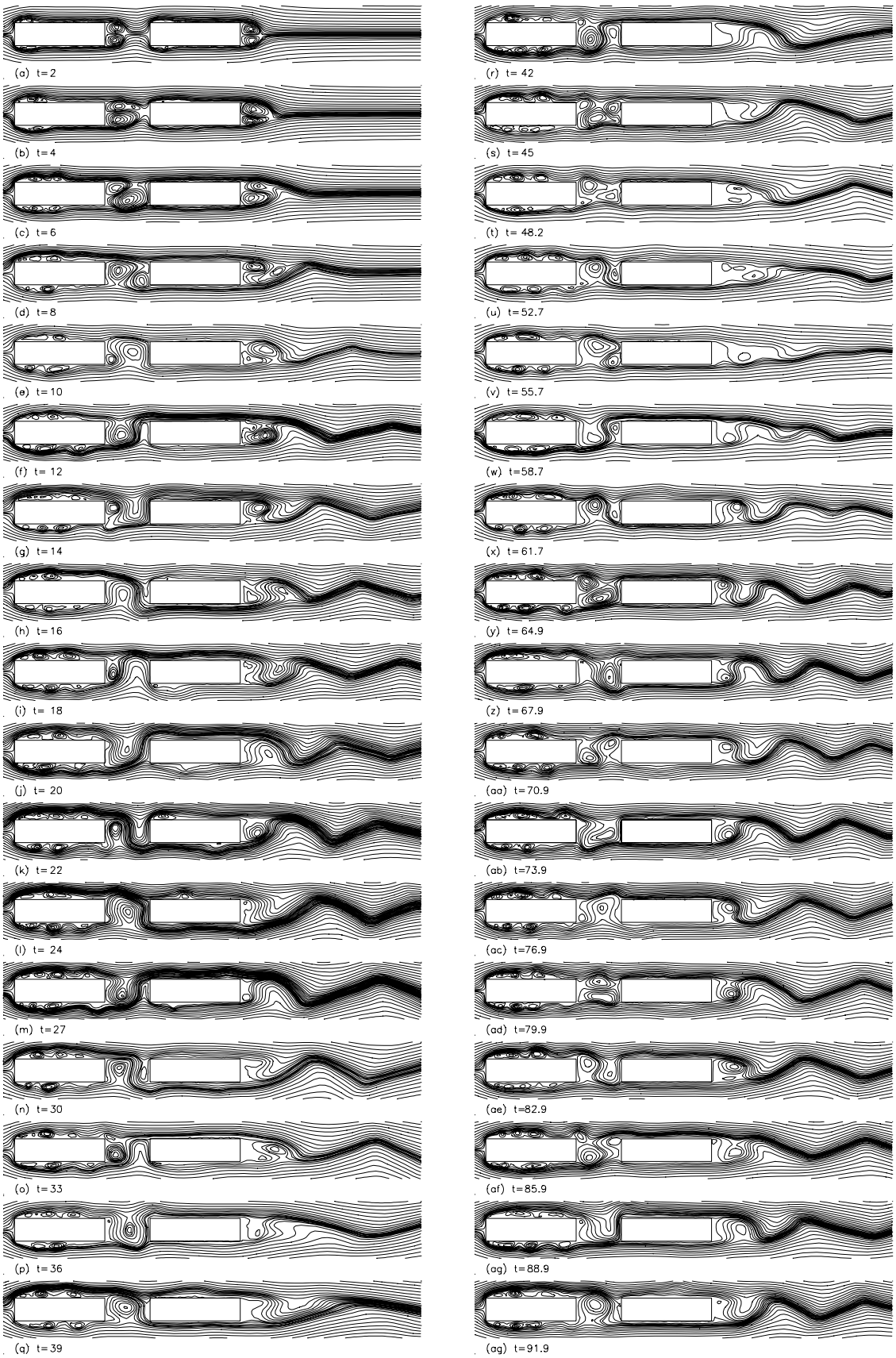

Figure 8.109. Calculated streamline patterns in flow over the ($C1$ = 4, $C2$ = 4, G = 2) array, showing flow development from an impulsive start from rest to the fully-developed flow.

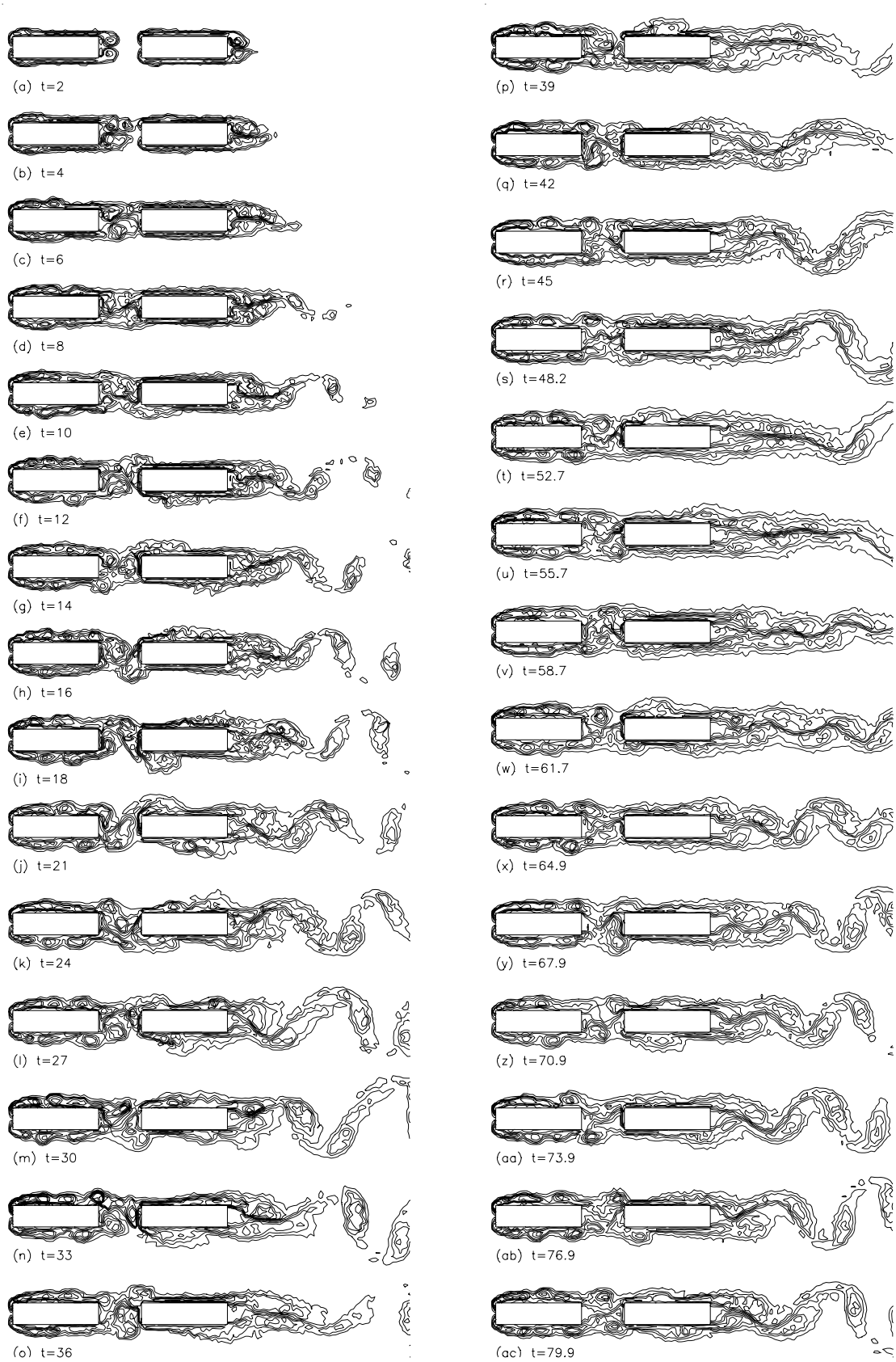

Figure 8.110. Vorticity contours in flow over the ($C1 = 4$, $C2 = 4$, $G = 2$) array, showing flow development from an impulsive start from rest to the fully-developed flow.

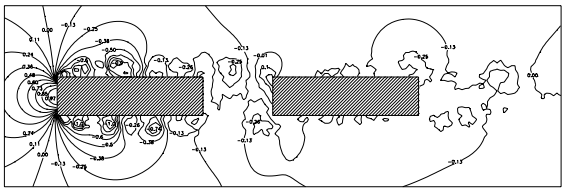

(a1) G = 2.0, t = 55.7

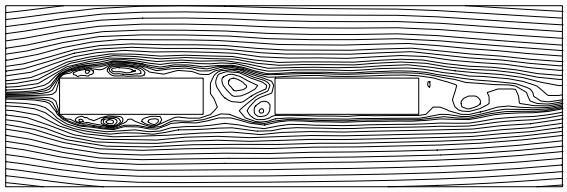

(a2) G = 2.0, t = 55.7

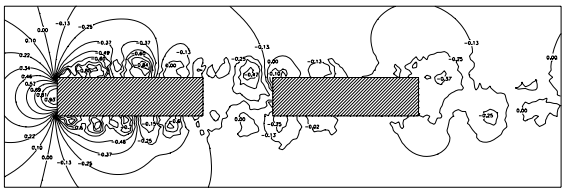

(b1) G = 2.0, t = 56.7

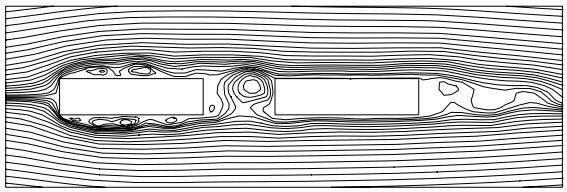

(b2) G = 2.0, t = 56.7

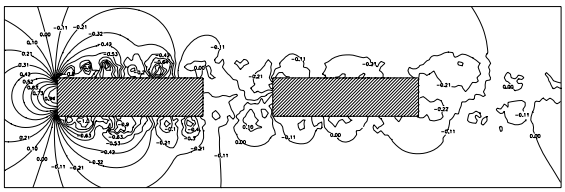

(c1) G = 2.0, t = 57.7

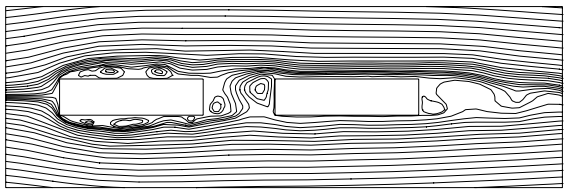

(c2) G = 2.0, t = 57.7

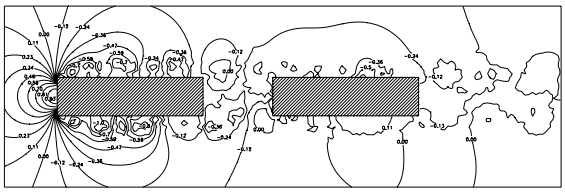

(d1) G = 2.0, t = 58.7

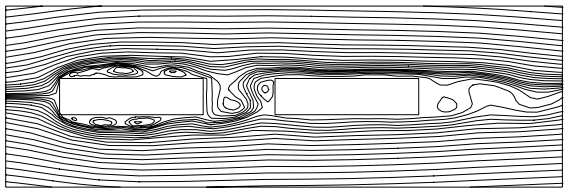

(d2) G = 2.0, t = 58.7

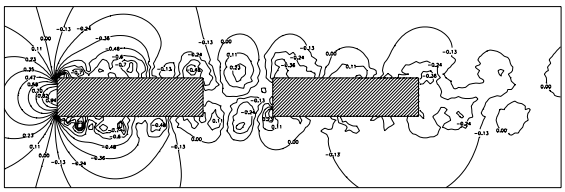

(e1) G = 2.0, t = 59.7

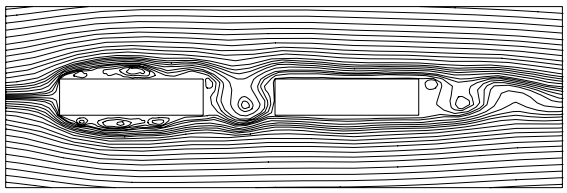

(e2) G = 2.0, t = 59.7

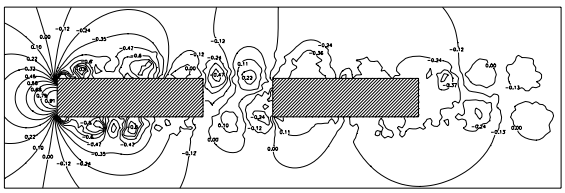

(f1) G = 2.0, t = 60.7

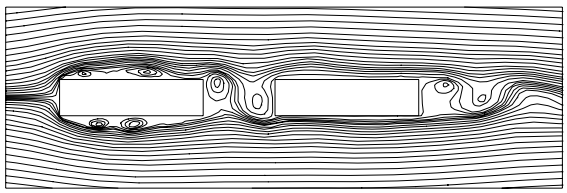

(f2) G = 2.0, t = 60.7

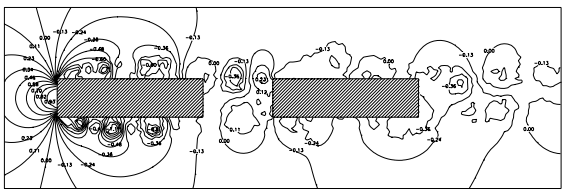

(g1) G = 2.0, t = 61.7

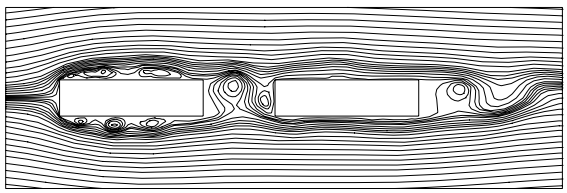

(g2) G = 2.0, t = 61.7

Figure 8.111. Instantaneous pressure fields and streamline patterns in fully-developed flow around the ($C1$ = 4, $C2$ = 4, G = 2) array.

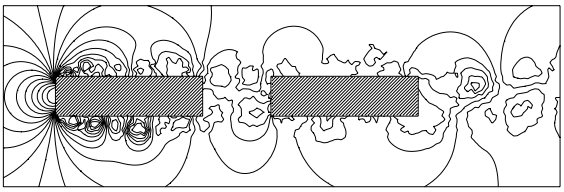

(h1) G = 2.0, t = 62.9

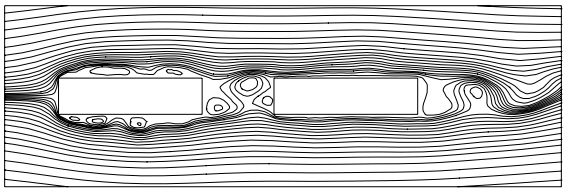

(h2) G = 2.0, t = 62.9

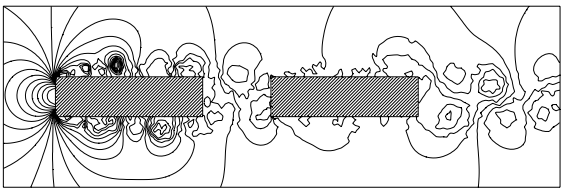

(i1) G = 2.0, t = 63.9

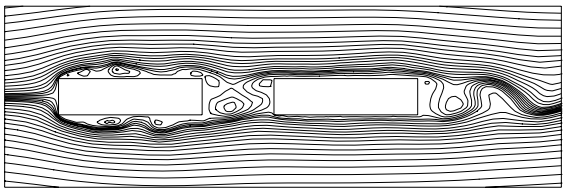

(i2) G = 2.0, t = 63.9

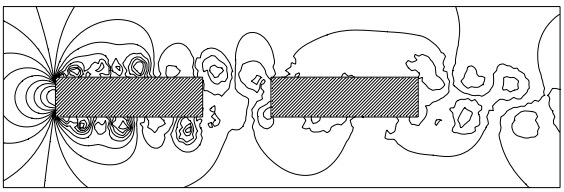

(j1) G = 2.0, t = 64.9

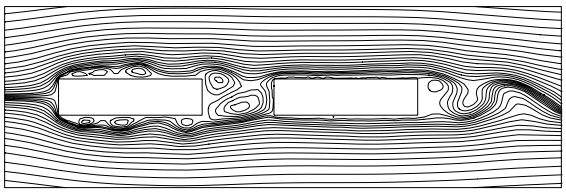

(j2) G = 2.0, t = 64.9

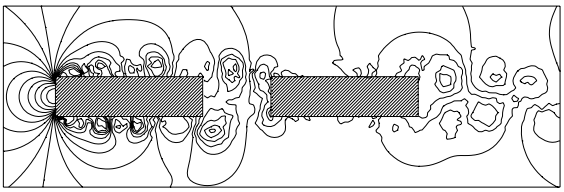

(k1) G = 2.0, t = 65.9

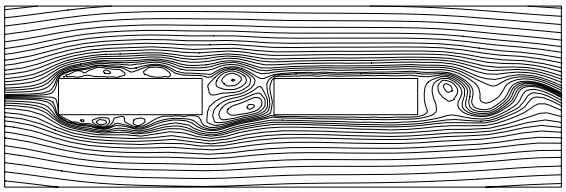

(k2) G = 2.0, t = 65.9

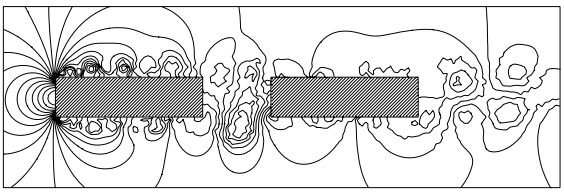

(l1) G = 2.0, t = 66.9

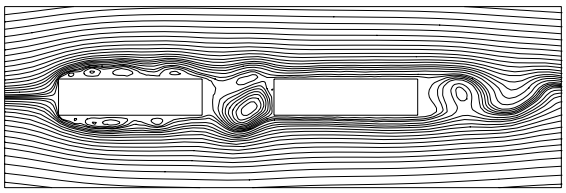

(l2) G = 2.0, t = 66.9

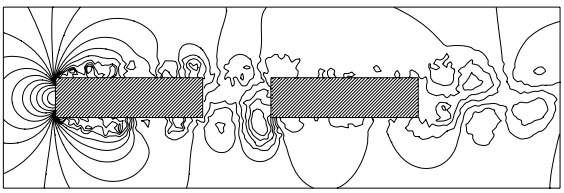

(m1) G = 2.0, t = 67.9

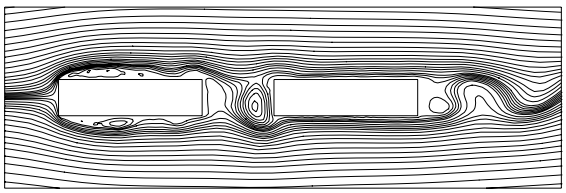

(m2) G = 2.0, t = 67.9

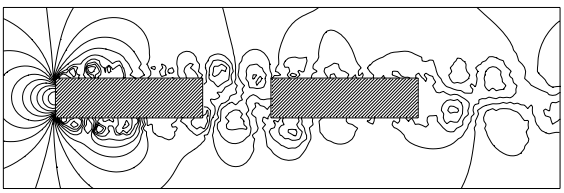

(n1) G = 2.0, t = 68.9

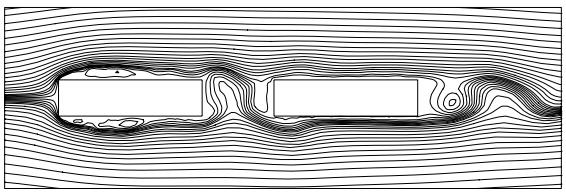

(n2) G = 2.0, t = 68.9

Figure 8.111. Cont'd.

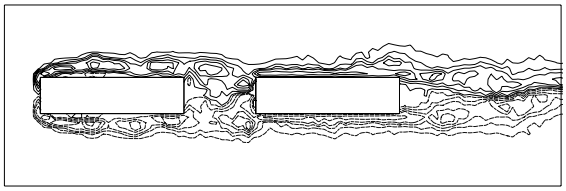

(a) G = 2.0, t = 55.7

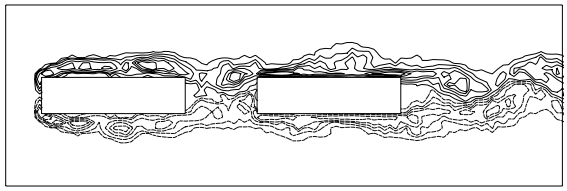

(h) G = 2.0, t = 62.9

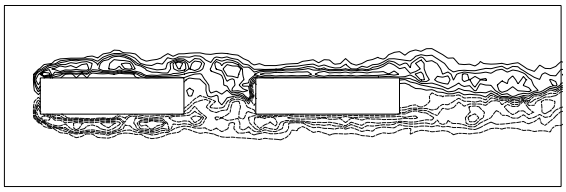

(b) G = 2.0, t = 56.7

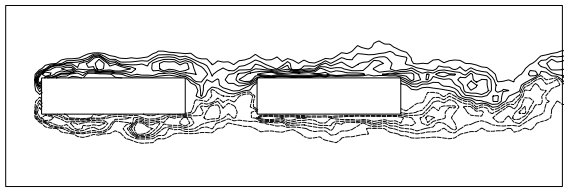

(i) G = 2.0, t = 63.9

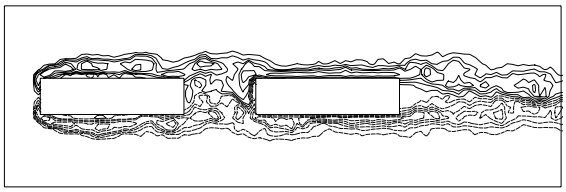

(c) G = 2.0, t = 57.7

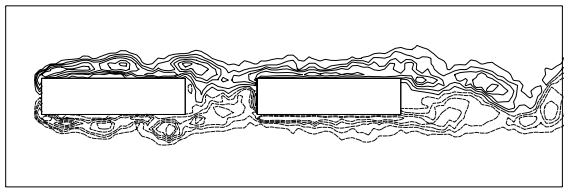

(j) G = 2.0, t = 64.9

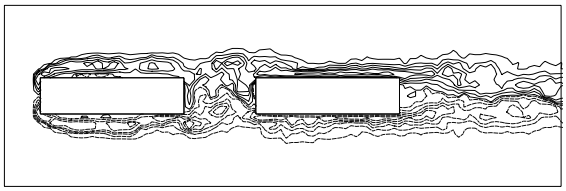

(d) G = 2.0, t = 58.7

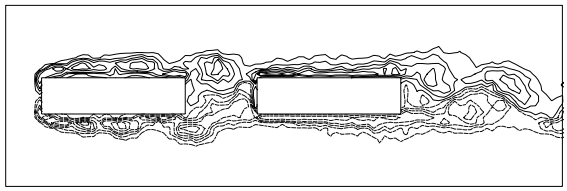

(k) G = 2.0, t = 65.9

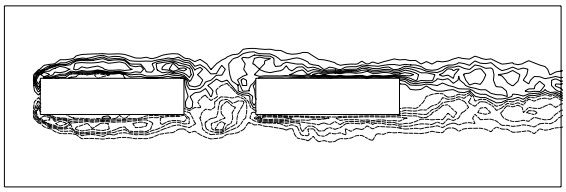

(e) G = 2.0, t = 59.7

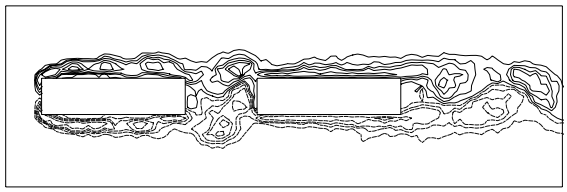

(l) G = 2.0, t = 66.9

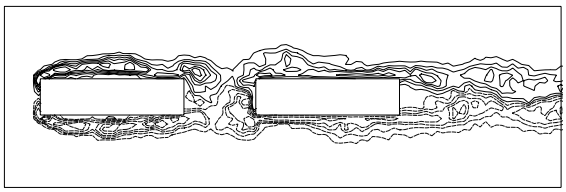

(f) G = 2.0, t = 60.7

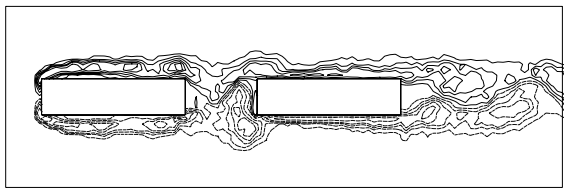

(m) G = 2.0, t = 67.9

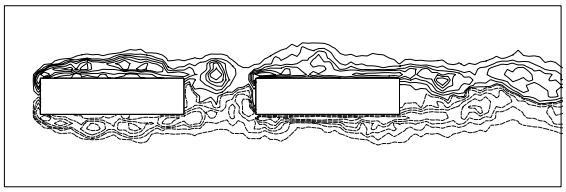

(g) G = 2.0, t = 61.7

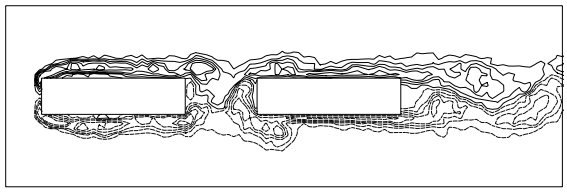

(n) G = 2.0, t = 68.9

Figure 8.112. Vorticity contours over one vortex-shedding period in flow over the ($C1$ = 4, $C2$ = 4, G = 2.0) array.

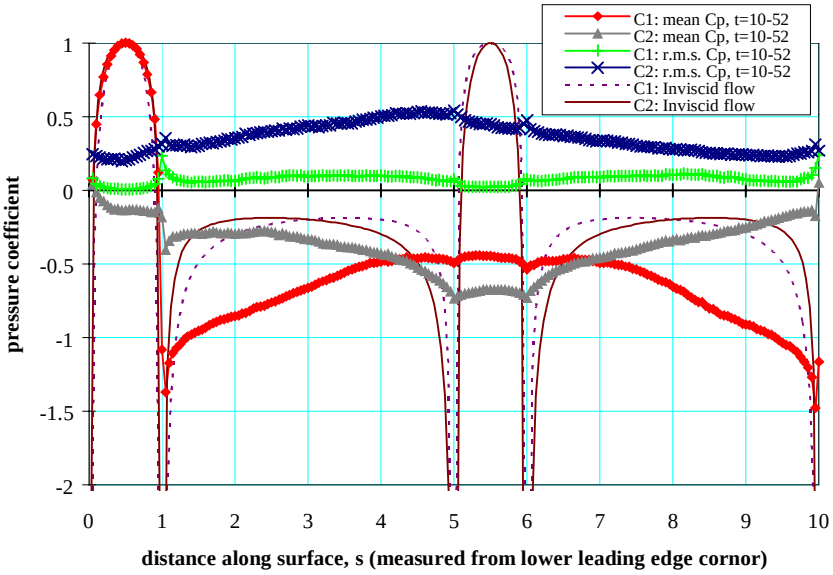

Figure 8.113. Calculated distributions of mean and r.m.s. pressure coefficients on the ($C1 = 4$, $C2 = 4$, $G = 1$) array.

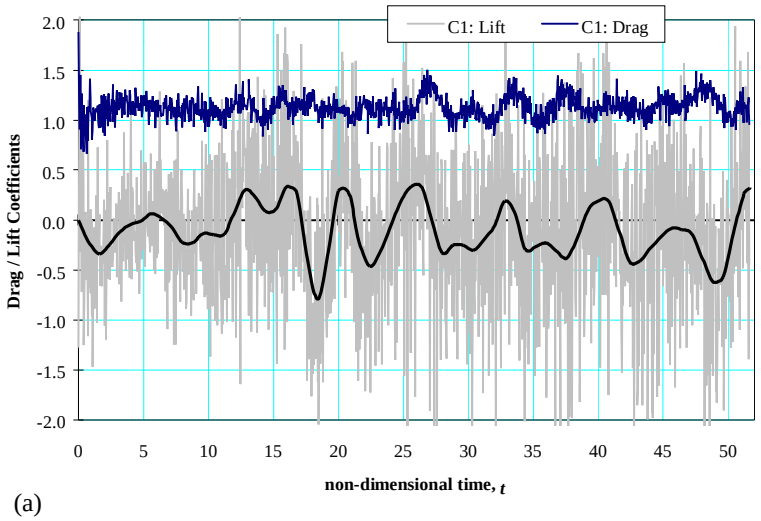

(a)

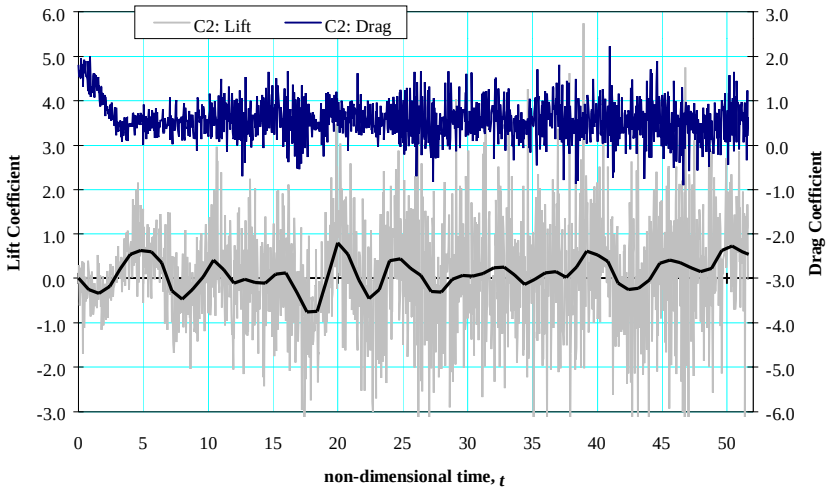

(b)

Figure 8.114. Time-histories of drag and lift on the ($C1 = 4$, $C2 = 4$, $G = 1$) array, (a) upstream plate, (b) downstream plate. Drag and lift are calculated for $\Delta t = 0.02$; highlighted values are averaged over $\Delta t = 0.4$.

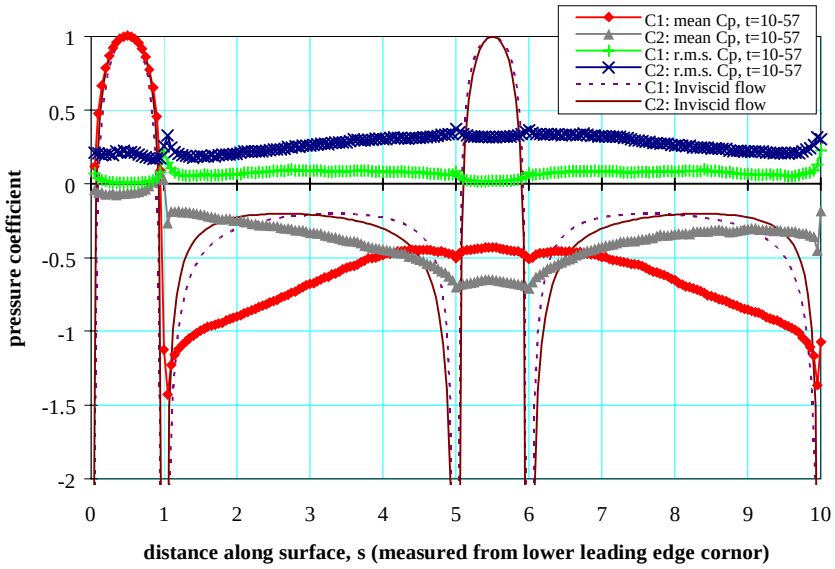

Figure 8.115. Calculated distributions of mean and r.m.s. pressure coefficients on the ($C1 = 4$, $C2 = 4$, $G = 1.5$) array.

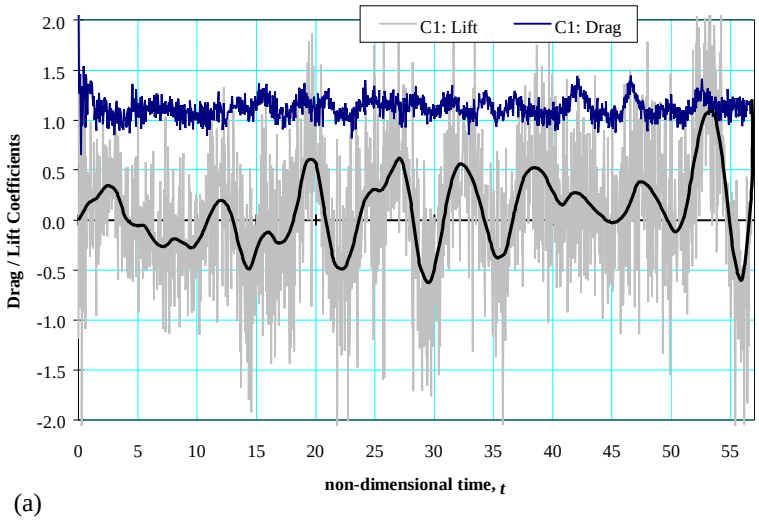

(a)

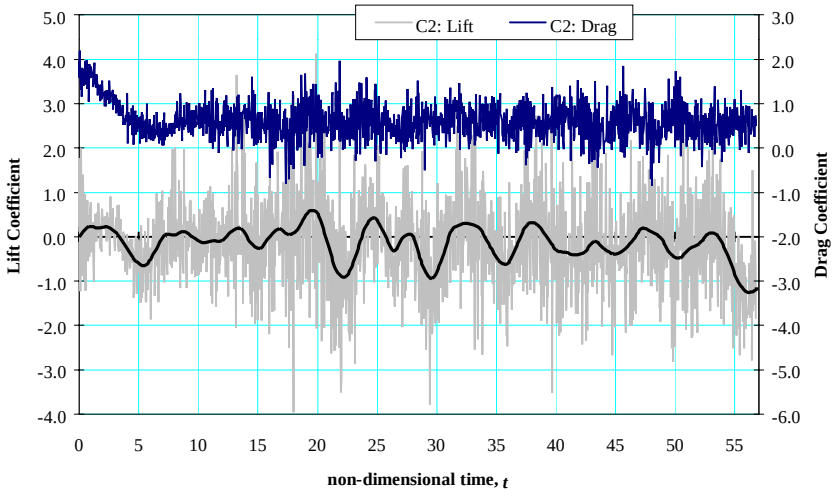

(b)

Figure 8.116. Time-histories of drag and lift on the ($C1 = 4$, $C2 = 4$, $G = 1$) array, (a) upstream plate, (b) downstream plate. Drag and lift are calculated for $\Delta t = 0.02$; highlighted values are averaged over $\Delta t = 0.4$.

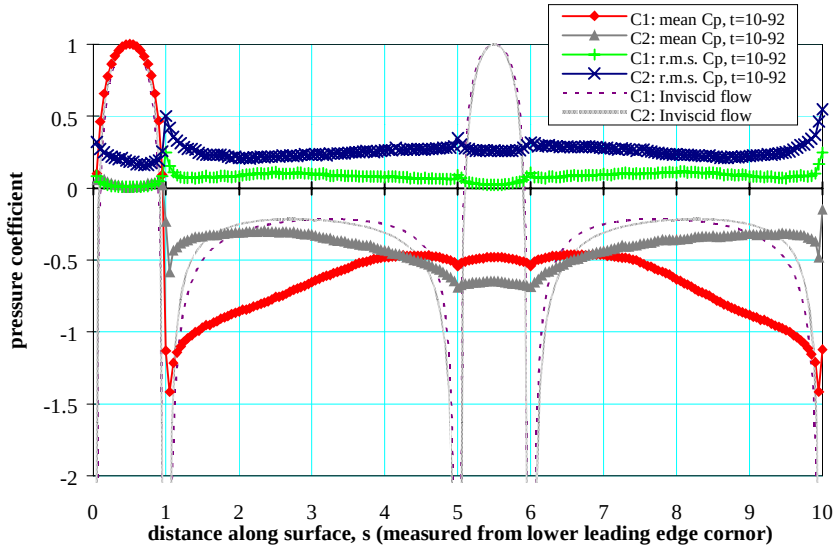

Figure 8.117. Calculated distributions of mean and r.m.s. pressure coefficients on the ($C1 = 4$, $C2 = 4$, $G = 2.0$) array.

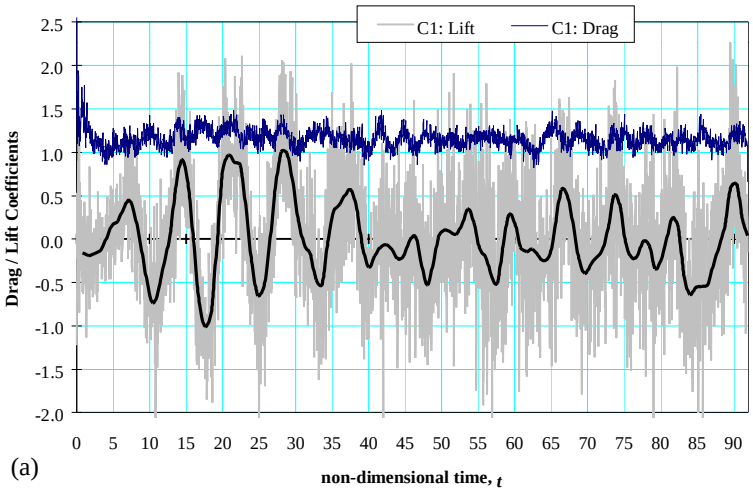

(a)

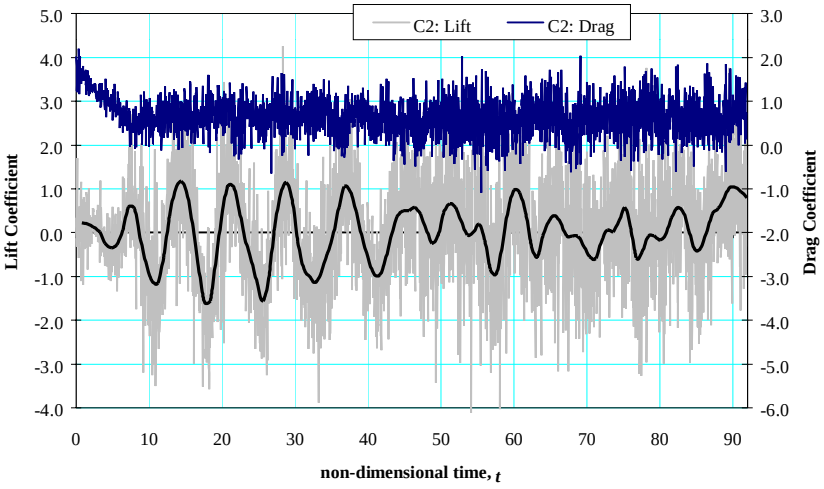

(b)

Figure 8.118. Time-histories of drag and lift on the ($C1 = 4$, $C2 = 4$, $G = 2.0$) array, (a) upstream plate, (b) downstream plate. Drag and lift are calculated for $\Delta t = 0.02$; highlighted values are averaged over $\Delta t = 0.4$.

8.5.3 Flow Regime for Large Gaps, $G \geq 4$

As the gap-to-thickness ratio is increased beyond $G = 2$, the vortex-street character of the flow in the gap, with vortex-impingement on the downstream plate, becomes more pronounced. Simulations have been made for arrays with $G = 4$, 6 and 8. The calculations show that the gap flows of these arrays are similar to each other, and in all cases the interaction between an impinging vortex and the leading corner of the downstream plate is as previously observed for the ($C1 = 1$, $C2 = 1$) and ($C1 = 1$, $C2 = 4$) arrays with large gaps.

Consider the flow on the $G = 4$ array which is typical of this group. The calculated results for elemental-vortex distributions, streamline patterns and vorticity patterns for this array are presented in Figs. 8.119–8.121. In addition, streamline patterns and instantaneous pressure fields around the array, over about two vortex-shedding periods, from time $t = 30$–42.8, are shown in Fig. 8.122.

In the early stages of flow development, before vortices from the upstream plate impinge on the downstream plate, the flow patterns on the upstream and downstream plates are very similar to each other and, as expected, to the developing flow on a single plate with $C = 4$ at the same Reynolds number of $Re_h = 500$. On both plates the flow is characterised by: symmetry about the centre-line of the array ($t < 4$); leading-edge separation and reattachment to the side-face to form a leading-edge-separation bubble; fully-attached side-face flow downstream of reattachment and subsequent separation at the trailing edge; formation and extension of a closed recirculation region behind the plate, which later gives way to vortex shedding from the plate following instability in the extended recirculation region ($t \approx 6$). A vortex street is then established in the gap, which impinges on the leading edge of the downstream plate ($t \approx 10$). As a result of vortex-street impingement, the flow on the downstream plate changes significantly from its initial pattern.

In the fully-developed state ($t \gtrsim 12$), the flow on the upstream plate is virtually unchanged from its initial pattern which closely resembles the flow over a single plate with $C = 4$ at $Re_h = 500$. The general form of pressure distribution on the upstream plate (Figs. 8.129, 131, 133 for $G = 4$, 6 and 8 respectively) is very similar to that of a single $C = 4$ plate at $Re_h = 500$, as in the arrays with smaller gaps $G \leq 2$. Vortex formation in the gap results mainly from separation of the side-face boundary layers from the trailing edge of the upstream plate but also involves

shedding of side-face vortices that originate from the separation bubble on the upstream plate, as in the single-plate flow. Because trailing-edge boundary-layer separation is the major effect, the vortex street in the gap is narrower than in the ($C1 = 1$, $C2 = 1$) and ($C1 = 1$, $C2 = 4$) arrays with an upstream square cylinder. Nevertheless, the vortex impingement on the downstream plate of the ($C1 = 4$, $C2 = 4$) array exhibits strong similarities to the impinging flow of the ($C1 = 1$, $C2 = 1$) and ($C1 = 1$, $C2 = 4$) arrays with the same gap. In all these cases, the impingement involves clipping of the impinging vortex, formation of a main and a secondary vortex, and the subsequent movement of the main and secondary vortices along a side-face of the downstream plate. In association with impingement of the vortex-street, the downstream plate experiences periodic changes – oscillation of the stagnation point on the leading face between the upper and lower leading-corners, alternation on the side-faces between fully attached flow and flow with a leading-edge separation bubble, and formation and shedding of secondary vortices alternately on the upper and lower side-faces – occurring in phase with the vortex-impingement cycle. The similarities can be clearly seen by comparison of the streamline patterns and instantaneous pressure fields for the ($C1 = 4$, $C2 = 4$) array with $G = 4$ over time $t = 34–40$ (Fig. 8.122) with the corresponding patterns for the ($C1 = 1$, $C2 = 4$) array over time $t = 36–44.5$ (Fig. 8.89) and the ($C1 = 1$, $C2 = 1$) array over time $t = 59.6–67.6$ (Fig. 8.48).

The differences in the vortex-street flow in the gap do have some bearing on the details of the impingement flow. For the ($C1 = 4$, $C2 = 4$) array, the main vortex and its associated secondary vortex are, in most cases, separately convected along a side-face of the downstream plate without merging. The secondary vortex generally lags behind the main vortex, and is shed into the wake of the array in the next successive vortex-shedding cycle after that in which the main vortex is shed.

However, the most significant effect is on the coupling, or lack of it, of the vortex shedding from the upstream and downstream plates. For the ($C1 = 1$, $C2 = 1$) and ($C1 = 1$, $C2 = 4$) arrays, the simulations for large gaps have indicated phase-locking of vortex shedding from the upstream plate, vortex impingement on the downstream plate, and vortex shedding from the downstream plate. The frequencies of vortex shedding into the gap from the upstream plate St_1 and of vortex shedding into the wake from the downstream plate St_2 are, in consequence, the same. This is no longer the case for the ($C1 = 4$, $C2 = 4$) arrays. Although the calculations show phase-locking can occur at the larger values of G in the small-gap flow regimes (recall

the results in section 8.5.2 for $G = 2$) – owing to the strength of the gap vortices increasing with increasing G in this range to the point where they are sufficiently strong to dominate the flow on the downstream plate – this does not carry over to the flow regimes in which a fully-established vortex-street occurs in the gap. In the latter cases, when the flow is fully-developed in time, the upstream and downstream plates exhibit different characteristic vortex-shedding frequencies. The shedding frequency of the upstream plate increases slowly with increasing G, from a value of $St_1 \sim 0.14$ at $G = 4$ towards the value of 0.16 for a single plate with $C = 4$ at $Re_h = 500$ (Fig. 7.122) as G exceeds 8; the shedding frequency of the downstream plate correspondingly decreases slowly from $St_2 \sim 0.19$ at $G = 4$ towards the single-plate value for $G > 8$. Phase-locking does not occur for $G = 4$ or 6, but does reappear at $G = 8$, as the characteristic shedding frequencies of the two plates approach each other. The Strouhal number variations and the phase-locking at $G = 8$ are reflected in the power spectra of lift fluctuation on the upstream and downstream plates (Fig. 8.1.35).

Close examinations of streamline and vorticity fields shows that for gaps corresponding to the vortex-street regime, the shedding frequency in the early stages of the motion, before the first arrival of a side-face vortex at the trailing-edge of the plate, is generally somewhat higher than in the fully-developed flow. This effect can lead to apparently anomalous fluctuations in lift in the early stage of the motion. When shedding of side-face vortices becomes established, the simultaneous shedding of these vortices (at $St \sim 0.27$) and trailing-face vortices (at $St < 0.2$) into the gap from the upstream plate at different frequencies, gives rise to additional irregularities – in vortex-street flow in the gap (which can be clearly seen in the streamline patterns, Figs. 8.120, 8.124 and 8.127, and vorticity contours, Figs. 8.121, 8.125 and 8.128), and in the time-histories of lift fluctuation, particularly on the upstream plates (Figs. 8.130, 8.132 and 8.134).

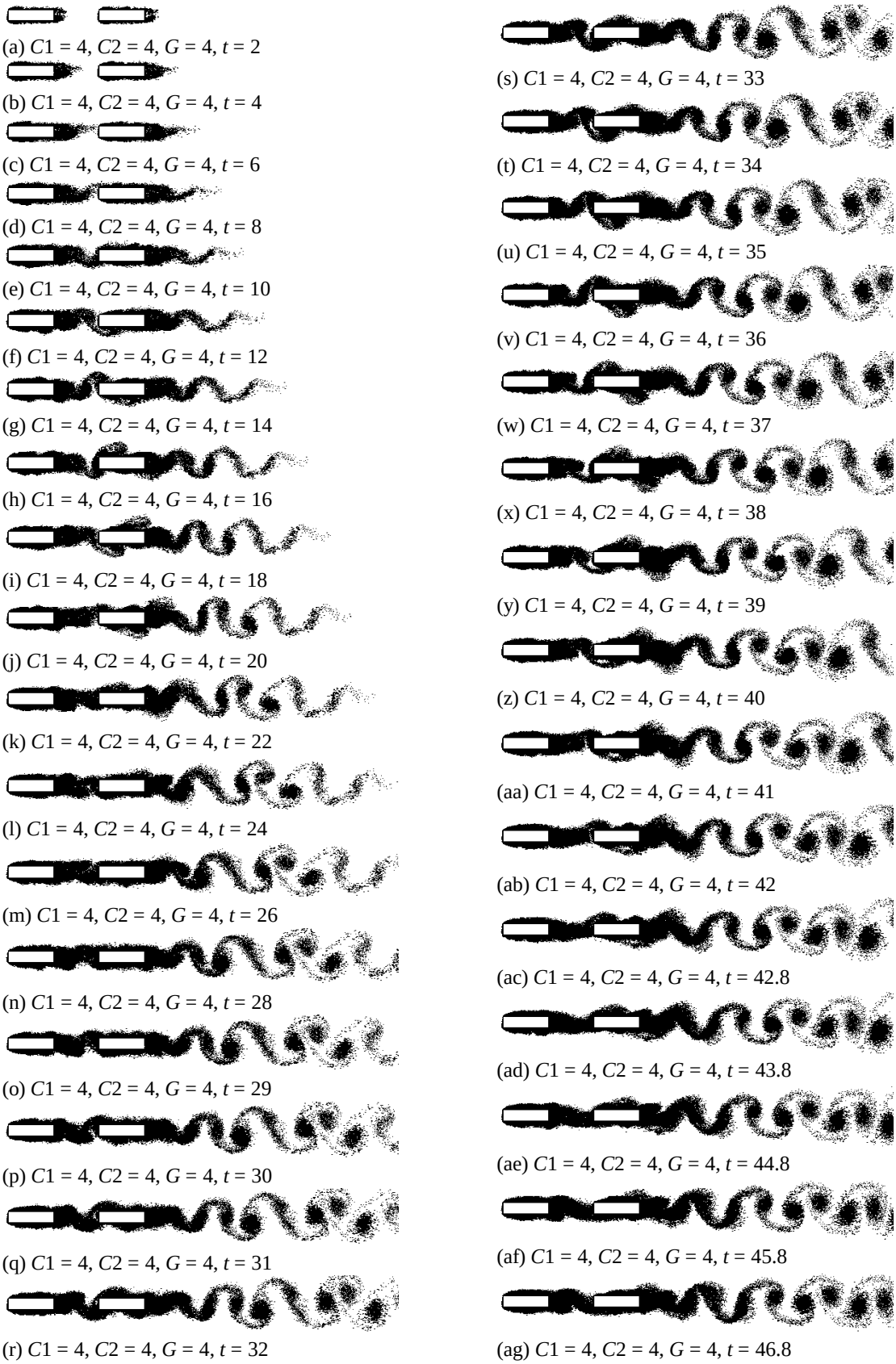

(a) $C1 = 4$, $C2 = 4$, $G = 4$, $t = 2$

(b) $C1 = 4$, $C2 = 4$, $G = 4$, $t = 4$

(c) $C1 = 4$, $C2 = 4$, $G = 4$, $t = 6$

(d) $C1 = 4$, $C2 = 4$, $G = 4$, $t = 8$

(e) $C1 = 4$, $C2 = 4$, $G = 4$, $t = 10$

(f) $C1 = 4$, $C2 = 4$, $G = 4$, $t = 12$

(g) $C1 = 4$, $C2 = 4$, $G = 4$, $t = 14$

(h) $C1 = 4$, $C2 = 4$, $G = 4$, $t = 16$

(i) $C1 = 4$, $C2 = 4$, $G = 4$, $t = 18$

(j) $C1 = 4$, $C2 = 4$, $G = 4$, $t = 20$

(k) $C1 = 4$, $C2 = 4$, $G = 4$, $t = 22$

(l) $C1 = 4$, $C2 = 4$, $G = 4$, $t = 24$

(m) $C1 = 4$, $C2 = 4$, $G = 4$, $t = 26$

(n) $C1 = 4$, $C2 = 4$, $G = 4$, $t = 28$

(o) $C1 = 4$, $C2 = 4$, $G = 4$, $t = 29$

(p) $C1 = 4$, $C2 = 4$, $G = 4$, $t = 30$

(q) $C1 = 4$, $C2 = 4$, $G = 4$, $t = 31$

(r) $C1 = 4$, $C2 = 4$, $G = 4$, $t = 32$

(s) $C1 = 4$, $C2 = 4$, $G = 4$, $t = 33$

(t) $C1 = 4$, $C2 = 4$, $G = 4$, $t = 34$

(u) $C1 = 4$, $C2 = 4$, $G = 4$, $t = 35$

(v) $C1 = 4$, $C2 = 4$, $G = 4$, $t = 36$

(w) $C1 = 4$, $C2 = 4$, $G = 4$, $t = 37$

(x) $C1 = 4$, $C2 = 4$, $G = 4$, $t = 38$

(y) $C1 = 4$, $C2 = 4$, $G = 4$, $t = 39$

(z) $C1 = 4$, $C2 = 4$, $G = 4$, $t = 40$

(aa) $C1 = 4$, $C2 = 4$, $G = 4$, $t = 41$

(ab) $C1 = 4$, $C2 = 4$, $G = 4$, $t = 42$

(ac) $C1 = 4$, $C2 = 4$, $G = 4$, $t = 42.8$

(ad) $C1 = 4$, $C2 = 4$, $G = 4$, $t = 43.8$

(ae) $C1 = 4$, $C2 = 4$, $G = 4$, $t = 44.8$

(af) $C1 = 4$, $C2 = 4$, $G = 4$, $t = 45.8$

(ag) $C1 = 4$, $C2 = 4$, $G = 4$, $t = 46.8$

Figure 8.119. Elemental-vortex distributions in flow over the ($C1 = 4$, $C2 = 4$, $G = 4$) array, showing flow development from an impulsive start from rest to the fully-developed flow.

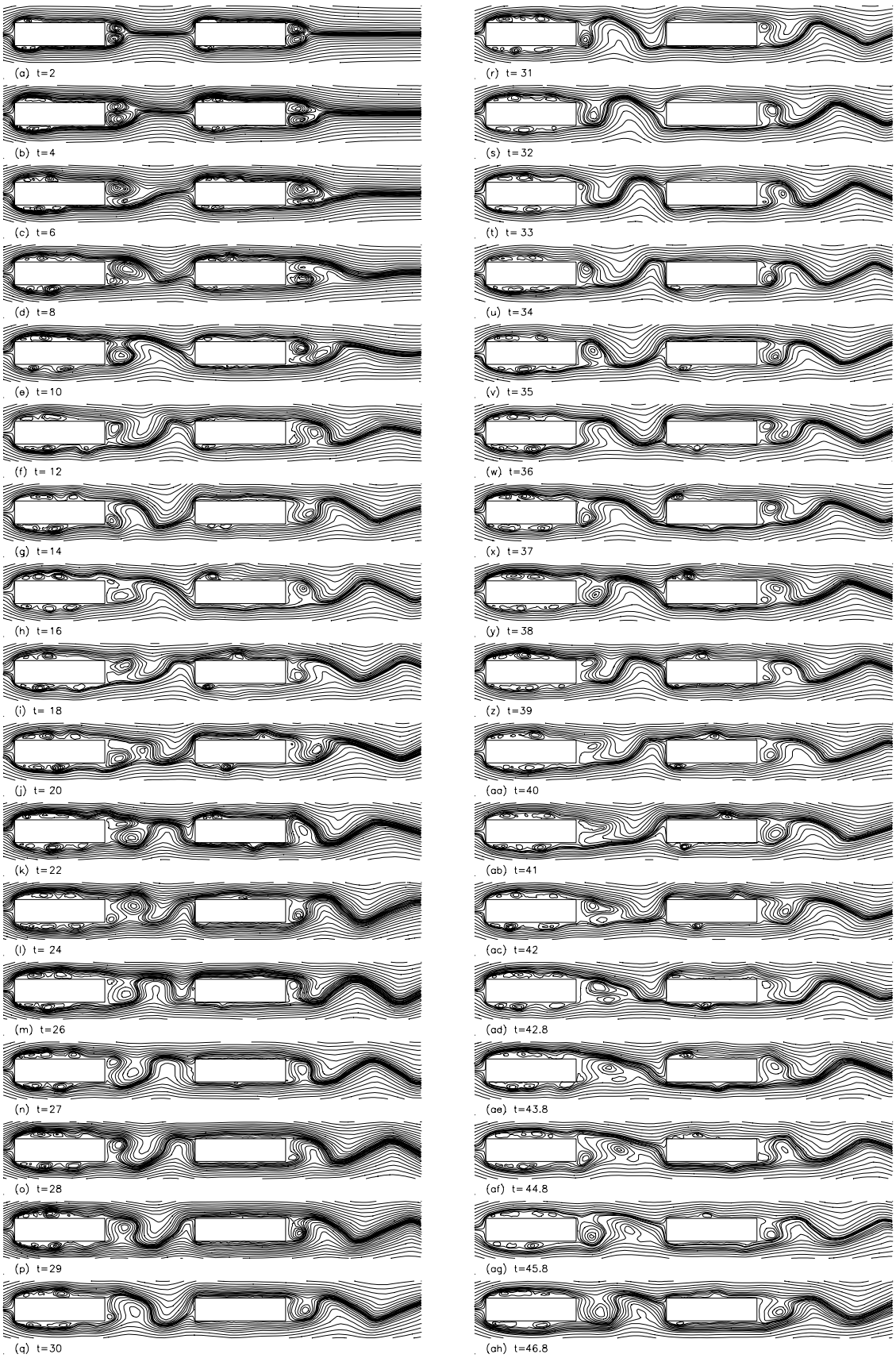

Figure 8.120. Calculated streamline patterns in flow over the ($C1$ = 4, $C2$ = 4, G = 4) array, showing flow development from an impulsive start from rest to the fully-developed flow.

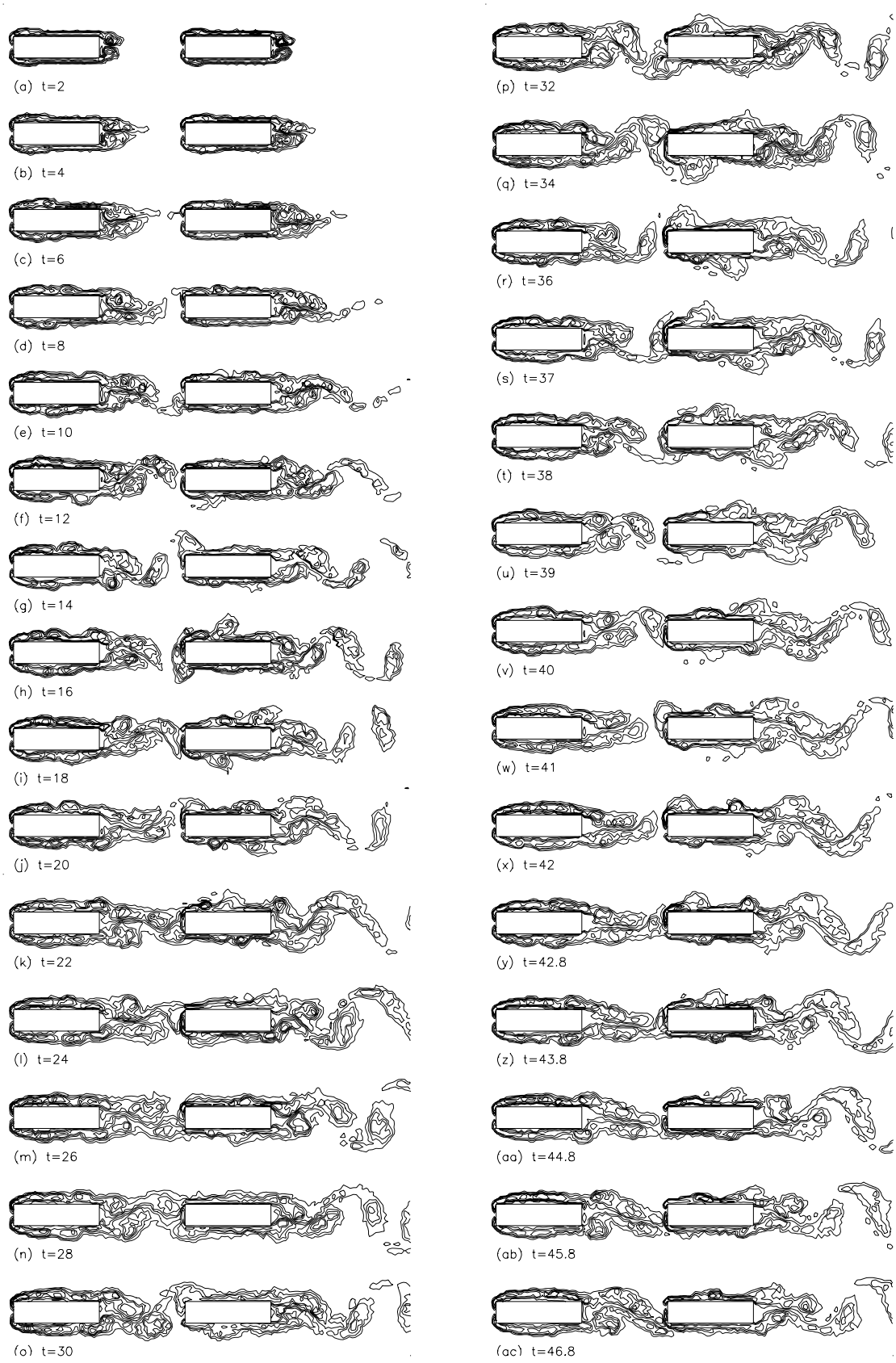

Figure 8.121. Vorticity contours in flow over the ($C1 = 4$, $C2 = 4$, $G = 4$) array, showing flow development from an impulsive start from rest to the fully-developed flow.

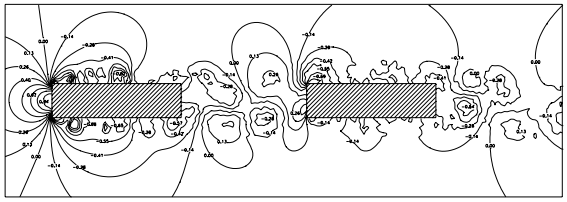

(a1) G = 4, t = 30

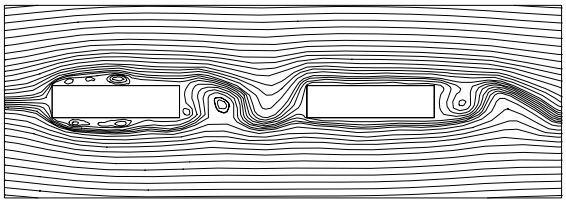

(a2) G = 4, t = 30

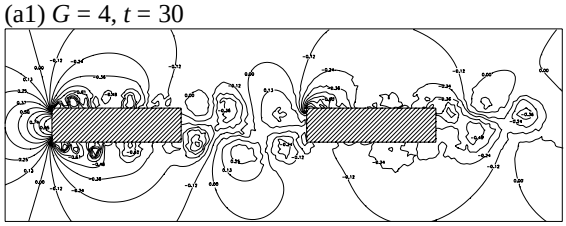

(b1) G = 4, t = 31

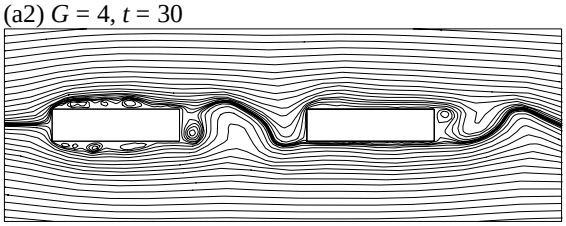

(b2) G = 4, t = 31

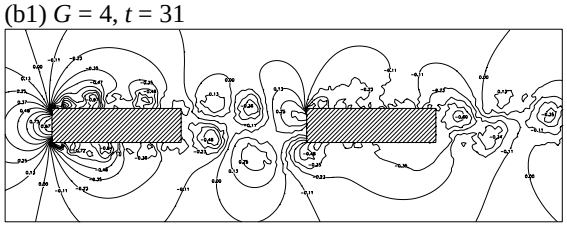

(c1) G = 4, t = 32

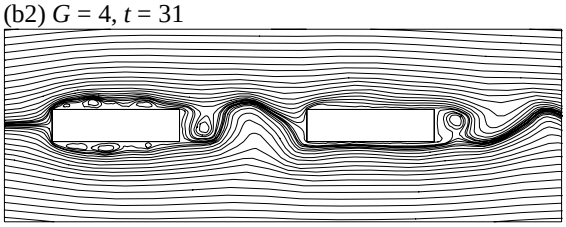

(c2) G = 4, t = 32

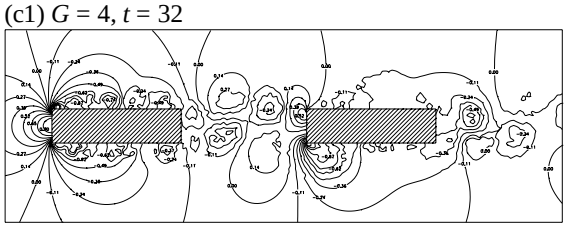

(d1) G = 4, t = 33

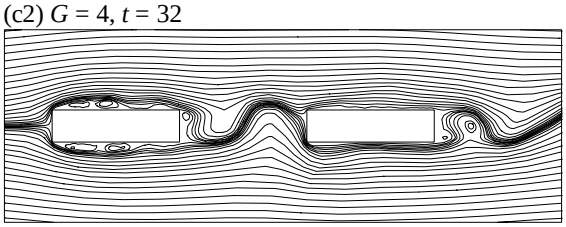

(d2) G = 4, t = 33

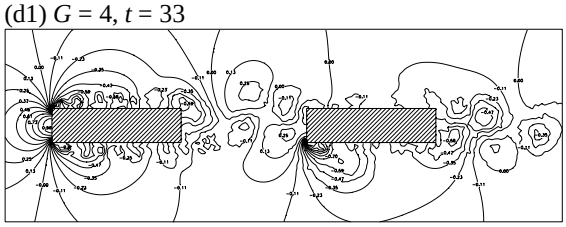

(e1) G = 4, t = 34

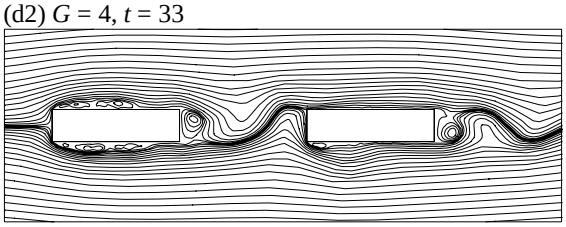

(e2) G = 4, t = 34

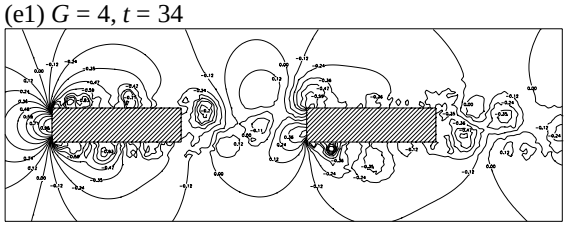

(f1) G = 4, t = 35

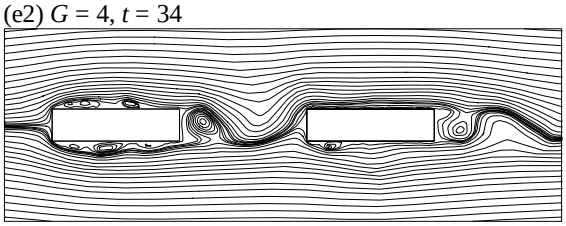

(f2) G = 4, t = 35

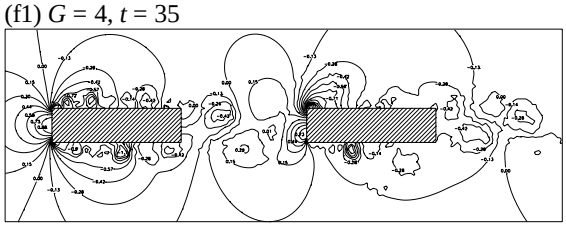

(g1) G = 4, t = 36

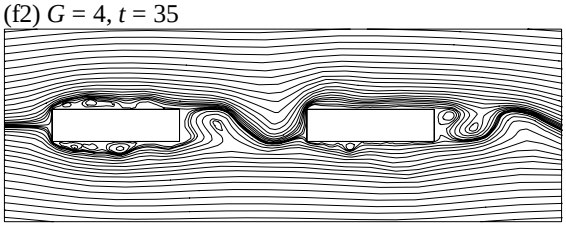

(g2) G = 4, t = 36

Figure 8.122. Instantaneous pressure fields and streamline patterns in fully-developed flow over the ($C1$ = 4, $C2$ = 4, G = 4) array.

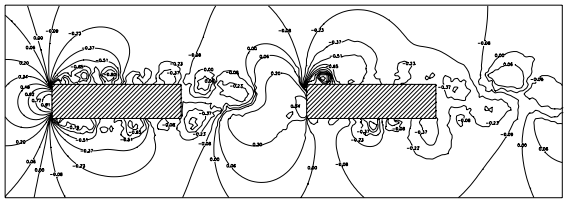

(h1) $G = 4$, $t = 37$

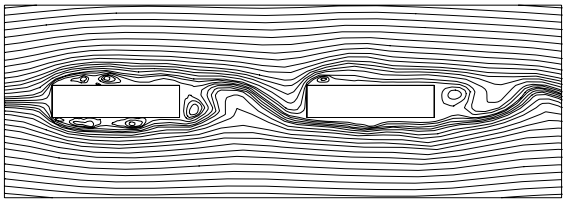

(h2) $G = 4$, $t = 37$

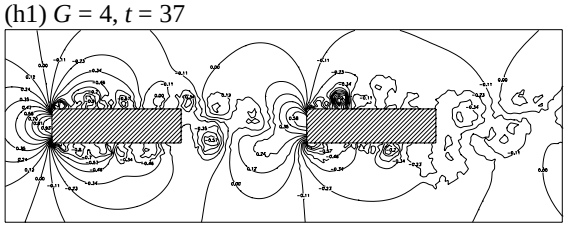

(i1) $G = 4$, $t = 38$

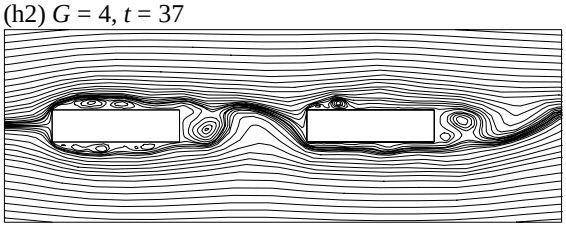

(i2) $G = 4$, $t = 38$

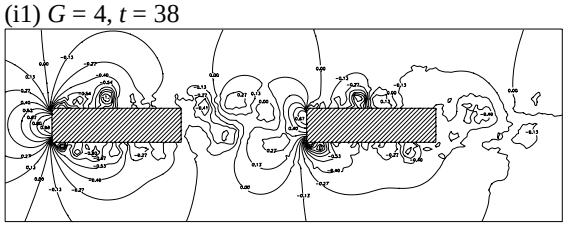

(j1) $G = 4$, $t = 39$

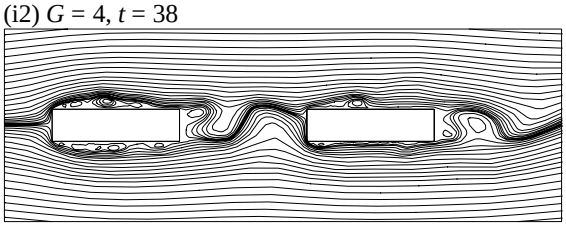

(j2) $G = 4$, $t = 39$

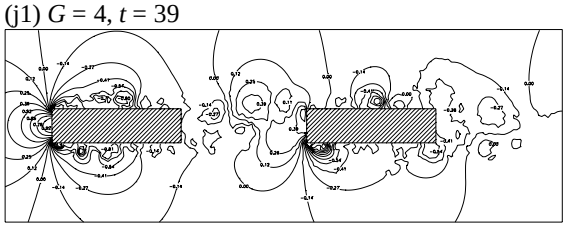

(k1) $G = 4$, $t = 40$

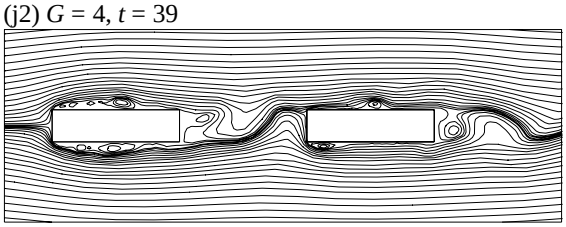

(k2) $G = 4$, $t = 40$

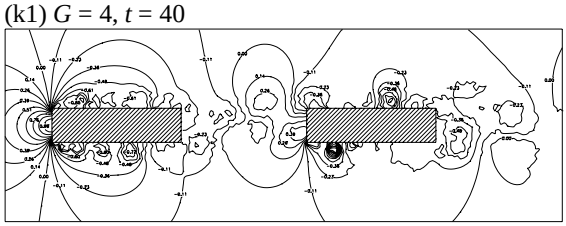

(l1) $G = 4$, $t = 41$

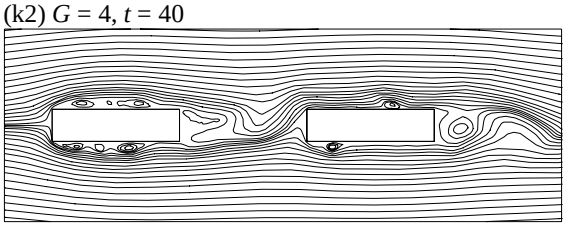

(l2) $G = 4$, $t = 41$

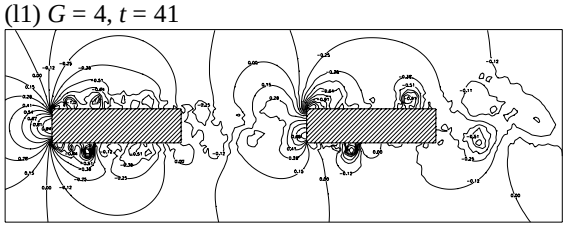

(m1) $G = 4$, $t = 42$

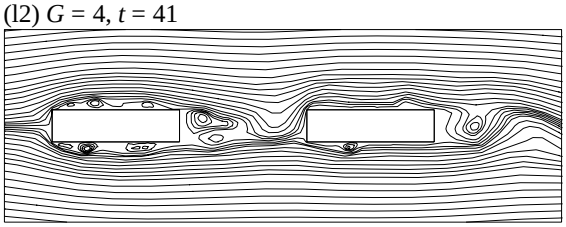

(m2) $G = 4$, $t = 42$

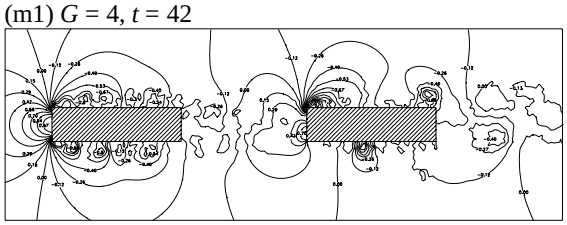

(n1) $G = 4$, $t = 43$

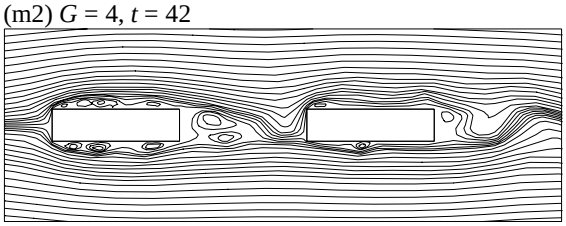

(n2) $G = 4$, $t = 43$

Figure 8.122. Cont'd.

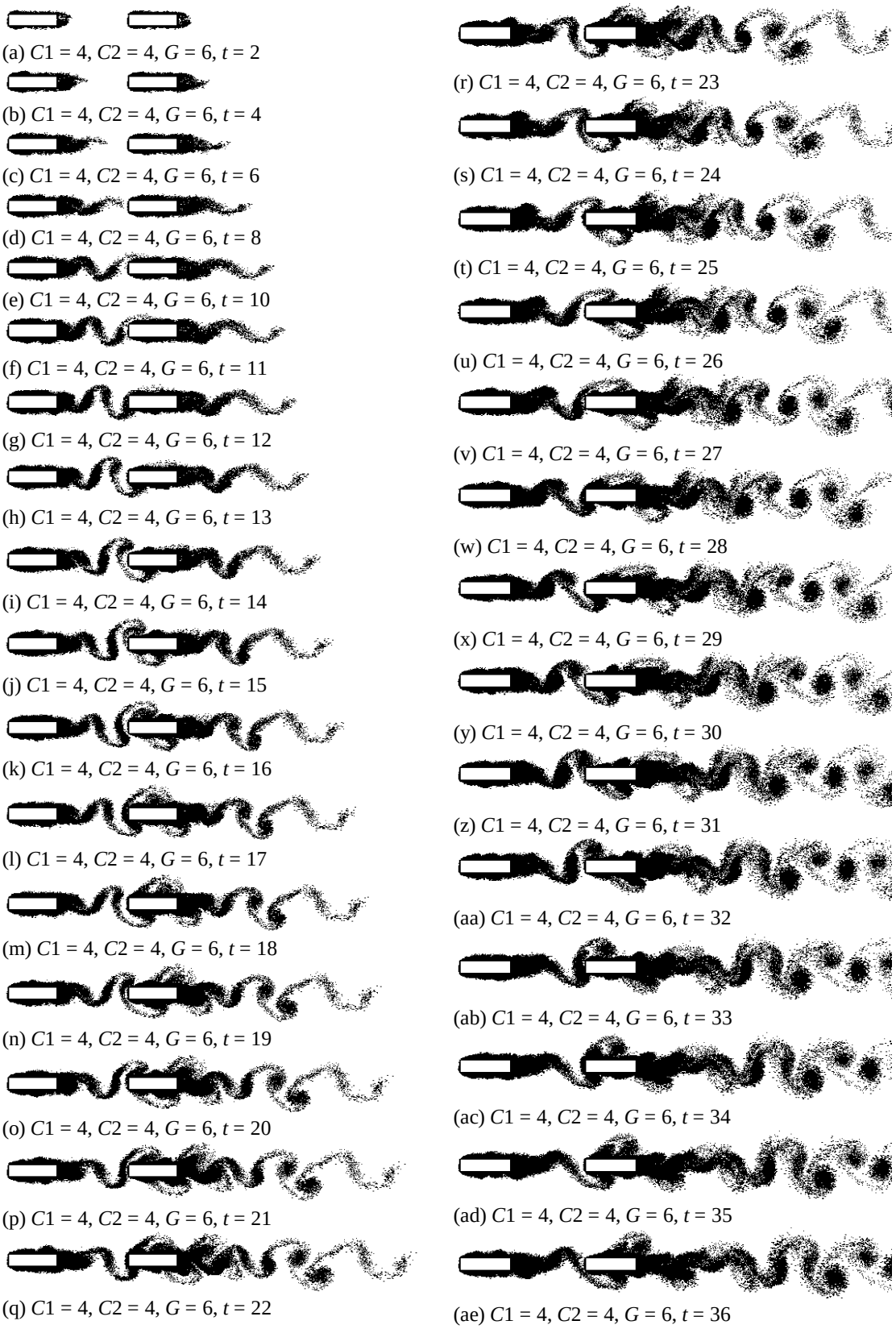

Figure 8.123. Elemental-vortex distributions in flow over the ($C1 = 4,\ C2 = 4,\ G = 6$) array, showing evolution of flow from the impulsive start to the fully-developed state.

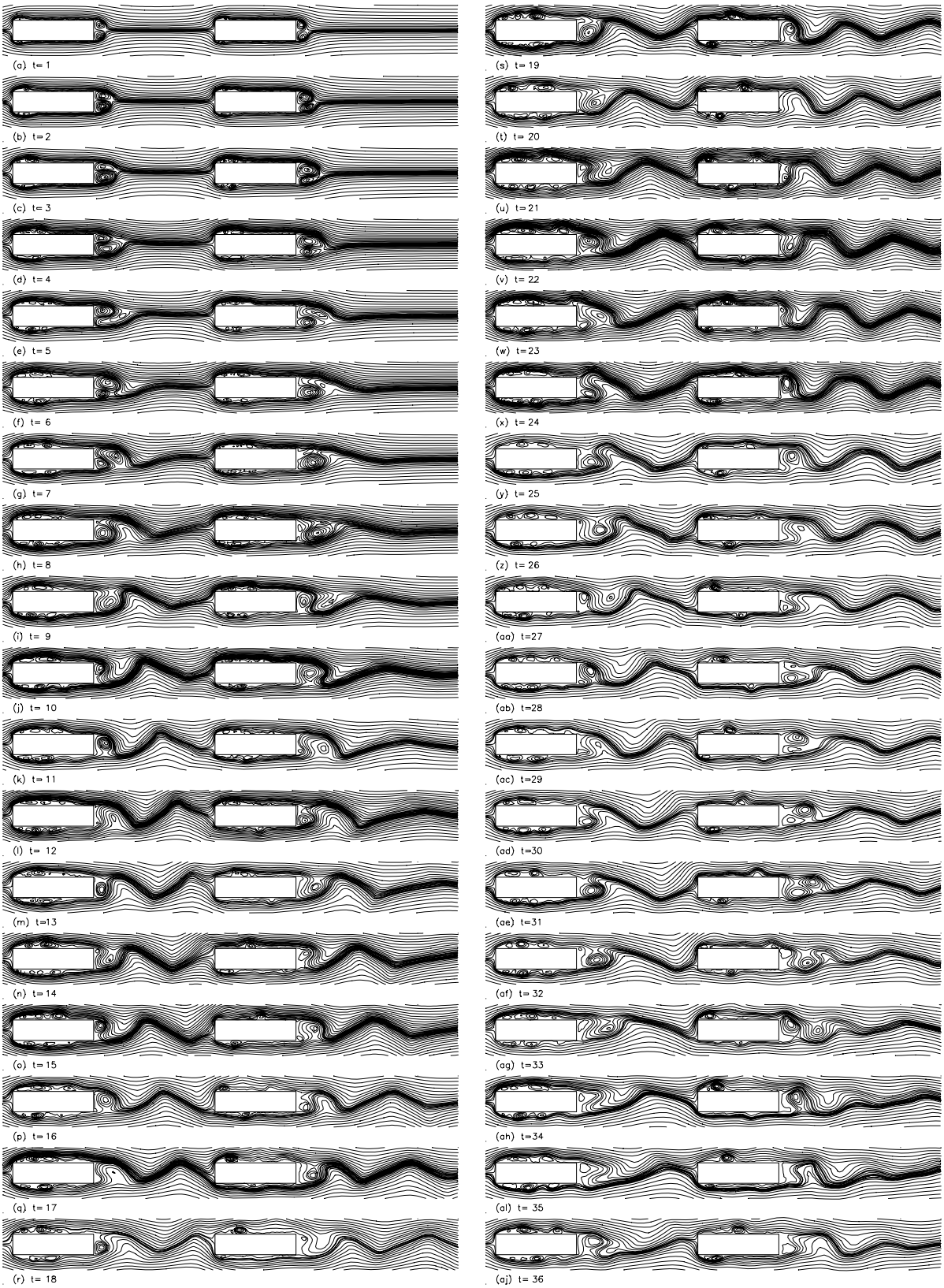

Figure 8.124. Streamline patterns in flow over the ($C1 = 4$, $C2 = 4$, $G = 6$) array, showing evolution of flow from the impulsive start to the fully-developed state.

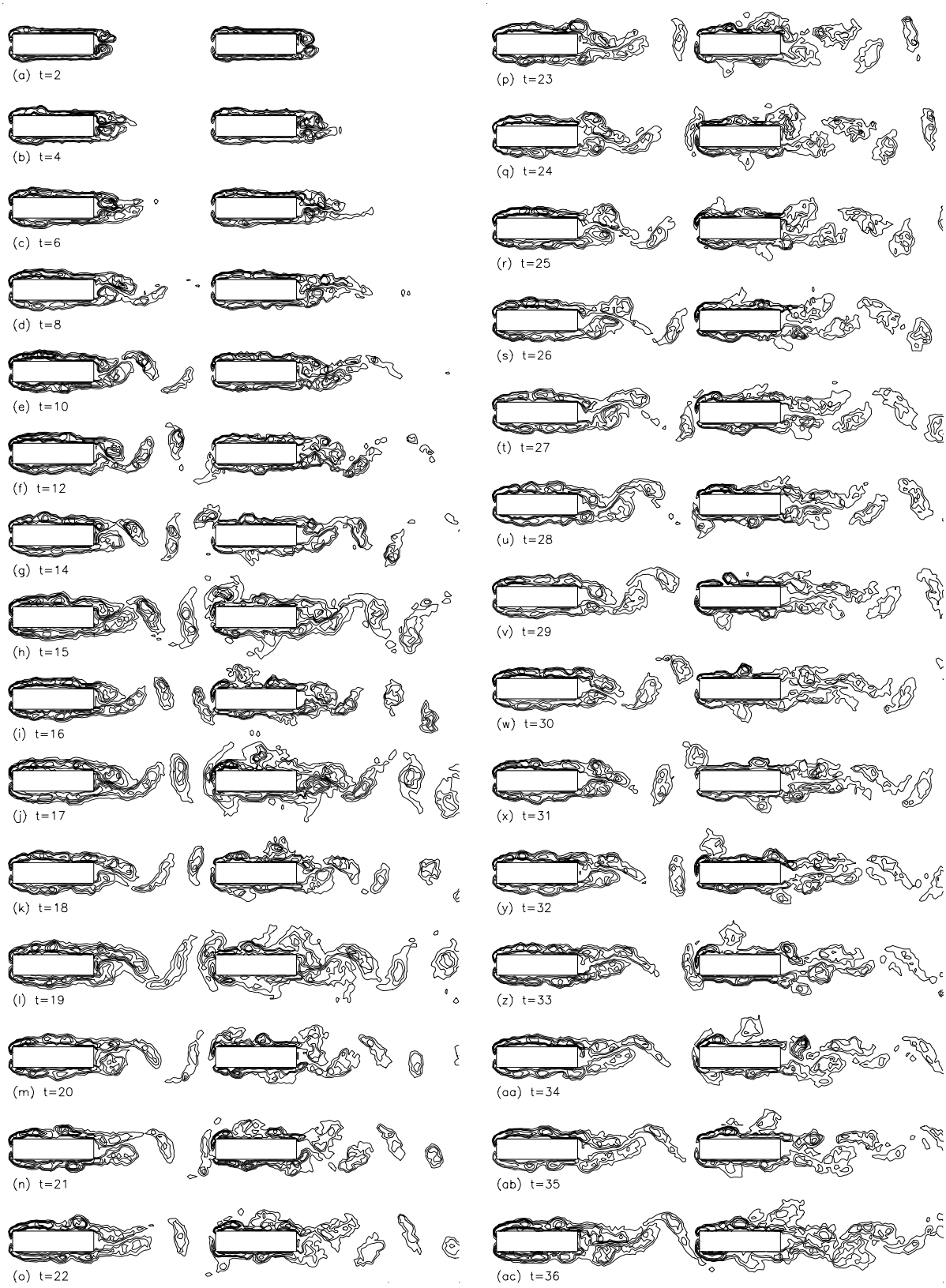

Figure 8.125. Vorticity contours in flow over the (*C*1 = 4, *C*2 = 4, *G* = 6) array, showing evolution of flow from the impulsive start to the fully-developed state.

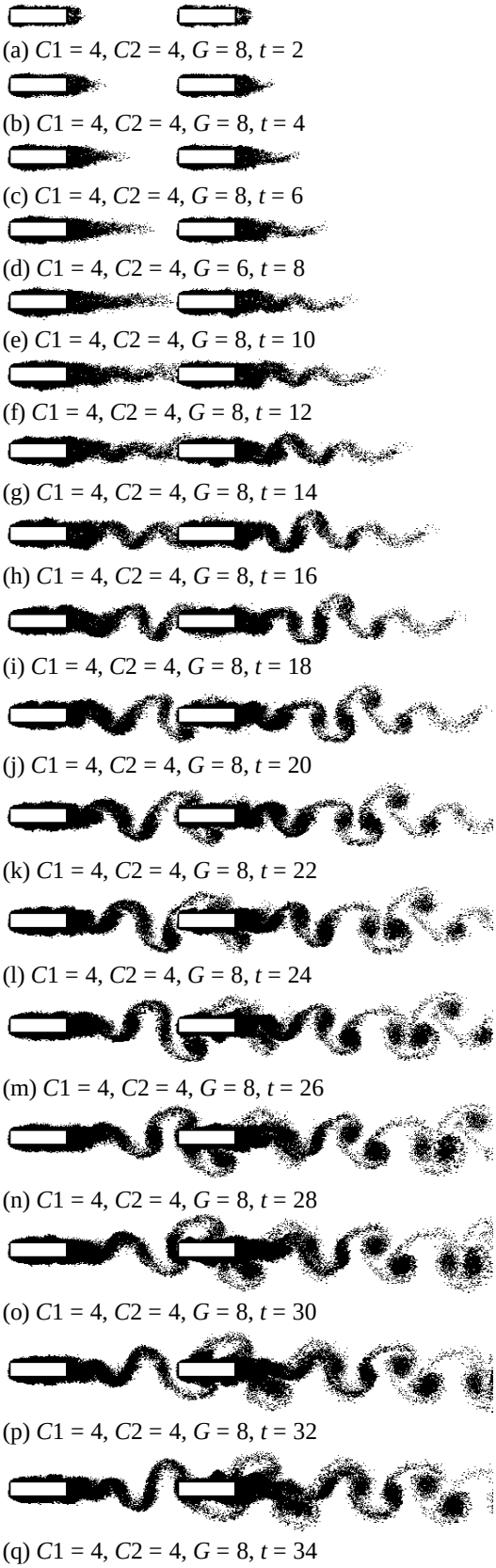

(a) $C1 = 4$, $C2 = 4$, $G = 8$, $t = 2$

(b) $C1 = 4$, $C2 = 4$, $G = 8$, $t = 4$

(c) $C1 = 4$, $C2 = 4$, $G = 8$, $t = 6$

(d) $C1 = 4$, $C2 = 4$, $G = 6$, $t = 8$

(e) $C1 = 4$, $C2 = 4$, $G = 8$, $t = 10$

(f) $C1 = 4$, $C2 = 4$, $G = 8$, $t = 12$

(g) $C1 = 4$, $C2 = 4$, $G = 8$, $t = 14$

(h) $C1 = 4$, $C2 = 4$, $G = 8$, $t = 16$

(i) $C1 = 4$, $C2 = 4$, $G = 8$, $t = 18$

(j) $C1 = 4$, $C2 = 4$, $G = 8$, $t = 20$

(k) $C1 = 4$, $C2 = 4$, $G = 8$, $t = 22$

(l) $C1 = 4$, $C2 = 4$, $G = 8$, $t = 24$

(m) $C1 = 4$, $C2 = 4$, $G = 8$, $t = 26$

(n) $C1 = 4$, $C2 = 4$, $G = 8$, $t = 28$

(o) $C1 = 4$, $C2 = 4$, $G = 8$, $t = 30$

(p) $C1 = 4$, $C2 = 4$, $G = 8$, $t = 32$

(q) $C1 = 4$, $C2 = 4$, $G = 8$, $t = 34$

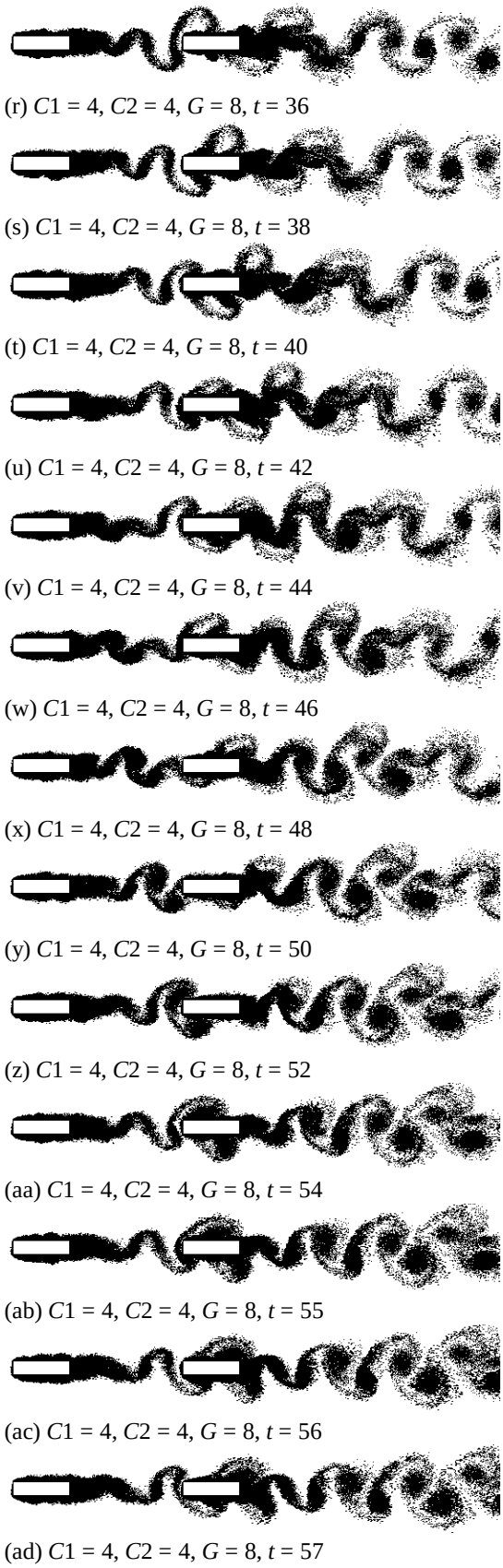

(r) $C1 = 4$, $C2 = 4$, $G = 8$, $t = 36$

(s) $C1 = 4$, $C2 = 4$, $G = 8$, $t = 38$

(t) $C1 = 4$, $C2 = 4$, $G = 8$, $t = 40$

(u) $C1 = 4$, $C2 = 4$, $G = 8$, $t = 42$

(v) $C1 = 4$, $C2 = 4$, $G = 8$, $t = 44$

(w) $C1 = 4$, $C2 = 4$, $G = 8$, $t = 46$

(x) $C1 = 4$, $C2 = 4$, $G = 8$, $t = 48$

(y) $C1 = 4$, $C2 = 4$, $G = 8$, $t = 50$

(z) $C1 = 4$, $C2 = 4$, $G = 8$, $t = 52$

(aa) $C1 = 4$, $C2 = 4$, $G = 8$, $t = 54$

(ab) $C1 = 4$, $C2 = 4$, $G = 8$, $t = 55$

(ac) $C1 = 4$, $C2 = 4$, $G = 8$, $t = 56$

(ad) $C1 = 4$, $C2 = 4$, $G = 8$, $t = 57$

Figure 8.126. Elemental-vortex distributions in flow over the ($C1 = 4$, $C2 = 4$, $G = 8$) array, showing development of flow from the impulsive start to the fully-developed state.

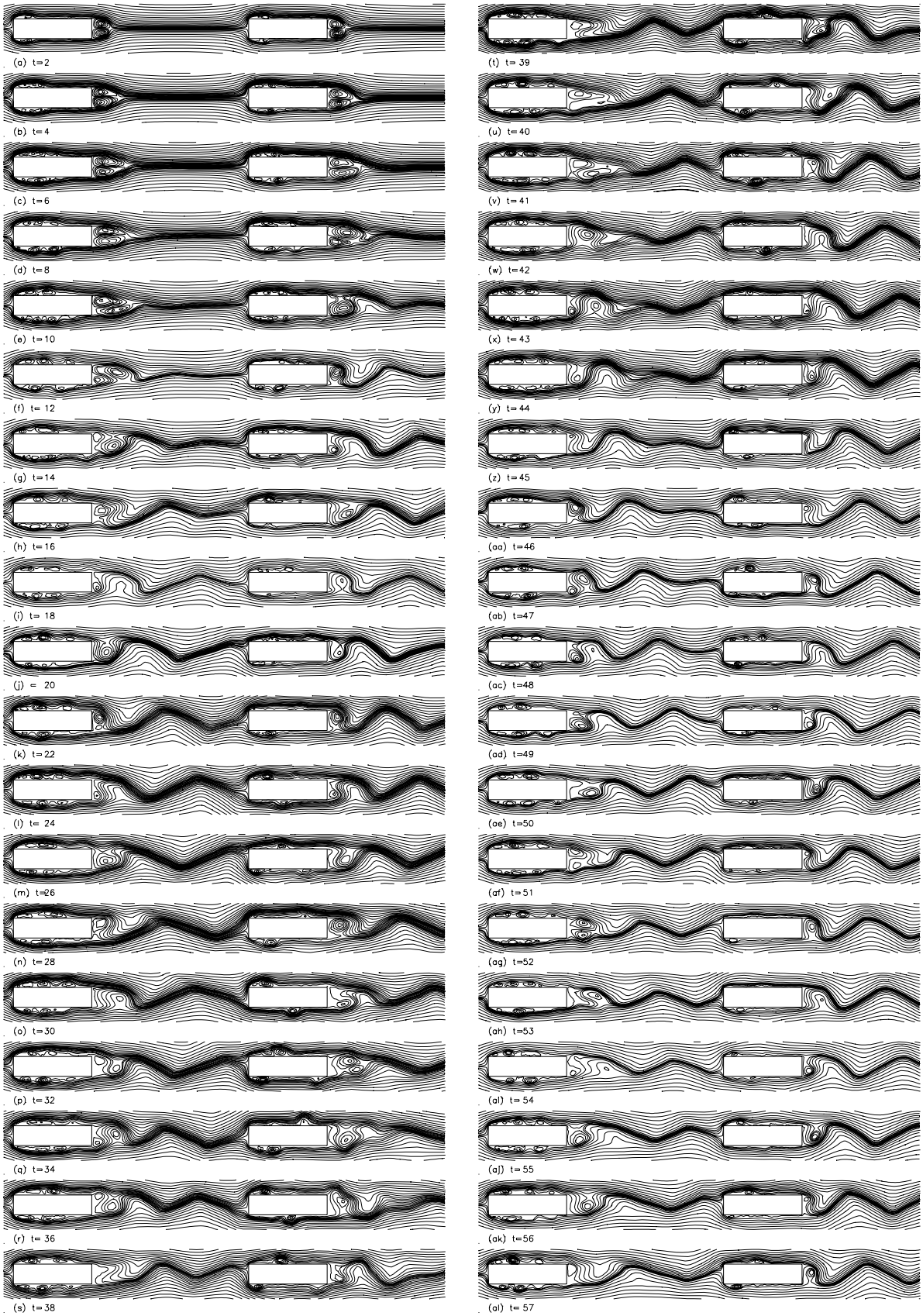

Figure 8.127. Calculated streamline patterns in flow over the ($C1 = 4$, $C2 = 4$, $G = 8$) array, showing development of flow from the impulsive start to the fully-developed state.

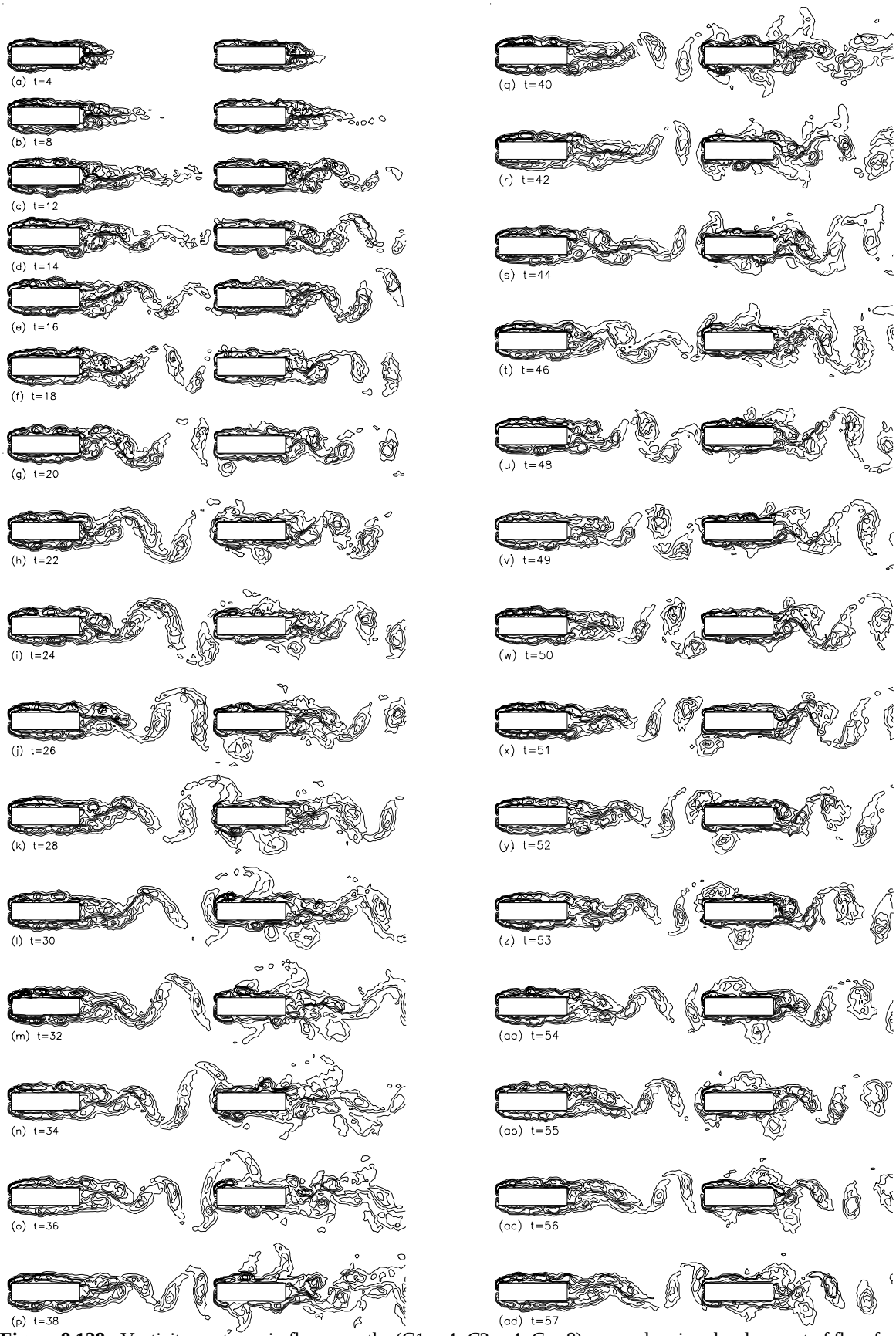

Figure 8.128. Vorticity contours in flow over the (C1 = 4, *C*2 = 4, *G* = 8) array, showing development of flow from the impulsive start to the fully-developed state.

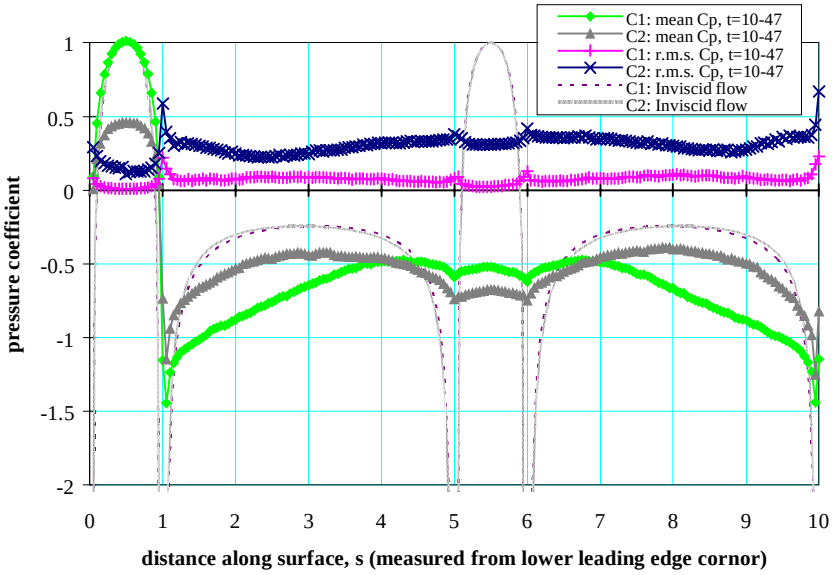

Figure 8.129. Calculated distributions of mean and r.m.s. pressure coefficients on the ($C1 = 4$, $C2 = 4$, $G = 4.0$) array.

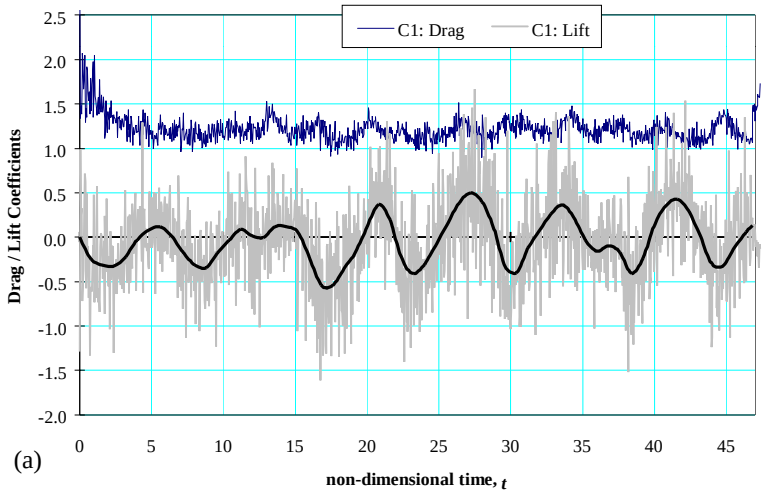

(a)

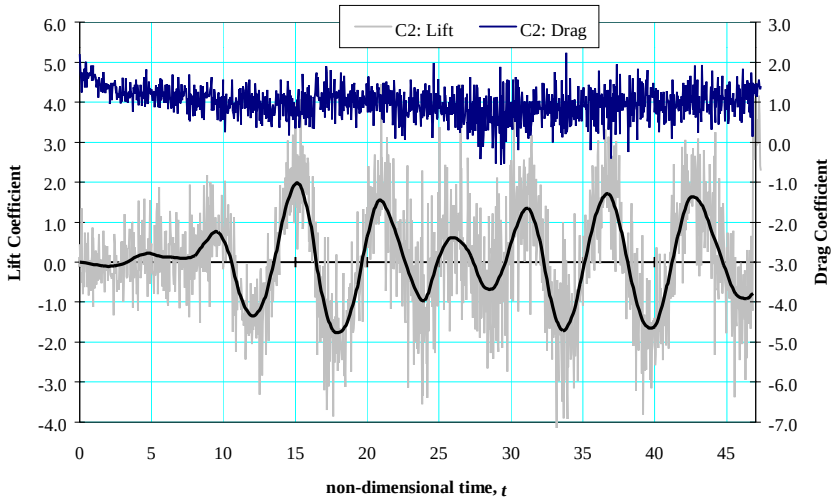

(b)

Figure 8.130. Time-histories of drag and lift on the ($C1 = 4$, $C2 = 4$, $G = 4.0$) array, (a) upstream plate, (b) downstream plate. Drag and lift are calculated for $\Delta t = 0.02$; highlighted values are averaged over $\Delta t = 0.4$.

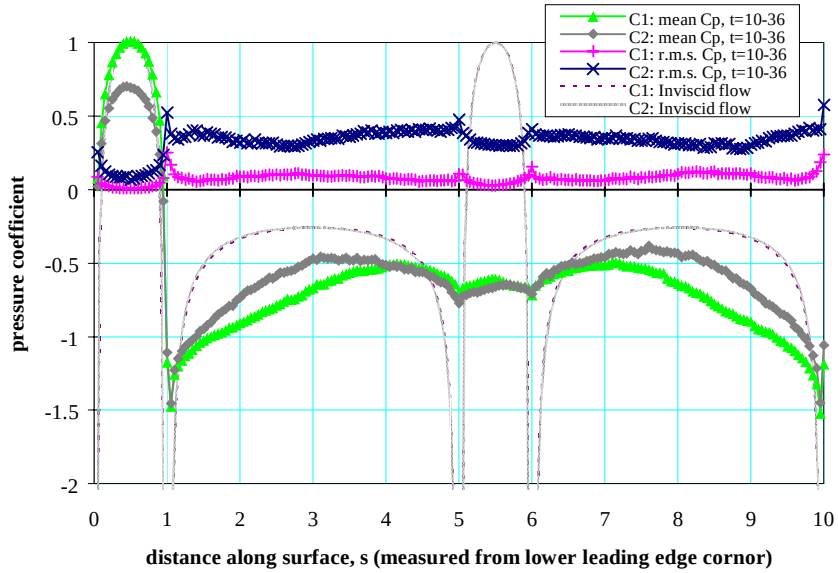

Figure 8.131. Calculated distributions of mean and r.m.s. pressure coefficients on the ($C1 = 4$, $C2 = 4$, $G = 6.0$) array.

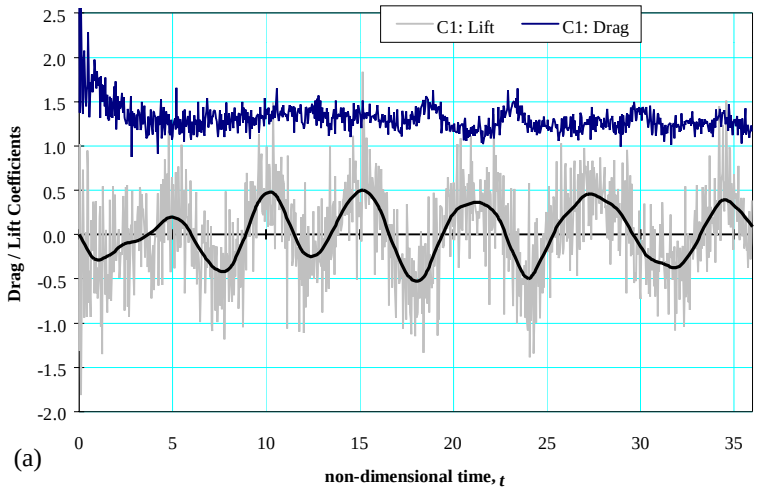

(a)

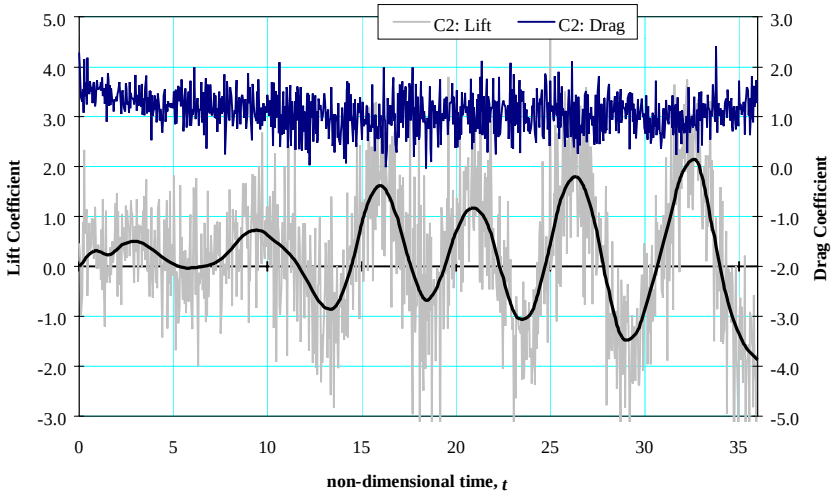

(b)

Figure 8.132. Time-histories of drag and lift on the ($C1 = 4$, $C2 = 4$, $G = 6.0$) array, (a) upstream plate, (b) downstream plate. Drag and lift are calculated for $\Delta t = 0.02$; highlighted values are averaged over $\Delta t = 0.4$.

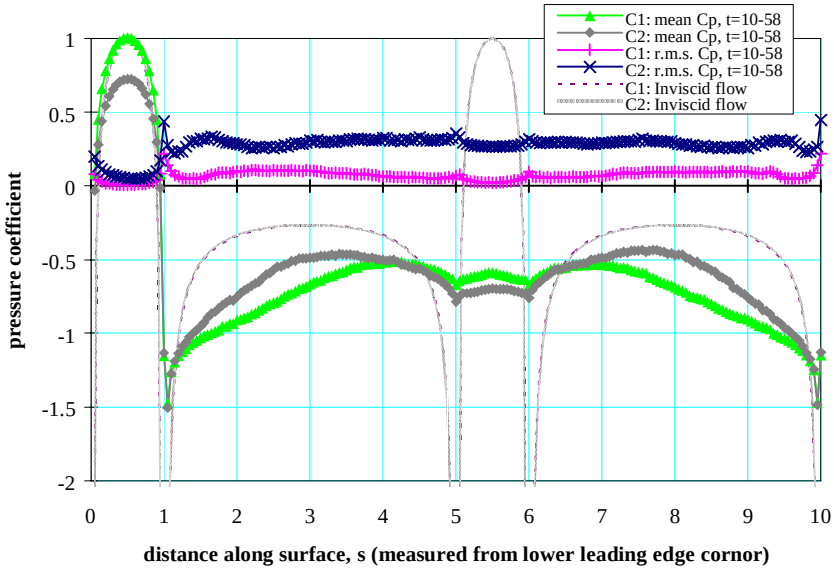

Figure 8.133. Calculated distributions of mean and r.m.s. pressure coefficients on the ($C1 = 4$, $C2 = 4$, $G = 8.0$) array.

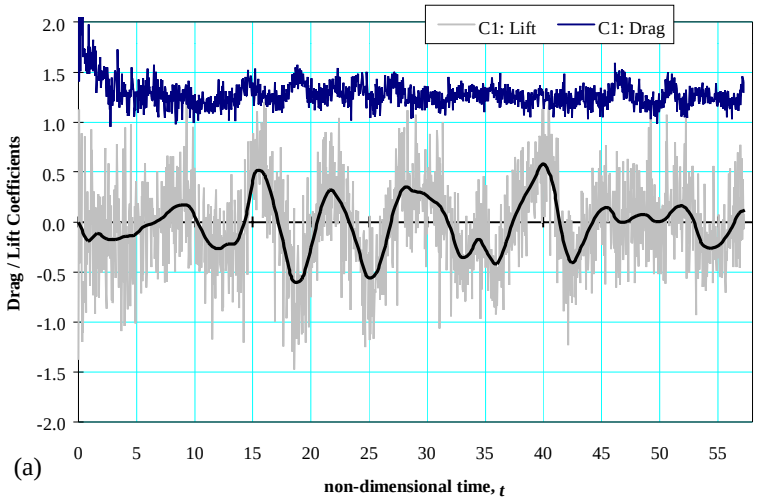

(a)

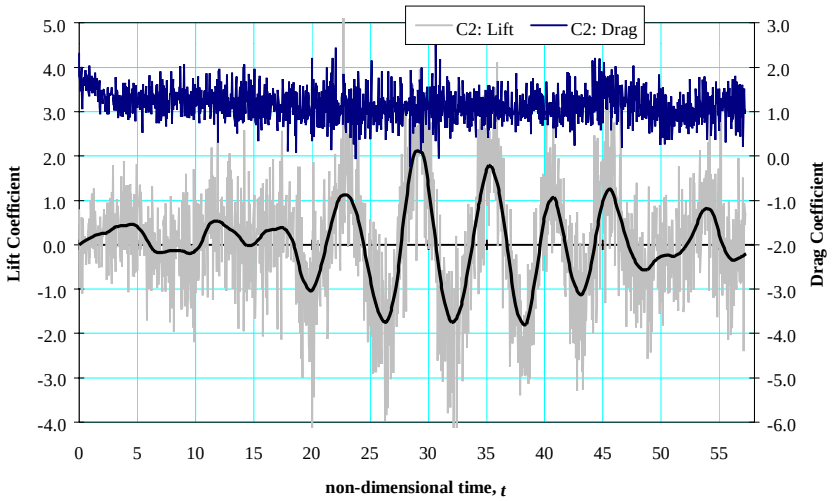

(b)

Figure 8.134. Time-histories of drag and lift on the ($C1 = 4$, $C2 = 4$, $G = 8.0$) array, (a) upstream plate, (b) downstream plate. Drag and lift are calculated for $\Delta t = 0.02$; highlighted values are averaged over $\Delta t = 0.4$.

8.5.4 Dependence of Flow Parameters on the Gap-to-Thickness Ratio

A summary of flow parameters, as a function of gap-to-thickness ratio G, is presented in Fig. 8.136. The figure shows the Strouhal numbers St_1 of vortex shedding from the upstream plate and St_2 of vortex shedding into the wake from the downstream plate derived from the power spectra of lift fluctuations of the plates (Fig. 8.135), the base-pressure coefficients C_{pb1} and C_{pb2} on the upstream and downstream plates, the leading-face pressure coefficient C_{pf2} of the downstream plate, and the drag coefficients C_{D1} and C_{D2} of the upstream and downstream plates.

The characteristic streamline patterns for gaps in the range $1 \le G \le 8$, viewed from a frame of reference moving at a velocity $U_{ref} = 0.8U_\infty$, which is approximately equal to the convection velocity of wake vortices, are given in Fig. 8.137. In this reference frame, vortical structures moving at this velocity are highlighted. The progressive change in the pattern of flow in the gap from the onset of vortex shedding from the upstream plate at $G = 1.0$, which produces essentially stationary vortices in the gap, to the fully-established vortex-street flow in the gap at $G = 8.0$, can be clearly seen.

The distributions of surface pressure and the time-histories of lift and drag coefficients of the upstream and downstream plates in the specific flow regimes, for each gap considered in the calculation range $1 \le G \le 8$, are shown in previous sections (Figs. 8.113, 8.115, 8.117, 8.129, 8.131 and 8.133). The general form of surface-pressure distribution on the upstream plate is, as in all previous cases of the ($C1 = 1$, $C2 = 1$) and ($C1 = 1$, $C2 = 4$) arrays with two rectangular plates, almost independent of gap length, and very similar to the pressure distribution on a single isolated plate at the same Reynolds number. The base pressure and drag of the upstream plate change slightly with G. The base pressure coefficient decreases from $C_{pb1} \approx -0.5$ to -0.65 as the gap is increased through the range $1 \le G \le 8$, approaching the base pressure $C_{pb} \approx -0.7$ of a single plate with $C = 4$ at $Re_h = 500$; the drag coefficient correspondingly increases from $C_{D1} \approx 1.1$ to 1.26, tending to the single-plate value $C_D \approx 1.27$.

On the downstream plate, the surface-pressure distribution exhibits greater dependence on gap-to-thickness ratio; its general form approaches that on the upstream plate as G increases. The base pressure of the downstream plate is fairly constant at $C_{pb2} \approx -0.7$ over the range of G, while the leading-face pressure increases from $C_{pf2} \approx -0.15$ at $G = 1.0$ to $C_{pf2} \approx 0.75$ at $G = 8$.

As a result, the drag on the downstream plate increases from $C_{D2} \approx 0.7$ to 1.2 as the gap is increased from $G = 1$ to 8. Both the pressure coefficients and drag coefficient of the downstream plate approach the single-plate values as the gap increases.

As already observed, alternate vortex-shedding from upper and lower surfaces of the upstream plate occurs even at as small a gap as $G = 1.0$. In this case, the vortices formed in the gap increase and then decrease in size, without significant convective motion. This type of flow changes progressively to vortex-street flow in the gap as G increases, and, correspondingly, the Strouhal number of vortex shedding from the upstream plate basically varies continuously with increasing G. Similarly, there is basically a continuous variation of the Strouhal number St_2 of vortex shedding from the downstream plate. There are, however, deviations, from these continuous variations when phase-locking of the shedding from the two plates occurs. At small gaps, phase-locking of the downstream plate to the upstream plate occurs at $G \sim 2$; calculations have not been done to indicate how far this persists to higher values of G, but phase-locking has ceased to occur at $G = 4$. The reverse process, phase-locking of the upstream plate to the downstream plate, occurs at large gaps, $G \geq 8$, when the shedding frequencies of both plates converge towards the $C = 4$ single-plate value, $St = 0.16$ at $Re_h = 500$.

8.5.5 Concluding Remarks on Flow Over the ($C1 = 4$, $C2 = 4$) Array

Calculations of flow over the ($C1 = 4$, $C2 = 4$) arrays have been made for gap-to-thickness ratios $G = 1.0$, 1.5, 2.0, 4.0, 6.0 and 8.0 at a Reynolds number of $Re_h = 500$. In all these cases the flow on the upstream plate features a leading-edge separation bubble and permanent reattachment to the side faces. The reattached shear layers separate from the trailing edge, leading to vortex shedding into the gap. Although it is found that the vortex shedding from the upstream plate has already started to occur at $G = 1$, a vortex street in the gap does not become fully established until the gap is increased beyond $G \approx 2$. There is a progressive evolution of the gap flow towards a vortex-street as G increased.

For small gaps $G \leq 2$, which are too short to allow a vortex street to become fully established in the gap, the vortices in the gap fill up the entire space between the upstream and downstream plates. In association with the vortex shedding from the upstream plate, these vortices undergo a cycle of formation, growth, shrinkage and disappearance at the vortex-shedding frequency of the upstream plate. The flow on the downstream plate is generally fully-attached on the side

faces, with intermittent passage of side-face vortices which originate from the gap vortices. Vortex formation downstream of the array results primarily from the rolling up of the shear layers separated from the trailing edges of the downstream plate. The vortex-shedding frequencies St_1 and St_2 of the upstream and downstream plates decrease slowly as the gap is increased in this range. The value of St_1 is generally lower than the value of St_2 until phase-locking between upstream and downstream plates occurs at $G \approx 2$ and the values of St_1 and St_2 become equal to each other.

As the length of the gap is increased beyond $G \sim 2$, convective movement of the gap vortices becomes more pronounced and the vortex street becomes fully established in the gap, the convected vortices in the street then impinging on the leading edge of the downstream plate. The vortex-impingement flow on the ($C1 = 4$, $C2 = 4$) arrays exhibits similar characteristics to the vortex-impingement flows on the ($C1 = 1$, $C2 = 1$) and ($C1 = 1$, $C2 = 4$) arrays with the same gap. In all these cases, the impingement process involves: periodic reversal of flow direction on the front face of the downstream plate; oscillation of the stagnation point between the upper and lower leading corners of the downstream plate; clipping of the impinging vortex by the leading edge of the downstream plate; formation of a primary and a secondary vortex at each impingement, and their subsequent movement along a side face of the downstream plate; and alternation between fully-attached flow and a leading-edge separation bubble on the side faces of the downstream plate. The wake of the array comprises the primary and secondary vortices formed during impingement, and the trailing-face vortex of the downstream plate formed by trailing-edge separation of the attached-flow on the side faces of the plate. The phase-locking of vortex shedding from the upstream and downstream plates, that generally occurs in the impingement flow of the ($C1 = 1$, $C2 = 1$) and ($C1 = 1$, $C2 = 4$) arrays, does not occur on the ($C1 = 4$, $C2 = 4$) array until the gap is increased to $G \gtrsim 8$ where both St_1 and St_2 approach the value $St = 0.16$ the frequency of wake-vortex shedding of a single $C = 4$ plate at $Re_h = 500$.

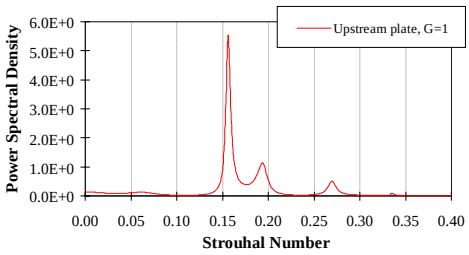

(a1) G = 1.0, upstream plate

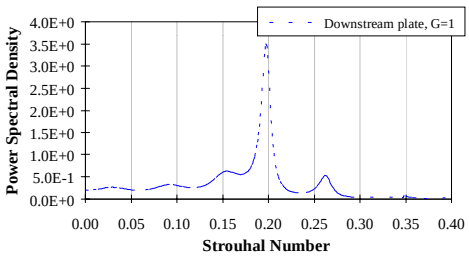

(a2) G = 1.0, downstream plate

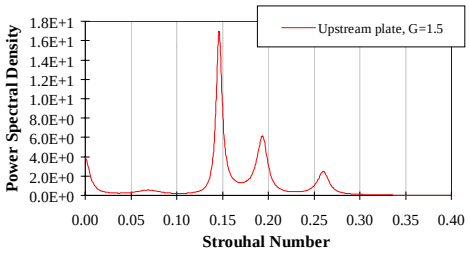

(b1) G = 1.5, upstream plate

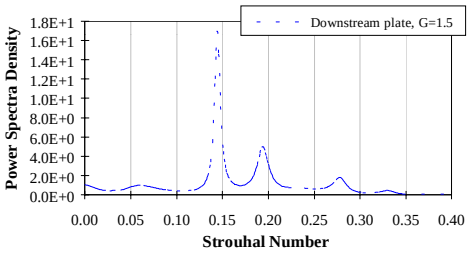

(b2) G = 1.5, downstream plate

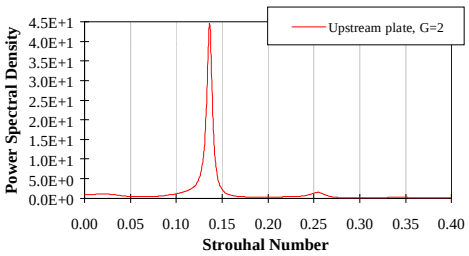

(c1) G = 2.0, upstream plate

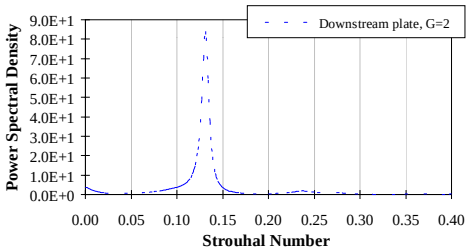

(c2) G = 2.0, downstream plate

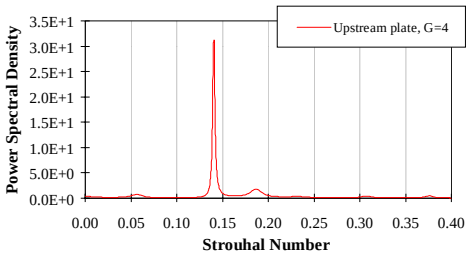

(d1) G = 4.0, upstream plate

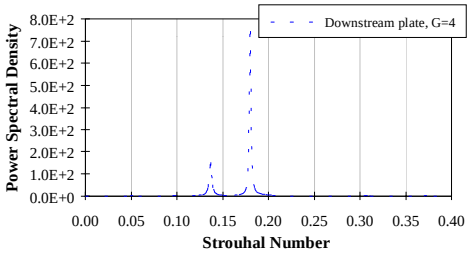

(d2) G = 4.0, downstream plate

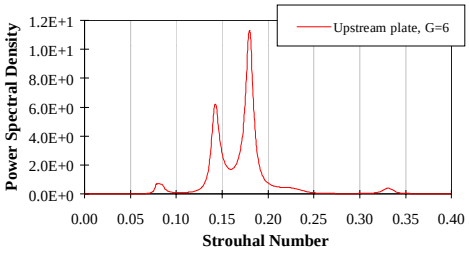

(e1) G = 6.0, upstream plate

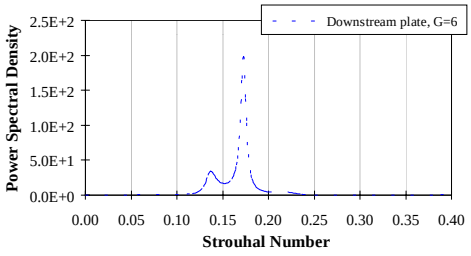

(e2) G = 6.0, downstream plate

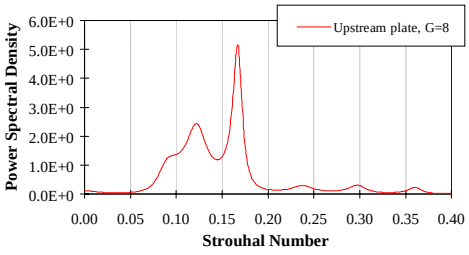

(f1) G = 8.0, upstream plate

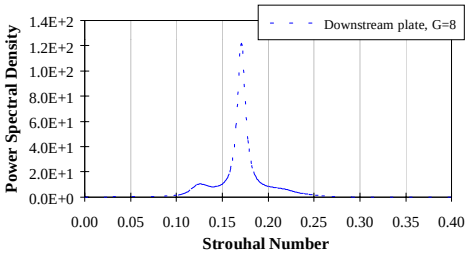

(f2) G = 8.0, downstream plate

Figure 8.135. Power spectra of fluctuating lift of the ($C1$ = 4, $C2$ = 4) array with various gap-to-thickness ratio in the range $1.0 \leq G \leq 8.0$.

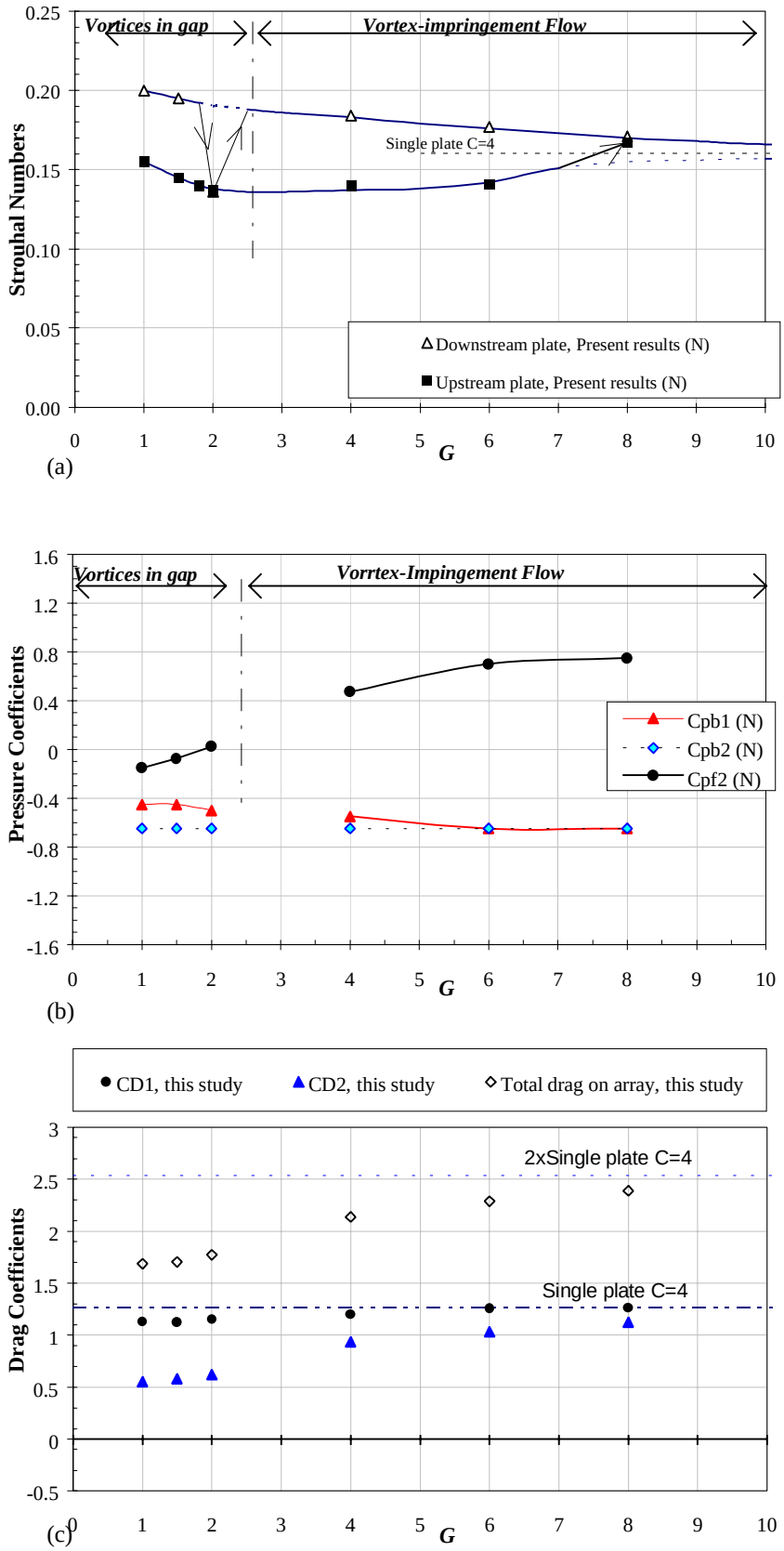

Figure 8.136. Variation of flow parameters with gap-to-thickness ratio of the ($C1$ = 4, $C2$ = 4) array: (a) Strouhal numbers of vortex shedding into the wake of the array, (b) pressure coefficients and (c) drag coefficients.

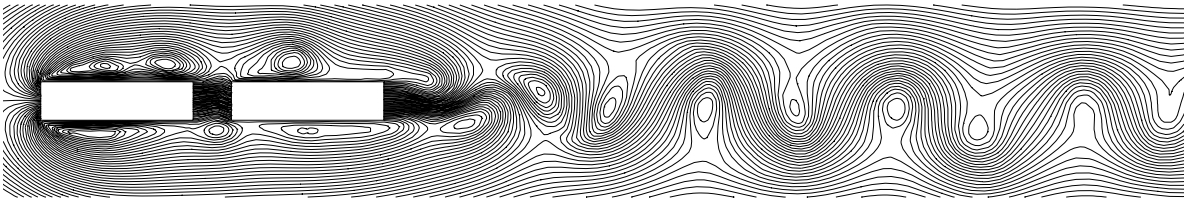

(a) G = 1, t = 51.7, *vortex-flow in the gap.*

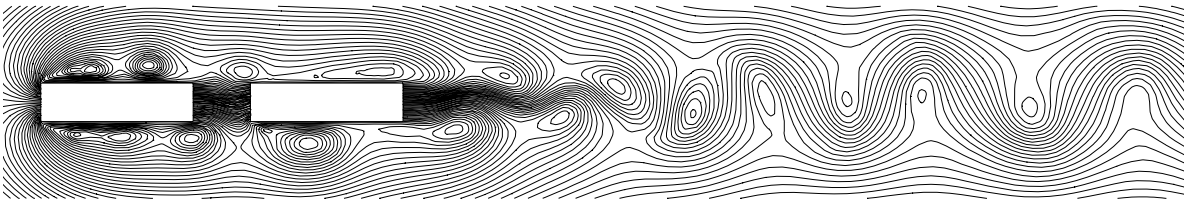

(b) G = 1.5, t = 56.7, *vortex-flow in the gap.*

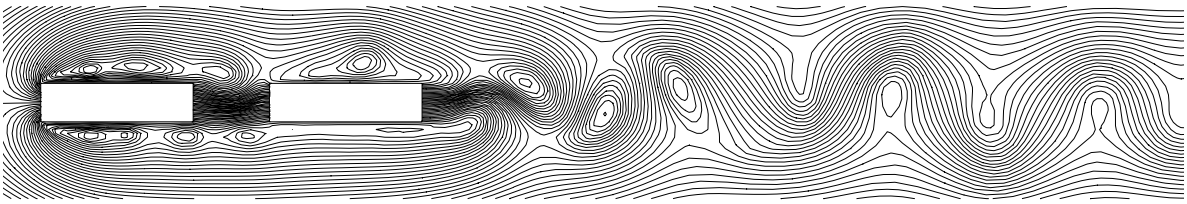

(c) G = 2, t = 91.9, *vortex-flow in the gap.*

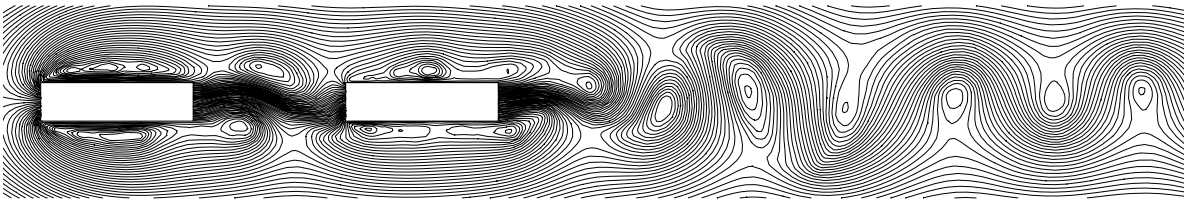

(d) G = 4, t = 46.8, *vortex-street impingement flow.*

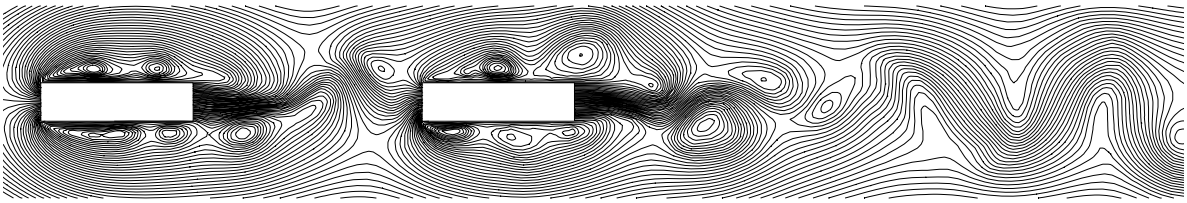

(e) G = 6, t = 36, *vortex-street impingement flow.*

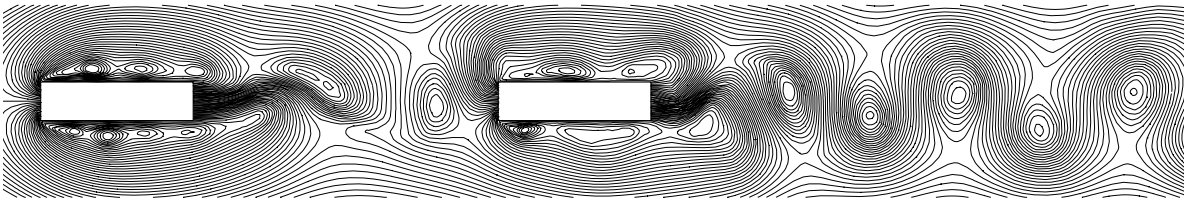

(f) G = 8, t = 57.3, *vortex-street impingement flow.*

Figure 8.137. Predicted streamline patterns in flow over the ($C1$ = 4, $C2$ = 4) array in various flow regimes; calculated in a reference frame moving at a velocity of $U_{ref} = 0.8U_{\infty}$

8.6 Overview of the Flow Over Tandem Arrays of Two Rectangular Plates based on the Numerical Simulations

Simulations of the flow over tandem arrays of two rectangular plates with ($C1 = 1$, $C2 = 1$), ($C1 = 1$, $C2 = 4$) and ($C1 = 4$, $C2 = 4$) demonstrate the effects of systematic variation of array geometry at one particular Reynolds number, in this case $Re_h = 500$. The calculations show that the most important factor determining the character of the flow is the location of the region of impingement on the array of the shear layers which in all cases separate from the sharp leading corners of the upstream plate. In general, characteristic flow regimes can be related to the streamwise position of impingement and the chord-lengths of the two plates and the gap between them. The combination of these parameters determines whether and where reattachment of the separated shear layers to either of the plates in the array may occur. In the case of two short-chord plates, as in the ($C1 = 1$, $C2 = 1$) array, completely detached flow may alternate with reattachment on a side-face of the downstream plate at small gaps ($F1/F2$ regimes); impingement of the shear layers on the gap may alternate with reattachment on the downstream plate at larger gaps ($E1/E2$ regimes); while, at large gaps, alternation of gap impingement with reattachment on the upstream plate may occur (the B regime). For a short upstream plate and long downstream plate, such as the ($C1 = 1$, $C2 = 4$) array, alternating gap impingement and downstream-plate reattachment ($E1/E2$) occurs at small gaps, and alternating upstream-plate reattachment and gap impingement (B) at large gaps. When the array has a long upstream plate, for example the ($C1 = 4$, $C2 = 4$) array, there may be permanent reattachment on the upstream plate (regime A). Changes from one regime to another, brought about by changes in gap, are frequently associated with discontinuities in or changes in the character of the variation of flow parameters.

Within any one of the broad flow regimes referred to above, significant variations in the details of the flow, particularly as a result of changes to the gap between the plates, may occur. Thus, from the predicted flow patterns, pressure forces and Strouhal numbers, a number of characteristic sub-regimes, relating particularly to flow in the gap, can be identified. These include transverse flow through the gap, trapped-vortex flow in the gap, vortex shedding into the gap from the upstream plate without vortex-street formation, and vortex-street flow within the gap. There are few experimental data with which comparisons can be made. Where such comparisons are possible, the calculations are generally in good agreement with experiment, and in most cases provide supplementary fine detail which would be difficult or impossible to obtain

experimentally. The gap flows in these sub-regimes have similar characteristics in all the arrays considered; there are, however, differences in the finer details, very much dependent on the $C1$ value which largely determines the vortex-shedding process of the upstream plate. The flow on the downstream plate, the nature of vortex shedding into the wake of the array and the influence of the wake of the array on the gap flow can vary significantly, according to the value of $C2$ of the downstream plate.

Irrespective of the flow regime determined by array geometry and shear-layer separation from the leading edges of the upstream plate, two general types of array flow can be distinguished. This results from the flow between the plates taking two different forms depending on the gap length – at small values of G, typically $G < 1$, the flow in the gap is confined within the gap and vortex shedding from the upstream plate does not occur; whereas, at larger G ($\gtrsim 1$) vortex shedding from the upstream plate does take place and the vortices formed become part of the general flow. The confined gap flow takes the form of periodically-reversing flow for very small gaps, $G < 0.5$, and a quasi-steady trapped-vortex flow for somewhat larger gaps, $0.5 < G \lesssim 1$. In either case, the two plates act like one single body and vortex shedding into the wake occurs only from the downstream plate. Vortex shedding from the upstream plate, alternately from the upper and lower sides, begins when the gap is increased just beyond $G \approx 1$. Successive vortices grow until they fill the gap, but undergo no convective movement within the gap. The gap vortices undergo a cycle of formation, growth (in which vorticity is gained from the side-face shear layers from the upstream plate), shrinkage and disappearance (by progressive loss of vorticity to the main flow). For larger gaps in the range $1 \lesssim G \lesssim 2$, a similar process of vortex formation, growth and shrinkage takes place, now with limited convective movement of vortices in the gap, but not sufficient to allow establishment of a vortex street in the gap. For large gaps, $G > 2$, a fully-established vortex street occurs in the gap. Its development with increasing G is essentially continuous, following the onset of vortex shedding for $G \gtrsim 1$. Once vortex shedding from the upstream plate begins, the array no longer behaves as a single plate, as interactions between the shed vortices and the downstream plate come into play.

When vortex-street flow occurs in the gap, vortices impinge on the leading edge of the downstream plate. The mechanism of impingement is virtually identical on the ($C1 = 1$, $C2 = 1$), ($C1 = 1$, $C2 = 4$) and ($C1 = 4$, $C2 = 4$) arrays. The same process of periodic oscillation of the stagnation flow on the leading face of the downstream plate, and clipping of the impinging vortex by the leading edge of the downstream plate to form primary and secondary vortices

takes place, essentially as described by Tang and Rockwell [1983], occurs on these arrays. In the impingement flow of the ($C1 = 1$, $C2 = 1$) and ($C1 = 1$, $C2 = 4$) arrays, the vortex shedding from the downstream plate is coupled with the vortex shedding from the upstream plate through vortex-street impingement. Consequently, there is a phase difference between the lift fluctuations on the upstream and downstream plates, determined by the time taken for vortices to be convected along the gap between the plates, it is therefore expected to vary linearly with G, and is found to be $(1.0 + G/3)\pi$ for the ($C1 = 1$, $C2 = 1$) array, and $(1.1 + G/3)\pi$ for the ($C1 = 1$, $C2 = 4$) array. For the ($C1 = 4$, $C2 = 4$) array, however, this phase-locking does not occur until the gap is increased beyond $G \approx 8$. In this case, for $G < 8$, the frequency of vortex shedding from the upstream plate approaches that for a single $C = 4$ plate from below, while that from the downstream plate approaches it from above. It is not until the two frequencies become close to each other that phase-locking takes place.

The general form of pressure distribution on the upstream cylinder remains virtually unchanged as G is varied, despite changes in flow regime, and is very similar to the pressure distribution on a single isolated cylinder at the same Reynolds number. The surface pressure on the downstream plate does, however, vary with G and the associated changes in flow regime. The general trend of the variation is that, as G increases, the leading-face pressure increases while the base-pressure remains fairly constant; at large G the overall pressure distribution approaches that on a single plate at the same Reynolds number.

The drag of the upstream plate is close to the single-plate value at all G, while that of the downstream plate is significantly less at small G and rises towards the single-plate value at large G. Thus, at small G where confined gap flow occurs, the overall drag of the array has a value typical of a single plate with $C = C1 + C2$ (although numerical values have not been directly calculated for single plate with $C = C1 + C2$), and, at large G, approaches the total drag of two isolated $C1$ and $C2$ plates.

Chapter 9

Conclusion

The main aim of this research project has been to develop numerical methods for calculating the time-dependent flow over arrays of solid bodies of arbitrary cross-section arranged in any arbitrary configuration. The objective is to establish a calculation procedure for real viscous flows, sufficiently reliable in predicting flow details for it to be used to complement and illuminate physical measurements. In the present work, procedures have been developed for two-dimensional flow, and validated by simulations of the flow over circular cylinders and thick rectangular plates, bodies for which a large amount of experimental data is available for comparison. At low to moderate Reynolds numbers, the simulations faithfully reproduce salient features of the experimentally-observed flows over these bodies, and generally yield accurate values for flow parameters such as pressure and force coefficients and Strouhal numbers of vortex shedding. This success in predicting the characteristics of these flows is then the justification for accepting the results of application of the numerical procedure to configurations for which few experimental measurements have been made. An example of such a configuration, which has been investigated in the present work, is that of a tandem array of two plates of rectangular cross-section. The simulations provide details of the flow, particularly in the gap between the plates, which are difficult or in some cases impossible to obtain experimentally.

9.1 Brief Account of the Numerical Scheme Developed

The present numerical scheme is based on the discrete-vortex and surface-vorticity boundary-integral methods for solving the governing equations of fluid motion – the Navier-Stokes equations, for this purpose formulated in terms of vorticity. The crux of the numerical scheme is the modelling of the natural processes of generation of vorticity at solid boundaries and its

subsequent diffusion into the flow domain, and the evolution of the vorticity distribution in the flow domain as a result of convection and diffusion. In this connection, the surface-vorticity boundary-integral method provides the potential-flow model to realise the boundary conditions at solid surfaces, and the tool to simulate the mechanism of vorticity creation at solid boundaries in viscous flow. The surface vorticity created at solid boundaries is introduced into the flow domain, where the distributed vorticity field is approximated and replaced by a system of discrete elemental vortices. The simultaneous convective and diffusive motions of the vorticity field are simulated by two successive independent motions of discrete vortices, according to the split-operator algorithm. Flow development within the solution domain is then derived from the trajectories of the discrete elemental vortices. Calculations yield directly the time-histories of elemental-vortex distributions and the pressure distribution on the solid surfaces (but not the pressure distribution in the general flow field).

When the Navier-Stokes equation is formulated as a vorticity transport equation, the pressure term is eliminated. The pressure is therefore not given directly by the solution procedures, but must be derived from the evolution of the vorticity field, taking account of the transport of distributed vorticity in the flow domain and the rate of change of surface vorticity on solid boundaries. In the approximation of the vorticity field by a distribution of elemental discrete vortices, construction of the pressure field presents conceptual difficulties, in that the single-valued pressure field has to be determined from the multi-valued velocity potentials of the discrete vortices. An innovative numerical procedure, which makes use of the closure of the pressure distribution around a solid body and a selectively drawn reference axis (between the body and any point at which the pressure is to be evaluated) to avoid a multiplicity of pressure values, has been developed to compute the pressure field from the vorticity distribution. The instantaneous pressure field, together with the streamline patterns and vorticity contours constructed from the elemental-vortex distributions, gives a complete representation of the flow.

As a prelude to the calculations of viscous flow over solid bodies, the formulation of the surface-vorticity boundary-integral method developed here has been validated by using it to obtain potential-flow solutions for a variety of smooth-profiled and sharp-edged bodies, configured in single and multiple-body arrays. This validation exercise has led to the development of what has been termed the *zero circulation correction* procedure, which takes into account the shapes of solid bodies to regularise the coupling coefficient matrix and improve

the accuracy of the surface-vorticity boundary-integral method. With the use of the *zero circulation correction*, the potential-flow solutions obtained in the present study are in very good agreement with the theoretical solutions: in the case of the circular cylinder, the error in the calculated potential-flow solution relative to the exact theoretical solution is in the order of 10^{-11}.

Calculation of the mutually-induced convection velocities of the discrete vortices by the Biot-Savart method imposes huge computational loads which become prohibitive when the number of vortices is large. Faster and more efficient computation has been achieved by incorporating the cell-to-cell method in the numerical procedure. The computational efficiency of the cell-to-cell method itself has been further improved by the use of sub-cell structures and a self-monitoring procedure, which optimises the number of vortices per cell by re-sizing the grid structure for the distribution of discrete vortices occurring in any given time-step. The use of two levels of sub-cell structure reduces computing time to 40% of that required for the Biot-Savart method.

9.2 Simulation of Viscous Flow Over Solid Bodies

To verify the numerical scheme developed, it was necessary to show that it was capable of yielding valid results for the flow over both bodies with a smooth-profiled cross-section and bodies with a cross-section characterised by sharp edges. For the former, the circular cylinder was chosen as the datum case because of the wealth of published experimental and numerical results for it. The validation process was then extended to flow over a representative class of bodies with sharp-edged profile, namely thick plates of rectangular cross-section, for which also there is an abundance of results of experimental and numerical studies. When the validity of the numerical scheme was established, the solution procedures were applied to simulate the flow over tandem arrays of two rectangular plates.

9.2.1 Validation

Calculations of flow over a circular cylinder, at Reynolds numbers Re_d = 100, 500, 1,000 and 10,000, lead to the conclusion that the numerical procedures give an accurate representation of the detailed flow patterns which have been revealed experimentally, in both the initial flow development and the fully-developed flow. For the fully-developed flow, the calculated

streamline patterns, boundary-layer separation points, and Strouhal numbers of vortex shedding are in good agreement with experimental data. The calculated pressure distributions around the cylinder and lift and drag coefficients, like those given by other numerical methods, agree well with experiment at low Reynolds numbers, but the agreement becomes less good as the Reynolds number increases. The present numerical scheme, developed for calculation of two-dimensional flows, becomes less accurate in representing real flows as the effects of three-dimensionality, which increase with increasing Reynolds number, become more significant. Three-dimensionality in bluff-body flows generally becomes identifiable experimentally for $Re \gtrsim 180$, although the good agreement between the present calculated results and experiment, even at $Re = 500$, suggests that its effects are not strongly felt until the Reynolds number is increased well beyond 180. Nevertheless, with the recognition that three-dimensionality will eventually have significant effects on the flow, the present calculations have been confined to Reynolds numbers $Re_d \leq 1{,}000$.

The simulations which have been made of flow over rectangular plates with chord-to-thickness ratios $C = 1$, 2 and 4, for Reynolds numbers in the range $100 \leq Re_h \leq 1{,}000$, serve two purposes: they extend validation of the numerical scheme to bluff bodies with sharp edges, and, once the scheme is deemed to be valid, they provide greater insight into the detailed mechanics of such flows. The flow regimes predicted by the simulations follow the general classification of characteristic flow regimes as a function of chord length and Reynolds number (Fig. 7.1), constructed on the basis of previous experimental and numerical results. In general, the predicted flow patterns, flow parameters (Strouhal numbers, pressure coefficients and drag coefficients) and their variation with Reynolds number, for the $C = 1$ plates, $C = 2$ plates, and $C = 4$ plates at low Reynolds numbers, $Re_h \leq 250$, correspond very well with the results of previous experimental and numerical studies. (For the $C = 4$ plates at the higher Reynolds numbers of $Re_h = 500$ and 1000, however, the simulations indicate permanent reattachment to the side faces rather than the experimentally-observed intermittent reattachment. This suggests some fine tuning of the numerical scheme is required for longer plates at high Reynolds numbers.)

The simulations indicate, in accord with experiment, that shear layers separate from the sharp leading corners of the plates in all cases. At low Reynolds numbers, for example $Re_h = 100$, the separated shear layers reattach permanently to the side faces at a position near the leading corner; the flow on a side face is then fully-attached all the way to the trailing edge where it

separates and rolls up to form wake vortices. For $Re_h \gtrsim 100$, the separated shear layers reattach to the plate at a position further downstream from the leading corners, and the characteristics of the flow become strongly dependent on the reattachment length in relation to the chord length of the plate. For short plates (for example, the $C = 1$ plate at $Re_h \gtrsim 500$) where side-face reattachment does not occur, the flow can remain fully-separated; for long plates (for example, $C = 4$) permanent reattachment takes place, a leading-edge-separation bubble is formed, and a second separation takes place from the trailing edge; for plates with intermediate chord length (for example, $C = 2$), both intermittently-reattached flow and fully-separated flow can occur, depending on Reynolds number, and at a certain critical Reynolds number ($Re_h \approx 500$ for the $C = 2$ plate) a sudden change from one flow regime to the other takes place. The simulations show that, in the last case, the sudden change in flow regime is accompanied by a discontinuity in Strouhal-number variation with Reynolds number, in accord with experimental findings, and the critical Reynolds number is well predicted.

The calculated results which have been obtained amply demonstrate the capacity of the simulations to supply details of the mechanics of the flow which would be difficult to obtain experimentally. A particular example is the process of formation of a leading-edge-separation bubble, the development of vortex motion within it, its bifurcation, and the consequent generation and shedding of side-face vortices, which complements the experimental investigation of Kiya [1989]; in this case, the role of side-face vortices in determining the main vortex-shedding frequency is brought out, and even finer detail, in the identification of variations in the strength of side-face vortices with amplitude modulation of the lift force on the plate, obtained.

The results of the flow simulations for these two types of bluff body, the circular cylinder and thick plates of rectangular cross-section, are generally in very good agreement with available experimental data over an extensive range of flow variables. On this basis, it was concluded that the numerical scheme developed in the present study could be applied with confidence to address the main aim of the work, namely the investigation of the flow over tandem arrays of rectangular plates. Configurations of this type have been much less extensively investigated, either experimentally or numerically, than other bluff-body flows. Consequently, for determination of the fine details and identification of mechanisms in these flows, particularly in the gaps between plates, reliance is very heavily on the numerical analysis.

9.2.2 Application to Flow Over Rectangular Plates in Tandem

The configurations which have been considered are tandem arrays of two rectangular plates with ($C1 = 1$, $C2 = 1$), ($C1 = 1$, $C2 = 4$) and ($C1 = 4$, $C2 = 4$), with gap-to-thickness ratio in the range $0.2 \leq G \leq 8$, all at a Reynolds number of $Re_h = 500$. The combinations of chord length have been chosen to show differences in the flow over two short plates in tandem and two long plates in tandem, and the differences brought about by the change from a short to a long downstream plate in tandem with a short upstream plate. The characteristic flow regimes which, according to the simulations, occur on the arrays, can be related to various classes in the broad general classification scheme of Bull, Blazewicz and Pickles [1997], based on the position of impingement on the array of the shear layers separated from the leading corners of the upstream plate. Depending on the gap between the plates, impingement may occur on the gap itself or may occur, with reattachment, on either the upstream plate or downstream plate. Fluctuations in the impingement position can therefore produce intermittent changes from one type of flow to another. The geometry of the array in conjunction with the fluctuations in impingement location determines the flow regime actually established. Thus, the simulations indicate that the characteristic regimes which occur on the ($C1 = 1$, $C2 = 1$) array are :

(i) completely detached flow alternating with reattachment on the downstream plate (regimes $F1/F2$), at small gaps;

(ii) gap impingement alternating with reattachment on the downstream plate (regimes $E1/E2$) at intermediate gaps; and

(iii) gap impingement alternating with reattachment on the upstream plate (regime B) at large gaps.

The effect of replacing the short downstream plate by a long plate to form the ($C1 = 1$, $C2 = 4$) array is to eliminate the occurrence of completely detached flow; and so only the $E1/E2$ and B regimes occur for this combination. When the upstream plate is long, there is a permanent reattachment to it (regime A); this is the flow regime which occurs on the ($C1 = 4$, $C2 = 4$) array at all gaps.

In addition to the broad flow regimes, the simulations have identified a number of characteristic sub-regimes in the gap flow, providing significant insights into the mechanics of array flows. For arrays with a small gap, generally for $G < 1$, vortex shedding into the wake of the array take places on the downstream plate only. In this case, the two plates act essentially like one single body. Two forms of gap flow have been identified for flows of this type:

(i) periodically-reversing transverse flow through the gap for very small gaps, $G < 0.5$, synchronised with the vortex shedding into the wake from the downstream plate in the array; and

(ii) trapped-vortex flow between the plates for small gaps, $0.5 < G < 1.0$, in which the gap vortices oscillate slightly in size at the frequency of vortex shedding into the wake of the array.

The onset of vortex shedding from the upstream plate, alternately from the upper and lower sides, occurs at about $G \approx 1$. Therefore, for gaps larger than $G \approx 1$, the two plates no longer behave as one single body; vortices shed from both the upstream and downstream plates contribute to the structure of the final vortex wake of the array. When vortex shedding from the upstream plate occurs, several other forms of gap flow become possible. These are (continuing the above classification):

(iii) for gaps at about $G \approx 1$, periodic vortex-formation between the plates, in which successive vortices grow, without convective movement, until they fill the gap (by gaining vorticity from the side-face shear layer from the upstream plate), shrink and disappear (by progressive loss of vorticity to the main flow);

(iv) periodic vortex-formation for gaps in the range $1 \lesssim G < 2$, in which a similar process of formation, growth, shrinkage and disappearance of gap vortices takes place, now with limited convective movement of vortices within the gap but not sufficient to allow establishment of a vortex street between the plates; and

(v) fully-established vortex-street flow within the gap for large gaps, $G > 2$, in which the impingement of gap vortices on the leading edge of the downstream plate involves: oscillation of the stagnation point on the downstream plate between the upper and lower leading corners with periodic reversal of flow direction on the front face; clipping of the impinging vortex by the leading edge; formation of a primary and a secondary vortex at each impingement, and their subsequent movement along a side face of the downstream plate; and alternation between fully-attached flow and flow with a leading-edge separation bubble on each of the side faces of the downstream plate.

This fine detail revealed by the simulations gives a comprehensive picture of the development of the gap flow as the gap between the plates is increased.

In the large-gap flows, with a fully-established vortex street between the plates, the details of vortex impingement on the downstream plate are consistent with and complement the experimental findings of Tang and Rockwell [1983]. In the impingement flow on the ($C1$= 1, $C2$ = 1) and ($C1$ = 1, $C2$ = 4) arrays, the process of vortex shedding from the downstream plate is coupled with that from the upstream plate. The phase difference between the lift forces on the two plates, brought about by the time taken for the vortex shed from the upstream plate to traverse the gap, is linearly proportional to the gap length; the predicted values of phase lag of the downstream plate can be closely represented empirically by $(1 + G/3)\pi$ and $(1.1 + G/3)\pi$ for the ($C1$ = 1, $C2$ = 1) and ($C1$ = 1, $C2$ = 4) arrays respectively. The former is virtually identical to the relation obtained experimentally by Sakamoto, Haniu and Obata [1987] for a ($C1$ = 1, $C2$ = 1) array. Phase-locking does not occur on the ($C1$ = 4, $C2$ = 4) array until the gap is increased beyond $G \approx 8$ when the vortex-shedding frequencies of the upstream and downstream plates, both approaching that of a single C = 4 plate as G increases, come close to each other.

As in the case of single plates of rectangular cross-section, the simulations yield flow parameters such as Strouhal number, pressure coefficients and drag coefficients. These parameters vary with gap and, in most cases, changes in the form of the variation mark changes in flow regime.

9.3 Extension of the Calculation Scheme

The numerical scheme developed in the present work, which is specific to two-dimensional flow, can be regarded as the first stage in the development of a computational code for simulating the flow over bluff-body arrays, over a wide range of Reynolds number. While the scheme does appear to be generally valid, the validation procedure has indicated some aspects in which refinement could, with advantage, be made. In particular, the results of the calculations of flow over thick rectangular plates with sharp corners show, in some cases, a sensitivity to the details of the method used to model viscous diffusion of surface-vorticity from solid boundaries into the flow domain. Before any extension of the calculation procedure is made, improvement of this modelling is desirable.

On the evidence of single-body flows that departures from two-dimensionality occur to an increasing extent as Reynolds number is increased, the calculations which have been made have been confined to Reynolds numbers less than 1,000. The single-body results lead to the expectation that the procedure will precisely reproduce the characteristics of real flows for Re_h < 250, but that at Reynolds numbers approaching 1,000 some loss of accuracy, because of the effect of increasing three-dimensionality, may occur. Significant differences between flow patterns predicted by two- and three-dimensional calculations are shown by the results obtained by Tamura *et al*. [1993] for the flow over long-chord plates at a Reynolds number of 104. Differences in the detailed vortical structure of leading-edge separation bubbles and the development of three-dimensionality in that study, and experimental evidence for three-dimensionality in the flow over single plates with rectangular cross-section at lower Reynolds numbers, make it clear that there is a need for development of a procedure which can take account of three-dimensionality.

Extension of the calculations to higher Reynolds numbers (typically Re_h > 1,000) will require incorporation of the vorticity dynamics of three-dimensional flows in the numerical scheme. In this connection, the surface-vorticity boundary-integral algorithm is readily extendable to three-dimensional solid bodies. Outstanding problems are the representation of the distributed vorticity field in three-dimensional space (by vortex filaments of an appropriate form) and accounting for the stretching of vortex filaments as well as the transport of vorticity by convection and diffusion. The procedure for the derivation of the pressure field from the vorticity field also needs to be extended. The other outstanding problem of simulating viscous

flow at high Reynolds numbers is that of turbulence. In principle, given that the vortex methods do indeed genuinely represent the vorticity dynamics, they should be able to simulate turbulent flow without the use of turbulence models. However, the requirement for a much larger number of vortices in the flow field compounds the problem already faced for low Reynolds number flow. It therefore seems more than likely that the introduction of turbulence models would become unavoidable.

Vortex methods have been used in the present study on the basis of their providing a grid-independent computational scheme. This inherent characteristic of the vortex method makes it particularly suitable for bluff bodies of arbitrary cross-section, in any arbitrary configuration. The present study has been focused on time-dependent flow over arrays of rigid bodies. However, with little modification, the method could be applied to flow over moving flexible bodies (of which the cross-sectional shape is a function of time) and to flow-induced vibration of structures.

References

Abbott, I.H. and Von Doenhoff, A.E. (1959). *Theory of Wing Sections.* New York, Dover Publications Inc..

Arnal, M.P., Goering, D.J. and Humphrey, J.A.C. (1991). Vortex shedding from a bluff body adjacent to a plane sliding wall. *Trans. ASME,* **113,** 384-398.

Batchelor, G.K. (1967). *An Introduction to Fluid Dynamics.* Cambridge: Cambridge University Press, 1967.

Bearman, P.W. (1992). Challenging problems in bluff body wakes, *IUTAM Symposium on Bluff-body Wakes, Dynamics and Instabilities,* Göttingen, Germany, Springer-Verlag, 1-10.

Bearman, P.W. and Obasaju, E.D. (1982). An experimental study of pressure fluctuations on fixed and oscillating square-section cylinders. *J. Fluid Mech.*, **119**, 297-321.

Bearman, P.W. and Kamemoto, K. (1978). *IC Aero Note,* 78-108.

Bearman, P.W. and Trueman, D.M. (1972). An investigation of the flow around rectangular cylinder. *Aeronautical Quarterly,* **XXII**, 229-237.

Bearman, P.W. (1967). On vortex street wakes. *J. Fluid Mech.*, **28,** part 4, 625-641.

Belotserkovsky, S.M., Kotovskii, V.N., Nisht, M.I. & Fedorov, R.M. (1992). *Two Dimensional Separated Flows.* CRC Press Inc., 1992.

Bienkiewicz, B., Kutz, R.F. (1993). Aerodynamic loading and flow past bluff bodies using discrete vortex method. *J. Wind Eng. and Ind. Aero.,* **46 & 47**, 619-628.

Birkhoff, G.D. and Fisher, J. (1959). Do vortex sheet roll up ? *Rendi. Circ. Mat.* Palermo, Ser. 2, **8**, 77-90.

Blazewicz, A.M., Bull, M.K. and Pickles, J.M. (1995). Flow regimes and base pressures on tandem arrays of plates of rectangular cross-section. *Proc. Twelfth Aust. Fluid Mech. Conf., Sydney, Dec. 1995.*

Blazewicz, A.M., Pickles, J.M. and Bull, M.K. (1993). Noise generation mechanisms in the flow around rectangular section bluff bodies. *Proc. Inter-Noise-93, Leuven, Belgium*, 1631-1634.

Blazewicz, A.M. (1998). Private communication.

Bloor, M.S. (1964). The transition to turbulence in the wake of a circular cylinder. *J. Fluid Mech.*, **19**, 290-304.

Bostock, B.R. and Mair, W.A. (1971). Pressure distributions and forces on rectangular and D-shaped cylinders. *Aeronautical Quarterly*, 1-6.

Bouard, R. and Coutanceau, M. (1980). The early stage of development of the wake behind an impulsively started cylinder for $40 < Re < 10^4$. *J. Fluid Mech.*, **101**, 583-607.

Bull, M.K., Blazewicz, A.M. and Pickles, J.M. (1997). Acoustic radiation from a tandem two-plate array in a fluid flow: dependence on array geometry and flow regime. *Proc. Fifth International Congress on Sound and Vibration, Adelaide, South Australia, Dec. 1997.*

Bull, M.K., Bies, D.A., Pickles, J.M. and Blazewicz, A.M. (1992). Acoustic radiation from a plate in a vortex wake. *Proc. Inter-Noise 92,* Toronto, 629-632.

Bull, M.K., Pickles, J.M. and Li, Y. (1992). On vortex-wake/bluff-body interactions and noise from circular saw. *Proc 14th International Congress on Acoustics,* Beijing.

Bull, M.K. and Pickles, J.M. (1992). The influence of a downstream body on wake formation behind a bluff body. *IUTAM Symposium on Bluff-body Wakes, Dynamics and Instabilities,* Göttingen, Germany, Springer-Verlag, 185-188.

Bull, M.K. and Pickles, J.M. (1991). Noise generation mechanisms in the interaction between a vortex wake and a bluff body. *Proc. Inter-Noise 91,* Sydney.

Bull, M.K., Bies, D.A. and Pickles, J.M. (1990). Generation of aerodynamic noise by a free running circular saw. *Proc. Inter-Noise 90,* Gothenberg.

Bull, M.K., Pickles, J.M., Martin, B.T. and Welsh, M.C. (1989). Vortex shedding from rectangular plates in tandem. *Proc. 10th Aust. Fluid Mech. Conf.,* 4.17-4.20

Cherry, N.J., Hillier, R. and Latour, M.E.E.P. (1984). Unsteady measurement in a separated and reattaching flow. *J. Fluid Mech.,* **144**, 13-46.

Cho, H.S. and Mote, C.D., Jr. (1979). On the aerodynamics noise source in circular saws. *J. Acoustical Society of America,* **65**(3), 662-671.

Chorin, A.J. (1969). On the convergence of discrete approximation to the Navier-Stokes equation. *Math. Comp.,* **23,** 341.

Chorin, A.J. (1972). A vortex method for the study of rapid flow. *Proc. 3rd Int. Conf. on Numerical Methods in Fluid Mech.,* Springer-Verlag.

Chorin, A.J. (1973). Numerical study of slightly viscous flow. *J. Fluid Mech*., **57**, 785-796.

Chorin, A.J., Bernard, P.S. (1973). Discretization of a vortex sheet, with an example of roll-up. *J. Comp. Phys.* **13**, 423-429.

Chorin, A.J. (1978). Vortex sheet approximation of boundary layers. *J. Comp Phys*., **27**, 428-442.

Christiansen, J.P. (1973). Numerical simulation of hydrodynamics by the method of point vortices. *J. Comp Phys*., **13**, 363-379

Clements, R.R. (1973). An inviscid model of two-dimensional vortex shedding. *J. Fluid Mech.*, **57**, part 2, 321-336.

Clements, R.R. and Maull, D.J. (1975). The representation of sheets of vorticity by discrete vortices. *Prog. Aero. Sci.,* **16**, part 2, 129-146.

Collins, W.M. and Dennis, S.C.R. (1973). The initial flow past an impulsively started circular cylinder. *Quart. J. Mech. Appl. Math.,* **26**, 53.

D'Alessio, S.J.D. and Dennis, S.C.R., (1994). A vorticity model for viscous flow past a cylinder. *Computers Fluids,* **23, No. 2**, 279-293.

Davis, R.W. and Moore, E.F. (1982). A numerical study of vortex shedding from rectangles. *J. Fluid Mech.,* **116**, 475-506.

Deffenbaugh, F.D. and Marshall, F.J. (1976). Time development of the flow about an impulsively started cylinder. *AIAA*, **14, No. 7**, 908-913.

Djilali, N, and Gartshore, I.S. (1991). Turbulent flow around a bluff rectangular plate. Part I: Experimental investigation. *J. Fluids Engineering*, **113**, 51-59.

Djilali, N, Gartshore, I.S. and Salcudean, M. (1991). Turbulent flow around a bluff rectangular plate. Part II: Numerical predictions. *J. Fluids Engineering*, **113**, 51-59.

Dugdale, D.S. (1969). Discrete frequency noise from free running circular saws. *J. Sound and Vibration*, **10**(2), 296-304.

Dennis, S.C.R. and Chang, G.-Z. (1970). Numerical solution for steady flow past a circular cylinder at Reynolds number up to 100. *J. Fluid Mech.,* **42**, 471-489.

Fage, A. & Johansen, F.C. (1927). On the flow of air behind an inclined plate of infinite span. *Proc. Roy. Soc. A.,* **116,** 170-197.

Fink, P.T. and Soh, W.K. (1974). Calculation of vortex sheets in unsteady flow and applications in ship hydrodynamics. *Proc. of the 10th Symposium on Naval Hydro.,* Cambridge, Mass., 463-488.

Fornberg, B. (1985). Steady viscous flow past a circular cylinder up to Reynolds Number 600. *J. Comp. Phys.* **98**, 819-855.

Franke, R., Rodi, W. and Schönung, B. (1990). Numerical calculation of laminar vortex-shedding flow past cylinders. *J. Wind Eng. and Ind. Aero.,* **35**, 237-257.

Gerrard, J.H. (1967). Numerical computation of the magnitude and frequency of the lift on a circular cylinder. *Phil. Trans. Roy. Soc.* **A.261**, 137-62.

Goldstein, S. (1938). *Modern developments in fluid dynamics, Vol I & II*. Oxford: Clarendon Press.

Graham, J.M.R. (1988). Computation of viscous separated flow using a particle method. *Numerical Methods for Fluid Dynamics III (Editors K.W. Morton and M.J. Baines),* Oxford Science Publications, 310-317.

Graham, J.M.R. (1992). Report on the session comparing computation of flow past circular cylinders with experimental data. *IUTAM Symposium on Bluff-body Wakes, Dynamics and Instabilities,* Göttingen, Germany, Springer-Verlag, 317-323.

Graham, J.M.R. (1993). A hybrid discrete vortex method for viscous flows. *Proc. SERC Community Club in CFD: Modelling Fluid Flow using Vortex Methods,* Manchester.

Greengard, C. (1985). The core spreading vortex method approximates the wrong equation. *J. Comp. Phys.,* **61, No. 2,** 345-348.

Gursul, I. and Rockwell, D. (1990). Vortex Street Impinging upon an Elliptical Leading Edge. *J. Fluid Mech.*, **211**, 211-242.

Hald, O.H., (1979). Convergence of Vortex Methods for Euler's Equations II. *SIAM J. Numer Anal,* **16, No. 5,** 726-755.

Hama, F.R. and Burke, E.R. (1960). On the rolling up of vortex sheet. *Univ. of Maryland TN No. BN-220*.

Helmholtz, H. (1858). On integrals of the hydrodynamical equation which express vortex motion. Transl., P.G., Tait, *Phil. Mag.,* **Vol 4**, 485-512.

Hillier, R. and Cherry, N.J., (1981). The effects of stream turbulence on separation bubbles. *J. Wind Eng. and Ind. Aero.,* **8**, 49-58.

Hockney, R.W. (1970). The Potential Calculation and Some Applications. *Methods in Comp. Phys,* **9**, 135-211.

Honji, H. and Taneda, S. (1969). Unsteady flow past a circular cylinder. *J. Phys. Soc. Japan,* **27**.

Hou, T.Y. (1991). A survey on convergency analysis for point vortex methods. *Lectures in Applied Mathematics*, **28**, 327-339.

Hou, T.Y., Lowengrub, J., Shelley, M.J. (1991). Exact desingularization and local regridding for vortex methods. *Lectures in Applied Mathematics*, **28**, 341-362.

Inamuro, T., Saito, T. and Adachi, T. (1984). A numerical analysis of unsteady separated flow by the discrete vortex method combined with the singularity method. *Computers and Structures*, **19**, No. 1-2, 75-84.

Inamuro, T., Adachi, T. and Sakata, H. (1983). A numerical analysis of unsteady separated flow by vortex shedding model. *Bulletin of JSME,* **26** (222), 2106-2112.

Inamuro, T. (1993). Numerical simulation of aerodynamic instability of bluff body by the discrete vortex method. *J. Wind Eng.and Ind. Aero.*, **46** & **47**, 885-892.

Jacob, K. and Riegels, F.W. (1963). The calculation of the pressure distribution over aerofoil sections of finite thickness with and without flaps and slats. *Z. Flugwiss*, **11**, 357-367. (Available as R.A.E. Library translation No. 1101, 1965)

Kanapathipillai, S. (1982). *On aerodynamic noise generation by circular saws*. Master Degree Thesis, Department of Mechanical Engineering, University of Adelaide.

Kaya, M.O., Kaykayoglu, C.R., Bayar, K.C. and Graham, J.M.R. (1991). Numerical Simulation of Vortex Street-Edge Interaction. *Advisory Group for Aerospace Research & Development Conference Proceedings*, **494**, 32-1 – 32-12.

Kaykayoglu, C.R. (1992). Hybrid moving vortex diffusive method simulation of the challenging aspects of vorticity field-edge interaction. Unpublished.

Kaykayoglu, C.R. and Rockwell, D. (1985). Vortices Incident upon a Leading-Edge: Instantaneous Pressure Fields. *J. Fluid Mech.*, **156**, 439-461.

Kelkar, K.M. and Patankar, S.V. (1992). Numerical prediction of vortex shedding behind a square cylinder. *Int. J. for Numerical Methods in Fluids*, **14**, 327-341.

Kiya, M. and Sasaki, K. (1985). Structure of large-scale vortices and unsteady rverse flow in the reattaching zone of a turbulent separation bubble. *J. Fluid Mech*., **154**, 463-491.

Kiya, M. and Sasaki, K. (1983). Structure of a turbulent separation bubble. *J. Fluid Mech*., **137**, 83-113.

Kiya, M., Arie, A. and Harigane, K. (1979). Mem. Faculty of Eng., Univ. of Hokkaido, **15**.

Kovasznay, L.S.G. (1949). Hot-wire investigation of the wake behind circular cylinder at low Reynolds numbers. *Proc. R. Soc. London, Ser. A*, **198**, 174-190.

Kronauer, R.E. (1964). Predicting eddy frequency in separated wakes. *IUTAM Symposium on concentrated vortex motions in fluids,* Michigan, USA.

Kuwahara, K. & Takami, H. (1973). Numerical studies of two-dimensional vortex motion by a system of point vortices. *J. Phys. Soc. Japan*, **34**, 247-250.

Lane, J.C. and Loehrkem R.I. (1980). Leading edge separation from a blunt plate at low Reynolds number. *J. Fluid Eng.,* **102**, 494-496.

Lee, B.E. (1975). The effect of turbulence on the surface pressure field of a square prism. *J. Fluid Mech.,* **69**(2), 263-282.

Leonard, A. (1980). Vortex methods for flow simulation. *J. Comp. Phys*., **37**(3), 289-335.

Leu, M.C., Mote, C.D., Jr. (1984). Vortex shedding: The source of noise and vibration in idling circular saws. *J. Vib., Acous., Stress and Rel. in Design*, **106**, 434-440.

Lewis, R.I. (1980). *Simplification to surface vorticity aerofoil and cascade theory to facilitate computation.* Report No. Tb. 55, Department of Mechanical Engineering, University of Newcastle upon Tyne.

Lewis, R.I. (1981). Surface vorticity modelling of separated flows from two-dimensional bluff bodies of arbitrary shape. *J. Mech. Eng. Sci.* **23**, No.1, 1-12.

Lewis, R.I. (1991). *Vortex element methods for fluid dynamic analysis of engineering systems.* Cambridge: Cambridge Engine Technology Series.

Li, Y. (1991). Measurements of vortex wake and pressure fluctuation on plate surface immersed in vortex wake. *Interim Report*, Department of Mechanical Engineering, University of Adelaide.

Lighthill, M.J. (1963). *Laminar boundary layers, Part II* (ed. L. Rosenhead), Oxford University Press.

Linke, W. (1931). *Physik. Zeitschr.* **32**, 900-914.

Long, D.G. (1988). Convergence of the random vortex method in two dimensions. *J. American Math. Society*, **1** No. 4, 779-804.

Martensen, E. (1959). Calculation of pressure distribution over profiles in cascade in two-dimensional potential flow, by means of a Fredholm integral equation. *Arch. Rat. Mech. Analysis*, **3**, No.3.

Martin, B.T., Bies, D.A., (1990). On aerodynamic noise generation from vortex shedding in rotating blades. Internal report, University of Adelaide. (unpublished).

Mook, D.T. and Dong, B. (1994). Perspective : Numerical simulations of wakes and blade-vortex interaction. *J. of Fluids Engineering*, **116**, 5-21.

Moore, D.W. (1971). The discrete vortex approximation of a finite vortex sheet. *Calif. Inst. of Tech. Report AFOSR-1804-69*

Moore, D.W. (1974). A numerical study of the roll up of a finite vortex sheet. *J. Fluid Mech.*, **63**, part 2, 225-235.

Morton, B.R. (1984). The generation and decay of vorticity. *Geophys. Astrophys. Fluid Dynamics*, **28**, 277-308.

Nakamura, Y. (1993). Bluff-body aerodynamics and turbulence. *J. Wind Eng. and Ind. Aero.*, **49**, 65-78.

Nakamura, Y., Ohya, Y. and Tsuruta, H. (1991). Experiments on vortex shedding from flat plates with square leading and trailing edges. *J. Fluid Mech.*, **222,** 437-447.

Nakamura, Y. and Nakashima, M. (1986). Vortex excitation of prisms with elongated

rectangular, ⊦ and ⊢ cross-sections. *J. Fluid Mech.* **163,** 149-169.

Naylor, P.J. (1982). *A discrete vortex model for bluff bodies in oscillatory flow.* Ph.D. Thesis, University of London.

Norberg, C. (1993). Flow around rectangular cylinders: pressure forces and wake frequencies. *J. Wind Eng. and Ind. Aero.*, **49**, 187-196.

Ogawa, A. (1992). *Vortex Flow.* CRC Press Inc..

Ohya, Y., Nakamura, Y., Ozono, S., Tsuruta, H. and Nakayama, R. (1992). A numerical study of vortex shedding from flat plates with squares leading and trailing edges. *J. Fluid Mech.* **236,** 445-460.

Okajima, A., Ueno, H. and Sakai, H. (1992). Numerical simulation of laminar and turbulent flows around rectangular cylinders. *Int. J. for Num. Methods in Fluids*. **15,** 999-1012.

Okajima, A., Nagahisa, T. and Rokugoh, A. (1990). A numerical analysis of flow around rectangular cylinders. *JSME Int. J.* Series II, **33,** No. 4, 702-711.

Okajima, A. (1990). Numerical simulation of flow around rectangular cylinders. *J. of Wind Eng. and Ind. Aero.*, **33,** 171-180.

Okajima, A. and Sugitani, K. (1984). Strouhal number and base pressure coefficient of rectangular cylinders (The effects of Reynolds Number), *Trans. JSME.* **Ser. B, 50:457**, pp 2004

Okajima, A., Mizota, T. and Tanida, Y. (1983). Observation of flows around rectangular cylinders. *Proc. 3rd International Symp. of flow Visualisation.* Michigan; 193-199.

Okajima, A. (1982). Strouhal numbers of rectangular cylinders. *J. Fluid Mech.* **123**, 379-398.

Ota, T., Asano, Y. and Okawa, J. (1981). Reattachment length and transition of the separated flow over blunt flat plates. *Bulletin of the JSME.* **24**(192), 941-947.

Ozono, S., Ohya, Y., Nakamura, Y. and Nakayama, R. (1992). Stepwise increase in Strouhal number for flows around flat plates. *Int. J. for Numer. Methods in Fluids,* **15,** 1025-1036.

Panikker, P.K.G & Lavan, Z. (1975). Flow past impulsively started bodies using Green's functions. *J. Comp. Phys.* **18**, 46-50.

Parker, R. and Welsh, M.C. (1983). Effects of sound on flow separation from blunt flat plate. *Int. J. Heat and Fluid Flow.* **4**(2), 113-127.

Perlman, M., (1985). On the accuracy of vortex methods. *J. Comp. Phys.* **59,** 200-223.

Pickles, J.M., Martin, B.T., Bull, M.K. and Zockel, M. (1988). On noise generation mechanisms in idling circular saws. *Proc. Australian Acoustical Society 1988 Annual Conference - Victor Harbor, 24-25 Nov*., 17.1-8.

Porthouse, D.T.C. and Lewis, R.I. (1981). Simulation of viscous diffusion for extension of the surface vorticity method to boundary and separated flows. *J. Mech. Eng. Sci., I. Mech. E.,* **23,** No. 3, 157-167.

Porthouse, D.T.C. (1983). *Numerical simulation of aerofoil and bluff body flows by vortex dynamics*. Ph.D. Thesis, University of Newcastle upon Tyne.

Prandtl, L. and Tietjens, O.G., *Fundamentals of Hydro- & Aerodynamics.* United Engineering Trustees, Inc. 1934. Reprinted by Dover Publications, New York, 1934.

Prandtl, L. and Tietjens, O.G., *Applied Hydro- and Aeromechanics.* United Engineering Trustees, Inc. 1934. Reproduced by Dover Publications, New York, 1957.

Rockwell, D.O. (1977). Organised fluctuations due to flow past a square cross section cylinder. *J. of Fluids Engineering.* **99**, 511-516.

Rockwell, D., Kaykayoglu, C.R., Sohn, D. and Kuo, C.H. (1985). An Assessment of Some Vorticity Field-Leading Edge Interactions. *Shear Flow-Structure Phenomena,* Edited by A. Akay and M. Reischman, ASME NCA **Vol. 1**, 79-88.

Rockwell, D. and Knisely, G. (1979). The Organised Nature of Flow Impingement upon a Corner. *J. Fluid Mech.,* **93**, 413-432.

Rockwell, D. and Naudasher, E. (1978). Review – Self-sustaining oscillations of flow past cavities. *J. of Fluids Engineering.* **100**, 152-165.

Roshko, A. (1953). On the development of turbulent wakes from vortex streets. *Natl. Advis. Comm. Aeronaut., Tech. Note* **No. 2913**.

Roshko, A. (1993). Perspectives on bluff body aerodynamics. *J. Wind Eng. and Ind. Aero.*, **49**, 79-100.

Rosenhead, L. (1931). The formation of vortices from a surface of discontinuity. *Proc. R. Soc. Lond.* **A134**.

Saffman, P.G. (1992). *Vortex Dynamics.* Cambridge: Cambridge University Press.

Sakamoto, H., Haniu, H., and Obata, Y. (1987). Fluctuating forces acting on two prisms in a tandem arrangement. *J. Wind Eng. and Ind. Aero.*, **26**, 85-103.

Sarpkaya, T. (1966). Separated flow about lifting bodies and impulsive flow about cylinders. *AIAA Journal* **4**, 414-420.

Sarpkaya, T. (1968). An analytical study of separated flow about circular cylinders. *ASME J. of Basic Engineering*, **90**, 511-520.

Sarpkaya, T. (1975). An inviscid model of two-dimensional vortex shedding for transient and asymptotically steady separated flow over an inclined plate. *J. Fluid Mech.*, **68**, Part I, 109-128.

Sarpkaya, T. and Schoaff, R. (1979). Inviscid model of two-dimensional vortex shedding by a circular cylinder. *AIAA Journal*, **17**, 1193-1199.

Sarpkaya, T. (1989). Computational methods with vortices – The 1988 Freeman Scholar Lecture. *J. Fluids Engineering*, **111**, 5-52.

Sasaki, K. and Kiya, M. (1991). Three-dimensional vortex structure in a leading-edge separation bubble at moderate Reynolds numbers. *J. Fluids Engineering*, **113**, 405-410.

Schwabe, M. (1935). Über Druckermittlung in der nichtstationären ebenen Strömung. *Ingénieur Archiv.* **6**, 34.

Schlichting, H., *Boundary layer theory*. McGraw Hill, New York, 1979.

Smith, P.A. and Stansby, P.K. (1987). Generalised discrete vortex method for cylinders without sharp edges. *AIAA J.* **25**, 199.

Smith, P.A. and Stansby, P.K. (1989). An efficient surface algorithm for random particle simulation of vorticity and heat transport. *J. Comp. Phys.* **81**, 349.

Sohankar, A., Davidson, L. and Norberg, C. (1995). Numerical simulation of unsteady flow around a square two-dimensional cylinder. *Twelfth Australasian Fluid Mechanics Conference, The University of Sydney, Australia 1995,* 517-520.

Soria, J., Sheridan, M. and Wu, J. (1993). Spatial evolution of the separated shear layer from a square leading-edge flat plate. *J. Wind Eng. and Ind. Aero.*, **49**, 237-246.

Spalart, P.R. and Leonard, A. (1981). Computation of separated flows by a vortex tracing algorithm. *AIAA 14th Fluid and Plasma Dynamics Conference*, Palo Alto, California, AIAA-81-1246.

Stansby, P.K. (1985). A generalized discrete-vortex method for sharp-edged cylinders. *AIAA Journal*, **23**(6), 856-861.

Stansby, P.K. (1993). A hybrid discrete vortex method for viscous flows. *Proc. SERC Community Club in CFD: Modelling Fluid Flow using Vortex Methods,* Manchester.

Stewart, J.S. (1978). An investigation of the aerodynamic noise generation mechanisms of circular saw blades. *J. Noise Control Eng.*, **11**(1), 5-11.

Stokes, A.N. and Welsh, M.C. (1986). Flow-resonant sound interaction in a duct containing a plate, part II: square leading edge. *J. Sound and Vibration*, **104**(1), 55-73.

Suzuki, H., Inoue, Y., Nishimura, T., Fukutani, K. and Suzuki, K. (1993). Unsteady flow in a channel obstructed by a square rod (crisscross motion of vortex). *Int. J. Heat and Fluid Flow,* **14**(1), 2-9.

Tafti, D.K. and Vanka, S.P. (1991). Numerical study of flow separation and reattachment on a blunt plate. *Phys. Fluids A*, **3**(7), 1749-1759.

Takami, H. (1964). A numerical experiment with discrete vortex approximation, with reference to the rolling up of a vortex sheet. *Dept. Aero. and Astronaut. Stanford Univ.* Rep SUDAER 202.

Takeuchi, T. and Matsumoto, M. (1992). Aerodynamic response characteristics of rectangular cylinders in tandem arrangement. *J. Wind Eng. and Ind. Aero.,* **41**-**44**, 565-575.

Tamura, T., Itoh, Y. and Kuwahara, K. (1993). Computational separated-reattaching flows around a rectangular cylinder. *J. Wind Eng. and Ind. Aero.,* **50**, 9-18.

Tamura, T. and Kuwahara, K. (1990). Numerical study of aerodynamic behaviour of a square cylinder. *J. Wind Eng. and Ind. Aero.,* **33**, 161-170.

Tang, Y.-P., and Rockwell, D. (1983). Instantaneous pressure fields at a corner associated with vortex impingement. *J. of Fluids Engineering.* **126**, 187-204.

Thom, A. (1929). *A.R.C. Report and Memoranda*, No. 1194.

Thoman, D.C. & Szewczyk, A.A. (1969). Time-dependent viscous flow over a circular cylinder. *Phys. Fluids Suppl.* **12**(II), 76-81.

Vickery, B.J. (1966). Fluctuating lift and drag on a long cylinder of square cross-section in a smooth and in a turbulent stream. *J. Fluid Mech.* **25**(3), 481-494.

Welsh, M.C., Stokes, A.N. and Parker, R. (1984). Flow-resonant sound interaction in a duct containing a plate, part I: semi-circular leading edge. *J. Sound and Vibration*, **95**(3), 305-323.

Westwater, F.L. (1935). The rolling up of a surface of discontinuity behind an aerofoil of finite span. *ARC R&M No. 1962.*

Wilkinson, D.H. (1967). A numerical solution of the analysis and design problems for the flow past one or more aerofoils or cascades. *Aeronautical Research Council Reports and Memoranda. No. 3545.*

Williamson, C.H.K. (1988). The existence of two stages in the transition to three-dimensionality of a cylinder wake. *Phys. Fluids*, **31**, 3165-3168.

Williamson, C.H.K. and Roshko, A. (1990). Measurements of base pressure in the wake of a cylinder at low Reynolds numbers. *Z. Flugwiss. Weltraumforsch*. **14**, 38-46.

Williamson, C.H.K. (1996). Vortex dynamics in the cylinder wake. *Ann. Rev. Fluid Mech*., **28**, 477-539.

Ziada, S. and Rockwell, D. (1982). Vortex-Leading Edge Interaction. *J. Fluid Mech*., **118**, 79-107.

Appendix A

Source Code Disk

Floppy disk containing source codes of the numerical scheme is attached to the back cover.